

Experimental impact damage resistance and tolerance study of symmetrical and unsymmetrical composite sandwich panels

By

Peter Nash

A Doctoral Thesis Submitted in Partial Fulfilment of the
Requirements for the Award of Doctor of Philosophy of
Loughborough University

February 2016

Department of Aeronautical and Automotive Engineering
Loughborough University
Leicestershire
United Kingdom

© by Peter Nash, 2016

Abstract

This thesis presents the work of an experimental investigation into the impact damage resistance and damage tolerance for symmetrical and unsymmetrical composite honeycomb sandwich panels through in-plane compression. The primary aim of this research is to examine the impact damage resistance of various types of primarily carbon/epoxy skinned sandwich panels with varying skin thickness, skin lay-up, skin material, sandwich asymmetry and core density and investigate the residual in-plane compressive strengths of these panels with a specific focus on how the core of the sandwich contributes to the in-plane compressive behaviour. This aim is supported by four specifically constructed preconditions introduced into panels to provide an additional physical insight into the loading-bearing compression mechanisms.

Impact damage was introduced into the panels over a range of IKEs via an instrumented drop-weight impact test rig with a hemi-spherical nosed impactor. The damage resistance in terms of the onset and propagation of various dominant damage mechanisms was characterised using damage extent in both impacted skin and core, absorbed energy and dent depth. Primary damage mechanisms were found to be impacted skin delamination and core crushing, regardless of skin and core combinations and at high energies, the impacted skin was fractured. In rare cases, interfacial skin/core debonding was found to occur. Significant increases in damage resistance were observed when skin thickness and core density were increased.

The reduction trends of the residual in-plane compressive strengths of all the panels were evaluated using IKE, delamination and crushed core extents and dent depth. The majority of impact damaged panels were found to fail in the mid-section and suffered an initial decline in their residual compressive strengths. Thicker skinned and higher density core panels maintained their residual strength over a larger impact energy range. Final CAI strength reductions were observed in all panels when fibre fracture in the impacted skin was present after impact. Thinner skinned panels had a greater compressive strength over the thicker skinned panels, and panel asymmetry in thin symmetrical panels appeared to result in an improving damage tolerance trend as IKE was increased due to that the impact damage balanced the in-plane compressive resistance in the skins with respect to the pre-existing neutral plane shift due to the uneven skin thickness.

Keywords: Unsymmetrical sandwich panel, honeycomb, carbon fibre, E-glass fibre, impact damage, damage mechanisms, energy absorption, damage tolerance, compression-after-impact, in-plane compression, skin-core interaction.

ACKNOWLEDGEMENTS

Firstly I would like to take this opportunity to extend my most sincere gratitude to my Project Supervisor, Dr Gang Zhou, for his support, guidance, expertise, and extensive patience and understanding over the years of my PhD and undergraduate study. I would also like to thank the Department of Aeronautical Engineering at Loughborough University for providing me with the support and facilities without which I would not have been unable to undertake this research. Also, I would like to extend my gratitude to Nigel Hookham of Hexcel Composites for his assistance in providing the core materials to help complete this research.

Moreover, I would like to acknowledge Chris Isherwood, Neal Coles, Luke Boston, Daniel Jones, Jasdeep Lall, Richen Mascrenas, Mark Burt, Sahdev Gahlay, Harpal Dhamu, Abhishek Ramanjaneya and Ankush Gami for their assistance in the manufacturing and testing of specimens in this investigation, helping me obtain the experimental data contained in this thesis.

I would also like to thank Grenville Cunningham, Nigel Lines, Drew Mason, and all other staff in the mechanical workshop in the AAE department that assisted me greatly in a number of aspects over the years of the investigation, whose expertise and hard work allowed for the successful and accurate completion of all testing included in this research.

I would like to take time to thank my family for their unwavering love and support over the years of my study, although the words here cannot do justice to my appreciation for all they have done for me. I also wish to express my appreciation to all my friends, across the country, the names of whom are too numerous to list here. Finally, I wish to express my deepest gratitude to Rosie, for her continued and un-ending support, patience and tolerance of me throughout the last few years.

Thanks to you all!

TABLE OF CONTENTS

1. INTRODUCTION.....	1
1.1. Applications of composite sandwich structures	1
1.2. Review of damage resistance in sandwich panels	2
1.2.1. Review of standard methods for introducing impact damage in composite sandwich panels	2
1.2.2. Review of damage mechanisms.....	7
1.2.3. Non-destructive and destructive characterisation techniques	10
1.2.4. Additional characterisation techniques.....	12
1.2.5. Intrinsic variables affecting damage resistance.....	13
1.2.6. Extrinsic variables affecting damage resistance	20
1.3. Review of damage tolerance in sandwich panels	22
1.3.1. In-plane compression methods of supported sandwich panels.....	23
1.3.2. Damage characteristics under in-plane compression.....	25
1.4. Outline of the thesis with aims and objectives	29
2. SANDWICH MATERIALS AND PANEL MANUFACTURE.....	44
2.1. Sandwich materials.....	44
2.1.1. Unavailable mechanical properties of skin materials	47
2.1.2. Core materials and mechanical properties.....	59
2.1.3. Adhesives	60
2.2. Skin lamination and cures	61
2.3. Sandwich panel bonding	67
2.3.1. Adhesive preparation.....	69
2.3.2. Bonding procedure	69
2.4. Introduction of pre-conditions in sandwich panels.....	70
2.4.1. Core removal.....	71

2.4.2. Skin removal via hole drilling	72
2.5. Impact panel preparation.....	73
3. EXPERIMENTAL PROCEDURES AND SETUP FOR LOW VELOCITY IMPACT TESTS	75
3.1. Main features of instrumented drop-weight low-velocity impact rig and test set-up.....	75
3.2. Low-velocity impact testing procedure	76
3.3. Typical impact measurements.....	77
4. DAMAGE MECHANISMS AND CHARACTERISATION	83
4.1. Identification of impact damage mechanisms	83
4.2. Examination of panel response under impact	86
4.2.1. Identification of damage mechanisms using panel response curve	86
4.2.2. Development of panel response over impact range	92
4.2.3. Parametric study	96
4.3. Effects varying skin thickness and skin lay-up on damage mechanisms.....	102
4.4. Effect of panel symmetry on damage mechanisms.....	114
4.5. Effects of varying panel composition on damage mechanisms.....	120
4.5.1. Core densities.....	120
4.5.2. Skin materials.....	126
4.6. Concluding remarks	131
5. EXPERIMENTAL PROCEDURES AND SETUP FOR CAI TESTS.....	141
5.1. Panel Specimen Preparations for CAI Testing.....	141
5.1.1. End potting and machining	142
5.1.2. Strain gauging	144
5.1.3. Removing core	146
5.2. Compression jig and testing approach	147

5.3. CAI testing set-up, measurements and procedures	148
6. IN-PLANE COMPRESSIVE BEHAVIOUR OF BASELINE SANDWICH PANELS.....	153
6.1. Test results from in-plane compression baseline panels.....	153
6.2. In-plane compressive response in terms of load-strain.....	158
6.3. Parametric studies	164
6.3.1. Effect of varying thickness	164
6.3.2. Effect of varying symmetry and lay-up	167
6.3.3. Effect of varying core density	173
6.3.4. Effect of varying skin material	175
6.4. Closing remarks	177
7. DAMAGE TOLERANCE OF IMPACTED AND PRE-CONDITIONED PANELS.....	179
7.1. Damage tolerance measures and test results.....	179
7.2. Dominant mean and curvature strain responses from compression testing	189
7.2.1. Dominant responses of impact damaged panels.....	189
7.2.2. Dominant responses of pre-conditioned panels	196
7.3. Major failure mechanisms of compression panels.....	214
7.3.1. Major failure mechanisms of impact damaged panels.....	214
7.3.2. Major failure mechanisms of pre-conditioned panels.....	218
7.4. Effects of skin lay-up and thickness on CAI strengths of carbon/epoxy skinned sandwich panels.....	220
7.5. Effects of panel symmetry on CAI strengths of carbon/epoxy skinned sandwich panels ...	226
7.6. Effects of core density on CAI strengths of carbon/epoxy skinned sandwich panels	228
7.7. Effects of different skin material on CAI strengths	230
7.8. Effects of removed core on CAI strengths of carbon/epoxy skinned sandwich panels.....	233
7.9. Effects of holes on CAI strengths of thin carbon/epoxy skinned sandwich panels.....	236

7.10. Deformation interactions between skins and core under in-plane compression.....	237
8. CONCLUSIONS AND RECOMMENDATIONS	243
8.1. Conclusions	243
8.2. Recommendations of further work.....	245
9. REFERENCES.....	246
APPENDIX A.....	253
APPENDIX B	267
APPENDIX C	279
APPENDIX D.....	323

LIST OF FIGURES

Figure 1.2.1. Sample drop weight tower apparatus suggested in ASTM D7766/D7766M-11, image from ASTM D7136/D7316M-07	3
Figure 1.2.2. Clamping arrangement recommended by ASTM D7766/D7766M-11, image from ASTM D7136/D7316M-07	4
Figure 1.3.1. Four point bending flexure testing on impact damaged beams.....	22
Figure 1.3.2. C364 Edge wise compressive testing	23
Figure 1.3.3. Schematic of compressive residual strength support fixture with specimen in place for monolithic laminates as detailed by ASTM D7137/D7317M-12.	24
Figure 1.3.4. In-plane compression set up with clamped loaded ends and simply supported at the unloaded sides	25
Figure 1.3.5. Failure modes observed in impact damaged sandwich panels under in-plane compression loading from Raju [33]	28
Figure 2.1.1. Tensile stress/strain response from 6 ply multi-directional laminate showing chord point used in modulus calculation, specimen T62.....	50
Figure 2.1.2. Failed specimens T125 and T126 showing premature failure modes (a) failure near end tab (b) top ply sheared off under tab	52
Figure 2.1.3. Celanese compression test jig used to obtain compressive strength and modulus.....	52
Figure 2.1.4. Compressive stress/strain response from 12 ply multi-directional laminate showing chord point used in modulus calculation, specimen C123	53
Figure 2.1.5. Flexural strength/strain response from 6 ply multi-directional laminate	55
Figure 2.1.6. Difference in fibre orientation between in-plane shear test coupon (left) and tensile test coupon (right)	56
Figure 2.1.7. In-plane shear stress vs. longitudinal, transverse and shear strain responses for specimen IPS61	57
Figure 2.1.8. Examples of core defects in honeycomb material from handling, storage or manufacturing	60
Figure 2.2.1. Prepreg cutting on the guillotine	61
Figure 2.2.2. Cutting plan for 45° plies (A: primary, B: secondary, C: waste)	62
Figure 2.2.3. Alignment of pieces A and B creating 45° ply joined temporarily with tape	62
Figure 2.2.4. Picture showing completed 45° ply	63
Figure 2.2.5. Angle guide on glass layup table with plies in situ.....	64
Figure 2.2.6. Autoclave cure cycle for PP1062/LTM26 and 34-700/LTM45-EL	64
Figure 2.2.7. Diagrammatic representation of order of consumable materials used in autoclave cure process [124].....	65
Figure 2.2.8. (a) Autoclave with lid off showing bagging film and breather layers (b) autoclave with steel cross members held in place by bolts	66
Figure 2.2.9. Example of panel marking	67
Figure 2.2.10. Diamond edged radial saw	67

Figure 2.3.1. Diagrammatic representation of honeycomb elements and key geometric definitions.....	68
Figure 2.3.2. Oven table with bagging release film tapped down ready for skin/core bonding	69
Figure 2.3.3. Oven configuration	70
Figure 2.4.1. Adhesive placement on 300 x 300mm skin for in-plane compression core removal specimens	71
Figure 2.4.2. Hole locations on 300 x 300mm skin before bonding to core	73
Figure 2.5.1. Cutting measurements applied to panels before cutting	74
Figure 2.5.2. Surface markings for LVI specimens, and strain gauge locations	74
Figure 3.1.1. Drop test rig for low velocity impact testing	76
Figure 3.3.1. Raw data response for a thin unsymmetrical CP carbon/epoxy panel with 70kg/m ³ core density impacted at 20J (HD-8-6-CP-20J)	78
Figure 3.3.2. Load time response for a thin unsymmetrical CP carbon/epoxy panel with 70kg/m ³ core density impacted at 20J (HD-8-6-CP-20J)	79
Figure 3.3.3. Acceleration time response for a thin unsymmetrical CP carbon/epoxy panel with 70kg/m ³ core density impacted at 20J (HD-8-6-CP-20J).....	79
Figure 3.3.4. Velocity time response for a thin unsymmetrical CP carbon/epoxy panel with 70kg/m ³ core density impacted at 20J (HD-8-6-CP-20J).....	80
Figure 3.3.5. Displacement time response for a thin unsymmetrical CP carbon/epoxy panel with 70kg/m ³ core density impacted at 20J (HD-8-6-CP-20J).....	81
Figure 3.3.6. Load displacement response for a thin unsymmetrical CP carbon/epoxy panel with 70kg/m ³ core density impacted at 20J (HD-8-6-CP-20J).....	82
Figure 4.1.1. Cross section of a thin unsymmetrical CP carbon/epoxy panel with 70kg/m ³ core density impacted at 5J (DJ-8-6-CP-5J-B1)	83
Figure 4.1.2. Cross section of a thin symmetrical CP carbon/epoxy panel with 70kg/m ³ core density impacted at 23J (CI-8-8-CP-23J-B).....	84
Figure 4.1.3. Cross section of thick symmetrical CP carbon/epoxy panel with 70kg/m ³ core density impacted at 60J (CI-16-16-CP-60J-B).....	84
Figure 4.1.4. Impact damage in a thin symmetrical QI carbon/epoxy panel with 70kg/m ³ core impacted at 10J showing an example of surface indentation (JL-8-8-QI-10J-A)	84
Figure 4.1.5. Impact damage in a thin symmetrical CP E-glass/epoxy panel with 70kg/m ³ core impacted at 15J as seen through the skin surface (SG-8-8-CP-15J)	85
Figure 4.1.6. Cross sections showing the occurrence of debond in carbon/epoxy panels with 135kg/m ³ core density and E-glass/epoxy thick skinned panel.....	85
Figure 4.2.1. Load vs time response for thin symmetrical CP carbon/epoxy panels with 70kg/m ³ core density impacted at 16J and 23J.....	87
Figure 4.2.2. Cross section of thin symmetrical CP carbon/epoxy panel with 70 kg/m ³ core density impacted with 16J	87
Figure 4.2.3. Cross section of thin symmetrical CP carbon/epoxy panel with 70 kg/m ³ core density impacted with 23J	87

Figure 4.2.4. Load and displacement vs time response for thin symmetrical CP carbon/epoxy panels with 70kg/m ³ core density impacted at 16J (CI-8-8-CP-16J).....	88
Figure 4.2.5. Load vs time response for thick symmetrical CP carbon/epoxy panels with 70kg/m ³ core density impacted at 45J and 60J.....	89
Figure 4.2.6. Cross section of thick symmetrical CP carbon/epoxy panel with 70 kg/m ³ core density impacted at 45J	89
Figure 4.2.7. Cross section of thick symmetrical CP carbon/epoxy panel with 70 kg/m ³ core density impacted at 60J	89
Figure 4.2.8. Load and displacement vs time response for thick symmetrical CP carbon/epoxy panel with 70kg/m ³ core impacted at 60J (CI-16-16-CP-60J-B)	90
Figure 4.2.9. Load vs time response for thin symmetrical CP carbon/epoxy panels with 135 kg/m ³ core density impacted at 20J, 30J and 40J	91
Figure 4.2.10. Cross section of thin symmetrical CP carbon/epoxy panel with 135 kg/m ³ core density impacted at 20J.....	91
Figure 4.2.11. Cross section of thin symmetrical CP carbon/epoxy panel with 135 kg/m ³ core density impacted at 30J.....	91
Figure 4.2.12. Cross section of thin symmetrical CP carbon/epoxy panel with 135 kg/m ³ core density impacted at 40J.....	92
Figure 4.2.13. Load vs displacement response for thin unsymmetrical CP carbon/epoxy panels with 70kg/m ³ core density impacted at 5J, 20J, and 30J.....	93
Figure 4.2.14. Load vs displacement response for thick symmetrical and unsymmetrical CP carbon/epoxy panels with 70kg/m ³ core density impacted at 15J and 60J	93
Figure 4.2.15. Load vs displacement response for thin symmetrical CP E-glass/epoxy panels with 70kg/m ³ impacted at 8J, 25J, and 35J	94
Figure 4.2.16. Load vs displacement response for thin symmetrical CP carbon/epoxy panels with 135kg/m ³ core density impacted at 15J, 25J, 30J, and 40J.....	95
Figure 4.2.17. Load vs displacement response for thin symmetrical CP carbon/epoxy panels with 110kg/m ³ core density impacted at 20J and 30J	95
Figure 4.2.18. Load vs displacement response comparison for thin symmetrical and unsymmetrical CP carbon/epoxy panels with 70kg/m ³ core density impacted at 16J and 18J respectively	96
Figure 4.2.19. Load vs displacement response comparison for thin symmetrical and unsymmetrical CP carbon/epoxy panels with 70kg/m ³ core density impacted at 23J.....	97
Figure 4.2.20. Load vs displacement response comparison for thin symmetrical and unsymmetrical QI carbon/epoxy panels with 70kg/m ³ core density impacted at 25J.....	97
Figure 4.2.21. Load vs displacement response comparison for thin symmetrical CP and QI carbon/epoxy panels with 70kg/m ³ core density impacted at 16J and 15J respectively	98
Figure 4.2.22. Load vs displacement response comparison for thin symmetrical CP and QI carbon/epoxy panels with 70kg/m ³ core impacted at 23J and 25J respectively.....	99

Figure 4.2.23. Load vs displacement response comparison for thick and thin unsymmetrical CP carbon/epoxy panels with 70kg/m ³ core density impacted at 30J	99
Figure 4.2.24. Load vs displacement response comparison for thin symmetrical CP carbon and E-glass/epoxy panels with 70kg/m ³ core density impacted 16J and 15J respectively	100
Figure 4.2.25. Load vs displacement response comparison for thin symmetrical CP carbon and E-glass/epoxy panels with 70kg/m ³ core density impacted at 23J and 25J respectively	101
Figure 4.2.26 Load vs displacement response comparison for thin symmetrical CP carbon/epoxy panels with 70, 110 and 135kg/m ³ core densities impacted at 23J, 20J and 20J respectively	102
Figure 4.3.1. Delamination length vs incident kinetic energy for thin and thick symmetrical CP carbon/epoxy and QI panels with 70 kg/m ³ core density	104
Figure 4.3.2. Delamination length vs incident kinetic energy for thin and thick unsymmetrical CP and QI carbon/epoxy panels with 70 kg/m ³ core density	104
Figure 4.3.3 Core crush length vs incident kinetic energy for thin and thick symmetrical CP and QI carbon/epoxy panels with 70 kg/m ³ core density	105
Figure 4.3.4. Core crush length vs incident kinetic energy for thin and thick unsymmetrical CP and QI carbon/epoxy panels with 70 kg/m ³ core density	106
Figure 4.3.5. Dent depth vs incident kinetic energy for thin and thick symmetrical CP and QI carbon/epoxy panels with 70 kg/m ³ core density.....	107
Figure 4.3.6. Dent depth vs incident kinetic energy for thin and thick unsymmetrical CP and QI carbon/epoxy panels with 70 kg/m ³ core density.....	108
Figure 4.3.7. Absorbed energy vs incident kinetic energy for thin and thick symmetrical CP and QI carbon/epoxy panels with 70 kg/m ³ core density	109
Figure 4.3.8. Absorbed energy vs incident kinetic energy for thin and thick unsymmetrical CP and QI carbon/epoxy panels with 70 kg/m ³ core density	110
Figure 4.3.9. Dent depth vs maximum impact force for thin and thick symmetrical CP and QI carbon/epoxy panels with 70 kg/m ³ core density.....	111
Figure 4.3.10. Dent depth vs maximum impact force for thin and thick unsymmetrical CP and QI carbon/epoxy panels with 70 kg/m ³ core density.....	111
Figure 4.3.11. Core crush length vs dent depth for thin and thick symmetrical CP and QI carbon/epoxy panels with 70 kg/m ³ core density	113
Figure 4.3.12. Core crush length vs dent depth for thin and thick unsymmetrical CP and QI carbon/epoxy panels with 70 kg/m ³ core density	113
Figure 4.4.1. Delamination length vs incident kinetic energy for thick symmetrical and unsymmetrical CP and QI carbon/epoxy panels with 70 kg/m ³ core density	114
Figure 4.4.2. Delamination length vs incident kinetic energy for thin symmetrical and unsymmetrical CP and QI carbon/epoxy panels with 70 kg/m ³ core density	115
Figure 4.4.3. Core crush length vs incident kinetic energy for thick symmetrical and unsymmetrical CP and QI carbon/epoxy panels with 70 kg/m ³ core density	116

Figure 4.4.4. Core crush length vs incident kinetic energy for thin symmetrical and unsymmetrical CP and QI carbon/epoxy panels with 70 kg/m ³ core density	116
Figure 4.4.5. Dent depth vs incident kinetic energy for thick symmetrical and unsymmetrical CP and QI carbon/epoxy panels with 70 kg/m ³ core density	117
Figure 4.4.6. Dent depth vs incident kinetic energy for thin symmetrical and unsymmetrical CP and QI carbon/epoxy panels with 70 kg/m ³ core density	118
Figure 4.4.7. Absorbed energy vs incident kinetic energy for thick symmetrical and unsymmetrical CP and QI carbon/epoxy panels with 70 kg/m ³ core density	119
Figure 4.4.8. Absorbed energy vs incident kinetic energy for thin symmetrical and unsymmetrical CP and QI carbon/epoxy panels with 70 kg/m ³ core density	119
Figure 4.5.1. Delamination length vs incident kinetic energy for thin symmetrical and unsymmetrical CP carbon/epoxy panels with 70 and 135 kg/m ³ core densities.....	121
Figure 4.5.2. Core crush length vs incident kinetic energy for thin symmetrical and unsymmetrical CP carbon/epoxy panels with 70 and 135 kg/m ³ core densities.....	121
Figure 4.5.3. Dent depth vs incident kinetic energy for thin symmetrical CP carbon/epoxy panels with 70, 110 and 135 kg/m ³ core densities	122
Figure 4.5.4. Dent depth vs incident kinetic energy for thin unsymmetrical CP carbon/epoxy panels with 70, 110 and 135 kg/m ³ core densities	123
Figure 4.5.5. Absorbed energy vs incident kinetic energy for thin symmetrical CP carbon/epoxy panels with 70, 110 and 135 kg/m ³ core densities	124
Figure 4.5.6. Absorbed energy vs incident kinetic energy for thin unsymmetrical CP carbon/epoxy panels with 70, 110 and 135 kg/m ³ core densities.....	124
Figure 4.5.7. Maximum impact force vs incident kinetic energy for thin symmetrical and unsymmetrical CP carbon/epoxy panels with 70, 110, and 135kg/m ³ core densities.....	125
Figure 4.5.8. Core crush length vs dent depth for thin symmetrical and unsymmetrical CP and QI carbon/epoxy panels with 70 and 135 kg/m ³ core densities	126
Figure 4.5.9. Delamination length vs incident kinetic energy for thin and thick symmetrical CP carbon and E-glass/epoxy panels with 70 kg/m ³ core density.....	127
Figure 4.5.10. Core crush length vs incident kinetic energy for thin and thick symmetrical CP carbon and E-glass/epoxy panels with 70 kg/m ³ core density.....	127
Figure 4.5.11. Dent depth vs incident kinetic energy for thin and thick symmetrical CP carbon and E-glass/epoxy panels with 70 kg/m ³ core density.....	129
Figure 4.5.12. Absorbed energy vs incident kinetic energy for thin and thick symmetrical CP carbon and E-glass/epoxy panels with 70 kg/m ³ core density.....	129
Figure 4.5.13. Dent depth vs max impact force for thin and thick symmetrical CP carbon and E-glass/epoxy panels with 70 kg/m ³ core density.....	130
Figure 4.5.14. Dent depth vs delamination length for thin and thick symmetrical CP carbon and E-glass/epoxy panels with 70 kg/m ³ core density.....	131

Figure 5.1.1. Photo of end potting mould with epoxy resin inside	143
Figure 5.1.2. Photo of V-notch cut into top of panel to improve epoxy penetration.....	143
Figure 5.1.3. Photo of a cured end pot at one end, and showing the configuration of the panel while curing the other end	144
Figure 5.1.4. Strain gauge locations on panels plus strain gauge numbering	145
Figure 5.1.5. Bonded and soldered single and rosette strain gauges	146
Figure 5.2.1. CAI testing jig	148
Figure 5.3.1. Exaggerated illustration showing solution put in place to eliminate the effects of bowing	149
Figure 5.3.2. Assignment of strain gauges and wires to data logger channels.....	150
Figure 5.3.3. Compressive load against in-plane LVDT displacement for a thick symmetrical QI carbon/epoxy control panel with 70kg/m ³ core density (CI-16-16-QI-0J-A).....	152
Figure 5.3.4. Strain response from a thick symmetrical QI carbon/epoxy control panel with 70kg/m ³ core density (CI-16-16-QI-0J-A).....	152
Figure 6.1.1. Diagram showing the three discrete regions of the panel used in identifying the location of the panel failure after in-plane compression.....	154
Figure 6.1.2. Two different failures types in in-plane compression control panels with carbon/epoxy skins and 70kg/m ³ core (a) thin unsymmetrical CP panel showing shear bands in skins only (DJ-8-6-CP-0J-B) (b) thick symmetrical CP panel showing end crushing (CI-16-16-CP-0J-A)	155
Figure 6.1.3. Observed end crushing mechanism failure in thin symmetrical CP carbon/epoxy panels with 110kg/m ³ core (AR-8-8-CP-0J-B).....	155
Figure 6.1.4. Observed shear band mechanism failure in thin symmetrical CP carbon/epoxy panels with 135kg/m ³ core (RM-8-8-CP-0J-B).....	156
Figure 6.2.1. Mean and curvature strain response for a thin symmetrical CP carbon/epoxy control panel with 135kg/m ³ core density (RM-8-8-CP-0J-B)	159
Figure 6.2.2. Mean and curvature strain response for a thick symmetrical CP carbon/epoxy control panel with 70kg/m ³ core density (CI-16-16-CP-0J-A).....	160
Figure 6.2.3. A deformation sequence of end region at-the-side view based on measured strain responses (a) unloaded state (b) initial compressive failure of front skin (c) transfer of load to un-failed skin	161
Figure 6.2.4. Top down view of transverse buckling developing in the mid-section region of panel based on strain responses (a) even compressive loading (b), (c) transverse buckling that could occur.....	162
Figure 6.2.5. Mean and curvature strain response for a thin unsymmetrical QI carbon/epoxy control panel with 70kg/m ³ core density (LB-8-6-QI-0J-A)	163
Figure 6.2.6. Mean and curvature strain response for a thin unsymmetrical QI carbon/epoxy control panel with 70kg/m ³ core density (LB-8-6-QI-0J-B).....	164
Figure 6.3.1. Average compressive stresses of thick and thin symmetrical CP and QI carbon/epoxy control panels with 70kg/m ³ density	166
Figure 6.3.2. Average compressive stresses of thick and thin unsymmetrical CP and QI carbon/epoxy control panels with 70kg/m ³ density	166

Figure 6.3.3. Mean strain response from the far-field region for thin and thick symmetrical QI carbon/epoxy control panels with 70kg/m ³ core density	167
Figure 6.3.4. Average compressive stresses of thick symmetrical and unsymmetrical CP and QI carbon/epoxy control panels with 70kg/m ³ core density	168
Figure 6.3.5. Average compressive stresses of thin symmetrical and unsymmetrical CP and QI carbon/epoxy control panels with 70kg/m ³ core density	169
Figure 6.3.6. Mean strain response from the far-field region for thick symmetrical and unsymmetrical CP carbon/epoxy control panels with 70kg/m ³ core density	170
Figure 6.3.7. Mean strain response from the far-field region for thin symmetrical and unsymmetrical QI carbon/epoxy control panels with 70kg/m ³ core density	171
Figure 6.3.8. Curvature strain response from the far-field region for thin symmetrical and unsymmetrical QI carbon/epoxy control panels with 70kg/m ³ core density	171
Figure 6.3.9. Mean strain response from the far-field region for thick symmetrical CP and QI carbon/epoxy control panels with 70kg/m ³ core density	172
Figure 6.3.10. Mean strain response from the far-field region for thin unsymmetrical CP and QI carbon/epoxy control panels with 70kg/m ³ core density	173
Figure 6.3.11. Average compressive stresses of thin symmetrical and unsymmetrical CP carbon/epoxy panels with 70, 110 and 135kg/m ³ core density	174
Figure 6.3.12. Mean strain response from the far-field region for thin symmetrical and unsymmetrical CP carbon/epoxy control panels with 70, 110 and 135kg/m ³ core density	175
Figure 6.3.13. Average compressive stresses of thin and thick symmetrical CP carbon and E-glass/epoxy panels with 70kg/m ³ core density	176
Figure 6.3.14. Mean strain response from the far-field region for thick symmetrical CP carbon and E-glass/epoxy panels with 70kg/m ³ core density	176
Figure 7.1.1. Sketches showing pre-conditions in panels (a) removed core at the mid-section region, (b) impacted removed core at the mid-section region, (c) drilled hole in a one skin and (d) drilled holes in both skins	180
Figure 7.1.2. End failures in impacted panels (a) thin symmetrical QI panel impacted at 20J (b) thin unsymmetrical CP panel impacted at 18J	189
Figure 7.2.1. Strain responses from thin symmetrical QI carbon/epoxy panel with 70kg/m ³ core density impacted at 25J (JL-8-8-QI-25J-B)	190
Figure 7.2.2. Mean and curvature strain responses from thin symmetrical QI carbon/epoxy panel with 70kg/m ³ core density impacted at 25J (JL-8-8-QI-25J-B)	191
Figure 7.2.3. Strain responses from thin unsymmetrical CP carbon/epoxy panel with 70kg/m ³ core density impacted at 10J (HD-8-6-CP-10J)	191
Figure 7.2.4. Mean and curvature strain responses from thin unsymmetrical CP carbon/epoxy panel with 70kg/m ³ core density impacted at 10J (HD-8-6-CP-10)	192

Figure 7.2.5. Strain responses from thick symmetrical QI carbon/epoxy panel with 70kg/m ³ core density impacted at 30J (CI-16-16-QI-30J-A)	192
Figure 7.2.6. Mean and curvature strain responses from thick symmetrical QI carbon/epoxy panel with 70kg/m ³ core density impacted at 30J (CI-16-16-QI-30J-A)	193
Figure 7.2.7. Strain responses from thick unsymmetrical QI carbon/epoxy panel with 70kg/m ³ core density impacted at 60J (LB-16-12-QI-60J-A)	193
Figure 7.2.8. Mean and curvature strain responses from thick unsymmetrical QI carbon/epoxy panel with 70kg/m ³ core density impacted at 60J (LB-16-12-QI-60J-A)	194
Figure 7.2.9. Mean and curvature strain responses from thin symmetrical QI carbon/epoxy control and 15J impacted panel (JL-8-8-QI-0J-A and JL-8-8-QI-15J-B)	195
Figure 7.2.10. Mean and curvature strain responses from thick symmetrical CP carbon/epoxy control and 15J impacted panel (CI-16-16-CP-0J-A and CI-16-16-CP-15J-A)	196
Figure 7.2.11. Strain responses from thin symmetrical CP carbon/epoxy panel with 40mm of core removed (CI-8-8-CP-CR-A)	198
Figure 7.2.12. Mean and curvature strain responses from thin symmetrical CP carbon/epoxy panel with 40mm of core removed (CI-8-8-CP-CR-A)	198
Figure 7.2.13. Progression of local skin buckling in mid-section in thin symmetrical CP carbon/epoxy panel with 40mm core removed (CI-8-8-CP-CR-A)	199
Figure 7.2.14. Strain responses from thin unsymmetrical QI carbon/epoxy panel with 40mm of core removed (LB-8-6-QI-CR-A)	200
Figure 7.2.15. Mean and curvature strain responses from thin unsymmetrical QI carbon/epoxy panel with 40mm of core removed (LB-8-6-QI-CR-A)	200
Figure 7.2.16. Progression of local skin buckling in mid-section in thin unsymmetrical QI carbon/epoxy panel with 40mm core removed (LB-8-6-QI-CR-A)	201
Figure 7.2.17. Strain responses from thick symmetrical CP carbon/epoxy panel with 40mm of core removed (CI-16-16-CP-CR-A)	202
Figure 7.2.18. Mean and curvature strain responses from thick symmetrical CP carbon/epoxy panel with 40mm of core removed (CI-16-16-CP-CR-A)	202
Figure 7.2.19. Strain responses from thick unsymmetrical CP carbon/epoxy panel with 40mm of core removed (NC-16-12-CP-CR-A)	203
Figure 7.2.20. Mean and curvature strain responses from thick unsymmetrical CP carbon/epoxy panel with 40mm of core removed (NC-16-12-CP-CR-A)	204
Figure 7.2.21. Strain responses from thin symmetrical CP carbon/epoxy panel with 20mm of core removed (HD-8-8-CP-CR-A)	205
Figure 7.2.22. Mean and curvature strain responses from thin symmetrical CP carbon/epoxy panel with 20mm of core removed (HD-8-8-CP-CR-A)	205
Figure 7.2.23. Strain responses from thin unsymmetrical CP carbon/epoxy panel with 20mm of core removed (HD-8-6-CP-CR-A)	206

Figure 7.2.24. Mean and curvature strain responses from thin unsymmetrical CP carbon/epoxy panel with 20mm of core removed (HD-8-6-CP-CR-A)	207
Figure 7.2.25. Strain responses from thin symmetrical CP carbon/epoxy panel with 20mm of core removed after a 10J impact (HD-8-8-CP-ICR-10J)	208
Figure 7.2.26. Mean and curvature strain responses from thin symmetrical CP carbon/epoxy panel with 20mm of core removed after a 10J impact (HD-8-8-CP-ICR-10J)	208
Figure 7.2.27. Strain responses from thin unsymmetrical CP carbon/epoxy panel with 20mm of core removed after a 20J impact (HD-8-6-CP-ICR-20J)	209
Figure 7.2.28. Mean and curvature strain responses from thin unsymmetrical CP carbon/epoxy panel with 20mm of core removed after a 20J impact (HD-8-6-CP-ICR-20J).....	210
Figure 7.2.29. Strain responses from thin symmetrical CP carbon/epoxy panel with one 40mm hole drilled in the top skin (HD-8-8-CP-1H-B)	211
Figure 7.2.30. Comparison of mean strain responses from thin symmetrical CP carbon/epoxy panels with one 40mm hole drilled (HD-8-8-CP-1H-B) and 10J impact with no precondition (HD-8-8-CP-10J)	211
Figure 7.2.31. Comparison of curvature strain responses from thin symmetrical CP carbon/epoxy panels with one 40mm hole drilled (HD-8-8-CP-1H-B) and 10J impact with no precondition (HD-8-8-CP-10J)	212
Figure 7.2.32. Strain responses from thin symmetrical CP carbon/epoxy panel with 40mm holes drilled in both skins (HD-8-8-CP-2H-A)	213
Figure 7.2.33. Comparison of mean strain responses from thin symmetrical CP carbon/epoxy panels with two 40mm holes (HD-8-8-CP-2H-A) and one 40mm hole drilled (HD-8-8-CP-1H-A)	213
Figure 7.2.34. Comparison of curvature strain responses from thin symmetrical CP carbon/epoxy panels with two 40mm holes (HD-8-8-CP-2H-A) and one 40mm hole drilled (HD-8-8-CP-1H-A)	214
Figure 7.3.1. Photograph of thin symmetrical QI carbon/epoxy panel impacted at 15J after in-plane compression showing left external edge and impacted skin front (JL-8-8-QI-15J).....	215
Figure 7.3.2. Photograph of thin unsymmetrical CP carbon/epoxy panel impacted at 10J after in-plane compression showing left external edge and impacted skin front (HD-8-6-CP-10J)	216
Figure 7.3.3. Photograph of thick symmetrical QI carbon/epoxy panel impacted at 30J after in-plane compression showing left external edge and impacted skin front (CI-16-16-QI-30J-A)	216
Figure 7.3.4. Photograph of thick unsymmetrical QI carbon/epoxy panel impacted at 60J after in-plane compression showing left external edge and impacted skin front (LB-16-12-QI-60J-A)	217
Figure 7.3.5. Photograph of thin symmetrical CP E-glass/epoxy panel impacted at 35J after in-plane compression showing left external edge and impacted skin front (SG-8-8-CP-35J)	218
Figure 7.3.6. Photograph of thick symmetrical CP E-glass/epoxy panel impacted at 45J after in-plane compression showing impacted skin front and right external edge (SG-16-16-CP-45J).....	218
Figure 7.3.7. Post failure image of thin symmetrical CP carbon/epoxy panel with 40mm core removed from mid-section (CI-8-8-CP-CR-1)	219
Figure 7.3.8. Post failure image of thick symmetrical CP carbon/epoxy panel with 40mm core removed from mid-section (CI-16-16-CP-CR-1)	219

Figure 7.3.9. Post failure image of thin symmetrical CP carbon/epoxy panel with 40mm holes in both skins (HD-8-8-CP-2H-A)	220
Figure 7.4.1. Compressive strength vs incident kinetic energy for thick and thin symmetrical CP and QI carbon/epoxy panels 70kg/m ³ core density	221
Figure 7.4.2. Compressive strength vs incident kinetic energy for thick and thin unsymmetrical CP and QI carbon/epoxy panels 70kg/m ³ core density	222
Figure 7.4.3. Compressive strength vs dent depth for thick and thin symmetrical CP and QI carbon/epoxy panels 70kg/m ³ core density	222
Figure 7.4.4. Compressive strength vs dent depth for thick and thin unsymmetrical CP and QI carbon/epoxy panels 70kg/m ³ core density	223
Figure 7.4.5. Compressive strength vs delamination length for thick and thin symmetrical CP and QI carbon/epoxy panels 70kg/m ³ core density	224
Figure 7.4.6. Compressive strength vs delamination length for thick and thin unsymmetrical CP and QI carbon/epoxy panels 70kg/m ³ core density	224
Figure 7.4.7. Compressive strength vs core crush length for thick and thin symmetrical CP and QI carbon/epoxy panels 70kg/m ³ core density	225
Figure 7.4.8. Compressive strength vs core crush length for thick and thin unsymmetrical CP and QI carbon/epoxy panels 70kg/m ³ core density	225
Figure 7.5.1. Compressive strength vs incident kinetic energy for thin symmetrical and unsymmetrical CP and QI carbon/epoxy panels with 70kg/m ³ core density.....	227
Figure 7.5.2. Compressive strength vs incident kinetic energy for thin symmetrical and unsymmetrical QI carbon/epoxy panels with 70kg/m ³ core density	227
Figure 7.5.3 Compressive strength vs incident kinetic energy for thick symmetrical and unsymmetrical CP and QI carbon/epoxy panels with 70kg/m ³ core density.....	228
Figure 7.6.1. Compressive strength vs incident kinetic energy for thin symmetrical and unsymmetrical CP carbon/epoxy panels with 70 and 110kg/m ³ core density	229
Figure 7.6.2. Compressive strength vs incident kinetic energy for thin symmetrical and unsymmetrical CP carbon/epoxy panels with 70 and 135kg/m ³ core density	229
Figure 7.7.1. Compressive strength vs incident kinetic energy for thin symmetrical CP carbon and E-glass/epoxy panels with 70kg/m ³ core density	231
Figure 7.7.2. Compressive strength vs delamination length for thin symmetrical CP carbon and E-glass/epoxy panels with 70kg/m ³ core density	231
Figure 7.7.3. Compressive strength vs incident kinetic energy for thick symmetrical CP carbon and E-glass/epoxy panels with 70kg/m ³ core density.....	232
Figure 7.7.4. Compressive strength vs delamination length for thick symmetrical CP carbon and E-glass/epoxy panels with 70kg/m ³ core density	232
Figure 7.8.1. Compressive strengths of core removed thin symmetrical and unsymmetrical CP and QI carbon/epoxy panels with 70kg/m ³ core density	233

Figure 7.8.2. Compressive strengths of core removed of thick symmetrical and unsymmetrical CP carbon/epoxy panels with 70kg/m ³ core density	234
Figure 7.8.3. Compressive strength against IKE for thin symmetrical CP carbon/epoxy panels with and without 20mm of core removed	235
Figure 7.8.4. Compressive strength against IKE for thin unsymmetrical CP carbon/epoxy panels with and without 20mm of core removed.....	235
Figure 7.9.1. Compressive strengths of thin symmetrical and unsymmetrical CP carbon/epoxy panels with 40mm hole drilled in skins	236
Figure 7.10.1. Illustration of the expected buckling deformation process of undamaged control panels under in-plane compression in the longitudinal loading direction	238
Figure 7.10.2. Illustration of the expected buckling deformation process of undamaged control panels under in-plane compression in the transverse direction	239
Figure 7.10.3. Illustration identifying panel regions, geometries, and critical regions	239
Figure 7.10.4. Illustration of the probable buckling deformation process of impact damaged panels under in-plane compression in the longitudinal loading direction.	240
Figure 7.10.5. Illustration of the probable buckling deformation process of impact damaged panels under in-plane compression in the transverse loading direction.....	241

LIST OF TABLES

Table 1.2.1. Summary of experimental conditions from impact test standards	3
Table 1.4.1. Details of cited literature in damage resistance	32
Table 1.4.2. Details of cited literature in impact damage tolerance	38
Table 2.1.1. Matrix of all panels manufactured and tested since 2007, including previous project work and all work encompassed in this investigation	46
Table 2.1.2. Material properties of 34-700/LTM45-EL UD tape	48
Table 2.1.3. Summary of CLT calculations	49
Table 2.1.4. Tensile test results for 6 and 12 ply multi-directional laminates	51
Table 2.1.5. Tensile properties of UD, CP, and MD laminates	51
Table 2.1.6. Compressive test results of 6 and 12 ply multi-directional laminates	53
Table 2.1.7. Compressive properties of UD, CP, and MD laminates	54
Table 2.1.8. Flexure test results of 6 and 12 ply multi-directional laminates	55
Table 2.1.9. Flexural properties of CP and MD laminates	56
Table 2.1.10. In-plane shear test results of 6 and 12 ply multi-directional laminates	58
Table 2.1.11. In-plane shear properties of UD and MD laminates	58
Table 2.1.12. Summary of all mechanical properties of UD, CP, and MD laminates	59
Table 2.1.13. Mechanical properties of Aluminium 5052 honeycomb core [123]	59
Table 2.1.14. Mechanical properties of adhesive VTA260 as supplied by Umeco Cytec [122]	60
Table 2.2.1. Tick sheet examples for thin cross ply and quasi-isotropic panels	63
Table 2.3.1. Geometric properties of honeycomb and results from area and force calculation for bond	68
Table 2.3.2. Oven material sizes	70
Table 4.7.1. Impact parameters and internal damage of carbon/epoxy thin CP and QI symmetrical panels with 70kg/m ³ core density	133
Table 4.7.2. Impact parameters and internal damage of carbon/epoxy thin CP and QI unsymmetrical panels with 70kg/m ³ core density (impact on thick skin)	134
Table 4.7.3. Impact parameters and internal damage of carbon/epoxy thick CP and QI symmetrical panels with 70kg/m ³ core density	135
Table 4.7.4. Impact parameters and internal damage of carbon/epoxy thick CP and QI unsymmetrical panels with 70kg/m ³ core density (impact on thick skin)	136
Table 4.7.5. Impact parameters and internal damage of carbon/epoxy thin CP symmetrical and unsymmetrical panels with 110kg/m ³ core density	137
Table 4.7.6. Impact parameters and internal damage of carbon/epoxy thin CP symmetrical panels with 135kg/m ³ core density	138
Table 4.7.7. Impact parameters and internal damage of carbon/epoxy thin CP unsymmetrical panels with 135kg/m ³ core density	139

Table 4.7.8. Impact parameters and internal damage of E-glass/epoxy thin and thick CP symmetrical panels with 70kg/m ³ core density	140
Table 4.7.9. Impact parameters and internal damage of preconditioned carbon/epoxy thin CP symmetrical and unsymmetrical panels with 70kg/m ³ core density (20mm of core was removed from mid-section after impact)	140
Table 6.1.1. Average compressive strengths of all control panels arrangements	156
Table 6.1.2. In-plane compressive tests of all individual thin control panels	157
Table 6.1.3. In-plane compressive tests of all individual thick control panels	158
Table 7.1.1. Impact-damaged thin symmetrical carbon/epoxy skinned panels	181
Table 7.1.2. Impact-damaged thin unsymmetrical carbon/epoxy skinned panels.....	182
Table 7.1.3. Impact-damaged thick symmetrical carbon/epoxy skinned panels	183
Table 7.1.4. Impact-damaged thick unsymmetrical carbon/epoxy skinned panels	184
Table 7.1.5. Impact-damaged thin symmetrical carbon/epoxy skinned panels with core density of 110 and 135 kg/m ³	185
Table 7.1.6. Impact-damaged thin unsymmetrical carbon/epoxy skinned panels with core density of 110 and 135 kg/m ³	186
Table 7.1.7. Impact-damaged glass/epoxy skinned panels	187
Table 7.1.8. All panels with skin with drilled hole(s)	187
Table 7.1.9. All pre-conditioned panels with core removed	188

NOMENCLATURE

1H – One hole precondition

2H – Two hole precondition

3PB – Three point bending

4PB – Four point bending

ABS – Anti-buckling support

AE – Absorbed energy

AR – Aspect ratio

ASTM – American Society for Testing and Materials

BVID – Barely visible impact damage

C – Clamped (support condition)

CAI – Compression after impact

CC – Core crushing

CF – Carbon fibre

CFRP – Carbon fibre reinforced plastic

CLT – Classical lamination theory

CP – Cross ply

CR – Core removal

F – Free (support condition)

FE – Flat end

GE – Glass fibre

GFRP – Glass fibre reinforced plastic

HC – Honeycomb core

HS – Hemi-spherical

HVI – High velocity impact

ICR – Impacted core removal

IKE – Incident kinetic energy

ILS – Interlaminar shear

IPS – In-plane shear

LVDT – Linear variable differential transformer

LVI – Low velocity impact

MD – Multi-direction

MS – Mid-section

MVI – Medium velocity impact

NDI – Non-destructive imaging
QI – Quasi-isotropic
QSI – Quasi-static indentation
RCS – Residual compressive strength
RE – Rebound energy
PET - Polyethylene terephthalate
PMI - Polymethacrylimide
PS - Polystyrene
PTFE - Polytetrafluoroethylene
PUR - Polyurethane
PWCF – Plain weave carbon fibre
PVC - Polyvinyl chloride
SB – Shear band
SG – Strain gauge
SS – Simply supported (support condition)
SWGF – Satin weave glass fibre
TTT – Through-the-thickness
UD – Uni-directional
VE - Vinyl ester
VID – Visible impact damage

PUBLICATIONS

1. Nash, P. and Zhou, G., "Investigation of in-plane compressive behaviour in unsymmetrical composite honeycomb sandwich panels", 15th European Conference on Composite Materials, Venice, Italy, 2012.
2. Nash, P. Zhou, G. Gahlay, S. & Burt, M., "Experimental study of impact damage resistance and tolerance of composite sandwich panels", 19th International Conference on Composite Materials, Montreal, Canada, 2013.
3. Zhou, G. Nash, P. Boston, L. Coles, N. & Campbell, L. "Experimental study of in-plane compressive behaviour of unsymmetrical sandwich panels", 18th International Conference on Composite Materials, South Korea, 2011.
4. Nash, P. Zhou, G. & Gahlay, S., "Experimental study of impact damage resistance and tolerance of E-glass/epoxy skinned sandwich panels", 16th European Conference on Composite Materials, Seville, Spain, 2014.

1. INTRODUCTION

1.1. Applications of composite sandwich structures

Composite materials have featured heavily in the aerospace, automotive and marine industry over the last 30 years, and now with a much higher frequency in some high end engineering structural systems. Examples include the tail structure of A380, 50% of the airframe of B787 Dreamliner, the monocoque shell of Formula 1 cars and hulls of high performance speedboats to name but a few. With the advancement of sandwich technology, the appeal of their high specific bending stiffness, strength and energy absorption in addition to enhanced buckling resistance has seen an influx of usage in modern structural engineering. However, performance of these composite structures after concentrated impact loads provides an uncertainty for the integrity of these structures, due to the complexity of the skin/core interaction and in the damage assessment. Safety concerns and cost-effectiveness demand a thorough understanding of the residual strengths of these panels, especially their in-plane compressive strengths. Some of the key issues of residual load-bearing capability lie in the interaction of the impact-damaged skin and the undamaged counterpart in compression with a partially damaged core.

The basic construction of a sandwich structure is made of two elements. The first element, the top and bottom skins of the sandwich panels, are comprised of thin, high density materials, which have high in-plane compressive and tensile properties. Most commonly, they consist of fibre reinforced systems such as carbon, glass or aramid fibre with an epoxy resin system, but can be made from metals and alloys such as aluminium sheets. The second element, the core of the sandwich construction, is a relatively thick, low density material with limited through-the-thickness compressive strength and stiffness, good energy absorption characteristics, allowing for an increase in the flexural rigidity of the panel as a whole, with little sacrifice in the weight of the panel. Typical core materials consist of aluminium or Nomex honeycombs and polymeric foams.

The effect of damage due to concentrated impact loads on the sandwich structures was evaluated throughout two sequential phases. The initial phase, damage resistance, is how the panels respond to the impact itself, involving the establishment of damage mechanisms in the skins and the core and the energy absorption characteristics over an impact range. The latter phase, damage tolerance, is how well the panel delivers the residual performance with loading after the impact event. They can include, but are not limited to, the following loading cases; in-plane compression and tension; bending, shear and torsion. In-plane compression is generally chosen over the other testing methods due to the in-plane compressive strength being lower than all other strengths, and it thus dictates the

composite structure design. The main aim of a damage tolerance study of composite sandwich panels is to ascertain how the in-plane compressive strengths are reduced specifically by the impact damage mechanisms of varying severity, with a focus on the contributions of local skin-core interaction.

In service, damage may arise from low speed impacts, such as runway debris thrown onto the aircraft during take-off and landing, damage from hail fall, bird strikes, tool drops during maintenance efforts, and similarly in marine and automotive industries, they can suffer in service from similar occurrences of contact with floating debris, wave impacts on the hulls, stones and other debris being thrown up by tyres into the car bodywork and so on. Furthermore, aircraft with a military application can be susceptible to high velocity ballistic impacts from fragments or shrapnel, and spacecraft can encounter super-high velocity impacts from collisions with debris at orbital speeds, or meteor impacts etc. Also, all vehicles with sandwich structures can be vulnerable to indentation impacts during low speed manoeuvring and collisions. Hence, investigating experimentally the effects of impact damage to further the understanding of the impact damage mechanisms and damage resistance and tolerance of a panel is very important. In this thesis, focus will be restricted to damage induced by Low Velocity Impact (LVI).

1.2. Review of damage resistance in sandwich panels

Damage resistance is the study of the onset and propagation of major quantifiable damage mechanisms during impact duration. How these damage mechanisms are defined and measured are essential to compression-after-impact (CAI) performance assessment. Extensive internal damage can be induced by even minor impacts, resulting in a significant loss of the local strength despite little visual evidence on the external surface of the panel. Methods to standardise the introduction of transverse impact damage have been developed over the years, mainly for monolithic laminates. Below is a brief review of main LVI standards and leading contributions to impact damage resistance of sandwich structures.

1.2.1. Review of standard methods for introducing impact damage in composite sandwich panels

Although a significant amount of research has been carried out, it wasn't until 2011 that the American Society for Testing and Materials (ASTM) released a standard that detailed the recommended experimental set-up for a transverse impact testing of sandwich panels. Unsurprisingly, since so much research had already been undertaken relating to the monolithic laminate standard, the standard ASTM D7766/D7766M – 11 [105] closely resembles ASTM D7136 [106] to allow for an easy transition to the principles of the standard. A comparison of the impact test standard experimental set ups,

including a summary of the Loughborough University's (LU) in-house impact set-up, are shown in Table 1.2.1 to show the similarities and differences between the standardised test set ups.

Table 1.2.1. Summary of experimental conditions from impact test standards

Parameter	Unit	ASTM D7766 [111]	ASTM D7316 [106]	NASA RP 1092 [108]	BS-ISO 18352 [109]	LU [1]
Specimen dimensions	mm	150 x 100	150 x 100	254-317 x 178	150 x 100	200 x 150
Impact test area	mm ²	125 x 75	125 x 75	127 x 127	125 x 75	100 dia circle
Boundary conditions	-	4 corners clamps (1100N)	4 corners clamps (1100N)	Fully clamped	4 corner clamps	Fully clamped 4Nm torque
Impactor mass	kg	5.5 ± 0.25	5.5 ± 0.25	4.55	5-6	1.49
Impactor size	mm	HS, 16 ± 0.1	HS, 16 ± 0.1	HS, 12.7	HS, 16 ± 0.1	HS, 20
Impact energy	J	26.8-40.2 (4-6mm laminate)	6.7-8.04 (1-1.2mm skin)	27	33.5 ± 6.7	0-60J
Drop height	m	0.3+	0.3+	0.508	0.3+	0-4.5
Specific panel requirements		1 – 1.2mm skins 13mm core	4-6mm QI	6.35mm QI	5 ± 1 mm QI	1-2mm skins 12.7mm core

As the table shows, there are certain parameters between the test standards that have a close or exact agreement, such as the shape, size and weight of the impactor, the size of the test area, and panel thickness, for both monolithic laminates and sandwich panels due to the related development of these standards. All standards utilise a typical drop weight tower arrangement to impact the panel, for example Figure 1.2.1 from ASTM D7766, avoiding a slightly more compact alternative such as pendulum based systems.

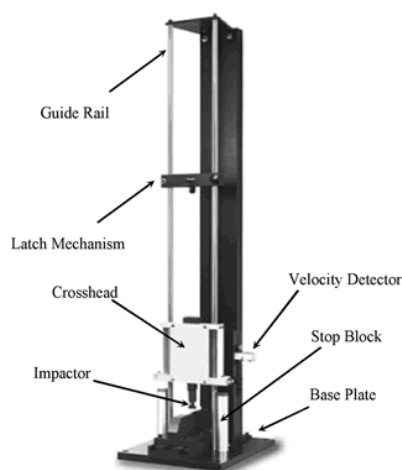


Figure 1.2.1. Sample drop weight tower apparatus suggested in ASTM D7766/D7766M-11, image from ASTM D7136/D7316M-07

All standards advise to employ methods to avoid secondary impacts from the rebounding impactor, such as a rebound catcher, as in ASTM D7766, which suggests a device that activates a latch that trips upon the initial impact, or a second-strike prohibition mechanism, as in BS-ISO 18352:2009, which employs a trigger mechanism based on the detected inertia of the dropping weight. Simple suggestions such as deploying a hard material of adequate thickness, such as wood or plastic, into the path of the second impact to absorb the impact are also accepted by the standards.

The standards uniformly recommend the use of a hemi-spherical shaped impactor nose. This allows for the damage to be introduced into the panel in a manner akin to the likely in-service occurrence of impact damage, since blunt objects such as tools and rocks are largely the cause of impact damage in such structures. The size of the impactor from ASTM D7766 is 16mm, such that the size of the impactor is not too localised from being too small which would create a higher chance of penetration and causing very obvious localised damage, and to ensure that the damage response is not too global due to the impactor size being too large. ASTM D7766 enforces a lower bound drop height of 0.3m, and suggests producing an impact energy equal to 6.7 times the thickness of the impacted skin of the sandwich panel. Thus, typical impact energies for an 8 ply sandwich skin would be 6.7J, and for a 16 ply sandwich skin would be 13.4J.

The clamping conditions and the impact test area are also a similarly controlled parameter in the test standards, with the majority of them recommending rectangular areas, around 100 x 75mm, the set-up recommended in ASTM D7766 is shown in Figure 1.2.2, where the panel is clamped on to a steel platform at the 4 corners using rubber ended toggle clamps.

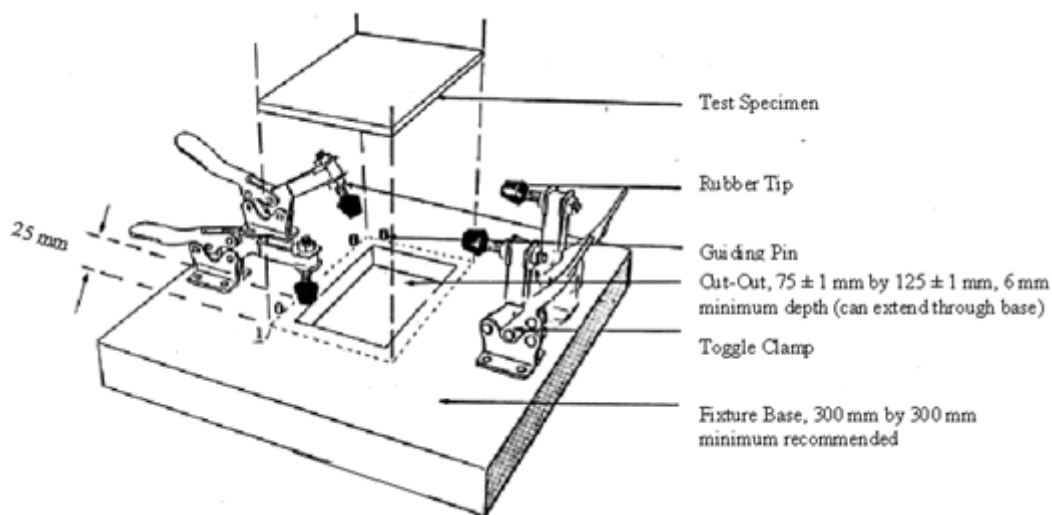


Figure 1.2.2. Clamping arrangement recommended by ASTM D7766/D7766M-11, image from ASTM D7136/D7316M-07

The in-plane dimensions for sandwich panels as recommended by ASTM D7766 are again drawn directly from ASTM D7136, and are specified at 150 x 100mm. The transfer of the monolithic in-plane dimensions to apply to the sandwich panel standard could be troublesome due to the relationship between the sandwich panel thickness and the impactor geometry, however, a significant reduction in recommended impact energy compared to the monolithic panels could account for this interaction in the sandwich panels. ASTM D7766 makes reference to the importance of the damage size in the panel after a standard impact, based on the level of energy, size and shape of impactor, that it be no more than half the size of the unsupported panel width. For any damage that occurs above this threshold, it is recommended that the panel size be increased. The importance of controlling the damage area is linked to the effect of the interaction between the damage area and the interaction with the edge support conditions. The recommended arrangement of the skin and core thicknesses for the composite sandwich structures is for skins of 1-1.2mm thick and a core 13mm thick. This will provide a width-to-thickness ratio of around 6.77, implying heavily that, at this stage, the standard has not been considered for the eventual continuation to damage tolerance testing through in-plane compression. Clearly, such transition of the testing set-up details could substantially underestimate the potential of the sandwich construction, since the core absorbs most of the impact energy, combined with the thickness, the sandwich panels could perform very well under in-plane compression.

Determining the damage resistance of sandwich structures using quasi-static indentation (QSI) or high velocity impact (HVI) as a method of introducing the damage into the structure were also commonly found in the literature. Standardisation of these test methods are, for QSI methods, laid out in ASTM D6264/D6264M-07 [105], and for HVI test methods, being developed under the ASTM Work Item ASTM WK36719 - New Test Method for Measuring the Ballistic Penetration Resistance of Composite Materials.

Review of impact damage methods in literature

As mentioned, there were three main damage methods, quasi-static indentation (QSI), and low and high velocity impact (LVI and HVI). For LVI and HVI testing the impact kinetic energy (IKE) was varied by altering either the impact mass or velocity. The majority of researchers varied the velocity of the impactor, keeping the mass constant. However, a number of papers achieved different IKE via altering the mass of the impactor [9,14,21]. LVI tests were typically achieved using drop weight impact towers, and less commonly pendulum impactors [29], and achieved velocities under 10m/s. HVI typically represented testing for ballistic levels or perforation studies of the panels, and was commonly achieved using gas or powder guns with a ball or projectile with sabot, of speeds up to 1000m/s. QSI

investigated the low end of the velocity spectrum, with energy being introduced into the panels via altering the level of the indentation.

QSI is generally used as an introduction to impact damage, to help assess the onset, development and propagation of damage in the panel when characterised in terms of threshold or critical loads and slope or panel stiffness, with the ability to do diagnostic investigation of changes in slope, load drops and audible cues to identify the onset of damage accurately. The use of QSI to introduce damage states into composite sandwich panels is only acceptable in composite structures that are not strain-rate sensitive. Typically, the types of structures that are shown to be strain-rate insensitive are brittle and moderately toughened carbon/epoxy systems, such as 34-700/LTM-45 [89], whereas glass based reinforcements, highly toughened carbon/epoxy systems and aluminium honeycomb cores are known to be strain-rate sensitive to varying degrees.

Before the use of QSI to introduce damage into a structure as a means to capture the main features of LVI response, a justification exercise for determining whether or not a sandwich construction will be sensitive to strain-rate must be performed, the importance of running such an exercise is highlighted in a number of studies. Herup et al [13] set out to validate the quasi-static assumption as an important simplification to modelling the dynamic impact event in damage initiation in sandwich constructions with cross-ply carbon/epoxy AS4/3501-6 skins at 4, 8, 16, 32, and 48 ply thicknesses with Nomex honeycomb core. Authors concluded that the assumption that low-velocity impact damage with a composite sandwich panel was absolutely dependent on the loading rate, stating that the static and dynamic events differed significantly in the load at which the major load drop occurs, as well as the energy absorbed in the damage process.

Wen et al [36] tested E-glass/polyester skinned sandwich panels with PVC foam cores under QSI, LVI and ballistic impacts. They found that the fracture patterns as well as the load-deflection characteristics of the GRP skin sandwich panels in dynamic loading were similar to those observed in the corresponding quasi-static case. However, authors found that the damage extent under dropped objects was less than that observed in the identical panels under QSI, and the perforation energies were 15-30% higher than the QSI equivalent. Moreover, the extent of debonding was larger in the dynamic impact tests, and the dynamic load to cause a given deflection was higher than the equivalent indentation load in QSI. This was solely attributed to the rate sensitivity of the material properties and inertia effects in the panels. The interplay between these and the core-skin bond strength influence the balance between the various mechanisms in the panel and their respective contributions to energy absorption. In [4,5,58], authors used similar skin materials, and appeared to reach similar conclusions regarding the strain-rate sensitivity in E-glass skinned sandwich panels.

At the extreme ends of loading rate, Bull et al [2] investigated the applicability of simulating the damage from ballistic HVI of sandwich panels with QSI experiments. They showed that the damage was different in both appearance and in extent. Entry wounds were of the same diameter in both cases, but, the fibre strands differed in their appearance, with QSI fibres being pressed into the core, and the HVI fibres were pointing outwardly from the core. Debonding under the top skin of the panel was found in both, with the HVI panels showing a higher area on average. The greatest difference was in the core, with the HVI test leaving a 20mm hole in the core, half that of the QSI test, which represented the size of the 40mm projectile. The authors concluded that the comparisons were in good agreement when taken through to damage tolerance testing, however, with the panels failing as a result of different compressive failure mechanisms due to different states of damage after perforation, the failure load differing only by 15% on average may have been fortuitous, and any further utilisation of QSI to model the behaviour of HVI is potentially unrealistic.

All impact methods so far discussed involved impacts perpendicular to the planar direction of the panel skins, however, oblique impacts have featured as the focus of some research publications. Since it is likely that in the event of a blunt object strike, the angle at which the object strikes the panel could vary from the 90° angle most commonly dealt with. This loading case is of secondary importance, since at any given IKE, in an oblique impact, only a portion of the IKE will go towards damaging the panel, with the rest going into the ricocheting of the impactor, and hence it cannot be the 'worst' critical impact scenario. Considering a critical impact perpendicular to the target, in which all the IKE would go towards damaging the panel, is sufficient to encompass an intermediate impact scenario. This was reported by Zhou et al [55], who investigated three different impact incident angles, 10, 20 and 30° on E-glass/foam sandwich constructions, and found that increasing the angle of incidence increased the energy to cause perforation, and there was no noticeable difference in damage mechanisms, other than their off axis nature relating to the angle of impact.

The focus of this investigation is on LVI, due to the critical nature of the damage induced by even minor impacts at low speed. The use of QSI to represent dynamic impact damage has been previously investigated in Hill [1], and therefore further use of this method for indentation studies is not considered for this investigation.

1.2.2. Review of damage mechanisms

After impact damage was introduced via the above methods, the fundamental damage mechanisms in a sandwich panel were observed to involve skin damage and/or core damage. The failure types, orders of occurrence and propagation of these mechanisms have been observed in a wide range of

skin-core combinations [4,5,8,19,20,23,30,37,49]. Determining which mechanism occurs first is extremely difficult to achieve in impact testing and would be reliant on impactor size, skin material, thickness and lay-ups, and core density and material. Extensive diagnostic investigation by Zhou et al [88,89] into the development of initial damage mechanisms through comprehensive QSI and LVI testing and systematic cross-sectioning of carbon/epoxy skinned honeycomb panels revealed that after the initial damage threshold was reached, this incipient damage was due to a combination of core crushing and small delaminations in the loaded/impacted skin in the shape of a cone towards the skin/core interface. The presence of the two damage mechanisms was not considered to be related. As impact energy was increased the damage mechanisms in the sandwich panels were characterized by the continued core crushing and by propagation of the top skin delaminations. Propagation of the core crushing was both in the thickness direction and all planar directions. The initiation energy for crushing to occur varied depending predominantly on the crush strength of the material. The onset of delamination was controlled by the interlaminar shear (ILS) properties of the skin, and its propagation depended on the bending stiffness and ply orientation of the skins as well as the through-the-thickness (TTT) support provided by the core. Once core crushing occurred, the support offered to the top skin was reduced, promoting increased bending deformation as the impact continued, leading to further delamination and core crushing propagation as the stress spread from the impact zone. Typically, as impact energy was increased further, the impact force was expected to increase, increasing the stresses in the top skin to the point where fracture in the top skin occurred. These three damage mechanisms represented the typical state of damage propagation observed in honeycomb panels and their development in a normal impact energy range. Continued loading led to the densification of the core, leading to the reloading of the back skin, ultimately leading to tensile fracturing of the back skin and finally to full perforation.

The onset of delamination, core crushing or fibre fracture is typically described by the impact load or IKE that causes its development, but would ideally be described by a level of stress. This information is a key measure that is fed through to the damage tolerance assessment procedure to help understand the effects of delamination on the residual strength of the impacted sandwich panels. The propagation of delamination is usually described by either delamination area or extent in a particular direction, this can be measured from C-scanning or destructive cross-sectioning, however, the former method can be confused with the core damage underneath, as described by Tomblin et al [94] where the C-scanned image was seen to correlate with the core crushing diameter. C-scanning could provide misleading observations in the damage tolerance assessment of sandwich panels, since transverse spread of delamination is expected to be the significant contributor to the reduction in compressive

resistance. The propagation of core crushing is described by extents in both transverse and loading directions, and can be typically represented by an area or diameter measurement.

Less common damage mechanisms include skin/core debonding [16,22,25,36,37] which is typical in co-cured sandwich panels, which offer a lower bonding strength between the skin and the core than a separate adhesive bonding, or in panels with high core density, limiting the core crushing and hence skin bending, increasing the stresses at the bond interface. Some researchers observed the spread of skin/core debonding at the back skin interface, typically in penetration cases with flat ended impactors that caused a plug of core material to be pushed through the core, or in foam cores where shear cracking occurred causing debonding on the back face [16,36,62,63].

Identifying the occurrence of an impact in composite structures in-service relies on visual inspection of dents left by the impact event, and assessing the expected effect of the observed damage on the residual strength of the panel in the desired loading cases. With an impact identified, damage can be assessed and repaired, which can be a timely and expensive process. The concept of barely visible impact damage (BVID) was initially created to drive the design process of such structures whilst using non-destructive methods to reduce this time and cost implication of in-service inspection. Boeing and Airbus BVID inspection criteria are widely used in the industry and define BVID as small damage, such as dents of 1.0/0.9mm deep, which could be caused by dropping a tool on the wing or fuselage, and which may not be found during heavy maintenance by general visual inspections using typical lighting conditions from a distance of 1.5m. The impacts that typically could cause such damage are associated with an 8J impact energy. The applicability of using dent depth to define BVID has been assessed by a number of researchers, and a number of issues associated with this damage mechanism were raised. All in all, BVID needs to be taken into account in the design of composite sandwich panels.

Anderson et al [14] identified substantial underlying damage in specimens with BVID in different arrangements of core and skin materials, and suggested a corresponding indentation level to identify the critical levels of damage. The dents were found by authors to be considerably lower than those suggested in the CMH. In PMI foam core with thin skins both high and low density, significant internal damage was visually identified at 8.5J and above, with visual indentation needing to be kept at or below 0.13mm to identify this level of internal damage. For thick skins and high density foam cores, considerable internal damage occurred at levels of 12.55J, corresponding again to indentation of 0.13mm. For honeycomb core of both high and low density with thin skins, considerable internal damage was identified at 8.07J, with the indentation corresponding to these levels at 0.25mm. Again, thicker skins withstood a higher impact energy level, up to 12.55J for considerable damage, with residual indentation that corresponded to this level of 0.30mm.

Edgren et al [39] also used dent depth as a measure of identifying BVID, suggesting an indentation level of 0.40mm on the impact surface, which occurred at 100J, whilst impacts causing VID were at 250J. Using C-scans, the interior damage was found to contain extensive delaminations with a circular projection through the thickness of the impacted skin laminate with an average diameter of 65mm. Panels with VID had a measured penetration region of 18-20mm, and a slightly increased delamination diameter of 70mm.

Raju et al [33] identified issues relating to the impactor diameter and the residual indentation and interior damage. With smaller diameter impactors, damage was more localised, hence indentation occurred more readily with lower levels of planar interior damage spread, and with larger impactors, they produced damage states with large core damage regions and low levels of residual indentation. Authors suggested that a visual inspection based damage assessment relying solely on residual dent region may not be suitable with the residual dent regions being much smaller and had a much less significant effect on the residual compressive performance compared to a large sub-laminar planar damage zone.

Kassapoglou et al [30] defined the level of BVID as an indentation left by an impact and the associated local damage must be barely visible from a distance of 120cm. Authors highlighted issues with visual inspection, suggesting that it was not reliable enough to guarantee the same damage level in each panel, finding that with different face arrangements, variation of dent depth at the impact site ranged from 1.14mm to 1.52mm.

Park et al [53] also used a method of visual inspection from a distance, but set at 1.5m away from the panel, to identify BVID. C-scanning was used to check the degree of internal damage in order to validate the visual inspection. At a level of 5J, slight internal damage was found, and after 6J, the level was visually significant from 1.5m. The internal damage was found to be severe enough that the damage needed to be repaired, which supported the use of visual inspection methods in this instance.

1.2.3. Non-destructive and destructive characterisation techniques

The characteristics and dimensions of the aforementioned damage mechanisms are achieved through one or a combination of a variety of non-destructive and destructive techniques. The techniques used for detecting damage in sandwich panels include C-scanning, acoustic emissions, X-ray, Moiré or digital speckle interferometry (shearography), thermography, digital image correlation (DIC), tapping and destructive cross-sectioning with the use of optical and scanning electron microscopes.

Acoustic emission is capable of monitoring radiation of acoustic (elastic) waves in solids that occurs instantly when a material undergoes irreversible changes in its internal structure, such as fibre fracture, delamination, or debond.

Moiré shadow or digitalised speckle pattern interferometry (DSPI) can also be used as a means to characterise the indentation propagation during quasi-static indentation [14,83]. The method typically involves a light reflective line grid being adhered to the panel surface, which is calibrated by directing a light source at the panel surface prior to testing. After or during testing, this same light source is directed at the panel surface, and the interference patterns (moiré fringe patterns) that are associated with the grid distortion can be used to calculate the out of plane deformation. This technique can also be used to track out of plane displacement during compression testing, as long as the surface of the panel is unobstructed by the test rig. A digitalised version using a video camera along with a laser beam has been developed [2,11]. Digital image correlation (DIC) is a variant of the SPI techniques and tracks 2D or 3D surface image changes [68]. The surface is prepared by spraying on a speckle pattern with a contrasting colour (i.e. white on black). The speckle pattern is a random array of dots that can be tracked by DIC software during the surface deformation by comparing the before and after the speckle grid images, allowing a calculation of the magnitude and direction of movement of the dots to provide information as to the deformation. This was often used to measure both displacement and strain and is so far limited to damage occurring either on the surface or in sub-surface areas.

Thermography technique uses a heat source to locate the presence and magnitude of damage in composite structures [24]. Typically, the surface of a sample is heated with a spatially uniform light pulse emitted from a xenon, flash lamp array, or an infrared camera. The time-dependent heat response of the sample in terms of 2D temperature interval contours is used to determine if the damage occurs and if yes, what the size of the damage is.

The most popular and effective method for detecting interior damage in composite laminates and sandwich structures was ultrasonic C-scanning [13,16-17,19,21,23,26,29,32-33,39,43,53,68]. C-Scan uses ultrasonic sound to measure the amount of time that the ultrasounds pass through the thickness of the part and needs a liquid medium to transmit ultrasonic signals. A C-scan can be done in one of two ways, scanning for damage through the entire thickness of the panel (through transmission) or scanning at predetermined positions by setting the scanning depth (pulse echo). The former method is the most straight-forward, however, when applied to a sandwich structure the scan shows all damage in the skin and core as well as any skin/core interfacial damage making it difficult to distinguish between core and skin laminate damage mechanisms. The pulse echo method depends on manually

setting the scanning depth and therefore can be very inaccurate if the materials at the selected depths are not uniform.

X-ray radiography and X-ray tomography (X-ray CT) are X-ray-based technologies that uses X-radiations to produce X ray wave responses, which could be computer-processed to generate tomographic images (virtual 'slices') of specific areas of a scanned object, allowing the user to see inside the object without cutting. It can be used to generate a three-dimensional image of the inside of the object from a large series of two-dimensional radiographic images taken around a single axis of rotation. X-ray CT is particularly useful in determining core defects, skin/core interfacial debonding and core damage, however, planar damage in the composite skins cannot be determined by using X-ray scanning. This technique was seen to be used in Koissin et al [10], Nanayakkara et al [44] and Avila et al [62]. In Nanayakkara et al, X-ray scanning provided adequate resolution to identify damage in reinforcing z-pin constructs in the core, by digitally removing the foam core from the image.

A popular destructive technique is visual inspection of the damage through a cut cross-sectioning of the panel and can provide quick estimations of the internal panel damage. The ease of this method leads to it being commonly used [2,4-5,8,14]. However, this method is limited by being able to provide information at the cut surface only, as well as not being compatible with further tolerance testing, increasing the costs and resources of an investigation. For limited damage, the specimens may need to be polished after cross-sectioning, and examined at a much higher magnification than through visual inspection, by either a simple optical microscope as in Lee et al [7], Shin et al et al [15] and Crupi [56] or a scanning electron microscope as in Bhuiyan et al [25], Hosur et al [63] and Thomson et al [82]. A 3D picture of the damage can be achieved by taking multiple cross-sections of the sample across the width, and stitching the composite image together to create a 3D map of the damage. Nevertheless, this technique could be very useful and adequate, when the most relevant damage characteristic is the transverse extent of damage in the width direction of panels that are intended to be tested under in-plane compression as in the present study.

1.2.4. Additional characterisation techniques

The use of the above methods for defining and measuring the onset and propagation of the major damage mechanisms can not only be costly and time consuming with a lot of the specialist equipment being expensive to own and operate or high material and manufacturing costs associated with destructive sectioning, but also have various limitations, especially in the quantification aspect. Hence, a number of researchers used the impact load-time or load-displacement curves as an additional aid in order to identify the onset and propagation characteristics of the damage in terms of changes in

gradients and load drops. It can also provide an insight into the behaviour of the whole structure under impact, which the NDT and destructive techniques could not do.

In [88,89], Zhou et al conducted extensive investigation into QSI load-displacement and load-strain curves and with LVI load-displacement responses, as well as systematic cross-section diagnostics, the characterisation of the damage mechanisms from the load-displacement responses has been established in either two or three distinctive deformation stages, identified by critical loads for initial or threshold damage, secondary damage and/or ultimate failure. The initial deformation stage was usually linear and ended at the threshold load. At this point and beyond, the curve became nonlinear with a distinct change in slope, and can be accompanied by a small load drop, and indicated the onset of initial damage mechanisms. Both the threshold load and the initial slope were heavily dependent on the skin thickness, core density and indenter/impactor shape. The second stage was significantly affected by the shape of the indenter/impactor. For FE shapes, the second stage contained a secondary critical load with a substantial release in stored energy, before the ultimate load of the panel was reached. In HS shapes, the load-displacement load was largely linear, although a small amount of slope steepening can be observed towards the ultimate load, and was attributed to the membrane stretching of the top skin. This final stage up to the ultimate load was noticeably steeper in FE indenter/impactor cases, due likely to the greater number of honeycomb cells being crushed in addition to the membrane stretching. The final deformation stage was signified by the failure of the indented/impacted skin, resulting in the loss of load bearing capabilities, causing a substantial decrease in load. The ultimate critical load was found to be dependent once again on the indenter/impactor nose shape, and the skin thickness, but not on the core density. In [58,67,97], authors appeared to reach similar conclusions regarding the stages of damage characterisation and load-displacement response in QSI and LVI testing.

1.2.5. Intrinsic variables affecting damage resistance

Skin material

The development of damage using the load/displacement responses for a sandwich panel with E-glass/polyester skins with a PVC foam core was reported by Wen et al [36], and showed a distinct difference to a sandwich construction with a honeycomb core due to the differing failure mechanisms associated with foam cores under transverse loading, citing seven steps A-G, which authors combined with images of diagnostic cross-sections of panels taken at each stage. At point A, damage was characterised by discolouring due to contact stresses beneath the indenter. As the load further increased towards point B, a crack was initiated in the core due to local shear stress together with the

punching through of the top skin, causing a major load drop to point C. The load increased slowly from C as the shear crack propagated towards the bottom skin. At point D, a further load drop was initiated to point E by the crack reaching the bottom skin causing debonding between the bottom skin and the core. Load increased slowly again through point F, and finally, point G saw the tensile failure of the back skin causing a final load drop. Intrinsic variables affecting damage resistance

Skin material

Composite sandwich panels are widely constructed using carbon, glass and aramid fibre reinforced plastics. Carbon fibres feature heavily in the aeronautical industry, and more recently the high performance areas of the automotive industry. Glass fibre reinforcements are often selected in more cost restrictive industries, and feature mainly in the marine industry. A variety of fibre arrangements are used, including uni-directional, plain weave, 2x2 twill, and 5 and 8 harness satin. Kevlar fibre reinforced composites are typically used in ballistic applications due to their high tensile properties, but have limited structural applications due to their poor compressive properties and high associated costs. In order to combine the advantages of these fibres some investigations have been carried out into the use of hybrid fibre reinforcements, weaving together carbon and Kevlar fibres [78]. Other possibilities of hybrid arrangements involves utilising different layers of materials in the skins, such as in Kassapoglou et al [29], Ishaï et al [28], Salehi-Khojin et al [54], Zheng et al [45] and Crupi et al [56].

These fibres are reinforced with a number of different resin systems. The variation of resins depend on the manufacturing processes and cure methods available, fiscal limitations and operating environments. The most common resin is epoxy, with alternatives such as vinyl ester, polyester, and bismaleimide, as seen in Table 1.4.1. Finally, it is possible to manufacture sandwich panels without the use of plastic reinforced fibre skins, and generally these are replaced by aluminium skins [7] or other light metal alloys, however impact damage resistance and tolerance prediction in metal skins is not a critical issue.

Raju et al [33] directly compared sandwich panels made of woven carbon (PWCF) and glass fabric epoxy (SWGf) skins with a QI layup, with identical thick and thin core material. In the thin core sandwich, PWCF exhibited higher dent depths of 0.6mm and planar damage size of 50mm in diameter at low impact energies, compared to SWGF panels with 0.3mm of dent depth and planar damage size of 40mm in diameter, when impacted with 25.4mm diameter impactor. As impact damage was increased, the delamination diameter of 70mm in diameter was for PWCF and 60mm for SWGF. Similarly, indentation of 4mm was found for PWCF panels and 3mm for SWGF panels. Skin fracture was delayed in the SWGF panels due to their higher failure strains and globally dominated

deformations, resulting in these smaller depths. However, when the panels were impacted with the larger impactor, the dent depth of 0.1mm was found for PWCF and 0.2mm for SWGF. Since panels with the thicker core could accommodate larger deformations, the PWCF panels failed earlier than SWGF panels.

Skin thickness

The effect of skin thickness was the more commonly varied parameter in studies of impact damage resistance of sandwich structures. The range of skin thicknesses found in the research are shown in Table 1.4.1, and varied from 0.25-7mm, and the most common thicknesses were 1 and 2mm skins with 4 or 8 plies.

It is widely agreed that the increase in skin thickness causes an increase in both load required for damage initiation and load required for top skin failure/penetration. The increase in damage resistance performance in the panels with the thicker skins is attributed to the increased flexural and contact resistances of the panel. This allows for the impact to be more efficiently spread across a larger area of the supporting core material, reducing localised damage such as dent depth and fibre fracturing, however, there is a trade-off in impact design efficiency given the increase in weight of the panels.. Herup et al [13] reported that in panels with very thin skins, the flexural stiffness was low enough such that it was unable to spread the contact stresses away from the impact centre, resulting in the damage becoming localised. Hence a small area of the core experienced all of the transverse loads, and thus, the onset of damage could be considered to be occurring in the core, rather than the skin and core jointly.

Zhou et al [90] investigated the effect of varying skin thicknesses in carbon/epoxy CP skins with varying densities of aluminium core densities under both HS and FE indenters, where the thickness in the sandwich skins was varied between 0.5-2mm. This increase was found to enhance not only the flexural rigidity of the sandwich panels but also the bending and local indentation resistance. The slopes before and after the initial threshold increased with increasing the skin thickness, and also, the initial threshold and ultimate loads were increased substantially. The occurrence of secondary damage, characterized by a load drop, was clearly seen from the panels with relatively thicker (1.5-2.0mm) skins. The greater load drops were found for the thicker skins thereby indicating more AE.

Herup et al [13] tested various carbon/epoxy sandwich panels over a wide range of impact energies. Authors observed that as skin thickness was increased, both the damage threshold load and the ultimate load of causing top skin fracture increased. Furthermore, they reported that for the larger threshold and ultimate loads, a larger load drop was observed and was accompanied by the larger

planar damage. Anderson et al [14], Tomblin et al [23] and Wang et al [68] all exhibited increased peak forces for thicker skin panels with both honeycomb and foam cores at the same IKE and reported that the onset of damage for panels with the thick skins occurred at higher IKE and that indentation depth was lower at any given IKE than thin skinned panels (Raju et al [33]). Kassapoglou et al [30] made similar observations relating to the onset of BVID, which was found to occur at higher IKE for thicker skinned panels. Tomblin et al [23] investigated impact damage in large sandwich panels with two different Nomex core thicknesses co-cured with three different carbon/epoxy skin thicknesses and found that the C-scanned planar damage area was found to be slightly higher in the thicker skinned panels at similar IKE levels, showing that the load was being spread more effectively away from the impact centre by the skins under impact. These effects were more apparent when the panels were impacted with a larger diameter impactor.

Skin lay-up

One of the main design features of composite materials is the unique customisable aspect of the fibre orientation in the laminate to specifically cater to the loading conditions, such as compression, tension, flexure and torsion. Various stacking variations can be seen in Table 1.4.1, ranging from uni-directional, cross ply, angle ply, multi-directional, and quasi-isotropic. From Dost et al [99] and Liu [100], they suggested that in monolithic laminates, the resistance to delamination propagation will be greater as the ply-to-ply angle is reduced between adjacent plies and further suggested that delamination area would be smaller in a quasi-isotropic lay-up than laminate in a cross-ply lay-up. Also, the longitudinal flexural rigidity of the panel will be reduced when more plies are orientated away from the 0° direction, which will result in larger global deformations in the panels. This has a high potential for providing a significant effect on the damage tolerance of the panels, where skin delamination and panel curvatures are expected to have a considerable effect on the in-plane compressive strength of sandwich panels, and will hence need to be a consideration in the design of sandwich panels.

Skin asymmetry

Lee et al [7,15] investigated the use of unsymmetrical glass fabric skins with aluminium honeycomb core, where the thicknesses of the front and back skins were 3mm and 1.5mm respectively. Impact load responses appeared to follow the same pattern as symmetrical sandwich structures, there was no damage reported in the distal skin, and the same damage mechanisms (delamination and core crushing) developed.

Counter to the intuitive deployment of an unsymmetrical sandwich panel such that the thicker of the skins would be open to impact damage, Crupi et al [56] impacted the thinner side of an unsymmetrical arrangement for reasons not specified. The impacted side was 3mm GFRP and the distal skin was 7mm GFRP, with a PVC foam core. However, once again, no conclusions on the effective damage resistance on this arrangement were made to a symmetrical panel or with impacting the thicker skin.

Li et al [58] investigated panels with E-glass fibre/phenolic resin skins of 1.2, 1.5 and 2.0mm thick. They indicated that for sandwich panels with the same impacted skin thickness and a thick distal skin, a lower specific energy absorption and a lower effectiveness factor were found. There was however, no assessment on the propagation of planar or through the thickness damage mechanisms of unsymmetrical skins.

Core material

Generally, two main types of core structures were used in sandwich constructions, either honeycomb or foam. The honeycomb core material consists of metallic honeycombs, represented by aluminium honeycomb and Nomex. Foam cores are represented by polyvinyl chloride (PVC), polymethylacrylimide (PMI), polystyrene (PS), polyurethane (PUR) and aluminium. Foam cores are usually closed cell and cross linked. The two most common trade names are Divinycell (PVC) and Rohacell (PMI).

Zhou et al. [89,90,96] made comparisons for both Aluminium and Nomex honeycomb cores for carbon/epoxy skinned sandwich panels for both QSI and LVI testing. Authors observed that both the critical threshold load and slope after the initial threshold load were similar between the core materials and that the major damage mechanisms were roughly the same. Diagnostic cross-sectioning revealed the Nomex cells were fractured with a lesser degree of cell folding and showed a substantial spring-back upon unloading. Furthermore, the initial flexural rigidity of the Nomex sandwich panels (within the elastic range) was significantly lower than those of the aluminium ones due to the fact that the shear properties of the Nomex cores were significantly lower, however, due to the spring-back characteristic of the Nomex core, panels with Nomex cores exhibited much less surface indentation with the maximum depth of crushed cells reaching not even the middle of the core thickness at the high IKE range. This appeared to agree with many of the observations made by Tstotsis et al [9] for similar core material with glass/epoxy skins.

Anderson et al [14] investigated panels of carbon/epoxy skins with high and low density Rohacell foams (52 and 110kg/m³) and Nomex cores (48 and 96kg/m³). Damage initiation in the foam panels

occurred earlier than the honeycomb panels. Over a similar range of IKE, the honeycomb panels also showed greater resistance with the greater impact force and lesser indentations than the foam panels.

Akay et al [17] used two panels of carbon/epoxy skins with Nomex honeycomb (48kg/m^3) and Rohacell PMI foam core (71kg/m^3). They showed that the measured damage area of the Nomex panels was much greater than that of the foam, as the foam core density was 48% greater.

Core density

The variation of core density can be seen in Table 1.4.1, and in honeycomb cores it ranged from 15-200 kg/m^3 , and 31-400 kg/m^3 for foam. Typically, foam core densities used were on average higher than the honeycomb cores due to the lower compressive and shear properties of the foam cores. It can be seen throughout the literature that where the core density was increased, skin thicknesses were typically increased with it to ensure compatibility of the core and skin material [11,26,38,39].

Zhou et al [90, 96] investigated a number of panels with various core densities in both Aluminium (50, 70, and 90 kg/m^3) and Nomex (64 and 96 kg/m^3) honeycomb cores. For HS indenters, the overall increase in ultimate load was small for panels with 0.5mm skins, modest for panels with 1.0mm and 1.5mm skins but became substantial for panels with 2.0mm skins. The increase in ultimate load for the thin skinned panels was expected, as the skins dictate the load-bearing capacity of the sandwich panels. These observations associated with the HS indenter were different to those associated with the FE indenter. While the ultimate loads here were unaffected by the density variation, the increase in initial threshold load was significant. This was because the higher contact pressure at the indenter edge spread the load to a larger core area through the top skin so that significantly more cells offered resistance before being crushed. Thus, the thicker the skins involved, the larger the core area, thereby inducing the increased transverse shear contribution. Moreover, for a given skin thickness, the moderate variation of core density did not affect the nature of the identified damage mechanisms nor the AE.

Anderson et al [14] found that the denser foam cores had much smaller planar spread of core crushing at similar levels of IKE and provided greater through-the-thickness damage resistance, along with the much smaller dent depths. These findings were similar to those presented by Zhou et al. [55], who investigated a wide range of cross-linked and linear PVC foams with densities ranging from 60-200 kg/m^3 . Authors found the lower density PVC foams exhibited a cylindrical shaped shear zone similar in size to the impactor, whereas mixed failure was found in the intermediate and higher densities, with a cylindrical shear pattern in the upper half, and frustum shaped failure shape in the lower half of the panel thickness, which is opposite to what would be expected. This was once again

linked to the increased shear properties in the higher density core, causing the failure mode to shift towards tensile failure.

Leijten et al [21] compared two different densities of two different foam materials, Rohacell XT and WF with densities of 71 and 110kg/m³. They observed that the specimens with the lower density foam core exhibited much larger planar damage area of around 2000mm² compared to 1000mm² in the higher density core panels, which was attributed to the difference in shear strengths of the foam material. They found that panels with the lower core density had far higher indentations than those of panels with the higher density cores.

Zhou et al [55] investigated a novel method of varying the core density, via varying the through the thickness properties by stacking different density cores on top of each other. They showed that placing the high density foam core against the top surface skin led to the greater perforation resistance than sandwich panels with the higher density core on the distal side as well as their constant density counterparts.

Core thickness

Leijten et al [21] compared sandwich panels with three Rohacell 100XT-HT foam core thicknesses of 10, 15 and 20mm. Authors observed that increasing the core thickness from 15 to 20mm only had a limited effect on the planar damage area, whereas reducing the thickness of the core to 10mm resulted in a major increase in planar damage area by almost five times.

Raju et al [33] found that the residual indentation was dependent on the core thickness, from testing two different core thicknesses of 9.525 and 19.05mm Nomex honeycomb of 48kg/m³ density. They observed that core crushing extent in the planar direction was larger in the thinner panels, whereas in the thicker panels the through-the-thickness crushing was more extensive. They found that panels in a thicker core accommodated greater indentation with smaller planar damage areas at the relatively lower energy levels. In the thinner (9.525mm Nomex honeycomb) core, the localised skin indentation was limited by the core thickness and thus top skin fracture was delayed. Also, they reported that the impact forces over the IKE range in the thinner cores were higher than that in the thicker cores which had a lower impact force required for indentation.

1.2.6. Extrinsic variables affecting damage resistance

Specimen dimensions

From the sandwich panel damage resistance standard, ASTM D7766, the panel size is recommended to be 150 x 100mm. However, the specimens reviewed in the literature were found to have the sizes ranging from 60 x 60mm to 1000 x 1000mm for square panels, and from 60 x 90mm to 305 x 1219.2 mm for rectangular panels, as seen in Table 1.4.1.

Panel configurations can be square or rectangular, though rectangular panels are more popular. They are less important as long as they are large enough to well contain the largest size of delamination induced by the upper end of an impact energy range. Tomblin et al [23] investigated various lengths and widths of square and rectangular panels of 8 x 8, 12 x 12, 16 x 16, 12 x 24, and 12 x 48" in a clamped condition. They found that the impact force decreased when both planar dimensions were increased and aspect ratio was maintained. The effects of increasing the size of both planar dimensions whilst maintaining aspect ratio on the planar damage size and dent depth exhibited a similar trend to that of the impact force, with planar damage diameters and dent depths decreasing as the planar dimensions were increased. Authors showed that the planar damage diameter did not exhibit any trend when aspect ratio was altered with only one dimension (length) changed, but a decrease in dent depth was observed.

Wen et al [36] found that failure mechanisms were found to change from shear failure in the smaller panels (0.3x0.3m) to global bending failure in some of the larger arrangements (0.9mx0.9m). Zhou et al [90] investigated the effect of increasing the circular testing area from 100 to 220 mm for the same panel thickness and found it increased the membrane effect but decreased the flexural and transverse shear effects. The total displacement and indentation response characteristics were similar, with the larger panel showing a greater displacement and a 30% decrease in initial slope in addition to a 15% increase in ultimate load. The damage mechanisms were also similar for both panel sizes and the crushed core area was larger for the larger panels loaded with the FE impactor. All observations made for the smaller panels could therefore be qualitatively applicable to the larger ones.

Support conditions

Three types of support conditions used in all reviewed damage resistance studies are clamped, simply supported and rigid support.

Zhou et al [90] reported that local indentation was significant for the initial panel response under bending situations and was lesser in sandwich panels with thicker skins, as the higher flexural rigidity of the panel offered a greater resistance and therefore greater reduction in bending.

Tomblin et al [23] investigated the difference in damage resistance after LVI between clamped and rigid supported 2-ply and 4-ply PWCF/epoxy panels with a 19.05mm thick Nomex core. They found that the planar damage diameter was consistently smaller for the sandwich panels with rigid-base supports for impacts at 6.5J, 10.8J, 15.3J and 17.7J. However, the residual dent depths were larger for the specimens supported by a rigid base at all energy levels. Thus, core crushing was propagated in the thickness direction when the specimens were supported on a rigid base, whereas the core damage propagation occurred along the lateral direction in specimens that have boundary supports that allowed some flexural deformation. Visible skin fractures were also observed in sandwich specimens with rigid base supports at the highest energy levels (17.7J).

Raju et al [33] investigated clamped and simply supported conditions along all four edges, again with PWCF/epoxy and Nomex core arrangements of panels sized 267 x 217mm. They did not find any significant differences on peak impact forces and that somewhat the simply supported specimens exhibited a slightly higher peak force than the clamped in some of the thicker core arrangements. They also found that for these sandwich configurations the local indentation stiffness was always less than the global bending stiffness so that the impact responses were governed by the local indentation responses of the specimen. Authors did not report on the influence on the boundary conditions on the damage type and its propagation. Zheng et al [45] also concluded that the characteristics of impact contact and damage were not sensitive to support conditions because of the buffer of the honeycomb.

Impactor geometry

The diameter and nose shape of impactors used in damage resistance studies can be seen in Table 1.4.1, with the latter including hemispherical (HS), flat-ended (FE), conical and pyramidal impactors. Other impactors that have been used on rare occasions include a medicine ball [22] in order to replicate water impact (slamming). The most common nose shape of impactors used was HS. Sizes ranged from 8 to 100mm.

Zhou et al. [90,96] studied the effect of the indenter nose shape of 20mm diameter HS and FE indenters on carbon/epoxy skinned aluminium and Nomex honeycomb sandwich panels. They showed that for panels loaded by the HS indenter, core crushing and the onset of delamination in the top skin occurred simultaneously at the initial damage stage and they continued until top skin fracture occurred as the ultimate failure of the sandwich panel and that for panels loaded by the FE indenter,

core crushing, top skin delamination and continued core crushing, and ultimate top skin shear-out characterised respectively the initial, secondary, and ultimate failure.

Kepler et al [4,5] found that the FE impactor created a cylindrical plug and distributed the forces to the back face of the panel more so than the HS impactor and that internal damage in panels loaded by the HS and FE impactors was larger than that associated with conical impactor.

Wen et al [36] reached similar conclusions that the blunter the impactor the higher the impact force required to cause fibre fracture in the impacted skin, with the highest found in the FE impactors, and the conical impactors with the lowest. Similar findings were put forward by Zenkert et al [11] and Nettles et al [24].

Kassapoglou et al [29] found using C-scanning that damage lengths found in the panel were consistently higher with the larger impactor (19.85mm) over the smaller impactor (12.7mm). Similarly, Meo et al [32] found that increasing the impactor size from 16mm to 50mm increased the delamination area in top skin considerably, as well as seeing a marked drop in indentation depth. This was also reported by Raju et al [33], Nettles et al [24] and Wang et al [68].

1.3. Review of damage tolerance in sandwich panels

The assessment methodology for impact damage tolerance in sandwich panels does not yet exist as an official testing standard. The most common and proven effective method in the damage tolerance assessment of monolithic laminates is through in-plane compression after impact (CAI), hence a number of test methods established for CAI testing of monolithic laminates were adopted for sandwich panels. Nevertheless, there are other approaches that could potentially be used to evaluate the residual in-plane compressive strength. Some researchers modified 4 point bending of sandwich beams from ASTM C393 [110] by making them wide enough to accommodate impact damage, with the impact damaged skin on the compression side, as shown in Figure 1.3.1. It could be very low cost and much simpler to execute.

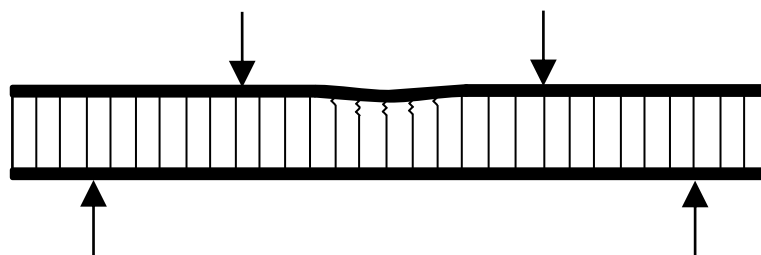


Figure 1.3.1. Four point bending flexure testing on impact damaged beams

Researchers also used a 'wide' coupon in accordance with ASTM C364 [103], as shown in Figure 1.3.2, to execute damage tolerance studies. This method normally uses specimens with a length less than or equal to 8 times the thickness, a minimum width of 50mm or 2 times the thickness, but less than the overall length. As this configuration is representative of a wide coupon, not a panel, the unloaded edges are unsupported, allowing column compression and global buckling, which does not typically duplicate either the structural conditions or specimen configurations of a panel even if the dimensions are scaled up. Furthermore, this standard does not allow the inclusion of impact damage for damage tolerance assessment, further undermining its usefulness.

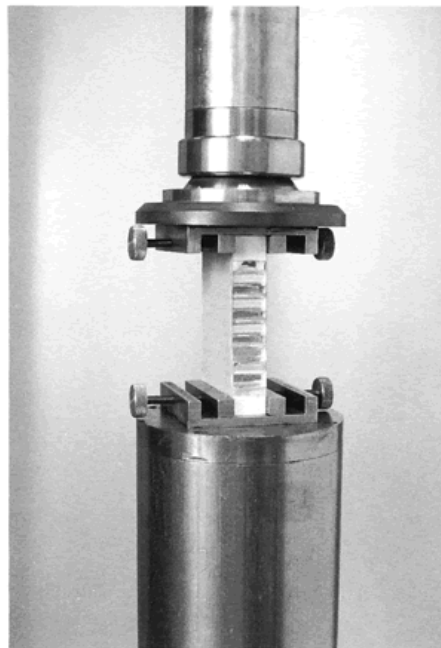


Figure 1.3.2. C364 Edge wise compressive testing

1.3.1. In-plane compression methods of supported sandwich panels

Early development of the CAI method for monolithic laminates came from Boeing and NASA, with a number of publications [108] detailing the methodology. It was adopted later by the Suppliers of Advanced Composite Materials (SACMA) and then by the ASTM as ASTM D7137/D7137M-12 [107] (sketch of typical test set-up shown in Figure 1.3.3). Other variants of this standard followed, firstly with Airbus AITM 1.0010 [119], and eventually by the British Standards Institute (BSI) and the International Standards Organisation (ISO) in BS-ISO 18352:2009 [109].

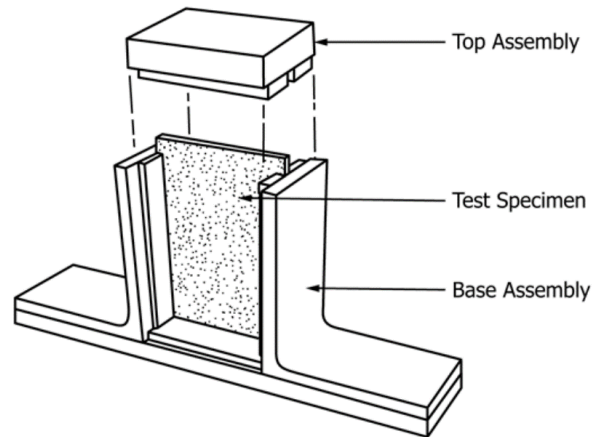


Figure 1.3.3. Schematic of compressive residual strength support fixture with specimen in place for monolithic laminates as detailed by ASTM D7137/D7317M-12.

Panels under in-plane compression for evaluating their CAI strengths are recommended to be clamped at the loading ends and simply supported at the unloaded sides, as shown in Figure 1.3.4. There are two techniques of applying the end clamping condition, one being direct clamping with metal blocks driven by screws and the other being potting the ends in an epoxy resin. The direct clamping could introduce strong clamping pressure at the ends, which could induce local stress concentrations and/or crushing the core. This could potentially be detrimental to the reliability of test results, considering that crush strengths of most core materials are very low. The end potting technique provides no through-the-thickness clamping force but slightly enlarged contact areas as is particularly suited to sandwich panels. Its advantage is that it minimises the stress concentrations at the ends at the initial stage of in-plane compressive loading. As potting epoxy could interlock with honeycomb cells or porous foam very well, aided with a substantial thickness of the sandwich panel, they usually perform well during compressive loading. The loaded ends of the panel usually need to be machined to ensure parallel.

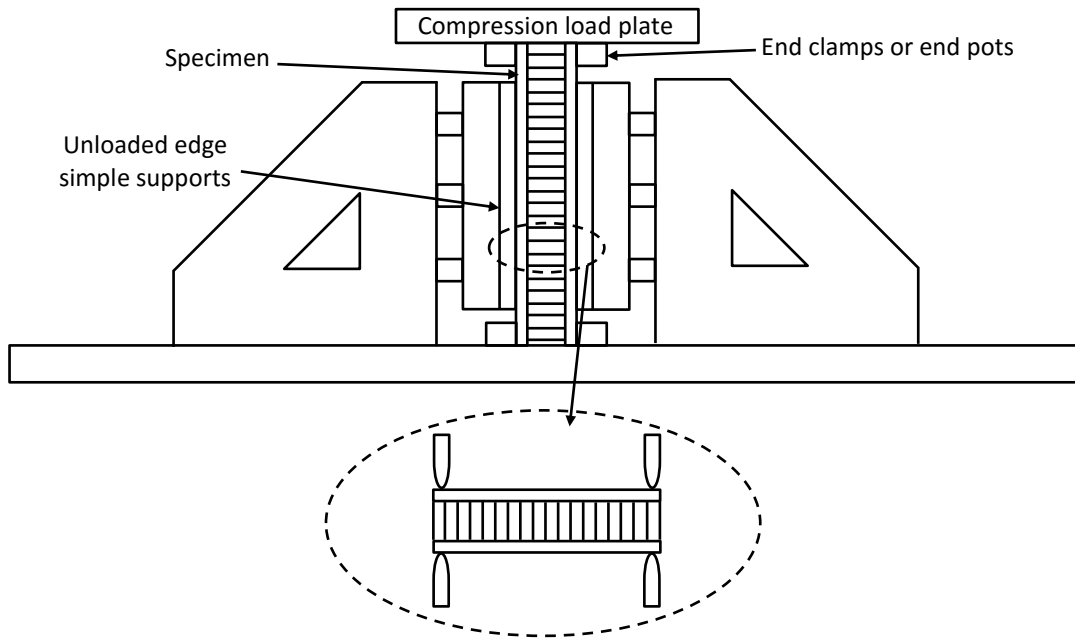


Figure 1.3.4. In-plane compression set up with clamped loaded ends and simply supported at the unloaded sides

Due to the lack of a standardised method, there was a wide range of panel geometries and thicknesses, thereby generating a wide range of width-to-thickness and aspect ratios.

1.3.2. Damage characteristics under in-plane compression

The in-plane compressive response of undamaged composite sandwich panels was studied both directly and as part of a wider study of the damage tolerance performance. Commonly, it was found that panels with no impact damage and with the insufficient width-to-thickness ratio suffered from premature failures at one of the loaded ends as seen in [78] ($w/t = 3.6-2.85$, $AR = 1$), [42] ($w/t = 13.53$, $AR = 1$). Panels that failed in this way were unrepresentative of in-plane compressive strengths of the panels, invalidating itself as a reference in judging the residual compressive strength values of the damaged panels. Failure modes of the baseline panels relied heavily on the width-to-thickness ratio of the sandwich construction, with the ideal ratio being expected to be above 35 on a basis of the CAI testing of monolithic laminates [87,88]. Some instances of in-plane compressive failure in undamaged panels were reported in [16]. Davies et al [16] tested two different very large carbon/epoxy panels with aluminium honeycomb cores with dimensions of 490 x 496mm. The first panel of about 14mm thick gave a width-to-thickness ratio of 35.5, and the second panel which was 27mm thick gave a width-to-thickness ratio of 18.4. Both single panel tests failed in the mid-section. Although the w/t ratios were largely different, the lower w/t ratio of the second panel type still resulted in in-plane

compressive failure due to the weak construction, comprising of very thin skins, with limited numbers of plies in the loading direction due to the QI lay-up.

It was largely recognised in the literature that with increasing impact energy the CAI strength of the panel decreased. However, it was found that at very low levels of impact energy the reduction in local resistances and the imbalance of local bending moments induced by the shift of the mid-plane towards the intact skin in the mid-section region could not overcome the stabilizing effect of the core so that the impact damage in the impacted skin could neither propagate transversely nor facilitate local buckling. This led to a number of low energy impact panels still failing in the loaded end regions of the panel [78,89].

Increasingly there has been a trend looking into the compressive response of sandwich panels containing artificial or simulated damage mechanisms instead of investigating impact damage. The damage can be represented in a number of different ways including notches/holes [26,81,102] and artificial delaminations [42,51], in order to ascertain the effects of a well-known delamination on compressive strengths. Due to the complex and shared interaction of the damage mechanisms that occur in sandwich panels between the skin and the core, experimental understanding and CAI modelling of the interactions between these constituents is extremely difficult to achieve. By simplifying the number of mechanisms that occur at any one time, i.e. introducing only laminate delamination or skin/core debond or core crushed regions, their influence on the compressive response and strength of the panel could be understood. Additionally, artificial damage simulations like notches and open holes, are far easier to create than impact damage, hence if an open hole or notch geometry can be compared with the surface curvature regions after an impact, the assessment of the damage tolerance capabilities of a wide range of panels can be modelled numerically, and a large saving in time and cost can be achieved by reducing the amount of experimental work.

Bull et al [26] set a hole with the radius equivalent to the radius of a circle representing an area under which all delaminations were found from C-scanning. They concluded that the modelling of the holes and notches did not take into account the significant effect of local curvatures and residual stiffness of the damaged zone in impacted panels in terms of predicted residual strength.

McGowan et al [101] investigated the CAI strengths of impact-damaged carbon/epoxy skinned Korex core sandwich panels with the width-to-thickness ratio of about 8. Impact damage was created using both a drop-weight rig and an air gun with an impact energy (IKE) level of up to 10.1J with a 12.7mm HS impactor. All impact damaged panels were found to fail through compressive failure through the impact site in the mid-section region but the failure location of the undamaged panel was not

reported. The CAI strength was found to be 54% of the undamaged panel strength for drop weight impacted panels at a maximum impact energy of 9.5J, and 45% of the undamaged panel strength for air gun impacted panels at a maximum impact energy of 10J. They also found that the inclusion of impact damage at the lowest levels of IKE reduced the CAI strength by 32%, decaying to only 46% reduction increasing the impact energy by 4.7 times in the drop weight samples. This shows a decreasing sensitivity to the further spread of planar damage in the panels indicated by a decaying parabolic trend against metrics such as IKE, planar damage and indentation depth. The CAI strength of the gas gun-impacted panels was found to be lower than that of the drop-weight rig at the as IKE was increased. Authors attributed this to the fact that the gas gun-impacted damage areas were substantially larger than the drop-weight impacted ones, while their respective dent depths were about the same. They further stated that the residual global stiffness was not affected by the presence of impact damage.

Tomblin et al [23,94,95] conducted the most extensive studies of CAI strengths of various sandwich panels with the width-to-thickness ratios of varying between 6.5 and 20 and aspect ratios between 0.6 and 1.6, impacted with three HS impactors. All impacted panels under in-plane compression were found to fail in the mid-section regardless of geometry, construction or impactor diameter. They showed that the reduction of CAI strengths in panels with 2 ply skins was 60% at the upper end of the IKE range, with little observed effect of increasing core thickness or impactor diameter and that with 4 ply and 6 ply thick skins, panels with the thinner core thickness suffered the greater reduction of CAI strengths of up to 60% than those with the thicker core with only 45%, when impacted only by the larger diameter impactor. Authors reported that the CAI strengths appeared to increase by 12% when the width of the specimen was increased from 6.5" to 16" for sandwich specimens with 2 ply skins and that no significant trend was observed for sandwich specimens with 4 ply skins. This finding is largely counter-intuitive since doubling the width should halve the local buckling resistance, however, authors make no comment on this expected effect.

Raju et al [33] tested the CAI strengths of various sandwich panels with 2 ply, 4 ply and 6 ply PWCF skins with 9.525 and 19.05mm Nomex cores. The width-to-thickness ratios of these panels were between 10 and 20. They found that the failure location of all panels with impact damage were at the mid-section of the panel, regardless of the panel construction or impactor geometry. Authors categorised all the compressive failures by three types of mechanisms, as illustrated in Figure 1.3.5. Panels with significant dent depth and skin fracture exhibited the first type of failure in Figure 1.3.5, designated as net section fracture (compressive skin failure). This failure was initiated from top skin fractures in the impacted area and propagated across the width to the lateral edge. For the second

type of failure, they observed in 2-ply skinned panels impacted with the 76.2mm impactor that the panel failed through net section fracture due to local buckling. For the third type of failure in Figure 1.3.5, they observed that the CAI strengths of the panels were consistently lower as the failure mode changed from the first through to the third and that CAI degradation in terms of damage mechanisms in the panel suggested that dents caused by a larger impactor produced the greater reductions in CAI strength so that a panel with a benign dent depth may be more detrimental than significant dent depth with skin damage. Authors found that the 2 ply skin panels did not exhibit dependence on impactor diameter, whereas the 4 and 6 ply skinned panels were found to have a dependence on the impactor geometry.

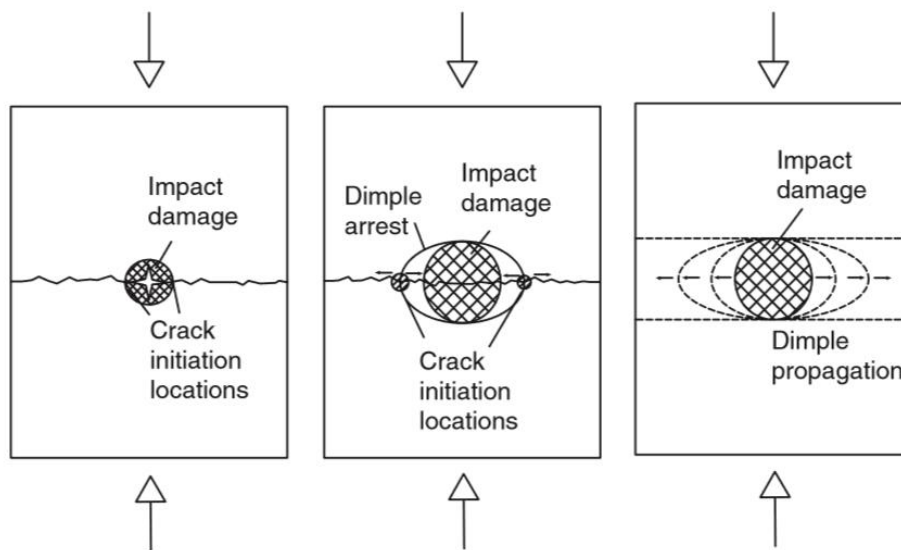


Figure 1.3.5. Failure modes observed in impact damaged sandwich panels under in-plane compression loading from Raju [33]

Davies et al [16] tested two types of impact damaged sandwich panels in in-plane compression. The first panel had 2mm thick carbon/epoxy skins with a 10mm thick aluminium honeycomb core, with the width-to-thickness ratio of 35 and aspect ratio of 1. These panels impacted at 80J and 120J failed in the mid-section with a 35% reduction in CAI strength for the latter panel. For the second panel with 1mm thick skins and a 25mm thick core giving a width-to-thickness ratio of 18.4 and aspect ratio of 1, these panels were impacted at 20J and 80J. They reported that in-plane compressive failure still occurred in the mid-section.

Zhou et al [89] investigated the CAI strengths of 8 ply carbon/epoxy skinned sandwich panels with both aluminium and Nomex core of 12.7 mm thick. Impact damage was created using a hemispherical impactor of 20 mm diameter up to 30 J, with the panel width-to-thickness ratio of about 10. They found that all undamaged panels, along with a third of the impact damaged aluminium honeycomb

core panels, failed at the loaded end region. They attributed this to that because the presence of the core counteracted the deleterious effect of the limited impact damage in such a way that local buckling or sideways propagation of the impact damage in those panels was constrained. They further reported that remaining two thirds of the impact damaged aluminium core panels and all impact damaged Nomex core panels failed in the impact damaged mid-section region. Authors showed that once the panels were impact damaged, there was an immediate but moderate reduction in compressive strength of approximately 30%, followed by a final reduction of CAI strengths for both aluminium and Nomex core sandwich panels to 50% of the undamaged panels at the upper end of the IKE range caused by fibre fracture of the impacted skin and that the effect of the core material on the CAI strengths appeared to be negligible.

The effects of skin asymmetry and skin lay-up alone were very uncommonly investigated aspects of the CAI performance of sandwich structures, while most of the focus was placed on the thickness of skins, core thickness, material type or density. It can be speculated that the compressive response of undamaged asymmetrical panels would be lower than in symmetrical equivalents due the induced bending moment due to the shifting of the neutral axis of the panel towards the thicker skin, if they fail in in-plane compression. No significant studies into the comparative performance of asymmetric and symmetric panels, or varying skin lay-ups were found.

1.4. Outline of the thesis with aims and objectives

The ultimate aim of this research is to examine the impact damage resistance of various types of primarily carbon/epoxy skinned sandwich panels and investigate the residual in-plane compressive strengths of the damaged panels with a specific focus on how the core of the sandwich contributes to the in-plane compressive behaviour.

The intrinsic variables involved in sandwich construction are skin thickness, skin lay-up, skin material, sandwich asymmetry and core density. These variables were selected because the overview of the literature at the outset of the project indicated that they play an important part in the in-plane compressive behaviour of impact damaged panels. The primary interest of employing E-glass/epoxy skin material was to use its translucent nature such that the visually clear size of impact damage could be re-examined after in-plane compression testing to see exactly how much the impact damage propagated under in-plane compression. Two lay-ups, cross-ply and quasi-isotropic, were considered in this study. The CP lay-up was useful to maximise the load-bearing capacity, whereas the angle plies in the QI lay-up was expected to make a useful contribution to resist in-plane compressive load. A need for introducing sandwich asymmetry stemmed from industrial weight reduction exercise by

removing plies from the non-impacted side without examining the consequence on the in-plane compressive behaviour. Core density not only affected impact damage resistance, but also provided a stabilising effect to the skins during compression. Hence three aluminium honeycomb densities will be investigated (70, 110 and 135kg/m³).

Extrinsic variables have been widely researched in the Department by Hill [1], and the effects of impactor size and shape, boundary conditions and loading speed have been duly considered on sandwich constructions. Additionally, core material variation has been previously studied, and further investigation would prove to be costly, and therefore will not be carried further.

To achieve the ultimate aim, firstly, various composite sandwich panels were impact damaged and their impact damage resistance was characterised through 'damage maps', which were established by combining impact response interrogation and post-mortem observations of tested specimens. Secondly, while in-plane compression testing all those impact damaged panels to establish 'damage tolerance maps', four different preconditions were introduced into specifically constructed panels and these panels were also compression tested to provide an additional physical insight into the loading-bearing compression mechanisms. These preconditions are removal of cores of a finite length, removal of core after impact, a single hole in one skin and two holes in two back-to-back skins.

To this end, the following specific objectives of this study must be accomplished:

(i). Fourteen groups of primarily carbon/epoxy sandwich panels were manufactured with skins individually cured in autoclave and with two-step skin-core bonding to ensure that 'telegraphic effects' would not occur. These groups covered two skin thicknesses, two skin lay-ups, two skin materials, symmetrical and unsymmetrical conditions and three different densities of aluminium honeycomb cores.

(ii). Of these groups the majority of panels were impact tested over varying ranges of IKEs using an instrumented drop-weight impact test rig such that the impact force responses were recorded for each test, including impact and rebound velocities. The non-destructive post-impact measurements were carried out on the impacted specimens. Selected specimens were cut up to confirm the dominant impact damage mechanisms. All these data and information allowed damage maps to be established with confidence.

(iii). The dimension design for in-plane compression panels was carried out to ensure that (a) the size of the panels was likely to be accepted by the industrial community without cost concern and (b) it is

big enough for impact damage to be well contained within the panels after being subjected to a substantial amount of IKE.

(iv). All those impact damaged panels after extensive preparations and instrumentations (strain gauges) were subjected to in-plane compression testing so that their corresponding CAI strengths were used to establish 'damage tolerance maps'. The strain gauge responses bonded back-to-back at several specifically selected pivotal locations from each panel were thoroughly interrogated to ascertain the occurrence of local buckling in a single half wave and its transition to two half waves, leading to catastrophic failure.

(v). Four types of preconditioned instrumented panels were also compression tested to provide an additional physical insight into the skin-core interaction during compression, which could in turn affect the in-plane compression failure mechanisms. The full width section of core with a longitudinal length of 20mm or 40mm was removed. In other groups, the panels were impact damaged before the removal to ensure the identical skin condition to the impact damaged panels. A hole size of 40mm was selected on the basis of previous experiences to ensure that it was big enough to affect the in-plane compressive resistance, while yielding a small or moderate hole size-to-width (of the panel) ratio.

(vi). The reduction trends of the residual in-plane compressive strengths of all the panels were evaluated using IKE, delamination and crushed core extents and dent depth with intent, through cross comparisons, to ascertain where, when and how the presence of core affected the in-plane compressive resistance of the skins in the sandwich panels.

Table 1.4.1. Details of cited literature in damage resistance

Ref.	Sandwich materials						Testing conditions							Damage details	Defects/ Preconditions
	Skin			Core			Panel thickness	Test type	B.C.	Test area	Impactor dia./weight	Vo/H	IKE		
	Material	Lay-up	t	Material	t	Density									
	-	-	mm	-	mm	kg/m ³	mm	-	-	mm ²	-	(m/s)/(m)	Joule	-	-
Bull [2]	GF/vinyl ester	[0,0,45,-45] ₆	4.2	PVC	50	200	58.4	QS, HVI	C	≤ 1x1m	40mm projectile	984, 988	3.8 – 6.9	ISP, Debond	-
Kepler [4], [5]	GF, aramid mid core insert (CSM)	[CSM/(90/0) ₃][CSM/(90/0)/(-30/60)/(30/-60)]	3mm	PVC	40mm	80kg/m ³	46	QS, MVI	SS	500 x 500	HS -r25 Cone 25 and 75mm 1kg	50mm/min, 70 and 93 m/s	1250-2170	Delam, Debond, core cracking	-
Lee [7]	Al., GF/Epoxy	Unsym	Al – 1.2mm GF - 1.5, 3.0 mm	Al. HC	16.0 25.4	59.26	29.9 18.4	LVI	C	≤ 100 x 100	15.86mm 1.95kg	-	1.3-6.0	Delam, CC	-
Shipsha [8]	GF/ Vinyl ester	QI	2.4	PMI	50	52	54.8	LVI	C	≤ 270 x 180	25mm 7.8kg	-	10- 60	Delam, CC, debond	-
Tsotsis [9]	GF/ Epoxy, Woven CF/ Epoxy, Al skins	UD, 2, 3 and 4 plies	-	Aramid HC- and Al HC	-	Aramid – 48, 80, 144, 184 Al – 96, 136	10	QSI LVI	SS	279.4 x 279.4	QSI, FE – 6.35, 12.7mm HS, LVI – 15.88mm 4, 6, 8 lb	-	2.5-27	CC, Core cracking	Si Rubber layer over plates to represent aircraft carpeting
Koissin [10]	GF/ VE	[0,-45,90,+45,-45,90,+45,)] _s , [0,45,90,-45] _s	1.6, 2.4	PVC and PMI	40, 50	130 52	54.8 43.2	QSI LVI	RB	270 x 180	25, 50mm HS 7.8	2mm/min	10-60	CC, delam debond	-
Zenkert [11]	CF T700/ VE	[0/90/45/-45] _s [0/90/45/-45] _{3s}	1.8 5.4	PVC foam core	60 50	80 200	63.6 60.8	LVI	-	300 x 300	HS 25mm Pyramid 15.29 kg	-	30-250	FF, debond, CC, delam	-
Williams [12]	GF/ epoxy	CP [0/90] _s	-	PMI	2 x 8	52	≥16	LVI	RB	60 x 90	HS 20mm 5.35kg	-	3	BVID	Self-healing panels, 2mm risers in core

Herup [13]	CF/ epoxy	[0/90] _{ns} n=1, 2, 4, 8, 12	-	Nomex HC	12.7	9.0 pcf	≥12.7	LVI, QSI	SS	127 x 127	HS 12.7mm 3.5kg	-	0.06 -25	Delam, CC, C	-
Anderson [14]	CF/epoxy 4x4 twill	[0/90/0] [0 ₂ /90 ₂ /0 ₂]	-	PMI Nomex HC	12.7 mm	110 96 51	≥12.7	LVI	SS	≤76.2 x 76.2	HS 25.4mm 1.8-2.7 kg	-/0.2 -1.2	5 – 25	BVID, ISP, CC, CS	-
Shin [15]	GF/ Epoxy AI	-	3.0/1.5 G/E 1.2/1.2 AI	AI HC, Balsa, AI foam	25.4 16	59 151 473	29.9 18.4	LVI	C	Circular	HS 15.86mm 1.4kg	-	1.3 – 6	Delam, CC, FF, debond	Asymmetry
Davies [16]	CF/epoxy prepreg	[+45/0/-45/90] _s , [0/90] _s	2 1	AI HC	10 25	72	14 27	LVI	C	≤490 x 496	FE, 20mm 5.45kg	-/0.375, 1.5, 2.25	20-120	CC, delam, debond (back face)	-
Akay [17]	CF A: Cycom 985 resin B, C, D, E: Fiberite 934 resin	Front Skin: [45,90 ₃ ,45] Back Skin: [90,45,90]	1.97 0.63	A: PMI B: Nomex HC C,E: PMI D:PMI	12.5 25	51 48 71 110	15.1 27.6	LVI	C	50, 90 diameter	HS 12.7mm	-/0.7	1.5-10	CC, delam	Asymmetry
Schubel [19], [20]	CF/epoxy	-	1.5mm	PVC Foam	25.4	250	28.2	LVI, QSI	SS	254 x 254	HS 254mm 6.22kg	1.6 – 5/-	7.8-108	CC, debond, delam	-
Leijten [21]	CF/epoxy fabric	[45/-45/0/90] _s	2.3	PMI foam	10 15 20	75 110	14.6 19.6 24.6	LVI	C (4Nm)	75 x 125	HS 16mm 2.4-4.2kg	-	0-60	FF, CC, delam	Interleaved sheets
Tomblin [23]	PW CF/epoxy	[90/45] _s [90/45] _{2s}	-	Nomex HC	0.75"	3.0 pcf	-	LVI	C	8x8 12x12 16x16 12x24 12x48"	FE 3"	-	58-157 lbf-in	CC, debond, delam, MC, cell wall fracture	Scaling effects
Nettles [24]	CF/epoxy	[45/0/-45/90] _{2s} [45/0/- 45/0/90/1/1/90/9 0] _s	-	AI HC	28.58	39.85	-	LVI	RB	102 x 152	HS 6.35, 12.7mm 1.23kg 38.1mm 1.7kg	-	0-20	Delam, CC	-

Bhuiyan [25]	Biaxial braided CF/epoxy	[±45]	3	PUR	12.5	240	18.5	LVI	C	80 x 80	HS 12.7mm, 6.62kg	-	15-44	Delam, debond, CC, cell collapse	Nanophased core
Bull [26]	CF/vinyl ester	[0/90/45/-45] _{sn}	1.8 5.4	PVC foam core	60 50	80 200	63.6 series 1 60.8 series 2	LVI	C	300 x 300 and 150 x 150	HS and pyramid 25mm 15.29kg	-	30, 50 for series 1 and 100, 200 for series 2	Delam, dent	Hole and Notch comparison
Ishai [28]	UD CF/BMI GF layers	[0/30/-30] _{3s}	2.52	Syntactic foam	25	0.6 g/cm ³	30	LVI, HVI	SS	350 x 76 210 x 76	HS -16mm 86N (LVI) 0.177N (HVI)	Up to 6m/s (LVI) Up to 160m/s (HVI)	0-160 0-220	Delam, MC	Interleaved layers of GF
Kassapoglu [29]	UD, PW, 5HS, 8HS CF/epoxy	Various Combo of all tape types	≤2	Nomex HC	12.7 19.05 25.4	14.68 29.36	-	LVI Pendulum	C, RB	9 x 6"	19.05mm 1.143kg pendulum 12.7, 38.1mm, 0.91kg Drop weight	-	0.269-2.69J	CC, MC, delam, dent	-
Kassapoglu [30]	3 types of CF/epoxy QI	(±45)/(0/90)/(±45), (±45)/(0/90) ₂ /(±45, (±45)/(0/90)	0.571 0.762 0.381	Nomex HC	25.4	3.0pcf	26-28	LVI	F	6 x 6"	HS 12.7mm, 3.48kg	-	3.03, 4.98 and 1.84	Delam, MC, FF, CC	-
JH Lee [31]	Woven CF/epoxy	-	4 2	AL. HC	36	-	42	LVI	SS	410 x 120	HS 12.7mm, 1.39kg	-	30-90	CC, MC, FF, delam	Asymmetry
Meo [32]	MD 69/GFE 3105 H AS4-8552 (MOD)	2 or 4 plies Modified – 3/2 or 4/3	-	Nomex HC	0.6" 0.25"	6.0pcf	-	LVI	SS	101.6 dia.	HS 16 and 50mm	-	5-20	Delam, dent	Asymmetry
K. Raju [33]	CF and GF/epoxy	[(0/45) _n /core/(45/0) _n] n=1,2,3	-	Nomex HC 4.76mm cell size	9.525 19.05	48.05	-	LVI	C, SS	203.2 x 203.2	HS 25.4, 76.2mm (weight varied)	2.43/-	5-35	Dent investigated only	-
M. Raju [34]	GF 2x2 twill/epoxy		0.65	PU Nomex HC	30 6.7	- 85kg/m ³	31.3 8	LVI	-	300 x 300	25mm 2.57kg	-/400 – 600	7.56-15.6	Delam, debond	Panel repair

Wen [36]	GF/PE Kevlar	3, 6 or 12 ply 0/90	1.7-7	PVC foam and vermilux cores.	25 20 25	130 400 475	28.5 – 56.5	HVI LVI QSI	SS	0.85, 0.2m ²	HS, FE, cone 5.25- 150mm 42.5kg	4.8 – 9.5 1.3 – 5	500-1918	Lower skin debond and FF, ISP	Mild steel or GF inserts for third skin
Koissin [38]	GF/VE	QI [0,45,90,-45] _s [0,-45,90,45,- 45,90,45,0] _s	2.4 1.6	PMI PVC	50 40	52 130	54.8 43.2	QSI LVI	RB	180 x 270	HS 25, 50mm 7.8kg	-	10-60	Delam, dent, CC, ISP	-
Edgren [39]	CF/ VE, biaxial 0/90, ±45	QI [0/90/45/-45] _{3s}	5.4	PVC	50	200	60.8	LVI	RB	300 x 300	HS 12.5mm	-	100 250	Delam, MC, FF	Notch and open hole specimens
Staal [43]	GF/epoxy prepreg	[0/90] _s	0.47	Nomex HC	25.5	3.0 pcf	26.5	LVI HVI	C	≤ 720 x (106, 150, 210, 320)	Ball 30, 50, 100mm	-	-	Indentation study	Crush tests after impact
Nanayakkar a [44]	CF/epoxy UD prepreg	QI	2	PMI	6	75	10	LVI	-	40 x 40 60 x 60	HS 25mm, 1.5kg	-	0-50	Delam, MC, CC	Z pinned core 0.28mm T300/BMI rods
Zheng [45]	CF/ epoxy	[(0/90) ₆ /45/- 45/0/-45/45C] _s	-	Nomex HC	-	-	9.5	QSI LVI	SS C	60mm dia	HS 20mm	-	1-10	Delam	(0/90) glass cloth top layer
Edgren [46]	CF,GF/VE, biaxial 0/90 (±45)	QI [0/90/45/-45] _s QI [0/90/45/-45] _{3s}	1.8 5.4	PVC	60 50	80 200	63.6 60.8	LVI	RB	300 x 300	HS 12.5mm 15.287kg	-/0.2 – 1.667	30-250	Delam, MC, FF	Hole and notch specimens
Aminanda [47]	Brass	-	0.5	Nomex HC	15	78	16	QSI	RB	150 x 100	HS 57.25mm	0.5mm/mi n	0, 0.5, 1, 1.5, 2mm	Indentation study	Metallic Skins
Nettles [49]	IM7/8552	[45,0,- 45,0,90,0,0,90, 0] _s	2.9	Al HC	25.4	50	31.2	LVI	C	≤152 x 102	HS 13mm 1.2kg	-	1-37.5	Delam,CC, FF, ISP, MC	Thermal protection system Sprayable PUR
Nettles [50]	IM7/8552	[45,0,-45,0,90,0,0, 90,0] _s	2.9	Al HC, 3.2mm cell size	25.4	50	31.2	LVI	C	≤152 x 102	HS 13mm 1.2kg	-	3.5-16.5	Delam, dent	Fatigue
Park [53]	CF/epoxy fabric	[(45/0) ₂ /core/(0/4 5) ₂]	1	Nomex HC	9.5	-	11.5	LVI	C	ASTM D7136			BVID/VID limits	Repair Environmental conditions	
Salehi- Khojin [54]	CF PW 3K CF/KF, 2x2 twill/epoxy	4 CF layers 1 Kevlar 3 CF 1 hybrid, 3 CF	1.2	Kraft paper HC	25.4	112	27.8	LVI	C	76.2mm dia	HS 12.7mm 7.25kg	-	12-45	FF, CC, backface cracking	Temperature affects, -50, 20,

															70, 120°C, Foam filled HC
Zhou [55]	Woven GF/triazine	2 ply	0.25	PVC crosslinked and linear PET	19.5	60-200	20	LVI	C	100mm dia	HS 10mm 5.56kg	-/0.2-1.4	-	CC, ISP	Oblique impact
Crupi [56]	1 – GF 2 –Al 3 –AlMn	1 – 6plies top and bottom 2,3 – Al	1- 3 top, 7 bottom 2,3 – 1	1 – PVC 2 –AlSi10 3 –AlSi7	15 9 9	75 950 870	1 – 25 2, 3 – 11	LVI	RB	60 x 60	HS 20mm 7kg	4-9/-	56-285	ISP, CC	-
Li [58]	Woven GF /phenolic	[0/90/0]	1.2 1.5 2.0	Al foam,	10 15 20 30	Relative density 0.06,0.085, 0.125, 0.2, 0.25	12.4 – 34	LVI QSI	C	90 x 90	Conical – 38mm FE, HS – 38mm 3-24kg	0.02mm/m in -/51-1275	6.5 – 155	FF, CC, ISP, BP	Unsymmetrical arrangements
Avila [62]	PW GF/ epoxy bisphenol	-	0.8	Closed cell PS	25.4	35	27	LVI HVI	C	50mm dia	HS 10mm 246-3414g	0-7.67/-	5-75	BVID, FF, CC, backface debond, skin tearing, BP	Nano structures – nanoclay 0wt. % to 10wt. %
Hosur [63]	PW CF 3K/ epoxy	3 layers	-	PUR	-	240	-	LVI	C	75mm dia	HS 12.7mm 6.62kg	-	15-45	Dent, CC, CS, backface debond, ISP, BP	Nanophased core
Wang [68]	Al	-	0.5, 0.8, 1	Al Foam and HC	10, 20, 30, 12.5	250	12-31	HVI	C, RB	300 x 40	Cylinder 36.5 dia	53.6-115.4/-	-	CS, CF, CC, wrinkling	-
Gustin [78]	CF and KF PW and Hybrid CF/KF epoxy	4 CF, 1KF/3 CF, 2KF/2CF, 3KF/1CF, 4KF, 1H/3CF, 2H/2CF, 3H/1CF, 4H	Approx. 1-1.2	Foam filled HC	25.4	112	Approx 27-28	LVI	C	76.2mm dia	HS 12.7mm 7.25kg	-	5-45	ISP, CC, delam top and bottom face sheet	-
Thomsen [83]	GF CSM PW/VE	3 CSM and 2 PW in each laminate	2.7	PVC cross linked foam	30	90	36	LVI	C	Clamped close to impact region	HS 25mm 1.3kg	-/2-3	20-30	MC, FF, core tearing, CC	-

Turner [84]	IM7/8552	[90/0] _s		Nomex HC	25.4 thick	48	-	LVI	C, RB	≤356 x 152	HS - 25.4mm 1.31kg	-/460	5.88	BVID	Integral stiffeners
Zhou [89]	CF/epoxy LTM45	[0/90] _{2s}	1.0	Al and Nomex HC	12.7	70 64	14.7	LVI	C	100mm dia.	HS 20mm	1.15-8.56/1.5	1-55J	CC, delam, FF	-
Zhou [90]	CF/epoxy LTM45	[0/90] _{ns} n = 1,2,3,4	0.5,1.0, 1.5,2.0	Al and Nomex HC	12.7	50,70,90 64,96	13.7-16.7	QSI	C	100 220mm dia.	HS, FE 20mm	5mm/min	-	CC, delam, FF	-
Czabaj [92]	IM7/8552	QI	8 ply	Al HC	25.4 16.5 25.4	49.7 49.7 72.1	-	QSI	C	178x152	HS 25.4, 76.2mm	-	0.5 1mm indentation	CC, delam, BVID dent	-
McQuigg [93]	GF/epoxy	[0/45]	2 ply 0.02"	Nomex HC	0.125, 0.75"	3.0, 6.0 pcf	0.165" 0.79"	QSI LVI	-	5x5"	HS 0.5"	-/2.49lbs	1.0-9.0 ft-lb	Delam, CC, dent, ISP, FF	-
Tomblin 00/44 [94]	PW CF/epoxy	[90/45] _s [90/45] _{2s} [90/45] _{3s}	-	Nomex HC	3/8, 3/4"	3.0 pcf	-	LVI	C	8x8"	HS 1.0, 3.0"	Max 12"/4.5-50lbs	50-350 (lbf-in)	CC, delam, FF, ISP	-
Tomblin 02/80 [95]	PW CF/epoxy	[90/45] _s [90/45] _{2s} [90/45] _{3s}	-	Nomex HC PVC	0.375, 0.750, 1.125"	3.0,4.5,6.0 2.6,4.2,5.5 pcf	-	LVI	C	-	HS 1.0,2.0,3.0"	-	84.6-155.7 (lbf-in)	CC, delam	-
Zhou [96]	CF/epoxy LTM45	[0/90] _{ns} n = 2,3,4	1.0, 1.5, 2.0	Al HC	12.7	70 50	14.7-16.7	QSI	C	100mm dia.	HS, FE 20mm	5mm/min	-	CC, delam, FF	-
Sharma [97]	GF/epoxy and polyester	-	-	PUR	-	0.6gm/cc	-	LVI Pendulum	C	-	HS 20mm	-	7.5-37.5	CC, delam, ISP	-
McGowan [101]	AS4/8552	QI	8 ply	Aramid HC	-	4.5pcf	-	LVI	C	10x5"	HS 0.5, 1.0" 2.5lb	-	0-13 (lbf-in)	BVID	-
McGowan [102]	AS4/8552	QI	36-50 plies	HRP HC	-	12pcf	1.53"	LVI	RB	10x5"	HS 1.0"	-/11.8lbs	40-100 (ft-lb)	Dent, damage area	-
Ratcliffe [121]	PWCF/epoxy	(±45)/(0/90)/(±45)	0.6mm	Nomex HC	25	48.1	26.2	-	-	140x140	-	-	-	-	6.35mm open hole

Damage mechanisms: CC – core crushing, FF – fibre fracture, MC – matrix cracking, ISP – impacted skin penetration, CS – core shear, BP – back face penetration, C - clamped, RB – rigid base, SS – simply supported, HC – honeycomb, CF – carbon fibre, GF – glass fibre, KF - Kevlar fibre, VE – vinyl ester

Table 1.4.2. Details of cited literature in impact damage tolerance

Reference	Sandwich materials						Testing conditions						Failure details	
	Skin			Core			Panel thickness	Specimen size	Load rate	B.C	IKE	Delam area	Dent depth	Failure location
	Material	Lay-up	Thickness	Material	Thickness	Density								
-	-	mm	-	mm	kg/m ³	mm	mm ²	mm/min	-	J	mm ²	mm	-	
Bull [2]	GF/VE	[0,0,45,-45] ₆	4.2	PVC	50	200	58.4	650 x 540	1.0	C, F	2.9 – 6.9	-	-	-
Vadakke [3]	E/S-Glass/VE	[0 90] ₂	3.6 2	PVC	50 12.5	75 100 200	57.2 57.2 16.5	25.4 x 37.5 75 x 25- 250 length	ASTM C364	C, F	-	-	-	LE MS
Shipsha [8]	GF/VE	QI	2.4	PMI	50	52	54.8	270 x 180	1.0	C, F	10- 60	-	0.5 – 1.2	MS
Koissin [10]	GF/VE	[0,-45,90,+45,-45,90,+45,)] _s , [0,45,90,-45] _s	1.6 2.4	PVC PMI	40 50	130 52	54.8 43.2	270 x 180	1.0	C, F	10-60	30 – 110mm	0 – 1.2	MS
Zenkert [11]	CF T700/VE	[0/90/45/-45] _s [0/90/45/-45] _{3s}	1.8 5.4	PVC	60 50	80 200	63.6 60.8	300 x 300	1.0	C,F	30 - 250	HS – 15-30mm P – 15-25mm dia.	-	MS
Williams [12]	GF/epoxy	CP [0/90] _s	-	PMI	2 sheets x 8	52	≥16	60 x 90	0.5	C,F	3	0° - 43mm 90° - 38mm Avg dia.	0.5	MS
Davies [16]	CF/epoxy prepreg	[+45/0/-45/90] _s , [0/90] _s	2 1	Al HC	10 25	72	14 27	490 x 496	-	C, SS Epoxy pots	20-120	60 – 170mm dia.	1.93 - 3.43	MS
Akay [17]	CF/ A: Cycom 985 B-E: Fiberite 934	Front Skin: [45,90 ₃ ,45] Back Skin: [90,45,90]	1.97 0.63	A: PMI B: Nomex HC C,E: PMI D:PMI	12.5 25	51 48 71 110	15.1 27.6	27 x 76	0.5	C, SS	1.5-10	0-150	-	MS
Schubel [19], [20]	CF/epoxy	-	1.5	PVC	25.4	250	28.2	73.1 x 25.4	-	C, F	7.8-108	-	-	LE MS
Leijten [21]	CF/epoxy	[45/-45/0/90] _s	2.3	PMI	10 15 20	75 110	14.6 19.6 24.6	150 x 100 End Pots	ASTM D7137	C, SS	0-60	0 – 5500	0 – 2.25	MS

Tomblin [23]	PW CF/epoxy	(90/45) _s (90/45) _{2s}	-	Nomex HC	0.75"	3.0 pcf	-	6.5 x 10.5 8.5 x 10.5 12.5 x 10.5 12.5 x 12.5 12.5 x 16.5 16.5 x 10.5 (")	NASA RP 1092 mod	C, SS	58- 157 lbf-in	0 – 6"	-	MS
Nettles [24]	CF/epoxy	[45/0/-45/90] _{2s} [45/0/- 45/0/90/1/1/9 0/90] _s	-	Al HC	28.58	39.85	-	102 x 102	-	C,F End pots Al	0-20	0-250	0.1 – 0.6	-
Bull [26]	Carbon fibre reinforced vinyl ester	[0/90/45/-45] _{sn}	1.8 5.4	PVC foam core	60 50	80 200	63.6 series 1 60.8 series 2	300 x 300	-	C, F End tabs	30- 200	-	-	MS
Ishai [28]	UD CF/BMI	[0/30/-30] _{3s}	2.52	Syntactic foam	25	600	30	330 x 127	1.84	4PB SS	0-160 0-220	0-230	0- 2.8	MS
Kassapoglou [29]	UD, PW, 5HS, 8HS CF/epoxy	Various	≤2	Nomex HC	12.7 19.05 25.4	14.68 29.36	-	228.6 length	1.27	C, F	2.69 – 11.93	2.25 – 5.5mm dia.	-	Control – global Impacted – MS
Kassapoglou [30]	3 types of CF/epoxy QI	(±45)/(0/90)/(± 45), (±45)/(0/90) ₂ / ±45, (±45)/(0/90)	0.571 0.762 0.381	Nomex HC	25.4	3.0pcf	26-28	6" x 6"	1.27	C, F	3.03, 4.98, 1.84	30mm dia.	-	-
JH Lee [31]	Woven CF /epoxy	-	4 2	Al. HC	36	-	42	410 length	20	3PB SS	30- 90	-	-	MS
Raju [33]	CF and GF/epoxy	[(0/45) _n /core/ 45/0] _n n=1,2,3	-	Nomex HC	9.525 19.05	48.05	-	266.7 x 215.9	1.27	C, SS	5-35	30 – 150mm dia.	0-4	MS
M. Raju [34]	GF/epoxy	-	0.65	PUR Nomex HC	30 6.7	- 85	31.3 8	200 x 60 x (30, 8) 60 x 60 x 30 50 x 50 x 8	0.5	4PB and C, F	7.56-15.6	-	-	-

Koissin [38]	GF/VE	QI [0,45,90,-45] _s [0,-45,90,45,-45,90,45,0] _s	2.4 1.6	PMI PVC	50 40	52 130	54.8 43.2	180 x 270	1.0	C, F End tabs	10-60	30 – 80mm dia.	0.1-1.25	MS
Edgren [39]	CF/VE biaxial 0/90, ±45	QI [0/90/45/-45] _{3s}	5.4	PVC	50	200	60.8	300 x 300	1.0	C, F	100 250	70mm dia.	-	MS
Moslemian [42]	GF/VE	A and B [0/45/90-45] ₃ C – [0/0/45/-45] ₃	2	PVC PMI	30	130 250 51	34	460	1.0	C, SS Wood insert	Artificial debonds 100, 200, 300mm			Intact – LE Impact – MS
Staal [43]	GF/epoxy	(0/90) _s	0.47	Nomex HC	25.5	3.0 pcf	26.5	670 and 300 length	2.0	C 393 SS	-	10 -145mm dia.	-	MS
Nanayakkara [44]	CF/epoxy	QI	2	PMI	6	75	10	60 x 50	0.5	ASTM C364 C, F	0-50	7.5 – 32.5 mm dia.	-	MS
Edgren [46]	CF and GF/VE, biaxial 0/90,(±45)	QI [0/90/45/-45] _s QI [0/90/45/-45] _{3s}	1.8 5.4	PVC	60 50	80 200	63.6 60.8	A : 300 x 300 B: 150 x 150	1.0	C, F End tabs	30- 250	A: BVID – 32,54 VID – 36, 69 B: BVID – 63, 68 VID – 69,72 mm dia.	A – BVID 0.8 B - BVID 0.4	MS
Aminanda [47]	Brass	-	0.5	Nomex HC	15	78	16	150x 100	0.5	C, SS AITM	0, 0.5, 1, 1.5, 2mm	-	Indentation of 0, 0.5, 1, 1.5 and 2mm	-
Henao [48]	Woven CF and GF/epoxy	[0/90] ₂	1.97 1.12	PVC PUR	30	80 40	32-35	140 x 70	1.0	ASTM C364 ASTM 393	-	-	-	CF – MS GF – MS
Nettles [49]	IM7/8552	[45,0,-45,0,90,0,0,90,0] _s	2.9	AI HC	25.4	50	31.2	152x 102	-	C, F AI pots	1-37.5	0-42mm dia.	-	-

Nettles [50]	IM7/8552	[45,0,-45,0,90,0,0,90,0] _s	2.9	Al HC	25.4	50	31.2	152 x 102	5Hz Load rate	C, F Al pots	3.5-16.5	11 – 25mm dia.	-	-
Aviles [51]	GF/epoxy	-	2	PVC Balsa wood	12.5 50 25	45 100 200 150	16.5 29 54	200x150x30	0.8	C, SS End U-tabs	Artificial debonds 50 – 100mm			-
Park [53]	CF/epoxy fabric	[(45/0) ₂ /core/(0/45) ₂]	1	Aramid reinforced phenolic core	9.5	-	11.5	150 x 100	-	C, F ASTM C364	10	-	-	-
Salehi-Khojin [54]	PW 3K CF KF CF/KF epoxy	4 CF layers 1 Kevlar 3 CF 1 hybrid, 3 CF	1.2	Kraft paper HC Foam filled	25.4	112	27.8	-	-	C, SS, NASA	12-45	-	-	-
Boyle [75]	PW GF/VE	-	0.125"	PVC Balsa wood	0.5"	69.5 150	0.75"	183x92 122 x 92	2.03cm in 480s	C, SS CSM end pot	-	-	-	Balsa – MS Foam – LE
Christopherson [76]	PW CF/ epoxy	UD 4 ply	-	Foam filled HC	15.9 25.4	-	-	127x127	-	C, SS	0-120.1	-	-	MS
Fagerberg [77]	UD CF/VE	[0/90] _s [90/0] _s	1	PVC foam	-	30-200	-	200x 150 200x 100	0.5	C, F CF end tabs	-	-	-	MS
Gustin [78]	CF and KF PW and Hybrid CF/KF epoxy	4 CF, 1KF/3 CF, 2KF/2CF, 3KF/1CF, 4KF, 1H/3CF, 2H/2CF, 3H/1CF, 4H	Approx. 1- 1.2	Foam filled HC 12.7mm cell size	25.4	112	Approx. 27- 28	100 x 100	-	C, SS Boeing CU-CI	5-45	-	-	LE – crushing MS
Lagace [79]	CF/epoxy	[0/90] [±45]	0.35	Nomex HC	25.4	48	26.1	170 x 89		C, F GF/E tabs Al HC 352 kg/m ³	Holes 3.18, 6.35, 9.53mm			Control – MS

Mahfuz [80]	GF/VE	UD 3 layers	1.9	Semi rigid PVC	12.7	75 130 260	14.5	520 x 254	0.25	C, F Steel end pot	Artificial debond 50.8mm			Control – MS
Soutis [81]	PW T300 3K CF/epoxy	[±45/0/90] [0/90]	0.422 0.211	Nomex HC	25.4	-	26.2 25.8	50.8x152.4 101.6x305 203x406.4	0.13	C, F	Notched 6.35mm high 12.7, 25.4, 50.8mm wide			MS
Thomsen [82]	UD HTS CF/epoxy	[±10,0,-+10] [±45,0,-+45] [±25,0,-+25]	0.25	Al HC	10	-	10.5	150 x 100	-	C, SS	-	-	-	MS
Thomsen [83]	PW GF CSM GF /VE	3 CSM and 2 PW in each laminate	2.7	PVC	30	90	35.4	225 x 75	0.5	C, F ASTM C364	20-30	Length – 88mm Width - 24mm Max	1.8 max	MS
Turner [84]	IM7/8552	[90/0] _s	-	Nomex HC	25.4 thick	48	-	356 x 152	1.5	C, F Bismuth alloy end pots	5.88	-	-	MS
Wadee [85]	Al alloy Pure Al	-	0.25 0.25 0.9 1	PS PUR	25	-	25.5	322 x 70 322 x 152 500 x 90 210 x 102	-	SS and C LE F unloaded	-	-	-	MS
Zhou [89]	CF/epoxy LTM45	[0/90] _{2s}	1.0	Al and Nomex HC	12.7	70 64	14.7	200 x 150	1.0	C, SS	1-30	29-67mm (Al) 35-75mm (Nomex)	0.2-4.5 0.25-2.0	Control/ low IKE – LE Mid-high IKE - MS
Czabaj [92]	IM7/8552	QI	8 ply	Al HC	25.4 16.5 25.4	49.7 49.7 72.1	-	178x152	0.005- 0.00125 mm/sec	C, F	-	180-420	0.2-1.8	MS
McQuigg [93]	GF/epoxy	[0/45]	2 ply 0.02"	Nomex HC	0.125, 0.75"	3.0, 6.0 pcf	0.165" 0.79"	5x5"	0.01 in/min	C,F	1.0-9.0 ft-lb	-	-	MS
Tomblin 00/44 [94]	PW CF/epoxy	[90/45] _s [90/45] _{2s} [90/45] _{3s}	-	Nomex HC	3/8, 3/4"	3.0 pcf	-	8x8"	NASA RP 1092 mod	C, SS	50-350 (lbf-in)	2-16 in ²	-	MS
Tomblin 02/80 [95]	PW CF/epoxy	[90/45] _s [90/45] _{2s} [90/45] _{3s}	-	Nomex HC PVC	0.375, 0.750, 1.125"	3,4.5,6 2.6,4.2,5. 5 pcf	-	-	NASA RP 1092 mod	C, SS	84.6- 155.7 lbf-in	Planar diameters given	-	-

McGowan [101]	AS4/8552	QI	8 ply	Aramid HC	-	4.5pcf	-	10x5"	-	C, SS	0-13 ft-lb	0.0285-0.26 in ²	0.003- 0.05 in	MS
McGowan [102]	AS4/8552	QI	36-50 plies	HRP HC	-	12pcf	1.53"	10x5"	-	C, F	40-100 ft-lb	1.5-4 in ²	0.01- 0.05in	MS
Ratcliffe [121]	PWCF/ epoxy	(±45)/(0/90)/(± 45)	0.6mm	Nomex HC	25	48.1	26.2	140x140	-	-	6.35mm open hole		MS	

LE – loaded end, MS – mid-section, SS – simply supported, C – clamped, F – free boundary, 3PB – three point bending, 4PB – four point bending, HC – honeycomb, CF – carbon fibre, GF – glass fibre, KF – Kevlar fibre, PW – plain weave

2. SANDWICH MATERIALS AND PANEL MANUFACTURE

2.1. Sandwich materials

The sandwich panels used in this study comprised of two different skin material systems, each with a variety of material characteristics and an aluminium honeycomb core of three different densities. Two skin materials, supplied by UMECO (previously ACG, now owned by Cytec), were a unidirectional (UD) tape-based carbon fibre/epoxy and a UD tape-based E-glass/epoxy. The former, supplied on 300mm wide rolls, was composed of 34-700 carbon fibre with LTM45 epoxy. The carbon fibres were substituted by T700S for a couple of groups of tests, during which the 34-700 carbon fibre was out of supply. The latter, supplied on a 430mm wide roll, was composed of E-glass fibre PPG1062 and LTM26 epoxy. Both prepregs were needed to be stored in the freezer at -18° in order to maintain their shelf lives.

Sandwich skins used in this investigation had a number of different lay-ups, thicknesses and skin-to-skin arrangement. The three different skin lay-ups used were cross ply, quasi-isotropic and multi-directional. The lay-up orientations were $[0/90]_{2n_s}$ or $[0/90/0]_{n_s}$ for cross ply panels, $[45/0/-45/90]_{n_s}$ for quasi-isotropic, and $[45/0/-45]_{n_s}$ for multi-directional, with $n=1$ for a “thin” arrangement of 8 or 6 plies equivalent to 0.75-1.0mm in thickness, and $n=2$ for a “thick” arrangement of 16 or 12 plies equivalent to 1.5-2.0mm in thickness. Skin to skin arrangements were varied in order to investigate the effect of asymmetry in sandwich constructions. In both thin and thick arrangements, the number of plies in the back skin were 25% less than those in the front skin resulting in a combination of 8 and 6 plies for “thin” constructions, and 16 and 12 plies for “thick” constructions. In creating unsymmetrical arrangements for the quasi-isotropic panels, either two or four plies needed to be removed from the laminate, which meant that it was not possible to include all four fibre orientations to create a similar symmetric quasi-isotropic lay-up. Hence, the 90° ply was removed entirely from the QI panels, resulting in multi-directional skins being used for the distal skin in combination with the quasi-isotropic face skin. All skin combinations were used for the carbon/epoxy systems, whereas only a basic study of varying the skin thickness of symmetrical cross ply panels was chosen for the E-glass/epoxy system.

The aluminium (5052) honeycomb core was obtained from Hexcel Distributors AIM, as well as directly from Hexcel. To analyse its influence over damage resistance and damage tolerance, three different densities of 70kg/m^3 , 110kg/m^3 and 135kg/m^3 were used, all with a cell size of $3/16''$ and thickness of 12.7mm. The adhesive used to bond the skin and core was VTA260, which again was supplied by UMECO Cytec, and like the prepreg was stored at -18° in a freezer in order maintain the shelf life, and

improve handling and cutting of the adhesive. The adhesive contains a mesh in order to prevent dripping of the adhesive during the elevated temperature in the cure cycle.

Bonding of the skins and the core material was done using two main steps, lay-up and curing of the skins, and the bonding of the cured skins to the honeycomb using a separate temperature cure cycle. Although it is possible to co-cure skin and core materials, saving on time and resource, in the case of these material systems, the skins can be susceptible to sagging in the cells of the honeycomb core causing the skin to dimple reducing its in-plane compressive performance, lending this method to other core types such as PVC foams, and also, the interfacial skin/core bond line can suffer from reduced strength compared to using an additional adhesive and cure cycle.

Due to the vast amount of specimens tested in this investigation, it was necessary to introduce a coding to help in identifying the ply orientation, thickness, symmetry, and core material through simple inspection. Below outlines the ID template for each panel, which will help identify the configuration of any specimen ID that may be referred to in latter chapters. The below ID is an example only, and does not refer to a specific panel:

PN-8/8CP-10J-A-ICR

The first identifier in the panel ID will signify the skin material and the core density used by the use of the initials of the assisting researcher. The second field refers to the number of plies, the symmetry of the skins, and the lay-up used. The third signifies the impact conditions the panel was subjected to by the target IKE selected for the test. For any panel that was tested in compression only to provide a baseline compressive strength, they were referenced to with OJ. The fourth field helped separate any repeated impact energies done on the same panel arrangements with a letter, i.e. A or B, if there were no duplicate energies in the test batch, this letter was omitted from the ID. Finally, for any panel that was preconditioned, the final assignment signifies what the precondition was. As mentioned, this investigation is to look into panels with the core removed, impacted and non-impacted, and panels with holes drilled in one or both skins. These will be identified as ICR (impact core removal), CR (core removal, no impact), 1H (drilled hole in 1 skin only) and 2H (holes drilled in both skins). Panels with no pre-condition had no fifth identifier.

Shown in Table 2.1.1 is the variance of panel properties tested over the years of this investigation and the associated undergraduate students' initials that will be included in the specimen ID. Here it can be seen what skin material and density of core was used, the number of total specimens and how they have been split into CAI, compression only, impact only and preconditioned panels.

Table 2.1.1. Matrix of all panels manufactured and tested since 2007, including previous project work and all work encompassed in this investigation

				34-700/LTM45											PPG1062 /LTM26
Sandwich type	Skin lay-up	No of plies in skin	Core density	Previous projects		10-11			11-12			12-13	13-14		12-13
				Hill	Campbell	NC	CI	LB	DJ	JL	RM	MB	AR	HD	SG
Symmetrical	CP	8	70kg/m ³	23/2/11/-			5/0/2/2							8/-/2/6	8/2/5/-
		8	110kg/m ³										8/2/5/-		
		8	135kg/m ³								10/2/3/-	8/2/5/-			
		16	70kg/m ³				12/2/4/2								8/2/5/-
	QI	8	70kg/m ³								14/2/6/-				
		16	70kg/m ³				6/2/2/-				10/2/4/-				
Unsymmetrical	CP	8/6	70kg/m ³		12/2/4/-	10/2/6/2				12/2/6/-				8/-/2/6	
		8/6	110kg/m ³										8/2/5/-		
		8/6	135kg/m ³								10/2/4/-	8/2/5/-			
		16/12	70kg/m ³		12/2/4/-	10/2/5/2				10/2/4/-					
	QI/MD	8/6	70kg/m ³						12/2/5/2						
		16/12	70kg/m ³						10/2/5/-						

A/B/C/D: A – total no of specimens, B – no of control specimens for in-plane compression, C – no of CAI specimens & D – no of in-plane compression specimens in other preconditions

2.1.1. Unavailable mechanical properties of skin materials

In order to start to assess the differences in performance in the damage resistance and tolerance between the thin and thick panels and cross ply, quasi-isotropic and multi-directional panels it is important to have the base material properties for the different skin lay-ups and thicknesses available. Properties for UD and CP skins made of 34-700/LTM45 have already been determined by Lloyd [120] and Hill [1], therefore, in this study, the effective mechanical properties of 34-700/LTM45 MD laminates in tension, compression, flexure, and in-plane shear have been determined experimentally and predicted theoretically to aid an analysis of subsequent in-plane compression results by adding to the database of material properties already determined.

Classical Lamination Theory (CLT)

To make the calculations using classical lamination theory (CLT), a number of assumptions were made. These assumptions are summed up in the Kirchoff-Love hypothesis. It was also assumed that the composite laminate is homogenous on a macroscopic scale.

To start the calculation it was required to calculate the reduced stiffness matrix $[Q_{ij}]$, in which $[Q_{ij}]$ is defined in Equation 2.1.1, and is obtained from the orthotropic stress strain relationship.

$$[Q_{ij}] = \begin{bmatrix} Q_{11} & Q_{12} & 0 \\ Q_{21} & Q_{22} & 0 \\ 0 & 0 & Q_{66} \end{bmatrix} \quad (2.1.1)$$

The terms in the reduced stiffness matrix are defined in Equations 2.1.2-2.1.5.

$$Q_{11} = \frac{E_1}{1-\nu_{12}\nu_{21}} \quad (2.1.2)$$

$$Q_{22} = \frac{E_2}{1-\nu_{12}\nu_{21}} \quad (2.1.3)$$

$$Q_{12} = \frac{\nu_{21}E_1}{1-\nu_{12}\nu_{21}} = Q_{21} \quad (2.1.4)$$

$$Q_{66} = G_{12} \quad (2.1.5)$$

Where the reciprocal relationship is given by

$$\frac{\nu_{12}}{E_1} = \frac{\nu_{21}}{E_2} \quad (2.1.6)$$

For unidirectional tape or prepreg of the type being considered here, E_1 is much greater than either E_2 or G_{12} because the former is a 'fibre dominated' property, while the latter are 'matrix dominated'. For

UD tape, ν_{12} is matrix dominated whereas contraction implied in ν_{21} is resisted by the fibres and so is much smaller than the former. Properties of the UD 34-700/LTM45 tape can be found in Table 2.1.2 [120] **Error! Reference source not found.**

Table 2.1.2. Material properties of 34-700/LTM45-EL UD tape

UD prepreg 34-700/LTM45-EL properties					
E_1	E_2	G_{12}	ν_{12}	ν_{21}	Ply thickness
127 GPa	9.1 GPa	5.6 GPa	0.31	0.022	0.128mm

Using Equations 2.1.2-2.1.5, the reduced stiffness matrix for a single UD 0° ply can be calculated to give:

$$(\bar{Q}_{ij})_0 = \begin{bmatrix} 127.886 & 2.841 & 0 \\ 2.841 & 9.105 & 0 \\ 0 & 0 & 5.600 \end{bmatrix} GPa$$

Since the laminates used in this investigation comprise of multiple differing angles, it was necessary to transform the reduced stiffness matrix, through 90° , and $\pm 45^\circ$, to be able to incorporate the properties of all plies which make up the laminates used. This is done using Equations 2.1.7-2.1.12.

$$\bar{Q}_{11} = Q_{11} \cos^4 \theta + 2(Q_{12} + 2Q_{66}) \sin^2 \theta \cos^2 \theta + Q_{22} \sin^4 \theta \quad (2.1.7)$$

$$\bar{Q}_{12} = (Q_{11} + Q_{22} - 4Q_{66}) \sin^2 \theta \cos^2 \theta + Q_{12}(\sin^4 \theta + \cos^4 \theta) \quad (2.1.8)$$

$$\bar{Q}_{22} = Q_{11} \sin^4 \theta + 2(Q_{12} + 2Q_{66}) \sin^2 \theta \cos^2 \theta + Q_{22} \cos^4 \theta \quad (2.1.9)$$

$$\bar{Q}_{16} = (Q_{11} - Q_{12} - 2Q_{66}) \sin \theta \cos^3 \theta + (Q_{12} - Q_{22} + 2Q_{66}) \sin^3 \theta \cos \theta \quad (2.1.10)$$

$$\bar{Q}_{26} = (Q_{11} - Q_{12} - 2Q_{66}) \sin^3 \theta \cos \theta + (Q_{12} - Q_{22} + 2Q_{66}) \sin \theta \cos^3 \theta \quad (2.1.11)$$

$$\bar{Q}_{66} = (Q_{11} + Q_{22} - 2Q_{12} - 4Q_{66}) \sin^2 \theta \cos^2 \theta + Q_{66}(\sin^4 \theta + \cos^4 \theta) \quad (2.1.12)$$

Applying this transformation gives the following transformed reduced stiffness matrices for 90° and $\pm 45^\circ$ plies:

$$(\bar{Q}_{ij})_{90} = \begin{bmatrix} 9.16 & 2.81 & 0 \\ 2.81 & 127.87 & 0 \\ 0 & 0 & 5.60 \end{bmatrix} GP$$

$$(\bar{Q}_{ij})_{45} = \begin{bmatrix} 41.27 & 30.07 & 29.68 \\ 30.0625 & 41.27 & 29.68 \\ 29.68 & 29.68 & 32.85 \end{bmatrix} GPa$$

$$(\bar{Q}_{ij})_{-45} = \begin{bmatrix} 41.27 & 30.07 & -29.68 \\ 30.0625 & 41.27 & -29.68 \\ -29.68 & -29.68 & 32.85 \end{bmatrix} GPa$$

It was then possible to calculate the extensional and bending stiffness matrices for the MD laminates used in this investigation. Assuming constant ply thickness after cure, t_k , the extensional and bending stiffness matrices were calculated using Equation 2.1.13-2.1.14.

$$A_{ij} = \sum_{k=1}^n (\bar{Q}_{ij})_k t_k \text{ GPa} \cdot \text{mm} \quad (2.1.13)$$

$$D_{ij} = \frac{1}{3} \sum_{k=1}^n (\bar{Q}_{ij})_k t_k (t_k^2 + 3z_k z_{k-1}) \text{ GPa} \cdot \text{mm}^3 \quad (2.1.14)$$

Where k is a counter for the number of plies in the stack, and was counted from the bottom laminate, i.e. in the negative coordinate, and z is the distance from the neutral axis.

With these matrices calculated, certain mechanical properties of laminates with a lay-up of other than UD can be estimated using the CLT. A longitudinal tensile modulus can be predicted using Equation 2.1.15.

$$E_x = \frac{A_{11}A_{22} - A_{12}^2}{tA_{22}} \quad (2.1.15)$$

Using the inverse of the bending matrix, D_{ij} , the flexural modulus can be calculated using Equation 2.1.16.

$$E_f = \frac{12}{D'_{11}t^3} \quad (2.1.16)$$

The pure in-plane shear modulus can be calculated using Equation 2.1.17.

$$G_{12} = \frac{E_x}{2(1+\nu_{xy})} \quad (2.1.17)$$

These predictions are summarised in Table 2.1.3 for CP, QI and MD thick and thin laminates.

Table 2.1.3. Summary of CLT calculations

Mechanical Property	8 ply CP, [0/90] _{2s}	16 ply CP, [0/90] _{4s}	8 ply QI, [45/0/-45/90] _s	16 ply QI, [45/0/-45/90] _{2s}	6 ply MD, [45/0/-45] _s	12 ply MD, [45/0/-45] _{2s}
Tensile modulus, GPa	68.40	68.40	49.97	49.97	55.73	55.73
Flexural modulus, GPa	90.60	79.51	51.17	53.03	45.10	53.27
Poisson's ratio, ν_{xy}	0.041	0.041	0.299	0.299	0.299	0.299
IPS modulus, GPa	-	-	-	-	9.35	9.35

Tensile properties of multi-directional laminates

A tensile test of MD laminates was conducted according to the ASTM D3039 standard [113]. To avoid an influx of grip failures, the coupons were end tabbed with aluminium, in order to transfer the force of the gripping jaws into tensile force in the coupon. To calculate the tensile strength (F_{ut}) of the test, the load at failure (P_{max}) was recorded, and using the cross sectional area of the coupon at the mid span, Equation 2.1.18 was used.

$$F_{ut} = P_{max}/A \quad (2.1.18)$$

To calculate tensile modulus, Equation 2.1.19 was used in conjunction with the stress/strain relationship.

$$E_{chord} = \frac{\Delta\sigma}{\Delta\varepsilon} \quad (2.1.19)$$

The linear strain up to 0.25% strain was used in a modulus calculation. A typical example of the stress strain curve is shown in Figure 2.1.1.

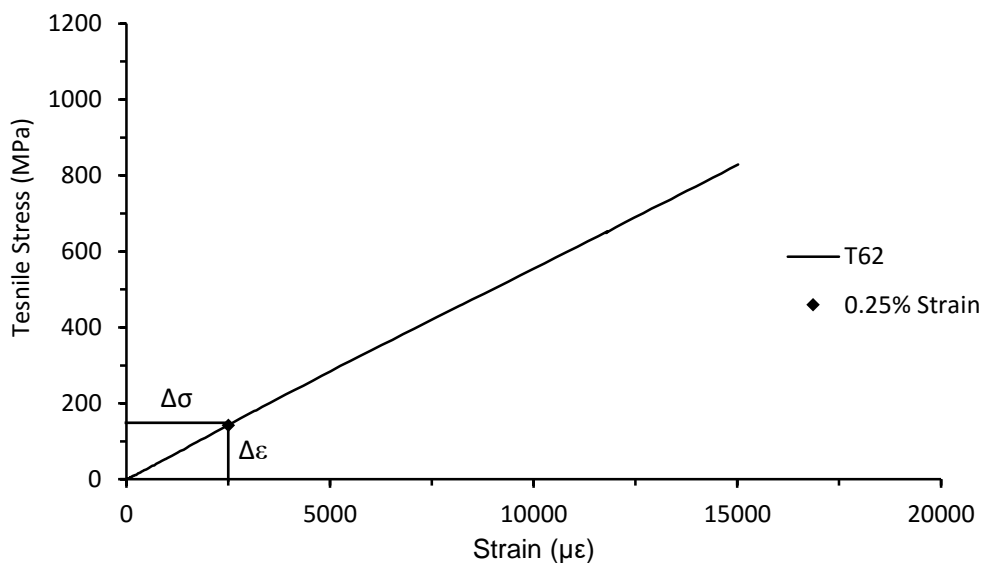


Figure 2.1.1. Tensile stress/strain response from 6 ply multi-directional laminate showing chord point used in modulus calculation, specimen T62

The results from the tests are shown in Table 2.1.4.

Table 2.1.4. Tensile test results for 6 and 12 ply multi-directional laminates

Specimen ID	Length (mm)	Width (mm)	Thickness (mm)	Failure Load (kN)	Tensile Strength (MPa)	Tensile Modulus (GPa)	Failure location from quadrants from left tab
T61	110.28	26.21	0.79	20.68	998.56	59.18	3
T62	109.91	26.04	0.78	16.84	828.91	56.89	1
T63	110.12	26.76	0.78	15.68	751.34	61.48	1
T64	110.06	26.96	0.79	20.41	958.27	60.20	1
T65	110.36	26.4	0.77	22.18	1091.01	60.47	3
T66	110.04	26.53	0.78	21.44	1036.13	62.61	3
T121	110.36	25.5	1.55	47.75	1208.17	-*	2
T122	110.82	25.24	1.5	40.74	1076.18	63.96	4
T123	110.5	25.51	1.51	42.43	1101.46	62.75	1
T124	110.29	25.86	1.49	39.26	1019.00	60.47	3
T125	110.01	25.36	1.54	37.06	948.96	61.14	1
T126	110.19	25.92	1.54	34.27	858.55	62.98	Under left tab

*- Strain gauge failure

The tensile mechanical properties of MD laminates are summarised in Table 2.1.5 along with those from UD and CP lay-ups.

Table 2.1.5. Tensile properties of UD, CP, and MD laminates

Mechanical Property	16 ply UD, [0] ₁₆	8 ply CP, [0/90] _{2s}	6 ply MD, [45/0/-45] _s	12 ply MD, [45/0/-45] _{2s}
Tensile Strength, MPa	1956.3±89.5	1060	944.04±129.34	1035.39±122.39
Tensile Modulus, GPa	126.7±4.0	68.69	60.03±1.80	61.86±1.45
Reference	[120]	[1]	Current	Current

As seen from the table, the tensile strength of the MD laminates suffers from a wide scatter, which was down to issues encountered in the set up and alignment of the tensile coupons. Failures in some of the coupons were indicative of premature failure due to gripping influences, two examples are shown in Figure 2.1.2. Issues with the gripping jaws and ease of coupon alignment during the set-up of the test resulted in stress concentrations in the tabbed regions or bending stresses in the gauge section, causing some of the specimens to fail prematurely, resulting in the observed scatter. It is of note as well that there is no significant difference between the strength and moduli of the thin and thick laminates, indicating no thickness effects in the tensile properties.



Figure 2.1.2. Failed specimens T125 and T126 showing premature failure modes (a) failure near end tab (b) top ply sheared off under tab

Compressive properties of multi-directional laminates

Similarly, the compressive properties of the composite laminates in a multi-directional lay-up were determined according to the ASTM D3410 standard [114]. The standard uses coupons of 12.7mm x 6.4mm dimensions (with a span/depth ratio of 2 and a minimum overall length of 140mm) in a Celanese compression jig, shown in Figure 2.1.3, to limit the specimen buckling. Specimen failures recorded in the gauge section only were considered acceptable, though slipping in the tabbed regions occurred occasionally.

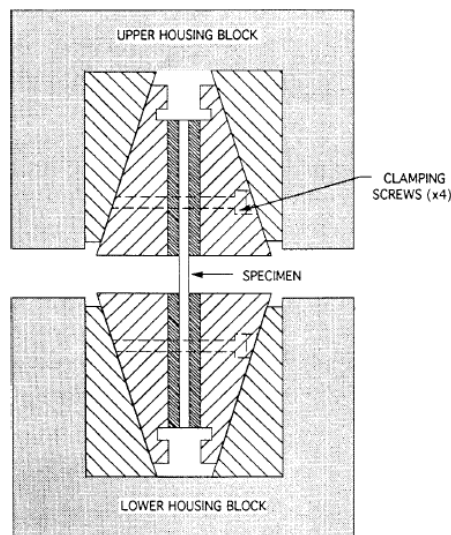


Figure 2.1.3. Celanese compression test jig used to obtain compressive strength and modulus

Compressive strength (F_{uc}) was calculated using Equation 2.1.18, and for the modulus of the material, the linear strain range up to 0.25% strain was used in the same way as in the tensile tests, as shown in Figure 2.1.4.

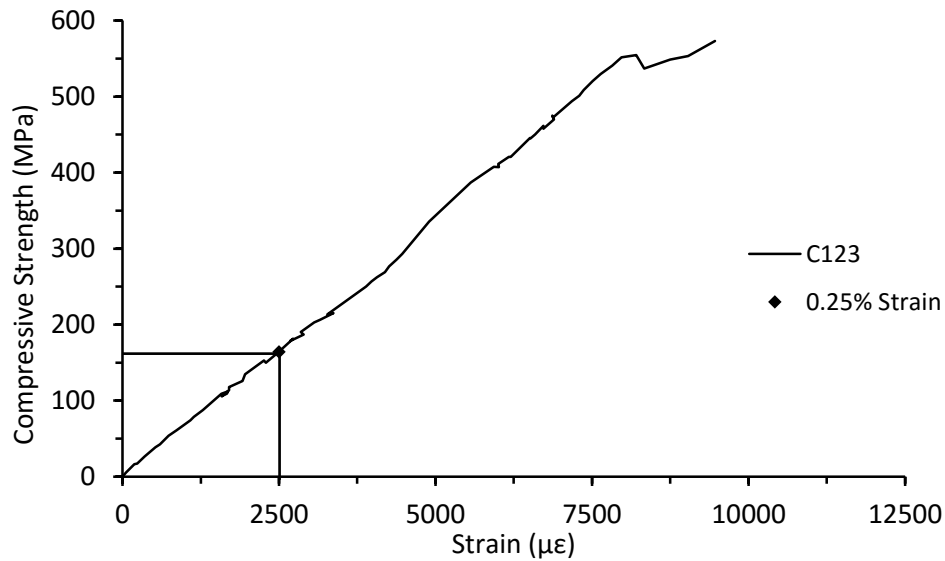


Figure 2.1.4. Compressive stress/strain response from 12 ply multi-directional laminate showing chord point used in modulus calculation, specimen C123

The results from the compressive tests are shown in Table 2.1.6.

Table 2.1.6. Compressive test results of 6 and 12 ply multi-directional laminates

Specimen ID	Length (mm)	Width (mm)	Thickness (mm)	Failure Load (kN)	Compressive Strength (MPa)	Compressive Modulus (GPa)
C61	13.34	7.55	0.78	1.93	328.12	49.08
C62	13.62	7.57	0.78	1.91	323.06	54.05
C63	12.46	7.67	0.78	2.15	359.86	42.02
C64	13.42	7.68	0.77	1.71	288.77	59.25
C65	13.41	7.58	0.79	2.13	355.72	65.63
C66	13.1	7.65	0.79	1.99	329.43	62.61
C121	13.42	7.14	1.52	5.94	547.15	65.55
C122	13.53	6.9	1.52	5.86	558.43	57.22
C123	13.2	6.17	1.52	5.38	573.26	65.75
C124	13.28	6.42	1.52	6.73	694.06	72.41
C125	13.47	7.25	1.52	6.90	626.43	-*
C126	12.81	7.7	1.51	7.30	628.10	58.78

*- Strain gauge failure

Using these methods the compressive data for MD laminates are summarised in Table 2.1.7, the average and standard deviations have been calculated to provide the spread of the data in the test groups.

Table 2.1.7. Compressive properties of UD, CP, and MD laminates

Mechanical Property	16 ply UD, [0]₁₆	8 ply CP, [0/90]_{2s}	6 ply MD, [45/0/-45]_s	12 ply MD, [45/0/-45]_{2s}
Compressive Strength, MPa	1032.0±5.9	548.78	330.83±25.70	604.57±55.58
Compressive Modulus, GPa	120.3±2.3	78.04	56.58±11.13	63.13±7.28
Reference	[120]	[1]	Current	Current

Flexural properties of multi-directional laminates via 3 point Bending

Flexural strength and modulus were determined using ASTM D790 standard [116]. During the test, the central deflection of the central loader and the force applied to the specimen were recorded. For the flexural strength, σ_f , the load at which the specimen achieved an acceptable failure was recorded, P, and was fed into Equation 2.1.20, along with specimen dimensions measured at the mid span of the gauge section, (b=width, d=thickness), to give the specimens flexural strength.

$$\sigma_f = \frac{\bar{M}E_x h}{2d} \quad (2.1.20)$$

For the flexural strain, since no strain gauges were bonded to the specimens, the nominal fractional change in the length of an element of the outer surface of the test specimen at mid-span where maximum strain, ε_f , would occur can be calculated for any deflection using Equation 2.1.21.

$$\varepsilon_f = \frac{6vd}{L^2} \quad (2.1.21)$$

In which v is deflection of the centre of the beam, L is the support span and d is the thickness, all of which are in mm. A typical flexural stress/strain response is shown in Figure 2.1.5. Maximum deflections when failure occurs were found to be on average 1.59±0.34mm for 6 ply laminates, and 2.02±0.17mm for 12 ply laminates.

The flexural modulus can be calculated as in previous material property tests using Equation 2.1.19. Due to the linear nature of the stress-strain response from all flexural specimens, the whole range of the response was used in the chord calculation, from the origin to the point failure occurred. The test results for both thin and thick specimens are shown in Table 2.1.8.

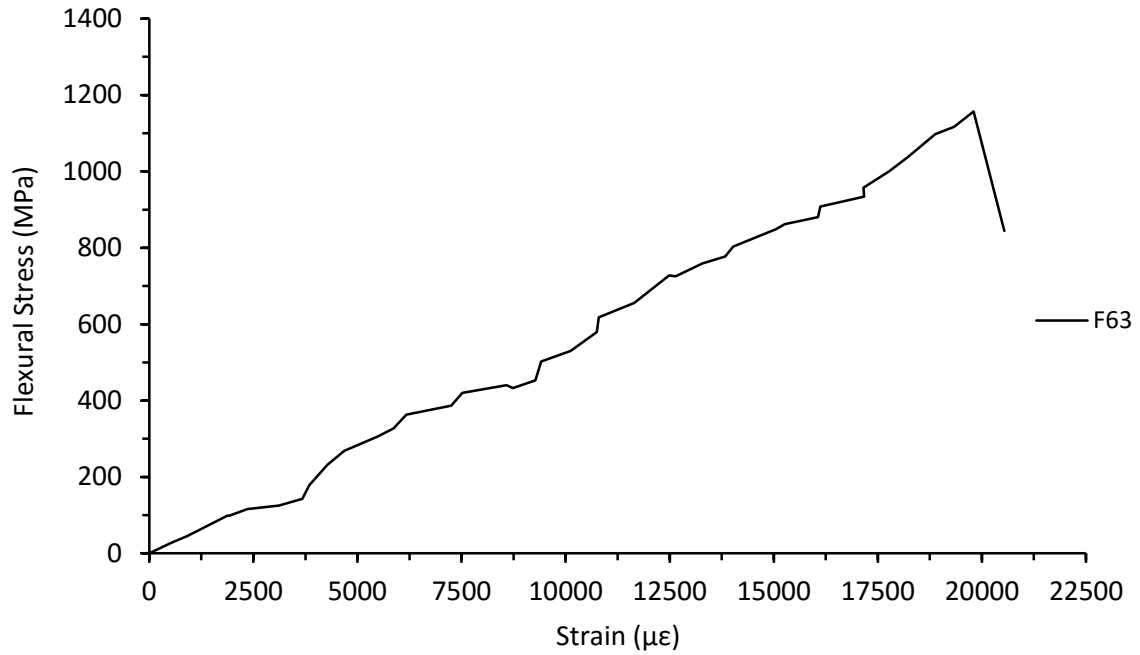


Figure 2.1.5. Flexural strength/strain response from 6 ply multi-directional laminate

Table 2.1.8. Flexure test results of 6 and 12 ply multi-directional laminates

Specimen code	Span (mm)	d (mm)	t (mm)	Flexural Strength (MPa)	Chord Modulus (GPa)	Displacement at failure
F61	15.21	4.38	0.77	1376.57	61.65	1.118
F62	15.63	3.73	0.77	1478.27	69.36	1.127
F63	18.45	3.88	0.76	1487.76	75.13	1.478
F64	18.30	3.90	0.76	1638.59	71.27	1.689
F65	18.34	3.74	0.79	1671.98	74.16	1.600
F66	18.71	4.73	0.78	1311.15	46.64	1.995
F67	17.84	4.13	0.77	1626.94	56.08	1.999
F68	17.94	3.86	0.76	1349.37	56.83	1.676
F121	30.16	3.86	1.54	1275.11	61.79	2.032
F122	30.60	3.11	1.51	1292.08	60.23	2.217
F123	29.87	3.72	1.53	1281.74	55.37	2.250
F124	30.41	3.07	1.50	1366.59	72.70	1.931
F125	30.32	3.88	1.52	1235.91	63.71	1.955
F126	30.10	3.72	1.52	1179.55	58.91	2.018
F127	30.29	3.24	1.52	907.23	35.60	1.685
F128	30.54	2.90	1.50	1261.39	59.76	2.188
F129	30.22	3.04	1.49	1127.98	57.98	1.987
F1210	30.34	3.30	1.50	1217.42	63.90	1.949

Using these methods the flexural data for CP and MD laminates is summarised in Table 2.1.9, the average and standard deviation has been calculated to provide the spread of the data in the test groups.

Table 2.1.9. Flexural properties of CP and MD laminates

Mechanical Property	8 ply CP, [0/90] _{2s}	12 ply CP, [0/90] _{3s}	16 ply CP, [0/90] _{4s}	6 ply MD, [45/0/-45] _s	12 ply MD, [45/0/-45] _{2s}
Flexural Strength, MPa	1140±142	1320±184	1160±1.0	1492.58±141	1214.50±126
Flexural Modulus, GPa	76.55±2.7	76.78±9.3	104.06±3.8	63.89±10.2	58.99±9.5
Reference	[1]			Current	

Theoretically, in a homogenous material, the tensile and flexural properties would be identical, due to the reliance on tensile failure in both test cases. However, it is likely that the gripping problems experienced in the tensile tests mentioned in the previous sections would account for the disparity between the two strengths.

In-plane Shear properties of multi-directional laminates

An in-plane shear response of laminates was achieved by the $\pm 45^\circ$ off-axis tensile shear test as described in ASTM 3518 [115]. Essentially the set-up of the test was the same as ASTM D3039 for the tensile properties, however in this test case the 0° ply was orientated to the transverse direction, as shown in Figure 2.1.6, and the longitudinal and transverse strain in the specimen was measured in order to determine the in-plane properties.

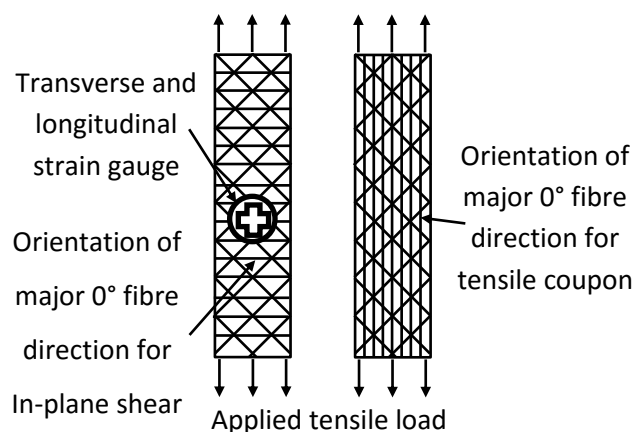


Figure 2.1.6. Difference in fibre orientation between in-plane shear test coupon (left) and tensile test coupon (right)

Once the test had been carried out, Equation 2.1.22 could be used to calculate the maximum shear stress in the specimen, and hence the ultimate in-plane shear strength, τ_{12} , of the specimen.

$$\tau_{12} = \frac{P}{2A} \quad (2.1.22)$$

Where, P is the failure load and A is the cross sectional area in the centre of the gauge section. The shear strain was calculated using the recorded strain data. Given the longitudinal, ε_l , and the transverse, ε_t , strain, Equation 2.1.23 gives the shear strain.

$$\gamma_{12} = \varepsilon_l - \varepsilon_t \quad (2.1.23)$$

A typical stress/strain response for a 6 ply multi-directional laminate is shown in Figure 2.1.7.

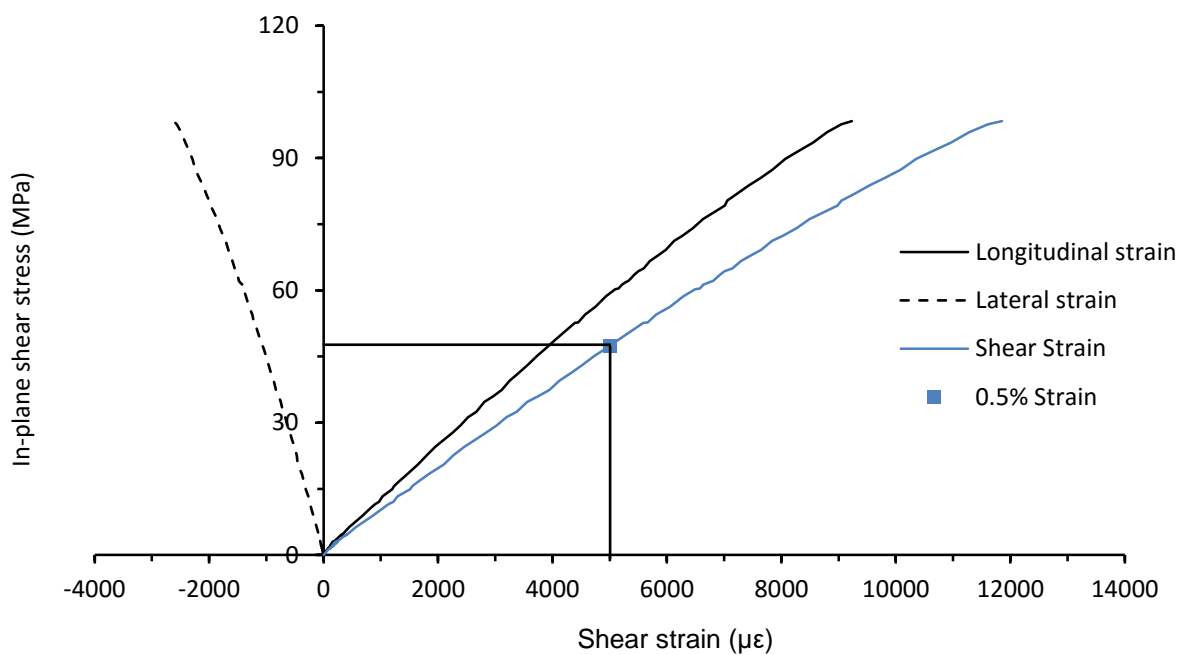


Figure 2.1.7. In-plane shear stress vs. longitudinal, transverse and shear strain responses for specimen IPS61

Using the shear stress-strain relationship, the modulus can be obtained from the chord at 0.5% strain. Poisson's ratio can also be obtained using Equation 2.1.23, using the longitudinal and transverse strain readings at 3000 $\mu\epsilon$ and 1000 $\mu\epsilon$.

$$\nu = \frac{-\Delta\varepsilon_t}{\Delta\varepsilon_l} \quad (2.1.23)$$

The results of the in-plane shear test in all thin and thick MD laminates are shown in Table 2.1.10.

Table 2.1.10. In-plane shear test results of 6 and 12 ply multi-directional laminates

Specimen code	l (mm)	d (mm)	t (mm)	IPS Strength (MPa)	IPS Modulus (GPa)	Poisson's Ratio
IPS61	110.41	25.35	0.76	98.36	9.48	0.269
IPS62	110.16	24.99	0.77	109.79	10.00	0.353
IPS63	110.59	25.73	0.78	111.12	9.83	0.287
IPS64	110.69	24.08	0.77	109.04	9.98	0.299
IPS121	111.04	25.49	1.53	118.03	10.55	0.288
IPS122	110.47	25.52	1.5	105.68	9.60	0.289
IPS123	110.86	25.39	1.53	94.67	10.27	0.295
IPS124	110.19	24.95	1.5	116.71	10.66	0.297

Using these methods the in-plane shear strength and modulus data for MD laminates is summarised in Table 2.1.11, the average and standard deviation has been calculated to provide the spread of the data in the test groups.

Table 2.1.11. In-plane shear properties of UD and MD laminates

Mechanical Property	16 ply UD, [0] ₁₆	6 ply MD, [45/0/-45] _s	12 ply MD, [45/0/-45] _{2s}
In-plane Shear Strength, MPa	72.5±1.8	107.08±5.88	108.77±10.91
In-plane Shear Modulus, GPa	-	9.82±0.24	10.27±0.47
Poisson's Ratio	-	0.302±0.036	0.292±0.004
Reference	[120]	Current	Current

Interlaminar Shear Properties

As Interlaminar shear properties are a major governing factor in the panel's resistance to transverse through the thickness loading, it is important to assess the strength capabilities of the different orientations of skins. However, due to the nature of the ILS testing, outlined in ASTM D2344 [112], the laminate thickness was limited to a minimum of 2.0mm. The thickness has a minimum to avoid difficulties in testing the very small specimens that would result from these thin laminates. As it is limited by the standard, it was not feasible to test 6, 8 or 12 ply laminates. However, background research suggests that the ILS strength (ILSS) has a small amount of variation with a changing thickness [1]. In this way, tests that have been carried out in previous research projects [1,120], will provide adequate values of 66.3MPa for ILSS for all laminate thicknesses. The research suggests that the laminates with lower numbers of plies will actually have a slightly higher ILSS, so the value used from the thicker laminates will be an adequate lower bound approximation.

Mechanical property summary

Below, in Table 2.1.12, is a summary of all mechanical properties of all laminates used in this investigation, as well as manufacturing data and CLT theory predictions for comparison.

Table 2.1.12. Summary of all mechanical properties of UD, CP, and MD laminates

Mechanical Property	16 ply UD, [0] ₁₆	8 ply CP, [0/90] _{2s}	12 ply CP, [0/90] _{3s}	16 ply CP, [0/90] _{4s}	6 ply MD, [45/0/-45] _s	12 ply MD, [45/0/-45] _{2s}
Tensile Strength, MPa	1956.3±89.5	1060	-	-	944.04±129.34	1035.39±122.39
Tensile Modulus, GPa	126.7±4.0	68.69	-	-	60.03±1.80	61.86±1.45
Compressive Strength, MPa	1032.0±5.9	548.78	-	-	330.83±25.70	604.57±55.58
Compressive Modulus, GPa	120.3±2.3	78.04	-	-	56.58±11.13	63.13±7.28
Flexural Strength, MPa	-	1140±142	1320±184	1160±1.0	1116.51±107.23	1145.93±90.09
Flexural Modulus, GPa	-	76.55±2.7	76.78±9.3	104.06±3.8	48.08±7.60	57.50±5.21
In-plane Shear Strength, MPa	72.5±1.8	-	-	-	107.08±5.88	108.77±10.91
In-plane Shear Modulus, GPa	-	-	-	-	9.71±0.26	10.08±0.48
Poisson's Ratio	-	-	-	-	0.302±0.036	0.292±0.004
Reference	[120]	[1]		Current		

2.1.2. Core materials and mechanical properties

Three aluminium honeycomb cores with CR-PAA and CR III coating used in this investigation, all from Hexcel, had a density of 70, 110 and 135 kg/m³. Below, in Table 2.1.13, are the mechanical properties of the three cores. The designation of each honeycomb material is in the format of Density (pcf)-Cell Size (inches)-Foil thickness (inches), as supplied by the manufacturer.

Table 2.1.13. Mechanical properties of Aluminium 5052 honeycomb core [123]

Honeycomb designation	Density (kg/m ³)	Compressive				Plate Shear			
		Bare Strength (MPa)	Stabilised		Crush Strength	L-direction		W-direction	
			Strength (MPa)	Modulus (MPa)		Strength (MPa)	Modulus (MPa)	Strength (MPa)	Modulus (MPa)
4.4-3/16"-0.0015"	70	3.59	3.79	1000	1.72	2.28	469	1.48	207
6.9-3/16"-0.0025"	110	7.72	8.10	1965	3.96	4.07	786	2.59	320
8.1-3/16"-0.003"	135	11.03	11.86	2413	5.17	5.00	931	3.31	372

During the handling of the honeycomb core it was imperative to ensure that none of the cell walls that will feature in the sandwich panel were damaged or dented. Any sections of honeycomb that were found to contain such defects, shown in Figure 2.1.8, were disregarded. Also, minimal contact with human skin was to be insured to reduce the chances of grease being left on the surface.

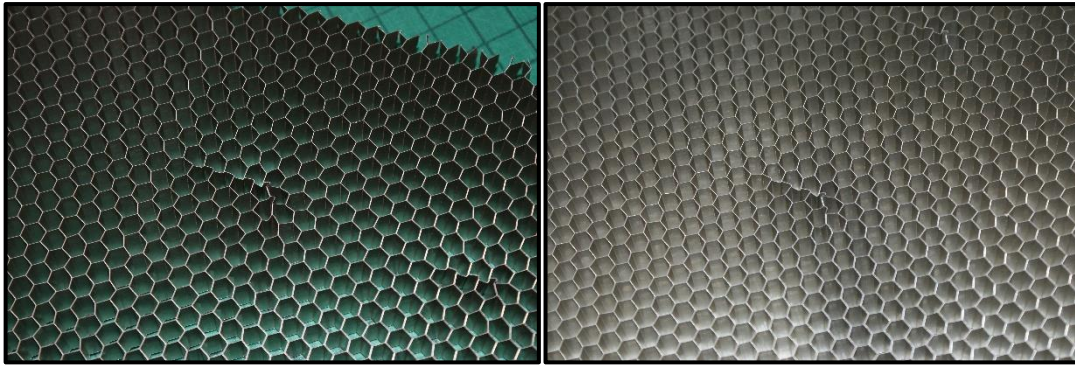


Figure 2.1.8. Examples of core defects in honeycomb material from handling, storage or manufacturing

To ensure these did not become factors, and also to help with the quality of the adhesive bond between core and skin at the edges of the panels, the honeycomb was cut into 340 x 340mm pieces to allow for a 20mm border on all sides protruding from the edge of the composite skin to allow for ease of handling. The honeycomb was cut with a Stanley knife, ensuring care was taken not to drag the blade through the material, causing major distortion of the cut cells and the surrounding areas. This could be avoided by scoring the core first, and also ensuring that the blades of the knife were regularly changed and kept sharp. Also, to make cutting easier and avoiding unnecessary damage, nodal walls were to be avoided when cutting if possible. The nodal walls of the honeycomb are where adjacent cells share a joined wall, and the thickness is double that of the free walls, making it harder to cut through.

2.1.3. Adhesives

The adhesive used was VTA260 from Cytec. The adhesive is critical in the sandwich construction, as it must provide great enough strength to ensure that the core and skin interface does not suffer from debonding under loading. The mechanical properties of the adhesive from the manufacturer are summarised in Table 2.1.14.

Table 2.1.14. Mechanical properties of adhesive VTA260 as supplied by Umeco Cytec [122]

Mechanical Property	Umeco VTA260
Areal Weight (g/m ²)	313
Lap Shear Strength (MPa) (ASTM D3165)	28-36
Climbing Drum Peel Strength (Nm/m) (ASTM D1781-76)	58-78
Flatwise tensile (MPa)	7.4-7.8

The data is given as a range due to the different cure cycles that the adhesive can be put through, the range covers cure temperatures of 65-120°C. The same adhesive was used in all panel configurations, to ensure no variation in the skin/core interaction.

2.2. Skin lamination and cures

Each laminate skin was manufactured at a size of 300 x 300mm, to allow 2 specimens to be cut out from each panel. Cutting and laying up of the prepreg plies was the first stage of the sandwich panel manufacturing procedure. Both carbon (34-700/LTM45) and E-glass (PPG1062/LTM26) UD prepreg tapes have only a 24hr shelf life at room temperature and could become tacky during cutting, handling and laying-up. Trapping of particulates between the ply layers, as well as moisture, can cause problems to the integrity and quality of the skin. Therefore the first stage of this procedure was to clean all surfaces of the lay-up area with propanol, to rid the surfaces of all dust, grease and debris. Then the prepreg drum was taken out of the freezer and the prepreg was fed through a guillotine, and a piece of 300mm long was cut for the 0° and 90° plies, shown in Figure 2.2.1, and with a Stanley knife and ruler for the ±45° plies. The cut plies were returned to the freezer temporarily to allow easier removal of the protective papers on the ply, whenever needed.

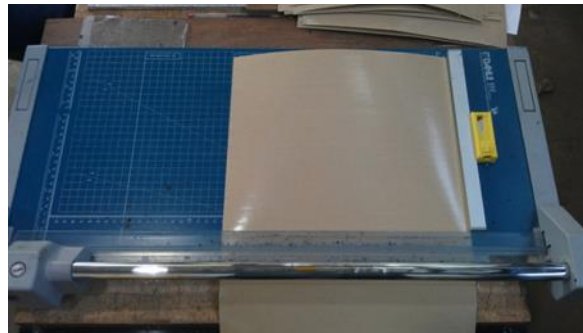


Figure 2.2.1. Prepreg cutting on the guillotine

Unlike the 0° or 90° plies, due to the width of the supplied carbon prepreg tape, a single piece 45° ply of the required 300x300mm size was constructed as shown in Figure 2.2.2, using the cutting procedure outlined provides three types of pieces, two of which could be used to form the required 45° ply. The primary piece ('A') provided the main body of the 45° ply, albeit with a corner piece missing. The secondary piece ('B') provided a piece to complete the whole 300x300mm 45° ply when combined with 'A'. Finally, parts labelled 'C' were waste. Approximately 30% of the prepreg has been wasted in this process of cutting angle plies; a minimum given the prepreg and required ply geometries.

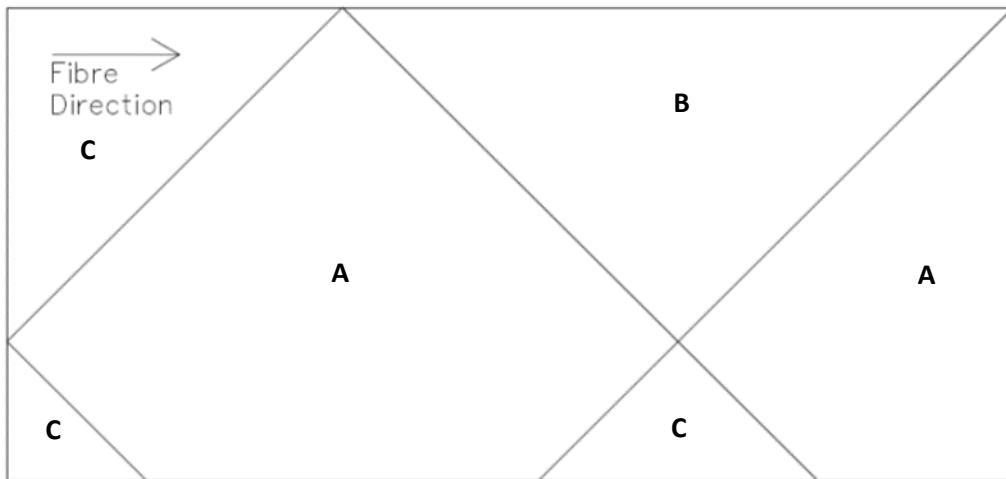


Figure 2.2.2. Cutting plan for 45° plies (A: primary, B: secondary, C: waste)

Once the two parts of the 45° ply were cut from the prepreg roll, they were aligned and fixed together using adhesive tape in preparation for a final cut (Figure 2.2.3).

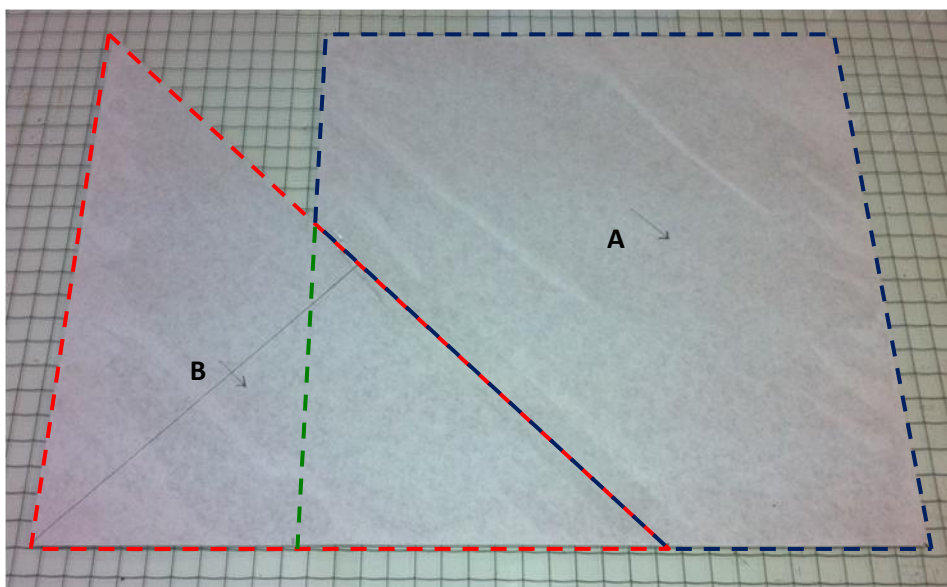


Figure 2.2.3. Alignment of pieces A and B creating 45° ply joined temporarily with tape

A final cut was then made using a knife along the green line in Figure 2.2.3, providing the final 300x300mm 45° ply observed in Figure 2.2.4. The piece with the red outline is set aside as waste.

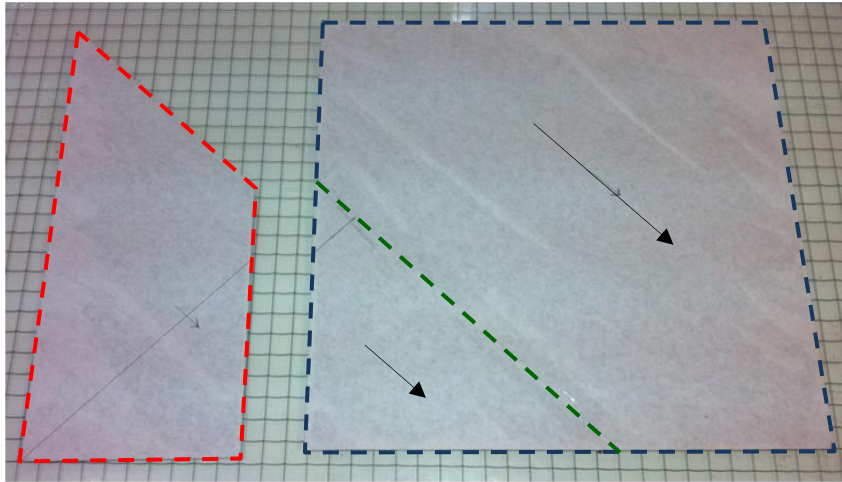


Figure 2.2.4. Picture showing completed 45° ply

It is important to note that the fibres were not broken using the method above, ensuring that performance compared to a single piece ply was not compromised.

Once all plies were cut up, their respective fibre orientations were marked on the protection paper of the ply sheet, arranged in the desired stacking sequence and returned to the freezer to reduce the resin tackiness. The lay-up procedure could be started with the preparation of a tick sheet, as shown in Table 2.2.1.

Table 2.2.1. Tick sheet examples for thin cross ply and quasi-isotropic panels

Layer	Orientation	Inserted?
1	0	
2	90	
3	0	
4	90	
5	90	
6	0	
7	90	
8	0	

Layer	Orientation	Inserted?
1	45	
2	0	
3	-45	
4	90	
5	90	
6	-45	
7	0	
8	45	

Using tick sheets to mark off each ply as it was stacked reduced the chances of wrong orientations or missing out plies. It was also common practice to create sets of sub laminates, to eliminate compounding lay-up mistakes throughout the panel. To ensure the plies were stacked in the right orientation, a right angled metal guide on the glass lay-up table was used to ensure the plies were stacked accurately on top of each other, shown in Figure 2.2.5.

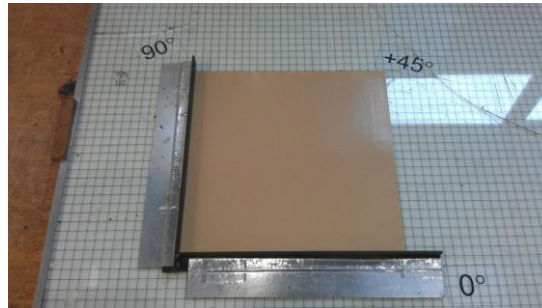


Figure 2.2.5. Angle guide on glass layup table with plies in situ

The completed laminate stacks were cured in an autoclave. This stage applied pressure, temperature and a vacuum to cure and consolidate the laminate stacks with a controlled single sequence. Before the laminate stacks were cured, they were removed from the freezer to defrost; this was to minimize moisture from being trapped in the cured panel. The manufacturer’s recommended single cure cycles are shown in Figure 2.2.6 for carbon and E-glass laminates.

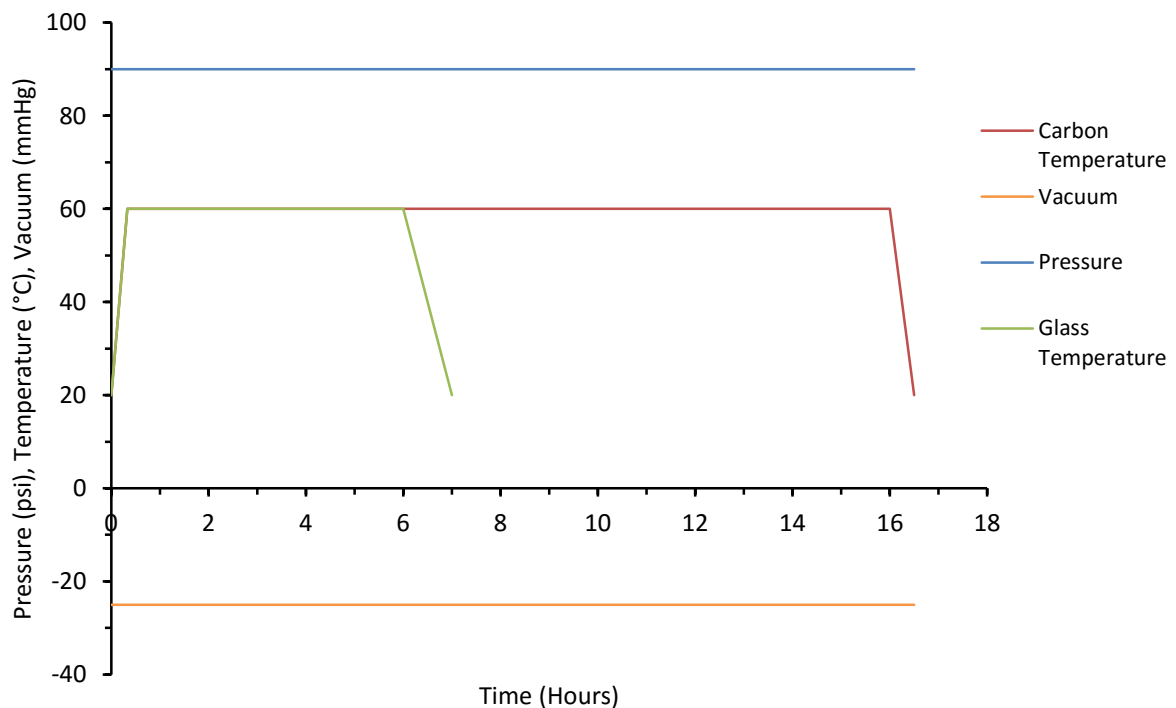


Figure 2.2.6. Autoclave cure cycle for PP1062/LTM26 and 34-700/LTM45-EL

The basic program details for the autoclave's controller was a 2°C/min temperature ramp rate, the dwell temperature was 60°C and the dwelling period was either 6 (for LTM26) or 16 hours (for LTM45). The pressure applied was 90psi and the vacuum that was required was -25mmHg. Maintaining the 90psi and vacuum was crucial to the consolidation of the laminate stack, during the preparation of the autoclave, extra care and attention was given to the seals of the autoclave lids, making sure that debris or creases in the bagging film did not allow air to escape from the chamber, causing a drop in pressure and vacuum. After the cycle was completed, the temperature receded naturally, and the pressure and vacuum were released manually.

The autoclave required a number of consumable and non-consumable materials to cure the panel effectively. Shown below, in Figure 2.2.7, is a diagrammatic representation of the bagging materials and their order of stacking in the autoclave.

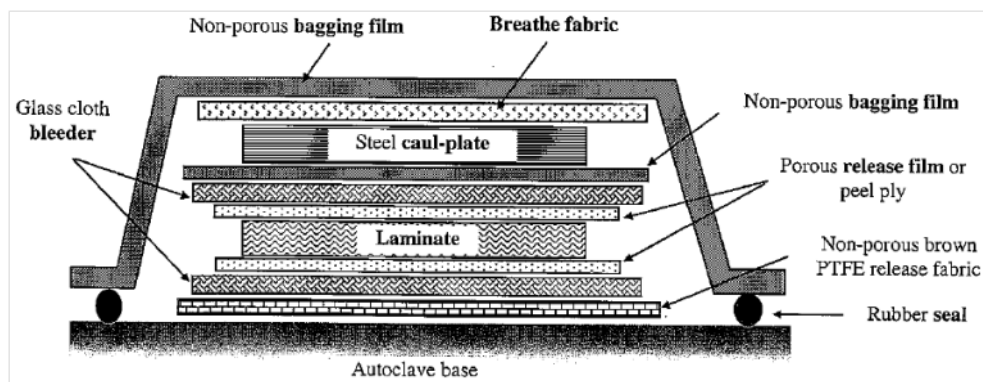


Figure 2.2.7. Diagrammatic representation of order of consumable materials used in autoclave cure process [124]

Before the materials were placed into the autoclave, the base and lid of the autoclave were cleaned using propanol, as well as the peel plies before they were stuck to the laminate. The bottom layer of non-porous brown PTFE release fabric provided a smooth surface on the bottom of the autoclave, so no blemishes or imperfections from the base of the autoclave had an effect on the surface of the panel, whilst ensuring no bled resin stuck to the bottom surface of the autoclave. The next layers of the bleeder cloths absorbed the resin bled throughout the laminate consolidation, the nylon cloths were thin enough to ensure that too much resin wasn't drawn from the panel which would create a resin starved laminate surface, but thick enough to ensure that the excess resin didn't spill into the vacuum pump mechanism of the autoclave. The number of bleeder cloths used depended on the thickness of the panel, with 2 bleeder cloths for the thin skins (8 or 6 ply laminates), and 4 bleeder cloths for the thicker skins (16 or 12 ply laminates). The next layer in between the bleeders was the peel plies, which were directly applied to the surface of the laminate. They ensured that all bagging

materials could be separated from the cured laminates at the end of the cure process, whilst allowing the resin to bleed through the pores in the peel ply. On top of these layers was a sheet of non-porous bagging film, which facilitated the protection of the machined surface of the steel caul plate, which was placed on top of the bagging film. The caul plate provided a flat surface to give a smooth finish to the panel, as well as evenly distributing the pressure to properly consolidate the laminate stack. On top of the caul plate, was a layer of breather fabric, allowing proper air circulation when applying the vacuum, as well as protecting the outer bagging film from splitting or puncturing on the caul plate edges. Care was taken over the storage of the top layer of bagging film whilst the autoclave was not being used, it was found on numerous occasions that a small slit or hole in the bagging film layer would allow the pressurised air above the bagging materials to rush through the bagging film, reducing drastically the quality of the vacuum.

With the bagging materials prepared and placed in the autoclave (Figure 2.2.8(a)), the lid was secured on to the autoclave using 3 steel cross members, and bolted down using 6 high tensile steel bolts, tightened, using a torque wrench, to 28Nm, to ensure the seals were not irreversibly damaged (Figure 2.2.8(b)).

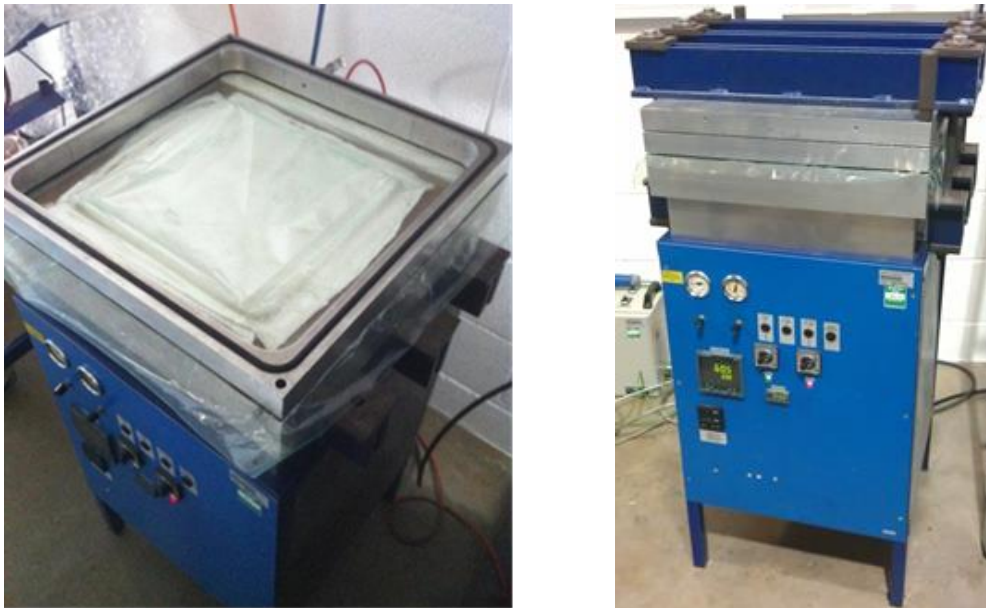


Figure 2.2.8. (a) Autoclave with lid off showing bagging film and breather layers (b) autoclave with steel cross members held in place by bolts

After the curing cycle in the autoclave, the cured laminate was marked with its lay-up, number of plies and the 0° direction as shown in Figure 2.2.9.



Figure 2.2.9. Example of panel marking

Before the cured laminate could be bonded to honeycomb core, its edges needed to be trimmed using the wet radial diamond edged grinder, shown in Figure 2.2.10. Trimming the skins was necessary due to the need to establish precisely the 0° direction, as well as removing uneven skin thicknesses created at the edge of the consolidated panel area. Once trimmed, the panel was then cleaned using propanol to remove all grease and debris from the skin, to make sure the adhesive used made good contact with the skin.



Figure 2.2.10. Diamond edged radial saw

2.3. Sandwich panel bonding

Two trimmed skin laminates were bonded to the honeycomb core using the VTA260 adhesive in an oven sequentially. Additional materials required for the bonding process were a 300 x 300mm caul plate of about 9.0kg, additional 1kg weights, and a layer of bagging film and breather fabric to protect the honeycomb or the already bonded skin, both cut to 340 x 340mm. The required cure pressure of 0.1MPa was applied by the 10mm thick steel caul plate being placed on top of the sandwich construction with the additional weights stacked on top during the cure cycle. To calculate the amount of additional weight needed to generate the required cure pressure for the different core densities, the cross-sectional area of the honeycomb walls needed to be estimated by calculating the cross-sectional area of a single hexagonal element, taking into account of the element sharing with a neighbouring cell and multiplying this by the number of cells contained within the 300 x 300mm area of the panel. Each element consists of 2 nodal walls, and 4 free walls, shown in Figure 2.3.1. The nodal

walls are in the L-direction, and signify the 0° direction of the honeycomb. Each nodal wall is of two foil thicknesses. The free walls are a single thickness. It was assumed for this area calculation that all cells are uniform hexagons with wall length a_w and have perfect internal angles of 60° (θ_w). Given the cell width (b_w) of 3/16" (4.7625mm), the wall length can be calculated using Equation 2.3.1.

$$b_w = 2 a_w \sin \theta_w \quad (2.3.1)$$

A single cell element also has the thickness of each wall halved, since it shares this thickness with an adjacent cell. This means that the nodal walls will effectively have a single thickness and the free walls have half a thickness. Therefore to calculate the elemental surface area, Equation 2.3.2 is used.

$$A_{element} = 0.5 \times (4t_w a_w) + 2t_w a_w \quad (2.3.2)$$

To work out the amount of elements that will be contained in the area under the bonded skin, it was necessary to identify the likely amount of cells in each direction. From the honeycomb array shown in Figure 2.3.1, it can be seen that in the W-direction, the cells are linearly stacked on top of each other, and that the number of cells is equal to width of the array divided by the cell width, b_w . In the L-direction, it can be seen that in the way they are stacked, a cell can have one of two lengths of either $2a_w$ or a_w . Therefore the number of cells in the L-direction is equal to the length of the array divided by the average cell length of $1.5a_w$. Once the number of elements in the 300 x 300mm honeycomb sheet had been estimated, the cross-sectional area can be calculated by multiplying the number of elements in the array by the elemental cross-sectional area. Summarised in

Table 2.3.1 are the geometric properties of the three honeycombs used, as well as the results of the area and force calculations.

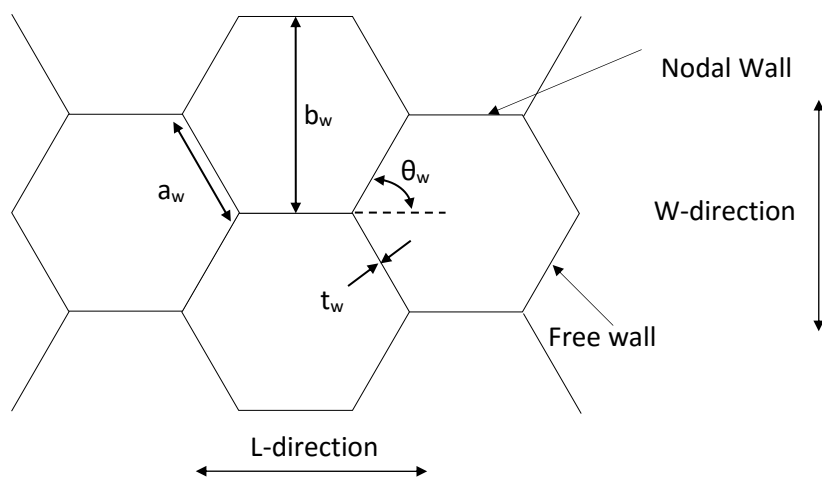


Figure 2.3.1. Diagrammatic representation of honeycomb elements and key geometric definitions

Table 2.3.1. Geometric properties of honeycomb and results from area and force calculation for bond

Honeycomb Designation	4.4-3/16-0.0015	6.9-3/16-0.0025	8.1-3/16-0.003
-----------------------	-----------------	-----------------	----------------

Cell Wall Length, a_w (mm)	2.72	2.72	2.72
Cell Width, b_w (mm)	4.763	4.763	4.763
Expansion Angle, θ_w (°)	60	60	60
Web thickness, t_w (mm)	0.0381	0.0635	0.0762
Elements in 300mm ² sheet	4632	4632	4632
Element Area, A_{element} (mm ²)	0.415	0.691	0.829
Total Surface Area (mm ²)	1920	3200	3840
Total Force Required (N)	192	320	384
Mass Required (kg)	20	33	39
Caul Plate Mass (kg)	9	9	9
Additional Mass required (kg)	11	24	30

2.3.1. Adhesive preparation

The adhesive VTA260 when removed from the freezer needed to thaw thoroughly before use to avoid damaging the adhesive's mesh. The adhesive sheets were cut using a Stanley knife into 340 x 340mm squares. The excess of 20mm on each side of the skin was to allow for high quality bonding at the edge of the sandwich panel. One sheet of adhesive was used per skin/core bond, and in order to prevent particulates and debris sticking to the adhesive the protective backing layers were left on until applied to the skins.

2.3.2. Bonding procedure

The two laminate skins were bonded to the core in two separate steps, wherein each time the laminate skin was needed to be located underneath the core to prevent resin dripping. The laminate skins were cleaned with propanol to remove all dirt and grease. One side of the backing sheet of the adhesive was removed and applied to the skin. The adhesive was then smoothed onto the skin. The second backing sheet was then removed and the honeycomb placed on top ensuring the L-direction of the honeycomb was in line with the 0° direction of the skin. The skin and core assembly were then placed on a piece of bagging film over a table in the oven, shown in Figure 2.3.2.



Figure 2.3.2. Oven table with bagging release film tapped down ready for skin/core bonding

The protective layers of bagging film and cotton breather material were placed underneath the caul plate and the additional weights were placed on top of the caul plate as illustrated in Figure 2.3.3. A list of the dimensions of everything involved is shown in Table 2.3.2.

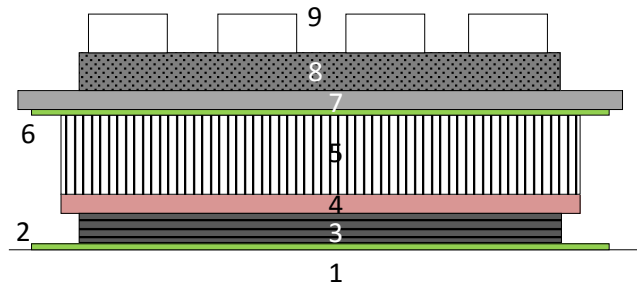


Figure 2.3.3. Oven configuration

Table 2.3.2. Oven material sizes

No.	Component	Size (mm)
1	Oven table base	-
2 & 6	Bagging film	340 x 340
3	Laminate panel	300 x 300
4	VTA260 adhesive	340 x 340
5	Aluminium honeycomb	340 x 340
7	Breather fabric	340 x 340
8	Caul plate	300 x 300
9	Dead weights	-

The curing cycle used was the same as that for LTM45 resin. Upon completion the oven was allowed to cool naturally to avoid the possibility of cracks and residual stresses occurring in the adhesive due to cooling too rapidly. Any excess honeycomb and adhesive overhanging from the skin was trimmed using a Stanley knife, with care and attention paid not to break the bond at the edges of the skin via dragging the blade through the honeycomb.

2.4. Introduction of pre-conditions in sandwich panels

Pre-conditions were purposefully introduced during manufacturing with intent to gain a physical insight of the skin-core interactions during in-plane compression. For this investigation there were four preconditions examined. The first two were removing the core material from the central region of the sandwich specimen in order to investigate the contribution of the core to the in-plane compressive resistance of the panel with 20mm and 40mm sections removed. For the third pre-condition, panels were impact damaged before the core material was removed to ensure identical

skin condition to the impact damaged panels. The fourth pre-condition was to drill holes into one or both skins, with the purpose of replicating impact damage in the skin only. This was to give a possible lead to simplification of prediction theories based on holes in skin as compared to impact damage, and also investigate the influence of the dent crater left after impact in the compressive performance of the panels. Manufacture of these panels was identical up to bonding of the core; all methods for laying-up the laminates and cure cycles for the skins and the core were the same as regular panels.

2.4.1. Core removal

Of the two different types of core removal panels, of those for in-plane compression only, there were two different sized core sections removed across the width of a panel, 20mm and 40mm in the loading direction, and for the CAI core removed specimens, only 20mm sections of core were removed. To manufacture the in-plane compression core removal panels, VTA260 adhesive was applied to a skin as shown in Figure 2.4.1, leaving either a 20mm or 40mm gap in the centre of the specimen. The honeycomb core was also applied in two separate pieces, and placed on top of the adhesive, ensuring the 0° fibre direction and nodal direction of the core were aligned. Both adhesive and core were cut with 20mm overhangs to maintain an effective bond line at the edges. The 20 or 40mm wide strip was left vacant of any core or adhesive material.

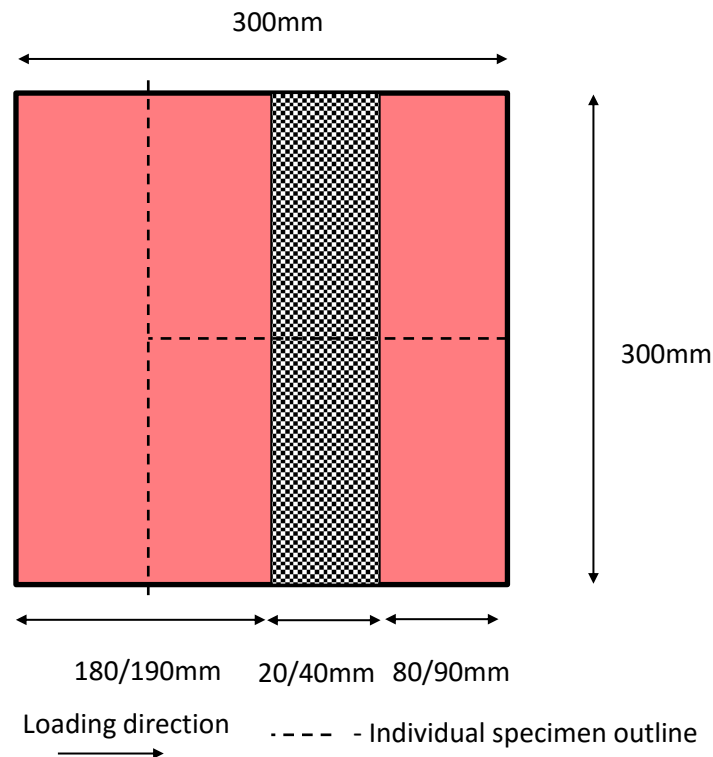


Figure 2.4.1. Adhesive placement on 300 x 300mm skin for in-plane compression core removal specimens

For the impact core removal specimens, it was necessary for the core to be present for the impact event, but to be removed as to have no influence on the subsequent compressive performance. This was achieved in several steps during the cure cycle. Firstly, to prepare for the first skin bonding, the adhesive was applied to give a 20mm gap in the centre of the specimen, as in Figure 2.4.1. Then a honeycomb sheet of 340 x 340mm was placed on top, aligning the nodal direction with the 0° fibre direction. To ensure that the skin did not bow into the unsupported area of honeycomb, two sheets of bagging film were put in the gap between the adhesive. Once the first cure cycle was completed, the un-bonded honeycomb was then cut out of the gap using a Stanley knife. The 20mm wide piece of honeycomb was cut at this stage as it was much easier to achieve the accuracy in width and straightness with two sections fully fixed by the cured adhesive. For the second skin bonding, this piece of honeycomb was left in between the two skins, with the adhesive and bagging film applied in the same manner as in the first skin. This left a fully cured panel, containing full coverage of honeycomb throughout the panel, with a 20 x 300mm section that could be removed. The core would then be removed after the impact test using a steel bar to push the core piece out of the panel.

2.4.2. Skin removal via hole drilling

For the panels with a hole precondition, 40mm holes were to be drilled in either one or both of the skins in the sandwich panel using a diamond-coated core drill. The skins had to be marked in order to position the holes in the centre of the 200x150mm specimen, shown in Figure 2.4.2. A diameter of 40 mm was estimated so that its effect on the compressive strength should be noticed but not overwhelming.

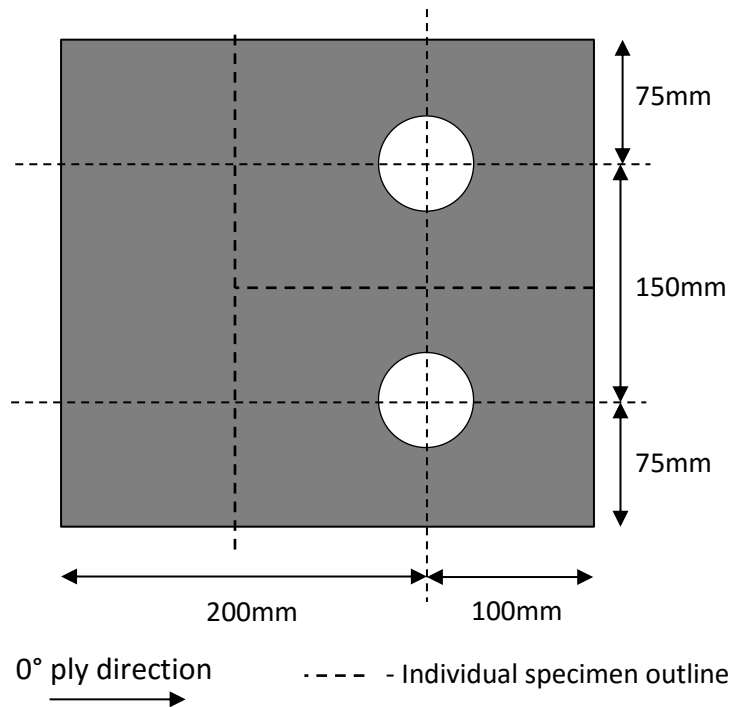


Figure 2.4.2. Hole locations on 300 x 300mm skin before bonding to core

For the panels with holes on both sides, more care needed to be taken to ensure that the holes were perfectly aligned back to back after the second cure cycle. To start, the panels were marked in the same manner as in Figure 2.4.2, however, two skins were selected such that their 90° dimensions were as equal as possible, and the markings were measured using the bottom left corner as a reference. After the honeycomb was bonded to the first skin, and trimmed, the second panel was secured to the honeycomb using the reference corner to align the panels. The adhesive in the holes on the second skin was cut away to help check the alignment of the holes.

2.5. Impact panel preparation

From a 300 x 300mm panel, it was possible to produce two 200 x 150mm specimens ready for testing, shown in Figure 2.5.1, by cutting the panel using the radial saw. As shown in Figure 2.5.1, the pre-conditioned panels were cut in a different formation to the normal sandwich panels in order to better maintain the longitudinal symmetry of the pre-conditions in the specimen. The cut specimens were 5mm longer in the 0° fibre direction to allow for trimming and machining, and cuts either side of the 0° dimension were made in order to ensure perpendicular and smooth edges were prominent for the loaded edges of the panel.

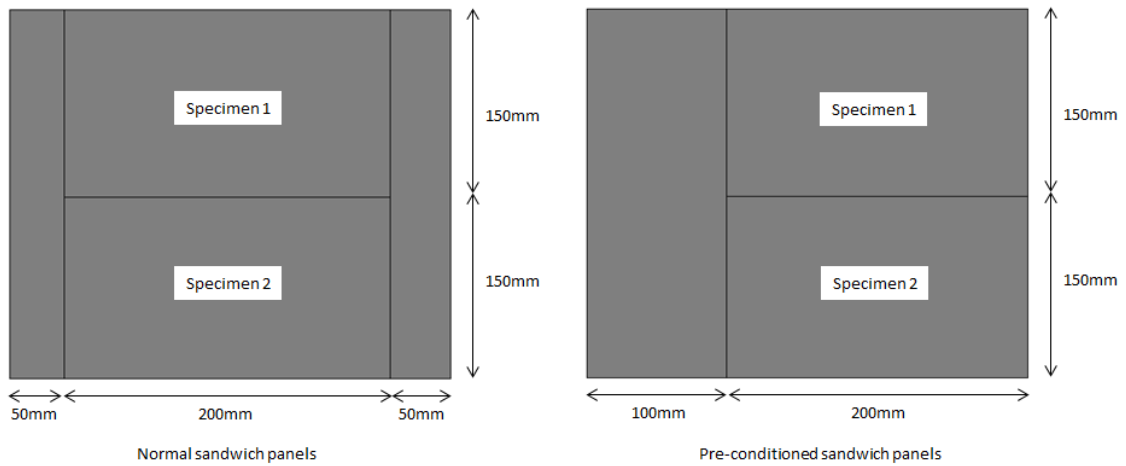


Figure 2.5.1. Cutting measurements applied to panels before cutting

Following the production of a test panel, those requiring impact testing were marked to allow the correct alignment within the impact testing apparatus, and all panels destined for in-plane compression testing were marked for the application of strain gauges, as shown in Figure 2.5.2. The horizontal and vertical lines were drawn at the centre point of the panel sides, and the circle in the middle was 100mm in diameter, and represents the testing area for the low velocity impact tests. The strain gauge placement and locations are detailed in Section 5.1.2. The markings were made with reference to a single corner to ensure that the strain gauges on the front and back of the panel were in line with each other.

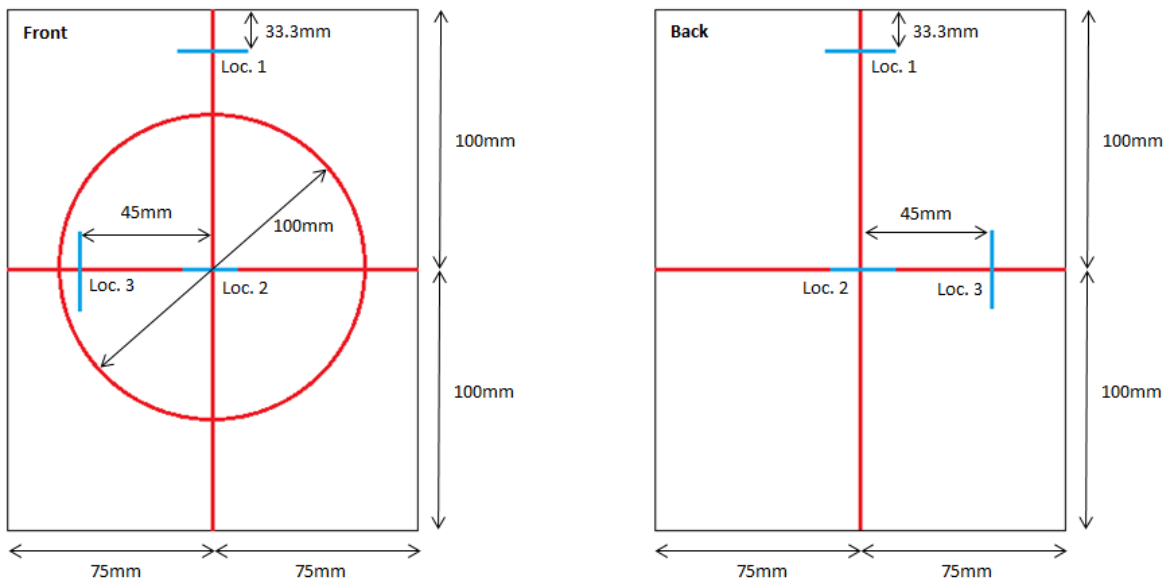


Figure 2.5.2. Surface markings for LVI specimens, and strain gauge locations

3. EXPERIMENTAL PROCEDURES AND SETUP FOR LOW VELOCITY IMPACT TESTS

In this section, the features of the test rig, the panel set-up and test operation used in this investigation are discussed. At the outset of this investigation, no precise testing standard existed for evaluating the damage resistance of composite sandwich panels with low velocity impacts. A small number of testing standards for the transverse testing of monolithic laminates exist in the literature, but are not directly applicable to the testing of sandwich structures.

3.1. Main features of instrumented drop-weight low-velocity impact rig and test set-up

Below, in Figure 3.1.1, is a close-up of the bespoke instrumented drop-weight impact test rig used to conduct low velocity impact tests of sandwich panels and assess their damage resistance characteristics. The impact rig is 4.5m tall with an impactor of 1.49kg with a 20mm hemispherical nose. The force of impact was recorded by an on-board load cell, and impact velocities could be calculated by using times recorded by two photodiodes set at a fixed distance of 51mm and triggered by a flag on the impactor. The position of the photodiodes was set depending on the thickness of the panel being tested to capture the point at which impact occurred. With the impactor secured in its housing, it could be raised to any height up to 4.5m using a winch system. The panels were clamped between two steel plates with a 100mm diameter opening at the centre as the testing area.

First stage of the test set-up, as already described in Section 2.5, was to ensure each panel had the 100mm diameter test area marked on the top skin in silver pen. Using this, the specimen was manoeuvred to ensure the opening in the top clamping plate aligned with the panel markings. As the distal clamping plate was fixed and was not visibly accessible, it was hard to ensure the top and bottom unclamped areas were matched up. However, the movement of the top plate was limited by four corner bolts, reducing this error to a minimum. With the panel specimen being held by the weight of the top clamping plate, the impactor was lowered down on to the panel and aligned such that the impactor would contact the centre of the 100mm diameter testing area. Then the clamping plates were secured by tightening the four bolts with a torque of 4Nm, enough torque to secure the panel and not crush or damage the honeycomb core. After this the impactor carriage was re-secured in the impactor housing, ensuring it was placed squarely in the housing so it would be released cleanly and in-line with the guide rails reducing friction as much as possible.

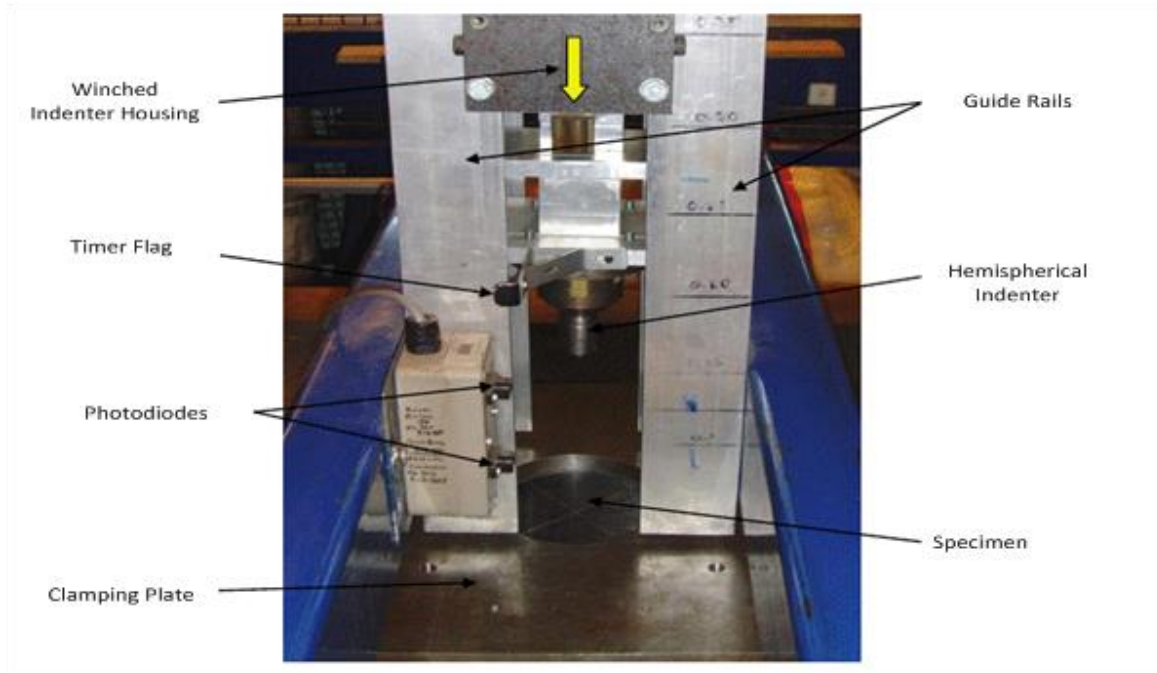


Figure 3.1.1. Drop test rig for low velocity impact testing

3.2. Low-velocity impact testing procedure

The height for the impact test was initially estimated using the target potential energy held by the impactor at a height (h) via Equation 3.2.1.

$$E = mgh \quad (3.2.1)$$

Taking $m=1.49\text{kg}$ and $g=9.81\text{kg/m}^3$, this provided an easy and quick estimation of the drop height to deliver the target impact energy. Impact energy or incident kinetic energy (IKE) was varied via altering the drop height of the impactor instead of increasing or decreasing weight. Since the impactor made contact with the insides of the free fall guide, there would be energy lost due to friction. Even though the best efforts were made to keep this friction to a minimum by applying grease to the guide, an adjustment of no more than 5% was added to the calculated drop height in order to achieve a desired IKE, especially at the lower end of the energy spectrum, for the group of impact tests. The housing was then winched up to the required height for each impact test, with the height being checked using a tape measure from the bottom of the impactor to the centre point of the impact test area. With the housing in position, the cables running from the load cell to the computer were taped against the drop tower frame to ensure they did not coil into the path of the impactor, which could interrupt the data reading, voiding the test.

Due to the need of ensuring a single impact, the impact tests was carried out by two people, one for operating the carriage release mechanism and rebound stopper and the other for triggering the data acquisition computer system. The software of WAVECAP was used to record the raw voltage data from the load cell during the impact, with a window of only 2.7 seconds for data capturing, due to the high sample rate of a reading every 50 μ s.

Before the impact test was started, all amplifier and conditioning units for the load cell and the photodiodes were switched on, and the timers for the photodiodes were both reset to clear any previous data from testing. The WAVECAP software was loaded and armed, then triggered to coincide with the impactor striking the panel. After the impactor struck the panel, a piece of wood was slid under the impactor path to prevent any rebound impact events. Once the carriage was at rest, the times on the photodiode read-outs were recorded before the housing was moved and the data was saved for post-processing. All the impact tests were conducted successfully, though one of the time counters was not triggered on a few occasions for an unknown reason.

3.3. Typical impact measurements

To work out IKE accurately, the impact velocity V_i was needed to be calculated using the time taken for the flag on the carriage to travel between two light gates, over the distance of 51mm. The IKE of the test is then obtained by Equation 3.3.1.

$$IKE = \frac{1}{2}mV_i^2 \quad (3.3.1)$$

As the carriage bounced off the panel, in the cases where total skin penetration didn't occur, a second timer captured the time taken for the rebound. This allowed for the rebound energy to be calculated in the same manner as in Equation 3.3.2

$$RE = \frac{1}{2}mV_r^2 \quad (3.3.2)$$

In instances where the impactor did not trigger the second time reading, it was assumed in these cases that all energy had been absorbed by the impact and that the impactor had in fact embedded itself in the panel. The rebound velocity was slightly underestimated, as the start of the rebound of the impactor was below the specimen surface where the photodiodes were referenced due to the deflection of the specimen during impact. Consequently, the greater deflection was, the severer the underestimation became, the sandwich panels did not deflect much but the impacted skin did sink in due to the core crushing. As a result, the absorbed energy was slightly overestimated. A typical raw

data response is shown in Figure 3.3.1, the major spike indicates the impact, and the residual spikes of the rebound can be seen.

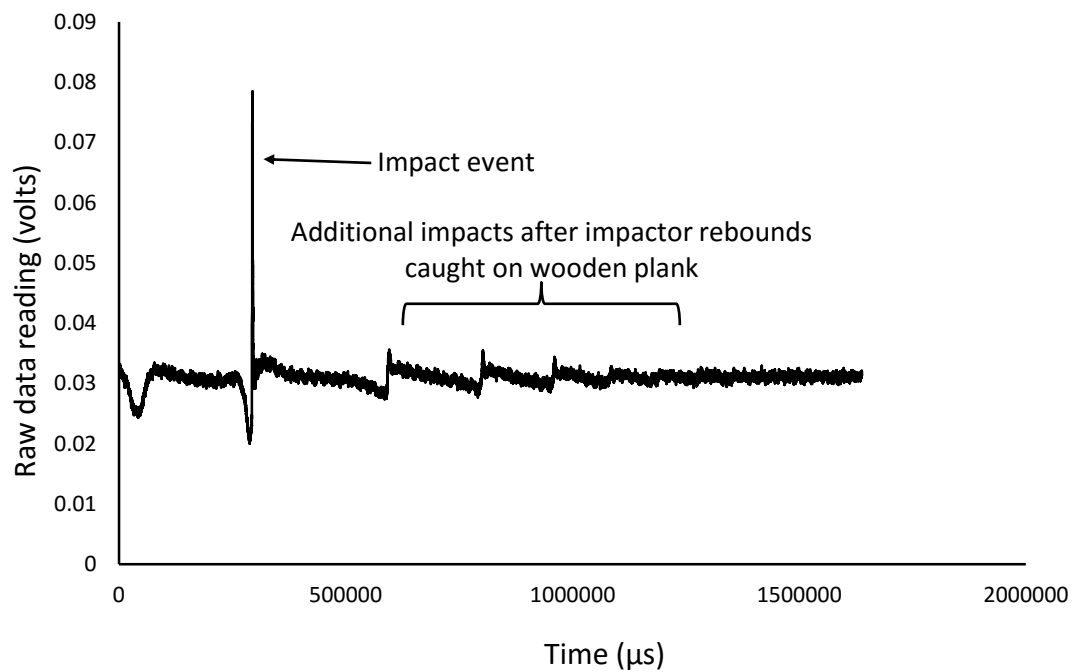


Figure 3.3.1. Raw data response for a thin unsymmetrical CP carbon/epoxy panel with 70kg/m³ core density impacted at 20J (HD-8-6-CP-20J)

It was then necessary to trim the data of the unwanted rebound spikes, and any noise in the lead up to the impact, to focus solely on the impact event. The voltage output could be converted to force using Equation 3.3.3, which was obtained from calibration tests from Hill [1],

$$Load (kN) = 0.128 \times (volts \times 1000) \quad (3.3.3)$$

which gives 7.79mV for 1kN. The converted load time response for each impact event could be seen in Figure 3.3.2, as an example. The use of these plots aided the study of the onset of damage mechanisms and the general response characteristics of the panels.

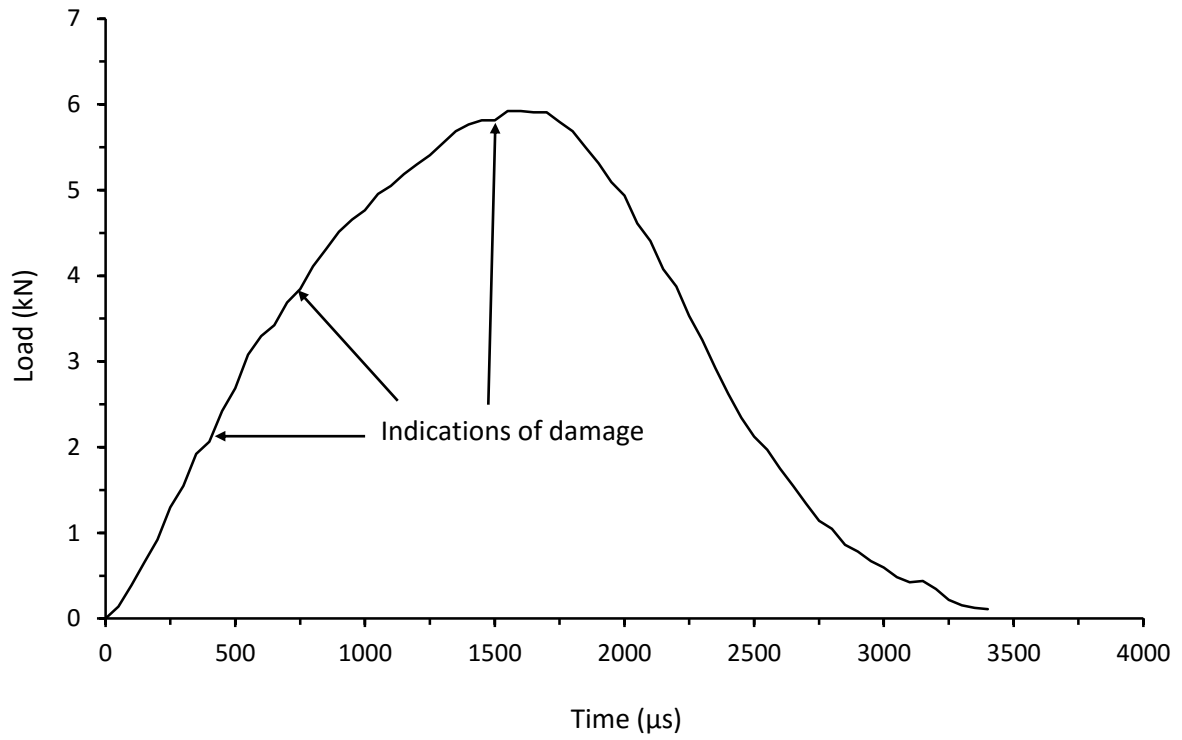


Figure 3.3.2. Load time response for a thin unsymmetrical CP carbon/epoxy panel with 70kg/m³ core density impacted at 20J (HD-8-6-CP-20J)

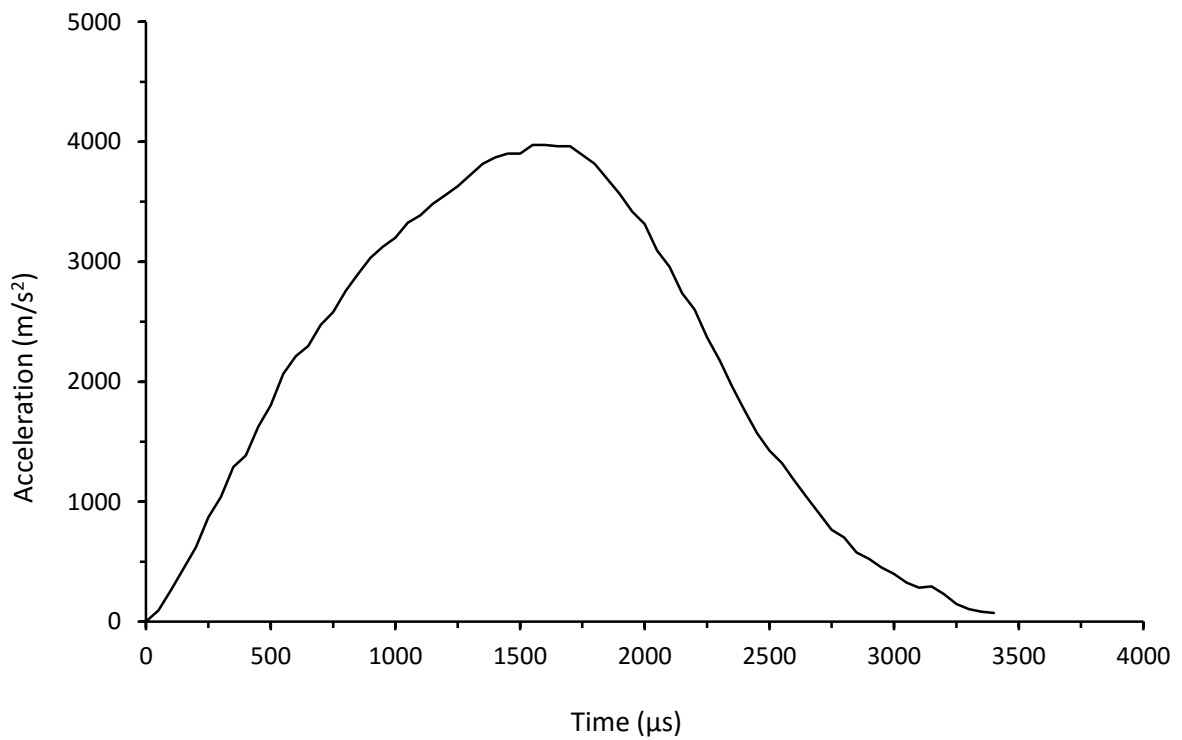


Figure 3.3.3. Acceleration time response for a thin unsymmetrical CP carbon/epoxy panel with 70kg/m³ core density impacted at 20J (HD-8-6-CP-20J)

Acceleration of the impactor was calculated from the force using Equation 3.3.4.

$$F = m_{indenter}a \quad (3.3.4)$$

Applying this formula over all force points throughout the time history, an acceleration-time plot was created for each impact, shown in Figure 3.3.3.

An integration of this acceleration curve over each 50 μ s interval with the known impact and rebound velocities gives the impact velocity response of the test, as shown by Equation 3.3.5

$$\Delta v = \int_{t_1}^{t_2} a. dt = v - v_o \quad (3.3.5)$$

This is shown in Figure 3.3.4 for panels with no fibre fracture or cracking, the peak load corresponds to zero velocity, where the rebound of the impactor started. For panels that suffered face sheet penetration or considerable top skin failures, there was a noticeable load drop due to the failure of the impacted skin to carry the load, therefore the peak load no longer corresponded to the start of the rebound of the impactor, and thus the change in velocity was used to identify the rebound. The velocity at the end was checked with the rebound velocity.

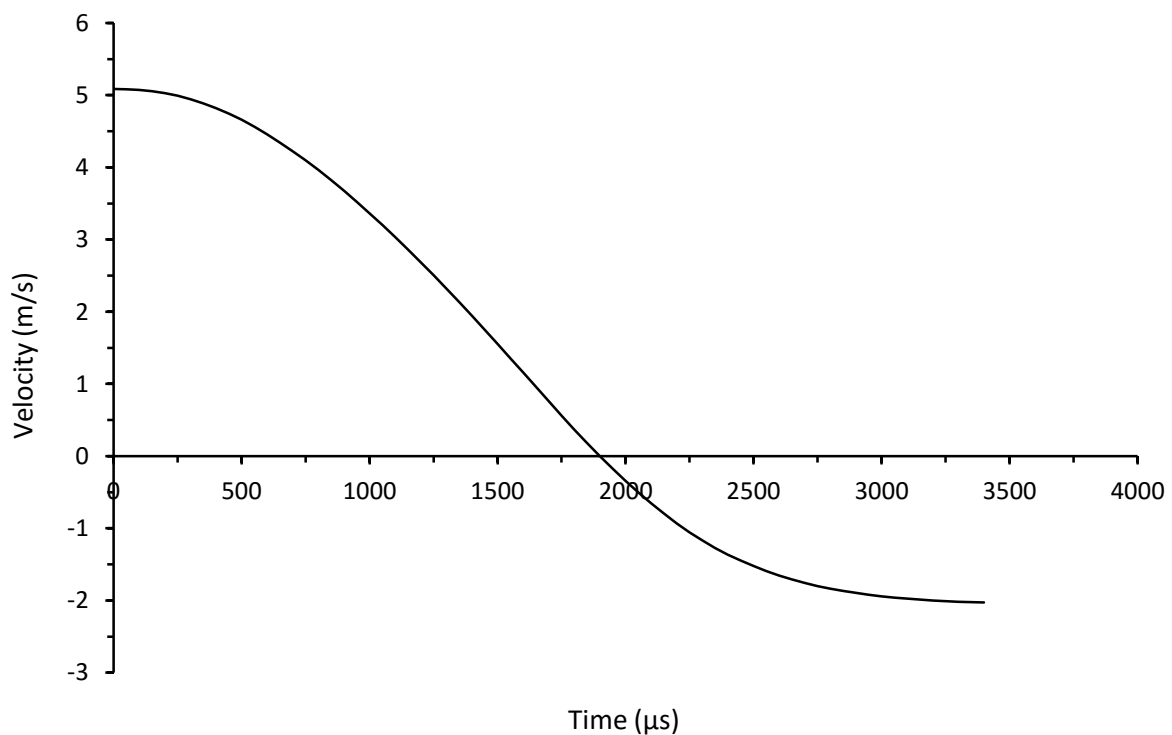


Figure 3.3.4. Velocity time response for a thin unsymmetrical CP carbon/epoxy panel with 70kg/m³ core density impacted at 20J (HD-8-6-CP-20J)

In a similar manner through the second integration of the velocity curve, the displacement of the impactor was calculated using Equation 3.3.6. The displacement response of the impactor is shown in Figure 3.3.5, and is seen never to return to its zero position at the end of the time frame. This was due to the residual core crush and skin indentation left in the panel after the impact. In panels with fibre fracture and extensive core crushing, the displacement-time response shows very little recovery after the maximum displacement. This indentation does not take into account for the recovery of the panel through spring back over a longer period of time, hence this value cannot be used as an accurate representation on the skin indentation on a panel being tested in compression, and a value has to be manually measured after the impact test.

$$\Delta w = \int_{t_1}^{t_2} v. dt = w - w_0 \quad (3.3.6)$$

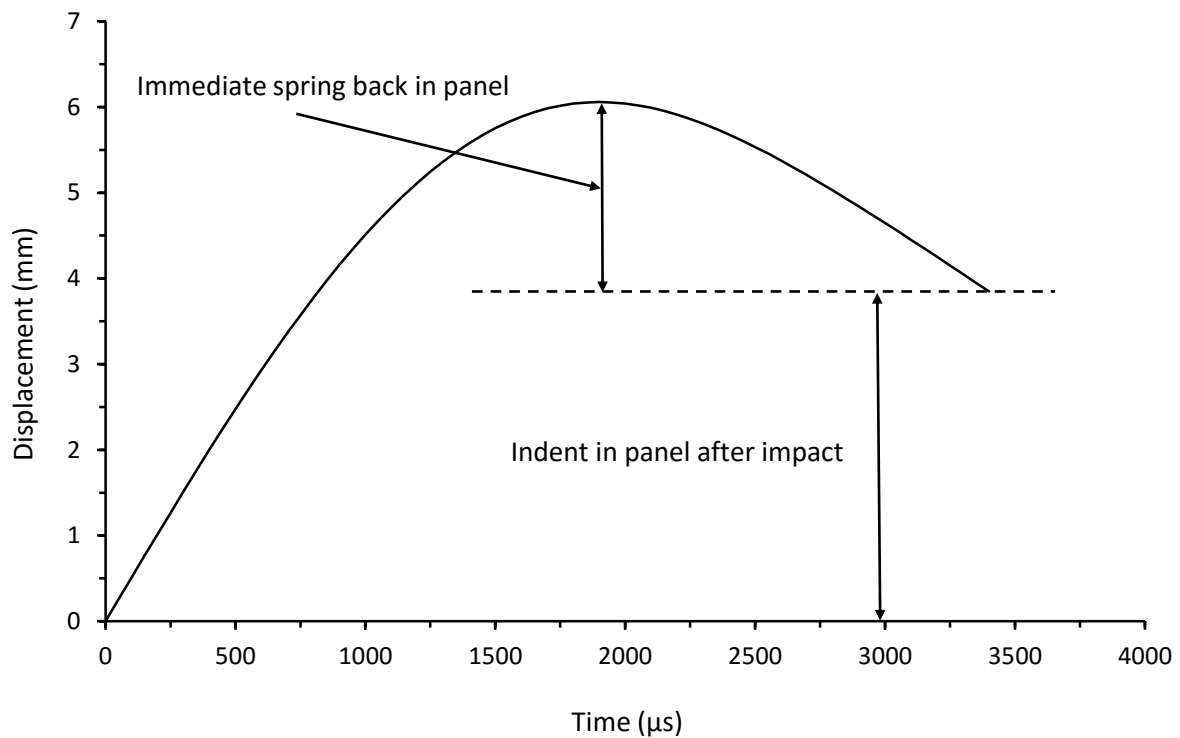


Figure 3.3.5. Displacement time response for a thin unsymmetrical CP carbon/epoxy panel with 70kg/m³ core density impacted at 20J (HD-8-6-CP-20J)

Finally with the displacement response obtained for the impact event, this was plotted against impact force, which can be used to compare the area under the response curve with the absorbed energy calculated from the incident and rebound velocities as well as comparing the response of the panels with varying arrangements and with those obtained quasi-statically. This is shown in Figure 3.3.6, as an example, from the same 8/6 CP panel impacted at 20J used in all previous examples.

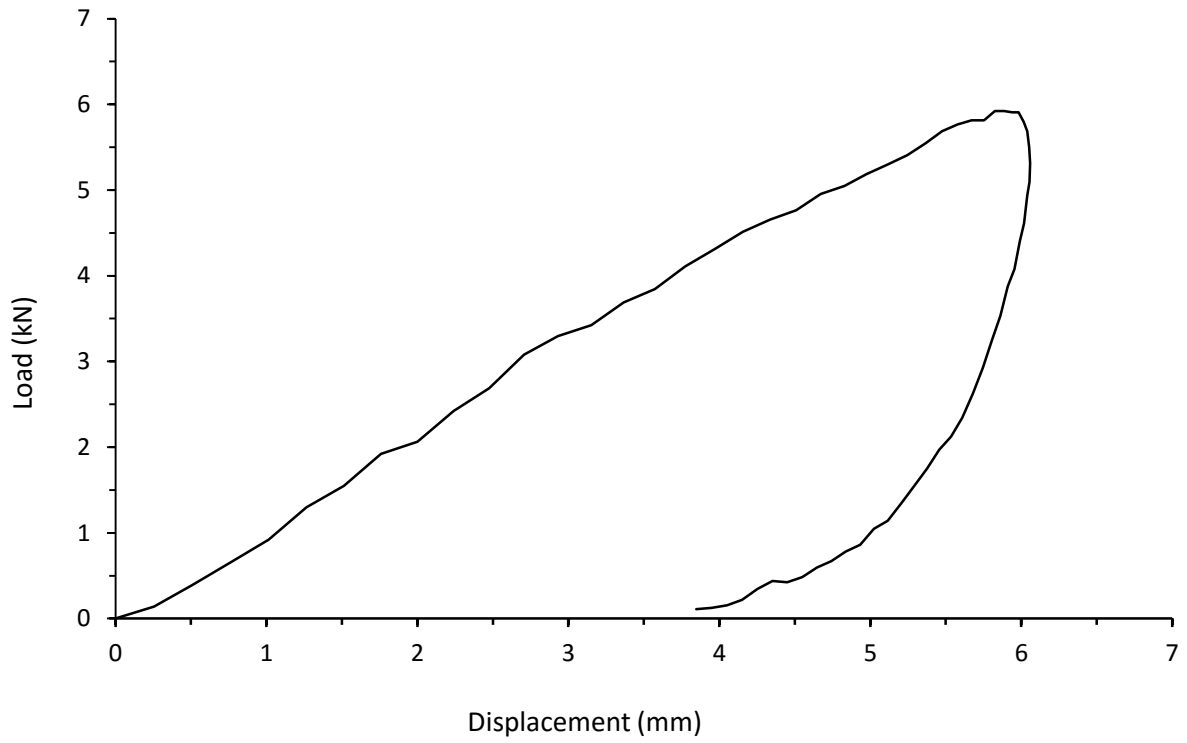


Figure 3.3.6. Load displacement response for a thin unsymmetrical CP carbon/epoxy panel with 70kg/m³ core density impacted at 20J (HD-8-6-CP-20J)

4. DAMAGE MECHANISMS AND CHARACTERISATION

Developing an in-depth understanding into the onset and propagation of damage mechanisms which sandwich panels experience throughout impact loading is important to enable designers to achieve efficient impact damage tolerant design in terms of skin material, ply orientation and thickness, core density and thickness, and panel asymmetry.

4.1. Identification of impact damage mechanisms

An assessment of the compressive strength reduction of these impacted sandwich panels requires quantitative information on damage mechanisms that occur in the panels over a range of impact energies. Diagnostic destructive cross-sectioning of panels was used to identify dominant damage mechanisms over the impact range. The first was a combination of delamination in the top skin, originating from the centre of the impact region in a cone shape towards the skin-core interface and spreading in both the 0° and 90° directions, coupled with core crushing spreading in all directions from the impact site, and was found to be the typical damage state in the panels from low levels of impact energy, an example of which is shown in Figure 4.1.1. Although these damage mechanisms were found to occur together, they are not assumed to be linked in their development. Material core crush strengths typically dictate the level at which core crushing would occur, however the early occurrence of core crushing could be attributed to the bending of the top skin causing honeycomb cell rotation, tearing and oblique crushing in addition to normal plastic folding. As impact energy was increased, the damage state in the panels was characterised by the propagation of core crushing and delamination in the top skin as seen in Figure 4.1.2. The final damage state to develop, typically at higher levels of IKE, was fibre fracture in the top skin, seen in Figure 4.1.3, causing extensive damage in the skin and core.



Figure 4.1.1. Cross section of a thin unsymmetrical CP carbon/epoxy panel with 70kg/m³ core density impacted at 5J (DJ-8-6-CP-5J-B1)



Figure 4.1.2. Cross section of a thin symmetrical CP carbon/epoxy panel with 70kg/m³ core density impacted at 23J (CI-8-8-CP-23J-B)

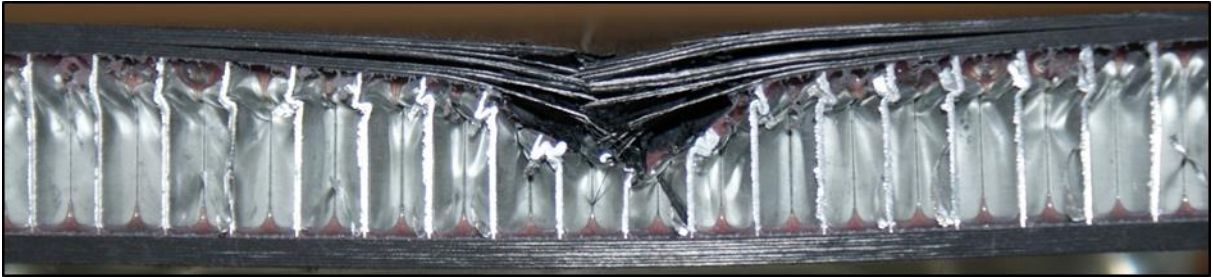


Figure 4.1.3. Cross section of thick symmetrical CP carbon/epoxy panel with 70kg/m³ core density impacted at 60J (CI-16-16-CP-60J-B)

Secondarily, damage mechanisms were measured where possible on the impacted panels before either cross-sectioning or compression. This was mainly limited to the surface indentation, an important damage measure, shown in Figure 4.1.4. Additionally, with the glass/epoxy panels, the three usually non visible damage mechanisms could be identified due to the translucency of the skins without the need for destructive inspection. As shown in Figure 4.1.5 by the 3 dashed circles, delamination, debond, and core crush (from inner to outer circles) are all easily recognisable by visual inspection. Interestingly the 0° and 90° directions for core crush and delamination regions can now be recorded, allowing comparison of damage propagation.

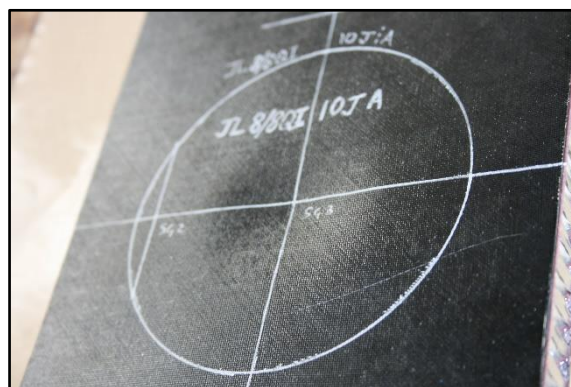


Figure 4.1.4. Impact damage in a thin symmetrical QI carbon/epoxy panel with 70kg/m³ core impacted at 10J showing an example of surface indentation (JL-8-8-QI-10J-A)



Figure 4.1.5. Impact damage in a thin symmetrical CP E-glass/epoxy panel with 70kg/m³ core impacted at 15J as seen through the skin surface (SG-8-8-CP-15J)

Although this progression of damage covers most of the test panels, there were some exceptions in both higher density core panels and panels with glass/epoxy skins. In these instances, interfacial skin-core debonding was found to occur before fibre fracture, as seen in Figure 4.1.6(a)-(c).



(a) Thin symmetrical CP carbon/epoxy panel with 135kg/m³ core density impacted at 20J (RM-8-8-CP-20J-B)



(b) Thin symmetrical CP carbon/epoxy panel with 135kg/m³ core density impacted at 45J (RM-8-8-CP-40J-B)



(c) Thin symmetrical CP E-glass/epoxy panel with 70kg/m³ core density impacted at 18J (SG-16-16-CP-18J-B)

Figure 4.1.6. Cross sections showing the occurrence of debond in carbon/epoxy panels with 135kg/m³ core density and E-glass/epoxy thick skinned panel

4.2. Examination of panel response under impact

4.2.1. Identification of damage mechanisms using panel response curve

As discussed in Section 3.3, the raw voltage load response was conditioned after the impact event to give load versus time, acceleration, velocity and displacement responses. Below, alongside the cross-sectioned panels, are typical and unique load time responses to see how they can be related to the damage states occurring in the panels, as well as general observations about the behaviour of the panels during the impact event.

In Figure 4.2.1 are two impacts in 8/8 CP symmetrical carbon fibre/epoxy panels with a 70kg/m^3 density core under 16J and 23J impacts. Figure 4.2.1 represents a typical load time response over the lower-mid range of impact energies exhibiting a sinusoidal response. The point of rebound was identified to coincide with the peak impact force in the majority of tests using the reversal of displacement and velocity. In the loading phase, small changes and fluctuations in the gradient possibly indicate the development of damage in the panel. As seen in Figure 4.2.3, the panels were found to have both delamination and core crushing extending in the planar direction away from the impact centre. It is not possible to ascertain from the response which of these mechanisms developed first. From the response it can be seen that the maximum impact force increases with the impact energy, and the cross-sections show clearly the result of the higher impact energy, with delamination, core damage and global bending being of a greater extent.

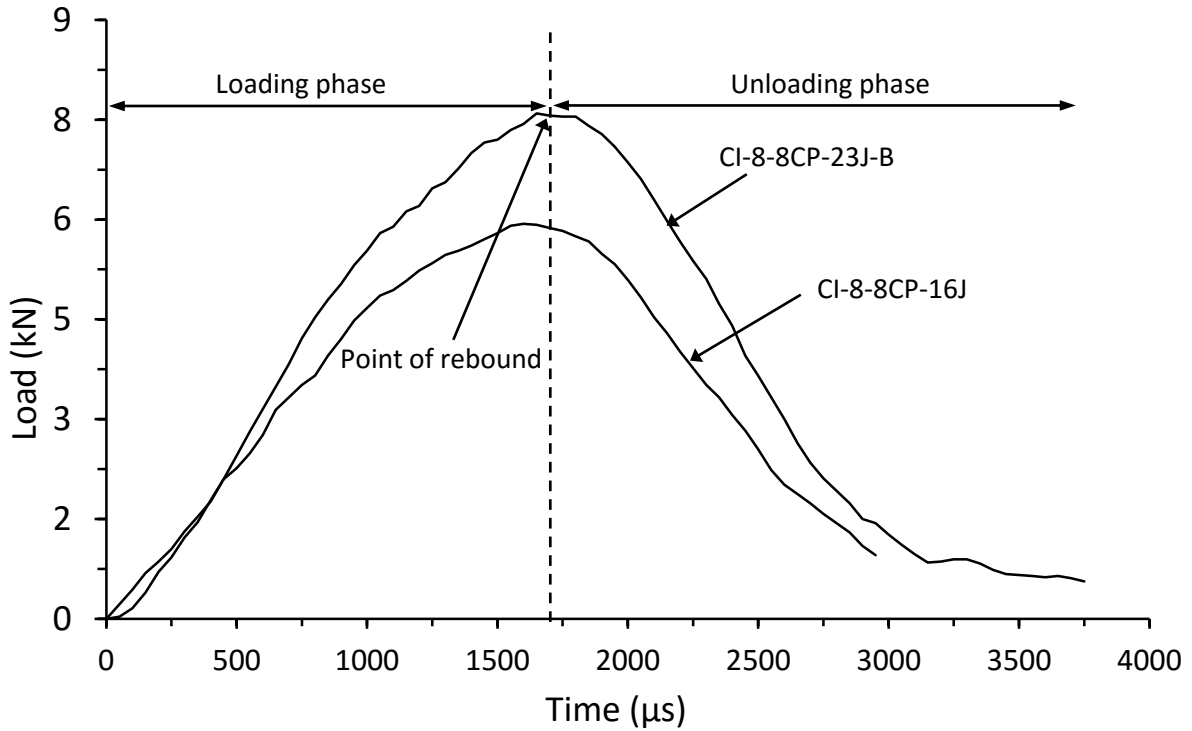


Figure 4.2.1. Load vs time response for thin symmetrical CP carbon/epoxy panels with 70kg/m^3 core density impacted at 16J and 23J



Figure 4.2.2. Cross section of thin symmetrical CP carbon/epoxy panel with 70 kg/m^3 core density impacted with 16J



Figure 4.2.3. Cross section of thin symmetrical CP carbon/epoxy panel with 70 kg/m^3 core density impacted with 23J

Figure 4.2.4 combines the load-time and the displacement-time response for the 8/8 CP panel impacted at 16J. From this graph the point at which the displacement stops increasing can be identified to be in phase with the reduction in load, signifying the reversal of the direction of the impactor. There was a small error induced in the double integral calculation of the displacement

related to inaccuracies in the time delta used and the position of the impactor being shifted due to the bending and displacement of the top skin which leads to the gap observed on the graph.

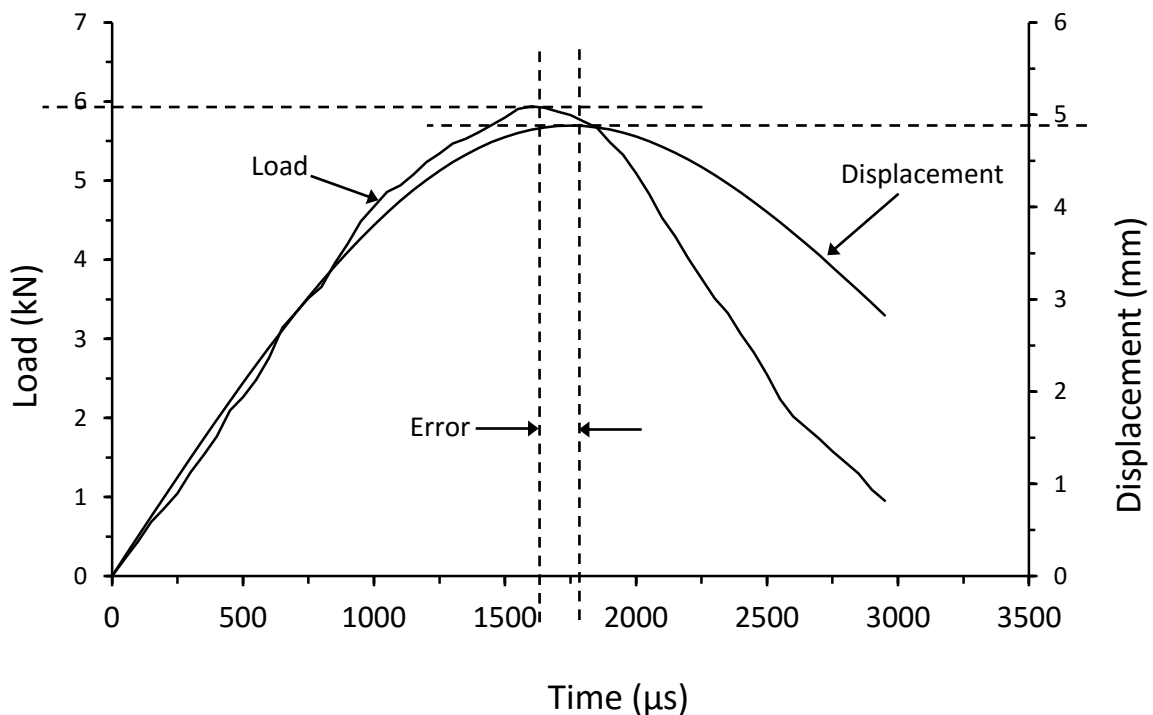


Figure 4.2.4. Load and displacement vs time response for thin symmetrical CP carbon/epoxy panels with 70kg/m³ core density impacted at 16J (CI-8-8-CP-16J)

In panels where fibre fracture occurred, at the higher range of impact energies for each panel arrangement, the load-time response varied from the above example. Shown in Figure 4.2.5, a comparison between a 45J and a 60J impact on a 16/16 CP carbon/epoxy panel with 70kg/m³ core density shows clearly the substantial difference in panel response under impact with the occurrence of fibre fracture. Unlike the occurrence of delamination and core crushing which were indistinguishable from the response, as in the 45J impact in Figure 4.2.5, fibre fracture is easily identifiable in the 60J impact load-time response, and can be seen to be split into three stages. The first stage sees the load rise to the peak load, at a faster rate than the lower impact, followed by a sharp decrease in load, signifying the fracture of the top skin, shown clearly in the cross-section in Figure 4.2.7, diverting the response from the expected pattern, shown by the dashed line in Figure 4.2.5. Stage two is from just after the load drops, and the impactor continues to penetrate the panel, as shown by the increasing displacement in Figure 4.2.8 as the top skin is no longer able to resist the through thickness propagation of the impactor travel, and the load carrying responsibility is shifted to the core, and eventually to the core and back skin jointly, signified by an extended zig-zag pattern in the response. The zig-zag pattern represents the plastic folding of the cells underneath the impactor. Finally in stage three, when the energy of the impactor is successfully dissipated by the crushing of

the core, further plastic folding is resisted which allows the load to be transferred through to the distal skin of the panel, resulting in the eventual reversal of the impactor, and unloading of the panel.

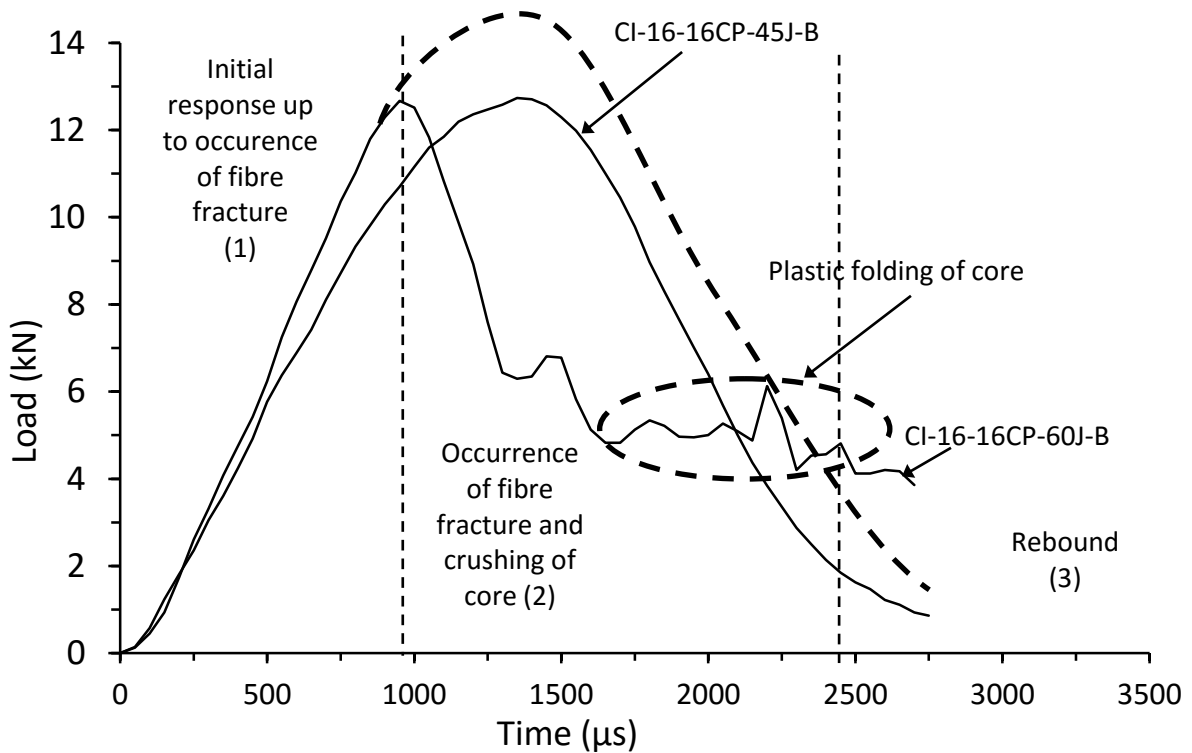


Figure 4.2.5. Load vs time response for thick symmetrical CP carbon/epoxy panels with 70kg/m³ core density impacted at 45J and 60J



Figure 4.2.6. Cross section of thick symmetrical CP carbon/epoxy panel with 70 kg/m³ core density impacted at 45J

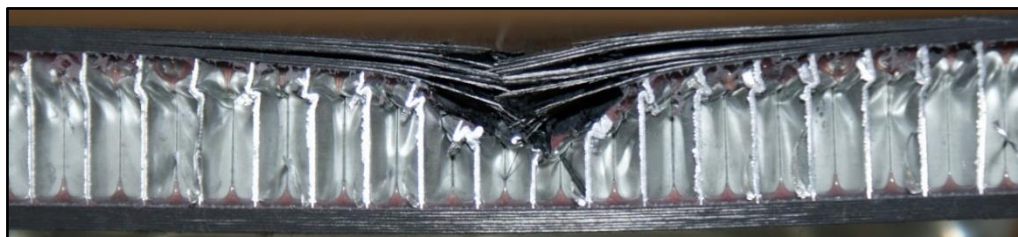


Figure 4.2.7. Cross section of thick symmetrical CP carbon/epoxy panel with 70 kg/m³ core density impacted at 60J

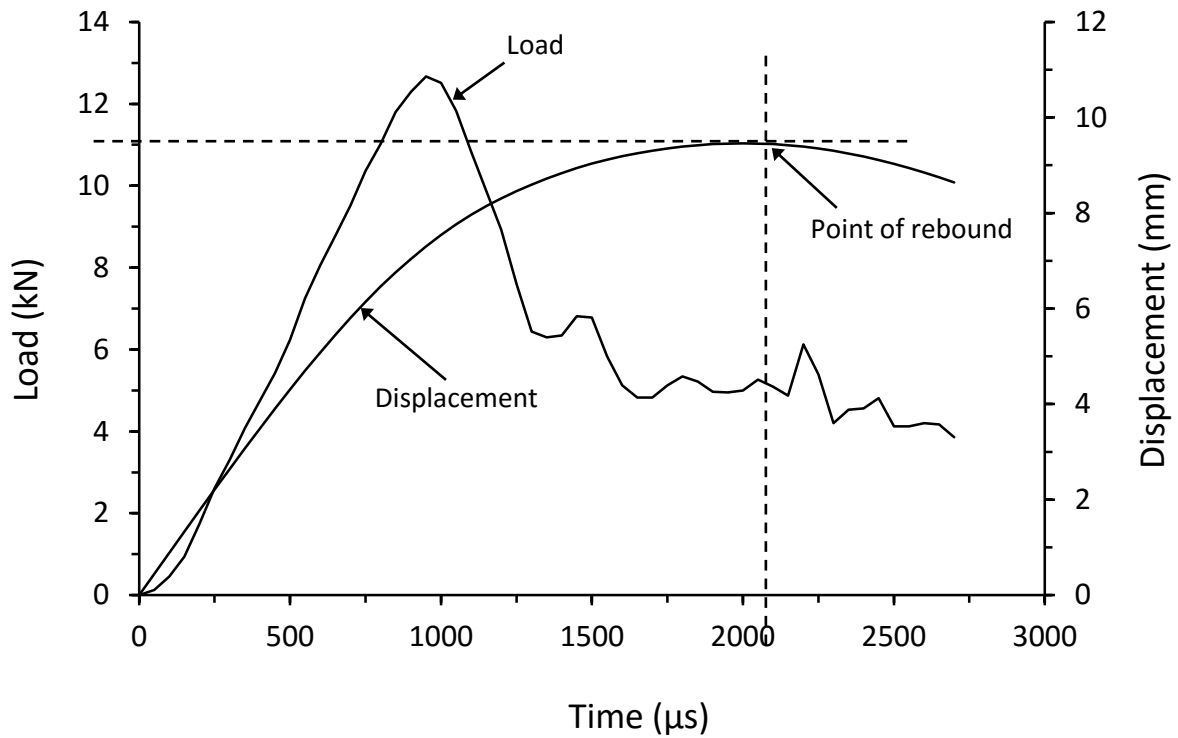


Figure 4.2.8. Load and displacement vs time response for thick symmetrical CP carbon/epoxy panel with 70kg/m³ core impacted at 60J (CI-16-16-CP-60J-B)

In Figure 4.2.9 are the responses from 8/8CP carbon epoxy panels with the 135kg/m³ density core. The two highest impacts showed interesting results, with large changes in gradient signifying damage in the panel, followed by the panel being reloaded before the impactor rebounded. Inspection of the panels showed no fibre splitting or fibre fracture in the top face sheet, which would have been the most likely reason given the substantial gradient changes that were not observed in the lower density panels prior to top skin damage. It is clear from the cross-section images in Figure 4.2.12, the higher density core suffered from extensive skin/core interfacial debonding, however, due to the similar levels of impact load compared to the lower density impact tests, it is likely that these debonds occurred during the unloading phase, and hence these gradient changes must be linked to the occurrence of delamination in the top skin. Peak impact load and impact duration were similar to those with 8/8CP panels with 70kg/m³ core arrangements, implying that these are a global function of the skin material.

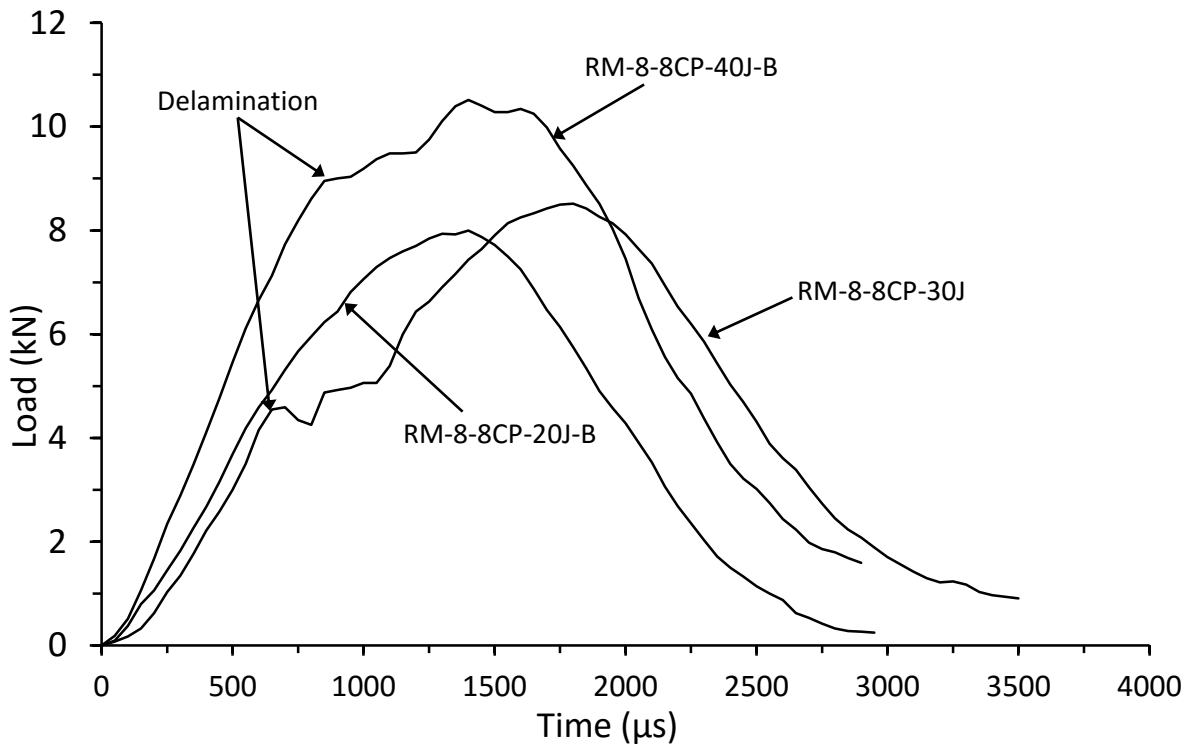


Figure 4.2.9. Load vs time response for thin symmetrical CP carbon/epoxy panels with 135 kg/m³ core density impacted at 20J, 30J and 40J



Figure 4.2.10. Cross section of thin symmetrical CP carbon/epoxy panel with 135 kg/m³ core density impacted at 20J



Figure 4.2.11. Cross section of thin symmetrical CP carbon/epoxy panel with 135 kg/m³ core density impacted at 30J



Figure 4.2.12. Cross section of thin symmetrical CP carbon/epoxy panel with 135 kg/m³ core density impacted at 40J

4.2.2. Development of panel response over impact range

Figure 4.2.13, Figure 4.2.14, and Figure 4.2.15 show the responses of thick and thin panels of symmetrical and unsymmetrical cross ply carbon/epoxy and symmetrical cross ply glass/epoxy panels with 70kg/m³ core density. It can be seen that the response in both the thin and thick arrangements throughout the impact ranges were fairly consistent, with a strong and intuitive correlation between the increase in IKE and the increase in panel displacements. It can be observed that the gradient of each curve goes through a small non-linear phase at the beginning of the panel response. As the impact begins, the response starts with a shallower gradient, which gradually increases to provide the main response gradient. After the slight densification of the core underneath the impactor, the load was more adequately spread through the skin, seeing a resultant stiffening in the response curve. Some curves, more prominently shown in Figure 4.2.14 in the thick unsymmetrical panels, see a further stiffening towards the end of the response curve. As the skin bends, more of the core underneath the skin was crushed, providing further support and stiffness to the skin.

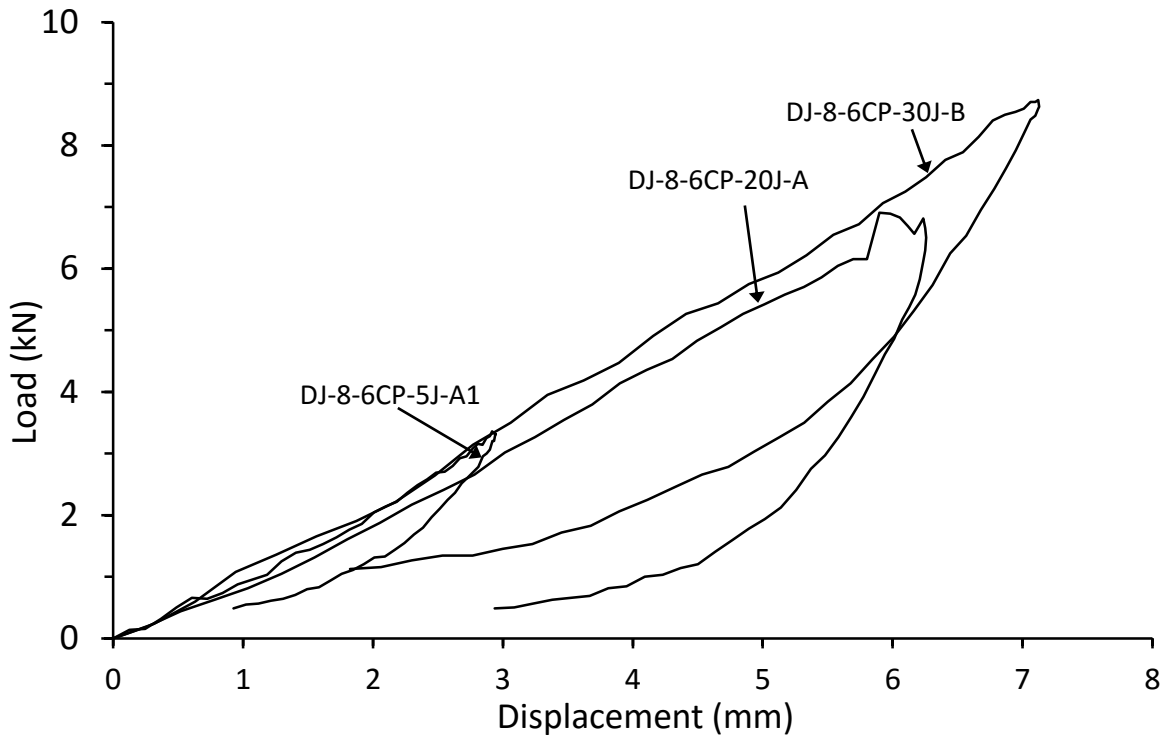


Figure 4.2.13. Load vs displacement response for thin unsymmetrical CP carbon/epoxy panels with 70kg/m³ core density impacted at 5J, 20J, and 30J

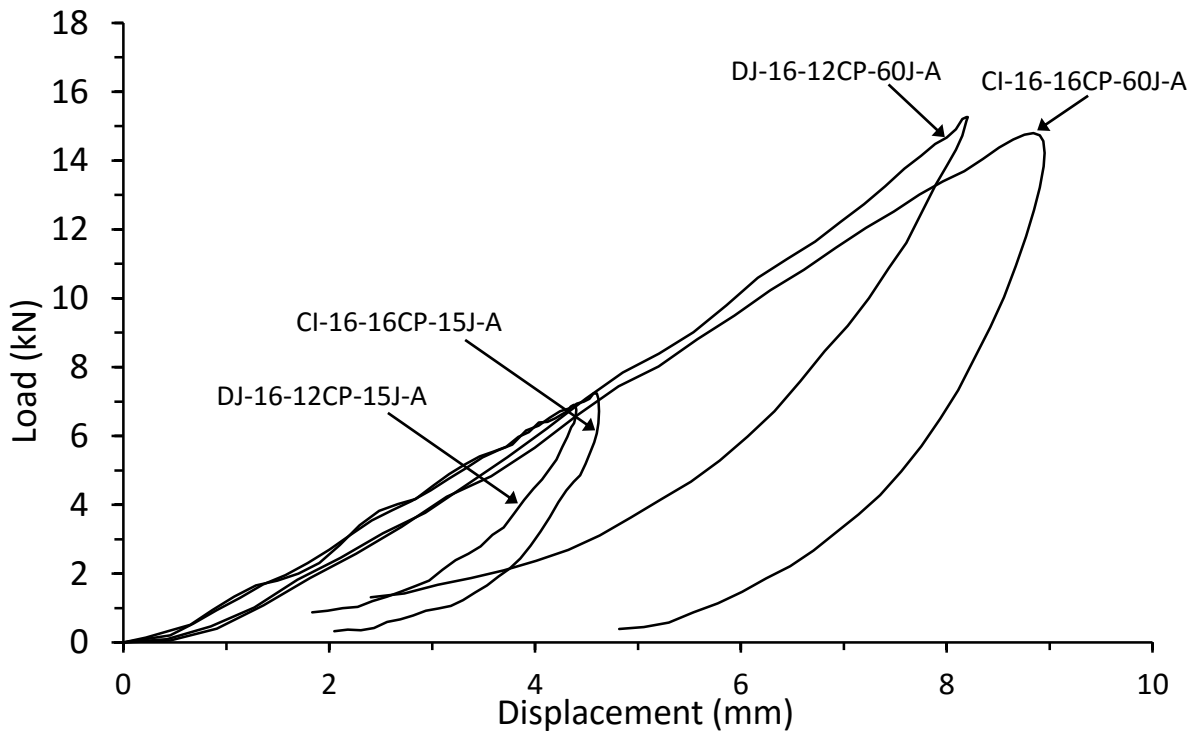


Figure 4.2.14. Load vs displacement response for thick symmetrical and unsymmetrical CP carbon/epoxy panels with 70kg/m³ core density impacted at 15J and 60J

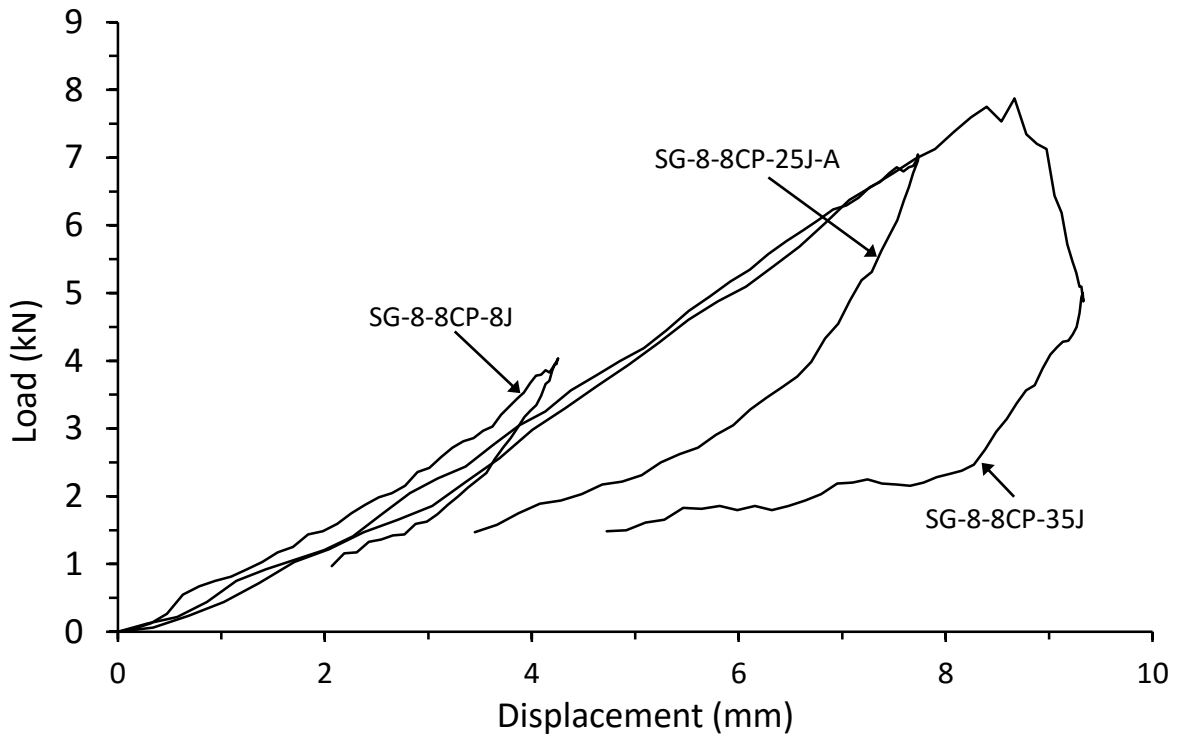


Figure 4.2.15. Load vs displacement response for thin symmetrical CP E-glass/epoxy panels with 70kg/m³ impacted at 8J, 25J, and 35J

In Section 4.2.1, the higher energy impacts suffered from deviations in their load-time curves, similar to the low density core panels, the initial response over the impact range starts in a non-linear fashion, stiffening slightly to provide the main response gradient. In the early range, displacement and IKE correlate as expected, however, the large gradient changes in the higher impact range differ to the lower density panels. This suggests that the higher resistance provided by the higher density core to the transverse load resulted in lower deformations at similar levels of load causing a more dramatic load drop when delamination occurred due to higher local ILS stresses.

The slopes across the IKE range for the 110kg/m³ are shown in in their load-displacement responses in Figure 4.2.17. The responses from the 110kg/m³ core density panels offered similar behaviour to those seen above from the higher density core panels. The increased resistance from the core created a more dramatic decrease in load due to the delamination of the top skin.

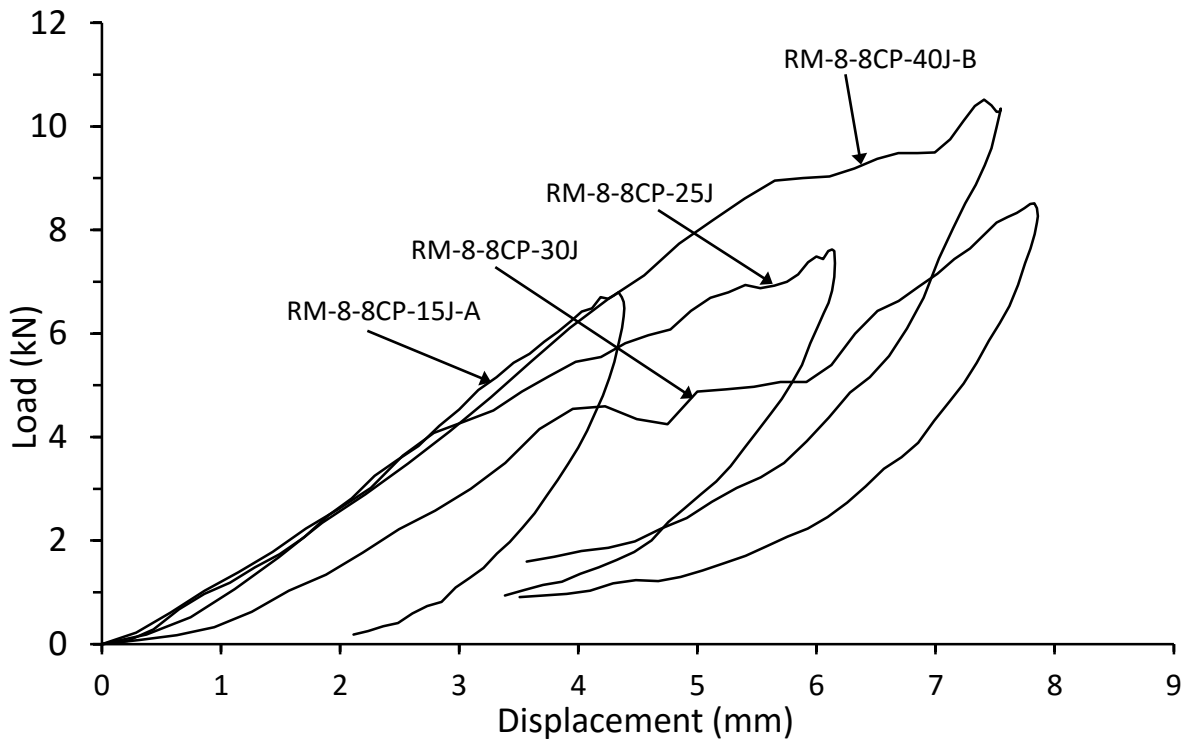


Figure 4.2.16. Load vs displacement response for thin symmetrical CP carbon/epoxy panels with 135kg/m³ core density impacted at 15J, 25J, 30J, and 40J

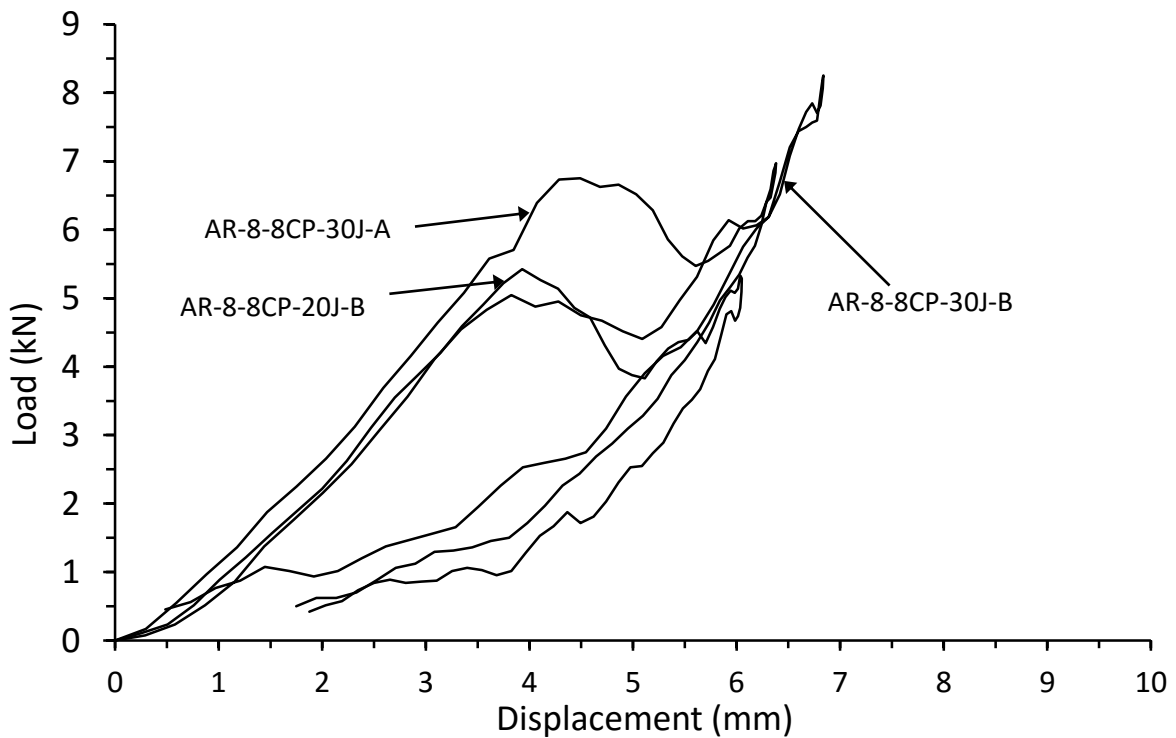


Figure 4.2.17. Load vs displacement response for thin symmetrical CP carbon/epoxy panels with 110kg/m³ core density impacted at 20J and 30J

4.2.3. Parametric study

Sandwich symmetry

Shown in Figure 4.2.18, Figure 4.2.19 and Figure 4.2.20 are the responses for symmetrical and unsymmetrical panels for thin CP and QI arrangements. From the graphs, very little difference in the slope of the responses can be seen even with the reduced number of plies in the distal skin. However, the onset of fibre fracture can be seen to be affected by the symmetry of the skins. The initiation of fibre fracture in the thin unsymmetrical panels was unanimously lower than in the symmetrical panels.

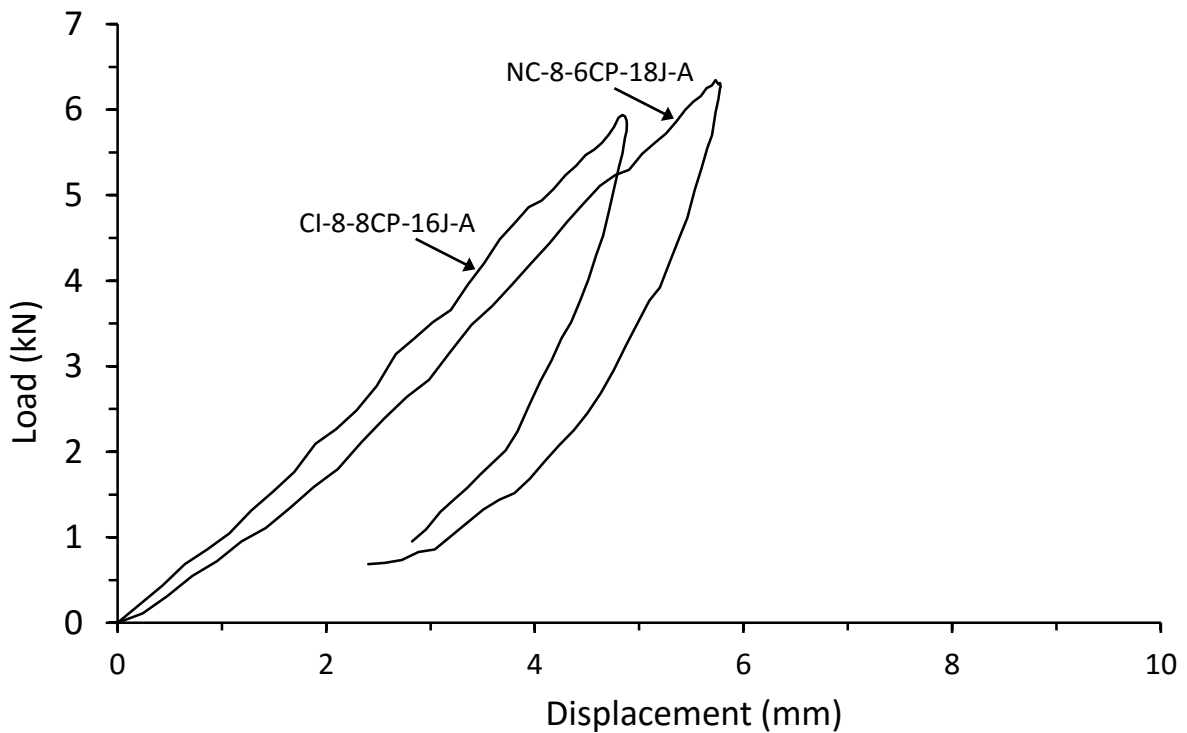


Figure 4.2.18. Load vs displacement response comparison for thin symmetrical and unsymmetrical CP carbon/epoxy panels with 70kg/m^3 core density impacted at 16J and 18J respectively

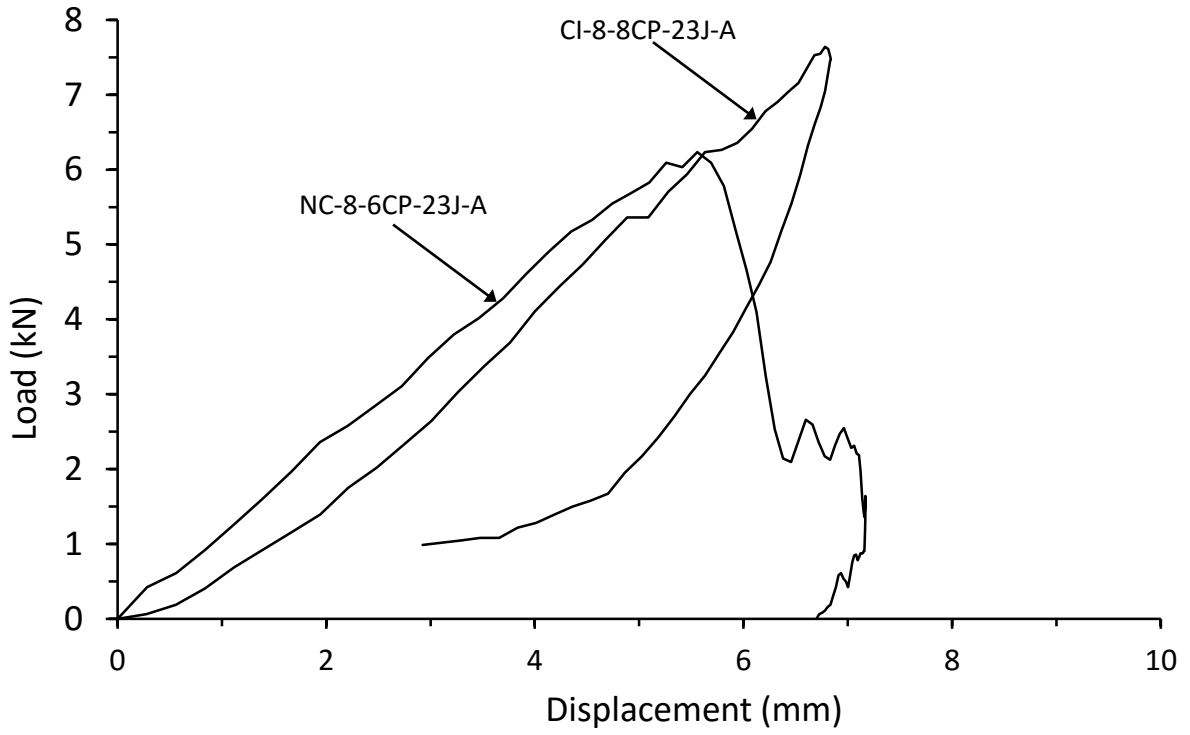


Figure 4.2.19. Load vs displacement response comparison for thin symmetrical and unsymmetrical CP carbon/epoxy panels with 70kg/m^3 core density impacted at 23J

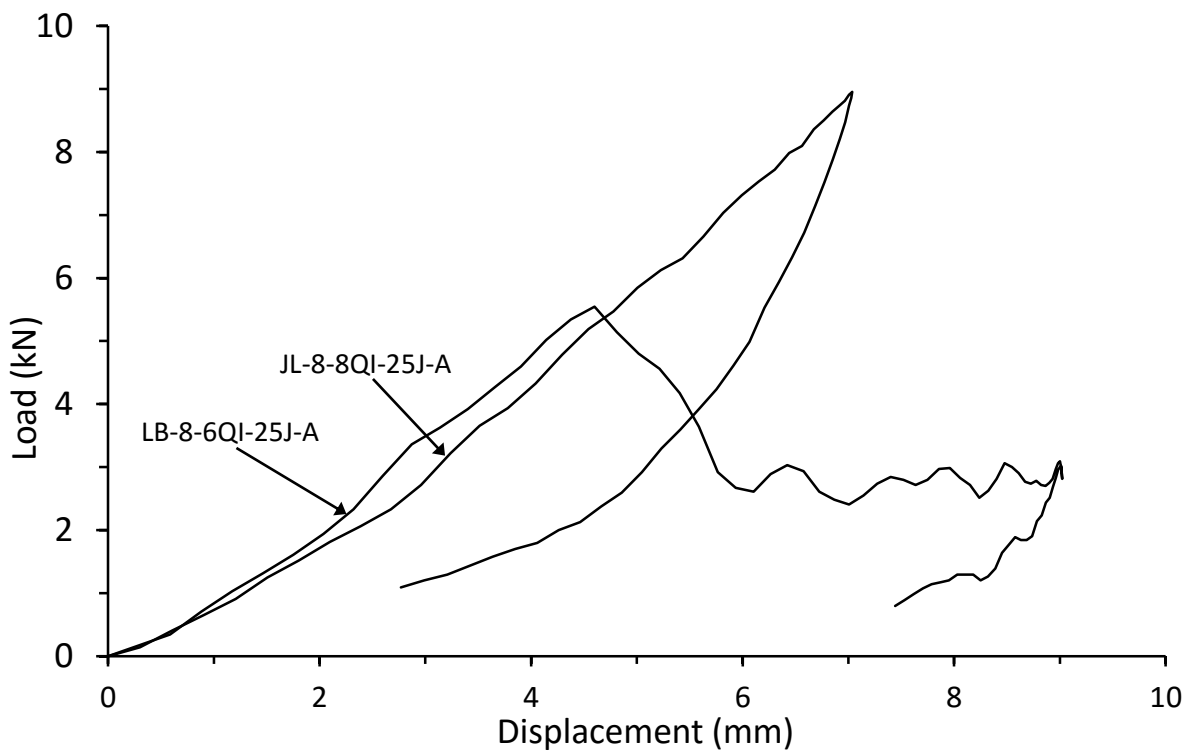


Figure 4.2.20. Load vs displacement response comparison for thin symmetrical and unsymmetrical QI carbon/epoxy panels with 70kg/m^3 core density impacted at 25J

Skin lay-up

In Figure 4.2.21 and Figure 4.2.22 are responses from thin symmetrical CP and QI panels respectively. With flexural modulus for QI panels being lower than for the CP panels, the expected result would be to see a difference in the load displacement slopes between CP and QI. Once again, there is no significant difference between the responses of the two arrangements, implying that the reduction in flexural properties of the skin was not significant enough to counter the role the core plays in dictating the through the thickness response of the panels. The increase in thickness of the skins saw a similar reaction to the change of skin lay-up under impact.

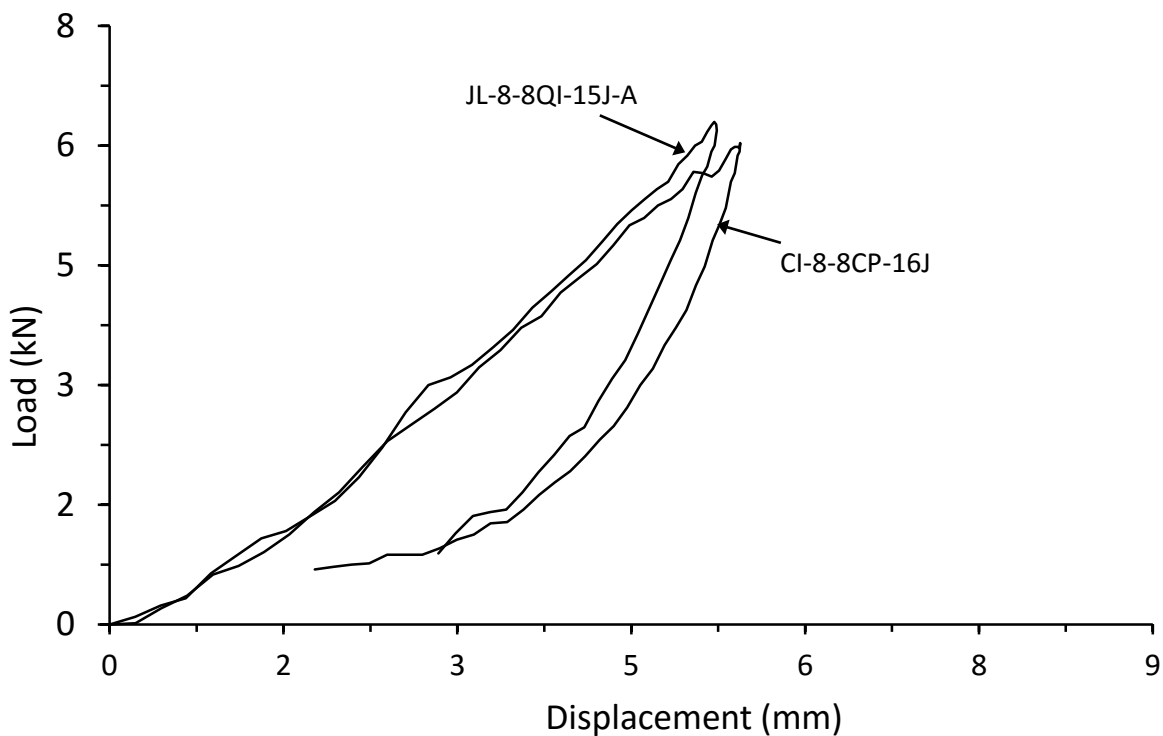


Figure 4.2.21. Load vs displacement response comparison for thin symmetrical CP and QI carbon/epoxy panels with 70kg/m^3 core density impacted at 16J and 15J respectively

Skin thickness

In Figure 4.2.23, a clear difference can be seen in comparing the thick and the thin unsymmetrical CP panels, the load displacement responses confirm a fairly instinctual notion that the thicker arrangements provide a stiffer resistance to the impact over the full range of impact energies, regardless of lay-up, skin asymmetry, and skin materials.

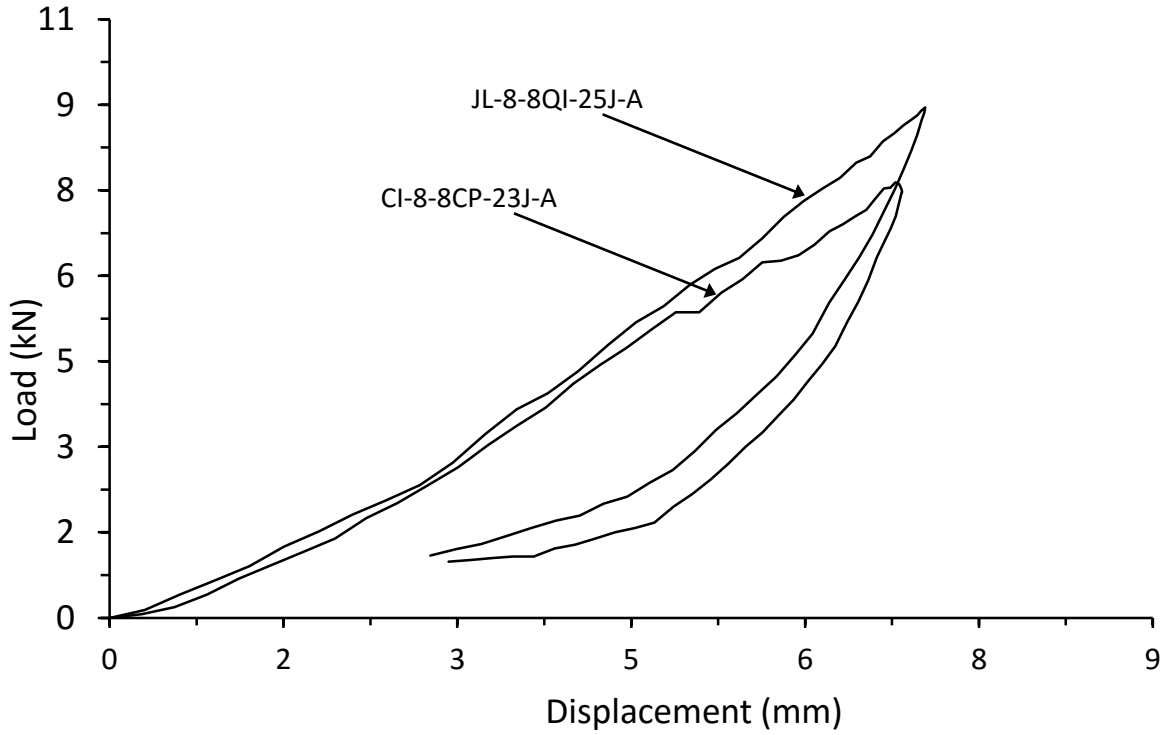


Figure 4.2.22. Load vs displacement response comparison for thin symmetrical CP and QI carbon/epoxy panels with 70kg/m³ core impacted at 23J and 25J respectively

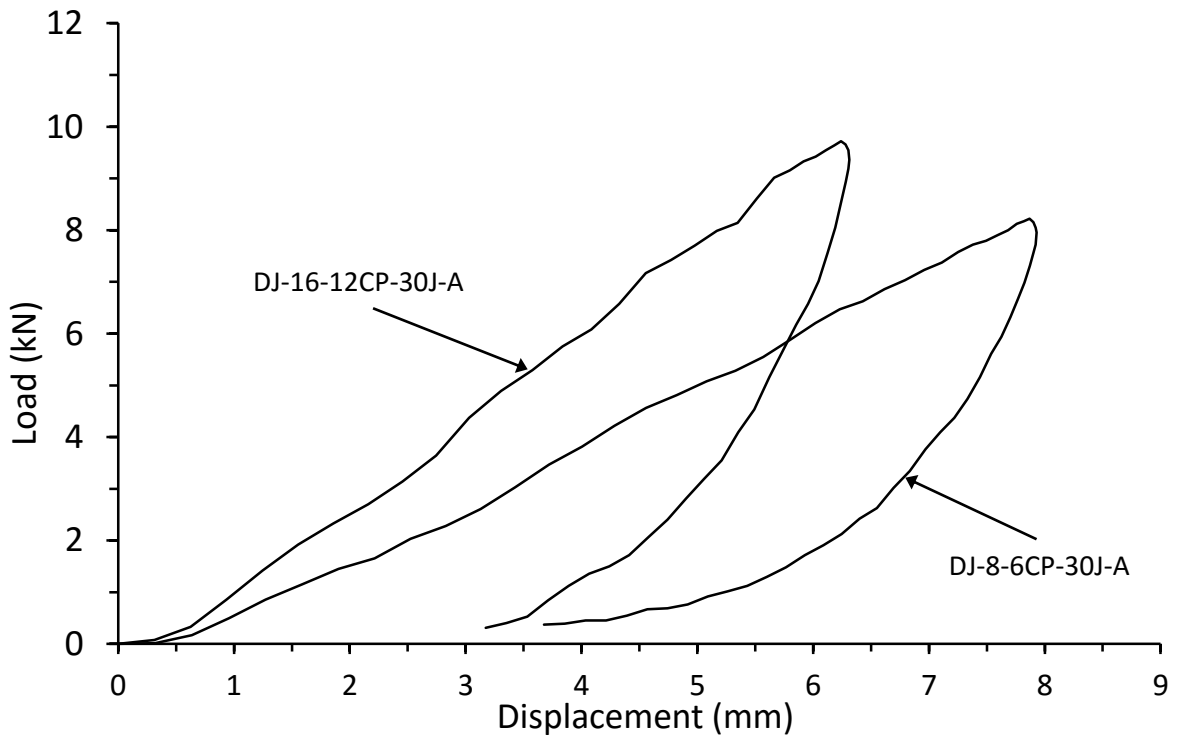


Figure 4.2.23. Load vs displacement response comparison for thick and thin unsymmetrical CP carbon/epoxy panels with 70kg/m³ core density impacted at 30J

Skin materials

Shown in Figure 4.2.24 and Figure 4.2.25 are the load displacement responses from thin glass and carbon/epoxy CP panels respectively. From the responses, there was a clear trend separating the two material types, with the gradients from the carbon panels being steeper, showing the carbon/epoxy panels are stiffer than the glass panels in both thin and thick arrangements. This result was expected, with the flexural and interlaminar moduli in particular being higher in the carbon/epoxy material. The glass/epoxy panels did carry some advantageous properties that assisted in the damage resistance of the panels. Although the panel underwent larger levels of deformation through global bending, with typical displacements of the impactor being higher than in the carbon panels impacted at a similar IKE, (just over 1mm more in thin panels and just over 0.5mm more in thick panels), the ability to endure high levels of tensile strain have provided the glass fibre skins with a remarkable fracture toughness, delaying the onset of fibre fracture in thin and thick panels when compared to the carbon/epoxy skins.

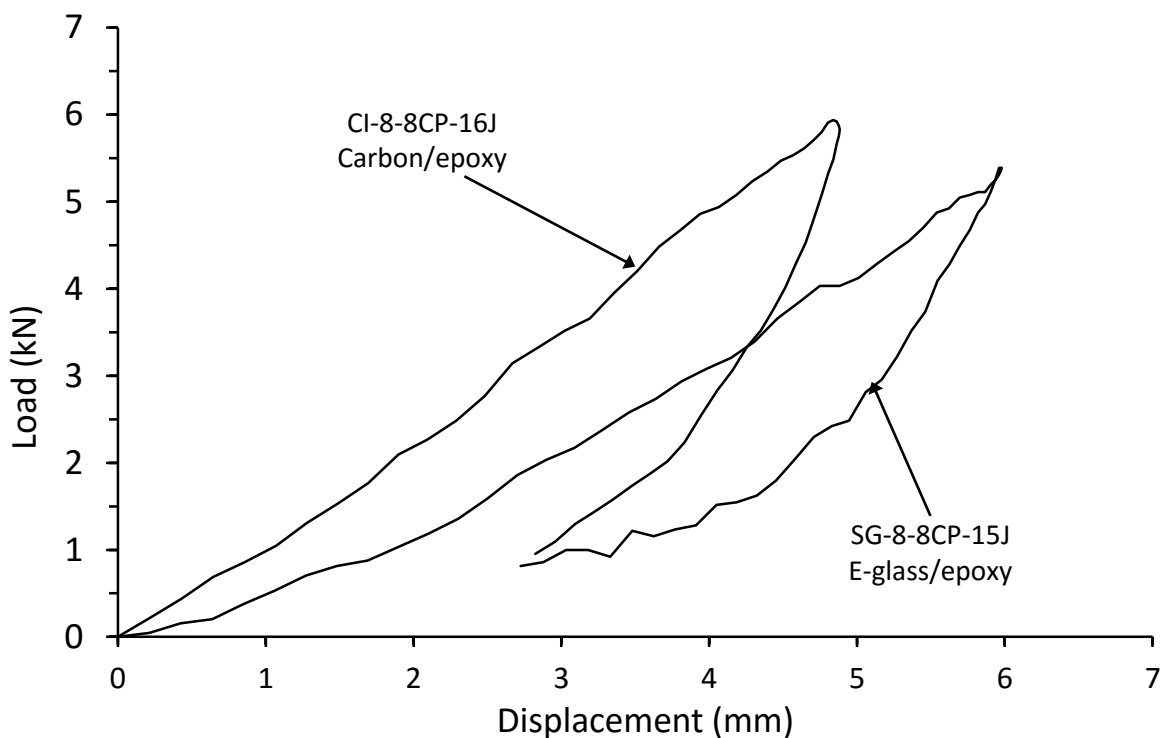


Figure 4.2.24. Load vs displacement response comparison for thin symmetrical CP carbon and E-glass/epoxy panels with 70kg/m³ core density impacted 16J and 15J respectively

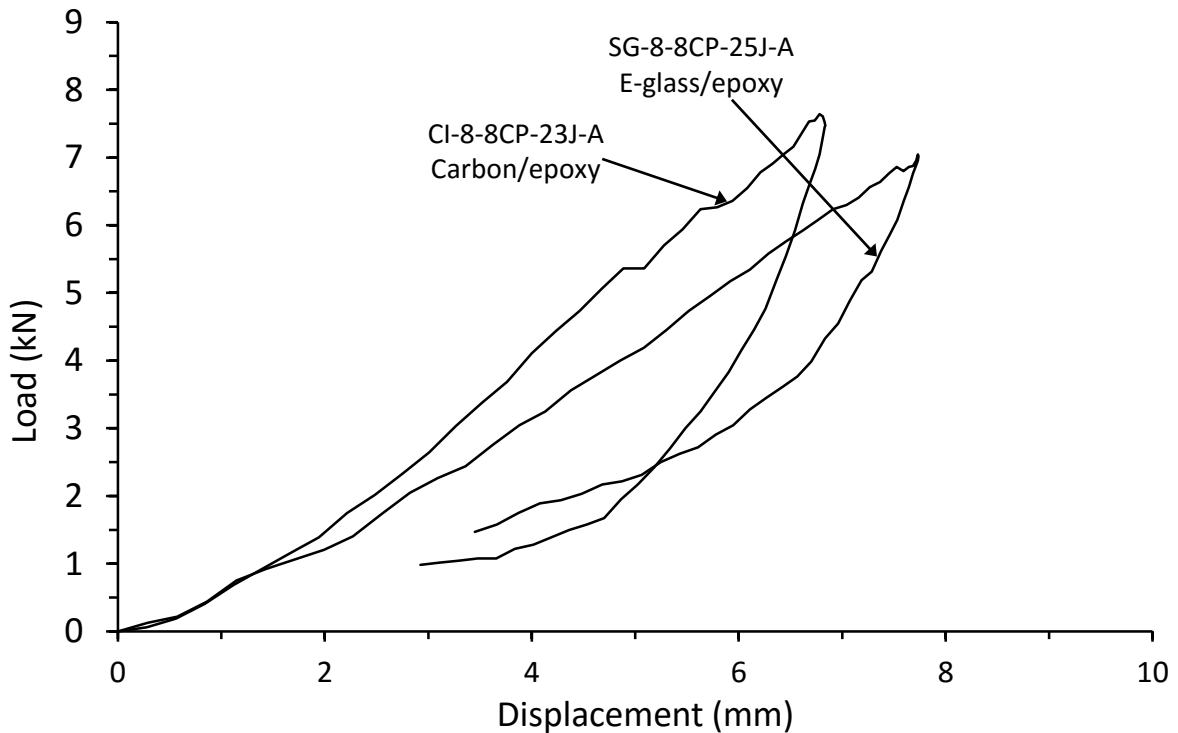


Figure 4.2.25. Load vs displacement response comparison for thin symmetrical CP carbon and E-glass/epoxy panels with 70kg/m³ core density impacted at 23J and 25J respectively

Core density

Shown in Figure 4.2.26 are the load displacement responses for thin symmetrical CP panels with core densities of 70, 110 and 135kg/m³. As seen from the material properties of the core in Section 2.1.2, with the core density almost doubled, the crush strength is increased almost threefold. As a result of this, a much stiffer response would be expected of the panel, as through the thickness travel of the impactor should be resisted by the denser core and the load would be expected to increase at a greater rate, but with lower displacement. As seen below, the load and displacement responses fit with this expectation, however, the difference seen was unsubstantial. This suggests that the initial stiffness portion was heavily influenced by the skin properties, however, through the thickness propagation at peak load was reduced at similar levels of IKE in the denser core panels but with little difference between the 110 and 135kg/m³ densities. Although the difference in slope was relatively small, it is of note that the IKE limit for the onset of fibre fracture was greatly increased.

The relationships between the three different core densities in the unsymmetrical carbon/epoxy panel arrangements were generally the same as the symmetrical arrangements where the panel rigidity increased as the core density was increased, however the difference between the densities was smaller, with almost no difference between the 110 and 135kg/m³ core panels. However, the overall

damage resistance of the panel was still affected by the increase in the core density, with increased displacement at lower impact loads and an earlier onset of fibre fracture the lower the core density.

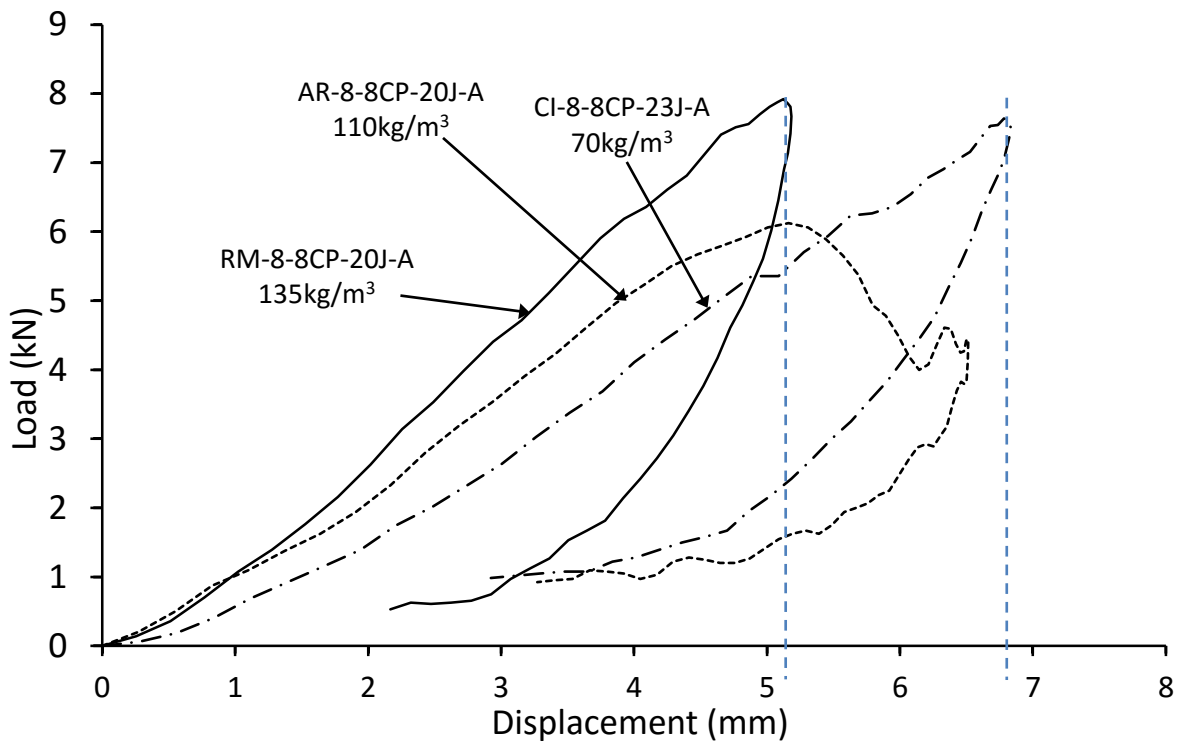


Figure 4.2.26 Load vs displacement response comparison for thin symmetrical CP carbon/epoxy panels with 70, 110 and 135kg/m³ core densities impacted at 23J, 20J and 20J respectively

4.3. Effects varying skin thickness and skin lay-up on damage mechanisms

In Figure 4.3.1 the extents of skin delaminations are given in terms of IKE for both thin and thick symmetrical panels. Trend lines drawn on these and all subsequent graphs in these sections are hand drawn, to illustrate the typical data trends of the individual test groups. Multiple delaminations that spread through different TTT interfaces were commonly observed and often were not at equal distance from the impact location. The delamination extent of the impacted skin used here was thus the largest extent projected through the thickness. The data trends in the rising stage were similarly parabolic in nature, shown in Figure 4.3.1. This indicated that the spread of delamination was initially swift but absorbed little energy and it decayed significantly from the delamination extent of about 40 mm onwards in CP and thick QI panels and 20mm in thin QI panels. As the front of the larger delaminations was far away from the immediate vicinity of the impact location, its local interlaminar shear (ILS) stresses could be low and thus it was very difficult for the supplied IKE to drive the level of the ILS stresses up further. These parabolic decaying trends suggest that the additional increase of absorbed energy could be due to the generation of multiple delaminations. As expected, those extents stopped increasing in the stage when ply fracture set in. Generally, the skin laminates in a QI lay-up

ought to be more delamination resistant with a ply-to-ply angle of 45° , this was evident in Figure 4.3.1 in the thin QI panel trend, with maximum measured delaminations of approximately 25mm, compared to almost 70mm in the thin CP arrangements at similar levels of IKE. Interestingly, thick panels with skins in a QI lay-up seemed to show the greater level of delaminations than those with a CP lay-up. This loss of lower ply-to-ply angle advantage in the thick arrangements showed a shift in the way the damage was being absorbed in the thicker panels, showing a reduction in the local ILS stresses around the impact area, shifting the focus more towards global deformation, accounting for the reduced performance of the relatively low flexural rigidity of the thick QI panels when compared with the thick CP skinned panels. Shown in Figure 4.3.2 are the skin delamination lengths in terms of IKE for both thin and thick unsymmetrical panels. Considering again the thickness and lay-up effects at play, there seems to be no change in the trends seen in the symmetrical panel signified by a sharp increase initially followed by a muted decay. Further proof of the improved delamination resistance of the thin QI panels can be seen, as well as the reduction of this effect with the increasing thickness of the skins. Interestingly, the further reduction of the flexural rigidity through panel asymmetry has collapsed the delamination curves for the thick CP and QI panels on to each other, further suggestion that the switch to a more globally dominated deformation under impact was changing the way in which the damage mechanisms were developing in the panel. Counter to the observed trends were three points from the thin CP unsymmetrical tests, highlighted by a dashed circle. The delaminations measured in these panels were almost half that of other panels in a similar arrangement, with no other damage mechanism showing an unusual value to explain the greatly reduced delamination extent.

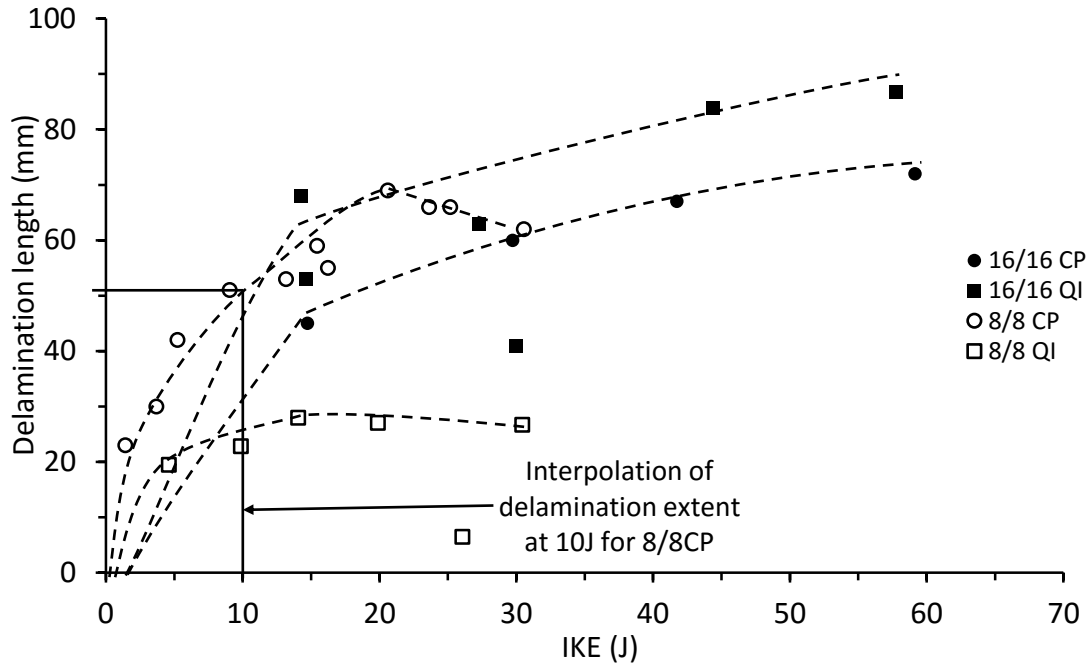


Figure 4.3.1. Delamination length vs incident kinetic energy for thin and thick symmetrical CP carbon/epoxy and QI panels with 70 kg/m³ core density

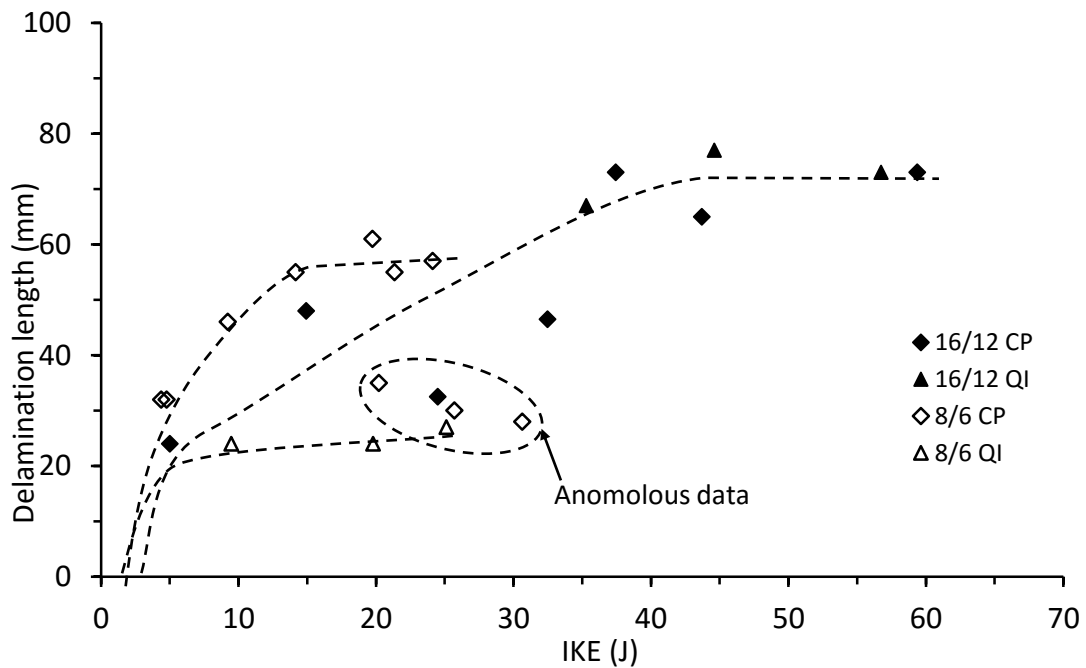


Figure 4.3.2. Delamination length vs incident kinetic energy for thin and thick unsymmetrical CP and QI carbon/epoxy panels with 70 kg/m³ core density

Figure 4.3.3 and Figure 4.3.4 exhibit the extents of core crushing in terms of IKE for both thin and thick symmetrical and unsymmetrical panels. Similar to the development of delaminations over the IKE range, core crush length against IKE also displayed an initial parabolic trend, indicating a swift development of core damage at low levels of IKE. Comparing the core damage in the thin symmetrical

panels, the QI panels show an increased level of core crushing, which was consistent with the increased resistance to the spread of delaminations seen above. This effect was less visible in the thin unsymmetrical panels, implying the spread of core damage was dependent on a certain level of panel rigidity interacting with the core. For the thick panels, both symmetrical and unsymmetrical, no difference existed when the lay-up of the skins was changed, with both trends being collapsed upon each other. The high panel rigidity in the thick skin arrangements saw the load being more effectively spread to the core than in the thin panels, removing the dependency on the differences in skin arrangement, and with the core material the same this resulted in a very similar level of core damage. Comparing the thick and thin panel trends for development of core crushing, only a small difference in core crushed extent exists, with thicker panels developing higher overall regions of crushed core, at a slightly faster rate. This difference was again due to the higher level of rigidity of the thicker panels, however, this damage mechanism was largely controlled by the core properties, since the effect of doubling the skin thickness had only a minor increase in the level of core damage over a full range of impact energies.

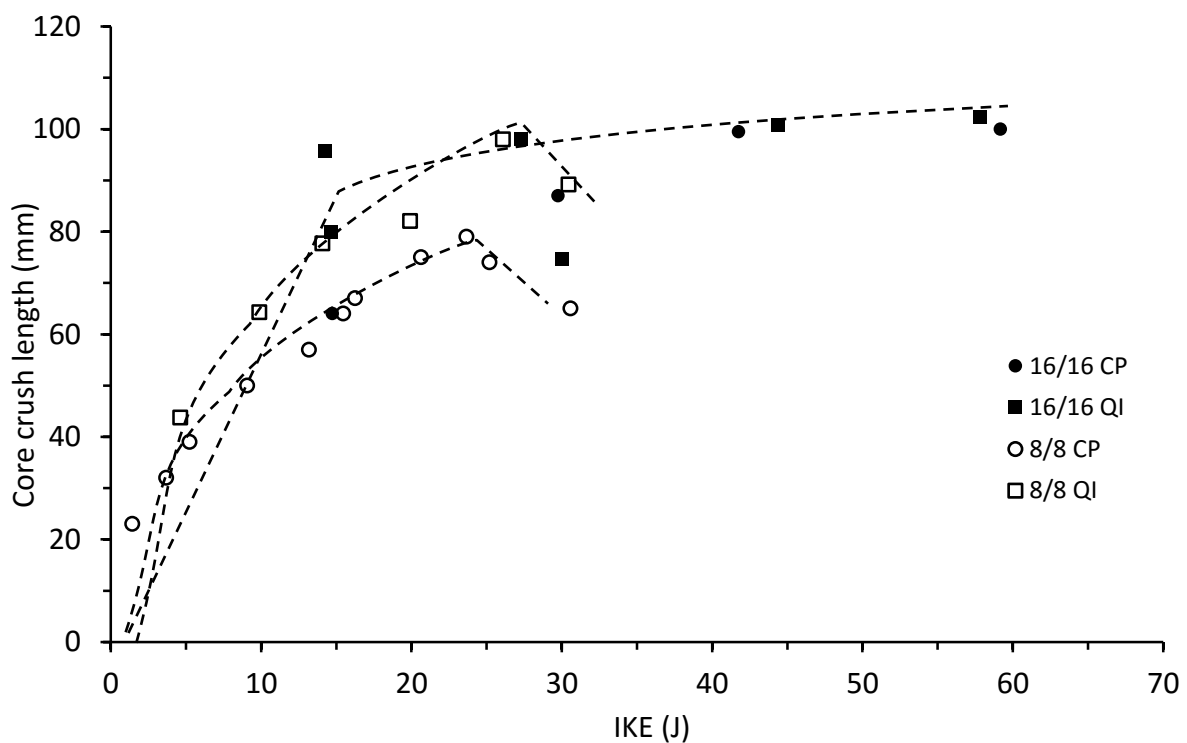


Figure 4.3.3 Core crush length vs incident kinetic energy for thin and thick symmetrical CP and QI carbon/epoxy panels with 70 kg/m³ core density

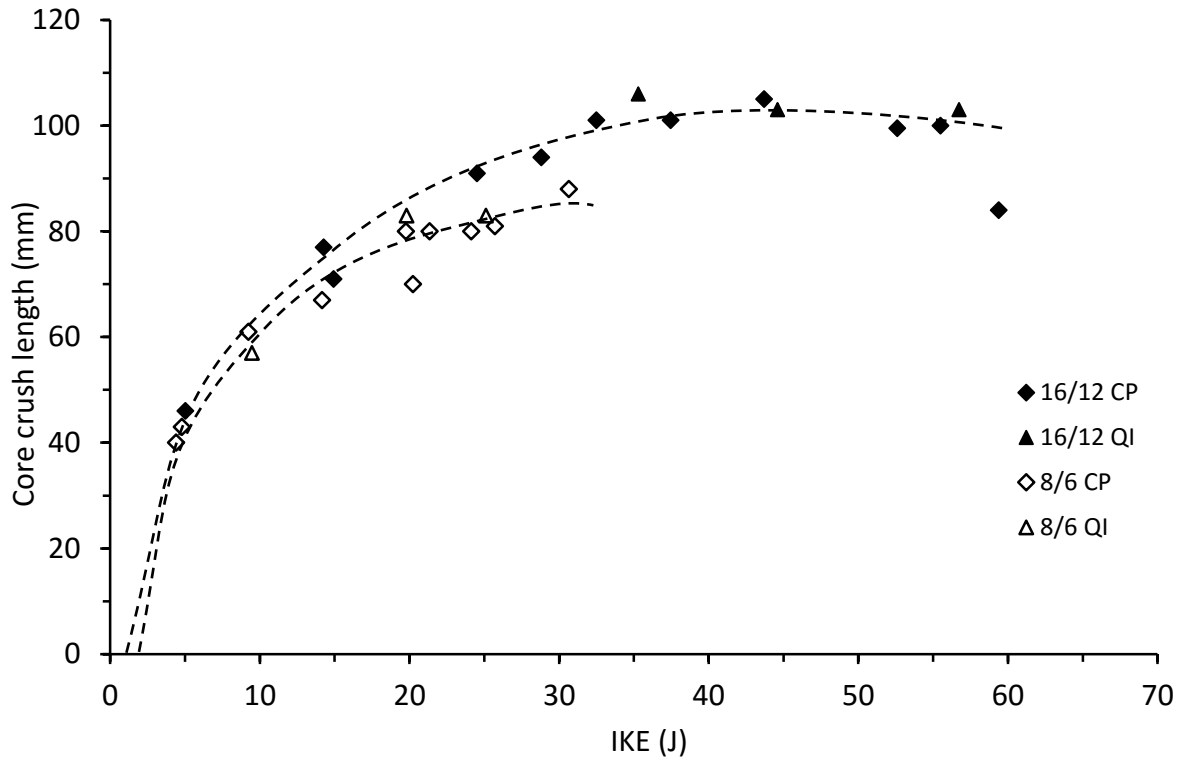
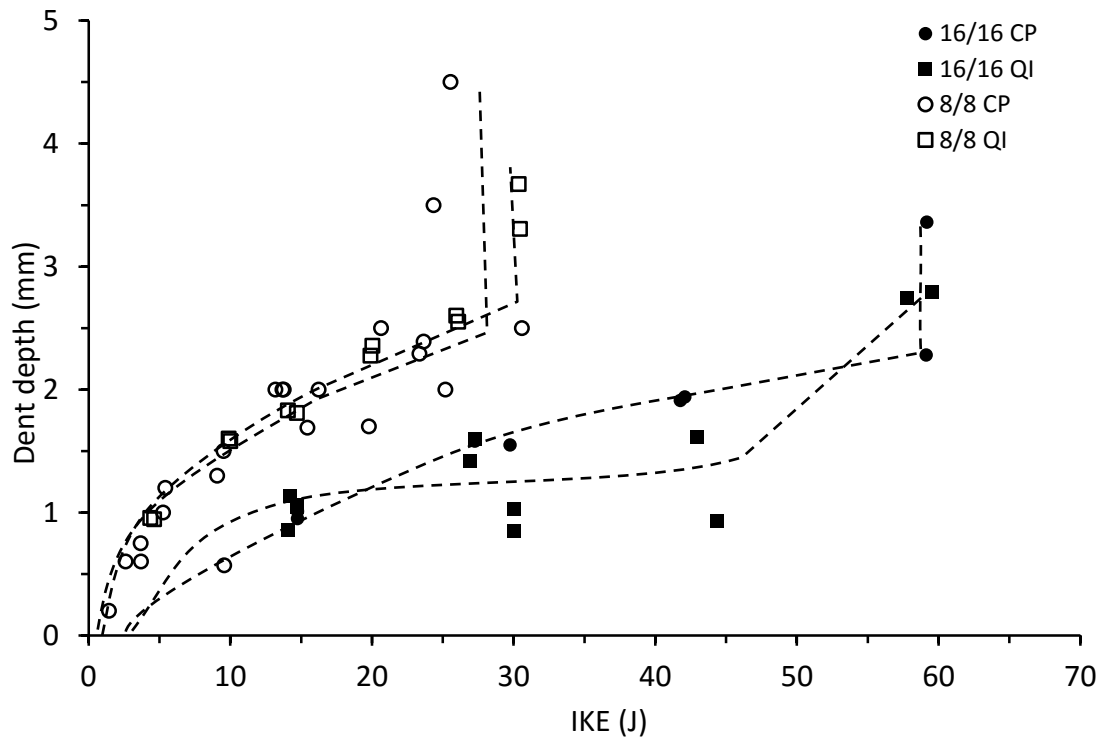


Figure 4.3.4. Core crush length vs incident kinetic energy for thin and thick unsymmetrical CP and QI carbon/epoxy panels with 70 kg/m³ core density

Figure 4.3.5 shows the development of dent depths from thin and thick symmetrical sandwich panels against an increase of IKE. For thin panels, the trend of this dent depth development was initially parabolic; decaying with IKE, but at the end follows a dramatic increase in dent depth at the upper end of the IKE range when fibre fracture in the impacted skins started occurring. Thus, the use of dent depth as damage metric before the occurrence of fibre fracture could still be viable. There was visible data scatter at the transitional region at about 25J. A partial loss of the primary resistance (i.e. the impacted skin) to the advancement of the impactor should be accompanied with the dramatic increase of dent depths via the majority of data points; a few data points that did not follow the trend could be due to spring back of broken delaminated sub-laminates, creating the uneven bottom of their craters. It is worth noting that there seems to be no effect on performance due to change of layup, due to the core being a major controlling factor of the through thickness propagation of this damage mechanism. All the observations established above for thin symmetrical and unsymmetrical panels were also very much true for thick panels, shown in the same figures, except that the late dramatic increase in dent depth here was less. This was expected, as the thicker skins offered much greater resistance against the vertical crushing from the impact. At any given IKE up to about 25J, doubling the skin thickness reduced the dent depths by 50%, including the initial thresholds and the level of IKE required to fracture fibres in the impacted skins was doubled. Figure 4.3.6 shows the comparison of the dent depth-IKE relationships from both thin and thick unsymmetrical panels, each with CP and QI

skins. All the key features obtained from the skin thickness comparison of symmetrical panels can be again observed for unsymmetrical panels. Due to the relative insignificance of the TTT properties between CP and QI lay-ups, the indentation depth over the IKE range was seen to be independent of changes in the lay-up in both thin and thick skinned panels, and propagation was controlled more significantly by the core properties, resulting no observable difference between indentation progression when lay-up was altered, and skin thickness was maintained.



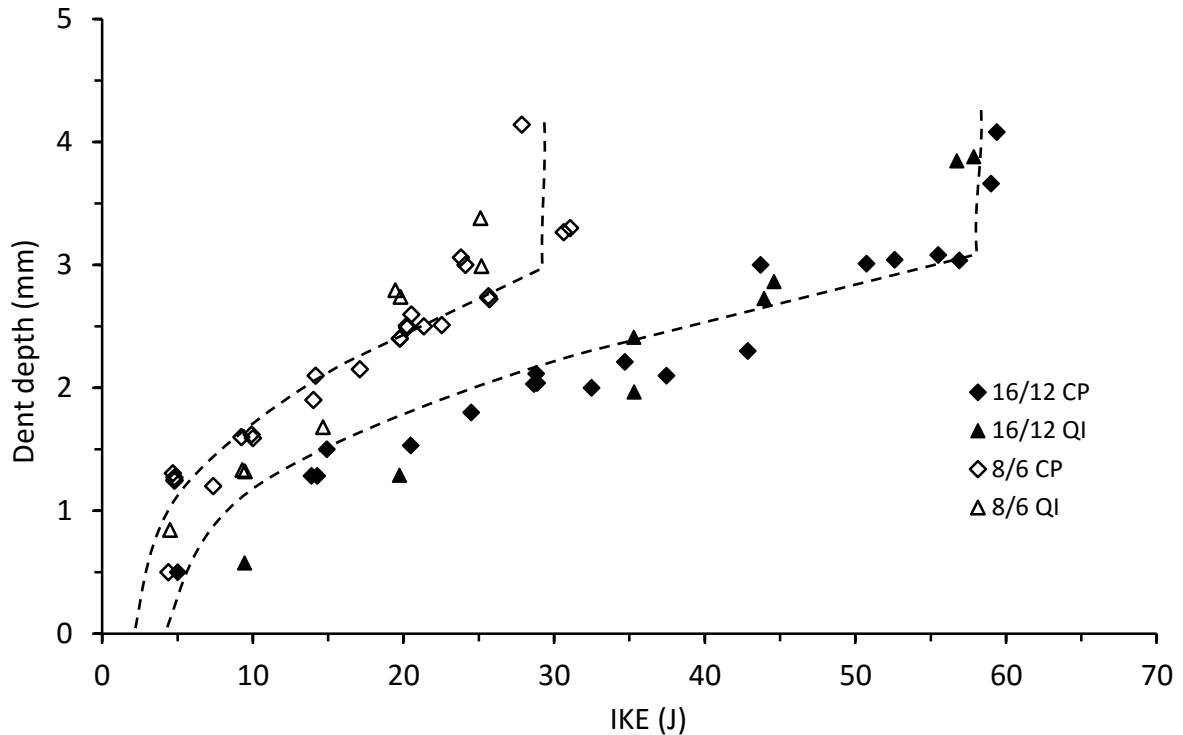


Figure 4.3.6. Dent depth vs incident kinetic energy for thin and thick unsymmetrical CP and QI carbon/epoxy panels with 70 kg/m³ core density

Looking at the energy absorption characteristics in sandwich panels, core crushing, delamination and ply fracture in impacted sandwich panels were found to be the main damage mechanisms and hence they absorbed almost all of supplied IKE. It was observed that the first two mechanisms were absorbing around 70% of the supplied IKE as shown in Figure 4.3.7 and Figure 4.3.8 irrespective of skin thickness or lay-up, which seems to suggest that it might be core crushing that contributed overwhelmingly to the 70% absorption. When skin fracture occurred, the percentage of absorbed energy went up abruptly over 93%. The thin and thick symmetrical specimens showed little variation in the threshold for the onset of fibre fracture between the CP and QI lay-ups. However, the relationships shown in the unsymmetrical panels suggest some transitional differences due to lay-up effects. In the thin arrangements, the QI specimens displayed a gradual, but distinct transition to the high level of absorbed energy, relating to failure in the face sheet such as splitting or partial fracture of the face sheet before full face sheet penetration occurs. The CP panels have a more ambiguous transition, with a number of panels following the QI trend, with fibre fracture occurring at 20J, as well as a number that further resist the onset of fibre fracture, with the face sheet of the panel remaining intact up to 30J. This trend was repeated in the thick unsymmetrical panels, where CP panels form a larger transition zone than the QI panels, indicated by the grey shaded area. These large transition zones and variations in the occurrence of fibre fracture could be related to the very inhomogeneous construction of the honeycomb. Unlike a foam core, aluminium honeycomb is made up of a cell

centres, free walls and nodes. If the impactor were to strike the skin where a cell centre was located, behaviour exhibited would be different to that if a node or free wall was struck. The nodes, which have double wall thickness, should provide the greatest through the thickness resistance to impact loading, resulting in higher local stresses in the skin, followed by the free wall and lastly, the cell centre which must rely on the surrounding cell structure. This could also relate to the varying level of impact energies, and hence impact velocities, resulting in a variation in the stiffening of the panel due to the dynamic response of the panel under different impact speeds. These phenomena could account for the delay in fibre fracture in panels with the same skin and core constructions.

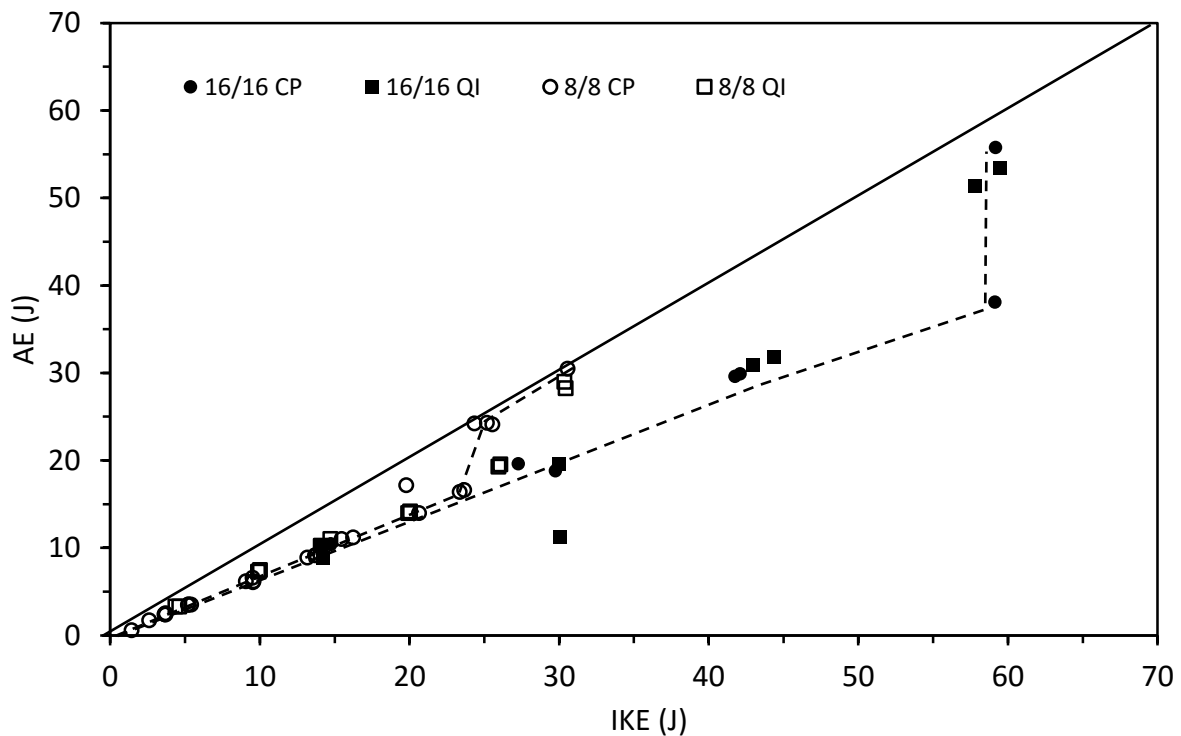


Figure 4.3.7. Absorbed energy vs incident kinetic energy for thin and thick symmetrical CP and QI carbon/epoxy panels with 70 kg/m³ core density

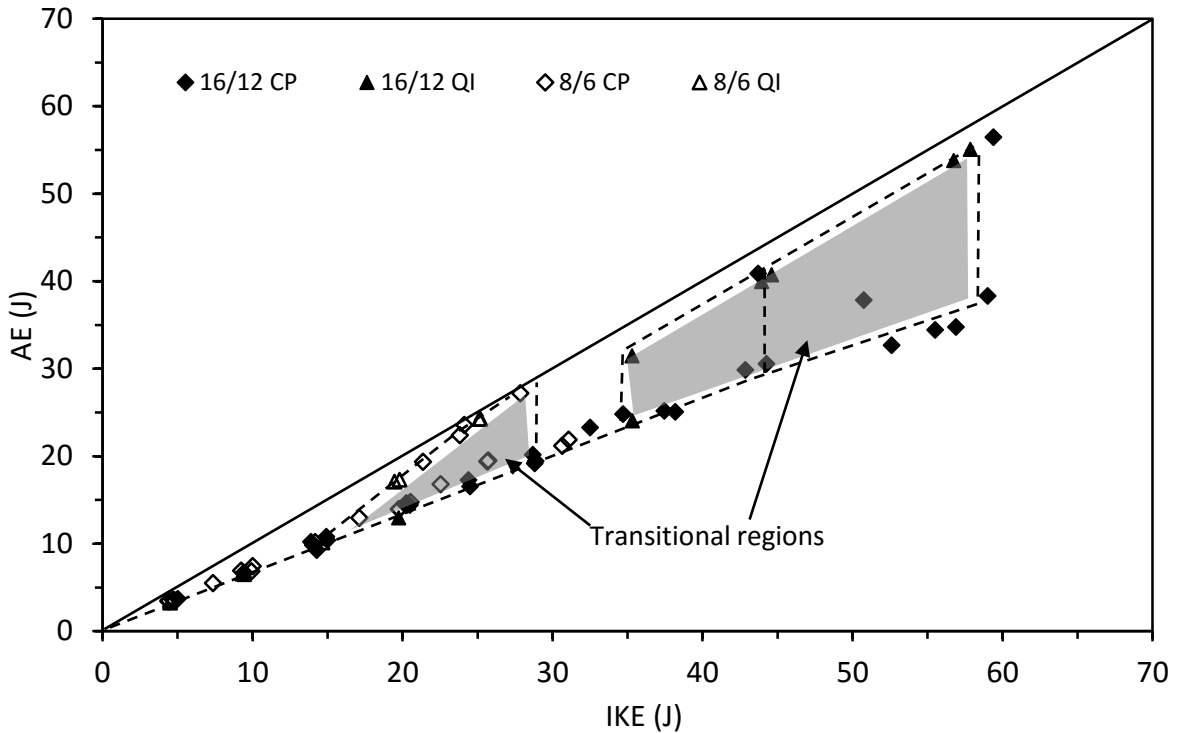


Figure 4.3.8. Absorbed energy vs incident kinetic energy for thin and thick unsymmetrical CP and QI carbon/epoxy panels with 70 kg/m³ core density

In Figure 4.3.9 and Figure 4.3.10, the growth of dent depths from thin and thick, CP and QI, symmetrical and unsymmetrical panels are shown against maximum impact force. Before the occurrence of fibre fracture the relationship between dent depth and impact force was essentially linear. Once fibre fracture occurs, the maximum impact forces stops increasing, signifying a specific yield load of the skin material. There was a small spread to the data, suggesting a further interaction between impact speed, impact location and the development of fibre fracture in the top skin. The effect of layup on the response of the panels was mixed. In the symmetrical panels, the onset of the trend reversal happened around the same threshold level between CP and QI skins, however, it is clear in the unsymmetrical panels that both thick and thin panels with QI skins suffer fibre fracture at an earlier peak load than the CP panels, signified by the blue dashed lines. This was likely to be connected again to the lower flexural rigidity in the panel causing the higher global bending and through thickness displacement of the impactor, resulting in a fibre fracture occurring at a lower level of impact force due to higher bending stresses in the impacted skin. The overall trend of the thick panels was similar, with a linear rise up to the onset of fibre fracture which halted the further increase in impact load with higher IKE. As indicated on the graph, the trend lines can be extrapolated to intercept the x-axis to provide the thresholds at which damage is likely to be initiated in the panels, hence comparing the performance of thick and thin skin panels, it can be seen that the increased skin thickness provides a

greater resistance to the through the thickness travel of the impactor, resulting in a damage initiation threshold of nearly three times larger than in the thinner panels.

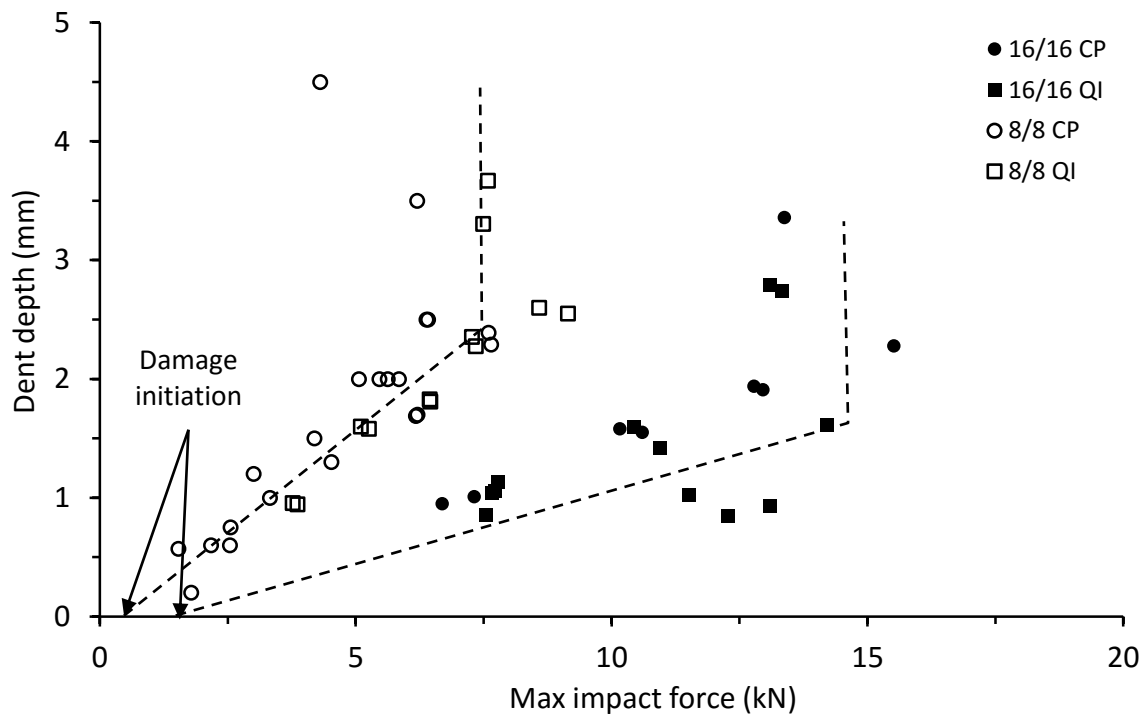


Figure 4.3.9. Dent depth vs maximum impact force for thin and thick symmetrical CP and QI carbon/epoxy panels with 70 kg/m³ core density

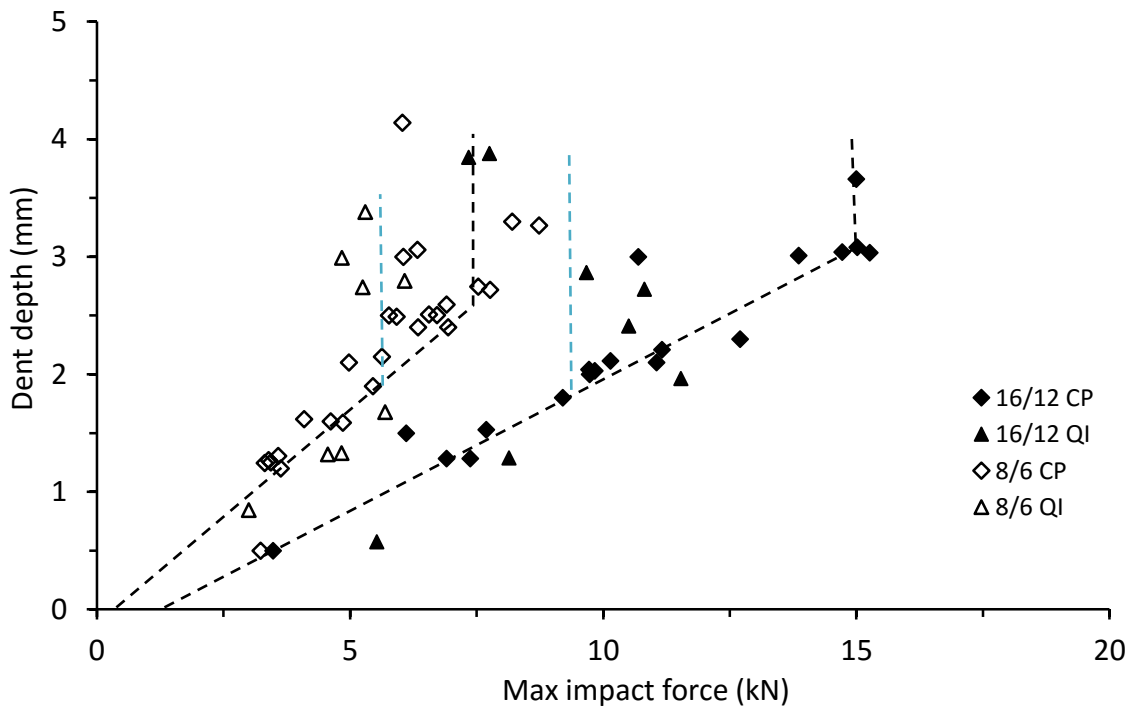


Figure 4.3.10. Dent depth vs maximum impact force for thin and thick unsymmetrical CP and QI carbon/epoxy panels with 70 kg/m³ core density

Following the early speculation of core crushing absorbing the most of the IKE, it was interesting to examine how core crushing grew with IKE in both transverse and TTT directions of impacted sandwich panels. Figure 4.3.11 and Figure 4.3.12 show the crushed core extent-dent depth relationship for both thin and thick symmetrical and unsymmetrical carbon/epoxy panels. Because of the hemispherical shape of the impactor, the contact with the skin of a sandwich panel at its apex upon impact increased continuously (up to the radius of the impactor) and thus the growth of core crushing in both directions took place simultaneously. The estimated growth rate for thin symmetrical CP panels was initially about 115 mm in the transverse direction for 1 mm in dent depth and then dipped by nearly five times, down to about 20 mm for 1 mm in dent depth. When fibre fracture occurred around 25J, such growth in the transverse direction ceased whereas it continued in the TTT direction. For thin QI symmetrical panels, the first phase was similar to the CP panels, however, the reduction in the transverse growth was lower, with a growth rate of core crushing in the planar direction of nearer 30mm per 1mm in the transverse direction. This once again reflected the increased delamination resistance in the QI panels leading to further development of other damage mechanisms to absorb the impact energy. For thick panels, the overall trends of the crushed core extent-dent depth relationship shown in Figure 4.3.11 and Figure 4.3.12 were similar to that of thin panels. The estimated initial growth rate was fractionally slower than that of thin panels, and the subsequent growth rate in the second phase remained constant from the first phase, resulting in a growth almost twice that of thin panels, as the thicker skins continued to spread the impact force much more effectively than the thin skins. Again, when fibre fracture occurred, the growth of crushed core ceased in the transverse direction but continued substantially in the TTT direction, representing the third phase. As in the thin panels, the thick QI panels displayed a larger growth rate in the planar direction compared to the CP panels. The unsymmetrical panels show similar trends between thicknesses and lay-up. However, in the thicker arrangements, there exists little to no difference between the growth rate of the CP and QI panels.

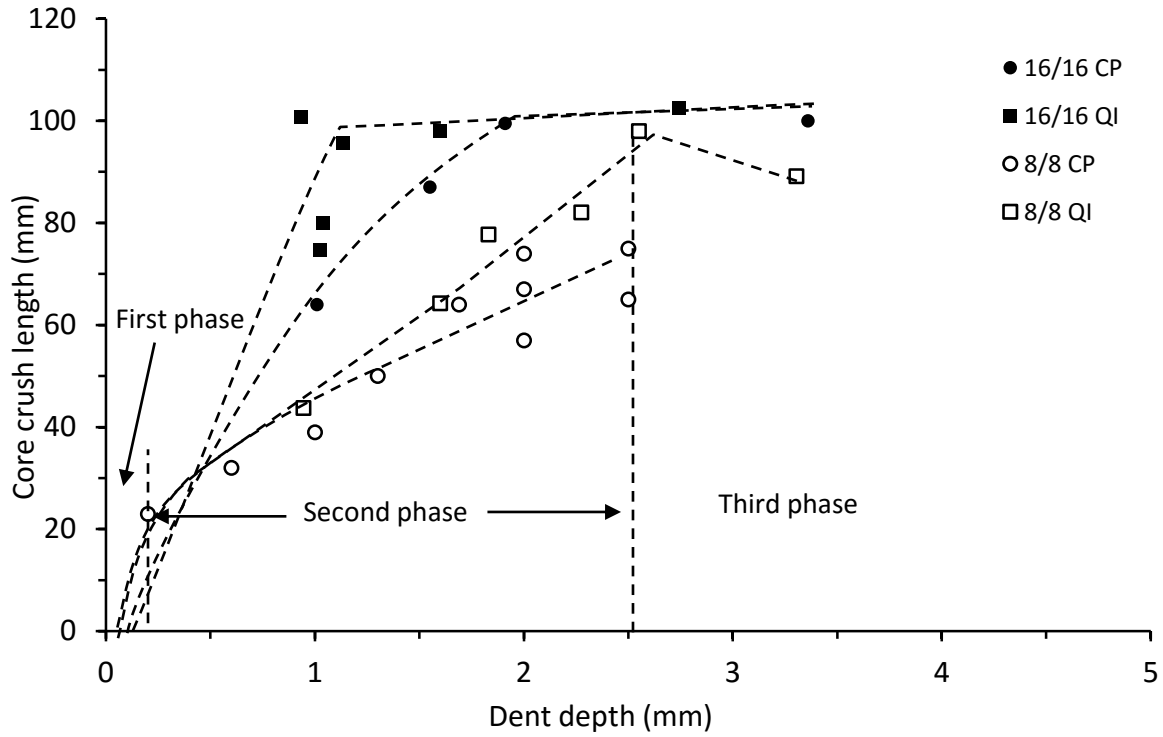


Figure 4.3.11. Core crush length vs dent depth for thin and thick symmetrical CP and QI carbon/epoxy panels with 70 kg/m³ core density

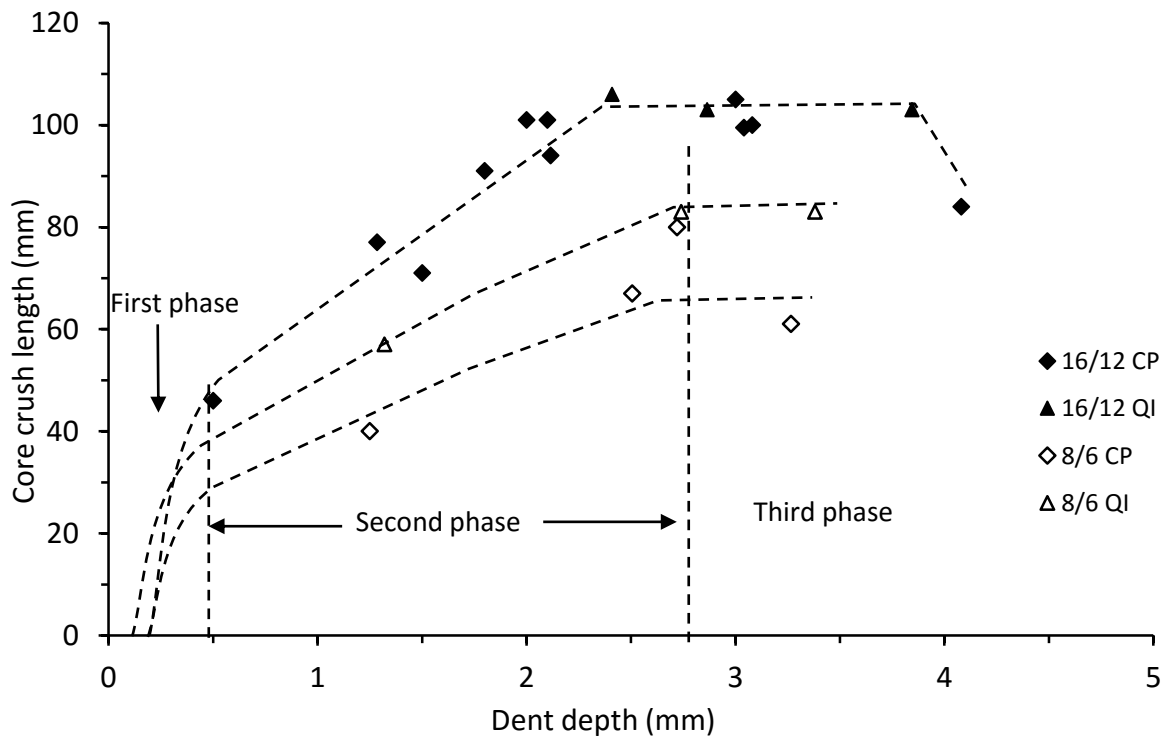


Figure 4.3.12. Core crush length vs dent depth for thin and thick unsymmetrical CP and QI carbon/epoxy panels with 70 kg/m³ core density

4.4. Effect of panel symmetry on damage mechanisms

This section will aim to investigate what differences, if any, the lack of symmetry through the thickness has on the performance of sandwich panels under impact. The previous section has outlined a number of general performance characteristics of some unsymmetrical arrangements with a focus on the effects of different thicknesses and lay-ups in unsymmetrical arrangements, this section will provide insight into the direct affects that thinner distal skin arrangements had on the impact performance and damage characteristics measured during testing.

Figure 4.4.1 and Figure 4.4.2 show the respective extents of skin delaminations as plotted against IKE and absorbed energy for thick and thin, CP and QI, symmetrical and unsymmetrical panels. Overall trends in the development of delaminations in thick panels sees very little difference between the symmetrical and unsymmetrical arrangements, with trends for the cross ply panels almost completely collapsed on to each other. The spread of delamination in the top skin of the panel can be assumed to be a function of the top skins characteristics and its interaction with the core. Similarly for the thin panels, the trends seen in the symmetrical CP and QI development of delamination length were repeated by the unsymmetrical arrangements, again, implying little reliance on the contribution of the distal skin to the resistance of delaminations forming under impact loading.

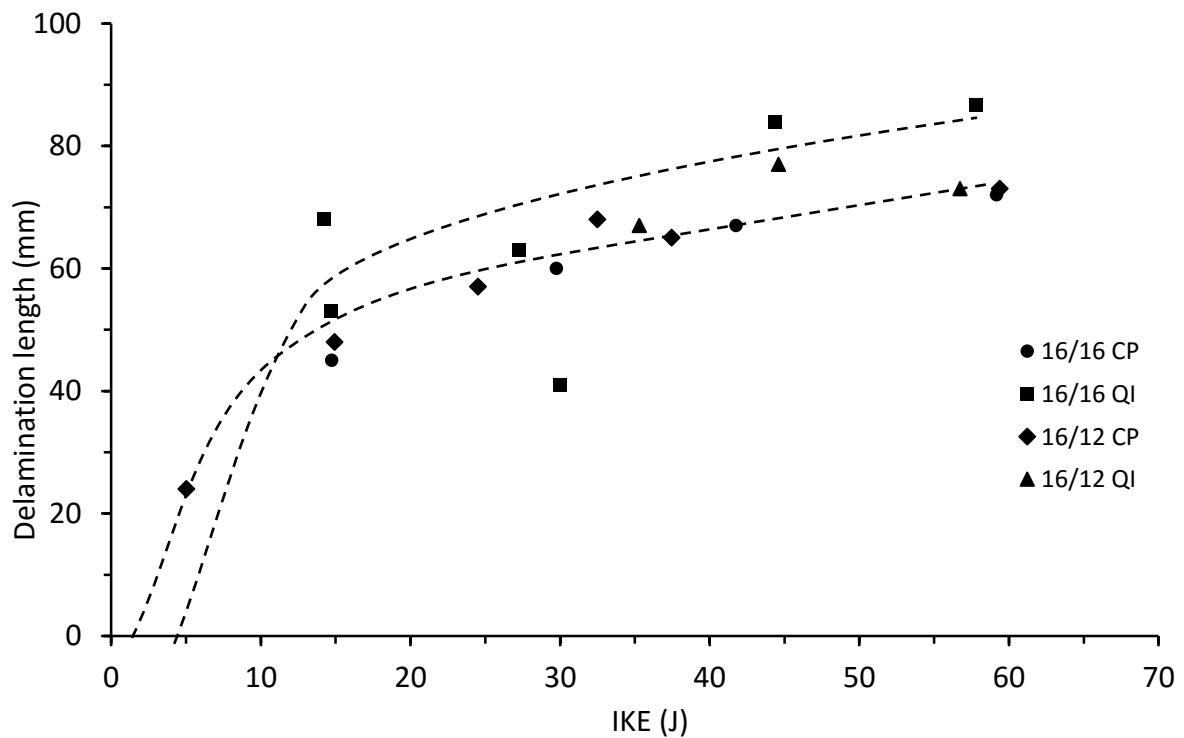


Figure 4.4.1. Delamination length vs incident kinetic energy for thick symmetrical and unsymmetrical CP and QI carbon/epoxy panels with 70 kg/m³ core density

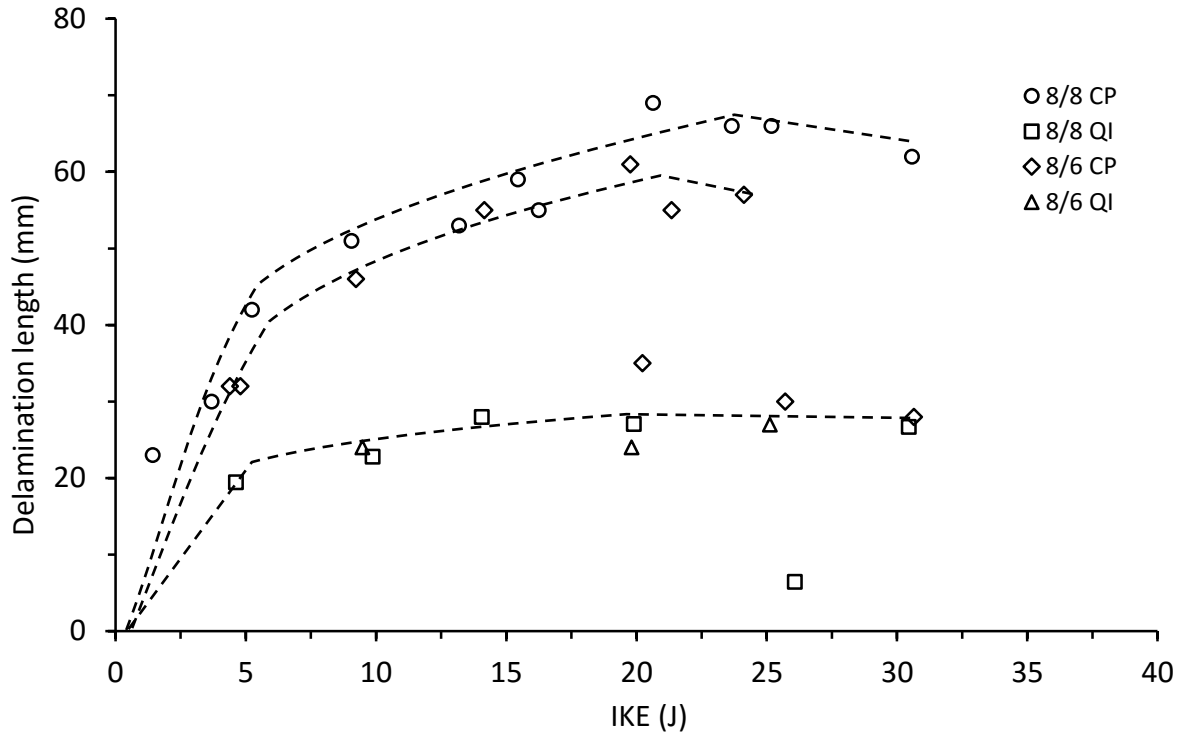


Figure 4.4.2. Delamination length vs incident kinetic energy for thin symmetrical and unsymmetrical CP and QI carbon/epoxy panels with 70 kg/m³ core density

Figure 4.4.3 and Figure 4.4.4 show the core crushing extents versus IKE for thick and thin, CP and QI, symmetrical and unsymmetrical panels. In both graphs, onset and propagation of core crushing appears to be insensitive to the reduction of plies in the distal skin, and therefore the interaction between the impacted skin and the core was intimately linked to the development of planar core crushing. The unsymmetrical panels had a slightly reduced flexural rigidity, resulting in a more global panel response, however, the effect of this difference was not reflected in the planar spread of core damage.

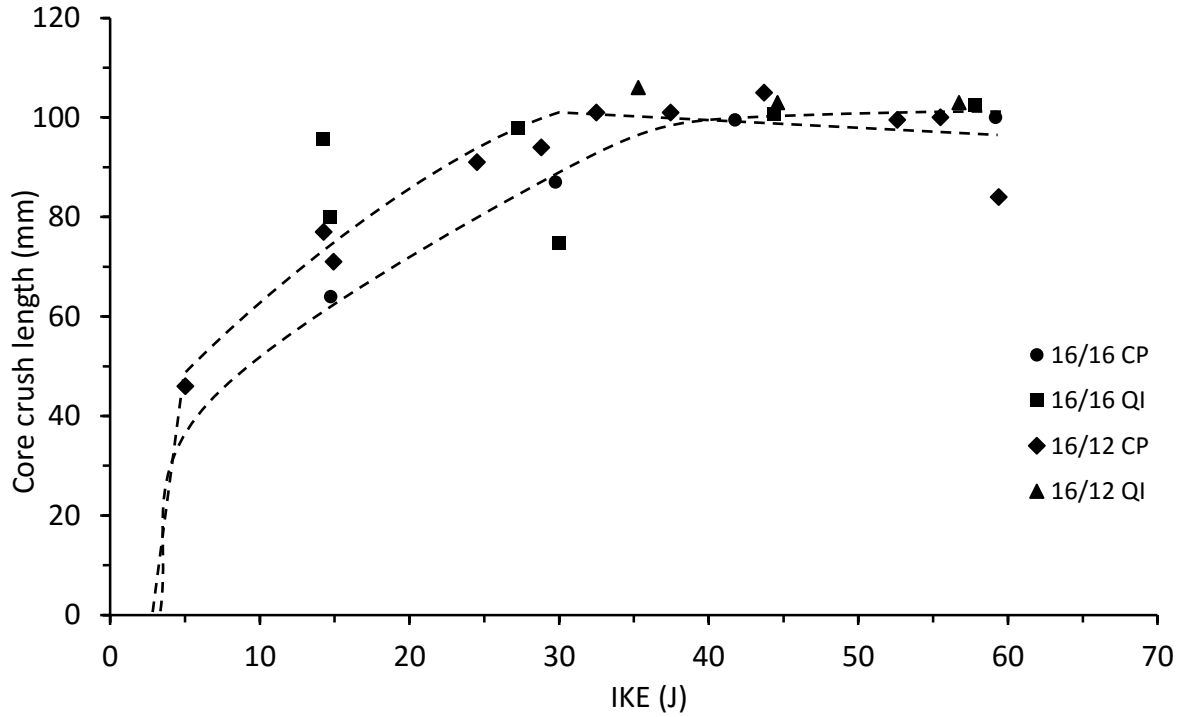


Figure 4.4.3. Core crush length vs incident kinetic energy for thick symmetrical and unsymmetrical CP and QI carbon/epoxy panels with 70 kg/m³ core density

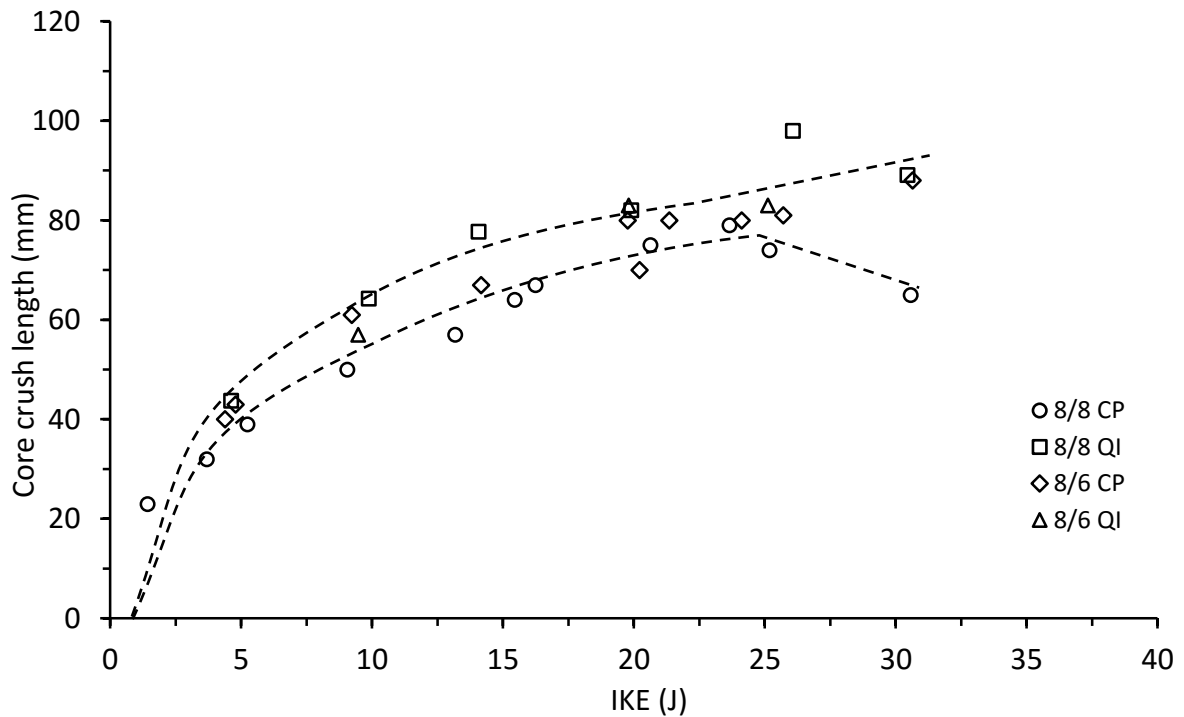


Figure 4.4.4. Core crush length vs incident kinetic energy for thin symmetrical and unsymmetrical CP and QI carbon/epoxy panels with 70 kg/m³ core density

Figure 4.4.5 and Figure 4.4.6 show the respective extents of residual indentation in thick and thin, CP and QI, symmetrical and unsymmetrical panels against the IKE. Overall, the trend of the damage development in both thin and thick panels was similar between the symmetrical and unsymmetrical arrangements, both showing a parabolic increase up to the occurrence of fibre fracture, where a drastic, vertical increase in the dent depth was observed. In terms of overall magnitudes of dent depth propagation for a given level of IKE, the symmetrical panels did offer a higher resistance compared to their unsymmetrical counterparts in both CP and QI arrangements for thick and thin panels. This suggested that the development of residual indentation after impact was linked to the global stiffness of the panel, unlike the planar propagation of core damage as discussed above. The development of indentation is controlled by two mechanisms, firstly, the local indentation of the impacted skin under the impactor is mainly controlled by the core properties, and local skin properties, which would be similar for both symmetrical and unsymmetrical panels. Secondly, the global deformations of the panel add to the level of residual indentation, and due to the lower flexural resistance of the unsymmetrical panels, will be more significant, hence the difference between the two panels. With delamination and core crush extent having been established as similar, the increased residual indentation in the unsymmetrical panels may prove troublesome in the post impact performance of the unsymmetrical panels.

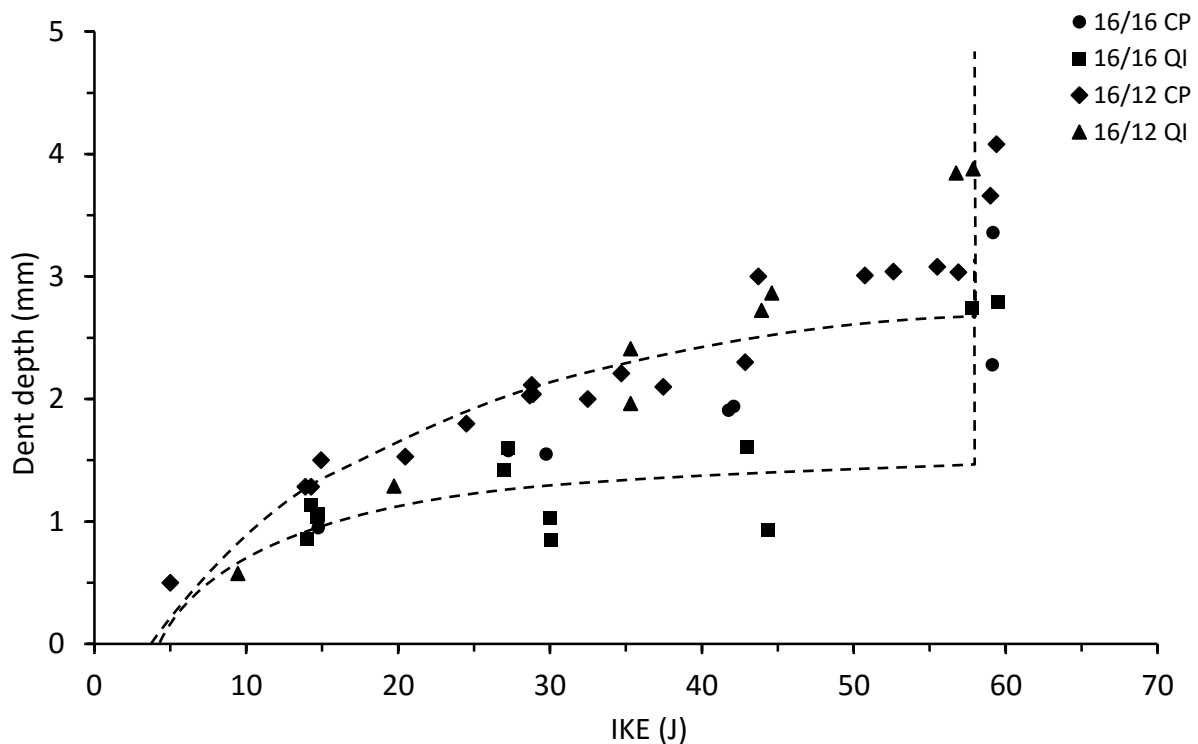


Figure 4.4.5. Dent depth vs incident kinetic energy for thick symmetrical and unsymmetrical CP and QI carbon/epoxy panels with 70 kg/m³ core density

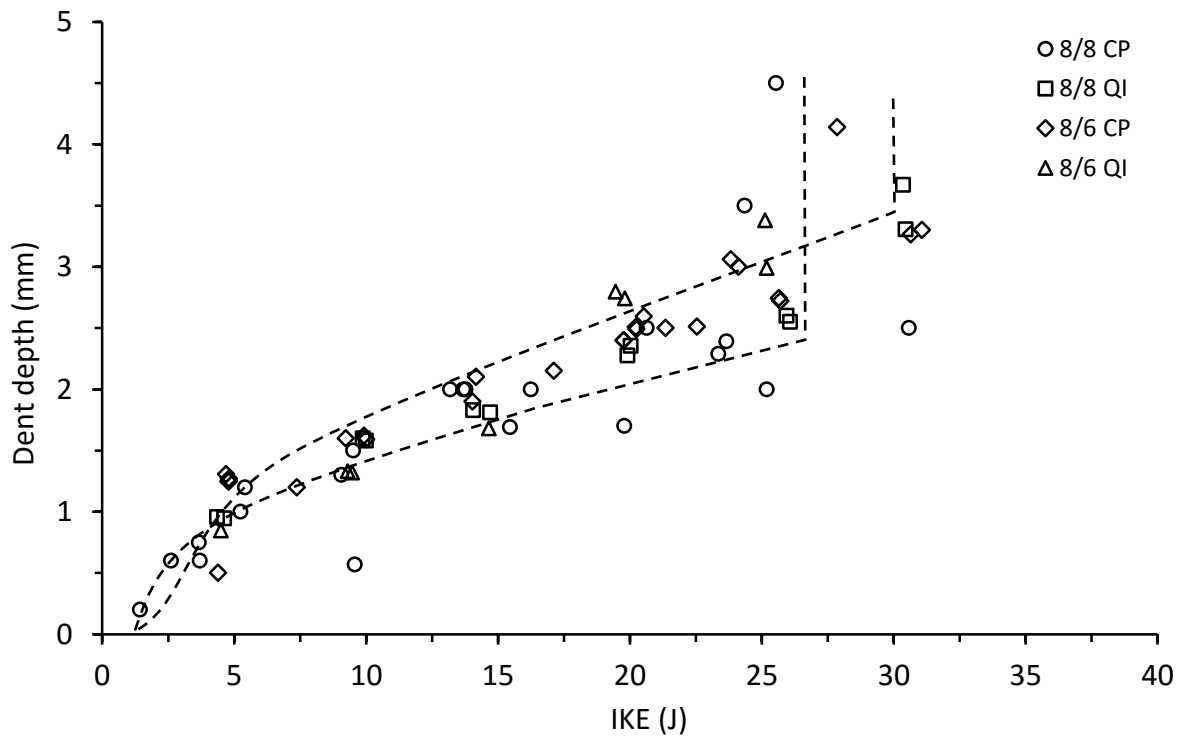


Figure 4.4.6. Dent depth vs incident kinetic energy for thin symmetrical and unsymmetrical CP and QI carbon/epoxy panels with 70 kg/m³ core density

Figure 4.4.7 and Figure 4.4.8 show the absorbed energy plotted against the IKE for thick and thin, CP and QI, symmetrical and unsymmetrical panels. Again, general trends between the symmetrical and unsymmetrical panels were similar, with both absorbing around 70% of the impact energy, being predominantly linked to the growth of delamination and core crushing, with a major increase in absorbed energy being signified by the occurrence of fibre fracture in the top skin. The unsymmetrical panels in both thick and thin, CP and QI, unanimously display an earlier threshold to the onset of fibre fracture. Clearly the lower level of flexural rigidity in these panels leads to lower local ILS stresses due to the larger overall global deformation of the panels, causing higher bending stresses in the top skins, resulting in an earlier failure threshold for fibre fracture in the panels in terms of both IKE and impact force.

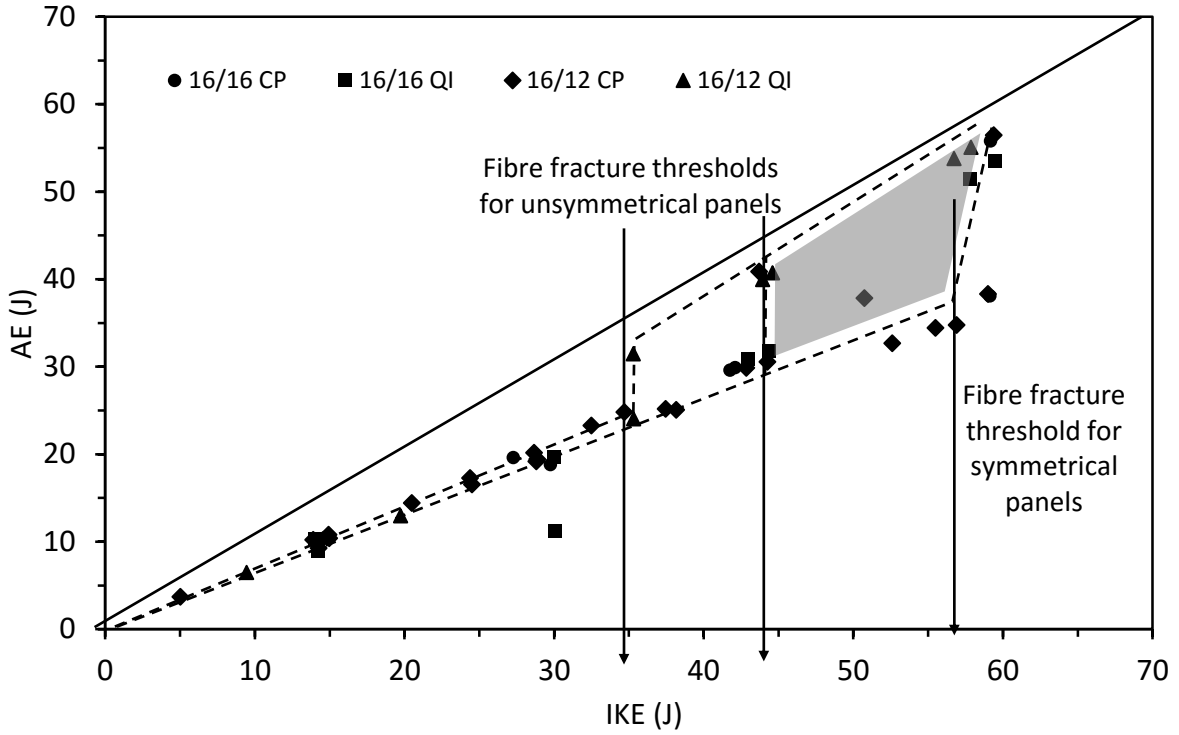


Figure 4.4.7. Absorbed energy vs incident kinetic energy for thick symmetrical and unsymmetrical CP and QI carbon/epoxy panels with 70 kg/m³ core density

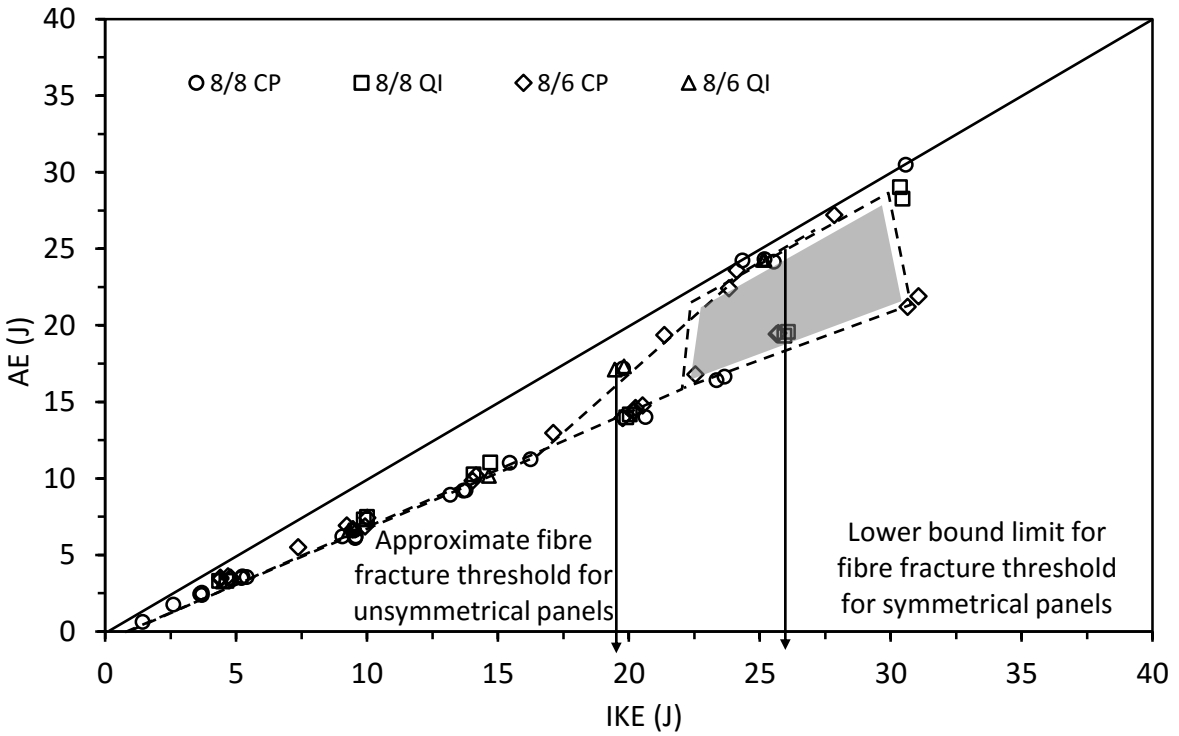


Figure 4.4.8. Absorbed energy vs incident kinetic energy for thin symmetrical and unsymmetrical CP and QI carbon/epoxy panels with 70 kg/m³ core density

4.5. Effects of varying panel composition on damage mechanisms

4.5.1. Core densities

Due to the lack of repeated impact testing in the 110kg/m^3 core panels, there was limited information on the internal damage mechanisms and their development for this type of panel arrangement, so the main comparisons will be made regarding the panels with 70 and 135kg/m^3 cores. Propagation of damage mechanisms for the 135kg/m^3 density core panels differed noticeably from the 70kg/m^3 density panels, due mainly to the higher compressive properties of the 135kg/m^3 core, the planar spread of core crush was typically similar to the delamination extent, whereas the measured core crush length was seen to be consistently higher than the delamination propagation in panels with a 70kg/m^3 core density. This is very clear in Figure 4.5.1 and Figure 4.5.2, displaying measured delamination and core crush length vs IKE respectively. In addition, panels with 70kg/m^3 core density developed core crush and delamination damage early in the IKE range, suggesting a threshold of between 1-2J for the development of internal damage mechanisms. Conversely, the 135kg/m^3 density core panels could have an IKE level of at least 5J before the development of these internal damage mechanisms. As the impact energies were increased the propagation of the delamination length and the crushed core length in the 135kg/m^3 density core panels were approximately 50% of the levels developed in the 70kg/m^3 panels. Unlike in the thicker skinned panel with the 70kg/m^3 core density, the increase in flexural rigidity from the skins alone was not sufficient to reduce the level of delamination and core crush lengths, showing that through the thickness propagation was linked closely to the development of both of these mechanisms, and with a higher core density the TTT propagation is expected to be limited. However, interfacial core/skin debond was found to occur in the midrange of the impact energies, which could prove troublesome in the in-plane compressive testing, since parts of the skin will be unsupported by the core, potentially increasing their susceptibility to local buckling.

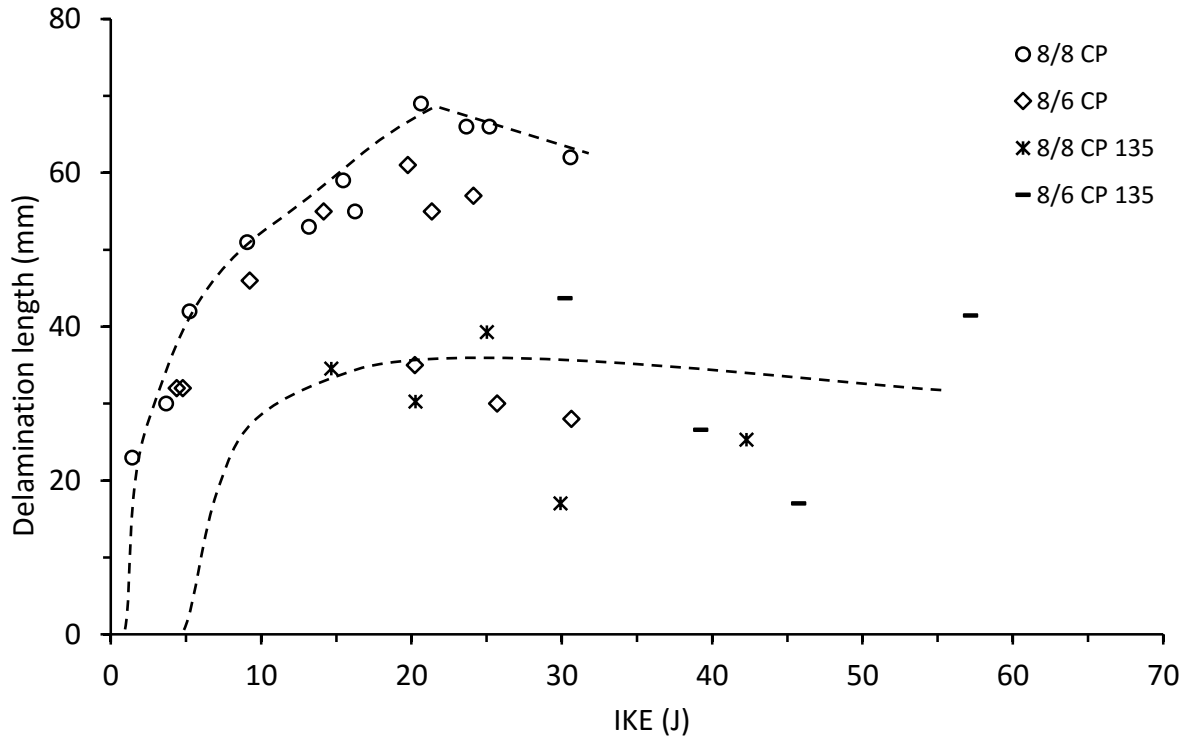


Figure 4.5.1. Delamination length vs incident kinetic energy for thin symmetrical and unsymmetrical CP carbon/epoxy panels with 70 and 135 kg/m³ core densities

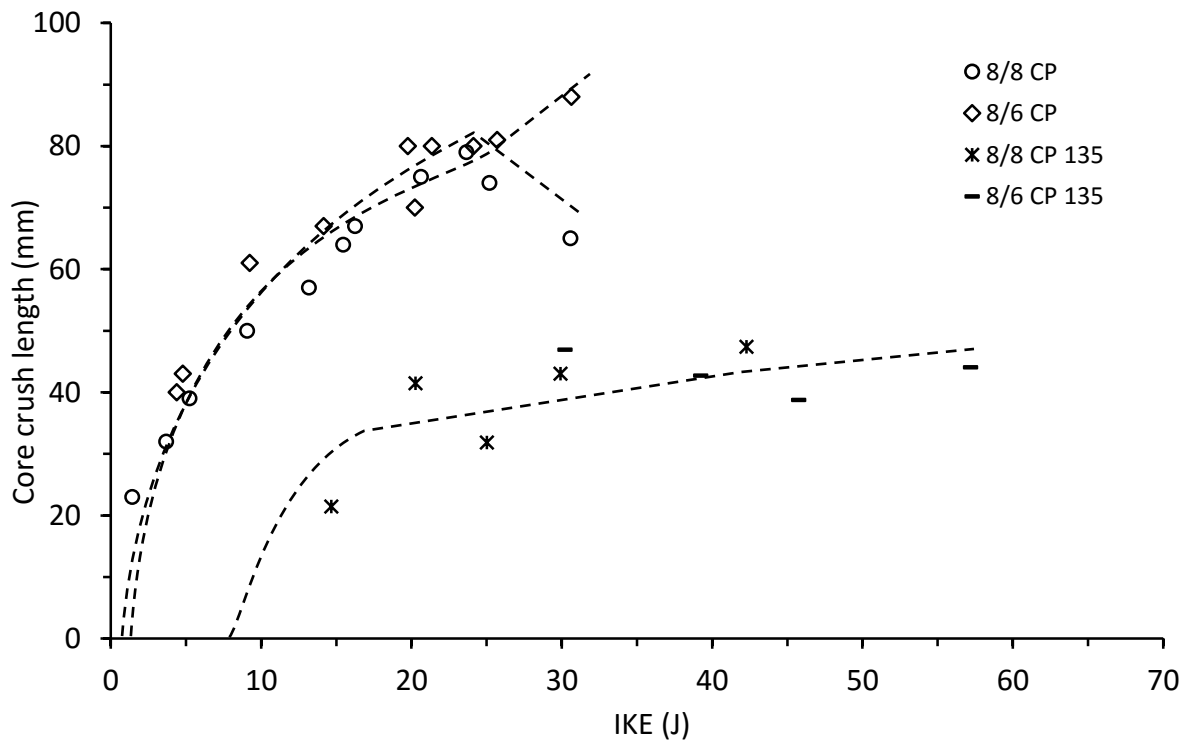


Figure 4.5.2. Core crush length vs incident kinetic energy for thin symmetrical and unsymmetrical CP carbon/epoxy panels with 70 and 135 kg/m³ core densities

Shown in Figure 4.5.3 and Figure 4.5.4 are the developments of the residual indentation of the top skin over the impact range of all three core densities for thin symmetrical and unsymmetrical carbon/epoxy panels. With a higher density core, the crush strength was increased, and it would be expected to resist plastic folding throughout the range of IKE compared to the low density core. This was backed up by the trends in the graphs. For symmetrical panels, the residual dent depth measured in the high density core panels was slower to develop over the early IKE range, and plateaued through the middle range, whilst the dent depth continued to rise in the low density panels. All three densities of core suffered the same extensive increase in dent depth with the occurrence of fibre fracture of the top skin, however, the maximum levels of indentation were lower and at higher levels of IKE for the higher density cored panels, for example the dent depth was 3.8mm at 40J for 135kg/m³ symmetrical panels compared to 4.5mm at 25J for the 70kg/m³ symmetrical panels. The unsymmetrical panels showed similar differences between the different core densities performances, with an increased resistance to the initial onset of indentation, delaying the occurrence of fibre fracture, and reduced maximum indentations at higher levels of IKE.

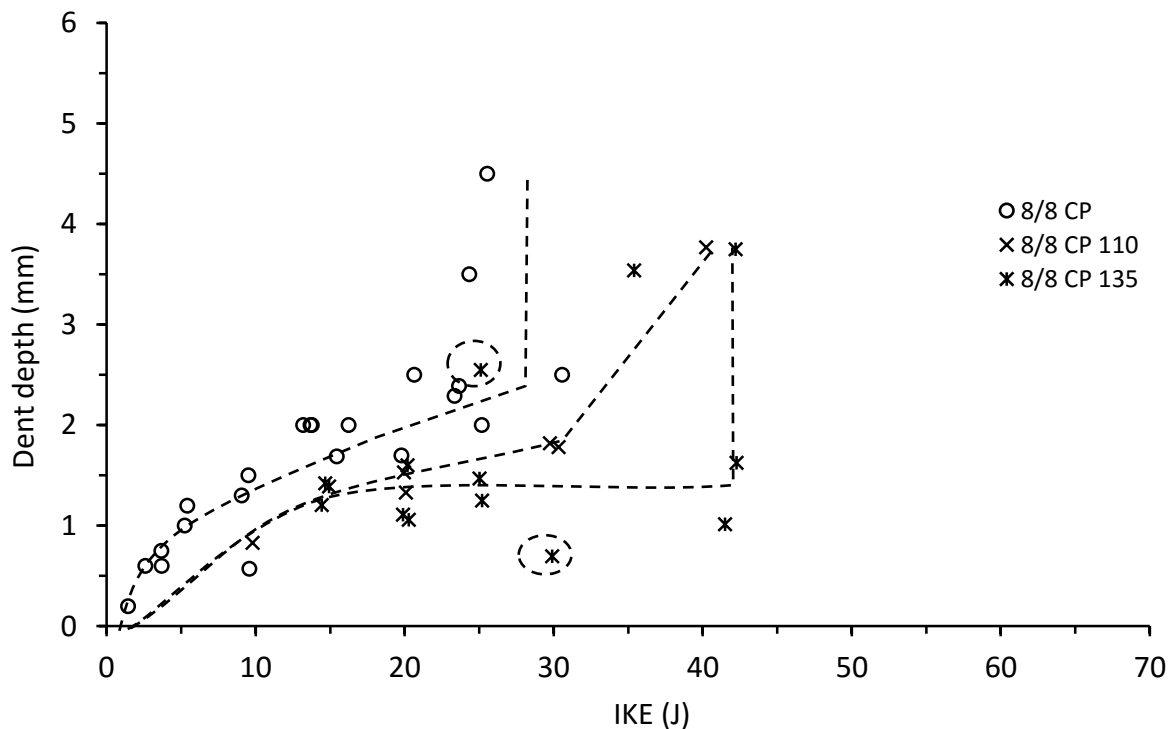


Figure 4.5.3. Dent depth vs incident kinetic energy for thin symmetrical CP carbon/epoxy panels with 70, 110 and 135 kg/m³ core densities

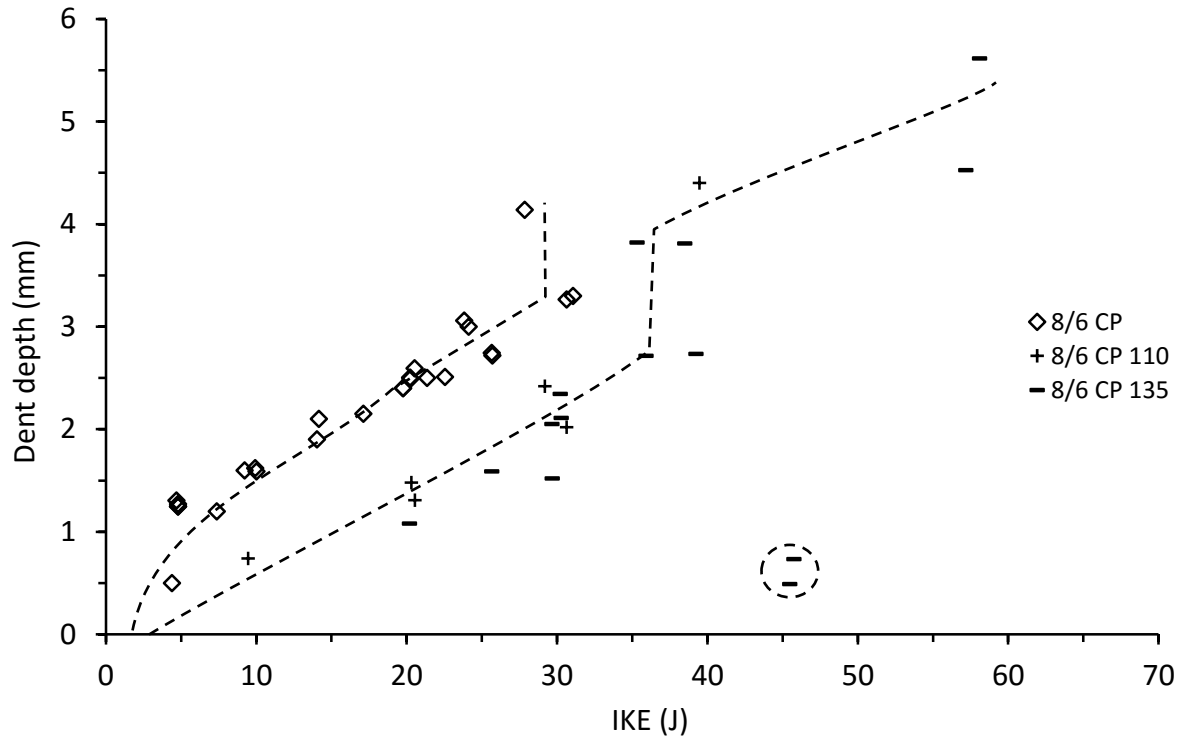


Figure 4.5.4. Dent depth vs incident kinetic energy for thin unsymmetrical CP carbon/epoxy panels with 70, 110 and 135 kg/m³ core densities

Energy absorption was once again found to be around 70% in the early IKE range which corresponds to similar mechanisms being found in the top skin and the core. The onset of fibre fracture in panels with a high density core in the impacted skin was coupled with the increase of absorbed energy to above 95%, shown in Figure 4.5.5 and Figure 4.5.6, a trend familiar with the lower density panels. The fibre fracture behaviour did not occur at a precise IKE energy, as indicated by the shaded regions of the graphs, another trend seen in the lower density core panels, namely the 8/6CP carbon panels (Figure 4.3.8). This phenomenon could relate to the location of the impact, as previously mentioned, and its vicinity to the nodal walls of the honeycomb. This inconsistency in impact location sees the paths through which the impact load was distributed resulting in different stress concentrations under the impactor. This could also relate to the varying dynamic response of the panel under different impact speeds, as mentioned previously. Very few differences in damage propagation and characteristics were noted between symmetrical and unsymmetrical dense core panel arrangements. The only difference of note, seen in Figure 4.5.5, was the earlier onset of fibre fracture in the high density core symmetrical panels as early as 25J, compared to 30J in the unsymmetrical panels. This difference could be due to the slightly higher stiffness of the symmetrical skins as well as the increased core properties, making them more susceptible to localised damage, causing them to be more likely to experience early fibre fracture. The influence of the higher core density and its interaction with the skins is an important difference in this trend being reversed compared to the 70kg/m³ panels.

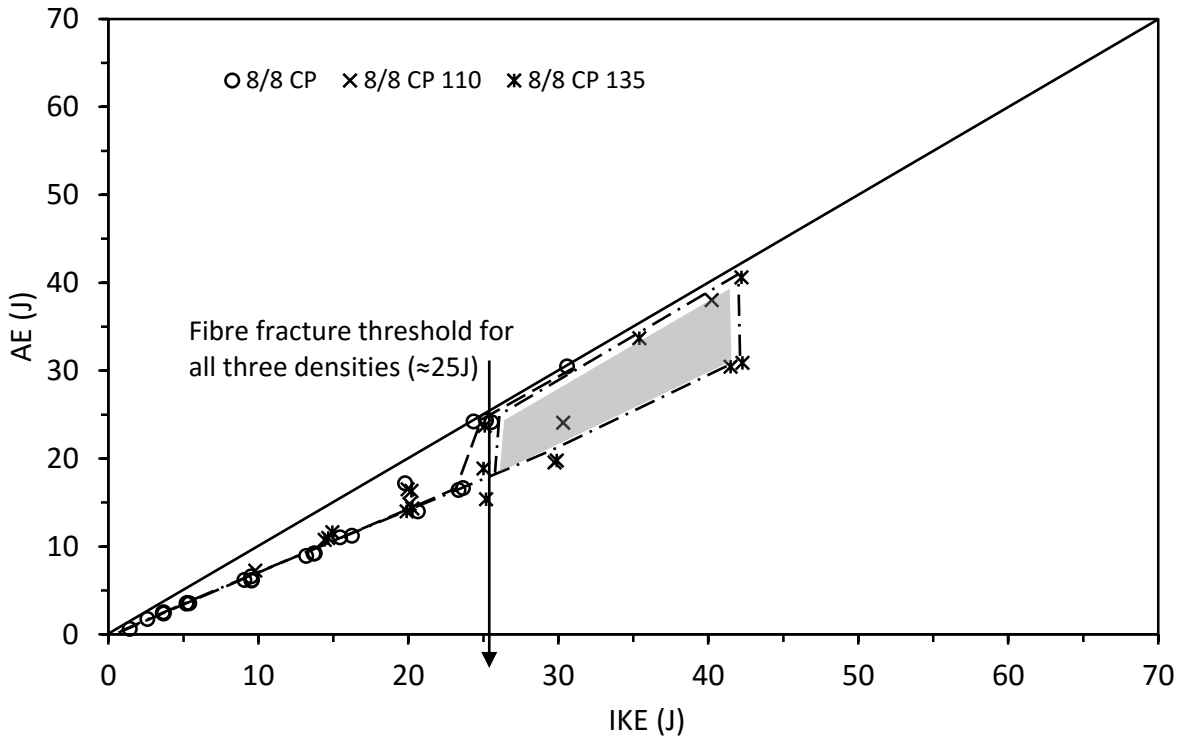


Figure 4.5.5. Absorbed energy vs incident kinetic energy for thin symmetrical CP carbon/epoxy panels with 70, 110 and 135 kg/m³ core densities

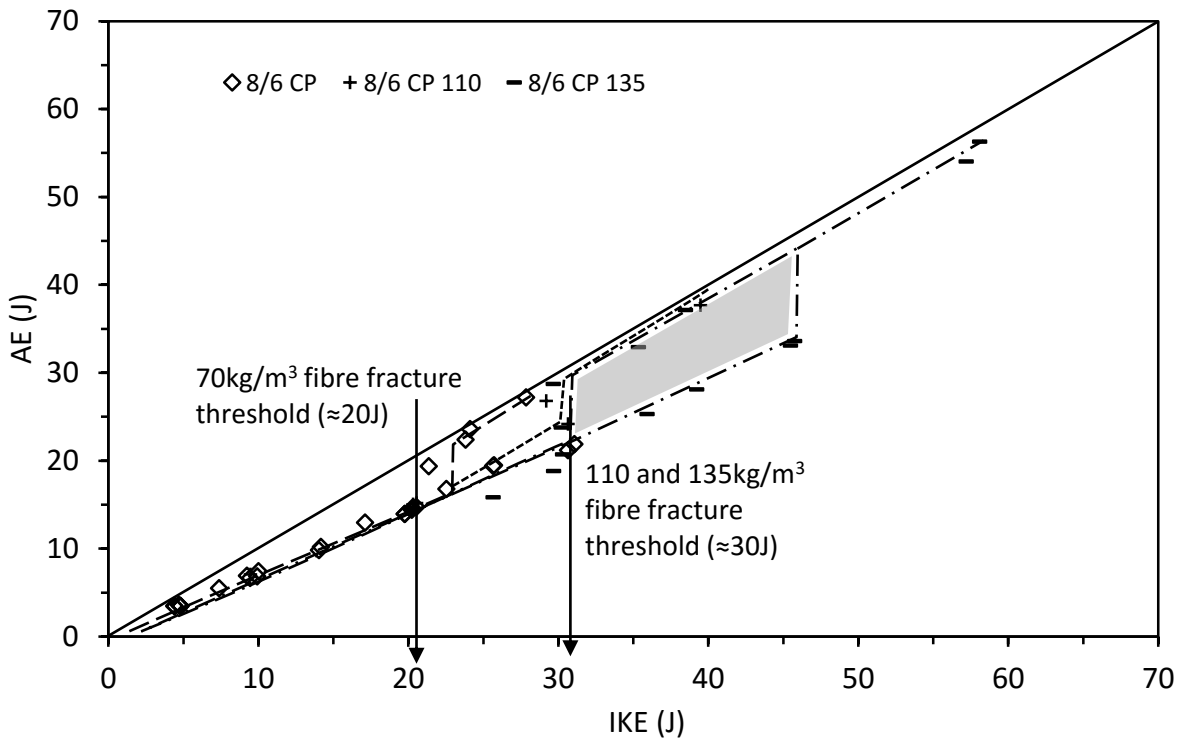


Figure 4.5.6. Absorbed energy vs incident kinetic energy for thin unsymmetrical CP carbon/epoxy panels with 70, 110 and 135 kg/m³ core densities

Shown in Figure 4.5.7 is the relationship between the maximum impact force and IKE. In Section 1 it was suggested that as core material density is increased, the maximum impact load should be higher at a similar level of IKE [9,14,17,55]. From the graph, there was no distinct or consistent correlation due to a high scatter in data to suggest that the impact load was higher at similar impact energies, suggesting this to be controlled by the skin material properties instead of the core material properties.

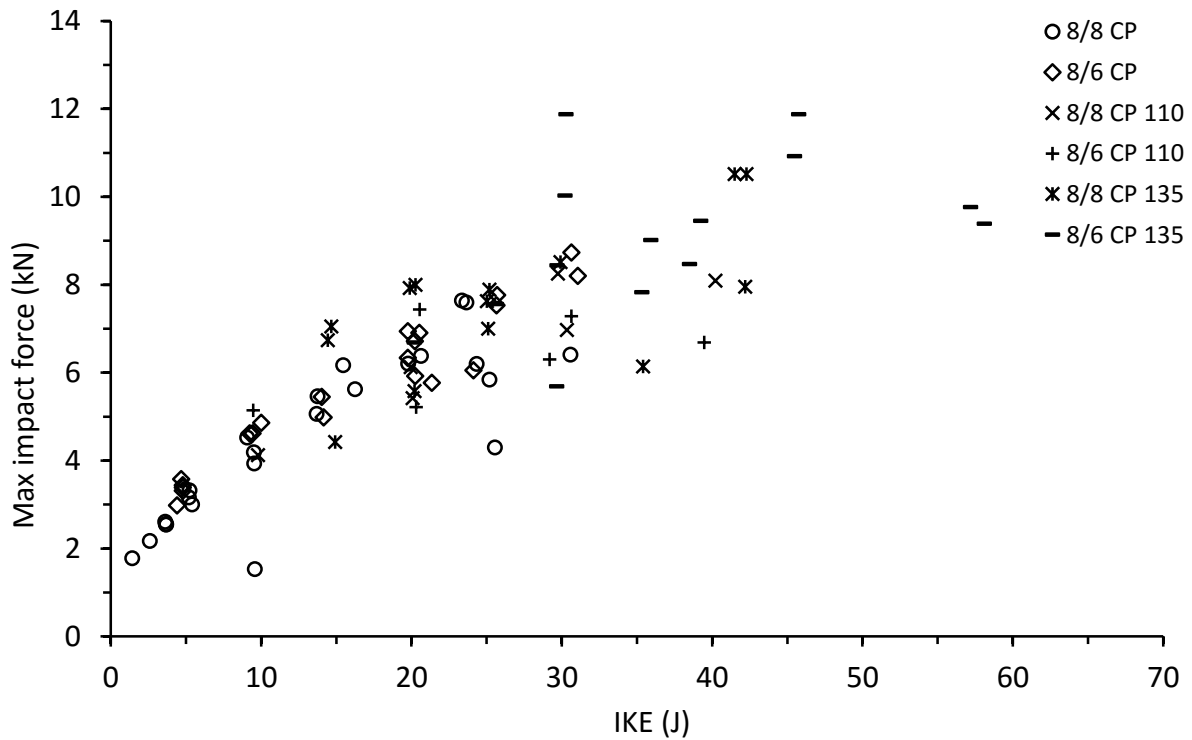


Figure 4.5.7. Maximum impact force vs incident kinetic energy for thin symmetrical and unsymmetrical CP carbon/epoxy panels with 70, 110, and 135kg/m³ core densities

Figure 4.5.8 shows the propagation of planar core damage against the residual indentation measured in thin symmetrical and unsymmetrical CP panels with 70 and 135kg/m³ core. Whereas damage in 70kg/m³ core panels was seen to spread successfully in both planar and TTT directions as the IKE was increased, implying a good role sharing relationship between the skin and the core, however, as shown by the 135kg/m³ core panels, planar spread of the core damage was stopped early on, showing that the increase in the core properties effectively limited the bending in the skin, severely localising the panel behaviour, indicating that the skin and the core were not as effective in spreading the impact damage as in the lower density arrangements, creating a more severe localised state of damage in the centre of the panel, which could be favourable to the damage tolerance of the panel.

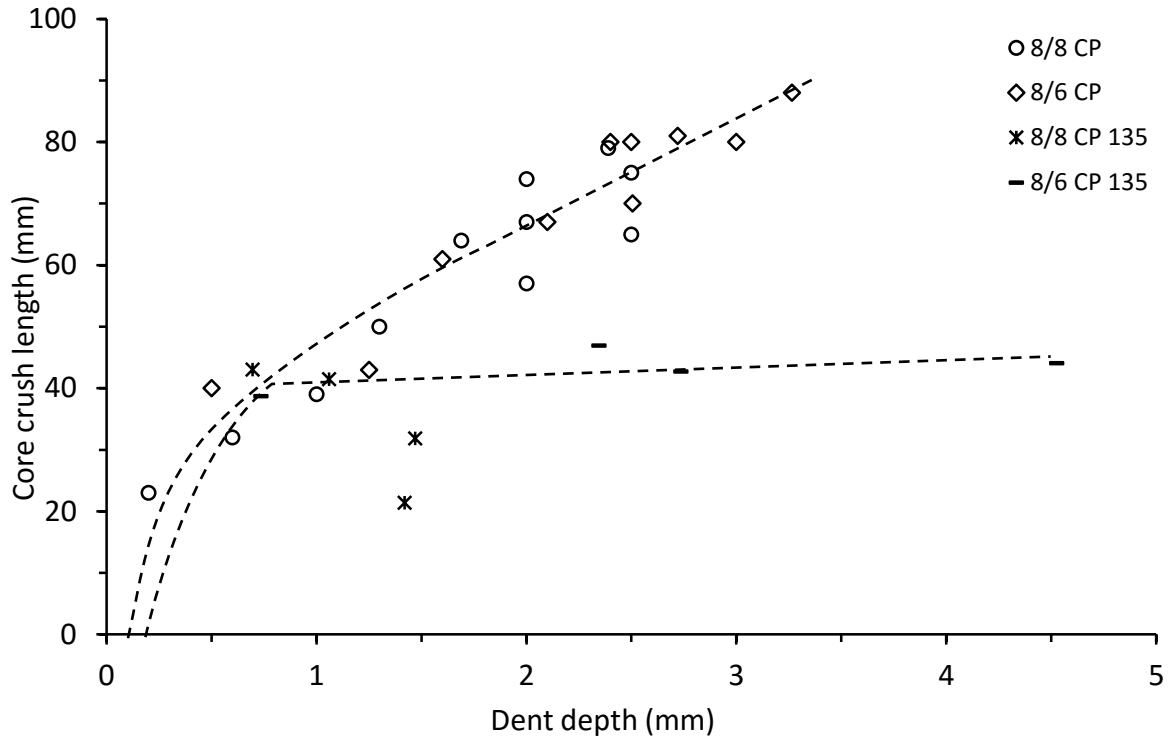


Figure 4.5.8. Core crush length vs dent depth for thin symmetrical and unsymmetrical CP and QI carbon/epoxy panels with 70 and 135 kg/m³ core densities

4.5.2. Skin materials

Initial internal damage was found to be delamination and core crushing in both carbon/epoxy and glass/epoxy panels, with a parabolic increase in delamination and core crush length, shown in Figure 4.5.9 and Figure 4.5.10 respectively. Delaminations were found only in the impacted skin in both thicknesses of glass/epoxy panel, with the thick glass/epoxy skins developing larger delaminations than then the thin glass/epoxy skins at the higher range of the impact energies. Delamination resistance in the glass/epoxy panels was far greater than in the carbon/epoxy panels, evident at even low levels of the IKE range, due to the known rate sensitivity of both E-glass fibre and aluminium core compared to the carbon/epoxy skins. Additionally, delaminations plateaued early in the IKE range in both thick and thin glass/epoxy panels, this was likely due to energy of the impact being absorbed by interfacial debonding in the middle IKE range. Due to the similarity in trends between the core crush lengths and the panels with different skin material, shown in Figure 4.5.10, most significantly in the lower range of impact energies, it can be further inferred that the core crushing was the primary damage mechanism in initially absorbing the impact, further confirming the importance of the cores role in the damage resistance, as seen in the carbon/epoxy tests.

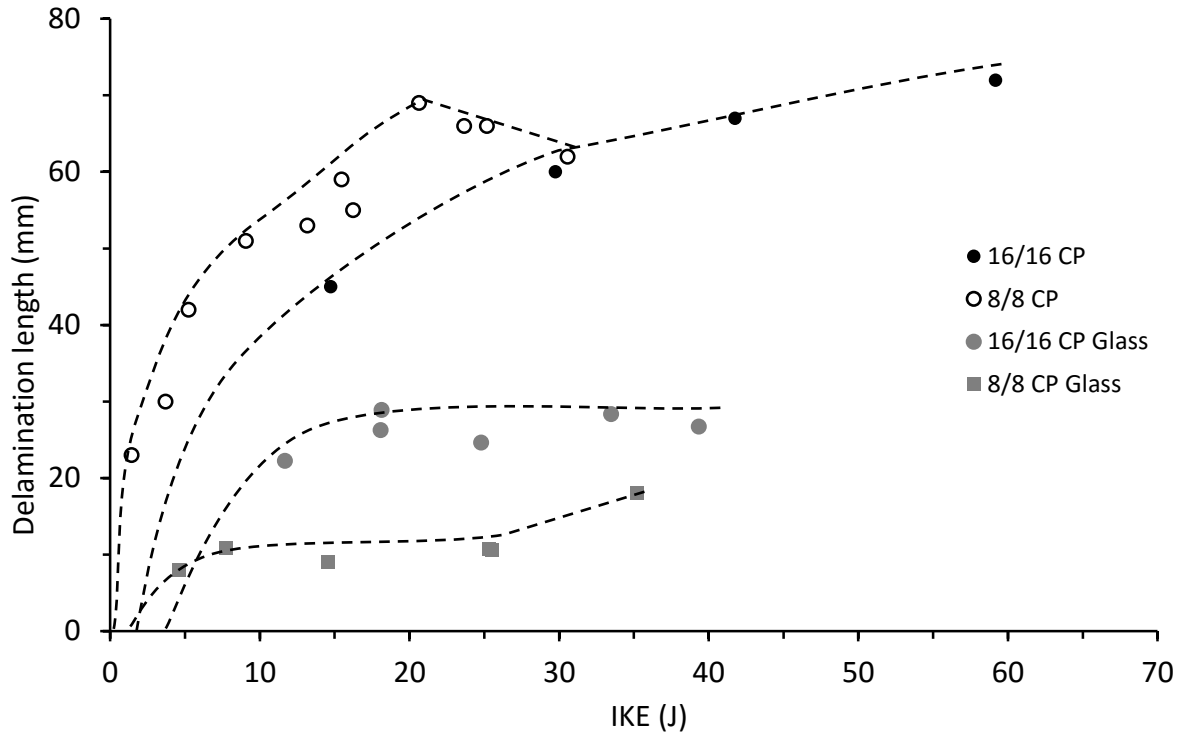


Figure 4.5.9. Delamination length vs incident kinetic energy for thin and thick symmetrical CP carbon and E-glass/epoxy panels with 70 kg/m³ core density

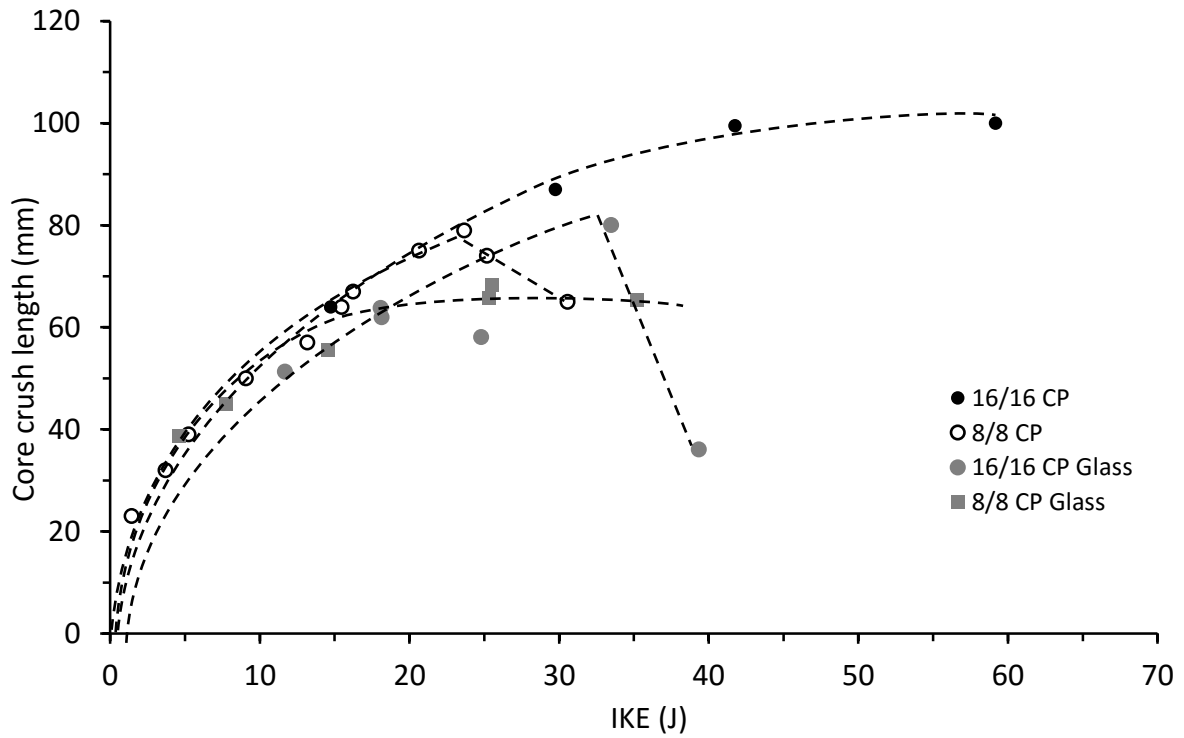


Figure 4.5.10. Core crush length vs incident kinetic energy for thin and thick symmetrical CP carbon and E-glass/epoxy panels with 70 kg/m³ core density

Initial external damage was found to be indentation of the top skin for both carbon and glass/epoxy skins, and is shown in Figure 4.5.11. It can be seen that thin and thick carbon/epoxy and glass/epoxy arrangements had similar levels of IKE where no dent was observed, and surprisingly similar levels of indentation development over the IKE range given the difference in flexural properties of the different skin materials. This could be linked to the slight development of debonding and lower level of delamination in the glass/epoxy panels allowing the skins to spring back, closing the expected gap between the two panel arrangements, but also shows the influence of the core material over the skin properties in the propagation of indentation in the panels. Fibre fracture was only observed in the thin skinned glass/epoxy panels at 35J, and can be seen in Figure 4.5.10 to cause the level of core crush extent to dramatically decrease, as well as in Figure 4.5.12, causing an increase in the energy absorbed to around 95%.

Figure 4.5.13 shows an initial linear relationship between IKE and impact load in both glass and carbon/epoxy panels, which leads to an eventual arrest of the trend at the occurrence of fibre fracture, resulting in the further increase in dent depth with no further increase in peak load. In this graph it can be seen that the thin glass/epoxy panels had a similar effective IKE range over the carbon/epoxy panels. The peak impact force to cause fibre fracture in the glass/epoxy panel was very similar to the carbon/epoxy panels, which was unexpected due to the higher flexural rigidity of the carbon/epoxy panels, and can be attributed to the increased delamination resistance and high strain tolerance of the glass/epoxy skins. A cautious approach was used in testing the thicker panels, with the final impact energies not being enough to cause fracture in the impacted skin, hence the trend was shown to be wholly linear in Figure 4.5.12 and Figure 4.5.13.

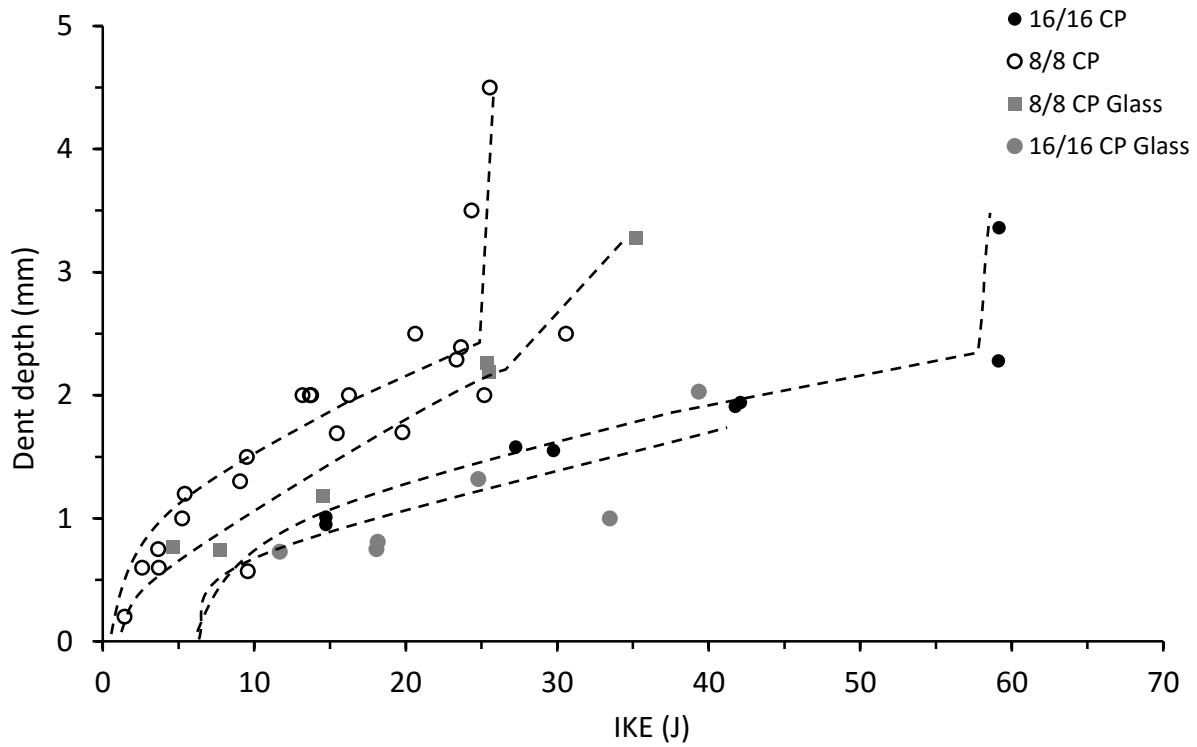


Figure 4.5.11. Dent depth vs incident kinetic energy for thin and thick symmetrical CP carbon and E-glass/epoxy panels with 70 kg/m³ core density

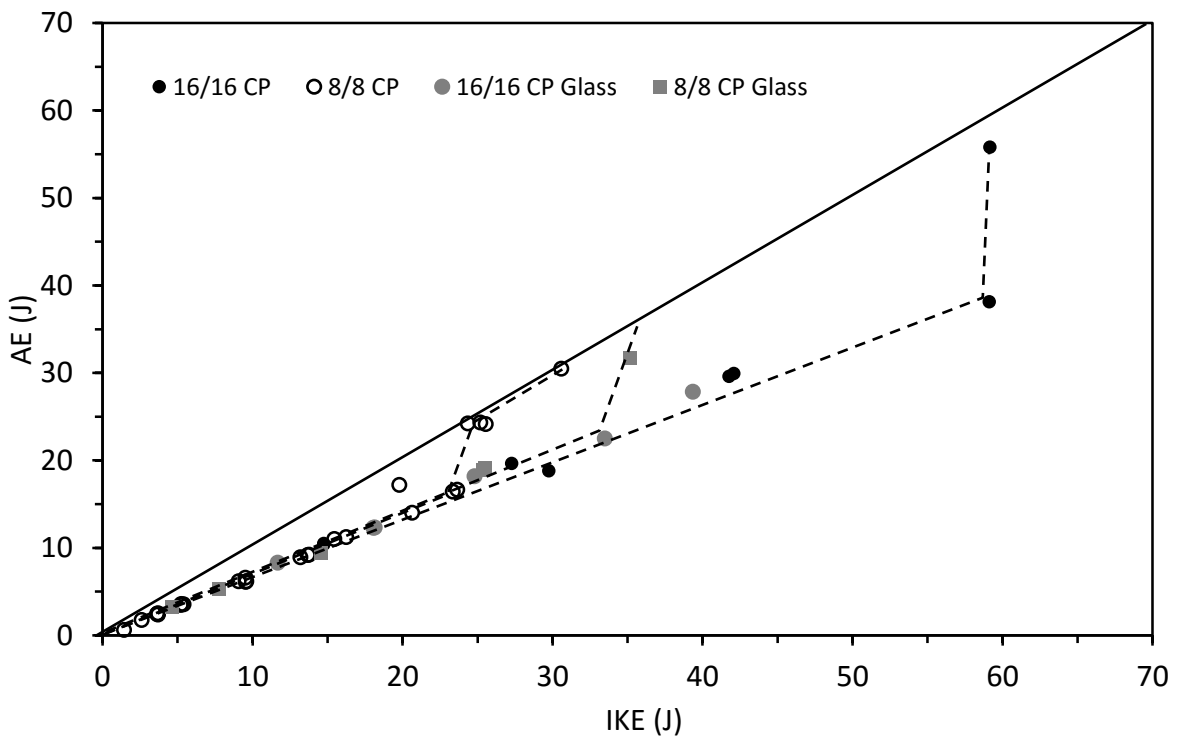


Figure 4.5.12. Absorbed energy vs incident kinetic energy for thin and thick symmetrical CP carbon and E-glass/epoxy panels with 70 kg/m³ core density

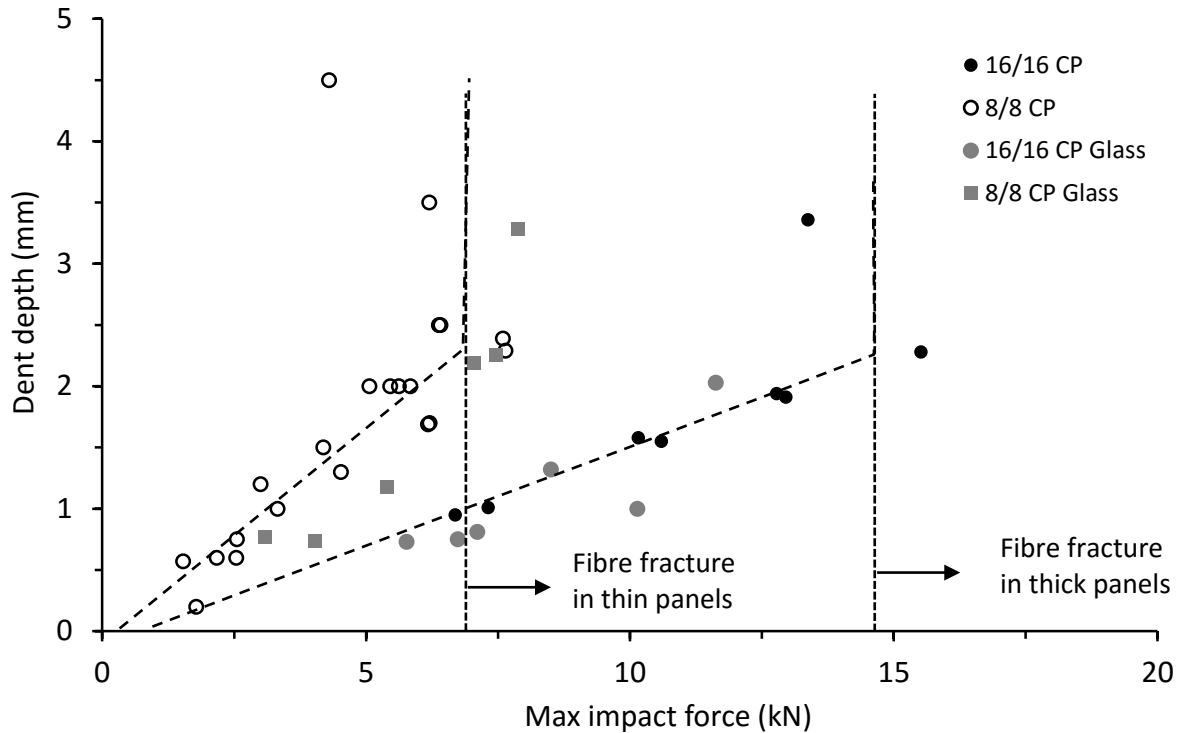


Figure 4.5.13. Dent depth vs max impact force for thin and thick symmetrical CP carbon and E-glass/epoxy panels with 70 kg/m³ core density

As previously mentioned, the use of the dent depth damage metric to quickly identify the amount of sub laminar damage in a structure after an impact is a key issue for in the field assessment of in-service products, its reliability however was called into question by a number of researchers [14,29,33,39,53] as discussed in Section 1.2.2. Shown in Figure 4.5.14 is a comparison of dent depth vs the planar delamination damage length for both thin and thick symmetrical CP carbon and glass/epoxy panels with a 70kg/m³ core. The trend for both thin and thick carbon panels shows very strong and reliable correlation between the two damage mechanisms, with dent depth increasing almost linearly with delamination length. Prediction of internal delamination lengths could be made with a fairly high level of confidence in these cases. Conversely the glass/epoxy panels displayed no such trend, with the occurrence of debonding and high delamination resistance in the glass/epoxy skins preventing the continued development of the planar length of the delaminations, resulting in an unconvincing trend against dent depth. However, with the translucent nature of the glass panels, the state of internal damage can be visually observed with no need for destructive sectioning or through the thickness imaging equipment.

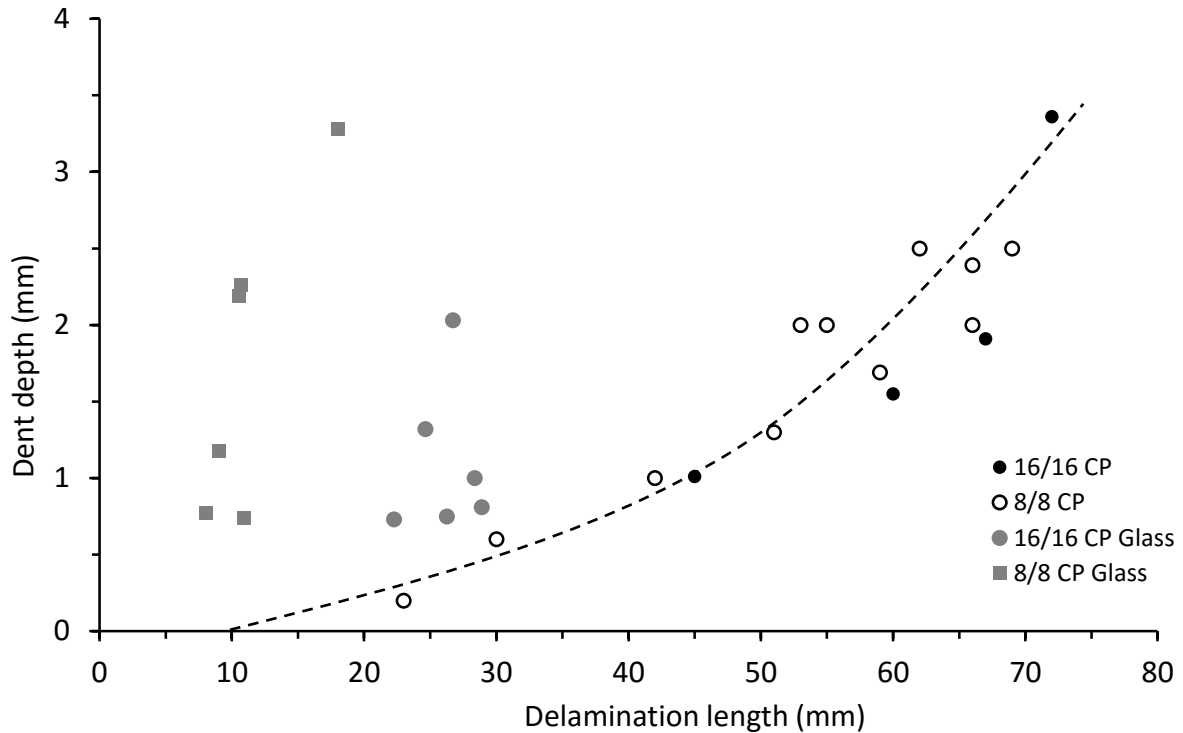


Figure 4.5.14. Dent depth vs delamination length for thin and thick symmetrical CP carbon and E-glass/epoxy panels with 70 kg/m³ core density

4.6. Concluding remarks

The damage resistance of composite sandwich panels was assessed in terms of the occurrence and propagation of damage mechanisms from destructive cross-sectioning, critical impact loads and energy absorption. After impact, a combination of delamination in the top skin coupled with core crushing was found to be the typical damage state from low levels of impact. The order of occurrence for these damage types was indistinguishable from the load-displacement/time responses, and were typically even in the loading and unloading phases with little deviation in the gradients. The second damage state to develop, typically at higher levels of IKE, was fibre fracture in the top skin which caused extensive damage in the skin and core. This damage type was clearly identifiable in the load-time/displacement responses by a large drop in load, and continued increase in displacement.

Altering the skin thickness in carbon/epoxy panels with 70kg/m³ core density provided a significant difference in the damage resistance of the panels. The increased flexural rigidity of the thicker skins allowed the energy to be absorbed more through global deformations, increasing the energy to cause fibre fracture, which overall doubled the effective impact range over thin skinned panels. The increase in skin thickness also reduced the sensitivity to changes in ply orientation and asymmetry in the thicker skinned panels. Skin lay-up was significant in the resistance of delamination spread in the thin skinned panels, with quasi-isotropic lay-ups experiencing measured lengths of delamination of up to 50%

lower than in cross-ply skins, and was attributed to the increased delamination resistance given by the lower ply-to-ply angle of 45° in the QI skins compared to 90° in the cross-ply skins. Panel asymmetry had limited effect on the damage resistance due to the overwhelming contribution of either the core in the thin panels, or the skins in the thick panels. The reduced number of plies in the distal skin lowered flexural rigidity allowing more global deformation compared to the symmetrical counterparts, and largely went unnoticed, until the onset of fibre fracture, which typically occurred earlier in the unsymmetrical arrangements. Panels with higher core density also had significant improvements in damage resistance in both the transverse and TTT propagation of damage mechanisms due to the far enhanced core properties, however this created a susceptibility to debonding between the skin and the core. The E-glass/epoxy skins proved to be almost far more delamination resistant than the carbon/epoxy skins, as well as a reduced planar propagation of crush core length due to the lower flexural rigidity of the E-glass/epoxy skins failing to spread the impact damage away from the impact zone as effectively as the carbon/epoxy skins.

Table 4.6.1. Impact parameters and internal damage of carbon/epoxy thin CP and QI symmetrical panels with 70kg/m³ core density

Specimen ID	Impact parameters					Panel damage			
	Inbound Velocity (m/s)	Rebound Velocity (m/s)	IKE* (J)	AE (J)	% AE	Delamination Extent (mm)	Crushed Core Extent (mm)	Surface Dent Depth (mm)	Max Impact Force (kN)
CI-8/8CP-16J-B	4.55	2.44	15.45	11.03	71.37	59	64	1.69	6.17
CI-8/8CP-23J-A	5.60	3.05	23.35	16.42	70.32	-	-	2.29	7.64
CI-8/8CP-23J-B	5.63	3.07	23.65	16.64	70.35	66	79	2.39	7.59
HD-8/8-CP-10J	3.58	2.13	9.57	6.20	64.79	-	-	0.57	1.53
HD-8/8-CP-20J	5.15	1.86	19.78	17.19	86.91	-	-	1.70	6.20
JL-8/8QI-5J-A	2.49	1.33	4.62	3.30	71.44	19	44	0.95	3.86
JL-8/8QI-5J-B	2.42	1.18	4.35	3.31	76.01	-	-	0.96	3.77
JL-8/8QI-10J-A	3.64	1.85	9.87	7.32	74.15	23	64	1.60	5.10
JL-8/8QI-10J-B	3.66	1.84	9.99	7.48	74.85	-	-	1.58	5.25
JL-8/8QI-15J-A	4.34	2.26	14.06	10.27	73.05	28	78	1.83	6.44
JL-8/8QI-15J-B	4.44	2.22	14.70	11.04	75.06	-	-	1.81	6.46
JL-8/8QI-20J-A	5.17	2.81	19.90	14.00	70.34	27	82	2.28	7.35
JL-8/8QI-20J-B	5.19	2.80	20.03	14.18	70.81	-	-	2.36	7.27
JL-8/8QI-25J-A	5.92	2.96	26.07	19.56	75.03	6	98	2.55	9.14
JL-8/8QI-25J-B	5.90	2.98	25.94	19.32	74.47	-	-	2.60	8.58
JL-8/8QI-30J-A	6.39	1.71	30.44	28.28	92.88	27	89	3.31	7.49
JL-8/8QI-30J-B	6.38	1.34	30.35	29.01	95.58	-	-	3.67	7.58

*Impact in top skin as panel is manufactured, or thicker skin in unsymmetrical panel

Table 4.6.2. Impact parameters and internal damage of carbon/epoxy thin CP and QI unsymmetrical panels with 70kg/m³ core density (impact on thick skin)

Specimen ID	Impact parameters					Panel damage			
	Inbound Velocity (m/s)	Rebound Velocity (m/s)	IKE* (J)	AE (J)	% AE	Delamination Extent (mm)	Crushed Core Extent (mm)	Surface Dent Depth (mm)	Max Impact Force (kN)
NC-8/6-CP-8J	3.15	1.59	7.37	5.49	74.49	-	-	1.2	3.63
NC-8/6CP-10J	3.65	2.03	9.92	6.85	69.05	-	-	1.62	4.09
NC-8/6CP-18J	4.79	2.36	17.11	12.96	75.75	-	-	2.15	5.63
NC-8/6CP-23J-A	5.65	1.38	23.82	22.41	94.08	-	-	3.06	6.33
NC-8/6CP-23J-B	5.50	2.78	22.54	16.8	74.53	-	-	2.51	6.56
NC-8/6CP-28J	6.11	0.93	27.85	27.2	97.67	-	-	4.14	6.03
DJ-8/6CP-5J-A1	2.51	1.21	4.69	3.60	76.67	-	-	1.31	3.58
DJ-8/6CP-5J-B1	2.53	1.31	4.79	3.51	73.28	32	43	1.25	3.44
DJ-8/6CP-5J-A2	2.54	1.33	4.79	3.47	72.53	-	-	1.25	3.31
DJ-8/6CP-5J-B2	2.54	1.33	4.80	3.48	72.48	-	-	1.27	3.39
DJ-8/6CP-20J-A	5.25	2.78	20.52	14.77	71.95	-	-	2.60	6.91
DJ-8/6CP-20J-B	5.21	2.79	20.22	14.41	71.27	35	70	2.51	6.72
DJ-8/6CP-25J-A	5.87	2.89	25.65	19.42	75.70	-	-	2.75	7.53
DJ-8/6CP-25J-B	5.87	2.89	25.71	19.50	75.84	30	81	2.72	7.77
DJ-8/6CP-30J-A	6.46	3.51	31.06	21.89	70.46	-	-	3.30	8.20
DJ-8/6CP-30J-B	6.41	3.56	30.64	21.21	69.22	28	88	3.27	8.73
HD-8/6-CP-10J	3.67	1.86	10.01	7.43	74.23	-	-	1.59	4.86
HD-8/6-CP-20J	5.21	2.75	20.25	14.60	72.10	-	-	2.49	5.92
LB-8/6QI-5J	2.46	1.29	4.50	3.26	72.50	-	-	0.84	3.00
LB-8/6QI-10J-A	3.57	1.91	9.47	6.76	71.37	24	57	1.32	4.56
LB-8/6QI-10J-B	3.53	1.90	9.31	6.61	70.99	-	-	1.33	4.83
LB-8/6QI-15J	4.43	2.46	14.65	10.15	69.30	-	-	1.68	5.69
LB-8/6QI-20J-A	5.16	1.83	19.81	17.32	87.42	24	83	2.74	5.25
LB-8/6QI-20J-B	5.11	1.78	19.46	17.10	87.87	-	-	2.80	6.08
LB-8/6QI-25J-A	5.81	1.09	25.18	24.28	96.46	-	-	2.99	4.84
LB-8/6QI-25J-B	5.81	1.06	25.12	24.28	96.64	27	83	3.38	5.30

Table 4.6.3. Impact parameters and internal damage of carbon/epoxy thick CP and QI symmetrical panels with 70kg/m³ core density

Specimen ID	Impact parameters					Panel damage			
	Inbound Velocity (m/s)	Rebound Velocity (m/s)	IKE* (J)	AE (J)	% AE	Delamination Extent (mm)	Crushed Core Extent (mm)	Surface Dent Depth (mm)	Max Impact Force (kN)
CI-16/16CP-15J-A	4.45	2.41	14.74	10.41	70.63	-	-	0.95	6.69
CI-16/16CP-15J-B	4.45	2.38	14.74	10.50	71.27	45	64	1.01	7.31
CI-16/16CP-28J-A	6.05	3.20	27.27	19.64	72.02	-	-	1.58	10.16
CI-16/16CP-28J-B	6.32	3.83	29.75	18.82	63.25	60	87	1.55	10.59
CI-16/16CP-45J-A	7.52	4.04	42.09	29.92	71.08	-	-	1.94	12.78
CI-16/16CP-45J-B	7.49	4.04	41.76	29.62	70.92	67	99.5	1.91	12.95
CI-16/16CP-60J-A	8.91	5.31	59.12	38.11	64.46	-	-	2.28	15.52
CI-16/16CP-60J-B	8.91	2.13	59.16	55.79	94.30	72	100	3.36	13.38
CI-16/16QI-16J-A	4.44	2.38	14.70	10.49	71.38	-	-	1.06	7.72
CI-16/16QI-16J-B	4.44	2.44	14.66	10.23	69.77	53	80	1.04	7.67
CI-16/16QI-28J-A	6.01	3.75	26.94	16.46	61.10	-	-	1.42	10.95
CI-16/16QI-28J-B	6.05	3.13	27.27	19.99	73.31	63	98	1.6	10.44
JL-16/16QI-15J-A	4.34	2.24	14.03	10.28	73.30	-	-	0.86	7.55
JL-16/16QI-15J-B	4.37	2.68	14.25	8.90	62.43	68	96	1.14	7.77
JL-16/16QI-30J-A	6.35	3.73	30.01	19.64	65.45	41	75	1.03	11.52
JL-16/16QI-30J-B	6.35	5.02	30.04	11.27	37.51	-	-	0.85	12.27
JL-16/16QI-45J-A	7.72	4.11	44.38	31.77	71.59	84	101	0.94	13.10
JL-16/16QI-45J-B	7.59	4.02	42.95	30.90	71.94	-	-	1.61	14.21
JL-16/16QI-60J-A	8.81	2.92	57.78	51.41	88.97	87	102	2.74	13.33
JL-16/16QI-60J-B	8.94	2.85	59.50	53.45	89.85	-	-	2.80	13.10

*Impact in top skin as panel is manufactured, or thicker skin in unsymmetrical panel

Table 4.6.4. Impact parameters and internal damage of carbon/epoxy thick CP and QI unsymmetrical panels with 70kg/m³ core density (impact on thick skin)

Specimen ID	Impact parameters					Panel damage			
	Inbound Velocity (m/s)	Rebound Velocity (m/s)	IKE* (J)	AE (J)	% AE	Delamination Extent (mm)	Crushed Core Extent (mm)	Surface Dent Depth (mm)	Max Impact Force (kN)
NC-16/12CP-20J	5.24	2.85	20.48	14.44	70.51	-	-	1.53	7.69
NC-16/12CP-30J	6.20	3.38	28.67	20.17	70.35	-	-	2.03	9.83
NC-16/12CP-35J	6.82	3.64	34.69	24.83	71.58	-	-	2.21	11.16
NC-16/12CP-45J	7.58	4.18	42.85	29.85	69.66	-	-	2.3	12.70
NC-16/12CP-60J-A	8.90	5.27	59	38.31	64.93	-	-	3.66	15.00
NC-16/12CP-60J-B	8.93	1.98	59.39	56.48	95.10	73	84	4.08	-
DJ-16/12CP-15J-A	4.32	2.22	13.90	10.21	73.48	-	-	1.29	6.91
DJ-16/12CP-15J-B	4.38	2.59	14.27	9.29	65.08	33	77	1.29	7.38
DJ-16/12CP-30J-A	6.23	3.56	28.88	19.45	67.35	-	-	2.04	9.72
DJ-16/12CP-30J-B	6.22	3.59	28.80	19.20	66.65	47	94	2.12	10.14
DJ-16/12CP-54J-A	8.25	4.16	50.74	37.84	74.58	-	-	3.01	13.86
DJ-16/12CP-54J-B	8.40	5.17	52.61	32.69	62.14	73	100	3.04	14.72
DJ-16/12CP-60J-A	8.74	5.45	56.89	34.77	61.11	-	-	3.04	15.27
DJ-16/12CP-60J-B	8.63	5.32	55.50	34.43	62.04	65	100	3.08	15.02
LB-16/12QI-10J	3.56	2.00	9.46	6.48	68.54	-	-	0.57	5.53
LB-16/12QI-20J	5.15	3.01	19.73	12.98	65.75	-	-	1.29	8.14
LB-16/12QI-35J-A	6.88	2.27	35.30	31.47	89.15	67	106	2.41	10.50
LB-16/12QI-35J-B	6.88	3.89	35.31	24.04	68.07	-	-	1.97	11.53
LB-16/12QI-45J-A	7.74	2.27	44.61	40.75	91.36	77	103	2.87	9.67
LB-16/12QI-45J-B	7.68	2.31	43.94	39.98	90.99	-	-	2.73	10.81
LB-16/12QI-60J-A	8.81	1.93	57.86	55.09	95.21	-	-	3.88	7.75
LB-16/12QI-60J-B	8.73	1.99	56.74	53.78	94.79	73	103	3.85	7.34

*Impact in top skin as panel is manufactured, or thicker skin in unsymmetrical panel

Table 4.6.5. Impact parameters and internal damage of carbon/epoxy thin CP symmetrical and unsymmetrical panels with 110kg/m³ core density

Specimen ID	Impact parameters					Panel damage			
	Inbound Velocity (m/s)	Rebound Velocity (m/s)	IKE* (J)	AE (J)	% AE	Delamination Extent (mm)	Crushed Core Extent (mm)	Surface Dent Depth (mm)	Max Impact Force (kN)
AR-8/8-CP-10J	3.62	1.84	9.79	7.25	74.11	-	-	0.83	4.13
AR-8/8-CP-20J-A	5.17	2.15	19.95	16.52	82.80	-	-	1.53	6.13
AR-8/8-CP-20J-B	5.19	2.66	20.08	14.82	73.80	-	-	1.33	5.42
AR-8/8-CP-30J-A	6.38	2.90	30.33	24.07	79.36	33	45	1.78	6.97
AR-8/8-CP-30J-B	6.32	3.70	29.75	19.56	65.77	-	-	1.82	8.25
AR-8/8-CP-40J	7.35	1.72	40.22	38.01	94.50	-	-	3.77	8.09
AR-8/6-CP-10J	3.56	1.80	9.46	7.05	74.54	-	-	0.74	5.14
AR-8/6-CP-20J-A	5.25	2.68	20.55	15.19	73.92	-	-	1.31	7.44
AR-8/6-CP-20J-B	5.22	2.66	20.31	15.03	74.00	-	-	1.48	5.22
AR-8/6-CP-30J-A	6.26	1.79	29.19	26.81	91.84	40	53	2.42	6.30
AR-8/6-CP-30J-B	6.41	2.95	30.64	24.16	78.85	-	-	2.02	7.28
AR-8/6-CP-40J	7.28	1.54	39.48	37.70	95.50	-	-	4.40	6.69

*Impact in top skin as panel is manufactured, or thicker skin in unsymmetrical panel

Table 4.6.6. Impact parameters and internal damage of carbon/epoxy thin CP symmetrical panels with 135kg/m³ core density

Specimen ID	Impact parameters					Panel damage			
	Inbound Velocity (m/s)	Rebound Velocity (m/s)	IKE* (J)	AE (J)	% AE	Delamination Extent (mm)	Crushed Core Extent (mm)	Surface Dent Depth (mm)	Max Impact Force (kN)
RM-8/8CP-15J-A	4.40	2.22	14.43	10.76	74.59	-	-	1.21	6.73
RM-8/8CP-15J-B	4.44	2.22	14.66	10.98	74.91	35	21	1.42	7.05
RM-8/8CP-20J-A	5.17	2.81	19.89	14.00	70.39	-	-	1.11	7.92
RM-8/8CP-20J-B	5.22	2.83	20.28	14.30	70.54	30	41	1.06	8.00
RM-8/8CP-25J	5.79	2.87	25.02	18.87	75.45	39	32	1.47	7.62
RM-8/8CP-30J	6.34	3.68	29.90	19.79	66.18	17	43	0.70	8.52
RM-8/8CP-40J-A	7.46	3.85	41.49	30.44	73.37	-	-	1.02	10.52
RM-8/8CP-40J-B	7.53	3.91	42.28	30.88	73.05	25	47	1.63	10.52
MB-8/8-CP-15J	4.48	2.10	14.93	11.63	77.91	-	-	1.39	4.42
MB-8/8-CP-20J	5.21	2.28	20.20	16.31	80.75	-	-	1.60	5.58
MB-8/8-CP-25J-A	5.81	3.63	25.18	15.38	61.08	-	-	1.25	7.89
MB-8/8-CP-25J-B	5.80	1.36	25.10	23.73	94.53	-	-	2.55	7.00
MB-8/8-CP-35J	6.89	1.52	35.40	33.68	95.16	-	-	3.54	6.14
MB-8/8-CP-45J	7.53	1.46	42.20	40.62	96.24	-	-	3.75	7.95

*Impact in top skin as panel is manufactured, or thicker skin in unsymmetrical panel

Table 4.6.7. Impact parameters and internal damage of carbon/epoxy thin CP unsymmetrical panels with 135kg/m³ core density

Specimen ID	Impact parameters					Panel damage			
	Inbound Velocity (m/s)	Rebound Velocity (m/s)	IKE* (J)	AE (J)	% AE	Delamination Extent (mm)	Crushed Core Extent (mm)	Surface Dent Depth (mm)	Max Impact Force (kN)
RM-8/6CP-30J-A	6.38	3.58	30.28	20.71	68.40	-	-	2.11	11.88
RM-8/6CP-30J-B	6.37	2.94	30.20	23.78	78.73	44	47	2.35	10.03
RM-8/6CP-38J-A	6.94	3.78	35.92	25.29	70.41	-	-	2.72	9.02
RM-8/6CP-38J-B	7.26	3.86	39.23	28.12	71.69	27	43	2.74	9.45
RM-8/6CP-45J-A	7.81	4.08	45.47	33.09	72.77	-	-	0.49	10.92
RM-8/6CP-45J-B	7.84	4.04	45.75	33.60	73.45	17	39	0.74	11.88
RM-8/6CP-60J-A	8.83	1.56	58.10	56.29	96.89	-	-	5.62	9.39
RM-8/6CP-60J-B	8.76	2.05	57.19	54.05	94.51	41	44	4.53	9.77
MB-8/6-CP-20J	5.21	2.73	20.18	14.65	72.58	-	-	1.08	6.69
MB-8/6-CP-25J	5.87	3.63	25.65	15.83	61.70	-	-	1.59	7.56
MB-8/6-CP-30J-A	6.31	3.82	29.69	18.83	63.43	-	-	1.52	8.44
MB-8/6-CP-30J-B	6.31	1.12	29.66	28.73	96.85	-	-	2.05	5.69
MB-8/6-CP-35J	6.89	1.80	35.33	32.91	93.16	-	-	3.82	7.83
MB-8/6-CP-40J	7.19	1.35	38.48	37.12	96.47	-	-	3.81	8.47

*Impact in top skin as panel is manufactured, or thicker skin in unsymmetrical panel

Table 4.6.8. Impact parameters and internal damage of E-glass/epoxy thin and thick CP symmetrical panels with 70kg/m³ core density

Specimen ID	Impact parameters					Panel damage			
	Inbound Velocity (m/s)	Rebound Velocity (m/s)	IKE* (J)	AE (J)	% AE	Delamination Extent (mm)	Crushed Core Extent (mm)	Surface Dent Depth (mm)	Max Impact Force (kN)
SG-8/8-CP-5J	2.49	1.38	4.61	3.20	69.40	8	39	0.77	3.08
SG-8/8-CP-8J	3.23	1.80	7.75	5.34	68.84	11	45	0.74	4.03
SG-8/8-CP-15J	4.42	2.63	14.53	9.37	64.49	9	56	1.18	5.39
SG-8/8-CP-25J-A	5.85	2.93	25.49	19.10	74.94	11	68	2.19	7.05
SG-8/8-CP-25J-B	5.83	2.94	25.33	18.87	74.50	11	66	2.26	7.47
SG-8/8-CP-35J	6.87	2.18	35.19	31.65	89.95	18	65	3.28	7.88
SG-16/16-CP-12J	3.96	2.13	11.67	8.31	71.15	22	51	0.73	5.77
SG-16/16-CP-18J-A	4.93	2.79	18.14	12.33	67.97	29	62	0.81	7.11
SG-16/16-CP-18J-B	4.92	2.78	18.06	12.30	68.10	26	64	0.75	6.73
SG-16/16-CP-25J	5.77	2.98	24.79	18.19	73.40	25	58	1.32	8.50
SG-16/16-CP-35J	6.70	3.84	33.48	22.51	67.24	28	80	1.00	10.14
SG-16/16-CP-45J	7.27	3.93	39.34	27.84	70.77	27	36	2.03	11.63

*Impact in top skin as panel is manufactured, or thicker skin in unsymmetrical panel

Table 4.6.9. Impact parameters and internal damage of preconditioned carbon/epoxy thin CP symmetrical and unsymmetrical panels with 70kg/m³ core density (20mm of core was removed from mid-section after impact)

Panel ID	Impact parameters					Panel damage			
	Inbound Velocity (m/s)	Rebound Velocity (m/s)	IKE* (J)	AE (J)	% AE	Delamination Extent (mm)	Crushed Core Extent (mm)	Surface Dent Depth (mm)	Max Impact Force (kN)
HD-8/8-CP-10J-ICR	3.58	2.15	9.54	6.10	63.94	-	-	0.47	4.45
HD-8/8-CP-20J-ICR	5.15	1.61	19.78	17.85	90.24	-	-	2.34	6.36
HD-8/6-CP-10J-ICR	3.65	2.22	9.90	6.23	62.93	-	-	0.84	4.16
HD-8/6-CP-20J-ICR	5.17	3.65	19.88	9.94	50.00	-	-	1.28	6.61

*Impact in top skin as panel is manufactured, or thicker skin in unsymmetrical panel

5. EXPERIMENTAL PROCEDURES AND SETUP FOR CAI TESTS

This section details the preparations of various sandwich panels for CAI testing and outline the testing methods and procedures used to produce the CAI results of the panels. A number of parameters that have been investigated for CAI strengths, include skin material, skin lay-up, skin thickness, sandwich asymmetry, and core density. The varying severity of impact damages has been estimated to adequately represent the whole range of the residual compressive performance of the selected sandwich panels. The level of impact damage contained within the panel has been ascertained by cross-sectioning an impact tested panel, and the panel of a duplicate impact test was used for a CAI test. A number of pre-conditions were also introduced into sandwich panels as a means to create a further understanding of the influence of the skin-core interaction over the compressive strength of the panels. They include removing core, hole drilling in a single skin and hole drilling in both panel skins. A pair of control panels for each panel configuration has been tested to provide a baseline compressive strength.

5.1. Panel Specimen Preparations for CAI Testing

Specimen size was maintained after impact testing, unlike in the NASA testing standard, where the width is to be trimmed down to eliminate any clamping or edge effects from the impact testing. Consideration of the specimen geometry was made by Hill [1]. Reviewing the suggested aspect ratios and width-to-thickness suggestions in the ASTM, NASA and BS-ISO standards, the ideal monolithic width-to-thickness ratio to cause failure in the mid-section was found to be 35 with an aspect ratio of 1.5, scaling up for sandwich panels similar to those used in this investigation gives ideal panel dimensions of 675x450mm. However, this would not only cost a considerable amount in terms of raw materials used, but also would not accommodate the use of the existing compression jig which was used throughout previous studies for monolithic laminate CAI testing. In addition, such dimensions would stand little chance to gain an industrial acceptance of generating impact damage tolerant design data. Due to these considerations, the panel size for CAI testing was set at 200x150mm, giving an aspect ratio of 1.33, well within the limits suggested by the existing CAI standards, with a width-to-thickness ratio of between 9 and 10, as well as allowing adequate width for the impact damage to spread through the panel, without interfering with the panel edges, as long as damage was limited to the penetration of the front face sheet only in all sandwich arrangements.

5.1.1. End potting and machining

Following impact testing, all the tested panels, except for those selected for destructive sectioning, had both of their ends potted in epoxy resin through the use of a metallic mould (see Figure 5.1.1). To ensure the interior and major central part of the panel ends made contact with the platen of the testing machine, rather than the corners, the moulds had a 5mm bend radius around all edges. This would ensure that there were no undesirable bending moments induced at the ends of the panel, causing premature failures. Before the resin was put into the moulds, they were coated in silicon grease to allow for easy release from the mould after the panels had cured. To achieve a good bond between the resin and the panel, as well as enhancing the load transmission from the ends to the middle section, especially in panels with undamaged mid-sections, whilst maintaining the skin/core interfacial bond, the core at the end of the panel was depressed into a 'V' shape by 5mm, shown in Figure 5.1.2. This was done by cutting the core with a Stanley knife to the depth of 3-4mm, then using the edge of a steel square block with a cross sectional area of approximately 1cm^2 , and a length more than the panel width, the core was dented by tapping the block with a hammer. In order to obtain the correct height of end pot, it was necessary to weigh the exact amount of epoxy, which could reach the desired height once poured into the mould. All end pots were created using 30-32g of epoxy each using a 1:1 ratio of resin to hardener, which was mixed vigorously for 5 minutes to ensure the resin and hardener was adequately reacted, then allowed to rest for 5 minutes to allow the air bubbles to escape. Care was taken to ensure no air became trapped in the ends whilst the panel was being lowered into the epoxy. To minimise wastage of mixed resin, as well as reducing possible variation of multiple batch manufacturing, the resin was mixed for six ends at once. This number was limited only by the number of moulds available. The panels were positioned in the mould centrally in order to provide an even thickness distribution of the epoxy around the perimeter of the panel, which would provide an even resistance to the loading stresses during testing. To ensure vertical alignment, a set square was used to align the length of the panel with the perpendicular surfaces on the mould, allowing for even distribution of the load across both skins during testing. Once set in position, aluminium bars were bolted into the mould against the surface of the panel, shown in Figure 5.1.3, to ensure that the panels did not move from their position during the cure process. For impacted panels with locally bowed areas, the set square was lined up against the edges of the panel where no damage existed. Misalignment at this stage would see the crosshead of the test machine come into contact with only one skin as the load was applied to the panel, causing uneven loading.



Figure 5.1.1. Photo of end potting mould with epoxy resin inside



Figure 5.1.2. Photo of V-notch cut into top of panel to improve epoxy penetration

Cured at room temperature for a period of 24 hours, the ends of all the potted panels then required machining using a vertical mill and a 10mm tungsten-carbide router to ensure that the two loaded ends were parallel to each other, and that these ends were perpendicular to the 0° loading direction, in order to avoid any localised stresses during compression testing causing an early failure at the ends of the panel. Also for any machining on panels with impact damage and preconditions, it was imperative to ensure that after the machining these regions remained in the centre of the length of the panel in the loading direction. An example of a finished end pot can be seen in Figure 5.1.3.

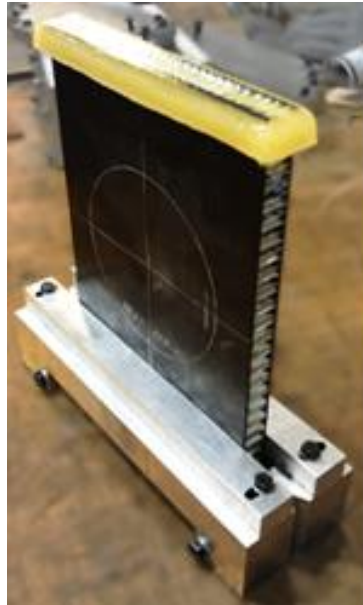


Figure 5.1.3. Photo of a cured end pot at one end, and showing the configuration of the panel while curing the other end

5.1.2. Strain gauging

Strain gauges were mounted to selected locations after the end machining was completed. Two single element, and four two-element rosette strain gauges were used in order to capture the strain profile of the panel to help develop an understanding over what is likely to have happened to the panel in order to cause the failure. The single element strain gauges were located on the centre line traversing the 0° fibre direction of the panel, at a distance of one sixth of the panel height (33.33mm) from the top edge of the panel. This distance was based on the relative placement of the far-field gauge from ASTM D7137 for monolithic CAI testing. This is a typical arrangement for measuring far-field response which would give information about the global response of the panel, as well as being able to identify onset of localised end failure of the panel at the loaded end. The ASTM standard suggests corner placements for the strain gauges for far-field responses, however, it has been found in previous research by Zhou et al [87] and Lloyd [120] that placing the strain gauges in the corners has potential short comings. It has been found that the earlier onset of contact during compressive testing with the corner regions causes areas of stress concentrations, as well as the corner regions being inherently stabilised by the presence of the anti-buckling supports, causing the panel to be stiffer in the corners, creating an untrustworthy location to gather information about the far-field response of the panel. Also, with the local response being captured in the centre of the panel, comparisons of the strain gauge response in order to ascertain the buckling modes of the panel are impractical if the strain gauge is not located on the same longitudinal path as the central gauge. The first pair of the rosette strain gauges was located at the central point of the panel, and measured the localised strain response

in both the 0° and 90° directions at the centre. Ideally, the second set of rosette strain gauges would be located on the edge of the delaminated area due to impact damage, however locating this region without destructive methods was not possible. So average face sheet indentation diameters to mark the damage front were relied on. Therefore the second pair of the rosettes were placed on the central line traversing the 90° fibre direction at a distance of 45mm from the centre spot, and provided information on the local response in the lateral section of the panel, as well as tracking propagation of impact damage, such as delamination, debond and indentation, in the panel. In the event of fibre fracture, or extreme localised dishing from the impact testing, there would be no strain gauge placed over the impact damage, due to the likelihood that the strain gauge would fail immediately or the reading be unrepresentative of the panels' behaviour due to the top ply detaching or splitting. The strain gauges were limited to one quadrant of the panel, as the response of sandwich panels in compression has been found by Lloyd [120] to be symmetrical about the horizontal and vertical bisectors. The strain gauge locations are shown below in Figure 5.1.4. In order to obtain mean and curvature strain responses, the strain gauges were bonded back-to-back. To ensure that the strain gauges were located back to back, a reference point in the bottom left hand corner (also shown in Figure 5.1.4) was used for all markings.

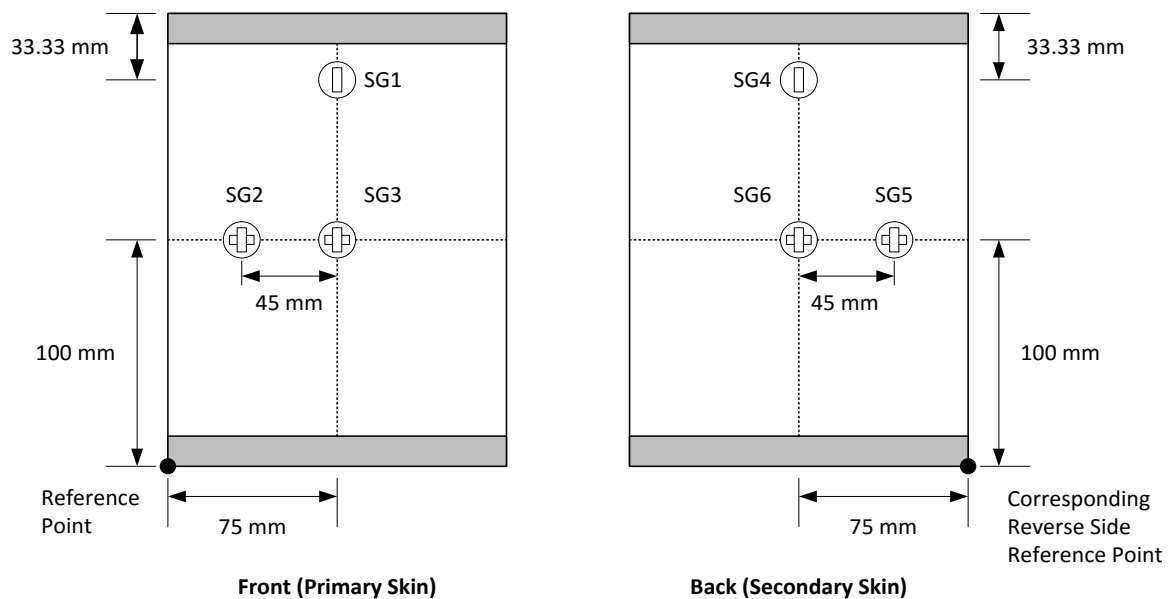


Figure 5.1.4. Strain gauge locations on panels plus strain gauge numbering

To ensure that the strain gauges survived the maximum loads of the panels, the following steps were taken during bonding them to the panel. First, the locations of the strain gauges were marked with a horizontal and vertical line in metallic pen, then the surface was prepared by sanding the mounting area lightly with 1200 grade wet and dry paper, which removed the central portion of the markings

whilst leaving enough to align the gauge accurately. Once the resin was smooth, the specimen was cleaned with propanol solution to remove dust and residues. To correctly locate the strain gauges, each gauge has 4 lines or arrows to help align them vertically and horizontally, which were matched up with the remaining marked silver lines. Tape was used to temporarily hold the gauge in this position. A side of the tape was lifted up which in turn lifted the strain gauge out of position, allowing cyanoacrylate glue to be applied to the back of the gauge. The tape was then placed back on the panel fixing the strain gauge in its correct position. This technique ensured that the strain gauge was correctly positioned before and after the application of the glue. Once the glue was dry, the tape could be removed, the legs of the strain gauge were then bent up and away to allow for the terminals to be mounted to the panel. The terminals were placed next to the strain gauges and fixed into place using the same technique as bonding of the strain gauges. These terminals gave an anchoring point for the strain gauge wires that connect the gauge to the data acquisition equipment, that, in the event the wires were pulled or jerked during connection, the possibility of the strain gauge from being ripped off was minimised. Once the glue under the terminal was set, the strain gauge legs were then bent back down directly over the terminal contacts. The legs were then soldered to the contacts and the excess portions could be trimmed off. Bonded and soldered single element and rosette strain gauges are shown in Figure 5.1.5. Wires were then soldered to the contacts.

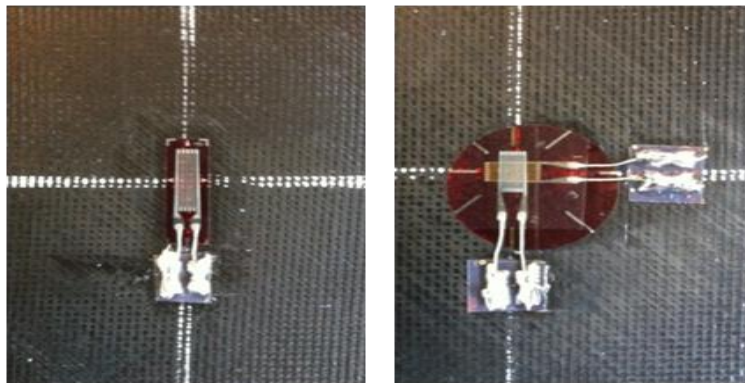


Figure 5.1.5. Bonded and soldered single and rosette strain gauges

5.1.3. Removing core

Following on from the manufacturing steps in Section 2.4.1 for the impact core removal panels, it was necessary at this stage to fully remove the section of core from the panel. This central section of honeycomb had pieces of bagging film on both the top and the bottom of the core during the sandwich bonding to prevent the skins from bonding the core. It was imperative that the core be removed without damaging or warping the core to an extent that the impact zone could not be analysed. The approach used to remove the core piece was to first remove the bagging film from around the core,

then gently push the core material through with a metal block from one side, whilst pulling the core from the other. Once the core was pushed out, it was set aside and labelled as to easily ascertain which panel it had been removed from, and to what impact energy it had been subjected to.

5.2. Compression jig and testing approach

The main contributions of the literature to the damage tolerance study of sandwich panels have been reviewed in Section 1.3, where it was clear that there is no established CAI test standard accepted globally for in-plane compression of sandwich panels. As discussed, the CAI test methods used for sandwich panels have evolved from the modifications and adaptations of the two main laminate CAI standards [107,108].

The in-plane compression jig as shown in Figure 5.2.1 was inherited from previous researchers. The jig consists of a 10mm steel base plate, with a welded steel frame mounted on top, 4 steel bolts provide lateral constraint, two steel plates with 160mm long cylindrical edge supports provide anti-buckling support, and 12 socket cap bolts to secure and position the anti-buckling supports. In this investigation, the boundary conditions that each compression panel was subjected to consisted of a 'quasi' clamped loaded end and a simply supported unloaded edges. The simply supported edges prevent the global buckling of the panel whilst still allowing local buckling to occur. Similar to monolithic laminates, it is still regarded as the most appropriate representation of the practical scenario. The cylindrical supports leave an allowance of a 20 mm length at each loaded end for the compressive deformation plus the height of epoxy pot, and allowing for the panel to experience transverse displacement and rotation. The effect of the clamped loaded ends was achieved by the increased contact area via the potted epoxy surrounding the cross section at the end. In this way, the degree of a physical clamping effect was drastically reduced so as to mitigate the stress concentration at the contact ends.

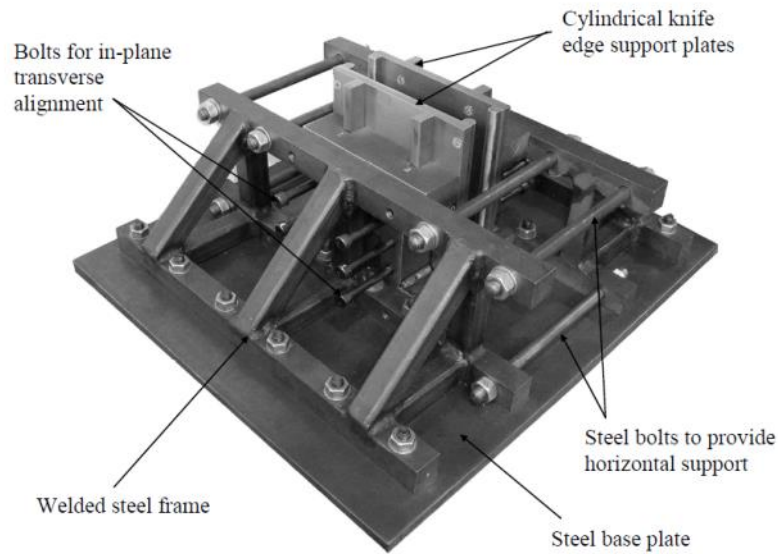


Figure 5.2.1. CAI testing jig

5.3. CAI testing set-up, measurements and procedures

All the in-plane compression tests were carried out on the seasoned Denison test machine, which has an upper load limit of 500kN with over a metre vertical test space. As a result, the CAI jig was required to sit on the top of a tall general-purpose base table such that loading a compression panel to failure would not require the cross head to travel more than 20 mm.

The CAI test setup started from the levelling of the base table. The most critical part of which was to ensure that all surfaces that lay perpendicular to the loading direction were all parallel to each other. This included the base table of the testing machine, the loading face of the machine, and the top and bottom surfaces of the test panels. Any slight misalignment could lead to an uneven contact, causing stress concentrations around one side of the loaded ends of the test panel, that could more than likely cause a premature failure of the panel at the end. Using a spirit level, all surfaces were checked that they were level. If there was any misalignment, the base table had adjustable feet to alter the height of each corner of the table.

The base of the Denison machine was found to be bowed in the central section where the jig was to be placed. The problem that bowing caused was noticed when testing a particular batch of control panels. The control panels all failed at loads that were much lower than expected, and in the central region. This was due to the lack of support under the loading area of the jig, which created greater local stresses to be present in the lower part of the specimen in the area left unsupported from the side supports. This meant that the jig had to be supported using additional metal shims underneath the panel area to ensure that loading was uniform. A vastly exaggerated depiction of the solution used

to eliminate the bowing effects are shown in Figure 5.3.1. In the event of any additional local misalignment of the test rig, thin metal shims were inserted beneath the base plate of the test rig to ensure it was level, as seen in Figure 5.3.1. Additionally, debris from failed panels in previous tests could also cause the specimen to sit out of alignment. To eradicate this eventuality the machine was brushed clear of debris before each test.

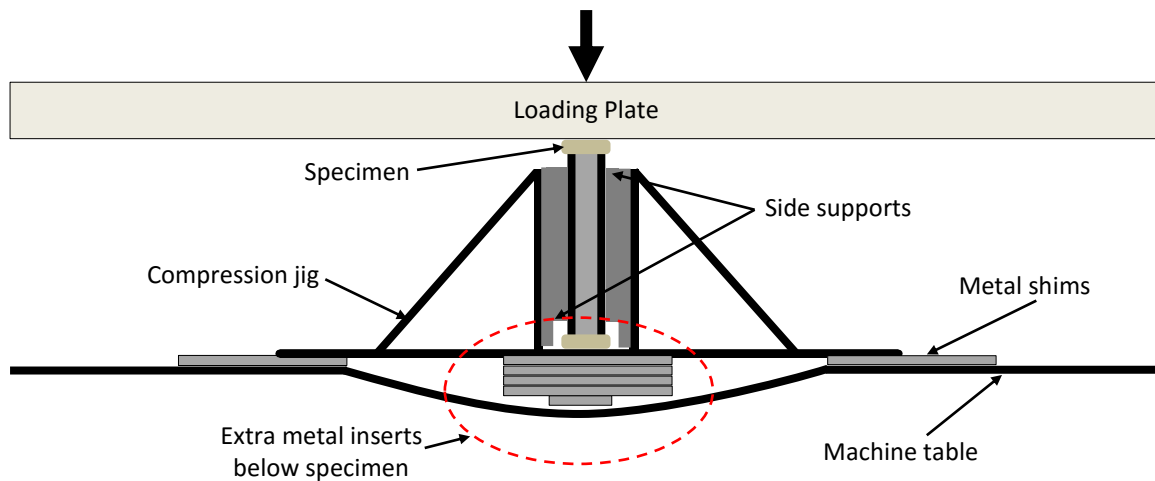


Figure 5.3.1. Exaggerated illustration showing solution put in place to eliminate the effects of bowing

Once the test rig was level, the specimen would then be loaded into the jig. This was a delicate procedure to ensure that none of the strain gauges were damaged, and to further ensure that the panel was upright and perpendicular to the loading crosshead. The anti-buckling supports were lifted out of the test rig, and positioned either side of the panel. At this stage, it was important to make sure that the strain gauge wires all passed underneath the anti-buckling supports and were not caught between the ABS and the panel surface, ensuring the wires were not damaged. With the panel in place between the ABS, the whole assembly was lowered back into the jig, care was taken to keep the strain gauge wires free from getting caught underneath the ABS when lowered. With the panel in the jig, it was essential that the panel was secured in an upright position. Using a spirit level to ensure that the panel was level and upright, the supports were secured in position by finger tightening the six bolts on each side. To ensure the panel did not get moved unevenly by the tightening of the bolts individually, they were all tightened to just touch the panel by one person either side, then in turn, starting from the middle four, tightened against the panel, turning the screws alternatively for the same number of revolutions each time. It was also important to ensure the sides of the panel overhung the ABS an equal amount on both sides, and that the panel was in the middle of the supports laterally, which was checked by eye by the operator. An LVDT (linear variable differential transformer) was positioned under the cross head to measure the in-plane compressive displacement, care was taken

to ensure the LVDT was vertically aligned, and just touching the crosshead at the beginning of the test. A magnetic stand was used to hold the sensor in place.

The strain gauge wires were then connected to the data logging device, the Orion Data Logger. To connect to the device, each wire was connected to one channel. There were 20 wires in total coming off of the panel, two from each gauge element. Each wire pair was labelled to identify which strain gauge it was from, and the same channels were used for each test to ensure the data could be easily linked to the strain gauge location when it was post-processed. The channels used and their associated strain gauge number are shown in Figure 5.3.2. When the wires had been securely screwed into the channel terminals, the resistance of the strain gauge was checked using a multi-meter on the tightened screws. At this stage, the resistance needed to read $120 \pm 1.0 \Omega$, which showed that the strain gauge had not been damaged during the set-up process, and that there was a connection between the strain gauge and the data logger. If there was no reading at this stage, the whole assembly needed to be taken apart, and the soldering and connections checked on the strain gauge which showed an errant resistance.

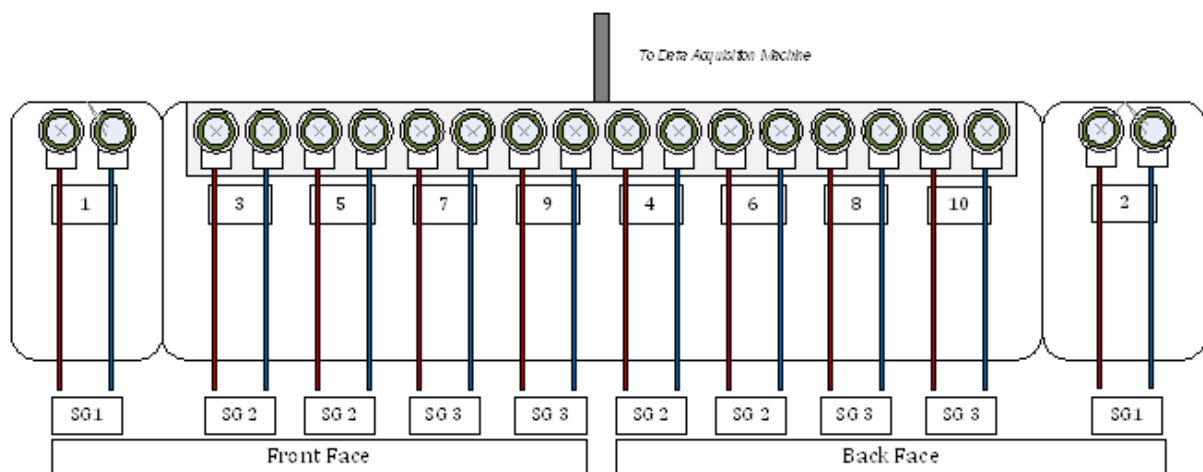


Figure 5.3.2. Assignment of strain gauges and wires to data logger channels

The Denison test machine outputted load during the test, and both load and displacement were fed into the data-logger through separate channels, 18 and 38. The LVDT passed through an amplifier box in order to condition the signal, and the load was also fed through an additional conditioning unit. It was imperative before each test these units were switched on, and that the feeds of both load and displacement were being read by the data-logging system. The signals of both the LVDT and the load were in volts.

At this stage, all data channels were connected to the data-logger, and the signals being read by the machine needed to be set-up. This included the set-up of each individual channel, whether the signal

inputted was in volts or strain, the sample rate required, and the details of the strain gauges used, including their excitation current and strain gauge factor. When all these channels were set up on the data-logger, the data capture software on the connected Windows computer, Data Logger 2000, needed to be linked and set-up to record the data stream to a text file during the test. Opening this file was crucial to the data being recorded, without it, the data streams to the computer, but would not be recorded, and all information about the test would be lost.

The Denison machine is a manually operated, load controlled machine, allowing the load to be applied by the user via the use of a main oil delivery wheel and fine strain control gauge. It was important before each test that the main oil delivery wheel, and the fine adjustment gauge, were fully rewound to ensure the full loading range could be applied to the panel. Another crucial part of the testing was the manual operation of the Denison, with attention being paid to the load rate of the machine. Consistency of load rate allows for comparison between tests easier to make, and avoiding loading the specimens too rapidly will ensure premature failures were not induced by a dynamic loading condition.

After each test, the raw data outputted from the Denison test machine needed to be saved and then converted from its ASCII format. After conversion, the data was outputted in columns related to the channel in which it was fed into, load in channel 18, displacement in channel 38, and strain gauges in channels 1-16 and 21-24. The data text file could then be opened in Microsoft Excel in order to start the data manipulation. Strain was outputted and recorded already in microstrain ($\mu\epsilon$), so no adjustment needed to be made, however load and LVDT displacement were outputted in volts. To convert the data, Equations 5.3.1 and 5.3.2 were used, which were verified by Hill [1].

$$\text{Load (kN)} = \text{Denison voltage output} \times 62.062 \quad (5.3.1)$$

$$\text{LVDT displacement (mm)} = \frac{\text{LVDT voltage output}}{0.5532} \quad (5.3.2)$$

After the data was all in the correct units for comparison, the start point of the test needed to be found and all data subsequently zeroed from that point. Tracking the point at which there was a noticeable and consistent increase in load was the easiest way of doing this. With all these steps followed, graphs for load vs displacement, and load vs strain responses could be plotted. Examples are shown in Figure 5.3.3 and Figure 5.3.4.

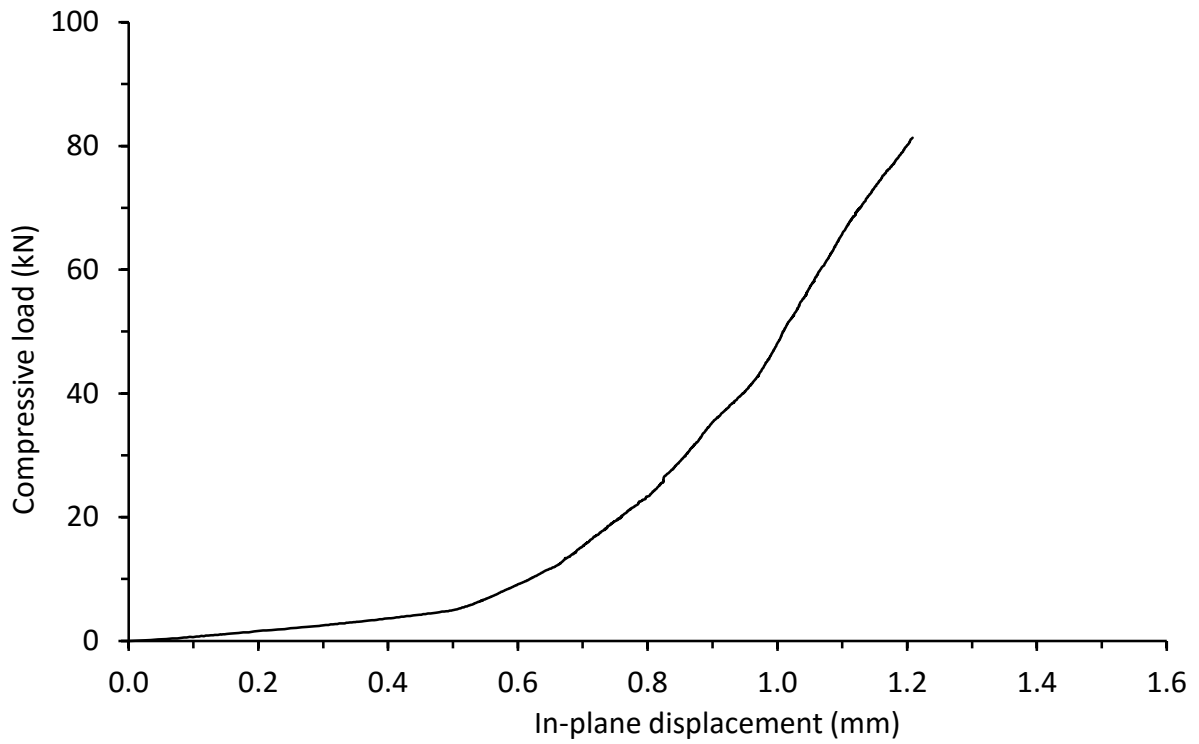


Figure 5.3.3. Compressive load against in-plane LVDT displacement for a thick symmetrical QI carbon/epoxy control panel with 70kg/m³ core density (CI-16-16-QI-0J-A)

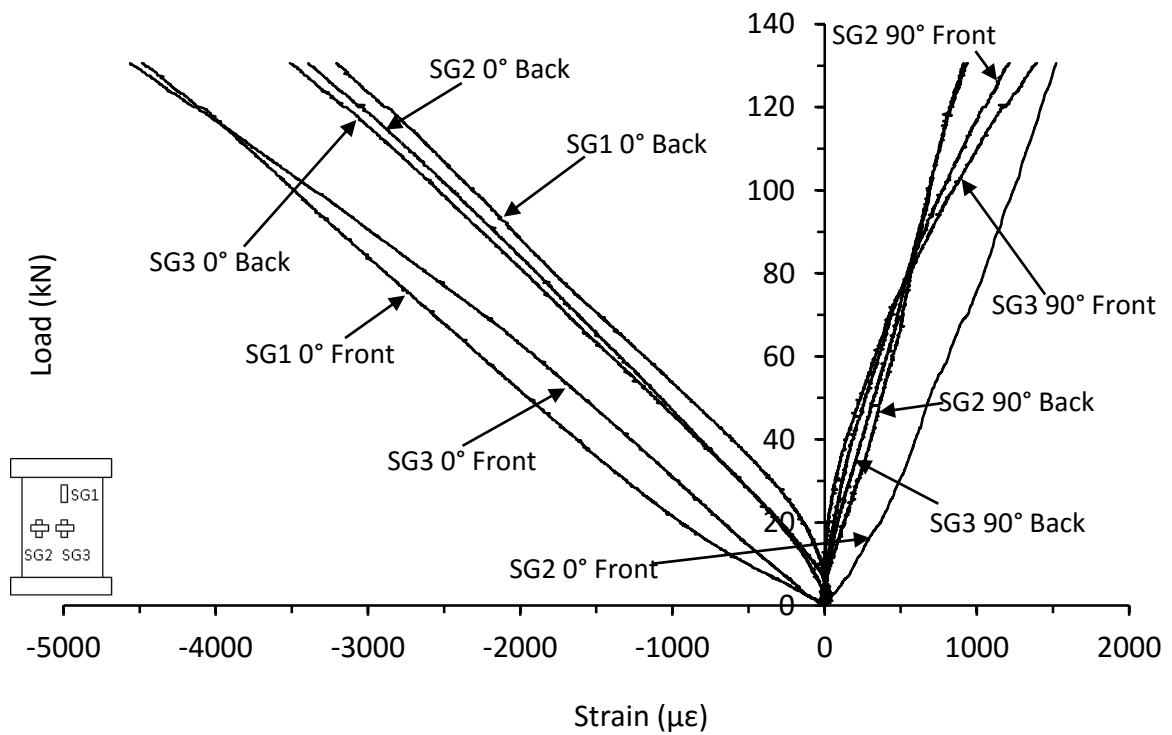


Figure 5.3.4. Strain response from a thick symmetrical QI carbon/epoxy control panel with 70kg/m³ core density (CI-16-16-QI-0J-A)

6. IN-PLANE COMPRESSIVE BEHAVIOUR OF BASELINE SANDWICH PANELS

6.1. Test results from in-plane compression baseline panels

Before the effects of either impact damage or other preconditions on the in-plane compressive behaviour could be understood, the in-plane compressive behaviour of intact or baseline sandwich panels must be examined so that any significant differences can be attributed to the presence of either impact damage or preconditions. The baseline panels include both carbon/epoxy and E-glass/epoxy skinned panels with honeycomb cores. For symmetrical panels with carbon/epoxy skins, both cross-ply lay-ups of $(0/90)_{2s}$ and $(0/90)_{4s}$ and quasi-isotropic lay-ups of $(45/0/-45/90)_s$ and $(45/0/-45/90)_{2s}$ were used for thin and thick skins, respectively. For unsymmetrical panels, skin combinations of 8 plies/6 plies were used for thin skinned panels and 16 plies/12 plies for thick skinned panels with both CP and QI lay-ups. When the lay-up was quasi-isotropic for unsymmetrical panels, the thinner skins were in multi-directional lay-ups of $(45/0/-45)_s$ and $(45/0/-45)_{2s}$ for thin and thick skins, respectively. Three densities of 5052 aluminium honeycomb core used were 70 kg/m^3 , 110 kg/m^3 and 135 kg/m^3 all with a thickness of 12.7 mm. The 70 kg/m^3 core density was used in all above arrangements, whereas each of the 110 kg/m^3 and 135 kg/m^3 core was coupled with the thin symmetrical and unsymmetrical cross ply skin arrangements only. For panels with E-glass/epoxy skins, thin 8/8 ply skin combinations in a cross ply lay-up of $(0/90)_{2s}$, and thick 16/16 ply skin combinations in a cross ply lay-up of $(0/90)_{4s}$, both with a core density of 70 kg/m^3 .

The performance of these baseline panels was assessed using their strain and displacement responses in conjunction with post-mortem observations of failed specimens. In this way, the baseline in-plane compressive behaviour of panels with varied skin material, skin thickness, skin lay-up, skin asymmetry and core density could be ascertained. A total of 13 types of in-plane compressive tests were conducted, with at least two tests in each type. Table 6.1.1 summarises the average compressive stresses at failure for all panel arrangements, and a summary of individual test details, along with post-mortem failure observations are shown in Table 6.1.2 and Table 6.1.3.

To help identify the failure locations, the panel was divided into three discrete sections, the loaded and far end and the mid-section regions, shown in Figure 6.1.1. All panels were found to fail at either the loaded end (LE) or the far end (FE) with none failing in the mid-section region (see Figure 6.1.2- Figure 6.1.4). Further examination of the tested panels indicated that some failed via end crushing, whereas the remaining failed through shear bands in the skins close to an end, which were approximately linked to the differences in construction. An example for the latter is shown in Figure 6.1.2(a) and an example for the former is shown in Figure 6.1.2(b). For this former type (Figure

6.1.2(b)), the middle part of the end pot is seen to be compressed into the core with the two skins bent outwards due to the fact that there was no lateral support over the end region of about 15mm from the contact. For the latter type, the panels commonly failed through shear bands in the skins close to the end. At the start of the test, the load was transmitted from the panel ends to the mid-section, as expected, however, due to high flexural rigidity of the panel and the high in-plane shear resistance, the longitudinal load transmission was very limited. As the loading continued, this led to a concentration of the load at the ends, where the resulting concentration of compressive stresses led to the failure at one of the ends (a detailed explanation on how this is linked to the strain responses and end deformation is given in the next section). It was generally found that the former was dominant in the thick panels, whereas the latter was dominant in the thin panels, as seen in the last column in Table 6.1.2 and Table 6.1.3. The increase in thickness in the panels provided the increased flexural rigidity and in-plane shear rigidity, which in turn made the load transmission to the mid-section more difficult, altering the manner of the failure in the panel.

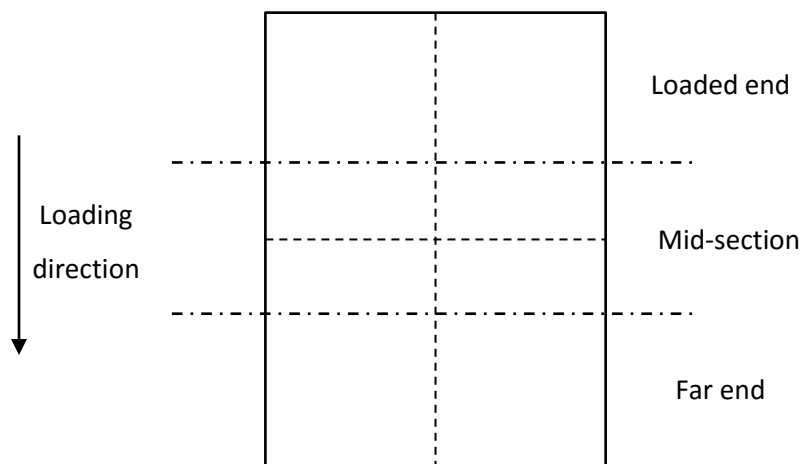


Figure 6.1.1. Diagram showing the three discrete regions of the panel used in identifying the location of the panel failure after in-plane compression

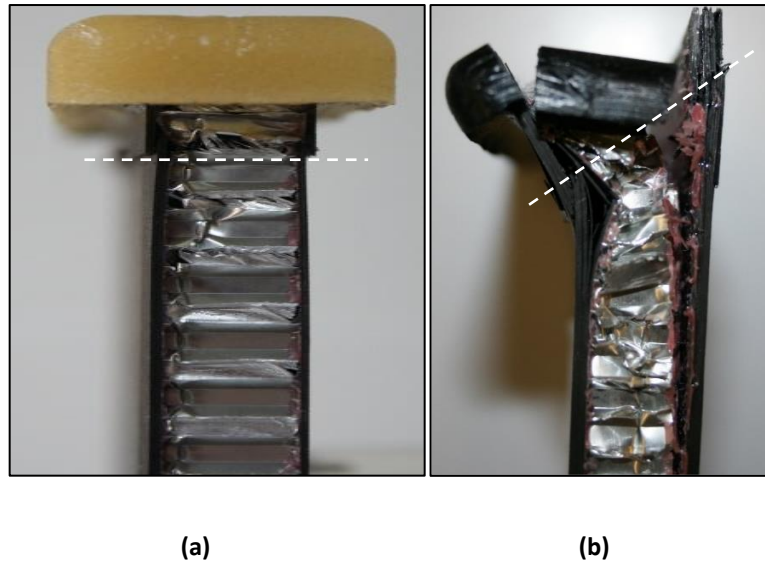


Figure 6.1.2. Two different failure types in in-plane compression control panels with carbon/epoxy skins and 70kg/m^3 core (a) thin unsymmetrical CP panel showing shear bands in skins only (DJ-8-6-CP-0J-B) (b) thick symmetrical CP panel showing end crushing (CI-16-16-CP-0J-A)

Nevertheless, in some cases, a few panels did not follow the trends and their failure types were significantly influenced by the other parameters such as core density. Increasing the core density increased both flexural rigidity and shear rigidity of the sandwich panels in addition to their normal compressive strengths. As a result, all the thin panels with a core density of 110kg/m^3 failed in end crushing, irrespective of panel symmetry, as can typically be seen in Figure 6.1.3. However, a further increase of the core density to 135kg/m^3 had the opposite effect. With the further enhanced flexural and in-plane shear rigidity, the thin panels with a core density of 135kg/m^3 failed in the skins close to the ends, as seen in Figure 6.1.4, rather than being crushed. Clearly, this further increasing of core density triggered a response mechanism, which has not been understood at this point.

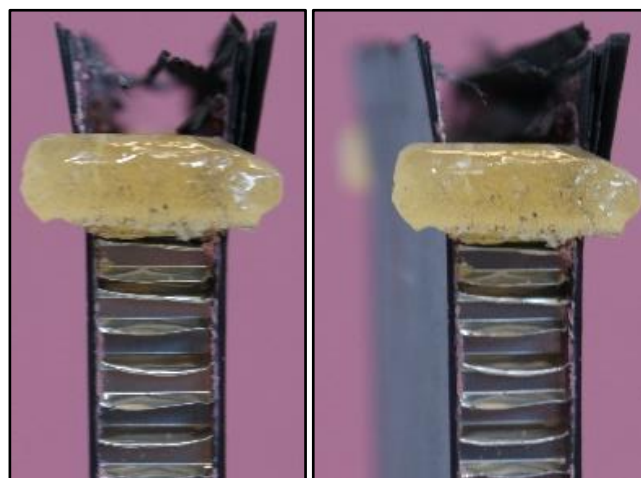


Figure 6.1.3. Observed end crushing mechanism failure in thin symmetrical CP carbon/epoxy panels with 110kg/m^3 core (AR-8-8-CP-0J-B)



Figure 6.1.4. Observed shear band mechanism failure in thin symmetrical CP carbon/epoxy panels with 135kg/m³ core (RM-8-8-CP-0J-B)

Table 6.1.1. Average compressive strengths of all control panels arrangements

	Core Density (kg/m ³)	Number of tests	Compressive stress at failure (MPa)	Standard Deviation (MPa)	% c.v
Thin CP Symmetrical ¹	70	2	296	36.35	12.27%
Thin CP Unsymmetrical		2	298	31.56	10.60%
Thin QI Symmetrical		2	293	29.17	9.95%
Thin QI Unsymmetrical		2	209	1.15	0.55%
Thick CP Symmetrical		2	223	14.96	6.72%
Thick CP Unsymmetrical		2	223	18.90	8.48%
Thick QI Symmetrical		4	239	22.54	9.43%
Thick QI Unsymmetrical		2	302	0.32	0.11%
Thin CP 110kg/m ³ core symmetrical	110	2	417	31.62	7.59%
Thin CP 110kg/m ³ core unsymmetrical		2	402	101.07	25.14%
Thin CP 135kg/m ³ core symmetrical	135	4	295	30.03	10.17%
Thin CP 135kg/m ³ core unsymmetrical		4	269	61.22	22.74%
Glass/epoxy thin CP	70	2	221	23.40	10.57%
Glass/epoxy thick CP		2	190	3.37	1.77%

1 - From Michelle Hill's tests [1]

Table 6.1.2. In-plane compressive tests of all individual thin control panels

Specimen ID	Upper Skin (mm)	Lower Skin (mm)	Panel Width (mm)	Core density (kg/m ³)	Compressive failure load (kN)	Compressive stress at failure (MPa)	Compressive Strain (μ ϵ)	Failure Location	Failure type	
NC-8/6-CP-OJ-1	0.99	0.74	148	70	81.94	320	-4222	LE	SF	
NC-8/6-CP-OJ-2	0.99	0.74	148		70.51	275	-3015	FE	EC ¹	
DJ-8/6-CP-OJ-A	0.96	0.72	144		32.82	136*	-1545	FE	SF	
DJ-8/6-CP-OJ-B	0.96	0.72	146		40.23	164*	-1826	FE	SF	
JL-8/8-QI-OJ-A	1.03	1.01	149		82.60	272	-4014	FE	SF	
JL-8/8-QI-OJ-B	1.03	1.01	147		94.15	314	-4541	FE	SF	
LB-8/6-QI-OJ-A	0.99	0.74	148		53.31	208	-3106	FE	SF	
LB-8/6-QI-OJ-B	0.99	0.74	148		53.72	210	-3110	FE	SF	
AR-8/8-CP-OJ-A	0.93	0.97	147		110	110.40	394	-5323	LE	EC
AR-8/8-CP-OJ-B	0.94	0.95	147			122.33	439	-5773	LE	EC
AR-8/6-CP-OJ-A	0.94	0.66	147	77.87		330	-3638	LE	EC	
AR-8/6-CP-OJ-B	0.94	0.66	145	110.03		473	-5411	FE	EC	
RM-8/8-CP-OJ-A	0.99	0.99	148	135	88.69	303	-3429	LE	SF	
RM-8/8-CP-OJ-B	0.99	0.99	148		88.67	303	-3945	LE	SF	
MB-8/8-CP-OJ-A	0.98	0.97	145		91.42	323	-3567	LE	SF	
MB-8/8-CP-OJ-B	0.97	1.00	147		73.00	253	-	FE	SF	
RM-8/6-CP-OJ-A	0.99	0.74	148		70.90	277	-2927	LE	SF	
RM-8/6-CP-OJ-B	0.99	0.74	148		89.75	351	-3462	LE	SF	
MB-8/6-CP-OJ-A	0.98	0.75	146		61.07	242	-2674	LE	SF	
MB-8/6-CP-OJ-B	0.98	0.74	145		51.74	207	-2418	LE	SF	
SG-8/8-CP-OJ-A	1.08	1.06	150	70	76.36	238	-6215	LE	EC	
SG-8/8-CP-OJ-B	1.08	1.15	150		68.35	205	-6329	LE	EC	

¹-End pot didn't cure properly

Table 6.1.3. In-plane compressive tests of all individual thick control panels

Specimen ID	Upper Skin (mm)	Lower Skin (mm)	Panel Width (mm)	Core density (kg/m ³)	Compressive failure load (kN)	Compressive stress at failure (MPa)	Compressive Strain** (μϵ)	Failure Location	Failure type
CI-16/16-CP-OJ-A	1.98	1.98	148	70	124.38	212	-2405	LE	EC
CI-16/16-CP-OJ-B	1.98	1.98	148		136.78	233	-2426	LE	EC
NC-16/12-CP-OJ-A	1.98	1.49	148		121.38	236	-2070	LE	EC
NC-16/12-CP-OJ-B	1.98	1.49	148		107.65	210	-2503	LE	EC
DJ-16/12-CP-OJ-A	1.88	1.40	145		61.21	128*	-1590	FE	EC
DJ-16/12-CP-OJ-B	1.88	1.40	145		87.40	183*	-2330	LE, FE	SF
CI-16/16-QI-OJ-A	1.98	1.98	148		130.56	223	-3845	LE	EC
CI-16/16-QI-OJ-B	1.98	1.98	148		121.37	207	-4054	LE	EC
JL-16/16-QI-OJ-A	1.90	1.89	149		152.84	271	-4524	LE	EC
JL-16/16-QI-OJ-B	1.90	1.89	147		134.08	240	-3868	LE	EC
LB-16/12-QI-OJ-A	1.98	1.49	148		155.08	302	-4508	FE	EC
LB-16/12-QI-OJ-B	1.98	1.49	148		155.32	302	-4962	FE	EC
SG-16/16-CP-OJ-A	2.15	2.14	150		121.00	188	-5703	LE	EC
SG-16/16-CP-OJ-B	2.15	2.21	150		125.92	193	-5332	LE	EC

LE – loaded end, FE – far end, SF – compressive skin failure close to the end, EC – end crushing, * - Compressive stresses removed from averages due to testing issues (Section 5.3) ** - Far-field mean strain.

6.2. In-plane compressive response in terms of load-strain

The in-plane compressive behaviour of the sandwich panels could be characterised by the combined local and far-field mean and curvature strain responses. These mean and curvature strains that were obtained by the back-to-back strains are given by

$$\epsilon_{mean} = \frac{\epsilon_{front} + \epsilon_{back}}{2} \quad (6.2.1)$$

$$\epsilon_{curvature} = \epsilon_{front} - \epsilon_{back} \quad (6.2.2)$$

The approach of cross-comparing the relative magnitudes of mean and curvature strains from both far-field and local locations of the panel in both loading and transverse directions could provide a qualitative indication of the in-plane compressive behaviour of the sandwich panel, if the panel was envisaged to have four portions (upper left, upper right, lower left and lower right). It was originally developed in Zhou et al [87,88] to characterise the monolithic laminates in in-plane compression, with the unloaded edges simply supported. Current loading and supporting conditions for sandwich panels are the same as those in the monolithic panels (except for the panel aspect and width-to-thickness ratios). If the panel undergoes pure local buckling as in one extreme case, the local mean strains ought to be zero, and if the panel undergoes pure in-plane compression as in the other extreme case and does not buckle locally the response from both the local and far-field mean strains will be large and

linear whilst the curvature strains ought to be zero or close to zero. For the remaining (cases) majority, the curvature strain response can be positive or negative depending on which way the skins buckle, and local buckling (at the mid-section region) can be picked up by combined mean and curvature strains from the mid-section gauges and will ultimately be identified by a reversal or large divergence in the curvature strain responses. With the use of simple supports at the unloaded edges the possibility of Euler (global) buckling is prevented.

The mean and curvature strain responses under in-plane compression shown in Figure 6.2.1 was typical of what can be closely considered to be a pure compressive response, and represents the majority of the responses from thin and thick, symmetrical and unsymmetrical, CP control panels, through all 3 core densities. After a brief initial bedding in phase, the linear increase in compressive mean strain in all three strain gauges in the loading (0°) direction, and the limited progression of the curvature strains in the far-field and mid-section of the panel, indicates no local buckling and the even compressive loading of the skins. The final catastrophic failure in the loaded end regions was sudden, due to stress concentrations. Nevertheless, the giving-in of one skin at the end at the early stage of the loading was clearly picked up by the far-field curvature strain, with the surge up to over 500 microstrains at less than 10kN. Yet, the mid-section region had a similar trend (from the centre and side mid-section curvature strain) but with much smaller magnitude. This pattern could be seen consistently in a clearer manner in another example in Figure 6.2.2.

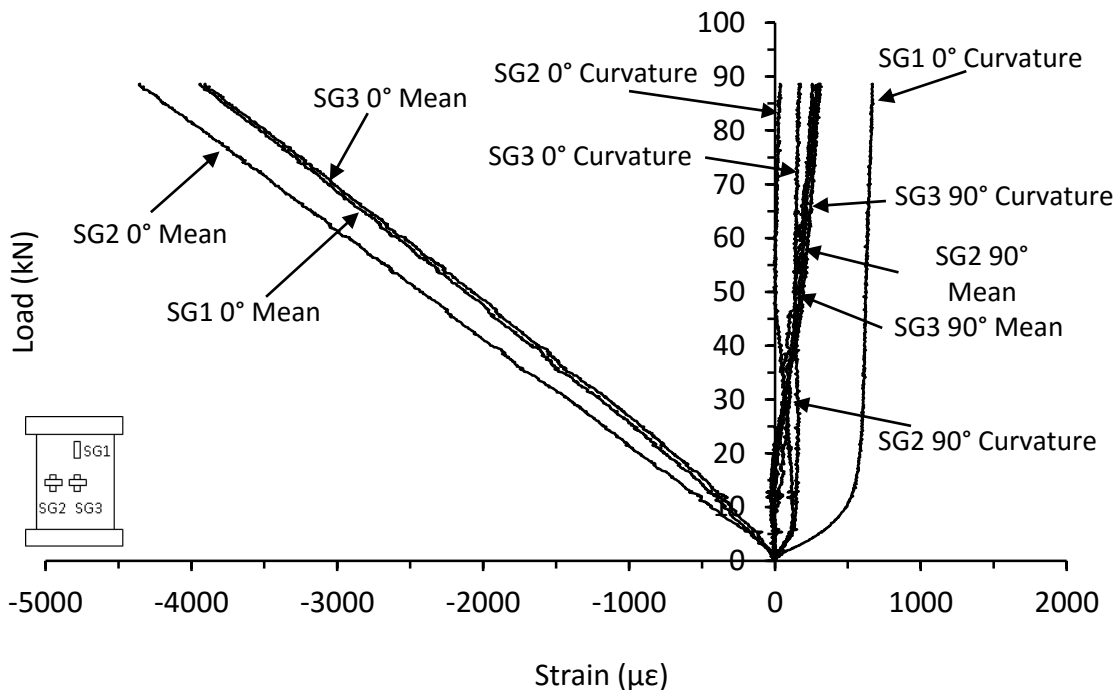


Figure 6.2.1. Mean and curvature strain response for a thin symmetrical CP carbon/epoxy control panel with 135kg/m^3 core density (RM-8-8-CP-0J-B)

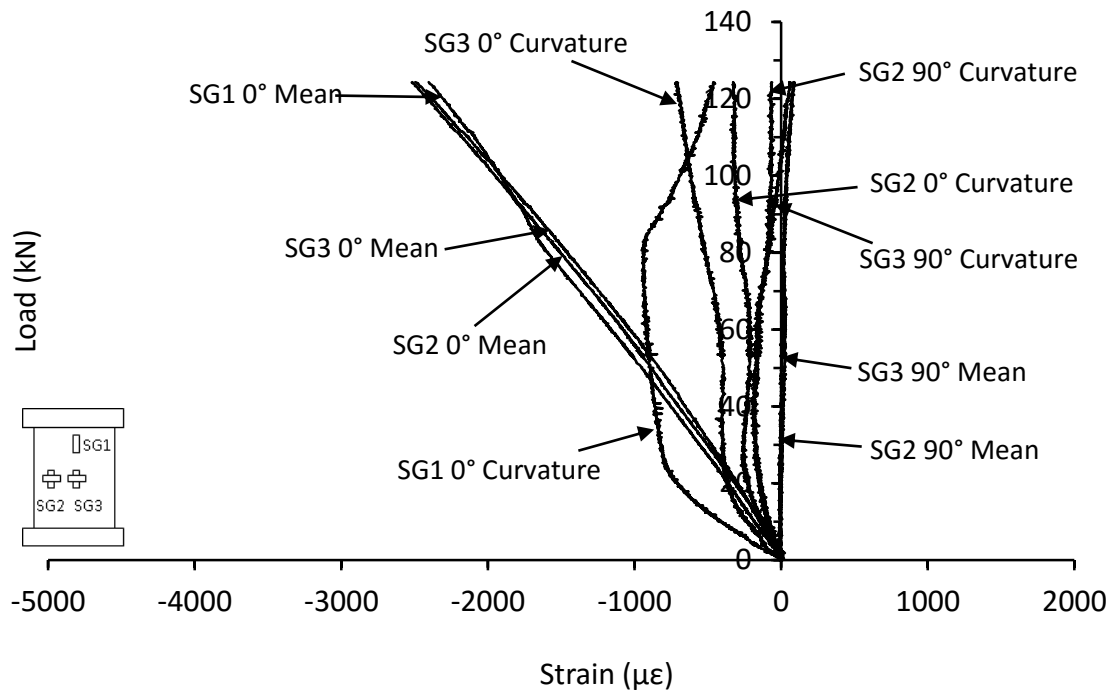


Figure 6.2.2. Mean and curvature strain response for a thick symmetrical CP carbon/epoxy control panel with 70kg/m³ core density (CI-16-16-CP-0J-A)

This consistent in-plane compressive failure sequence at an end is symbolised in Figure 6.2.3. From the unloaded state shown in Figure 6.2.3(a), a moderate increase of the curvature strain response from the far-field region, as seen in Figure 6.2.1 and Figure 6.2.2 as typical examples, and no full strain reversal up to the point of failure, would indicate failure of one skin close to an end in the skin with the higher strain, shown in Figure 6.2.3(b), which has been exaggerated for visual purposes. This would instantaneously lead to the major compressive resistance being shifted to the other skin, leading to the failure of the skin in in-plane compression. It was observed that the failure location between the two skins was rarely identical longitudinally, as seen in Figure 6.1.2(a), with the distance between the locations varying due to the construction of the panel, with the failure locations closer together in thin skinned panels.

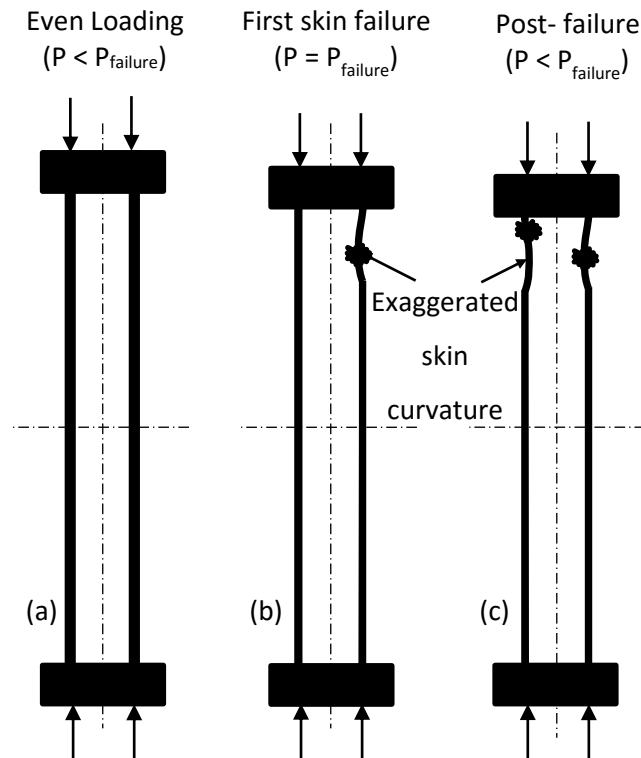


Figure 6.2.3. A deformation sequence of end region at-the-side view based on measured strain responses (a) unloaded state (b) initial compressive failure of front skin (c) transfer of load to un-failed skin

The mean and curvature responses in the transverse direction in both Figure 6.2.1 and Figure 6.2.2 are also typical of the transverse deformation behaviour of thin and thick, symmetrical and unsymmetrical CP control panels with all three core densities. Much in the same way that longitudinal buckling modes were not seen to properly develop in the mid-section, the concentration of the load in the end regions halted the development of the transverse deformation. The example responses show a small increase in the mid-section transverse mean strain, and the reversal of either the centre mid-section or centre and side mid-section curvature strains in the transverse directions, indicating the propagation of the buckling mode in Figure 6.2.4(b). However, due to the concentration of the loads at the ends, the deformation propagation seen in the strain responses was fortuitous. If proper in-plane compression failure was to occur here, the mid-section region would deform in the second mode shown in Figure 6.2.4(c).

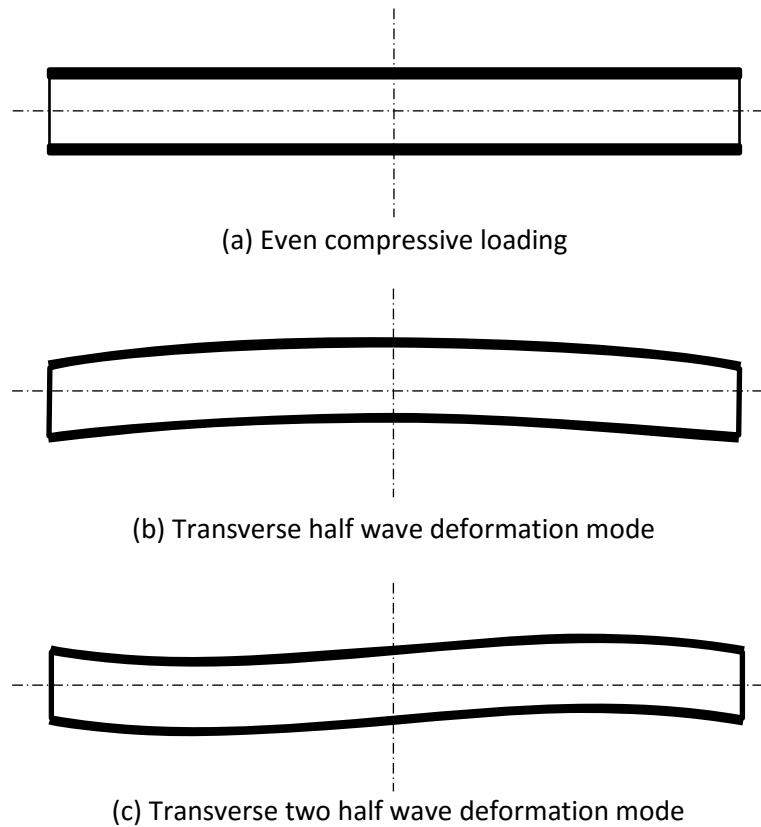


Figure 6.2.4. Top down view of transverse buckling developing in the mid-section region of panel based on strain responses (a) even compressive loading (b), (c) transverse buckling that could occur

Changing the lay-up in the skin material from CP to QI could increase the transverse deformation of the sandwich panels because of the 50% reduction of fibres, which could in turn increase the presence of the Poisson's effect, though the angle plies in $\pm 45^\circ$ could resist the in-plane compressive load very well. The Poisson's effect under in-plane compression in both 16 ply CP carbon/epoxy monolithic laminates and 8/8 CP sandwich panels with a honeycomb core was investigated in Hill [1], where not only strain gauges were used to monitor transverse displacement, but an LVDT was also positioned at the side of the panel at the mid-section. It was found that unlike in baseline 16 ply CP monolithic laminates, which exhibited transverse displacement and transverse mean strains before failure giving a Poisson's ratios of up to 0.24 (Fig 8.3 in Hill [1]). The baseline 8-8CP carbon/epoxy skinned sandwich panels did not show any transverse displacement under compression as measured by both the LVDT and strain gauges (Fig 8.17 in Hill [1]), and the lack of the transverse deformation was attributed to the presence of the core. As a result, the monitoring of transverse displacement was abandoned from this point onwards. For the majority of CP panels in this investigation, this result was confirmed; the strains in the mid-section region picked up by the 90° direction were minimal, as seen in Figure 6.2.1, which had a maximum transverse strain of approximately 300 microstrains in the mid-section, indicating little transverse deformation. However, as seen in Figure 6.2.5 and Figure 6.2.6, in two QI

carbon/epoxy panels, a large linear mean strain develops through the loading of the panel in both mid-section 90° gauges, up to 2000 microstrains near failure load, which is typically double or triple the values seen in CP panels (typically <1000 microstrains). This would indicate that the panel had experienced much greater transverse deformation in the skins, which is indicative of the Poisson's effect, though the panels still deformed in the first mode. This effect occurs most significantly in all QI control specimens.

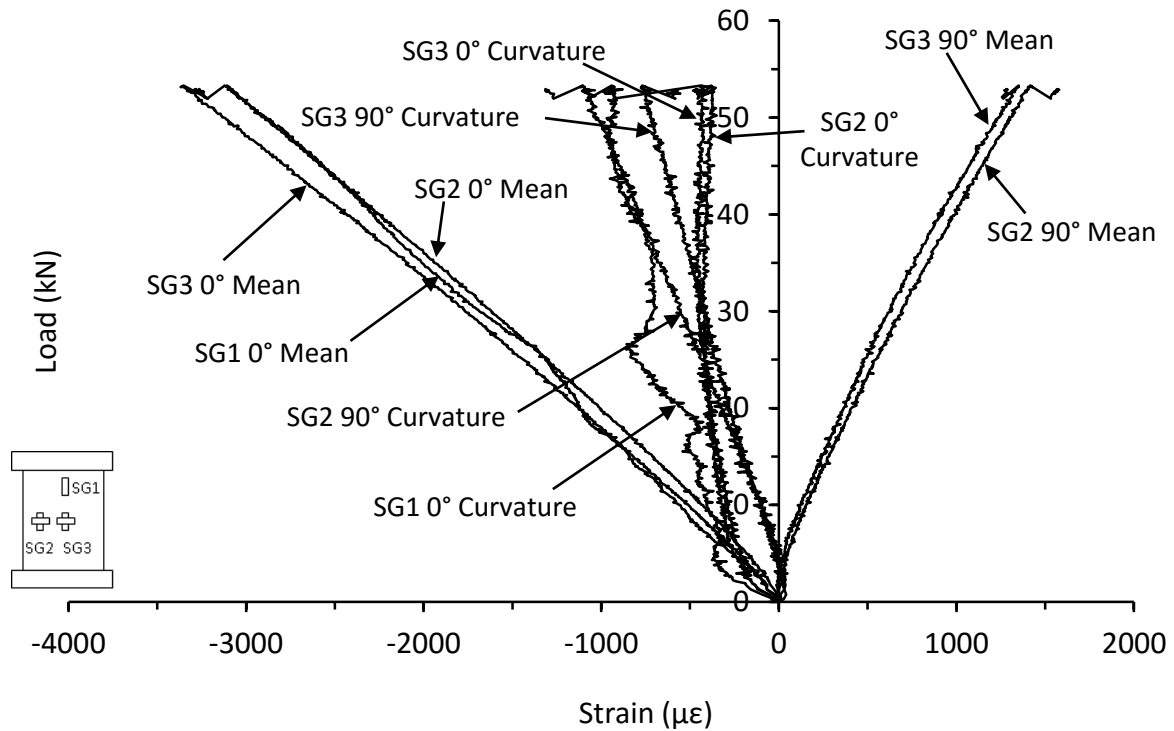


Figure 6.2.5. Mean and curvature strain response for a thin unsymmetrical QI carbon/epoxy control panel with 70kg/m³ core density (LB-8-6-QI-0J-A)

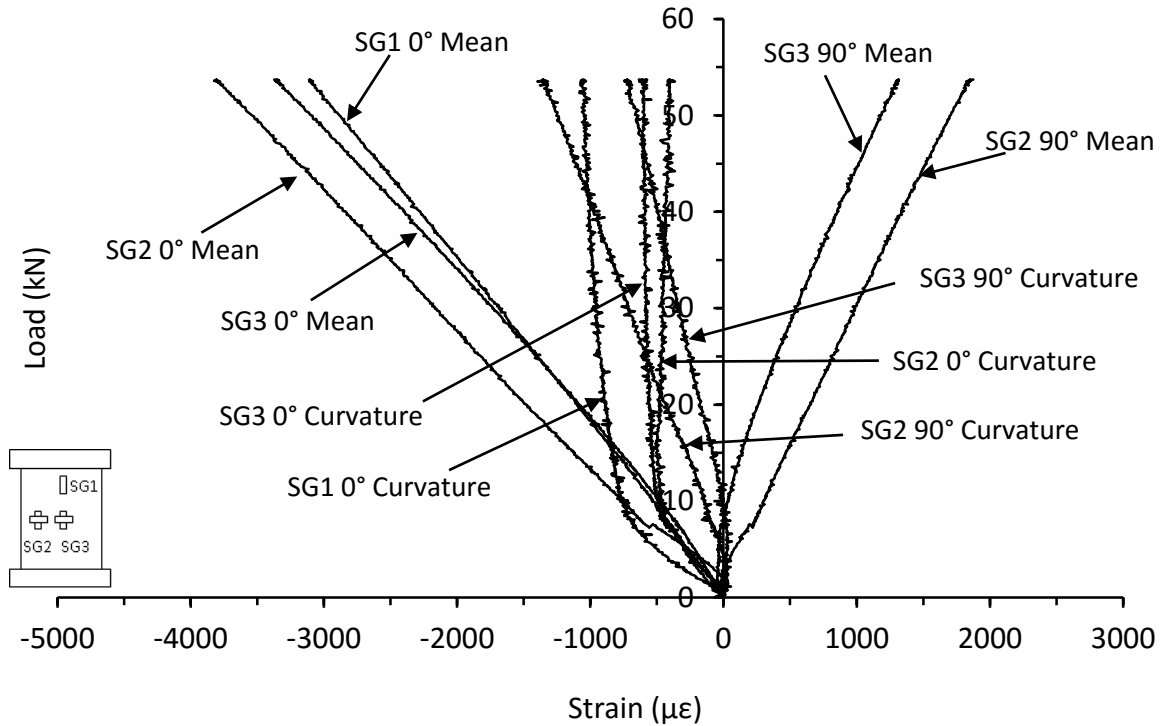


Figure 6.2.6. Mean and curvature strain response for a thin unsymmetrical QI carbon/epoxy control panel with 70kg/m³ core density (LB-8-6-QI-0J-B)

6.3. Parametric studies

The effects of changing skin thickness, lay-up, symmetry, material, or core density on the baseline in-plane compressive behaviour are re-focused here with regards to the potential variation in compressive strain response characteristics and especially failure characteristics.

The longitudinal displacement was measured using an LVDT (see Section 5.3), which was generally removed from the testing area before the catastrophic failure to avoid damage, leaving the majority of the tests without a final portion of the compressive displacement readings. Unfortunately, in some tests, this removal of the LVDT occurred much earlier throughout the loading history than others due to the lack of the familiarity of the in-plane compressive responses of the panels. The overall responses of the panels were similar across all variations of sandwich constructions. That is, there was a distinct non-linear portion at the beginning of each test and that was followed by a linear region, as could be seen in Figure 5.3.3.

6.3.1. Effect of varying thickness

The effect of skin thickness on the compressive load at failure was significant, as expected, with an average failure load of 130kN for the thick symmetrical CP panels and 137kN for thick QI panels and only 89kN and 88kN for the thin CP and QI symmetrical arrangements, respectively. However, it is

expected that the compressive strength of the panels with different thicknesses but similar skin symmetry and lay-up should be the same. As all control panels were found to fail prematurely, the comparative performance of the different constructions can really only be judged on how premature their failures were. As shown in Figure 6.3.1 and Figure 6.3.2, the dashed line represents the level of the assumed in-plane compressive strength that neither the CP nor QI symmetrical and unsymmetrical panels managed to achieve. In symmetrical thin panels, both the CP and QI lay-ups fail less prematurely than their thicker counterparts. That is, their respective stresses at failure from the thin panels are greater than those of the thick panels. Accounting for the effective area of the thicker panels, which is double that of the thin panels, the average compressive stress for the symmetrical thick CP panels is 222 MPa, which is 25% lower than the thin CP arrangements at 296 MPa. Similarly for the QI panels, the thick symmetrical panels have an average compressive stress at failure of 239 MPa, which is 18% lower than the thin QI symmetrical panels which had an average compressive stress of 293 MPa. This trend was repeated in the unsymmetrical CP panels, where the thick panels have an average compressive stress of 223 MPa, which is 25% lower than the thin panels which have an average compressive stress at failure of 298 MPa. In the unsymmetrical QI panels, this trend was reversed, where the thicker panels failed less prematurely, and have an average compressive stress of 302 MPa, and the thin panels have an average compressive stress 30% lower at 209 MPa. For symmetrical CP and QI and unsymmetrical CP panels, the increase in skin thickness, and hence flexural rigidity, in the panels has a clear effect on the ability of the panel to transmit the load from the ends to the mid-section, causing an earlier concentration of stress in the loaded ends, leading to a greater premature failure, and lower average compressive stresses in the panels. Since the unsymmetrical QI thick and thin panels exhibit their own trend, it is presumed that this is more a function of lay-up and asymmetry, and will be discussed further in the next section.

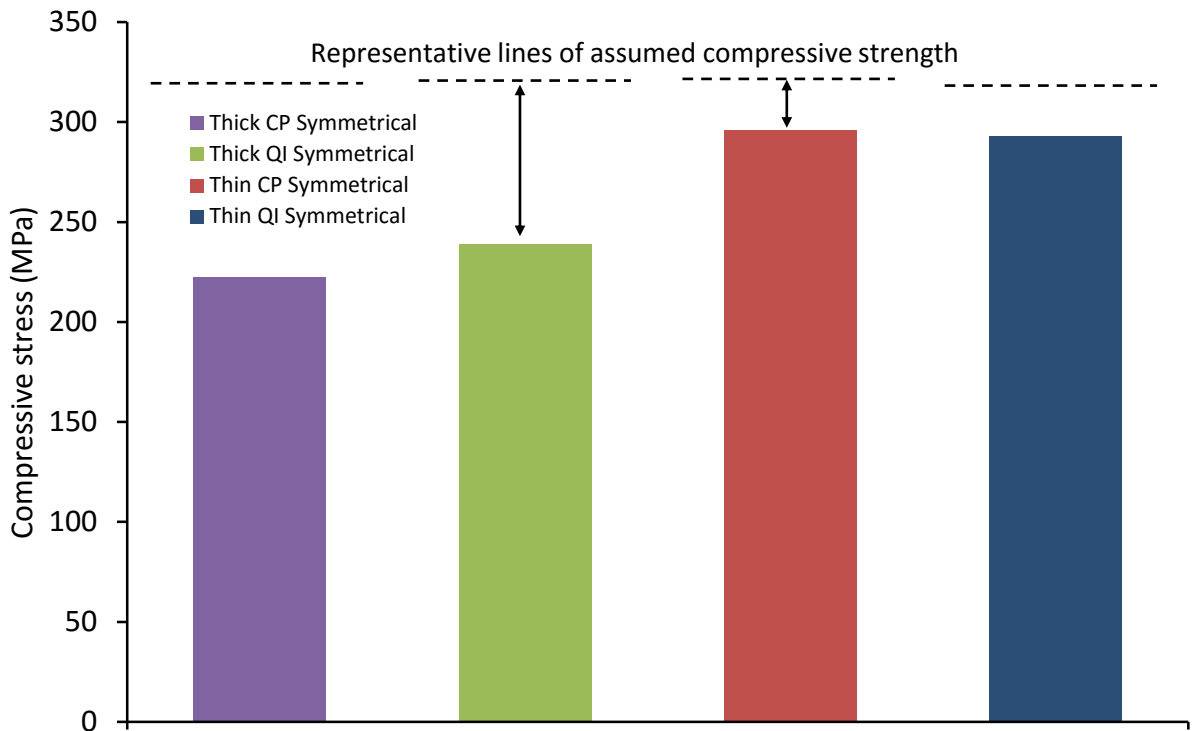


Figure 6.3.1. Average compressive stresses of thick and thin symmetrical CP and QI carbon/epoxy control panels with 70kg/m³ density

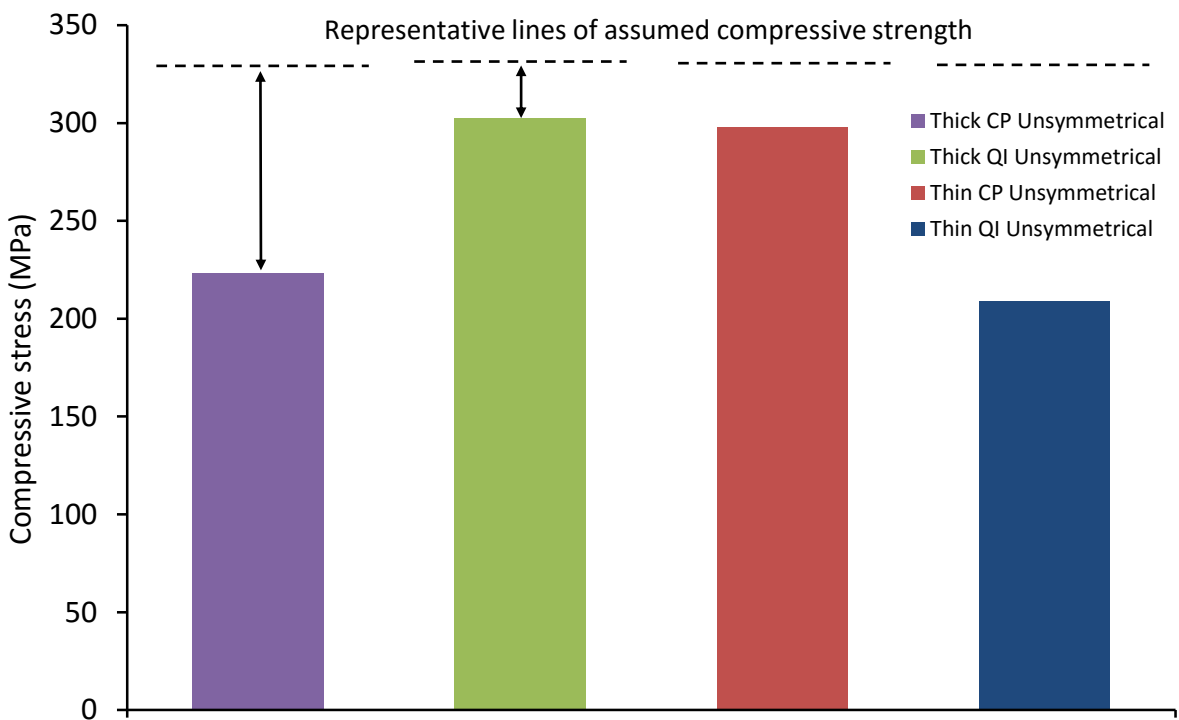


Figure 6.3.2. Average compressive stresses of thick and thin unsymmetrical CP and QI carbon/epoxy control panels with 70kg/m³ density

Shown in Figure 6.3.3 is a comparison between the far-field mean strain in thick and thin QI carbon/epoxy panels with 70kg/m^3 core density, which is representative of the majority of thin and thick panel strain responses. The thin panels developed a much higher level of strain under a similar load by approximately two times the amount than in the thicker panel, where both responses were pretty linear. This suggests that increasing the number of plies directly correlates to the development of strain in the skins, which suggests that the core has no direct effect on the linear response of the panel. The response from the mid-section of the thick and thin panels both suggest that there is no local buckling propagation in either skin under the compressive load, represented by linear increases in mean strain in both the front and back skin, and no significant curvature strain responses.

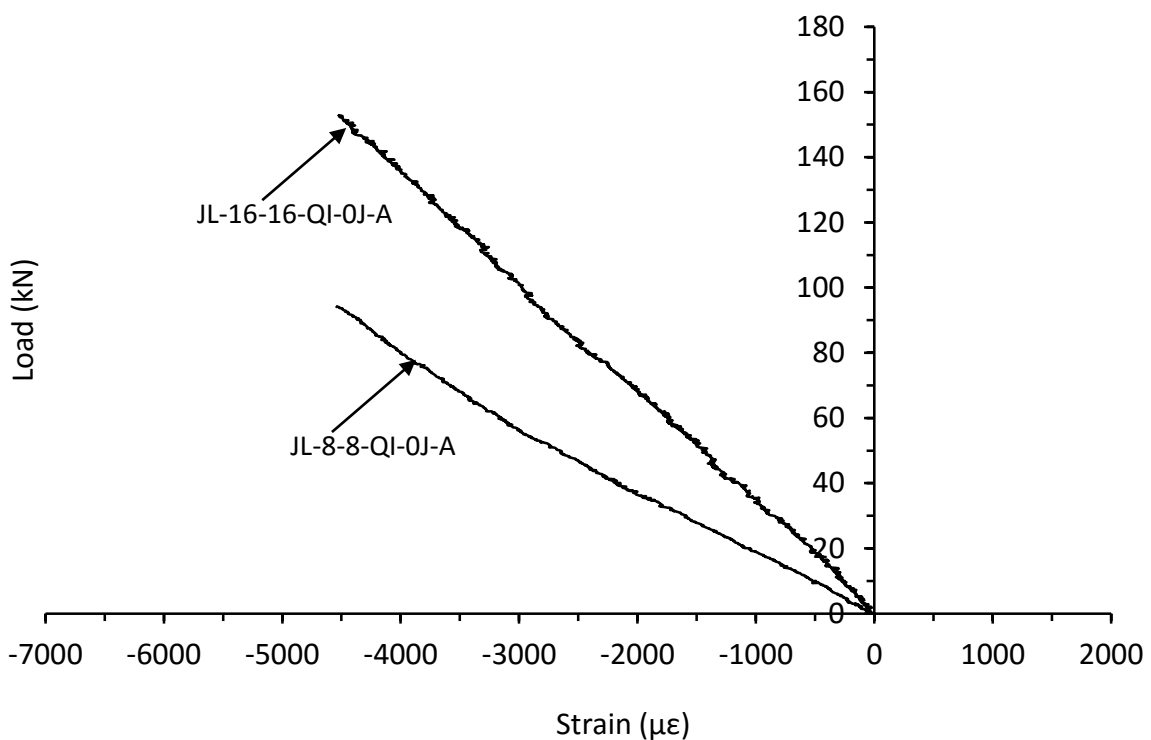


Figure 6.3.3. Mean strain response from the far-field region for thin and thick symmetrical QI carbon/epoxy control panels with 70kg/m^3 core density

6.3.2. Effect of varying symmetry and lay-up

The expected result of removing two or four plies from one side, depending on skin thickness, would shift the longitudinal neutral plane with respect to the in-plane compressive loading towards the side of the thicker skin, which could induce local bending moments around the mid-section and cause the panel to fail earlier than in the symmetrical arrangements if the bending moments are able to overcome the shear rigidity of the panel. Shown in Figure 6.3.4 and Figure 6.3.5 are the average compressive stresses at failure for thick and thin, symmetrical and unsymmetrical, CP and QI panels.

There was no apparent effect of panel symmetry in either thin or thick CP panels, with the panels failing at similar levels of compressive stress, suggesting that the concentration of stress in the loaded end was still dominant and the effect of panel symmetry was expected to influence only in the mid-section region. The thin unsymmetrical QI panels fail prematurely more than the symmetrical panels, which had a similar average compressive stress to the thin CP panels, which suggests that the effect of asymmetry could be prominent in the concentration of stress in the loaded ends, causing the unsymmetrical QI panels to fail at a lower compressive stress than the symmetrical counterparts. However, the average compressive stress at failure in thick unsymmetrical QI panels could be closest to the actual compressive strength out of these arrangements, and opposite to the expected result, the compressive stress at failure of thick symmetrical QI panels was 21% lower than the thick unsymmetrical QI panels. This merely confirms the random nature of the premature failures.

Skin lay-up should also have an effect on the compressive performance, with QI panels having higher in-plane shear properties in the skins due to plies orientated in the $\pm 45^\circ$ directions, leading to laminates with larger changes in orientation angles from layer to layer tending to result in lower CAI strength, as suggested in [99,100]. Both thick symmetrical and unsymmetrical CP panels, were seen to fail at earlier levels of stress than the QI counterparts, shown in Figure 6.3.4, as expected, with the differences between lay-up performances being more substantial in the unsymmetrical arrangements.

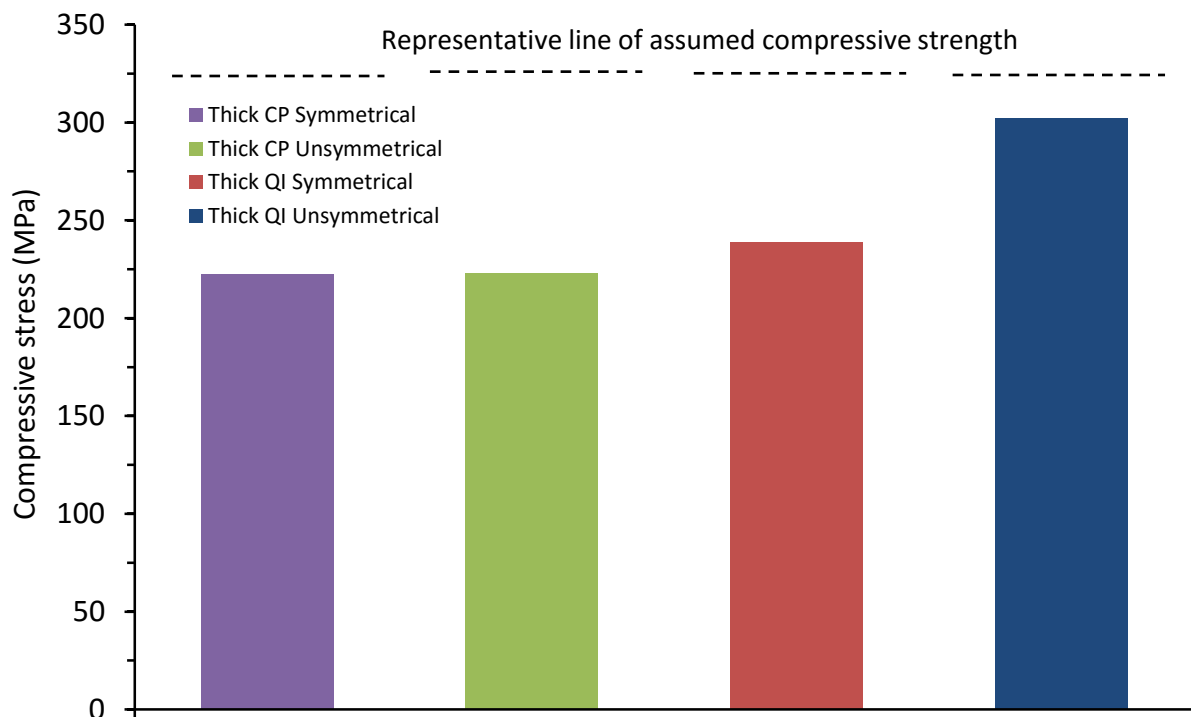


Figure 6.3.4. Average compressive stresses of thick symmetrical and unsymmetrical CP and QI carbon/epoxy control panels with 70kg/m³ core density

In Figure 6.3.5, the effect of lay-up in the thin panels is not as clear as in the thick panels. The thin symmetrical CP and QI panels have approximately the same level of average compressive stress at failure, which is not an expected result. The even level of premature failure in these panel arrangements, as well as in the unsymmetrical CP panels, suggests an additional factor in the skin/core interaction leading to the premature failure of these panels. Conversely, the thin unsymmetrical QI panels experienced the most premature of all failures in the carbon/epoxy sandwich constructions. With the lowest flexural rigidity of all arrangements, the inclusion of asymmetry appeared to overrule the increased in-plane shear properties of the QI lay-up, and caused the earliest concentration of stress in the loaded end of the panel.

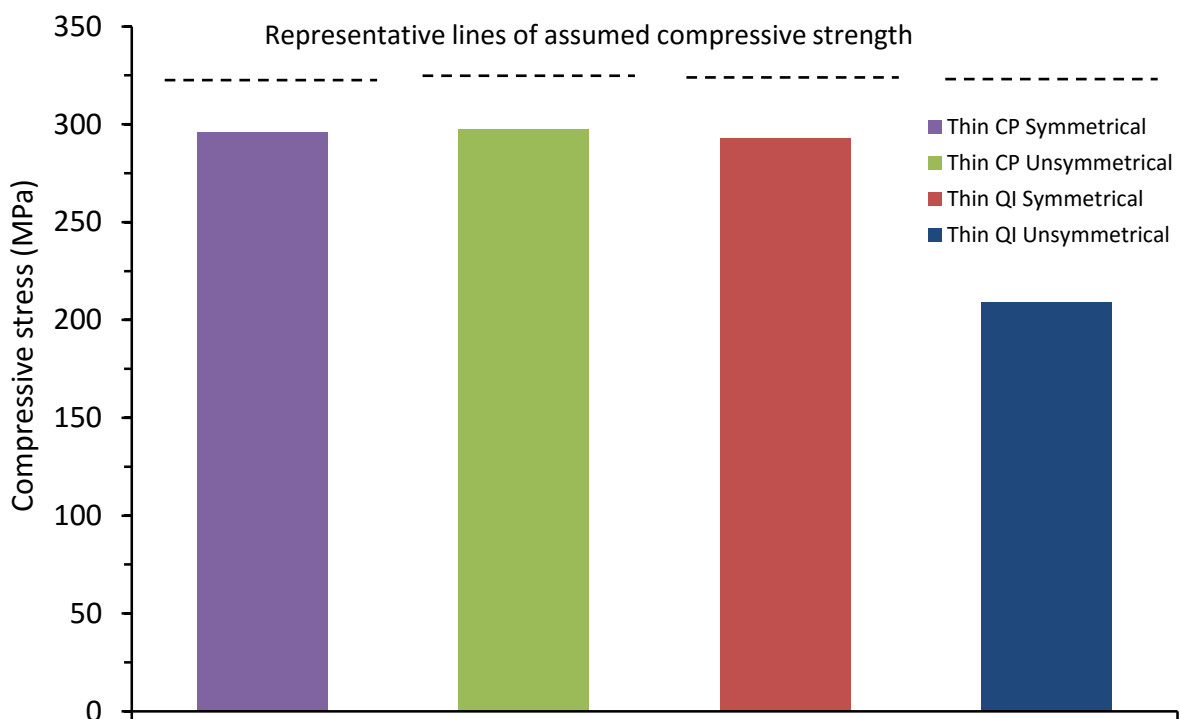


Figure 6.3.5. Average compressive stresses of thin symmetrical and unsymmetrical CP and QI carbon/epoxy control panels with 70kg/m³ core density

The effect of panel symmetry on the far-field mean strain response of thick CP symmetrical and unsymmetrical panels is shown in Figure 6.3.6. The thick unsymmetrical panel shows the higher levels of mean strain at the same level of load in all 0° gauges than in the thick symmetrical panel. The difference in mean strain in the far-field region in the example shown is approximately 25% higher at its maximum, suggesting a fortuitous correlation to the number of plies in the loading direction and the level of compressive strain in the panel. However, the difference in the far-field compressive mean strain in thin symmetrical and unsymmetrical QI panels was less significant, as shown in the example in Figure 6.3.7. The differences observed however appeared to be at different stages in the strain

development, due to the far more premature failure experienced by the thin unsymmetrical QI panel, suggesting that the trends may have been similar. Moreover, this suggests that the thicker panels offered a lower sensitivity to the imbalance in skin thicknesses. The differences in curvature strain responses were insignificant between the thin and thick symmetrical and unsymmetrical panels, as shown in Figure 6.3.8, indicating that neither panel type was developing local buckling in the mid-section region, which is consistent with even compressive loading of both skins.

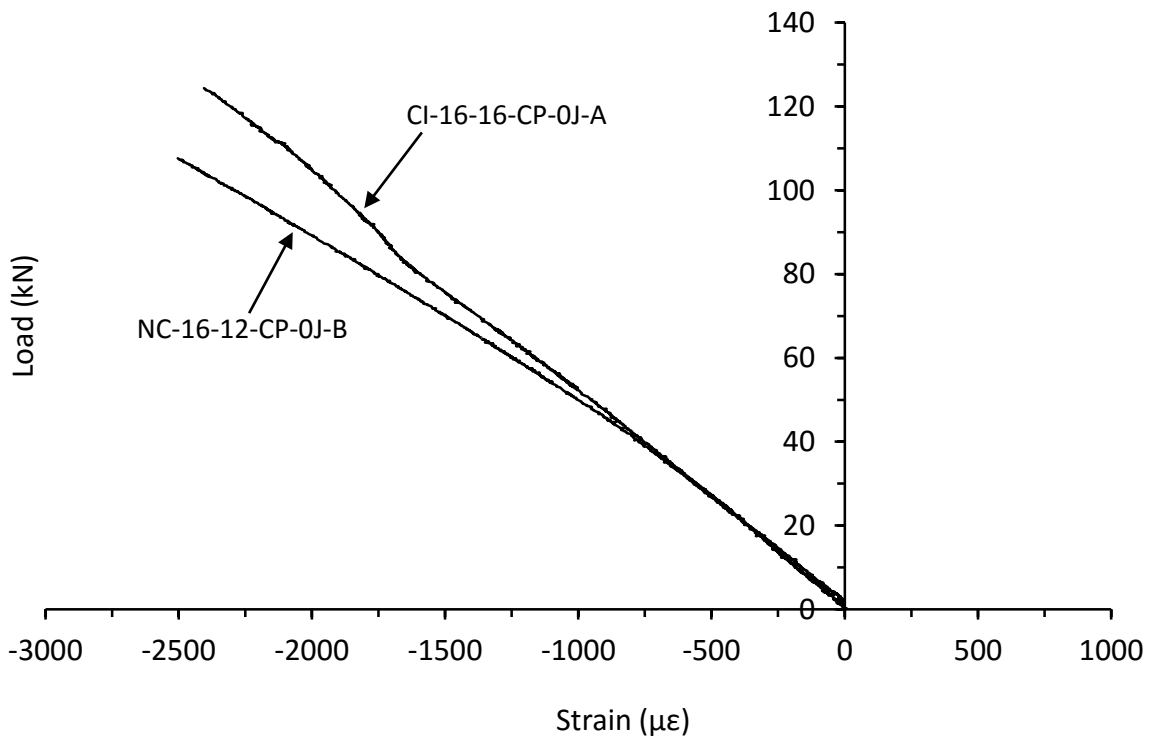


Figure 6.3.6. Mean strain response from the far-field region for thick symmetrical and unsymmetrical CP carbon/epoxy control panels with 70kg/m³ core density

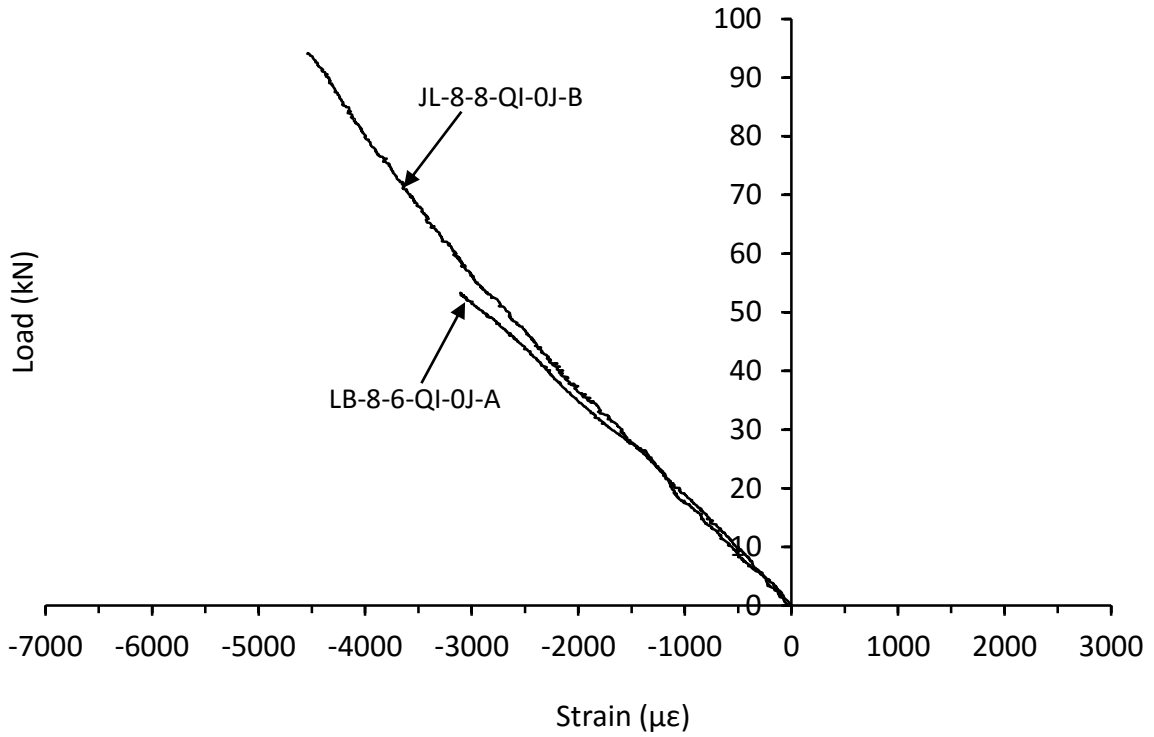


Figure 6.3.7. Mean strain response from the far-field region for thin symmetrical and unsymmetrical QI carbon/epoxy control panels with 70kg/m³ core density

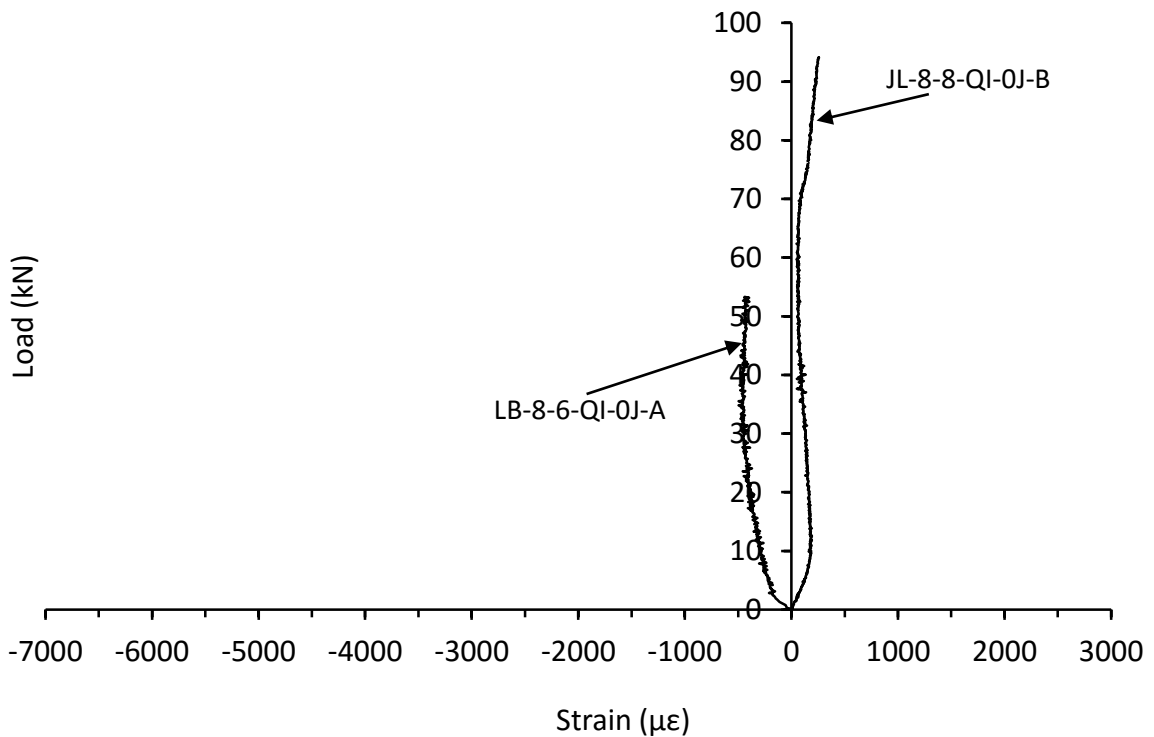


Figure 6.3.8. Curvature strain response from the far-field region for thin symmetrical and unsymmetrical QI carbon/epoxy control panels with 70kg/m³ core density

The effect of the ply lay-up on the compressive strain response saw a difference between the levels of strain across all gauges and directions between thick and thin symmetrical CP and QI arrangements, with typical examples shown in Figure 6.3.9 and Figure 6.3.10. This seems to promote the speculation that the 50% loss of fibres in the loading direction caused an increase in mean strain of approximately 50%. However, the responses from the thin unsymmetrical panels in Figure 6.3.10 show that the effect of panel symmetry is not only coupled with the effect of lay-up but could also be greater than the latter.

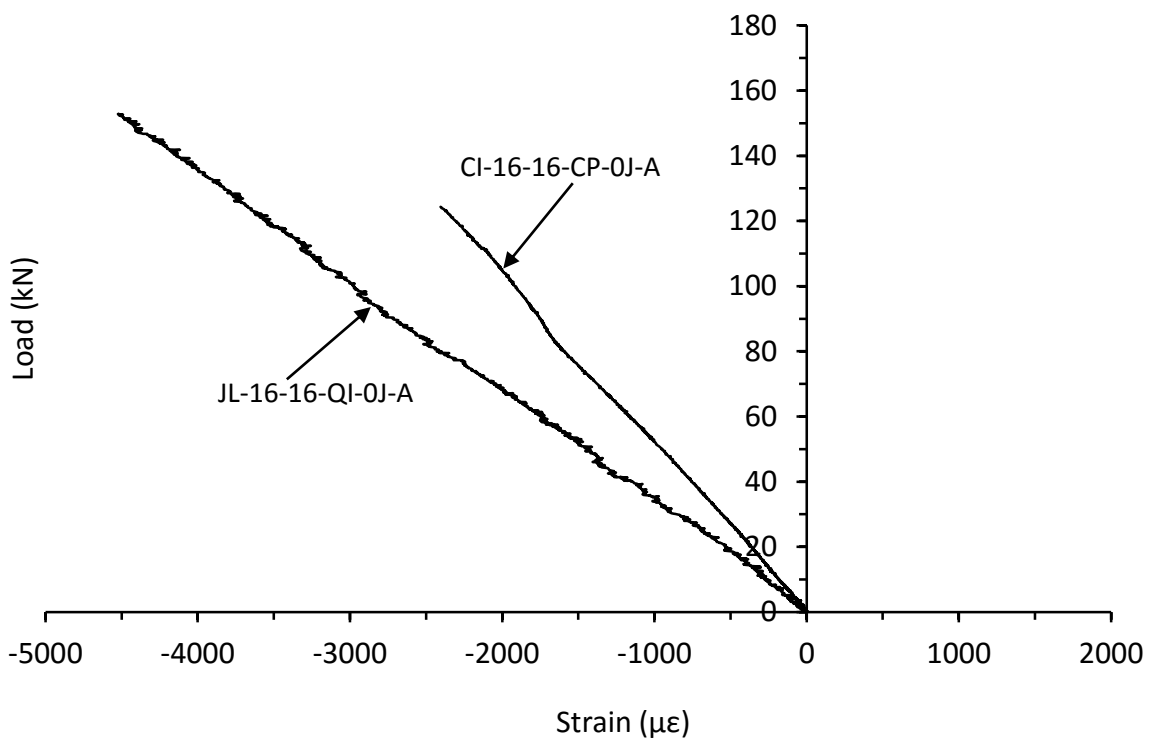


Figure 6.3.9. Mean strain response from the far-field region for thick symmetrical CP and QI carbon/epoxy control panels with 70kg/m³ core density

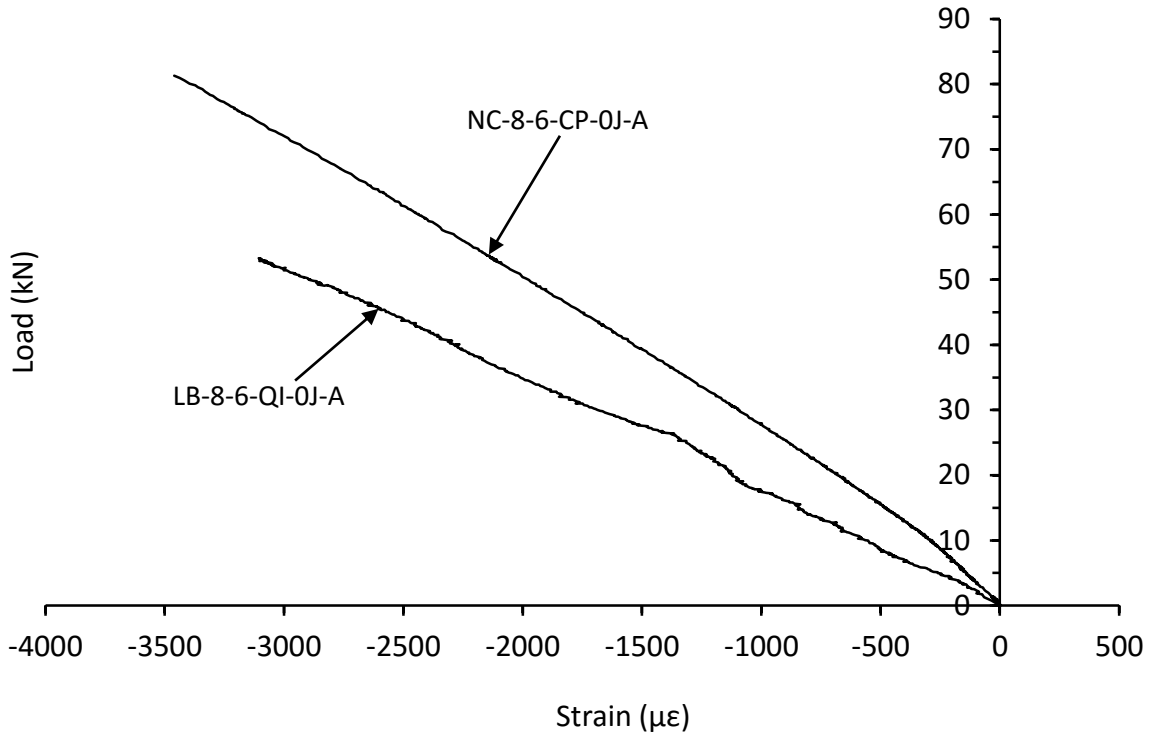


Figure 6.3.10. Mean strain response from the far-field region for thin unsymmetrical CP and QI carbon/epoxy control panels with 70kg/m³ core density

6.3.3. Effect of varying core density

It is expected that the two types of panels with only different core densities should have nearly identical undamaged compressive strengths since the skin constructions are the same, as their failure should be controlled by the compressive strength of the skins [93]. However, the premature nature of the failures precedes the occurrence of in-plane compressive failure in the mid-section and provides contradicting results in the failure stresses. Increasing the core density from 70kg/m³ to 110kg/m³ sees a large increase in the compressive stress at failure in both symmetrical and unsymmetrical panels, by 41% (from 296 MPa to 416 MPa) and 35% (from 298 MPa to 402 MPa) respectively. This could be attributed to the enhanced local stability at the loading ends. However, further increasing the core density from 110kg/m³ to 135kg/m³, the compressive stresses at failure of the symmetrical CP panels falls back to the level of the panels with 70kg/m³, whereas the compressive stresses at failure of the unsymmetrical panels was even 10% less (from 298 MPa to 269 MPa). Once again, this could merely be further indication of the random nature of the premature failures.

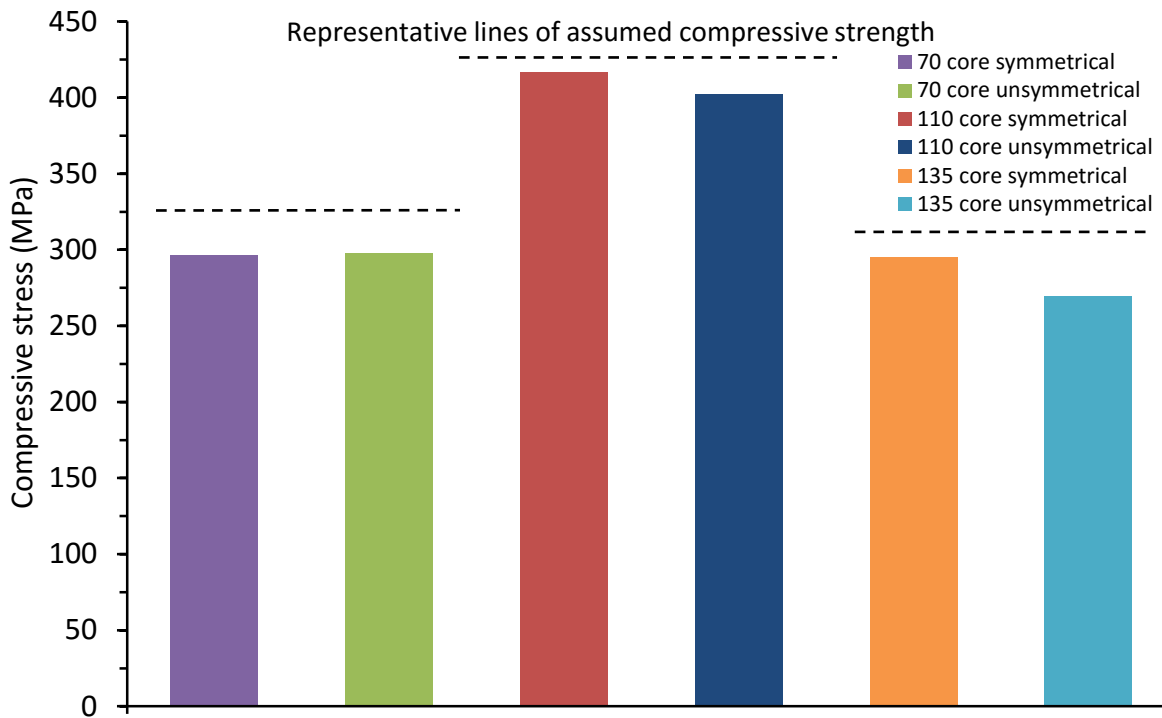


Figure 6.3.11. Average compressive stresses of thin symmetrical and unsymmetrical CP carbon/epoxy panels with 70, 110 and 135kg/m³ core density

The effect of core density on the compressive mean strain responses between the 70kg/m³ and 135kg/m³ core panels, shown in Figure 6.3.12, confirms that during even compressive loading the linear relationship between strain and load is governed entirely by the skins, and that the advantages of using higher density cores may become apparent with the introduction of impact damage. The response of a 110kg/m³ core control panel, also seen in the figure, had a similar gradient, but, the level of strain and load at failure surpasses the other panels. The larger level of strain in the thin carbon/epoxy 110kg/m³ panels indicates there was no early stress concentration in the skins causing premature failure due through shear bands allowing this higher level of strain to develop in the skins, causing the skins to fail instead through end crushing. The near identical linear response between panels with 70 and 135kg/m³ core densities once again indicate the influence of the core density was insignificant in the onset of stress concentrations in the loaded ends of the skins.

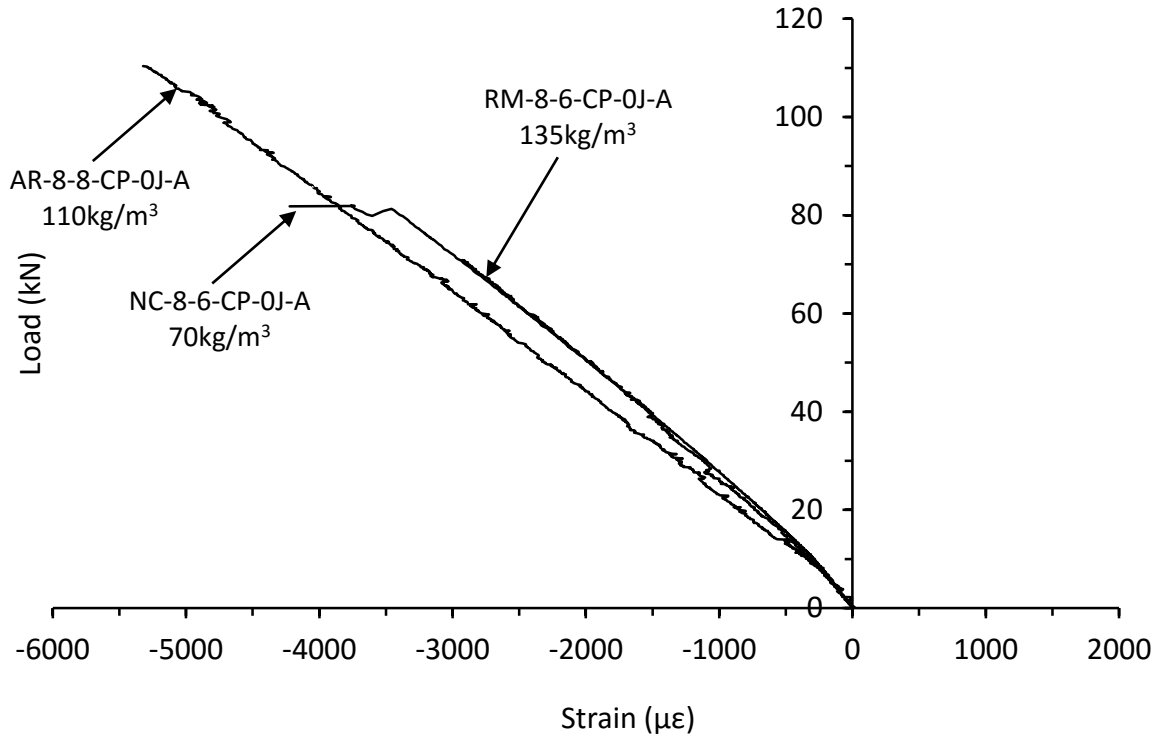


Figure 6.3.12. Mean strain response from the far-field region for thin symmetrical and unsymmetrical CP carbon/epoxy control panels with 70, 110 and 135kg/m³ core density

6.3.4. Effect of varying skin material

The effect of changing the skin material (only for symmetrical panels) sees the carbon/epoxy skinned panels having a greater compressive stress at failure than the glass/epoxy skinned panels by 17% and 34% in both thick and thin CP panels, respectively, which is expected due to the greater compressive properties of the carbon fibres. This could be seen in Figure 6.3.14 where the mean strains of the E-glass/epoxy skinned panel were roughly 2.4 times greater than those of the carbon/epoxy skinned panel.

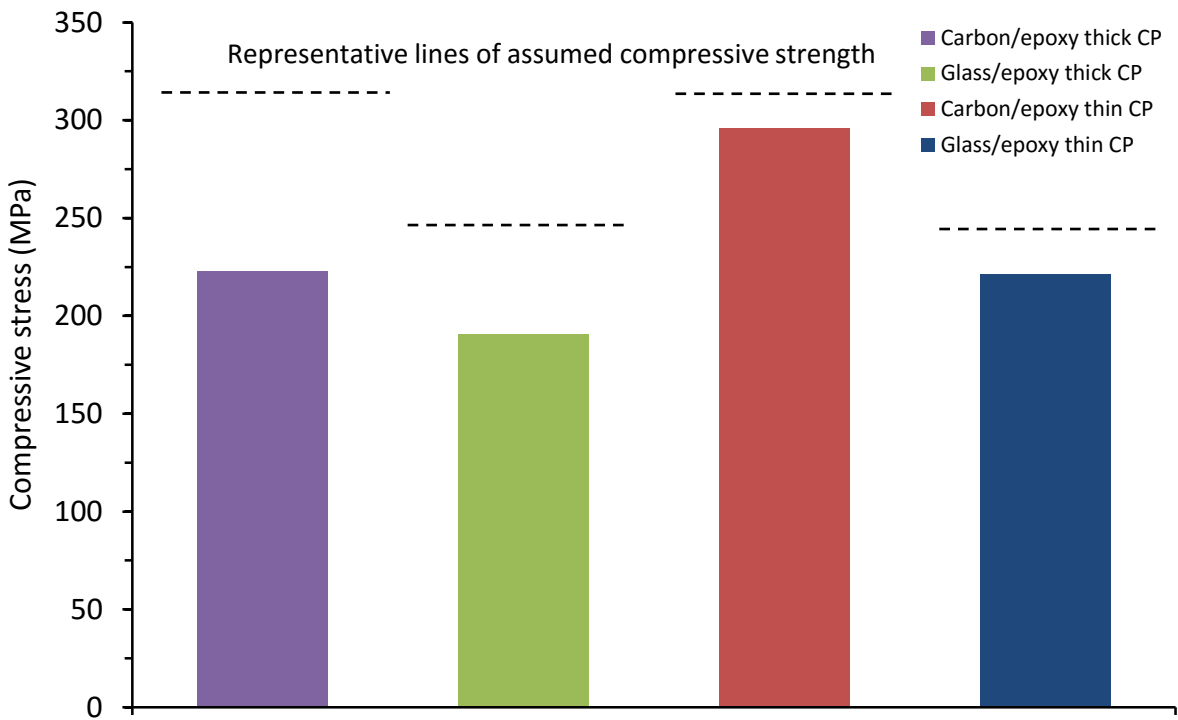


Figure 6.3.13. Average compressive stresses of thin and thick symmetrical CP carbon and E-glass/epoxy panels with 70kg/m³ core density

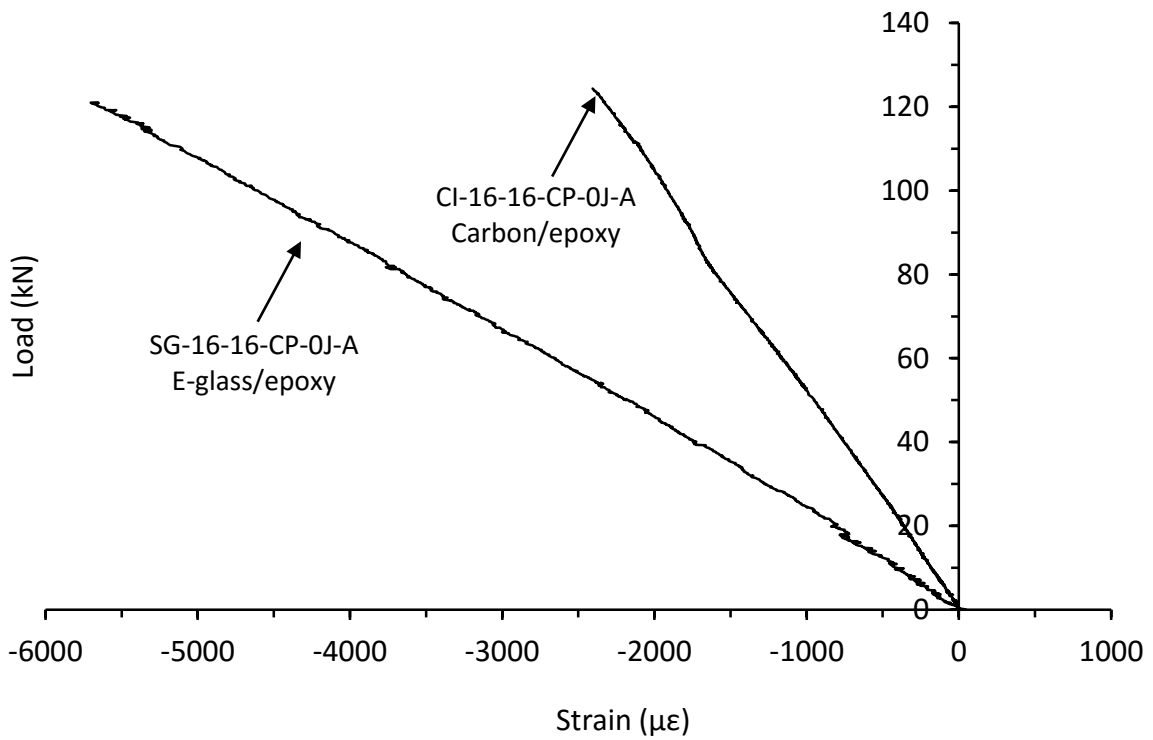


Figure 6.3.14. Mean strain response from the far-field region for thick symmetrical CP carbon and E-glass/epoxy panels with 70kg/m³ core density

6.4. Closing remarks

After carrying out baseline in-plane compressive tests on different arrangements of composite sandwich panels, altering the thickness, lay-up, symmetry and material in the skins, as well as the density of the aluminium core material, all panels were found to fail prematurely near the loaded ends of the panel in the skin, which was expected based on prior testing experience indicating that the width/thickness ratio of the panels were too small to cause in-plane compressive failure in the mid-section region. Some differences in the failure modes allows for some insight into skin/core interactions and load transmission properties of certain arrangements, where thick skinned panels and thin panels with 110kg/m^3 core density invariably succumb to end crushing, after the yielding of the ends of the skins, forcing them outwardly leading to catastrophic failure. All other thin panel arrangements failed through shear bands due to stress concentrations in one of both of the skins near the loaded ends.

These baseline sandwich panels have an average width-to-thickness ratio of around 10 only. A significant longitudinal flexural rigidity and high in-plane shear rigidity provided a local stabilising effect to the skins which caused the load to concentrate at the panel ends and helped prevent local buckling around the mid-section region. The premature nature of the failures means the stresses were not a true indication of the compressive strength of the panels. It was also not possible to predict how early these panels are failing relative to their true compressive strength.

Although the failure mechanisms were not representative of in-plane compressive failure, the compressive responses of the panels were still useful. The dominant features of the panel under compression were found to be large linear increases in the mean strains in the loading direction, indicating that the skins were being evenly loaded, resulting in low levels of curvature strain in the far-field and central gauges. For the majority of the panels, the deformation in the 90° direction was also found to be very limited, however, the Poisson effect was found to exist in panels with the QI lay-up, although the effect is not expected to be significant.

Finally, the effects of altering the panel construction on the in-plane compressive response were found to be varied. The most significant of these were changing the skin thickness, and altering the skin material. Doubling the skin thickness resulted in the compressive mean strain halving at similar loads, and altering the skin material reflected the increased compressive properties of the carbon fibre over the E-glass fibre, where strain in the E-glass panels developed to almost two and a half times the amount observed in the carbon panels. Reducing the number of plies in the back skin and changing the lay-up from cross-ply to quasi-isotropic resulted in an increase in mean strain at similar levels of

load, an effect that was more prominent in the thinner skinned panels. Increasing core density exhibited inconsistent results due likely to the fact that all the panels failed at the end, either through the skins or being crushed at the contact end, however, significant increases in the core density had no effect on the linear strain development under in-plane compression, confirming the linear relationship between strain and load was governed entirely by the skins.

7. DAMAGE TOLERANCE OF IMPACTED AND PRE-CONDITIONED PANELS

This chapter examines the influence of impact damage and other pre-conditions over the residual in-plane compressive performance of various sandwich panels in terms of a number of damage measures. In particular, it looks into how the variation of skin material, core density, skin thickness, skin lay-up and skin symmetry affects the residual compressive performance and damage tolerance of the panels. An attention will be specifically paid to the interaction between skins and core around the mid-section region. The preconditions, shown in Figure 7.1.1, include (a) removed core at the mid-section region, (b) impacted removed core at the mid-section region, (c) drilled hole in a one skin and (d) drilled holes in both skins.

7.1. Damage tolerance measures and test results

The impact damage tolerance of panels relates to the ability of the panel to perform within a certain limit of the baseline compressive value and can be assessed by plotting the variation of CAI strengths, strains, or central out of plane deflections against a damage measure such as IKE, absorbed energy, impact force, damage area, or transverse extent of damage, allowing the generation of damage maps to help identify the initial and critical threshold values of various damage mechanisms within the damage tolerance limits. All of these measures become problematic when applied to sandwich panels. This is because the primary amount of the supplied IKE in each impact event is absorbed by the core, as seen in Sections 4.4-4.6, which is generally believed to make a lesser contribution to the in-plane compressive strength. In addition, the damage areas or transverse damage extents in the impacted skin are different from the core, as shown earlier. Moreover, although it is ultimately necessary to normalise a residual compressive strength with the baseline compressive strength or strain in assessing the damage tolerance, however, using such ratio would be misleading if the baseline values of the panels were associated with premature failure. Under this circumstance, using a comprehensive set of damage measures was desirable, as shown in Tables 7.1.1-7.1.9, such that it is hoped that the damage tolerance of the sandwich panels could be assessed confidently without missing out important features or characteristics. In these tables the values of residual compressive strength were calculated using the cross-sectional area of the two skins, however, not all skin thicknesses were measured before they were bonded to the core and tested. In these cases, nominal values of 1.00mm for 8 ply skins, 0.75mm for 6ply skins were used to calculate the compressive strengths. Comparing these nominal skin thickness values to the average values of skin thicknesses taken from measurements on 8 ply and 6 ply skins before they were bonded, gives numerical differences of 2.4% and 2.8% respectively, therefore, the use of these nominal values can be assumed to be reasonable approximations based on this limited statistical comparison. Furthermore, by extension, utilising

nominal values of 2.0mm and 1.5mm for 16 ply and 12 ply skins respectively was also a reasonably good approximation. These testing results will be discussed in the subsequent sections.

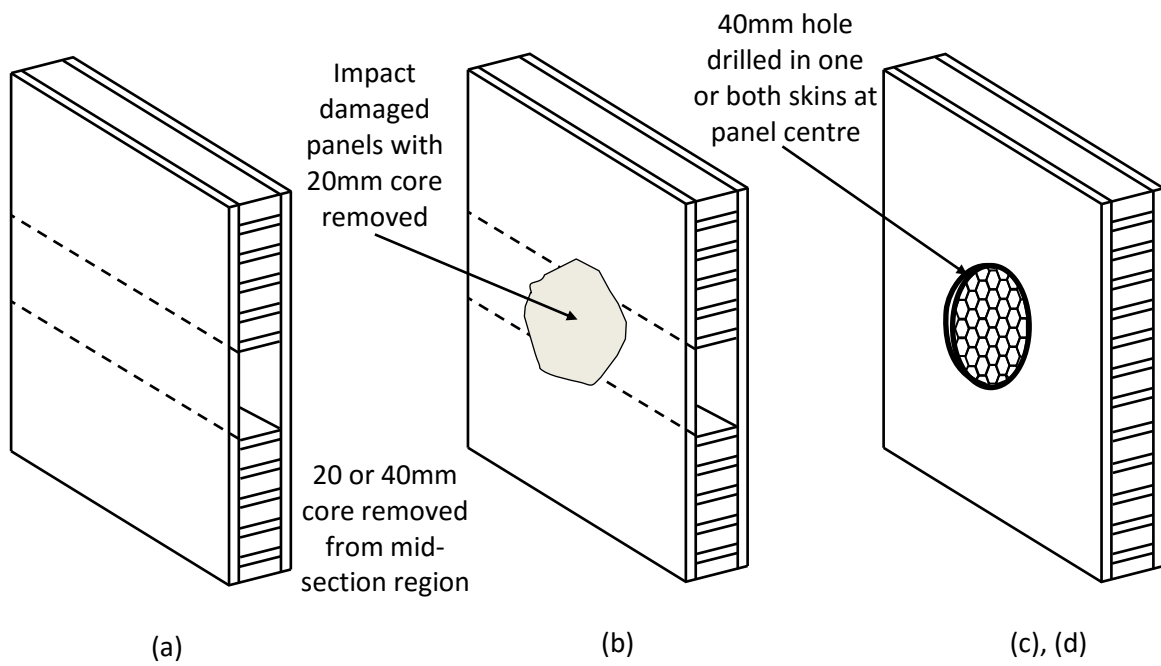


Figure 7.1.1. Sketches showing pre-conditions in panels (a) removed core at the mid-section region, (b) impacted removed core at the mid-section region, (c) drilled hole in a one skin and (d) drilled holes in both skins

Table 7.1.1. Impact-damaged thin symmetrical carbon/epoxy skinned panels

Specimen ID	Two skin thickness (mm)	Panel width (mm)	Core density (kg/m ³)	IKE (J)*	Dent depth (mm)	Delam length (mm)	Core crush length (mm)	Maximum impact force (kN)	Compressive failure load (kN)	Compressive strength (MPa)	Far-field mean compressive strain at failure (μ ϵ)	Compressive failure location
CI-8/8-CP-16J-A	2.0 [†]	149	70	15.45	1.69	59	64	6.17	67.10	226	-	MS
CI-8/8-CP-23J-A	2.0 [†]	148	70	23.35	2.29	66	79	7.64	57.45	194	-2088	MS
HD-8/8-CP-10J	2.0 [†]	147	70	9.57	0.57	-	-	1.53	69.13	235	-2787	MS
HD-8/8-CP-20J	2.0 [†]	148	70	19.78	1.70	-	-	6.20	59.38	201	-2176	MS
JL-8/8-QI-5J-B	2.0 [†]	149	70	4.35	0.96	19	44	3.77	64.48	213	-2800	MS
JL-8/8-QI-10J-B	2.0 [†]	149	70	9.99	1.58	23	64	5.25	60.89	204	-3569	MS
JL-8/8-QI-15J-B	2.0 [†]	149	70	14.70	1.81	28	78	6.46	71.52	241	-4008	MS
JL-8/8-QI-20J-B	2.0 [†]	149	70	20.03	2.36	27	82	7.27	91.53	305	-5386	LE
JL-8/8-QI-25J-B	2.0 [†]	149	70	25.94	2.60	6	98	8.58	92.21	315	-4299	MS
JL-8/8-QI-30J-B	2.0 [†]	149	70	30.35	3.67	27	89	7.58	73.56	246	-4170	MS

*Impact in top skin as panel is manufactured, or thicker skin in unsymmetrical panel

† - Based on nominal skin thickness of 1.00mm for 8 ply skins

Table 7.1.2. Impact-damaged thin unsymmetrical carbon/epoxy skinned panels

Specimen ID	Two skin thickness (mm)	Panel width (mm)	Core density (kg/m ³)	IKE (J)*	Dent depth (mm)	Delam length (mm)	Core crush length (mm)	Maximum impact force (kN)	Compressive failure load (kN)	Compressive strength (MPa)	Far-field mean compressive strain at failure (μ ϵ)	Compressive failure location
NC-8/6-CP-8J	1.75 [†]	148	70	7.37	1.20	-	-	3.63	59.50	232	-2904	MS
NC-8/6-CP-10J	1.75 [†]	148	70	9.92	1.62	-	-	4.09	73.08	285	-2884	MS
NC-8/6-CP-18J	1.75 [†]	148	70	17.11	2.15	-	-	5.63	67.29	263	-2811	FE
NC-8/6-CP-23J-A	1.75 [†]	148	70	23.82	3.06	-	-	6.33	65.07	254	-2349	MS
NC-8/6-CP-23J-B	1.75 [†]	148	70	22.54	2.51	-	-	6.56	69.68	272	-2471	MS
NC-8/6-CP-28J	1.75 [†]	148	70	27.85	4.14	-	-	6.03	55.74	218	-2199	MS
DJ-8/6-CP-5J-A1	1.76	149	70	4.69	1.31	32	43	3.58	60.87	233	-2995	LE
DJ-8/6-CP-5J-A2	1.62	148	70	4.79	1.25	32	43	3.31	44.62	186	-998	LE
DJ-8/6-CP-5J-B2	1.62	148	70	4.80	1.27	32	43	3.39	43.85	183	-1684	LE
DJ-8/6-CP-20J-A	1.65	144	70	20.52	2.60	35	70	6.91	49.50	208	-2255	FE
DJ-8/6-CP-25J-A	1.67	148	70	25.65	2.75	30	81	7.53	54.34	220	-2563	LE
DJ-8/6-CP-30J-A	1.60	146	70	31.06	3.30	28	88	8.20	62.34	267	-2029	MS
HD-8/6-CP-10J	1.75 [†]	147	70	10.01	1.59	-	-	4.86	81.01	310	-3479	MS
HD-8/6-CP-20J	1.75 [†]	147	70	20.25	2.49	-	-	5.92	70.16	268	-2793	MS
LB-8/6-QI-5J	1.75 [†]	148	70	4.50	0.84	-	-	3.00	56.78	222	-3398	MS
LB-8/6-QI-10J-B	1.75 [†]	148	70	9.31	1.33	24	57	4.83	57.58	225	-2230	MS
LB-8/6-QI-15J	1.75 [†]	148	70	14.65	1.68	-	-	5.69	61.00	238	-4093	MS
LB-8/6-QI-20J-B	1.75 [†]	148	70	19.46	2.80	24	83	6.08	42.80	167	-3557	MS
LB-8/6-QI-25J-A	1.75 [†]	148	70	25.18	2.99	27	83	4.84	48.57	190	-2755	MS

*Impact in top skin as panel is manufactured, or thicker skin in unsymmetrical panel

† - Based on nominal skin thickness of 1.00mm for 8 ply skins and 0.75mm for 6 ply skins.

Table 7.1.3. Impact-damaged thick symmetrical carbon/epoxy skinned panels

Specimen ID	Two skin thickness (mm)	Panel width (mm)	Core density (kg/m ³)	IKE (J)*	Dent depth (mm)	Delam length (mm)	Core crush length (mm)	Maximum impact force (kN)	Compressive failure load (kN)	Compressive strength (MPa)	Far-field mean compressive strain at failure (μ ϵ)	Compressive failure location
CI-16/16-CP-15J-A	4.00 [†]	149	70	14.74	0.95	45	64	6.69	102.81	174	-1875	MS
CI-16/16-CP-30J-A	4.00 [†]	148	70	27.27	1.58	60	87	10.16	107.00	183	-	MS
CI-16/16-CP-45J-A	4.00 [†]	148	70	42.09	1.94	67	100	12.78	96.46	165	-1729	MS
CI-16/16-CP-60J-A	4.00 [†]	148	70	59.12	2.28	72	100	15.52	100.22	171	-1858	MS
CI-16/16-QI-15J-A	4.00 [†]	148	70	14.70	1.06	53	80	7.72	106.99	183	-3936	MS
CI-16/16-QI-30J-A	4.00 [†]	148	70	26.94	1.42	63	98	10.95	100.98	172	-1629	MS
JL-16/16-QI-15J-A	4.00 [†]	148	70	14.03	0.86	68	96	7.55	135.28	241	-4016	MS
JL-16/16-QI-30J-B	4.00 [†]	146	70	30.04	0.85	41	75	12.27	90.38	157	-2548	MS
JL-16/16-QI-45J-B	4.00 [†]	149	70	42.95	1.61	84	101	14.21	132.06	226	-3158	MS
JL-16/16-QI-60J-B	4.00 [†]	149	70	59.50	2.80	87	102	13.10	121.07	208	-3079	MS

*Impact in top skin as panel is manufactured, or thicker skin in unsymmetrical panel

† - Based on nominal skin thickness of 2.00mm for 16 ply skins

Table 7.1.4. Impact-damaged thick unsymmetrical carbon/epoxy skinned panels

Specimen ID	Two skin thickness (mm)	Panel width (mm)	Core density (kg/m ³)	IKE (J)*	Dent depth (mm)	Delam length (mm)	Core crush length (mm)	Maximum impact force (kN)	Compressive failure load (kN)	Compressive strength (MPa)	Far-field mean compressive strain at failure (μ ϵ)	Compressive failure location
NC-16/12-CP-20J	3.50 [†]	148	70	20.48	1.53	-	-	7.69	88.88	173	-1725	MS
NC-16/12-CP-30J	3.50 [†]	148	70	28.67	2.03	-	-	9.83	102.59	200	-2502	MS
NC-16/12-CP-35J	3.50 [†]	148	70	34.69	2.21	-	-	11.16	80.47	157	-1653	MS
NC-16/12-CP-45J	3.50 [†]	148	70	42.85	2.30	-	-	12.70	96.50	188	-1912	MS
NC-16/12-CP-60J-A	3.50 [†]	148	70	59.00	3.66	73	84	15.00	88.85	173	-1715	MS
DJ-16/12-CP-15J-A	3.50 [†]	145	70	13.90	0.00	33	77	6.91	97.18	191	-2410	MS
DJ-16/12-CP-30J-A	3.50 [†]	146	70	28.88	2.04	47	94	9.72	72.52	142	-2240	LE
DJ-16/12-CP-54J-A	3.50 [†]	146	70	50.74	3.01	73	100	13.86	78.45	153	3039	MS
DJ-16/12-CP-60J-A	3.50 [†]	148	70	56.89	3.04	65	100	15.27	89.50	172	-2150	LE
LB-16/12-QI-10J	3.50 [†]	148	70	9.46	0.57	-	-	5.53	104.67	204	-2921	MS
LB-16/12-QI-20J	3.50 [†]	148	70	19.73	1.29	-	-	8.14	91.34	178	-2532	MS
LB-16/12-QI-35J-B	3.50 [†]	148	70	35.31	1.97	67	106	11.53	100.93	197	-2861	MS
LB-16/12-QI-45J-B	3.50 [†]	148	70	43.94	2.73	77	103	10.81	89.06	173	-2289	MS
LB-16/12-QI-60J-A	3.50 [†]	148	70	57.86	3.88	73	103	7.75	82.36	160	-2149	MS

*Impact in top skin as panel is manufactured, or thicker skin in unsymmetrical panel

† - Based on nominal skin thickness of 2.00mm for 16 ply skins and 1.50mm for 12 ply skins

Table 7.1.5. Impact-damaged thin symmetrical carbon/epoxy skinned panels with core density of 110 and 135 kg/m³

Specimen ID	Two skin thickness (mm)	Panel width (mm)	Core density (kg/m ³)	IKE (J)*	Dent depth (mm)	Delam length (mm)	Core crush length (mm)	Maximum impact force (kN)	Compressive failure load (kN)	Compressive strength (MPa)	Far-field mean compressive strain at failure (μ ϵ)	Compressive failure location
AR-8/8-CP-10J	1.90	149	110	9.79	0.83	-	-	4.13	76.56	270	-3066	MS
AR-8/8-CP-20J-A	1.90	146	110	19.95	1.53	-	-	6.13	51.61	186	-1696	MS
AR-8/8-CP-20J-B	1.90	147	110	20.08	1.33	-	-	5.42	50.94	182	-1664	MS
AR-8/8-CP-30J-B	1.90	147	110	29.75	1.82	33	45	8.25	52.26	188	-1673	MS
AR-8/8-CP-40J	1.89	148	110	40.22	3.77	-	-	8.09	48.00	172	-	MS
RM-8/8-CP-15J-A	2.00 [†]	148	135	14.43	1.21	35	21	6.73	72.09	246	-2940	MS
RM-8/8-CP-20J-A	2.00 [†]	148	135	19.89	1.11	30	41	7.92	55.38	189	-2107	MS
RM-8/8-CP-40J-A	2.00 [†]	148	135	41.49	1.02	25	47	10.52	45.55	155	-1077	MS
MB-8/8-CP-15J	1.96	149	135	14.93	1.39	-	-	4.42	61.03	210	-2222	MS
MB-8/8-CP-20J	1.96	150	135	20.20	1.60	-	-	5.58	63.16	215	-3258	MS
MB-8/8-CP-25-A	1.97	145	135	25.18	1.25	-	-	7.89	58.19	204	-2910	MS
MB-8/8-CP-35J	1.97	149	135	35.40	3.54	-	-	6.14	58.94	201	-1579	MS
MB-8/8-CP-45J	1.97	147	135	42.20	3.75	-	-	7.95	50.89	176	-1300	MS

*Impact in top skin as panel is manufactured, or thicker skin in unsymmetrical panel

† - Based on nominal skin thickness of 1.00mm for 8 ply skins

Table 7.1.6. Impact-damaged thin unsymmetrical carbon/epoxy skinned panels with core density of 110 and 135 kg/m³

Specimen ID	Two skin thickness (mm)	Panel width (mm)	Core density (kg/m ³)	IKE (J)*	Dent depth (mm)	Delam length (mm)	Core crush length (mm)	Maximum impact force (kN)	Compressive failure load (kN)	Compressive strength (MPa)	Far-field mean compressive strain at failure (μ ϵ)	Compressive failure location
AR-8/6-CP-10J	1.63	145	110	9.46	0.74	-	-	5.14	76.30	323	-3447	MS
AR-8/6-CP-20J-A	1.63	145	110	20.55	1.31	-	-	7.44	44.66	189	-1767	MS
AR-8/6-CP-20J-B	1.63	144	110	20.31	1.48	-	-	5.22	37.05	158	-1166	MS
AR-8/6-CP-30J-B	1.62	146	110	30.64	2.02	40	52.50	7.28	44.57	188	-1223	MS
AR-8/6-CP-40J	1.62	148	110	39.48	4.40	-	-	6.69	34.90	146	-1128	MS
RM-8/6-CP-30J-A	1.75 [†]	149	135	30.28	2.11	44	47	11.88	66.18	257	-2479	MS
RM-8/6-CP-38J-A	1.75 [†]	150	135	35.92	2.72	27	43	9.02	43.18	166	-1831	MS
RM-8/6-CP-45J-A	1.75 [†]	151	135	45.47	0.49	17	39	10.92	37.14	142	-1579	MS
RM-8/6-CP-60J-A	1.75 [†]	152	135	58.10	5.62	41	44.08	9.39	37.44	142	-1007	MS
MB-8/6-CP-20J	1.68	149	135	20.18	1.08	-	-	6.69	53.19	213	-2046	MS
MB-8/6-CP-25J	1.73	149	135	25.65	1.59	-	-	7.56	48.53	189	-1476	MS
MB-8/6-CP-30J-B	1.68	147	135	29.66	2.05	-	-	5.69	58.80	239	-2236	MS
MB-8/6-CP-35J	1.73	147	135	35.33	3.82	-	-	7.83	45.09	177	-2433	MS
MB-8/6-CP-40J	1.72	146	135	38.48	3.81	-	-	8.47	48.77	195	-1869	MS

*Impact in top skin as panel is manufactured, or thicker skin in unsymmetrical panel

† - Based on nominal skin thickness of 1.00mm for 8 ply skins and 0.75mm for 6 ply skins.

Table 7.1.7. Impact-damaged glass/epoxy skinned panels

Specimen ID	Two skin thickness (mm)	Panel width (mm)	Core density (kg/m ³)	IKE (J)*	Dent depth (mm)	Delam length (mm)	Core crush length (mm)	Maximum impact force (kN)	Compressive failure load (kN)	Compressive strength (MPa)	Far-field mean compressive strain at failure (μ ϵ)	Compressive failure location
SG-8/8-CP-5J	2.22	150	70	4.61	0.77	8	39	3.08	82.41	247	-	LE
SG-8/8-CP-8J	2.18	150	70	7.75	0.74	11	45	4.03	79.38	243	-7209	MS
SG-8/8-CP-15J	2.18	150	70	14.53	1.18	9	56	5.39	68.50	210	-5914	LE
SG-8/8-CP-25J-A	2.14	150	70	25.49	2.19	11	68	7.05	57.82	180	-5008	MS
SG-8/8-CP-35J	2.14	150	70	35.19	3.28	18	65	7.88	57.95	181	-4692	MS
SG-16/16-CP-12J	4.28	151	70	11.67	0.73	22	51	5.77	139.18	215	-6779	LE
SG-16/16-CP-18J-A	4.33	152	70	18.14	0.81	29	62	7.11	163.16	248	-7658	MS
SG-16/16-CP-25J	4.28	153	70	24.79	1.32	25	58	8.50	109.81	168	-3972	LE
SG-16/16-CP-35J	4.33	154	70	33.48	1.00	28	80	10.14	121.77	182	-5533	LE
SG-16/16-CP-45J	4.29	155	70	39.34	2.03	27	36	11.63	130.19	196	-5981	MS

*Impact in top skin as panel is manufactured, or thicker skin in unsymmetrical panel

Table 7.1.8. All panels with skin with drilled hole(s)

Specimen ID	Two skin thickness (mm)	Panel width (mm)	Core density (kg/m ³)	Number of skins with holes*	Diameter of holes drilled (mm)	Compressive failure load (kN)	Compressive strength (MPa)	Far-field mean compressive strain at failure (μ ϵ)	Failure location
HD-8/8-CP-1H-A	2.03	147	70	1	40	70.52	236	-2533	MS
HD-8/8-CP-1H-B	2.03	148	70	1	40	70.63	235	-2482	MS
HD-8/8-CP-2H-A	2.02	147	70	2	40	55.18	186	-1115	MS
HD-8/8-CP-2H-B	2.02	148	70	2	40	55.22	185	-1184	MS
HD-8/6-CP-1H-A	1.79	148	70	1	40	78.59	297	-2820	MS
HD-8/6-CP-1H-B	1.79	147	70	1	40	77.41	294	-2857	MS
HD-8/6-CP-2H-A	1.75	147	70	2	40	46.64	181	-958	MS
HD-8/6-CP-2H-B	1.75	147	70	2	40	54.86	213	-1034	MS

*In panels with only one hole drilled, hole is drilled in top/thicker skin

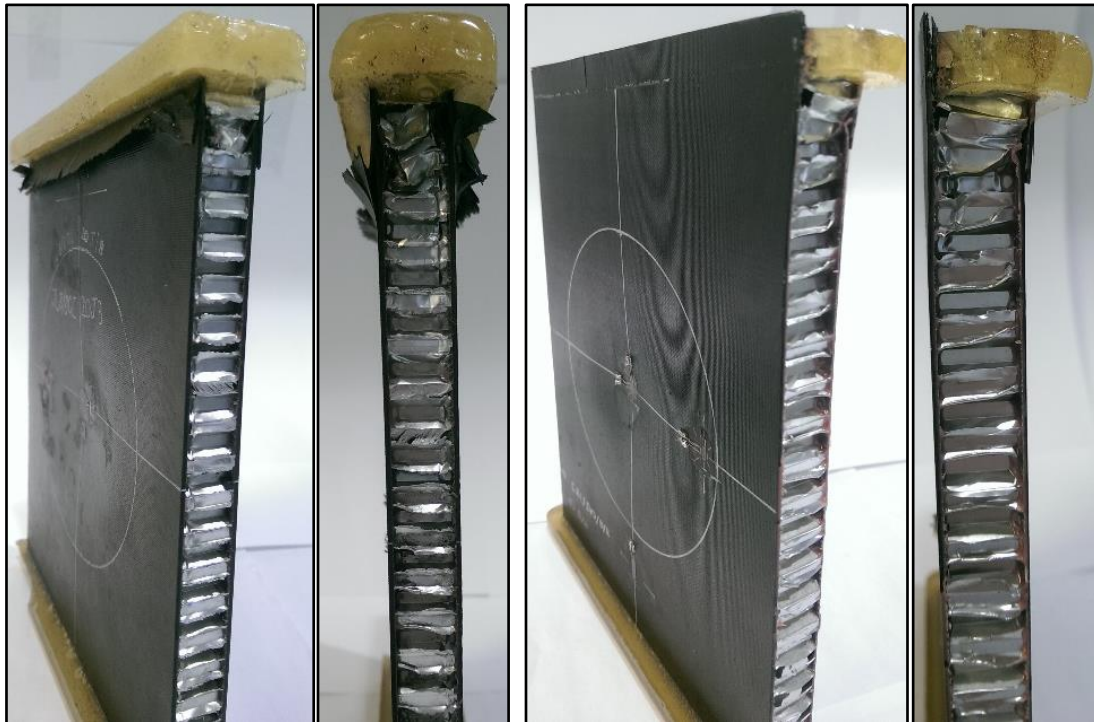
Table 7.1.9. All pre-conditioned panels with core removed

Specimen ID	Two skin thickness (mm)	Panel width (mm)	Core density (kg/m ³)	Longitudinal length of core removed	IKE (J)*	Maximum impact force (kN)	Compressive failure load (kN)	Compressive strength (MPa)	Far-field mean compressive strain at failure (με)	Failure location
CI-8/8-CP-CR-A	2.00 [†]	148	70	40	-	-	35.34	119	-749	MS
CI-8/8-CP-CR-B	2.00 [†]	148	70	40	-	-	33.35	113	-1647	MS
HD-8/8-CP-CR-A	2.00 [†]	147	70	20	-	-	61.33	209	-2650	MS
HD-8/8-CP-CR-B	2.00 [†]	146	70	20	-	-	63.87	219	-2733	MS
HD-8/8-CP-10J-ICR	2.00 [†]	146	70	20	9.54	4.45	56.75	195	-2060	MS
HD-8/8-CP-20J-ICR	2.00 [†]	146	70	20	19.78	6.36	27.28	94	-834	MS
NC-8/6-CP-CR-A	1.75 [†]	148	70	40	-	-	24.48	96	-978	MS
NC-8/6-CP-CR-B	1.75 [†]	148	70	40	-	-	24.75	97	-1006	MS
HD-8/6-CP-CR-A	1.75 [†]	148	70	20	-	-	32.62	123	-1355	MS
HD-8/6-CP-CR-B	1.75 [†]	147	70	20	-	-	31.69	120	-1134	MS
HD-8/6-CP-10J-ICR	1.75 [†]	146	70	20	9.90	4.16	28.63	111	-1095	MS
HD-8/6-CP-20J-ICR	1.75 [†]	146	70	20	19.88	6.61	28.50	110	-892	MS
LB-8/6-QI-CR-A	1.75 [†]	148	70	40	-	-	23.73	93	-1253	MS
LB-8/6-QI-CR-B	1.75 [†]	148	70	40	-	-	23.53	92	-1309	MS
CI-16/16-CP-CR-A	4.00 [†]	148	70	40	-	-	135.93	232	-2710	MS
CI-16/16-CP-CR-B	4.00 [†]	148	70	40	-	-	133.17	227	-2684	MS
NC-16/12-CP-CR-A	3.50 [†]	148	70	40	-	-	97.85	191	-2231	MS
NC-16/12-CP-CR-B	3.50 [†]	148	70	40	-	-	117.98	230	-2873	MS

*Impact in top skin as panel is manufactured, or thicker skin in unsymmetrical panel

† - Based on nominal skin thickness of 1.00mm for 8 ply skins and 0.75mm for 6 ply skins.

Several panels were found to fail in the loaded-end regions, despite the presence of substantial impact damage in the mid-section, as indicated in the last column in Tables 7.1.1-7.1.7 and seen in **Error! eference source not found.** (a) and (b). As the other panels that were impacted with lower IKEs failed in the mid-section under in-plane compression, the outcome of these panel results was attributed to unfortunate experimental errors, which were associated with poor test set-up.



(a) JL-8-8-QI-20J

(b) NC-8-6-CP-18J

Figure 7.1.2. End failures in impacted panels (a) thin symmetrical QI panel impacted at 20J (b) thin unsymmetrical CP panel impacted at 18J

7.2. Dominant mean and curvature strain responses from compression testing

7.2.1. Dominant responses of impact damaged panels

The overwhelming majority of impacted panels under in-plane compression failed in the mid-section region, irrespective of skin lay-up, asymmetry, thickness and core density. This is because the presence of impact damage had two effects on their compressive behaviour, namely, a curvature effect and material damage. Firstly, the local indentation of the panel caused significant local asymmetry with respect to in-plane compressive loading and the shift away from the mid-plane of the sandwich panels could induce local bending moments, which in turn could enhance the tendency of local buckling. Secondly, the impact damage through skin delamination and fibre fracture as well as core crushing directly reduced the in-plane compressive resistance of the sandwich panel, further reducing the local

buckling resistance in the mid-section. The combination of these two effects created sufficient local instability, resulting in the mid-section compressive failure. These characteristics are demonstrated in individual strain and mean and curvature strain responses in Figure 7.2.1 and Figure 7.2.2, in which classic strain reversal in the mid-section region is shown in the former figure just before the ultimate failure. This strain reversal phenomenon was observed in the majority of carbon/epoxy arrangements with different lay-up, symmetry and thickness, as further demonstrated by Figure 7.2.3-Figure 7.2.8. Photos of the panel failures are shown in Section 7.3.1. All mean and curvature strain responses for all tested panels can be found in Appendix C and D.

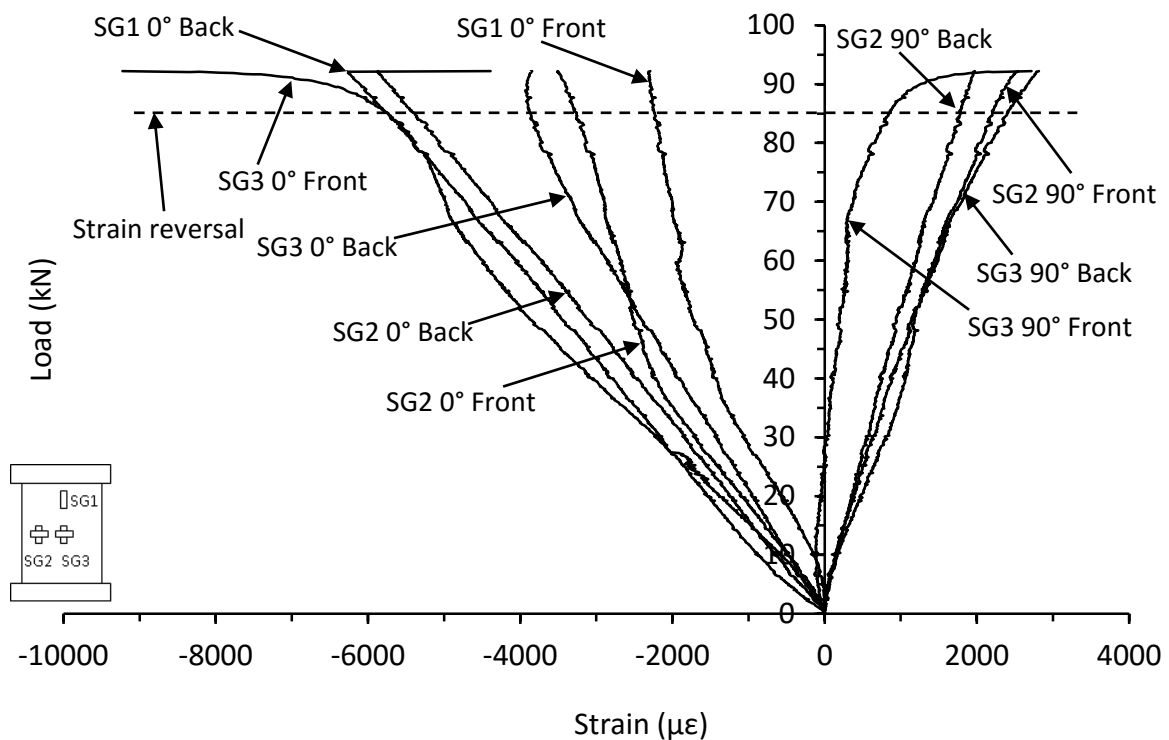


Figure 7.2.1. Strain responses from thin symmetrical QI carbon/epoxy panel with 70kg/m^3 core density impacted at 25J (JL-8-8-QI-25J-B)

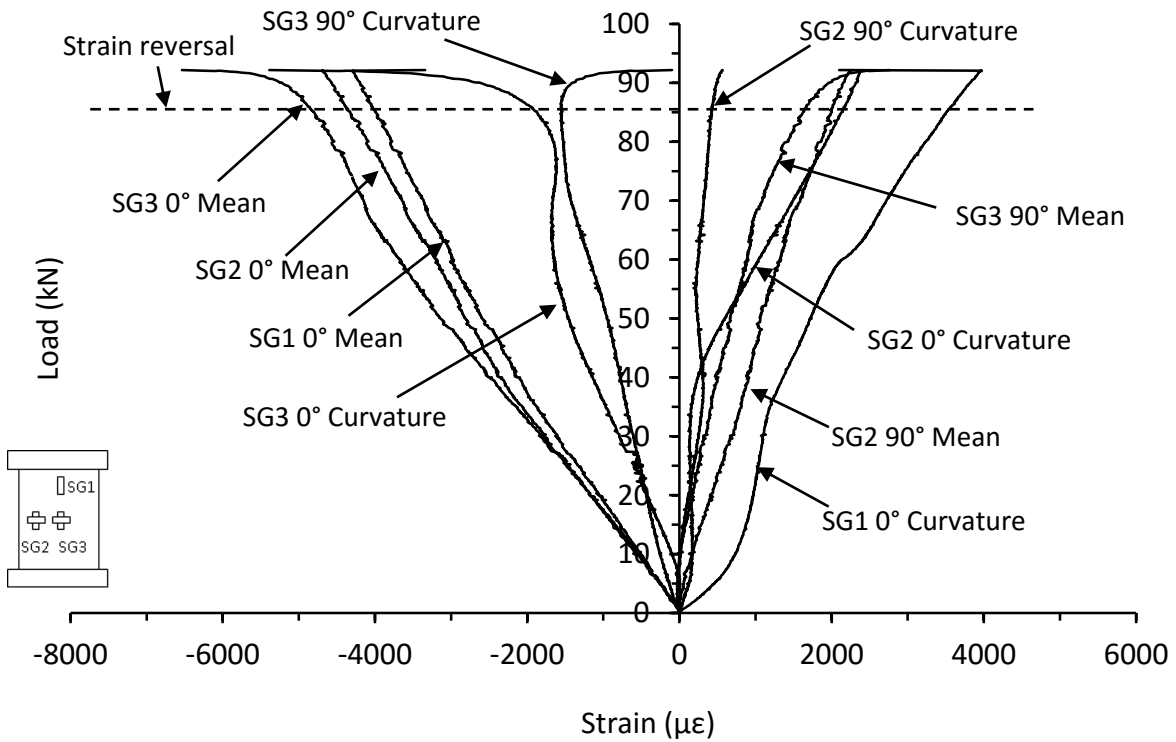


Figure 7.2.2. Mean and curvature strain responses from thin symmetrical QI carbon/epoxy panel with 70kg/m³ core density impacted at 25J (JL-8-8-QI-25J-B)

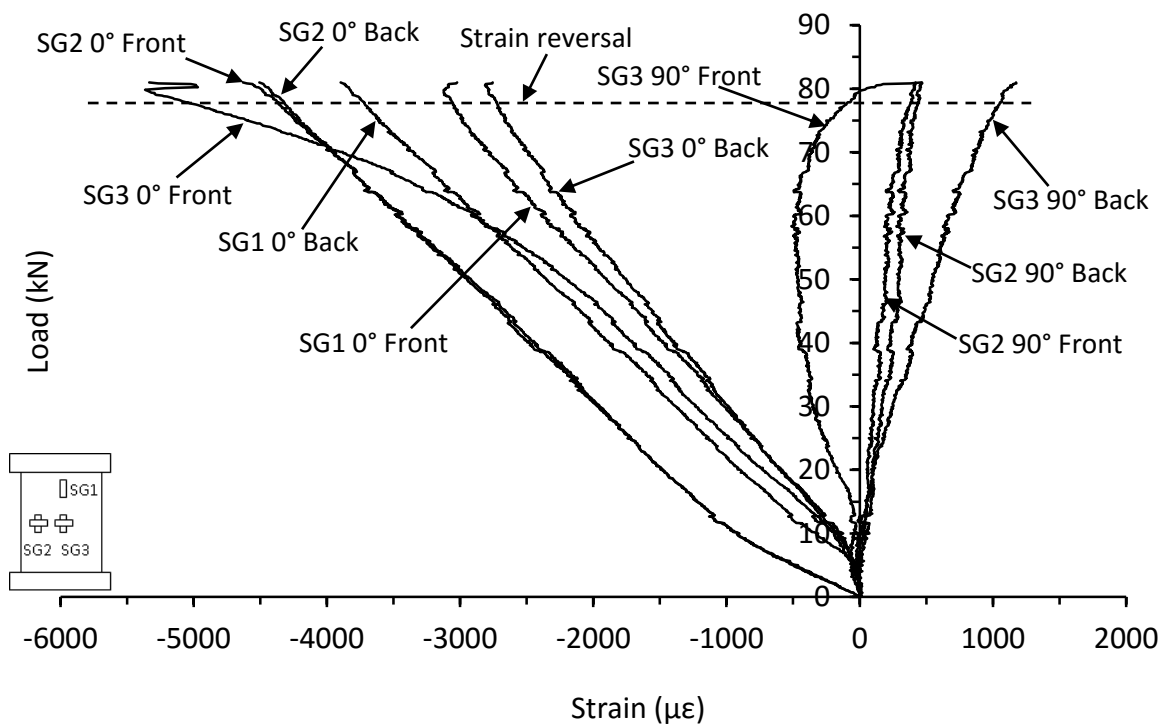


Figure 7.2.3. Strain responses from thin unsymmetrical CP carbon/epoxy panel with 70kg/m³ core density impacted at 10J (HD-8-6-CP-10J)

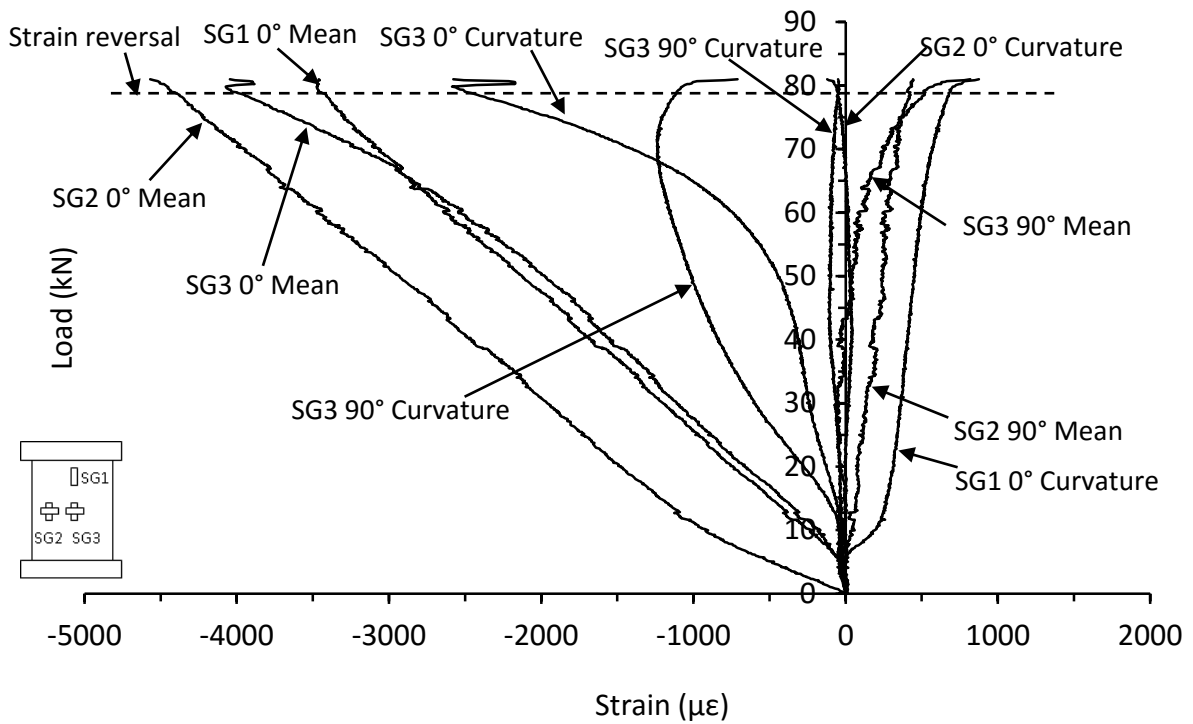


Figure 7.2.4. Mean and curvature strain responses from thin unsymmetrical CP carbon/epoxy panel with 70kg/m³ core density impacted at 10J (HD-8-6-CP-10)

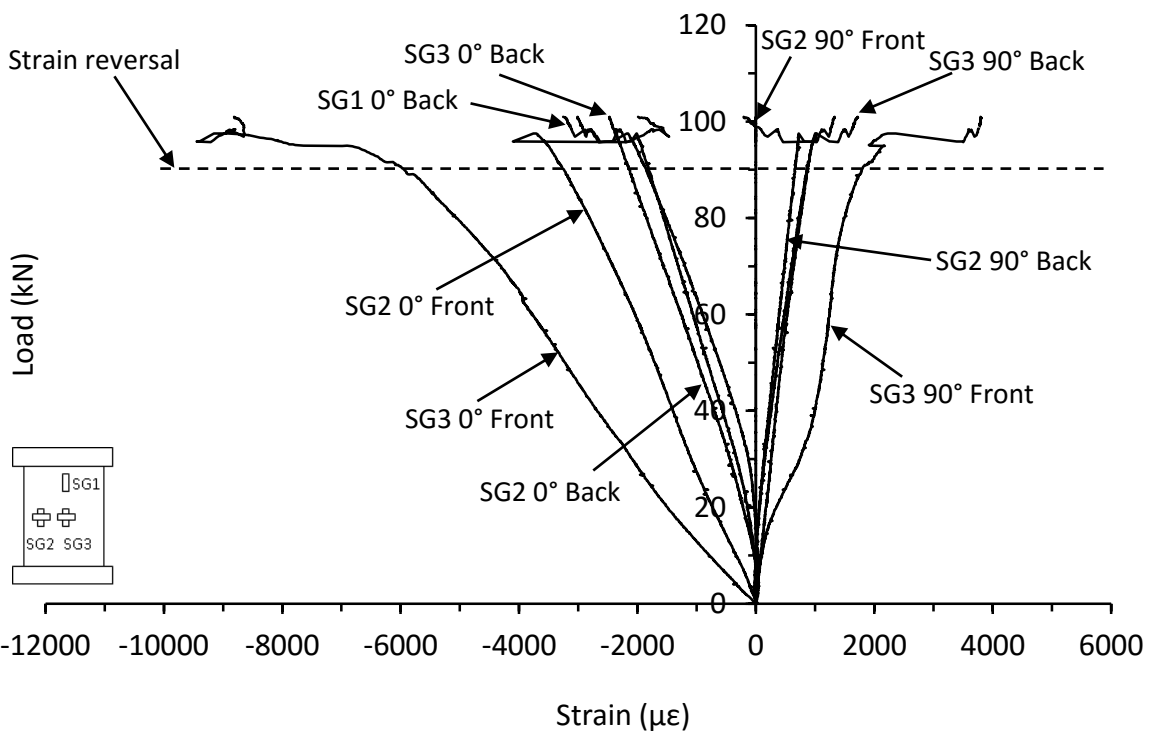


Figure 7.2.5. Strain responses from thick symmetrical QI carbon/epoxy panel with 70kg/m³ core density impacted at 30J (CI-16-16-QI-30J-A)

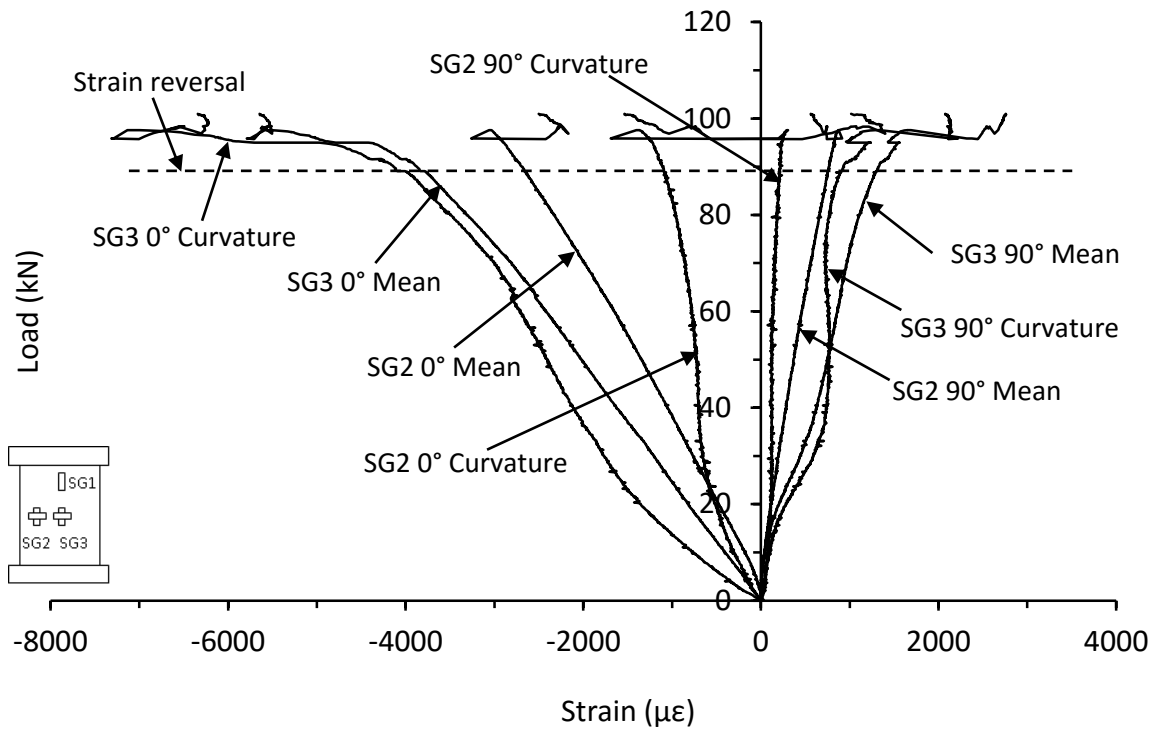


Figure 7.2.6. Mean and curvature strain responses from thick symmetrical QI carbon/epoxy panel with 70kg/m³ core density impacted at 30J (CI-16-16-QI-30J-A)

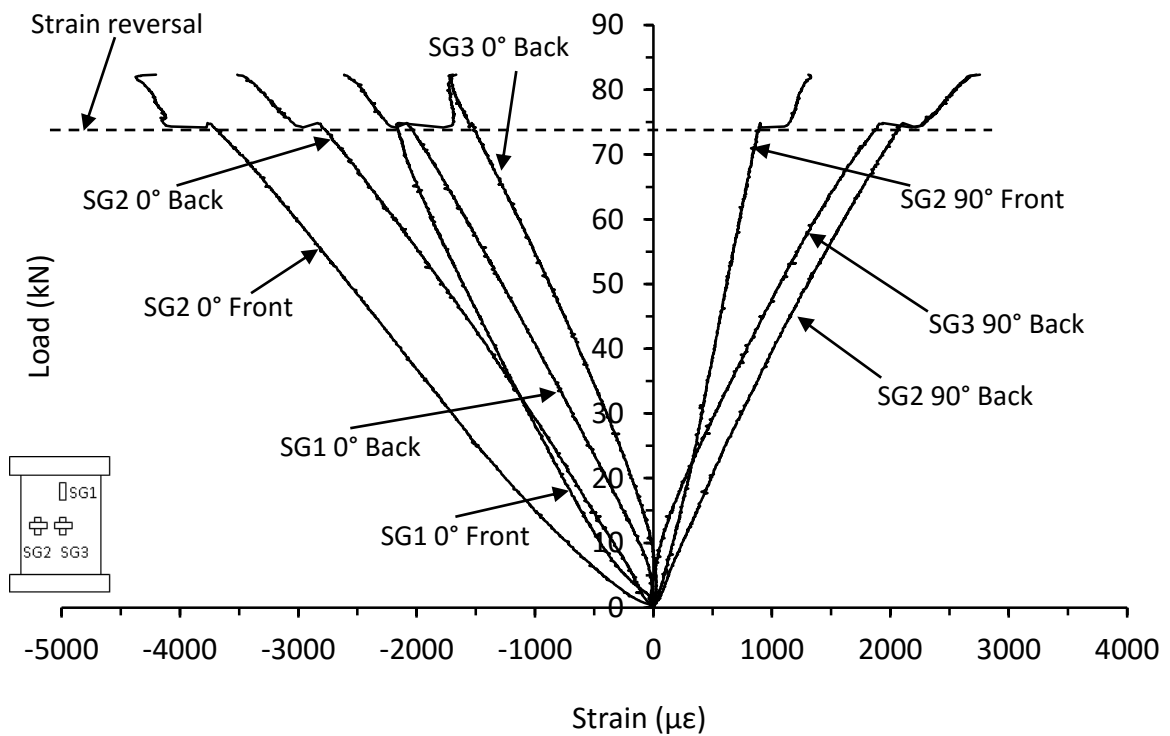


Figure 7.2.7. Strain responses from thick unsymmetrical QI carbon/epoxy panel with 70kg/m³ core density impacted at 60J (LB-16-12-QI-60J-A)

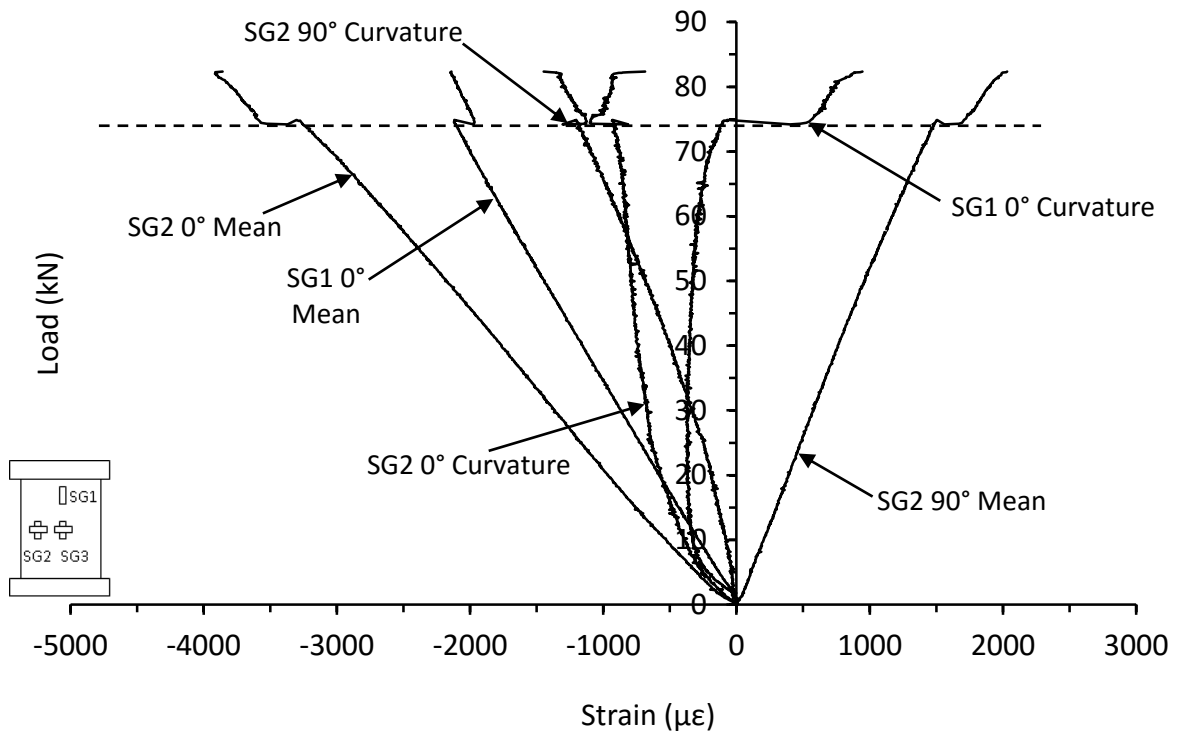


Figure 7.2.8. Mean and curvature strain responses from thick unsymmetrical QI carbon/epoxy panel with 70kg/m³ core density impacted at 60J (LB-16-12-QI-60J-A)

Although slightly subtle, it can be observed from Figure 7.2.2, Figure 7.2.4, Figure 7.2.6, and Figure 7.2.8 that in both 0° (longitudinal) and 90° directions the local buckling in those panels led them to deform into the ‘S’ shape towards the end of their compressive loads, which coincided with their respective mid-section failure locations. This finding is in agreement with the earlier results of symmetrical sandwich panels [89] and also with what was found from impact-damaged monolithic laminate panels [87,88]. In the panels impacted at the relatively low or moderate IKEs, there is a very prolonged propagation phase between the onset of the local buckling and the strain reversal. This suggests that the local residual flexural and TTT shear rigidities were still at a substantial level such that the transverse propagation of delaminations was difficult.

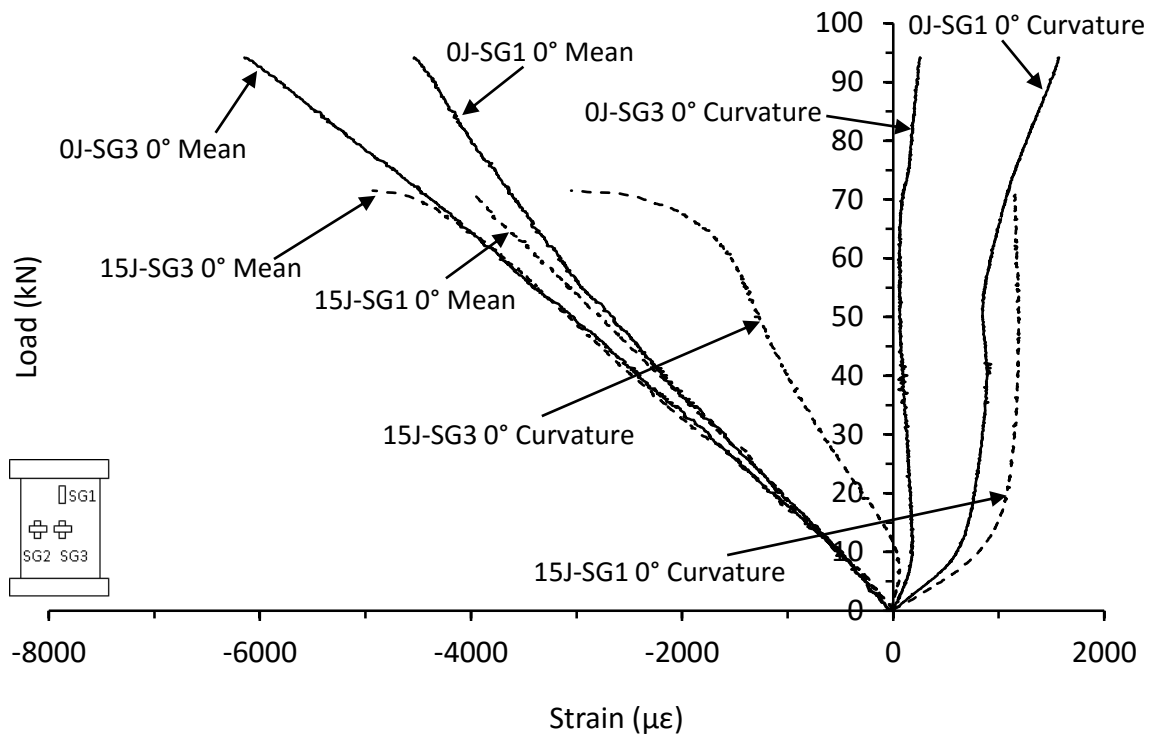


Figure 7.2.9. Mean and curvature strain responses from thin symmetrical QI carbon/epoxy control and 15J impacted panel (JL-8-8-QI-0J-A and JL-8-8-QI-15J-B)

Interestingly, some general characteristics found out of the control panel tests earlier were observed here from the CAI panels. Figure 7.2.9 and Figure 7.2.10 are from symmetrical thin QI and thick CP panels respectively. There was little to no variation between the linear mean strain response and magnitude of strain in the far-field region, which agrees with the observations of McGowan et al [101]. This indicates that the presence of impact damage may not have any effect on the initial global in-plane compressive resistance of the panels with small, up to moderate, impact damage and hence suggests that the local skin and core properties were the controlling factor in CAI strength. The variation in curvature strain from the mid-section region compared to the far-field responses in both figures indicates the increased compliance of the impacted skins over the control panel response, and the relative lack of strain progression in the far-field regions indicates little longitudinal propagation of the impact damage from the mid-section of the panel. The onset of strain reversal can be clearly seen in the impacted panels, whereas the control response remains linear up to the maximum recorded load in the mid-section region.

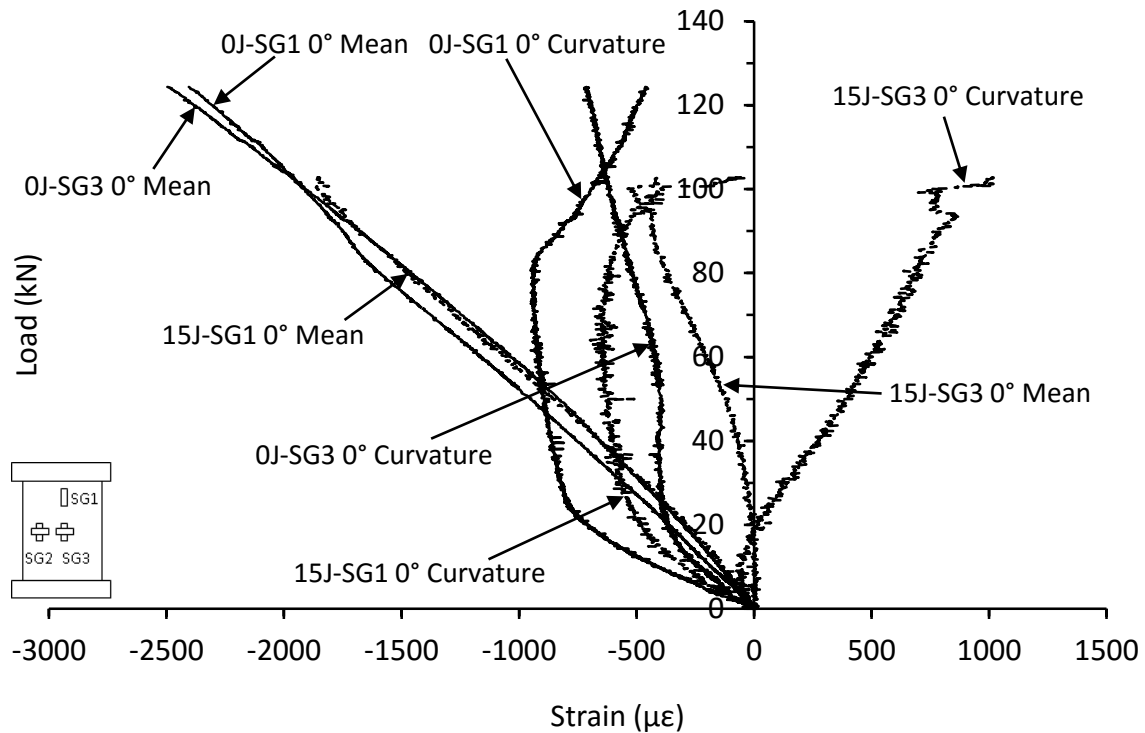


Figure 7.2.10. Mean and curvature strain responses from thick symmetrical CP carbon/epoxy control and 15J impacted panel (CI-16-16-CP-0J-A and CI-16-16-CP-15J-A)

7.2.2. Dominant responses of pre-conditioned panels

The preconditions that were examined over the course of the CAI testing included removal of 20mm of core material from the longitudinal direction across the whole panel width from the mid-section, in thin symmetrical and unsymmetrical CP panels, and 40mm in length in thick and thin symmetrical and unsymmetrical CP and unsymmetrical QI panels. Some thin symmetrical and unsymmetrical CP panels with 20mm of core material unbonded from the skins were impacted at 10J and 20J and then had the unbonded section of core removed after impact testing for in-plane compression testing. Additionally, thin CP symmetrical and unsymmetrical panels with hole(s) in the skins at the centre of the mid-section were tested. In one case, a 40mm diameter hole was drilled in one skin only for one type and in the other case, both skins had a 40mm diameter hole drilled. For some thin skinned core removal panel tests, photographs were taken during the compressive loading at the edge of the mid-section region. Those photographs will be used to help confirm the behaviour of the panel based on the strain responses wherever possible.

Symmetrical thin panels with 40mm long section of core removed

For thin symmetrical CP carbon/epoxy skinned panels with 40mm of core removed in the loading direction, the front and back individual strain responses from a typical test, CI-8-8-CP-CR-A, are shown in Figure 7.2.11, and the mean and curvature strains in the mid-section region are shown in Figure

7.2.12. Photographs of failed pre-conditioned panels are shown in Section 7.3.2. With a 40mm length of core removed from the mid-section, the local flexural and TTT resistance of the panel were significantly reduced, whilst the in-plane resistance of the skins was not affected. This pre-condition represented only damage done to the core in the mid-section region of the sandwich as to isolate the contribution of the core to the structure rather than replicating a particular impact event. Without the support of the core, the skins of the panel around the mid-section would be expected to buckle inwards. As seen in Figure 7.2.11 and Figure 7.2.12, the in-plane compressive resistance started right from the outset from the edge regions (indicated by SG2), as expected, whereas there was only very little compressive deformation at the far field region until about 8kN, where it continued to increase uniformly along with the rest of the central part of the mid-section region. Respective snap shots of photographs taken at 11kN and 18kN are shown in the first two frames in Figure 7.2.13 during this stage, exhibiting an already pronounced local buckling. At the load level of about 22kN, the in-plane compressive deformation at the edge region started escalating, whereas the rest of the mid-section region (SG3), and far-field region (SG1), continued linearly up to failure. This was where the mode switching in the transverse direction started emerging, which was correlated to the third frame of Figure 7.2.13 taken at 23kN. The central region in the longitudinal direction at this time could buckle either outwardly or inwardly, due to the lack of TTT constraint, so that the transition of local buckling mode from a single half wave to two smaller half waves was not clearly picked up (visible only in one skin). A strain reversal was completed at about 30kN, resulting in the failure of the panel along the nodal line of the two waves at about 35kN. The fact that the sandwich panel was able to offer the additional compressive resistance of 5kN after the strain reversal indicates the combined effect of the two individual skins, unlike the impact-damaged monolithic laminates which failed catastrophically almost immediately after the strain reversal [87, 88].

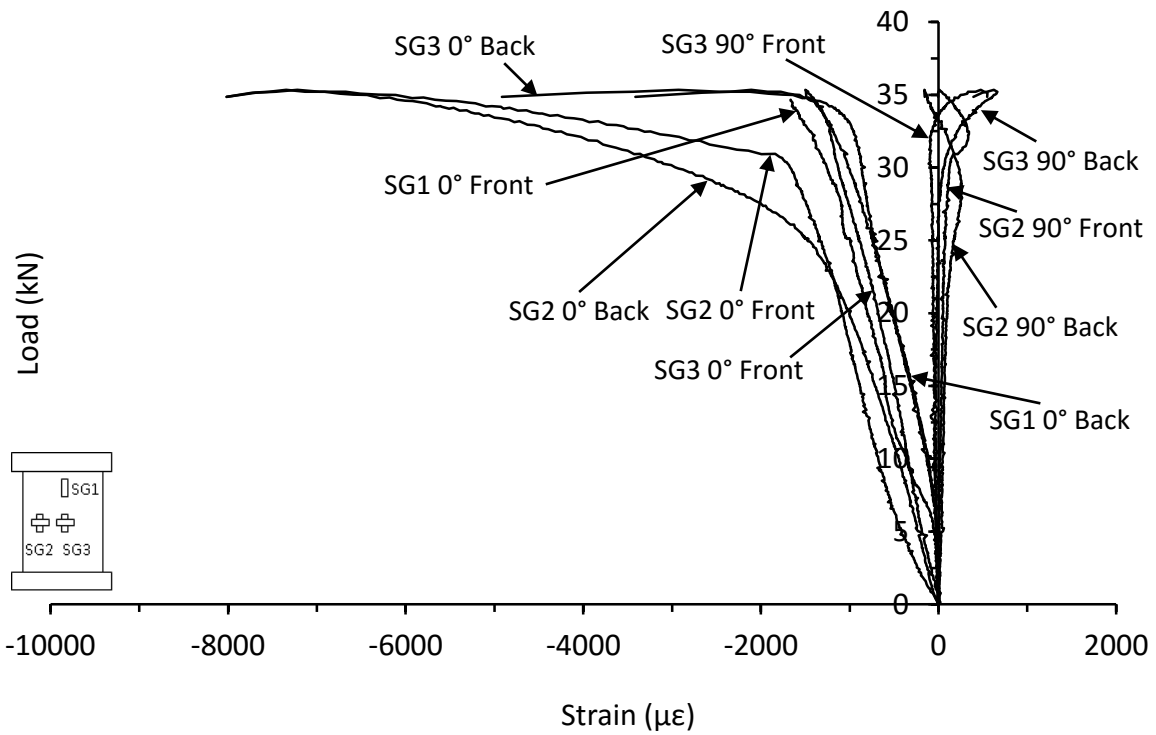


Figure 7.2.11. Strain responses from thin symmetrical CP carbon/epoxy panel with 40mm of core removed (CI-8-8-CP-CR-A)

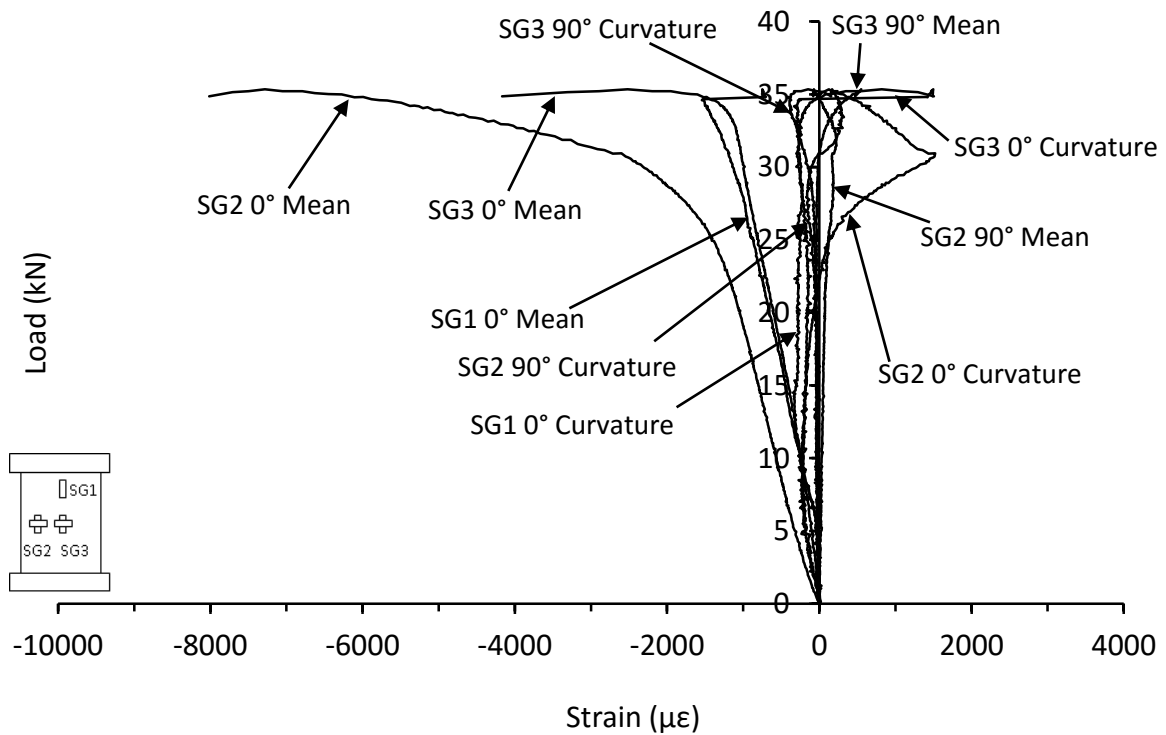


Figure 7.2.12. Mean and curvature strain responses from thin symmetrical CP carbon/epoxy panel with 40mm of core removed (CI-8-8-CP-CR-A)

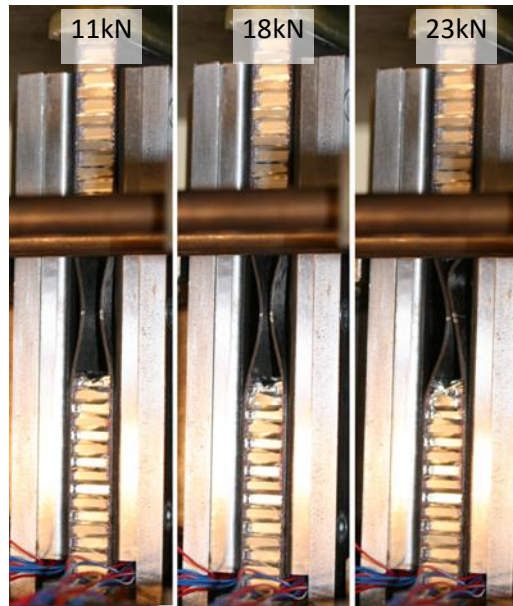


Figure 7.2.13. Progression of local skin buckling in mid-section in thin symmetrical CP carbon/epoxy panel with 40mm core removed (CI-8-8-CP-CR-A)

Unsymmetrical thin panels with 40mm long section of core removed

For unsymmetrical panels with the same section of core removed, an imbalance of two skin thicknesses could induce a bending moment due to a shift of the local neutral plane of the sandwich panel towards the thicker skin, in addition to the reduced local flexural and shear resistances of the sandwich panel. As can be seen through the strain responses of a thin QI panel in Figure 7.2.14 and Figure 7.2.15, the initial strain responses up to about 7kN were actually similar to those of the aforementioned thin symmetrical panel. The local inward buckling started again around 8kN at the edge regions and escalated about 10kN. It took further loading of about 2kN (to about 12kN) to spread to the centre of the mid-section region. All these features are largely attributed to the contributions of the 6 ply skin, as confirmed by the first frame of the photographs in Figure 7.2.16. Again this trend continued until about 20kN (also see the second frame of Figure 7.2.16) when the local buckling mode transition from a single half wave to two half waves occurred in the 8 ply skin but only in the longitudinal direction, as seen in the final frame (taken at 23kN) in Figure 7.2.16. Therefore, the significant effects of the lack of symmetry on these thin core removed panels were that the in-plane compressive behaviour of the unsymmetrical panels were dominated by the response of the thinner 6 ply skin so that their corresponding in-plane compressive strengths were reduced by about 16% (see Table 7.1.9) and that additionally there was no local buckling mode transition in the transverse direction.

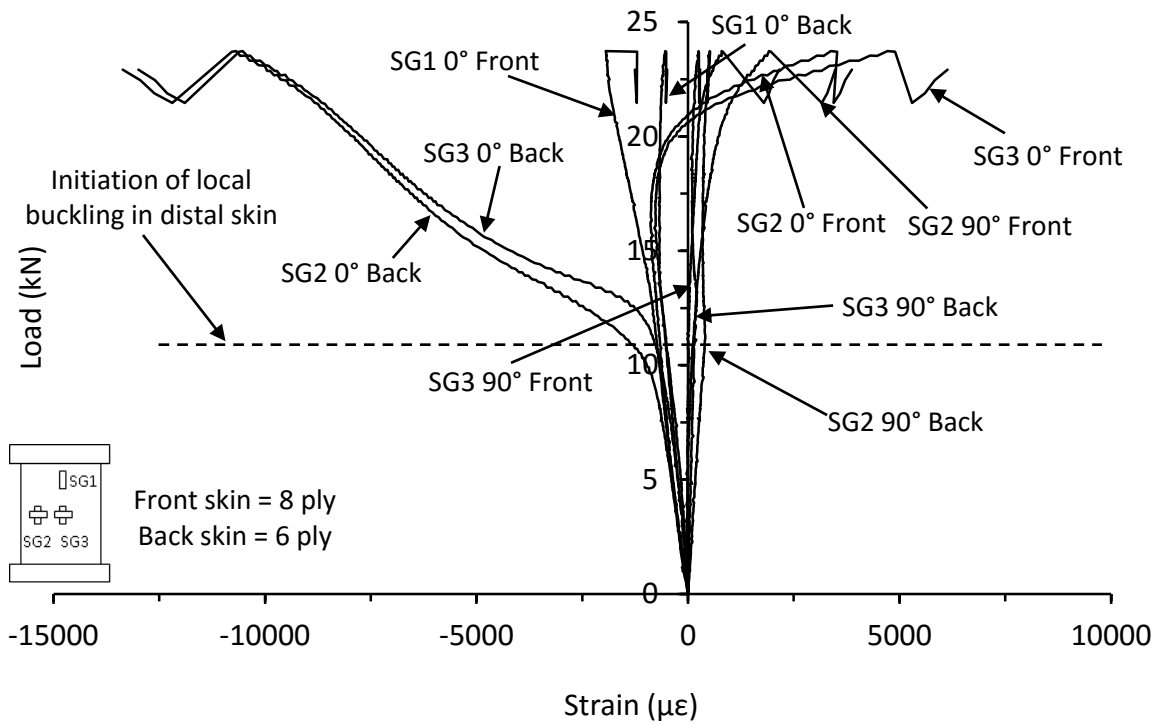


Figure 7.2.14. Strain responses from thin unsymmetrical QI carbon/epoxy panel with 40mm of core removed (LB-8-6-QI-CR-A)

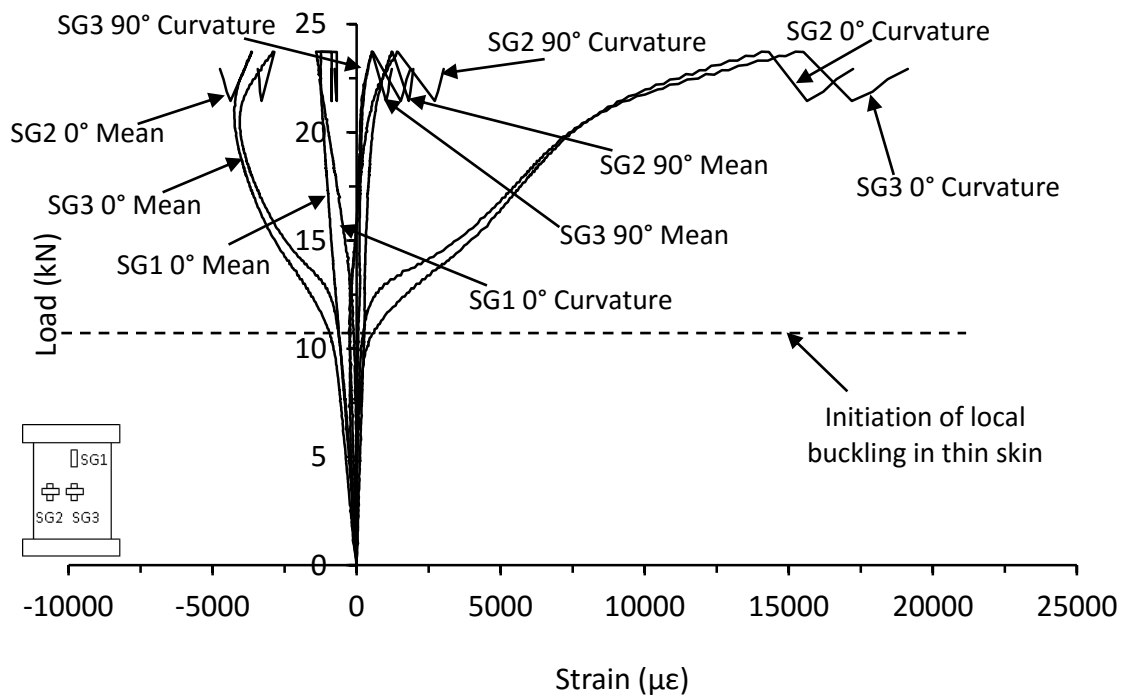


Figure 7.2.15. Mean and curvature strain responses from thin unsymmetrical QI carbon/epoxy panel with 40mm of core removed (LB-8-6-QI-CR-A)

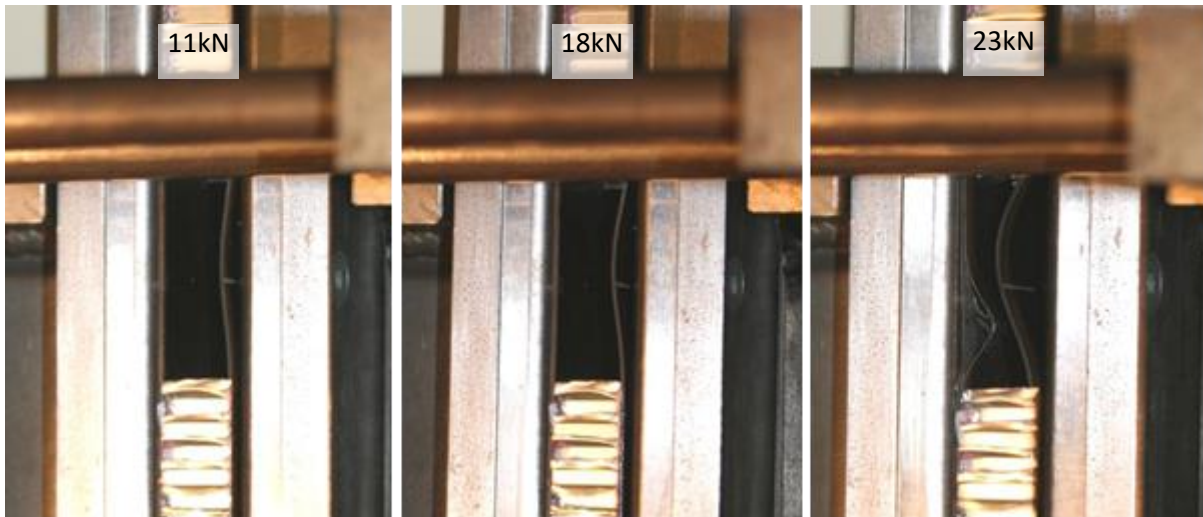


Figure 7.2.16. Progression of local skin buckling in mid-section in thin unsymmetrical QI carbon/epoxy panel with 40mm core removed (LB-8-6-QI-CR-A)

Symmetrical thick panels with 40mm long section of core removed

For thick symmetrical CP carbon/epoxy skinned panels with 40mm of core removed, the front and back individual strain responses of a typical test, CI-16-16-CP-CR-A, are shown in Figure 7.2.17 and the mean and curvature strain responses are shown in Figure 7.2.18, which again were both representative of the other panel tested in this arrangement. Once again, due to the lack of TTT support, the inward local buckling of the skins was observed to start at about 41kN and complete at about 121kN, with the local buckling model transition from a single half wave to two half waves in both directions resulting in the failure of the panel along the nodal line of the two waves. As doubling the skin thickness significantly increased the flexural resistance in the mid-section in addition to the in-plane shear resistance, the local buckling resistance increased. This delayed the onset of the local buckling from the edge of the panel to approximately 88% of the final failure load, compared to approximately 63% in the symmetrical thin panels with 40mm of core removed.

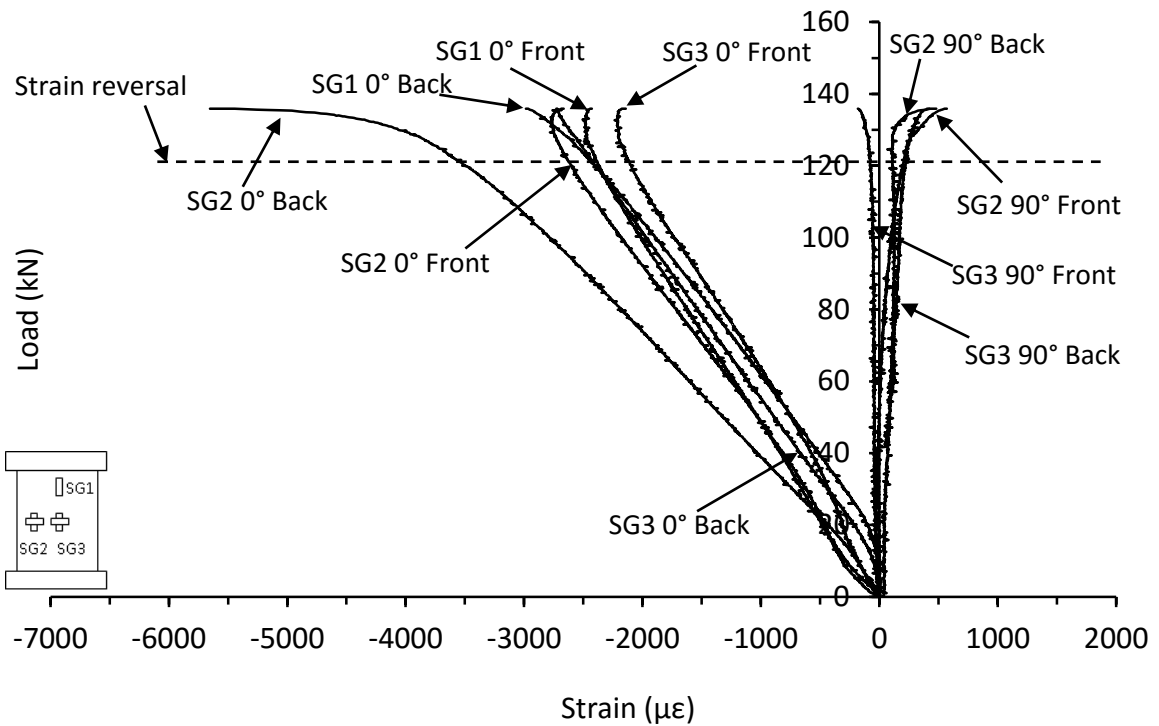


Figure 7.2.17. Strain responses from thick symmetrical CP carbon/epoxy panel with 40mm of core removed (CI-16-16-CP-CR-A)

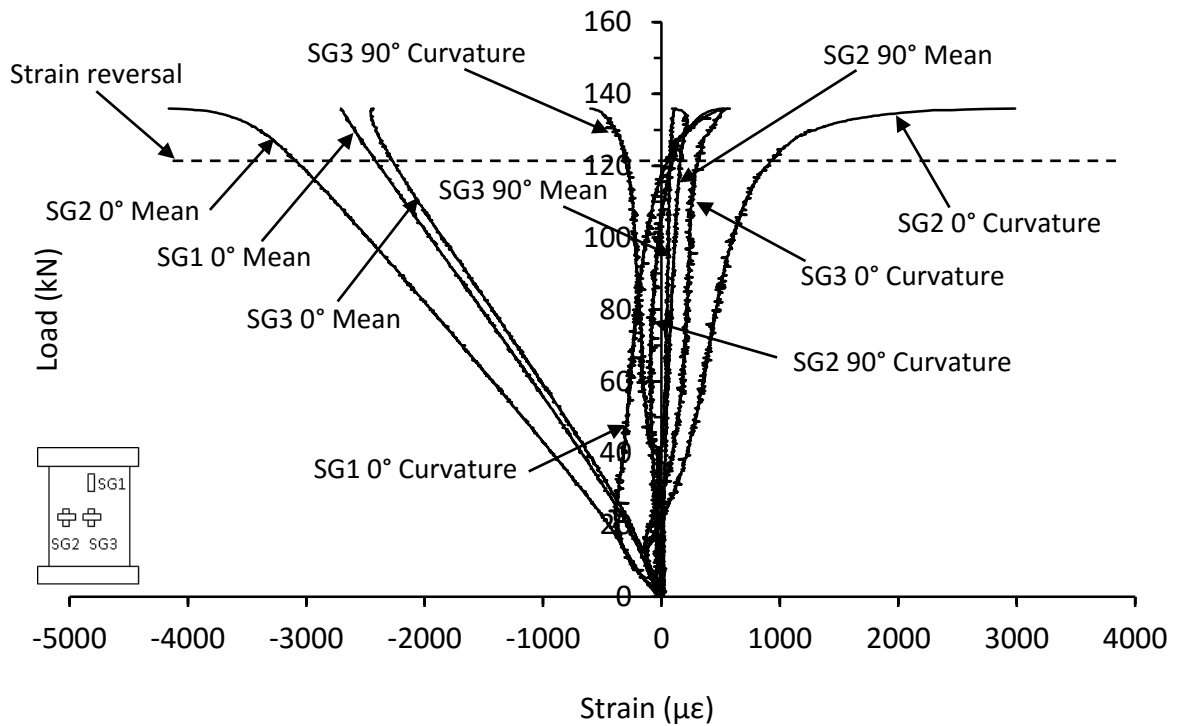


Figure 7.2.18. Mean and curvature strain responses from thick symmetrical CP carbon/epoxy panel with 40mm of core removed (CI-16-16-CP-CR-A)

Unsymmetrical thick panels with 40mm long section of core removed

For thick unsymmetrical CP carbon/epoxy skinned panels with 40mm of core removed, the front and back individual strain responses from a typical test, NC-16-12-CP-CR-A, are shown in in Figure 7.2.19 and mean and curvature strain responses are shown in Figure 7.2.20. Interestingly, the characteristics of these strain responses were much closer to those of the thick symmetrical panels. The local inward buckling started at about 70kN, compared to 121kN in the thick symmetrical panels and completed at about 81kN with the strain reversals in both directions. This suggests that with the sufficient thickness of the skins the same degree of the ply imbalance had a much smaller effect on their in-plane compressive behaviour so much so that their average in-plane compressive strength was similar to that of the symmetrical thick panels.

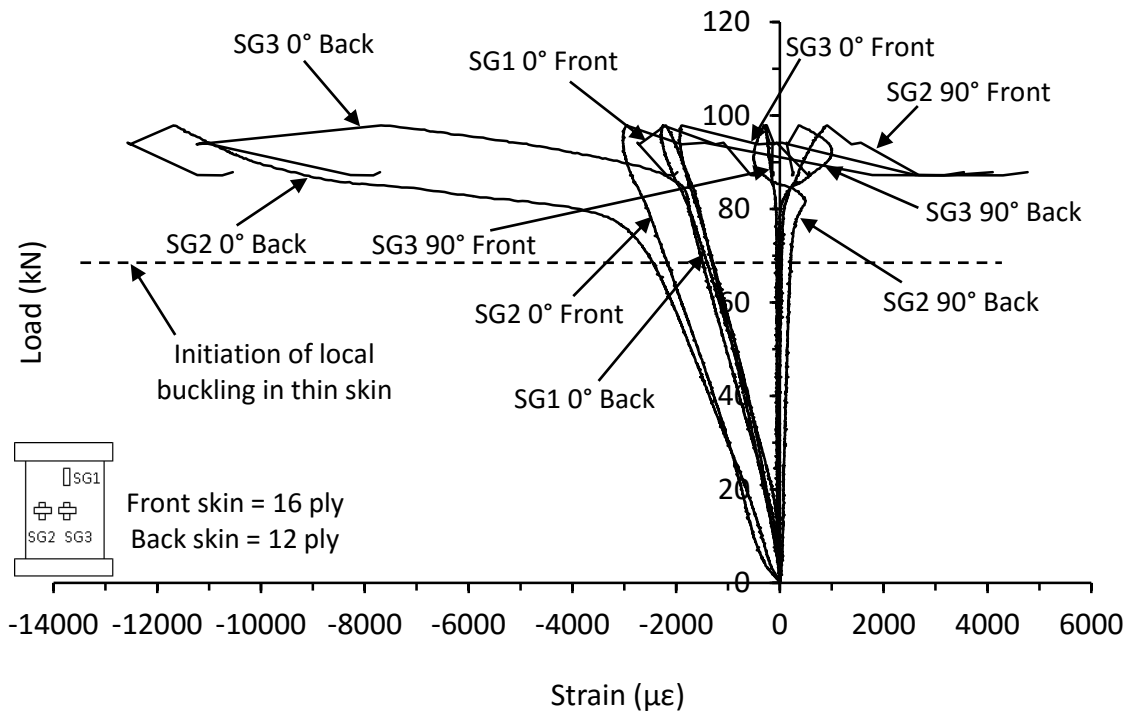


Figure 7.2.19. Strain responses from thick unsymmetrical CP carbon/epoxy panel with 40mm of core removed (NC-16-12-CP-CR-A)

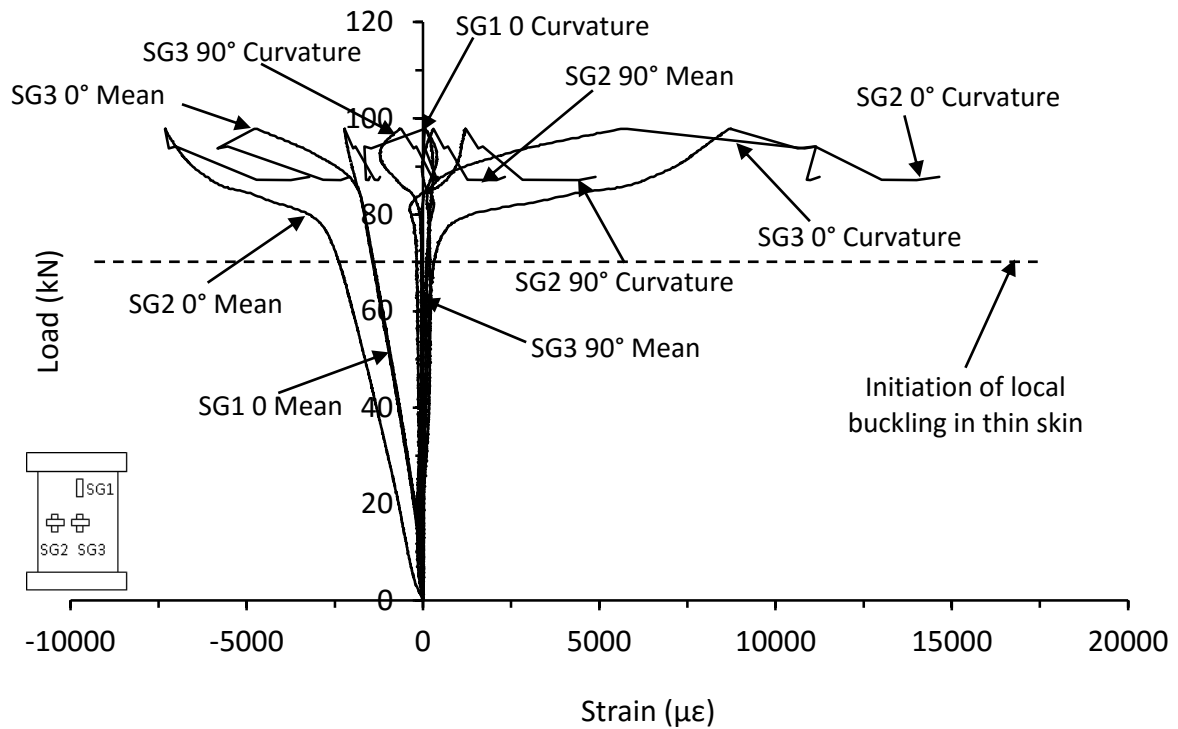


Figure 7.2.20. Mean and curvature strain responses from thick unsymmetrical CP carbon/epoxy panel with 40mm of core removed (NC-16-12-CP-CR-A)

Symmetrical panels with 20mm long section of core removed

Having examined the results of the 40mm core removed panels, it became clear that the 40mm section was overwhelming, especially to the thin skinned panels. Moreover, the results of the thick 40mm core removed panels did not show anything fundamentally new compared to the thin ones. Hence, further testing was performed only in thin panels with only a 20mm length of core removed. Typical individual front and back skin and mean and curvature strain responses for a symmetrical thin skinned CP panel, HD-8-8-CP-CR-A, are shown in Figure 7.2.21 and Figure 7.2.22. The onset of local buckling can be seen to occur from around 42kN, almost double the 22kN of the symmetrical thin panel with 40mm core removed and the strain reversals at about 54kN, which was again significantly greater than 34kN. The strain reversal in the transverse direction was much smaller and subtler with the SG2 90° Curvature and SG3 90° Curvature ending the opposite side at the catastrophic failure load.

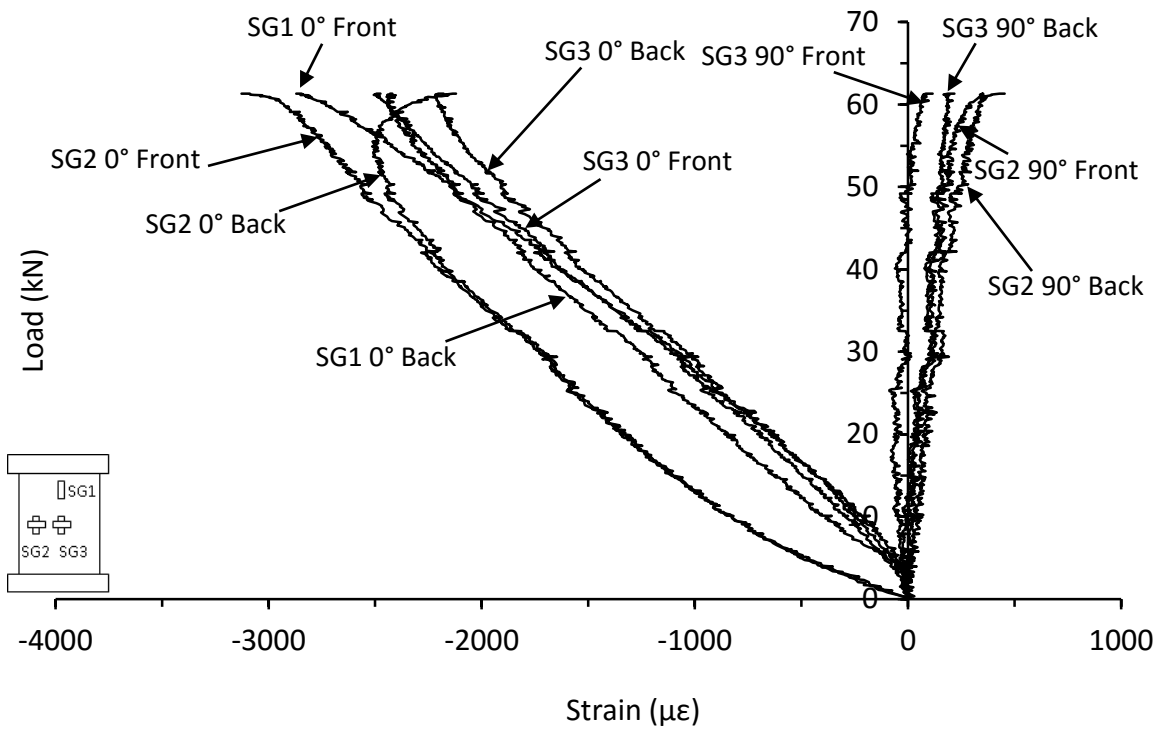


Figure 7.2.21. Strain responses from thin symmetrical CP carbon/epoxy panel with 20mm of core removed (HD-8-8-CP-CR-A)

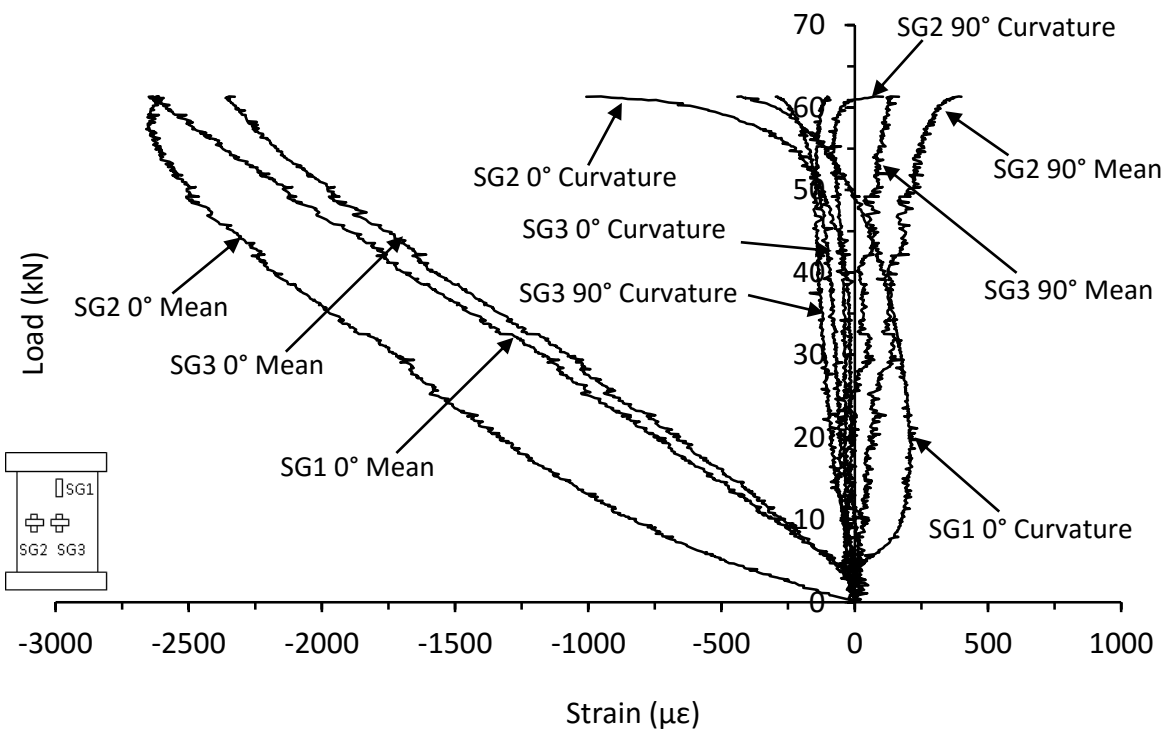


Figure 7.2.22. Mean and curvature strain responses from thin symmetrical CP carbon/epoxy panel with 20mm of core removed (HD-8-8-CP-CR-A)

Unsymmetrical panels with 20mm long section of core removed

The dominant strain responses in the unsymmetrical thin CP panels with 20mm of core removed, shown in Figure 7.2.23 and Figure 7.2.24, were found to be similar to those with 40mm of core removed. The local inward buckling started around 12kN at the edge regions and escalated about 18kN. While the strain reversal in the longitudinal direction was complete at around 24kN, in the transverse direction, the strain reversal occurred slightly later at about 27kN. Although these characteristics of the in-plane compressive behaviour of these shorter core removed panels were very similar to those of the 40mm core removed panels, the average in-plane compressive strength of these panels went up by 86% (see Table 7.1.9).

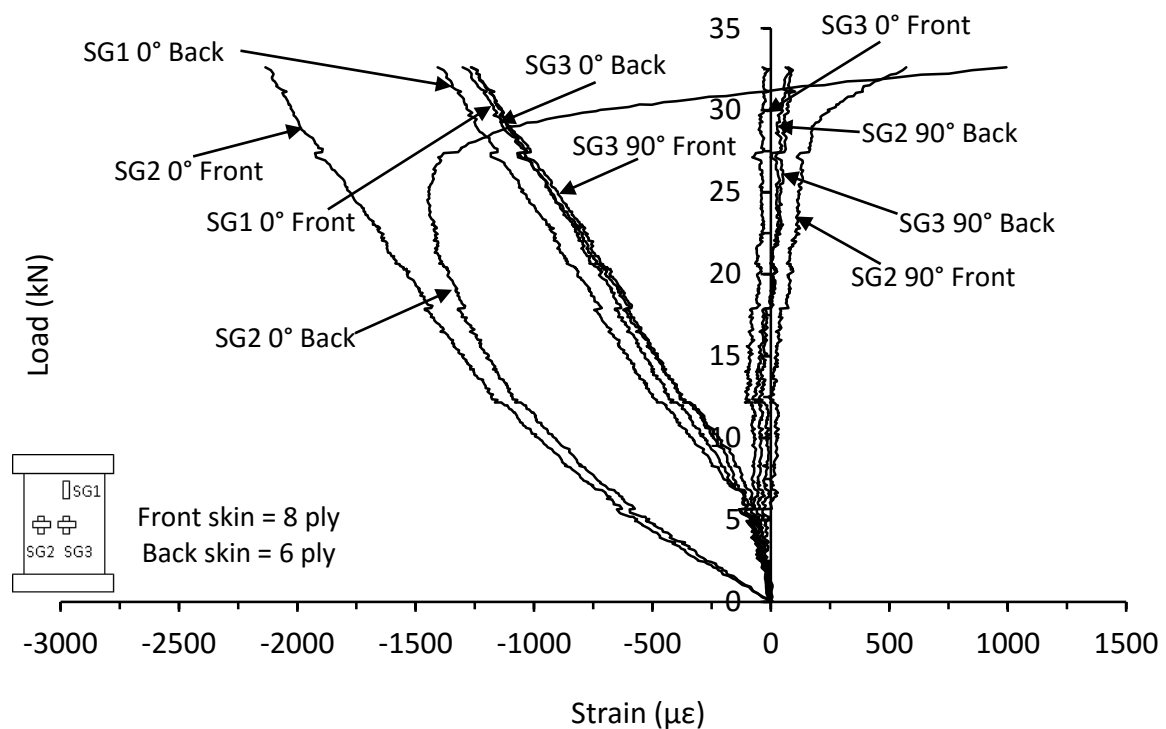


Figure 7.2.23. Strain responses from thin unsymmetrical CP carbon/epoxy panel with 20mm of core removed (HD-8-6-CP-CR-A)

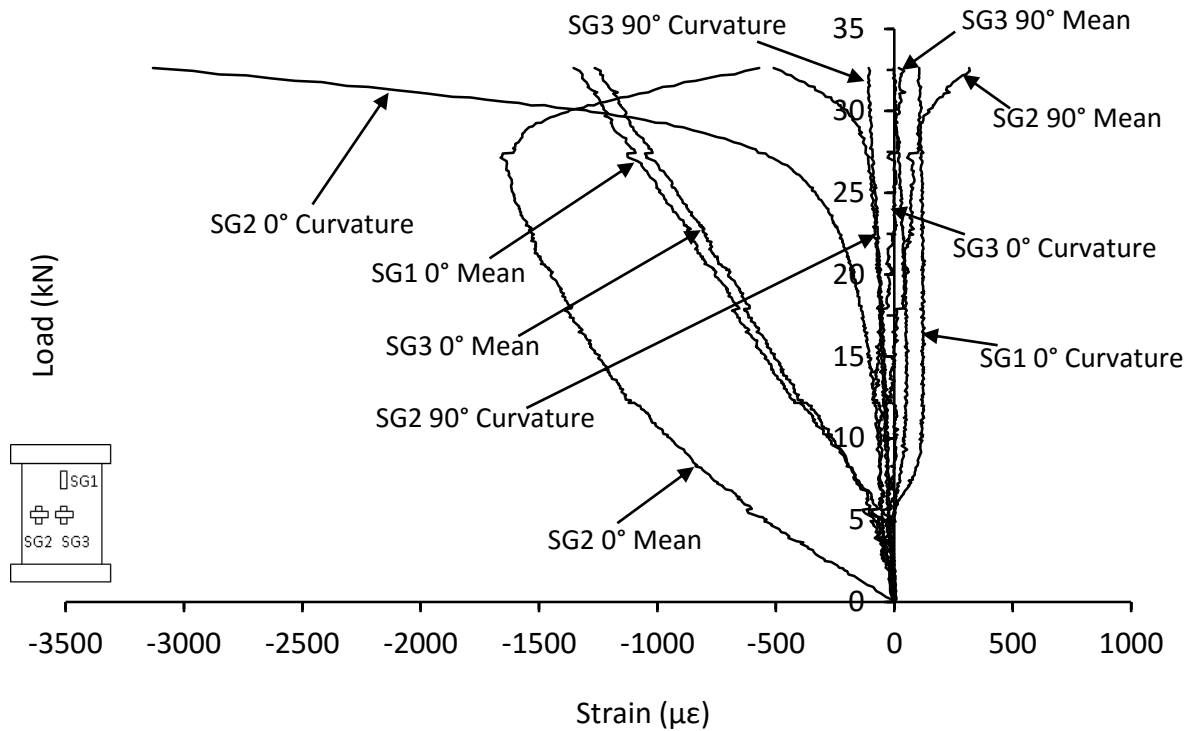


Figure 7.2.24. Mean and curvature strain responses from thin unsymmetrical CP carbon/epoxy panel with 20mm of core removed (HD-8-6-CP-CR-A)

Symmetrical panels with 20mm long section of core removed after impact test

Removing the core from the mid-section in thin symmetrical CP skinned panels after impact damage allowed for the effect of impact damage on the skin to be investigated. As with the aforementioned core removal panels, while local flexural and TTT resistance were significantly reduced without the core, the addition of impact damage should weaken the in-plane compressive resistance of the skins in the mid-section significantly, as well introducing local skin curvature and imbalance in the skins. Strain responses of a thin symmetrical CP panel with 20mm of core removed after a 10J impact are shown in Figure 7.2.25 and Figure 7.2.26. It can be seen that the inward local buckling started at about 12kN, much earlier than the non-impacted core removed panels. Amazingly, it took nearly 35kN for the strain reversal in the longitudinal direction to complete at 47kN and again further loading for the strain reversal in the transverse direction to occur, due likely to the relatively limited impact damage inflicted in the impact skin. Thus, the corresponding in-plane compressive strength of 195 MPa was just slightly less than 216 MPa for the non-impacted core removed panels.

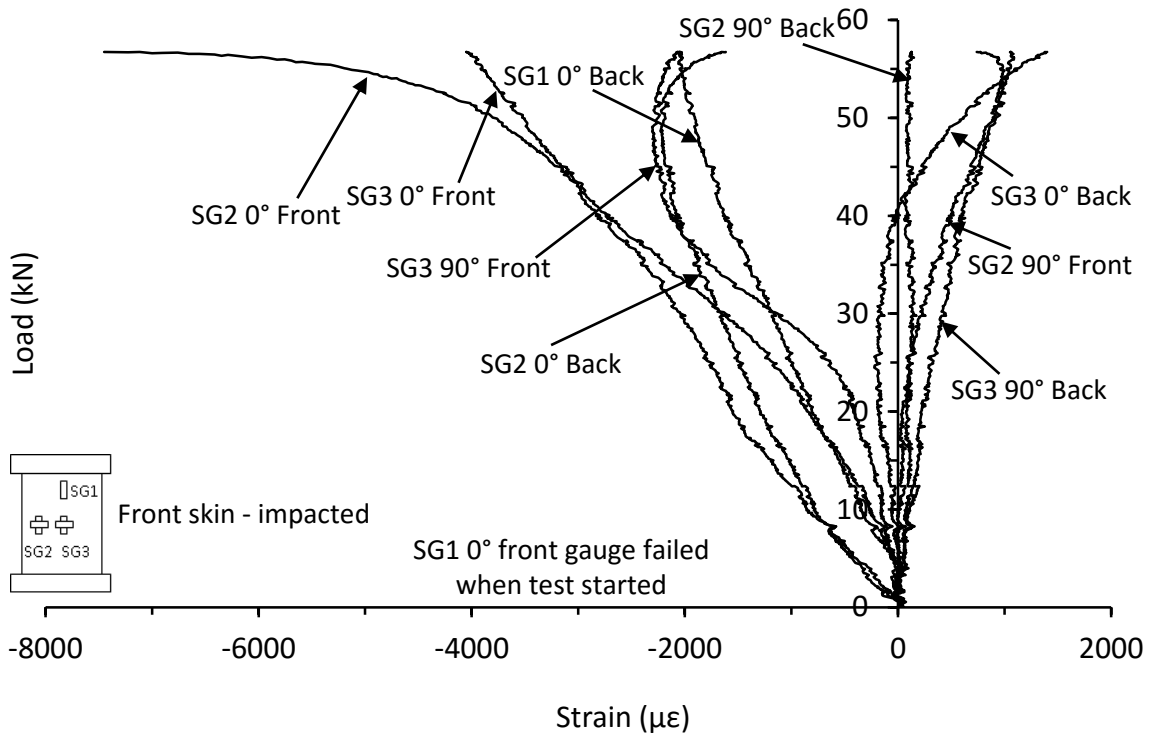


Figure 7.2.25. Strain responses from thin symmetrical CP carbon/epoxy panel with 20mm of core removed after a 10J impact (HD-8-8-CP-ICR-10J)

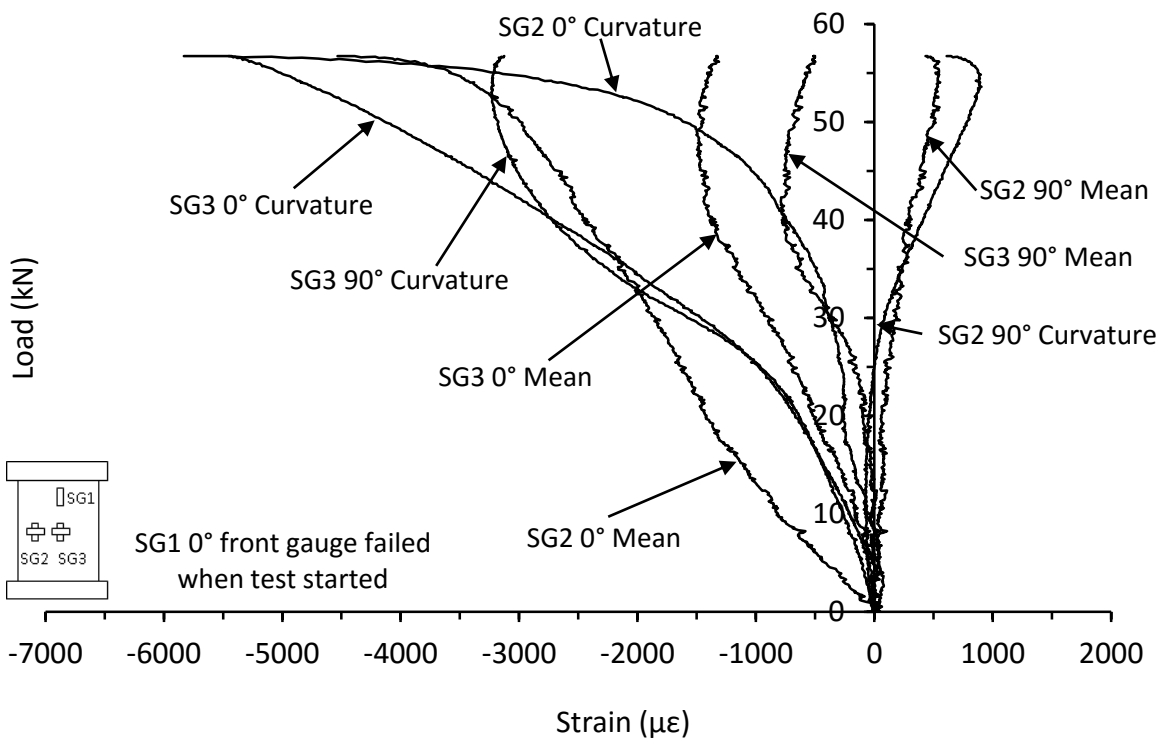


Figure 7.2.26. Mean and curvature strain responses from thin symmetrical CP carbon/epoxy panel with 20mm of core removed after a 10J impact (HD-8-8-CP-ICR-10J)

As expected, increasing the impact energy to 20J intensified the aforementioned features of the 10J case, including the effects of the panel curvature, on the dominant response of the panel without the TTT resistance and rigidity of the core. As shown in Figure 7.2.27 and Figure 7.2.28, the increase in the size of the dished area caused the direction of local buckling to shift from inward to outward in the back skin side region and severely reduced the load at which this local buckling was initiated at to about 7kN. The non-impacted skin appeared to delaminate at about 13kN, triggering a substantial instability and showed further propagation at about 25kN. Shortly after, the panel failed catastrophically. It was clear that the 20J impact significantly damaged the impacted skin, whose in-plane compressive resistance was severely reduced. Unsurprising, the in-plane compressive strength of this panel was only 94MPa.

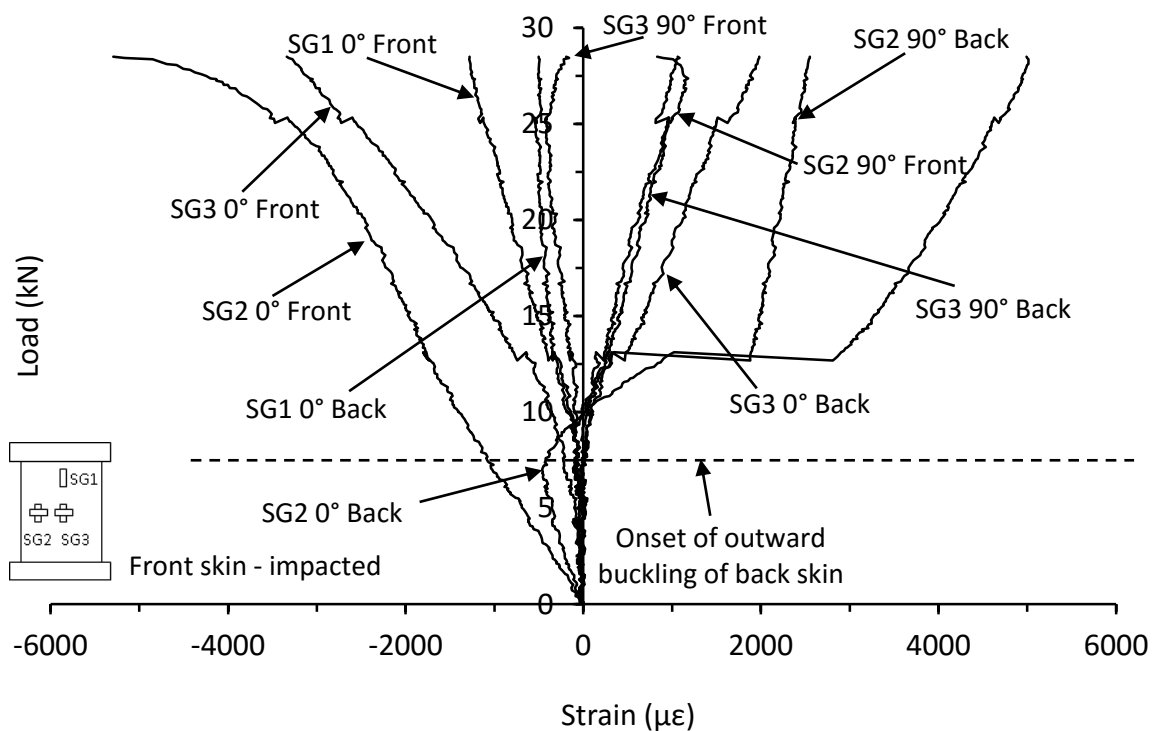


Figure 7.2.27. Strain responses from thin unsymmetrical CP carbon/epoxy panel with 20mm of core removed after a 20J impact (HD-8-6-CP-ICR-20J)

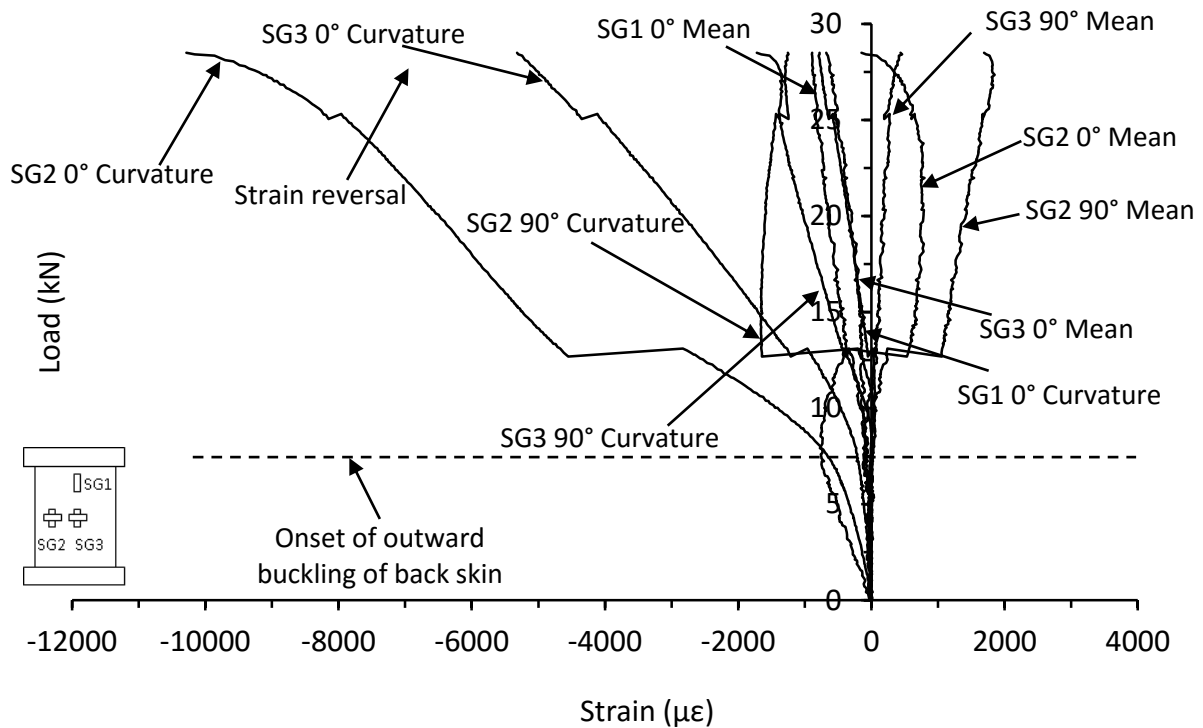


Figure 7.2.28. Mean and curvature strain responses from thin unsymmetrical CP carbon/epoxy panel with 20mm of core removed after a 20J impact (HD-8-6-CP-ICR-20J)

Panels with 40mm hole in one skin

Drilling a hole in the skin of sandwich panels is sometimes used as an extreme yet convenient measure of representing the effects of impact damage. Removal of the skin material reduces the global in-plane compressive resistance and the local flexural resistance of the skins, and the TTT shear resistance of the sandwich panel could be affected only moderately. With a hole in one skin, local asymmetry was introduced in the mid-section region inducing local bending moments, which in turn could increase the tendency of local buckling. Shown in Figure 7.2.29-Figure 7.2.31 are the individual strain responses for a typical panel with one hole in the front skin. In the mean and curvature strain responses, the corresponding strain responses of a 10J impact CAI panel are also included for comparison. As can be seen, the presence of a hole appeared to completely dominate the in-plane compressive behaviour of the panel with the linear resistance up to failure.

It is quite interesting to note in Figure 7.2.30 and Figure 7.2.31 that the mean and curvature strain responses of the panel with a hole compare very well with those of the panel impact damaged at 10J. From a damage map in Figure 4.3.1, it can be interpolated that the delamination extent in the impacted skin of such panel is about 51mm, which is slightly larger than the 40mm diameter hole. Thus, their respective in-plane compressive strengths of 236MPa are unsurprisingly identical, though fortuitous.

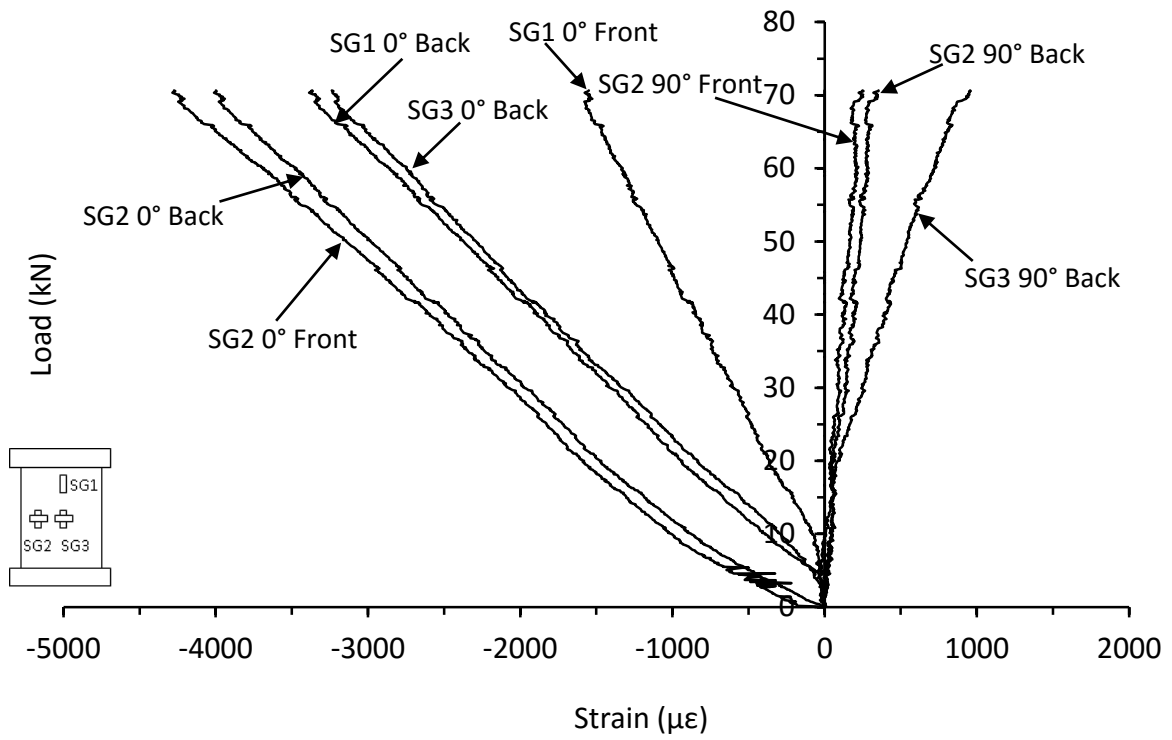


Figure 7.2.29. Strain responses from thin symmetrical CP carbon/epoxy panel with one 40mm hole drilled in the top skin (HD-8-8-CP-1H-B)

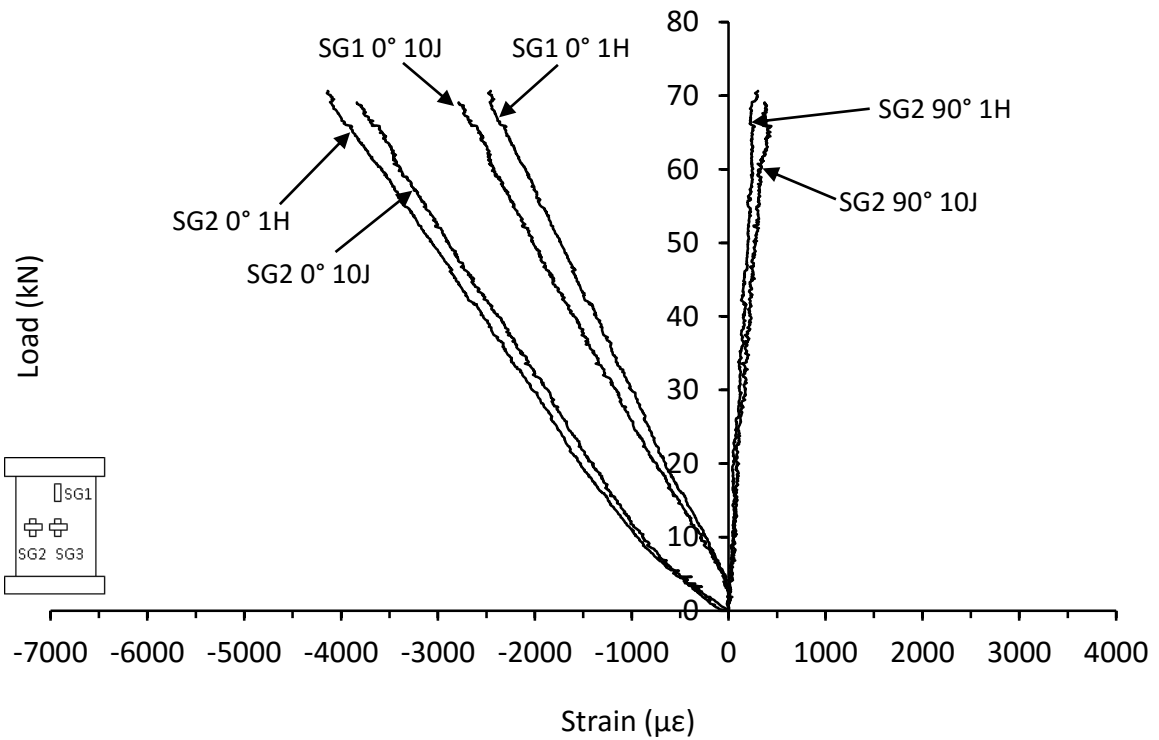


Figure 7.2.30. Comparison of mean strain responses from thin symmetrical CP carbon/epoxy panels with one 40mm hole drilled (HD-8-8-CP-1H-B) and 10J impact with no precondition (HD-8-8-CP-10J)

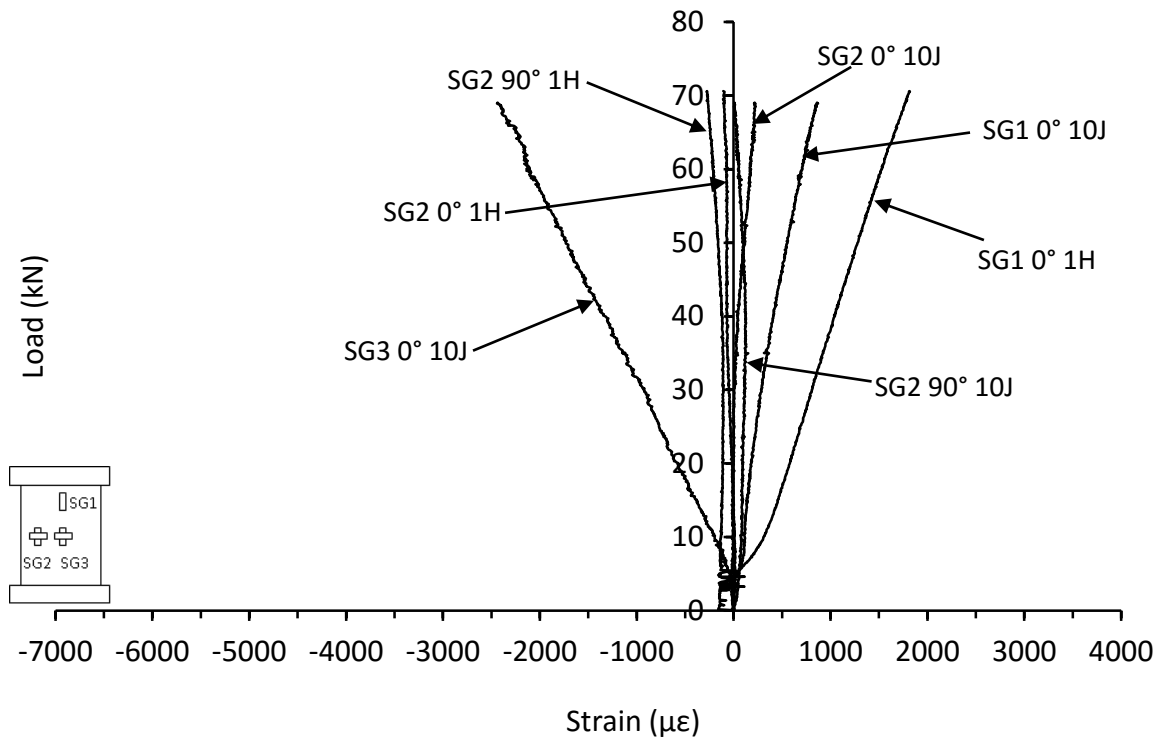


Figure 7.2.31. Comparison of curvature strain responses from thin symmetrical CP carbon/epoxy panels with one 40mm hole drilled (HD-8-8-CP-1H-B) and 10J impact with no precondition (HD-8-8-CP-10J)

Panels with 40mm hole in two skins

For panels with back-to-back holes in both skins, their in-plane compressive resistance, and local flexural and TTT shear resistance were reduced, similar to the panels with a hole in one skin. The most significant difference was that the panels with two holes were symmetrical, and hence under loading, should not generate any local bending moment in the mid-section region, as shown by the even development of strain in the front and back skins in Figure 7.2.32. This could also be seen in the comparative mean and curvature strain responses between the single hole and two hole panels shown in Figure 7.2.33 and Figure 7.2.34. Similar to the aforementioned single hole panels, the strain response of these two hole panels were completely dominated by the presence of the holes and were linear up to failure. The average in-plane compressive strength dropped down to 186MPa for panels with holes in both skins.

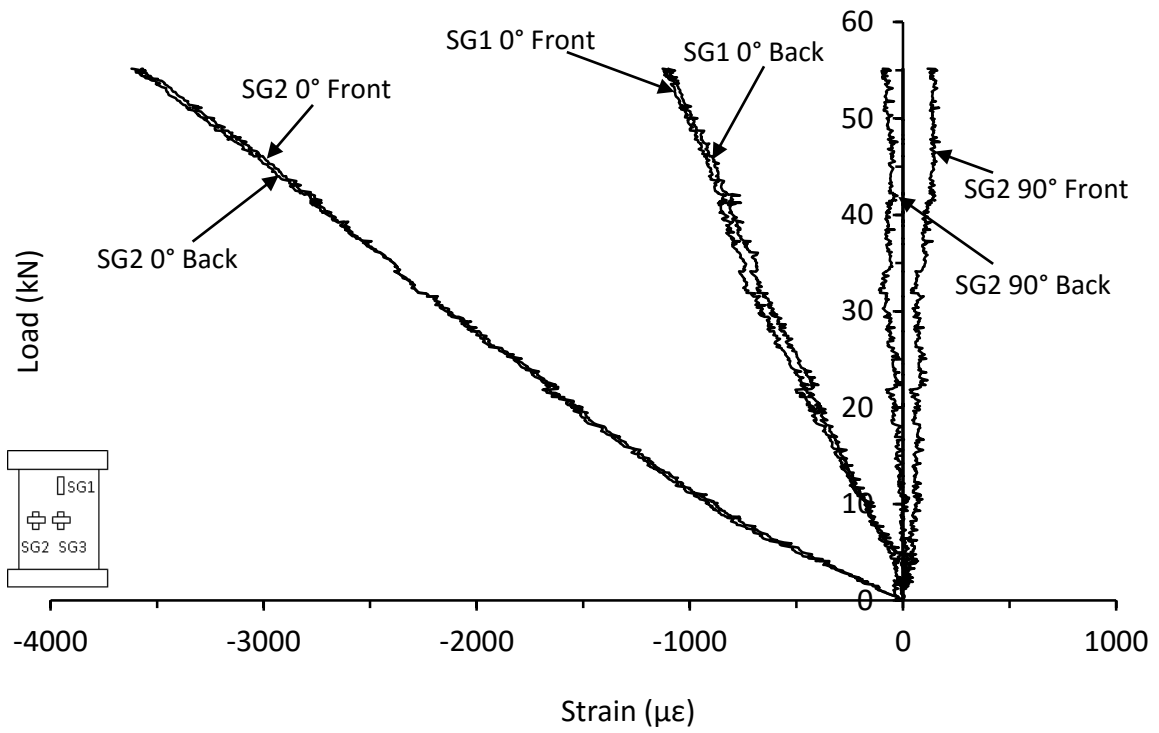


Figure 7.2.32. Strain responses from thin symmetrical CP carbon/epoxy panel with 40mm holes drilled in both skins (HD-8-8-CP-2H-A)

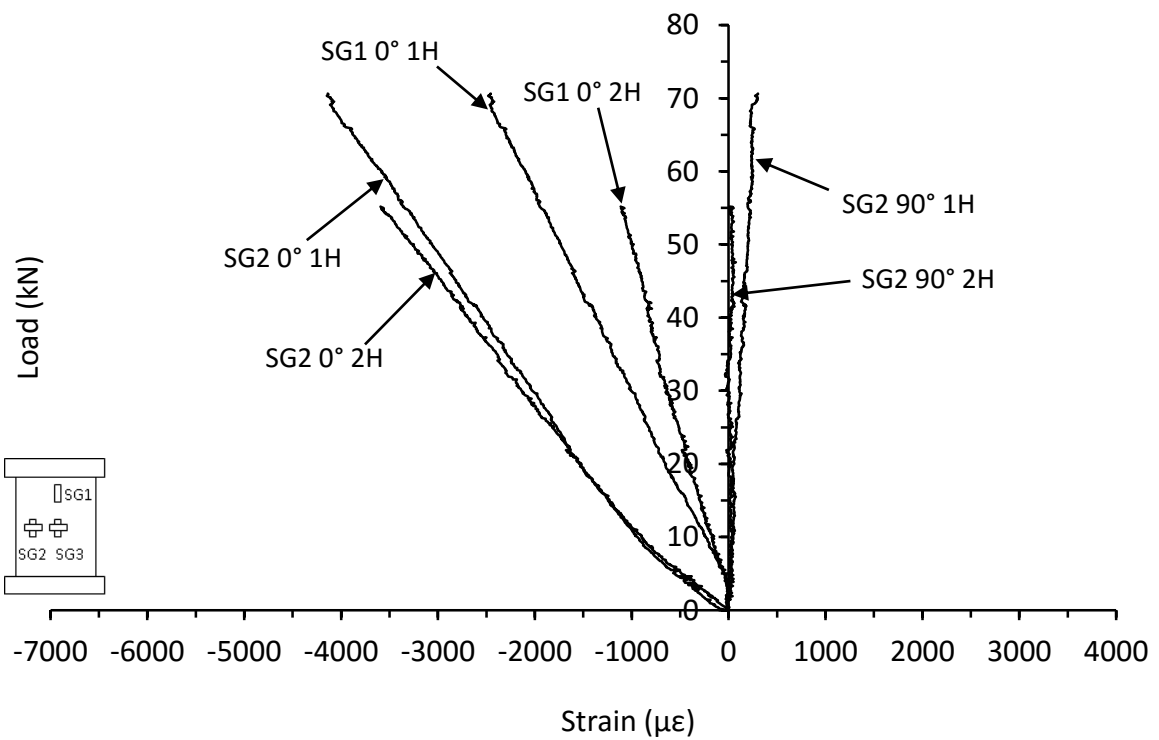


Figure 7.2.33. Comparison of mean strain responses from thin symmetrical CP carbon/epoxy panels with two 40mm holes (HD-8-8-CP-2H-A) and one 40mm hole drilled (HD-8-8-CP-1H-A)

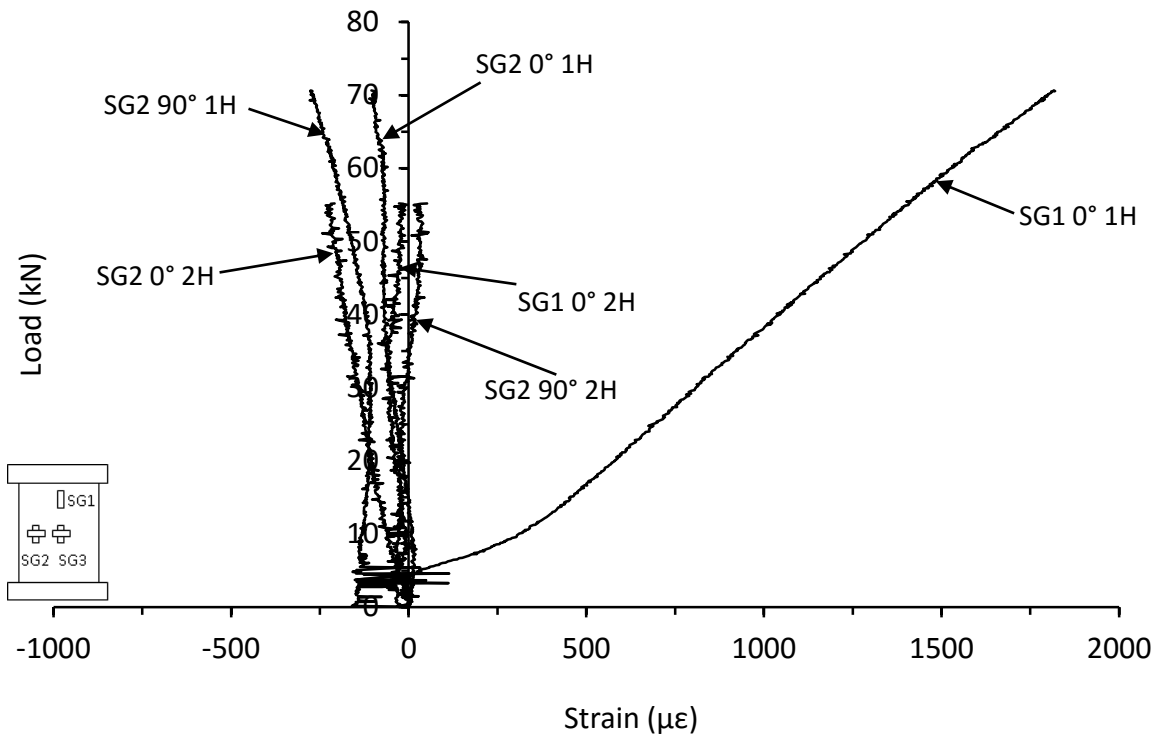


Figure 7.2.34. Comparison of curvature strain responses from thin symmetrical CP carbon/epoxy panels with two 40mm holes (HD-8-8-CP-2H-A) and one 40mm hole drilled (HD-8-8-CP-1H-A)

7.3. Major failure mechanisms of compression panels

7.3.1. Major failure mechanisms of impact damaged panels

As expected, the failure location under in-plane compression for the majority of panels coincided with the impact damaged area in the mid-section region. This suggests that the initiation and propagation of each panel under in-plane compression was due to the initiation and propagation of the impact damage, leading to catastrophic failure. As discussed in Section 4.1, two significant impact damage mechanisms that could affect the in-plane compressive behaviour were delamination and fibre fracture in the impacted skin. Firstly, from relatively low to moderate IKE in the IKE range for a specific sandwich construction, the panels were found to contain delamination(s) in the impacted skin, regions of crushed core and residual panel indentation, which had an effect on the in-plane compressive behaviour. Photos showing examples of failures from panels containing this type of damage are shown in Figure 7.3.1-Figure 7.3.3.

Secondly, at the upper end of the IKE range for a specific panel construction, fibre fracture occurred in the impacted skin. With local indentation up to 2.5-4.0mm, that caused a severe reduction in the in-plane compressive resistance and hence caused the reduction of the in-plane compressive strengths. An example of a panel failure containing fibre fracture from impact is shown in Figure 7.3.4.

The presence of delamination and/or fibre fracture initiated the local half wave buckling, which progressed into the 'S' shape, as indicated in the strain responses in Figure 7.2.1-Figure 7.2.8 and by the side view of all the failed panels through the sheared core. Although some core shearing was subtler than others, the transition of the single half wave to a double half wave resulted in the failure of the panel at the nodal point between the half waves.

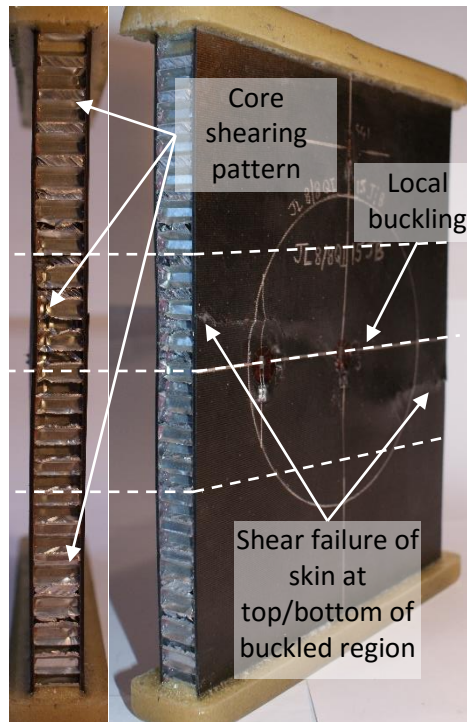


Figure 7.3.1. Photograph of thin symmetrical QI carbon/epoxy panel impacted at 15J after in-plane compression showing left external edge and impacted skin front (JL-8-8-QI-15J)

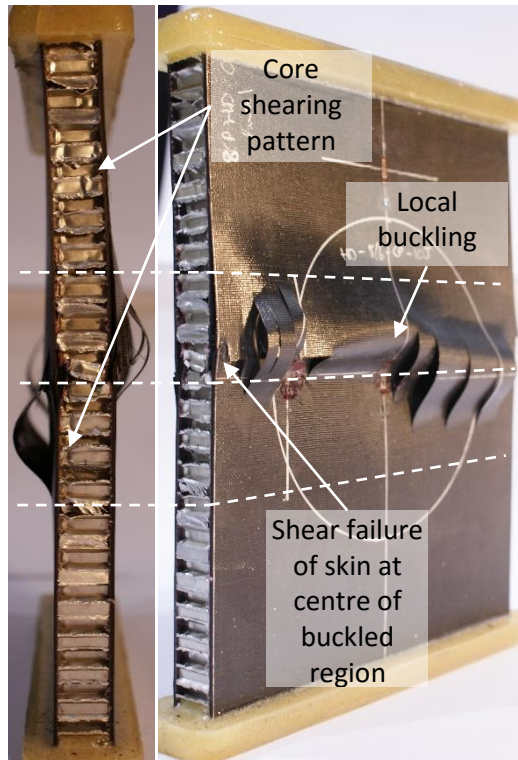


Figure 7.3.2. Photograph of thin unsymmetrical CP carbon/epoxy panel impacted at 10J after in-plane compression showing left external edge and impacted skin front (HD-8-6-CP-10J)

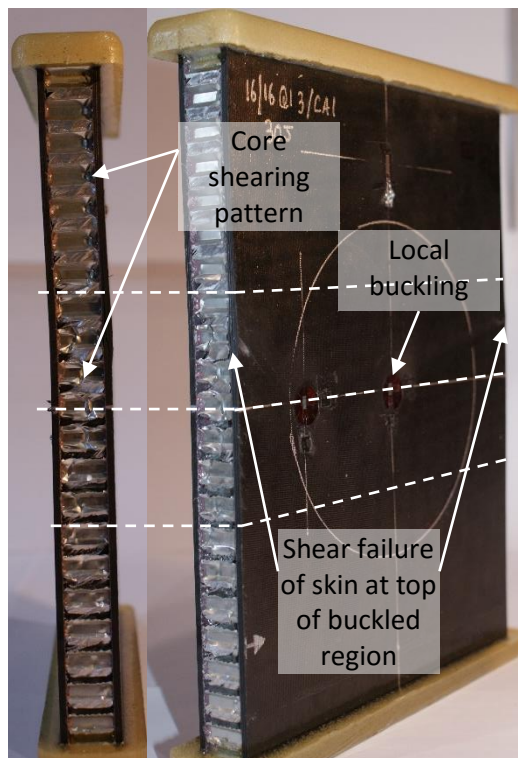


Figure 7.3.3. Photograph of thick symmetrical QI carbon/epoxy panel impacted at 30J after in-plane compression showing left external edge and impacted skin front (CI-16-16-QI-30J-A)

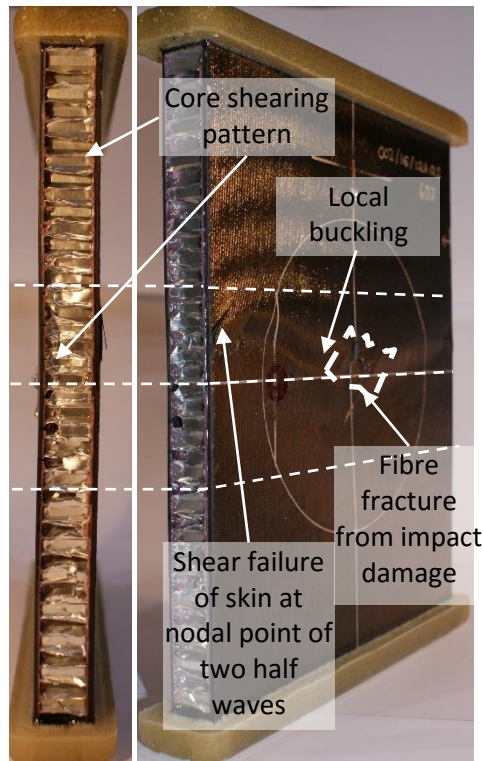


Figure 7.3.4. Photograph of thick unsymmetrical QI carbon/epoxy panel impacted at 60J after in-plane compression showing left external edge and impacted skin front (LB-16-12-QI-60J-A)

Since the initiation location and propagation paths of the in-plane compressive deformation originating from the impact damage in carbon/epoxy panels were not possible to monitor, a major advantage of using the E-glass/epoxy panels was their translucent nature to allow the failure appearances before and after in-plane compression testing to be examined. Figure 7.3.5 shows that a thin CP E-glass/epoxy panel impacted at 35J has got the relative limited impact damage, as circled by the dashed line and that the compressive failure mechanisms did not interact directly with the delamination of about 18mm. The lack of the transverse propagation triggering the compressive failure can be attributed to the relatively small size of the delamination.

For a thick CP E-glass/epoxy panel shown in Figure 7.3.6, the in-plane compressive failure band overlapped with the impact-induced delamination extent of about 27mm in the transverse direction. From the visual observation of this photo, the transverse propagation of the delamination under the in-plane compression may have occurred, but it was unclear whether or not such transverse propagation could trigger the in-plane compressive failure. All in all, the in-plane compressive behaviour of these E-glass/epoxy skinned sandwich panels was distinctively different from that of the carbon/epoxy skinned panels and was found to be much more damage tolerant than originally anticipated, even though the resin systems were very similar.

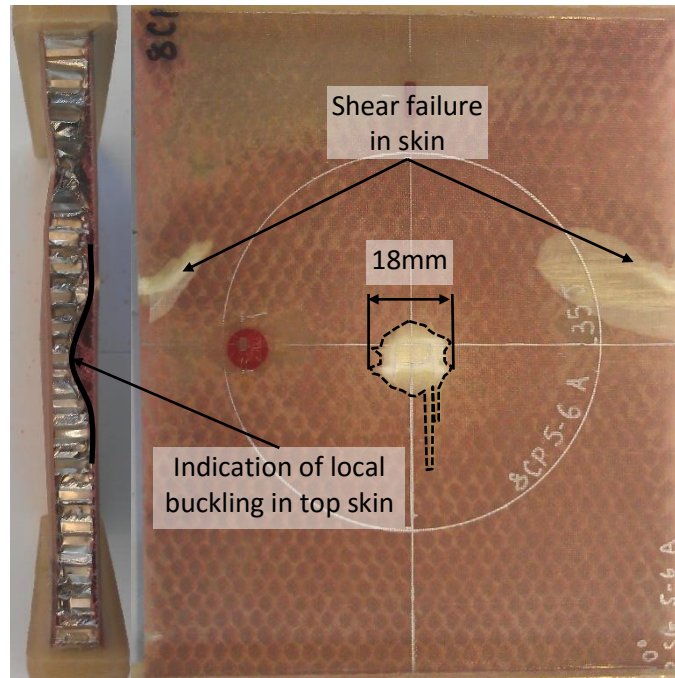


Figure 7.3.5. Photograph of thin symmetrical CP E-glass/epoxy panel impacted at 35J after in-plane compression showing left external edge and impacted skin front (SG-8-8-CP-35J)

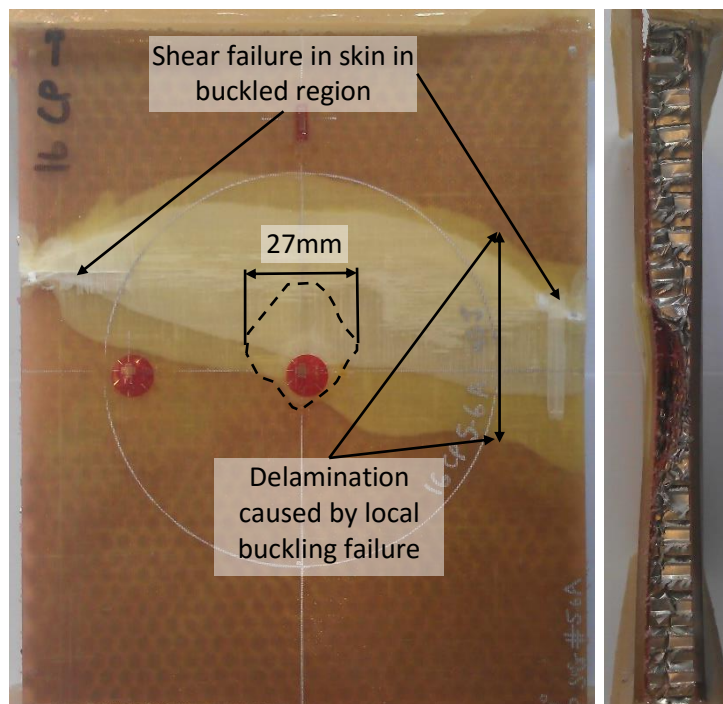


Figure 7.3.6. Photograph of thick symmetrical CP E-glass/epoxy panel impacted at 45J after in-plane compression showing impacted skin front and right external edge (SG-16-16-CP-45J)

7.3.2. Major failure mechanisms of pre-conditioned panels

All core removal panels at both lengths of 20mm and 40mm of core material removed failed, as expected, in in-plane compression in the core removed section. From the strain responses in Section

7.2.2, the inward local buckling initiated at the edge regions of the panel in the single half wave. The transition from a single half wave to the 'S' shaped buckling mode could have induced significant delaminations in the skin at the edge of the panel, as shown in Figure 7.3.7 for thin panels and Figure 7.3.8 for thick panels, resulting in the failure of the panels. Clearly, the delamination could have also occurred during the local buckling before the transition, which could depend on the sandwich constructions.

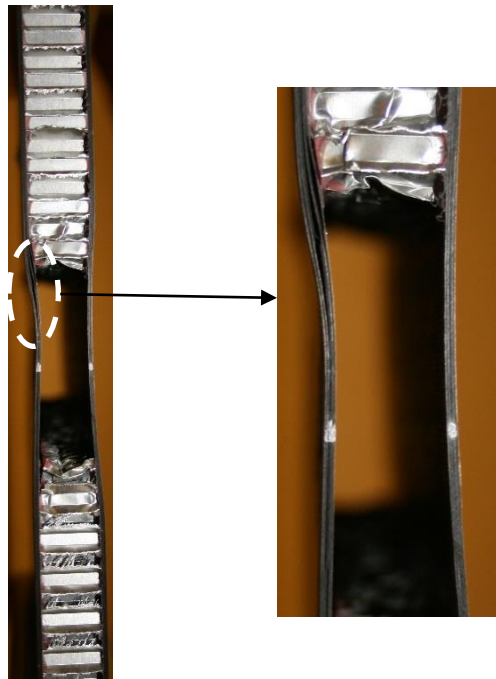


Figure 7.3.7. Post failure image of thin symmetrical CP carbon/epoxy panel with 40mm core removed from mid-section (CI-8-8-CP-CR-1)

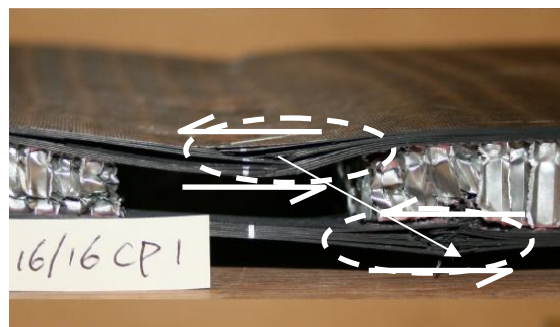


Figure 7.3.8. Post failure image of thick symmetrical CP carbon/epoxy panel with 40mm core removed from mid-section (CI-16-16-CP-CR-1)

The failure mechanisms for all panels with either one hole in the front skin, or a hole in both skins, were consistent, regardless of number of holes or skin symmetry in the panel. All panels exhibited compressive shear band fracture, emanating from the apex of the circle diameter in the transverse direction to the edge of the panel, as seen in Figure 7.3.9. Although limited strain information was

available from this region, it can be strongly inferred that the formation of kink bands at the edge of the holes propagated across the panel, as suggested by Ratcliffe et al [121], resulting in the failure of the panel.

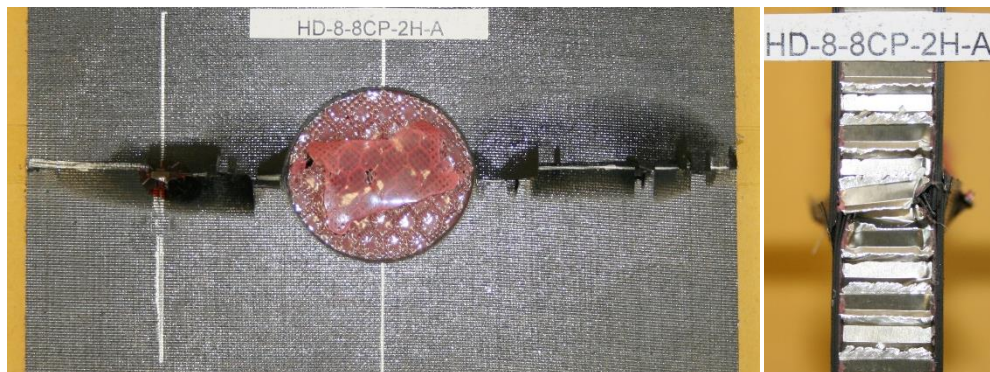


Figure 7.3.9. Post failure image of thin symmetrical CP carbon/epoxy panel with 40mm holes in both skins (HD-8-8-CP-2H-A)

7.4. Effects of skin lay-up and thickness on CAI strengths of carbon/epoxy skinned sandwich panels

As discussed in Section 6, the premature failure of all baseline panels' means that their true in-plane compressive strengths were not obtained, hence, the assessment of the percentage losses of their CAI strengths was not possible. However it is still possible to generate tolerance maps for all arrangements tested and make observations based on the residual performance of the panels over their respective tested IKE ranges, and compare the values of CAI strength to identify the effects of the damage measures on the in-plane compressive strengths of those sandwich panels in various constructions.

Lay-up effect

The effect of skin lay-up on the CAI strength has been known [99] due to a number of probable reasons. Swapping plies in the loading direction with $\pm 45^\circ$ plies could reduce the longitudinal flexural rigidity but increase the in-plane shear strength of the skins, which in turn could increase the in-plane compressive strength of the panel. Also, since the planar size of impact damage is expected to directly affect the CAI strength of the panels, the resistance to the propagation of delamination in the QI skins would be greater than that of the CP panels, which could lead to a lower level of CAI strength reduction. As seen in Figure 7.4.1 for symmetrical panels, at the relatively low IKE levels (from about 4J to about 17J) where the areas of delamination could be relatively small, there does not appear to be any effect of ply lay-up on CAI strength. However, for the IKE levels over 20J (large delaminations present with fibre fracture occurring over 25J), this lay-up effect is clearly shown. In the thick panels, this lay-up effect was upheld over the entire IKE range, though around about 28J, CAI strength values for CP and QI panels were about the same. For unsymmetrical panels in Figure 7.4.2, in which only the

impacted skins were in the QI lay-up, the lay-up effect was generally weak, due mainly to the early onset of fibre fracture in the QI panels causing a reduction in the CAI strength compared to the CP panels.

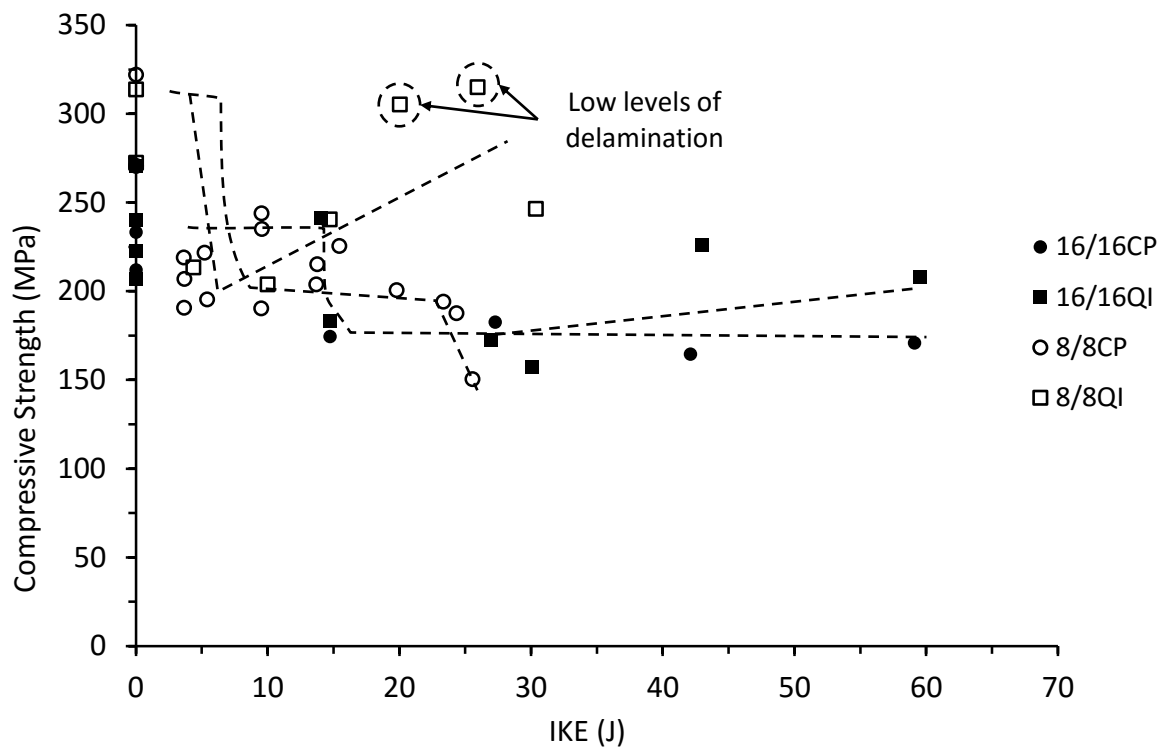


Figure 7.4.1. Compressive strength vs incident kinetic energy for thick and thin symmetrical CP and QI carbon/epoxy panels 70kg/m³ core density

Skin thickness effect

In Figure 7.4.1, the thin symmetrical panels of both lay-ups appear to have greater CAI strengths than the thick panels up to 30J. For unsymmetrical panels in Figure 7.4.2, the same trend is observed, especially for the CP panels, where the effect is most significant.

As mentioned earlier, the use of IKE for evaluating the trends of CAI strength degradation for sandwich panels has significant limitations. Thus, the damage tolerance comparison continues with dent depth, transverse delamination extent and transverse crushed core extent. Figure 7.4.3 and Figure 7.4.4 show the same CAI strength data plotted against the level of dent depth. All the trend characteristics for IKE for both lay-up and thickness effects are still observable qualitatively in both symmetrical and unsymmetrical panels for dent depth.

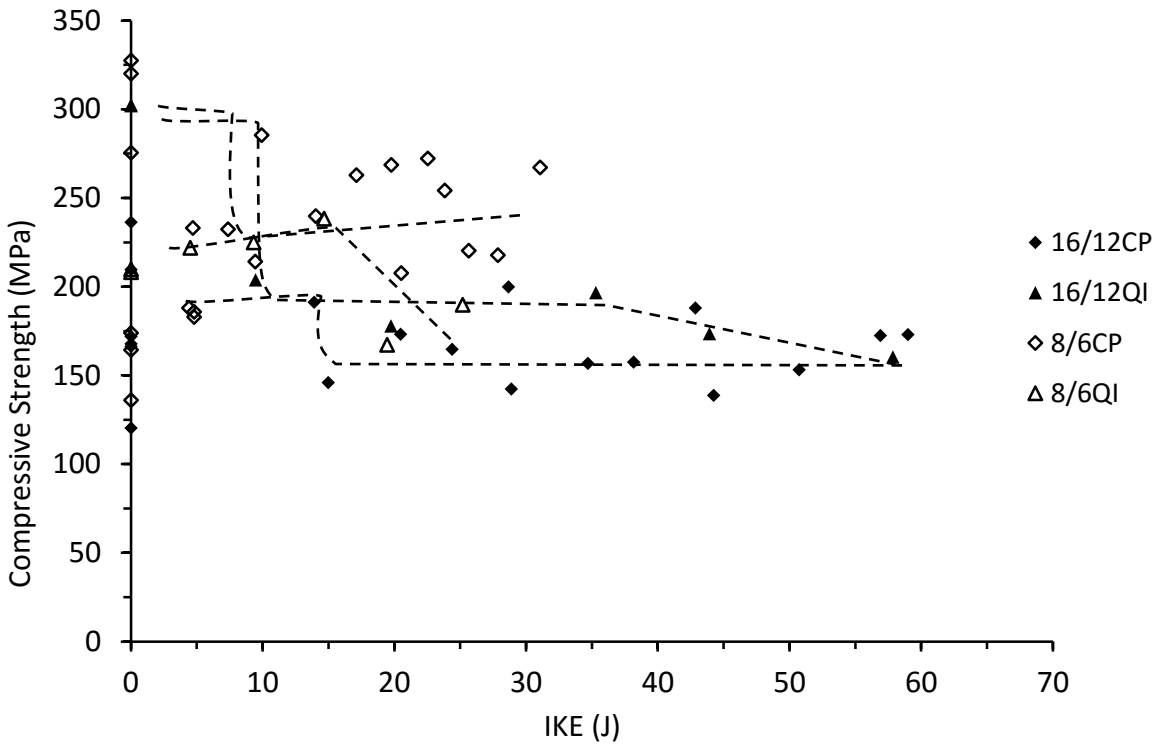


Figure 7.4.2. Compressive strength vs incident kinetic energy for thick and thin unsymmetrical CP and QI carbon/epoxy panels 70kg/m³ core density

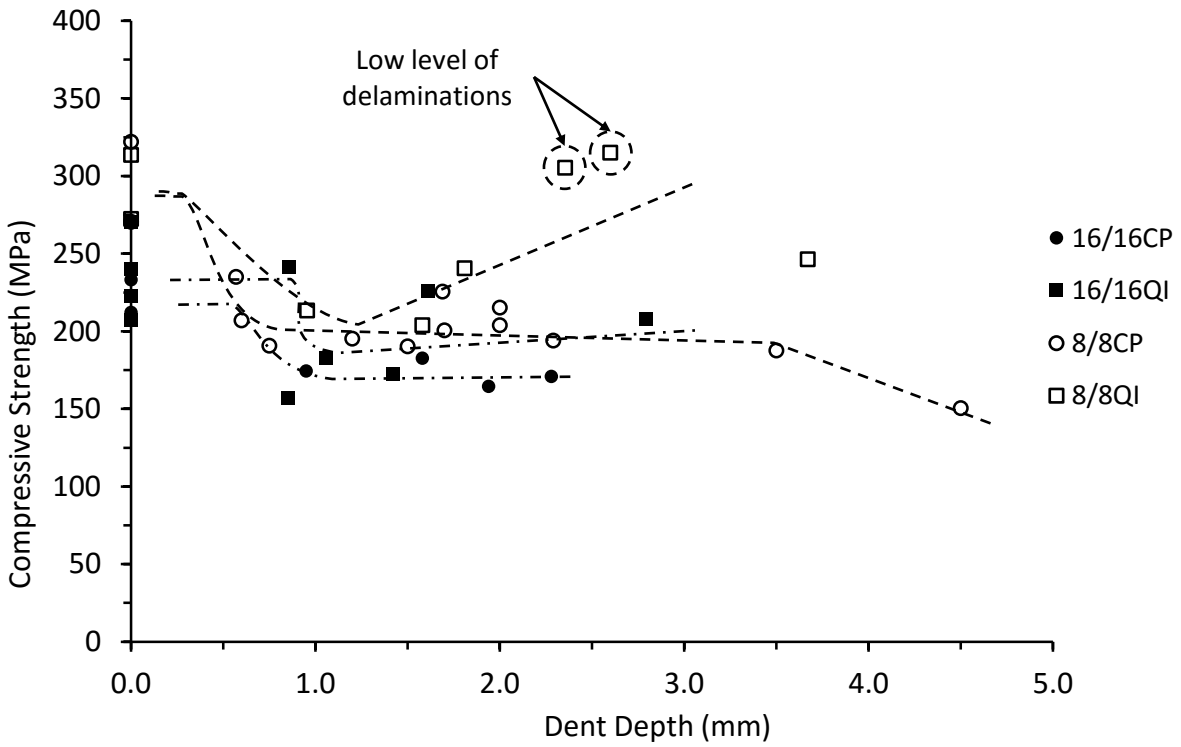


Figure 7.4.3. Compressive strength vs dent depth for thick and thin symmetrical CP and QI carbon/epoxy panels 70kg/m³ core density

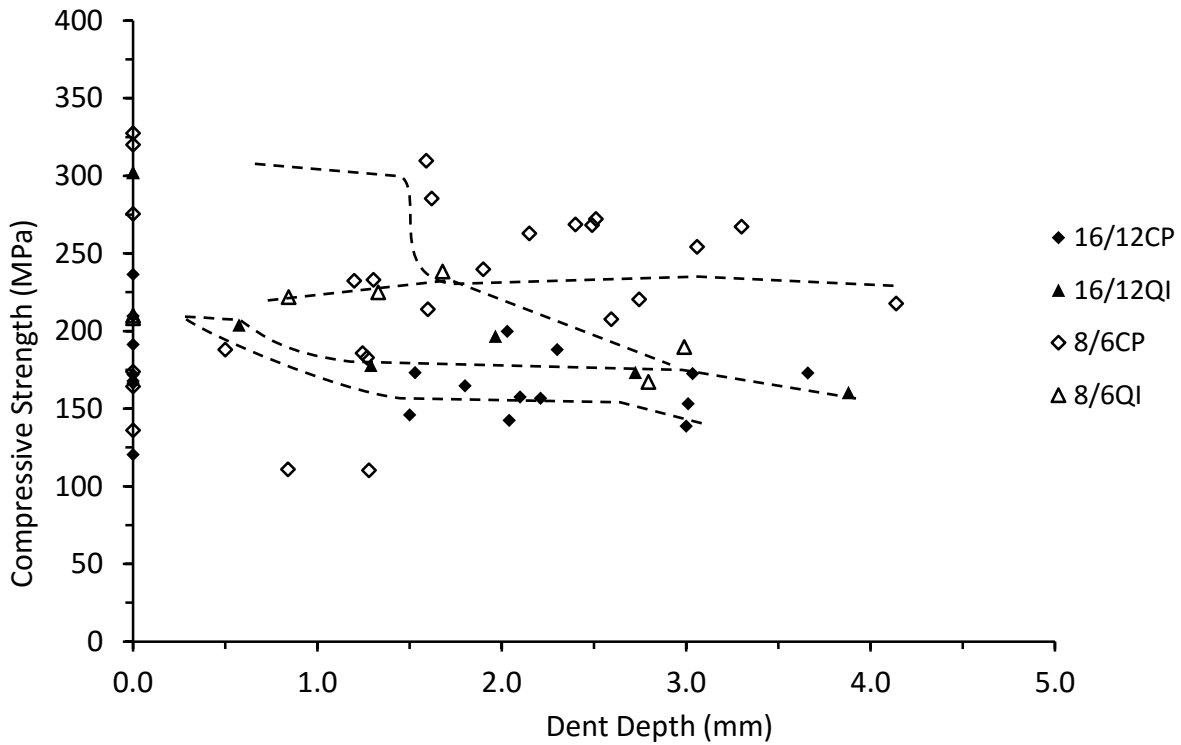


Figure 7.4.4. Compressive strength vs dent depth for thick and thin unsymmetrical CP and QI carbon/epoxy panels 70kg/m³ core density

In Figure 7.4.5 and Figure 7.4.6, the CAI strength data plotted against delamination extent of the impacted skin appears to be slightly scattered for the thin panels, because the CP panels had the far greater delamination sizes than the QI panels. Thus, it can be deduced that the thin QI symmetrical panels have the greater CAI strengths at the same IKEs due to the low level of delamination propagation, and due to the similar developments of delamination length in CP and QI thick symmetrical and unsymmetrical panels, the effect of lay-up on the CAI strength results in a similar trend. In the unsymmetrical thin panels, the CAI strength values of the CP panels are fractionally higher than those of the QI panels, as in the earlier cases when the IKE and dent depth were used as the limited propagation of delamination in the QI panels does not reflect the occurrence of extensive fibre fracture in the top skin. Moreover, the thickness effect in both symmetrical and unsymmetrical CP panels on the CAI strengths are in agreement with the findings when IKE and dent depth were used. Comparison for the thickness effect could not be made for the QI panels due to the fact that the thicker QI panels had far greater delamination extents than the thin ones.

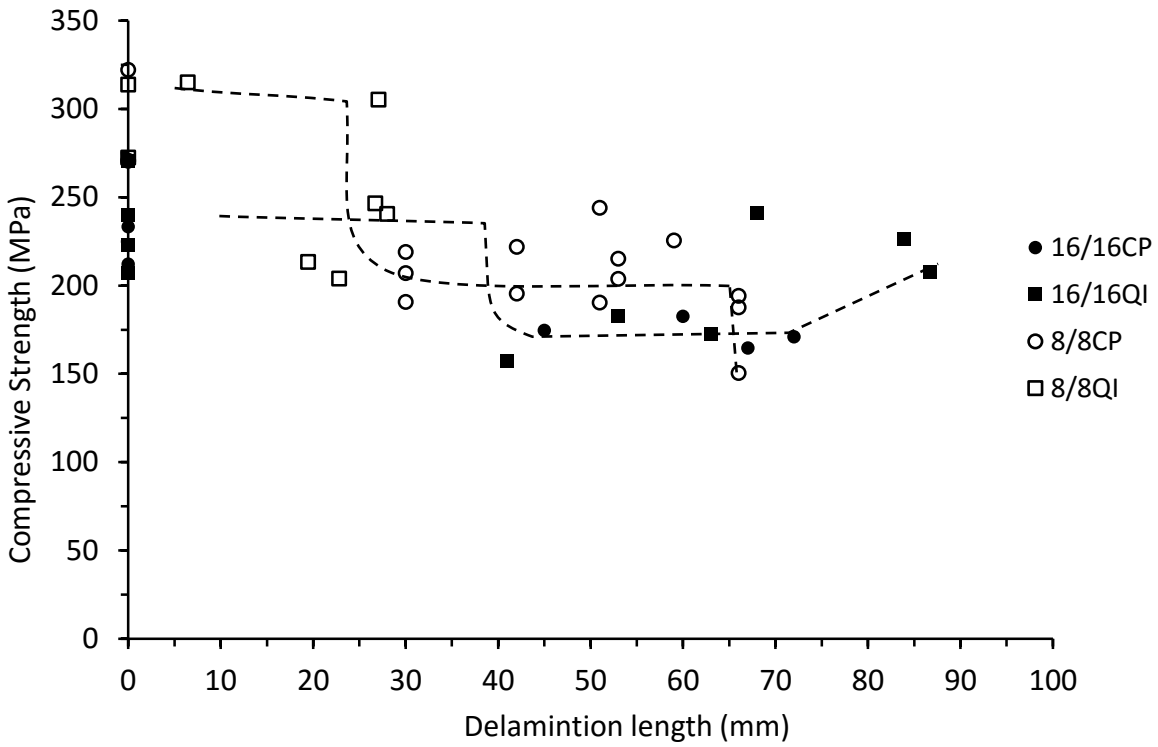


Figure 7.4.5. Compressive strength vs delamination length for thick and thin symmetrical CP and QI carbon/epoxy panels 70kg/m³ core density

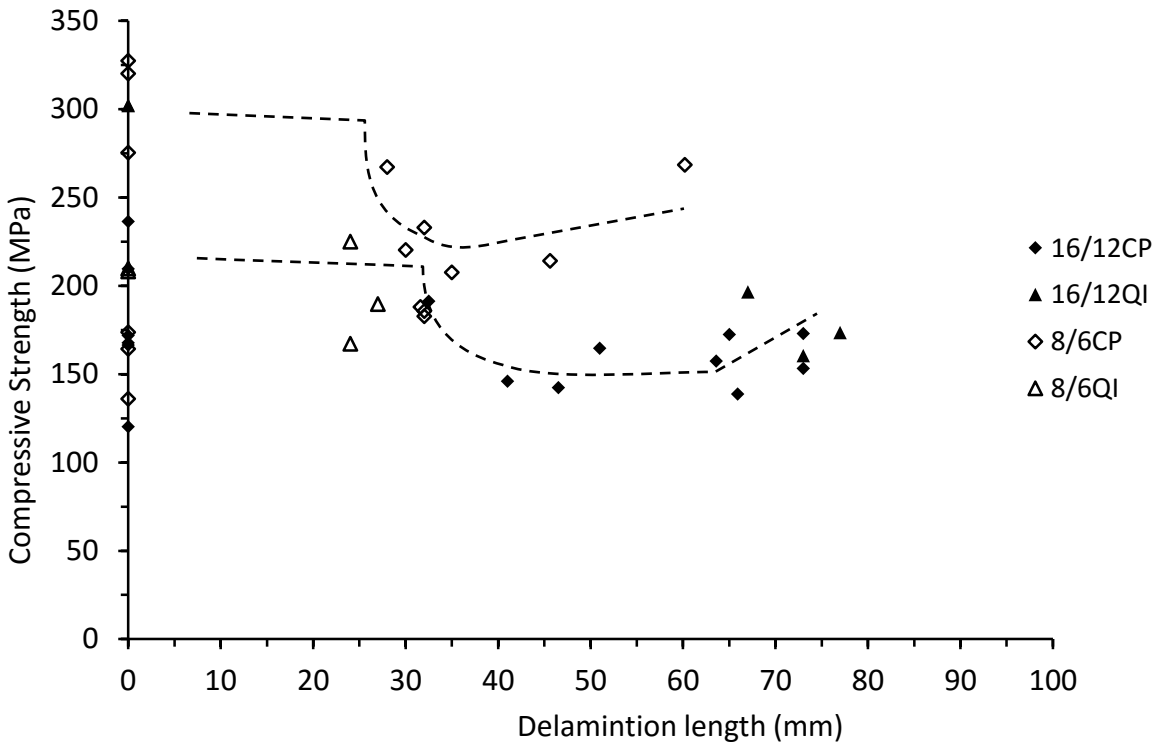


Figure 7.4.6. Compressive strength vs delamination length for thick and thin unsymmetrical CP and QI carbon/epoxy panels 70kg/m³ core density

It can be seen in Figure 7.4.7 and Figure 7.4.8 that the CAI strength data does not correlate with the variation of the crushed core extent for the lay-up effects, very much as expected, and that the visible

thickness effects are the simple indications that the extent of crushed core is coupled with the delamination extent of the impacted skin.

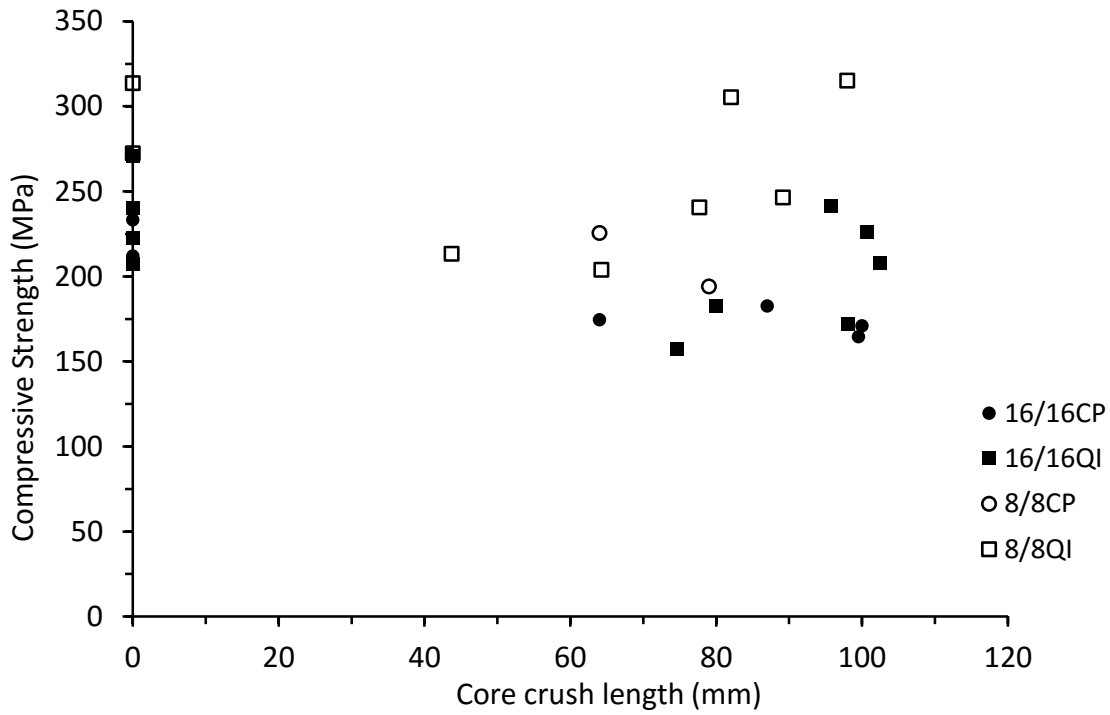


Figure 7.4.7. Compressive strength vs core crush length for thick and thin symmetrical CP and QI carbon/epoxy panels 70kg/m³ core density

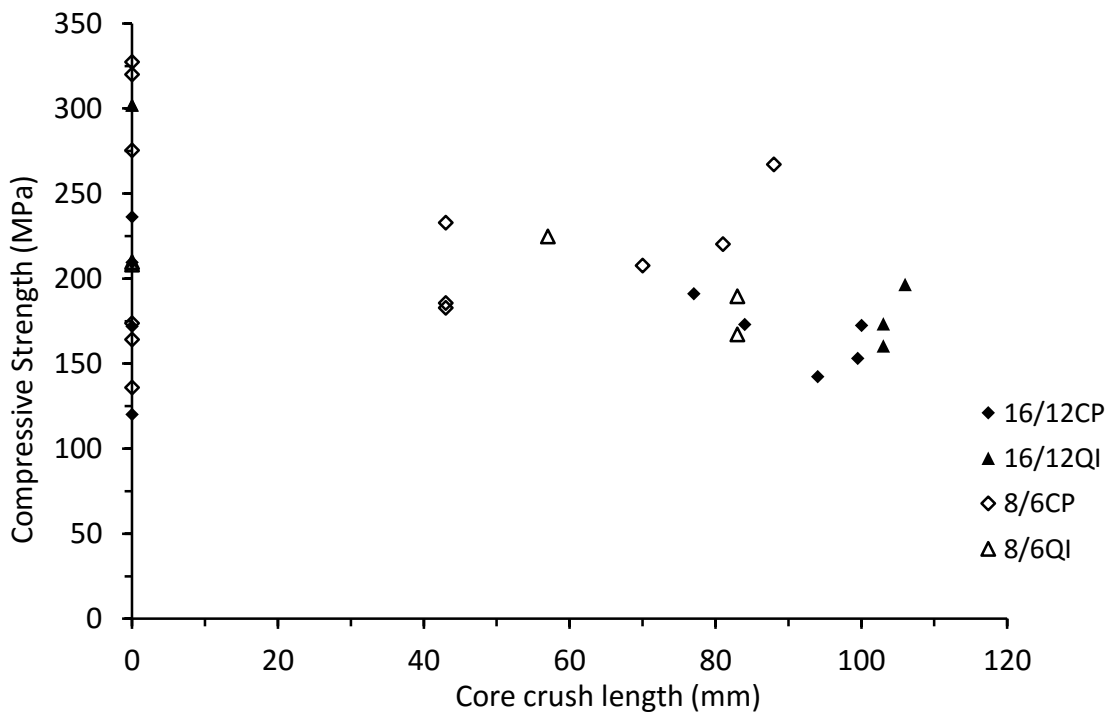


Figure 7.4.8. Compressive strength vs core crush length for thick and thin unsymmetrical CP and QI carbon/epoxy panels 70kg/m³ core density

7.5. Effects of panel symmetry on CAI strengths of carbon/epoxy skinned sandwich panels

Symmetrical sandwich panels under in-plane compression could lose symmetry locally in the mid-section region due to impact damage and local curvature. Unsymmetrical sandwich panels could still be unsymmetrical even if impact damaged but could provide symmetrical in-plane compressive resistance depending on the degree of impact damage and local curvature. A key feature is a shift in the neutral plane either towards the undamaged skin in the impact damaged section of the impact damaged symmetrical panels or towards the thicker skin of the undamaged unsymmetrical panels, inducing a local bending moment. Since this effect could not be examined directly due to the fact that the baseline panels did not fail in the mid-section regions, it could only be examined indirectly by comparing the in-plane compressive behaviour of both thin and thick panels. As seen in Figure 7.5.1 for thin CP panels, at the lower end (less than 10J) of IKE range, there was little difference between symmetrical and unsymmetrical panels. Beyond 10J, the unsymmetrical panels consistently exhibited greater CAI strengths to the end of IKE range. Moreover, the symmetrical panels showed the well-established degradation trend with the increase of IKE, whereas the unsymmetrical CP panels show a clear upward trend, indicating that the moderate and severe impact damage and local curvatures evened out the in-plane compressive resistance of the two unequal skins. This finding has not been experienced before, however, when the two groups of thin QI panels were in-plane compression tested, as shown in Figure 7.5.2, the same characteristic trend was not observed. It was found that in the unsymmetrical thin QI panels, fibre fracture occurred as early as 20J, compared to the symmetrical panels, where the onset of fibre fracture was established to occur at impacts 30J, resulting in the difference in trend compared to the CP panels. Although the findings here are preliminary, the implications of panel asymmetry having a deleterious effect on impact damage resulting in a resurgence of CAI strength is rather significant. At the cost of baseline performance, the removal of plies from the distal skin could provide designers with an effective damage tolerance solution while reducing the cost and weight of the structure.

The effects of asymmetry on the thick CP and QI skinned panels were far less significant. As seen in Figure 7.5.3, due to a high scatter in data points at similar levels of IKE, no significant trends on the average compressive strength of the panel over the impact range could be established. After an initial drop in CAI strength in all thick arrangements between 10-15J, the CAI strengths fluctuated showing neither significant increase nor decrease in the CAI strength.

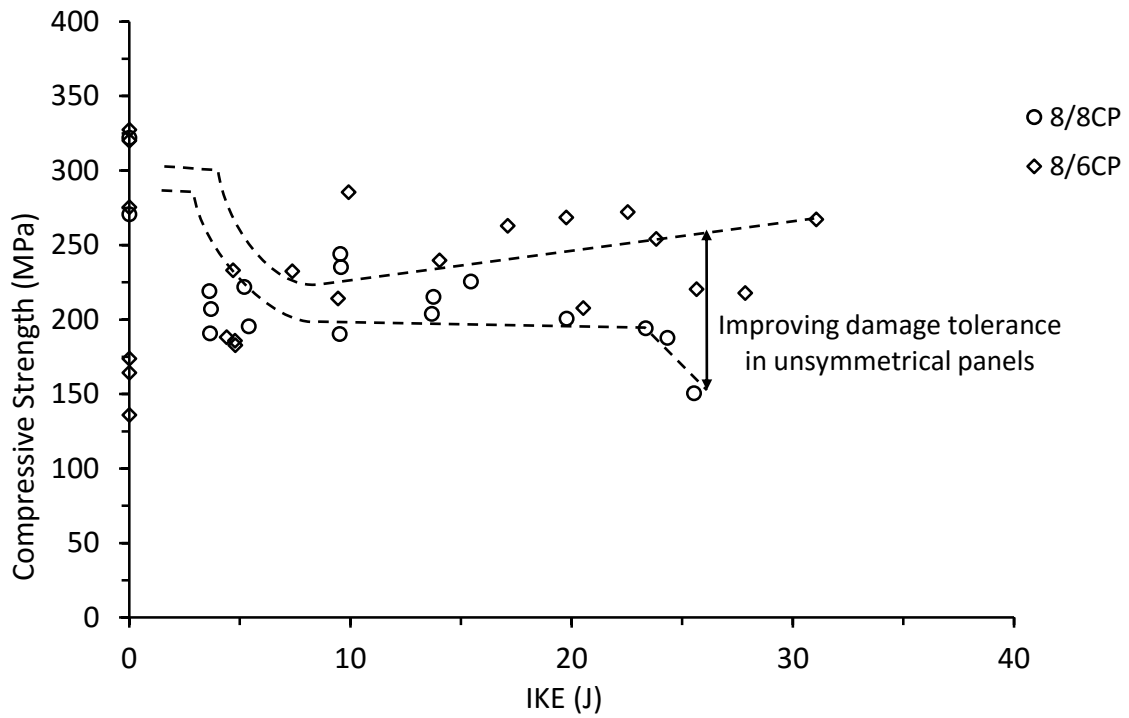


Figure 7.5.1. Compressive strength vs incident kinetic energy for thin symmetrical and unsymmetrical CP and QI carbon/epoxy panels with 70kg/m³ core density

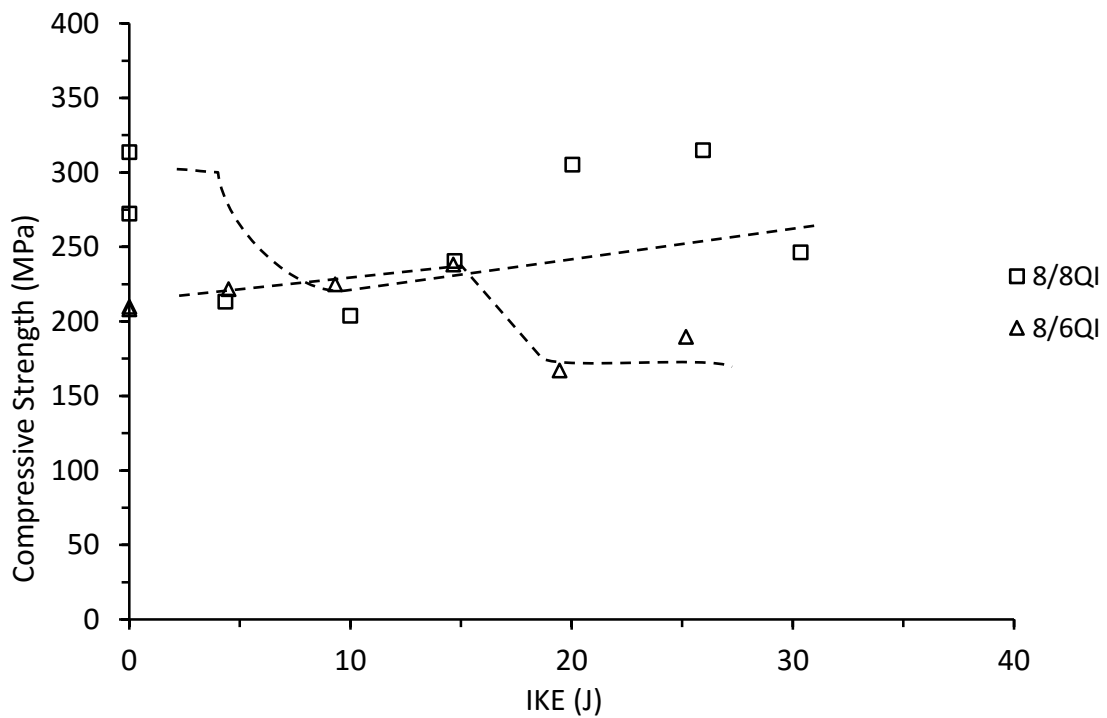


Figure 7.5.2. Compressive strength vs incident kinetic energy for thin symmetrical and unsymmetrical QI carbon/epoxy panels with 70kg/m³ core density

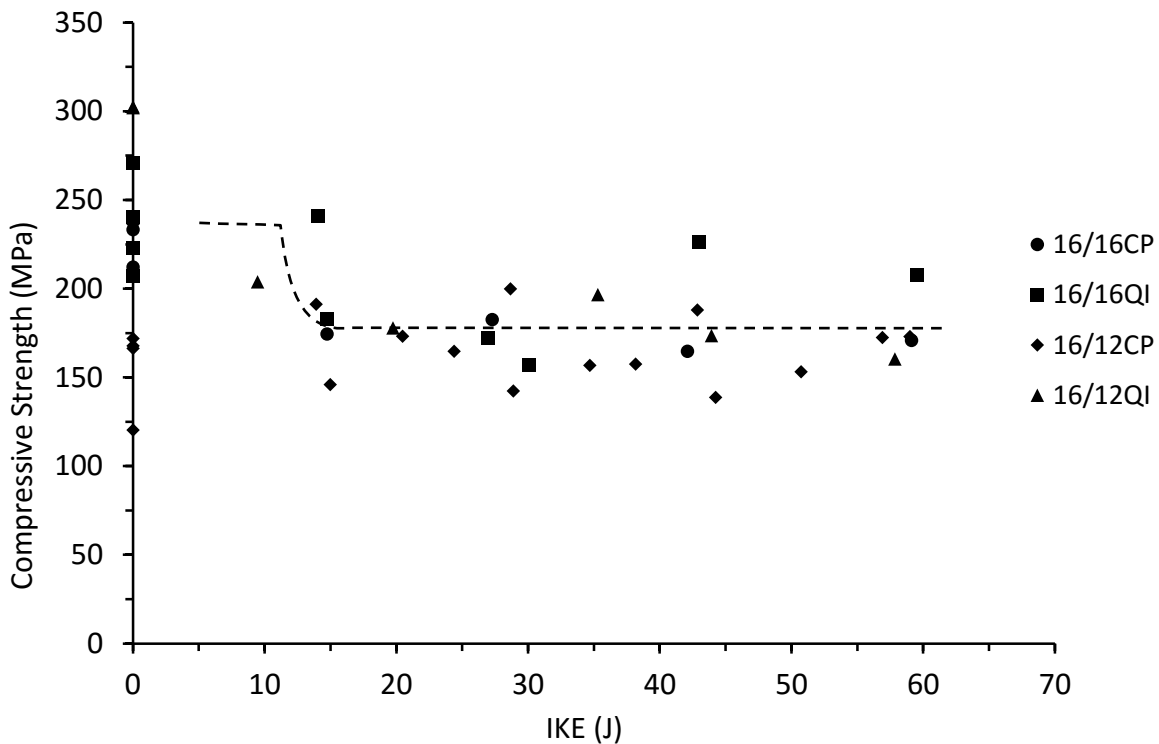


Figure 7.5.3 Compressive strength vs incident kinetic energy for thick symmetrical and unsymmetrical CP and QI carbon/epoxy panels with 70kg/m³ core density

7.6. Effects of core density on CAI strengths of carbon/epoxy skinned sandwich panels

In Figure 7.6.1 and Figure 7.6.2, the CAI strength data of thin sandwich panels with different core densities are compared. In the figures, the thin panels with 110kg/m³ core show much greater in-plane compressive resistance when impact damage was limited. This was very much expected, as core with the greater density increased the local flexural and TTT shear resistance in addition to the in-plane shear resistance of the panels. Nevertheless, once the skin delamination became substantial with the increase of IKE, the dominance of the skins in the in-plane compressive resistance took over and hence panels with the same or similar skins exhibited the same or similar CAI strengths. The further reduction of the CAI strength was again due to the occurrence of the fibre fracture mechanism. Finally, the damage tolerance of the 110kg/m³ panels was effective over a larger range of impact energies. This was due to the higher damage resistance of the core leading to reductions in delamination and core crush propagation, as well as delayed onset of fibre fracture, allowing for larger impacts to be absorbed in the panels, maintaining the CAI strength over a larger IKE range.

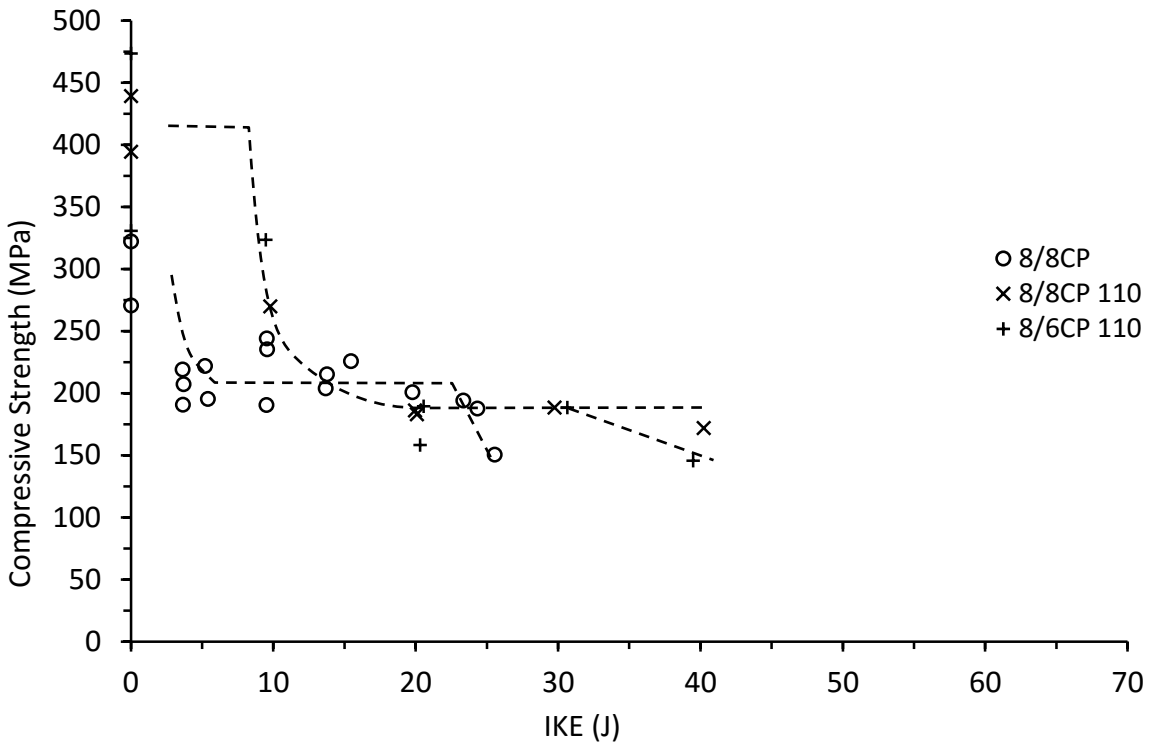


Figure 7.6.1. Compressive strength vs incident kinetic energy for thin symmetrical and unsymmetrical CP carbon/epoxy panels with 70 and 110kg/m³ core density

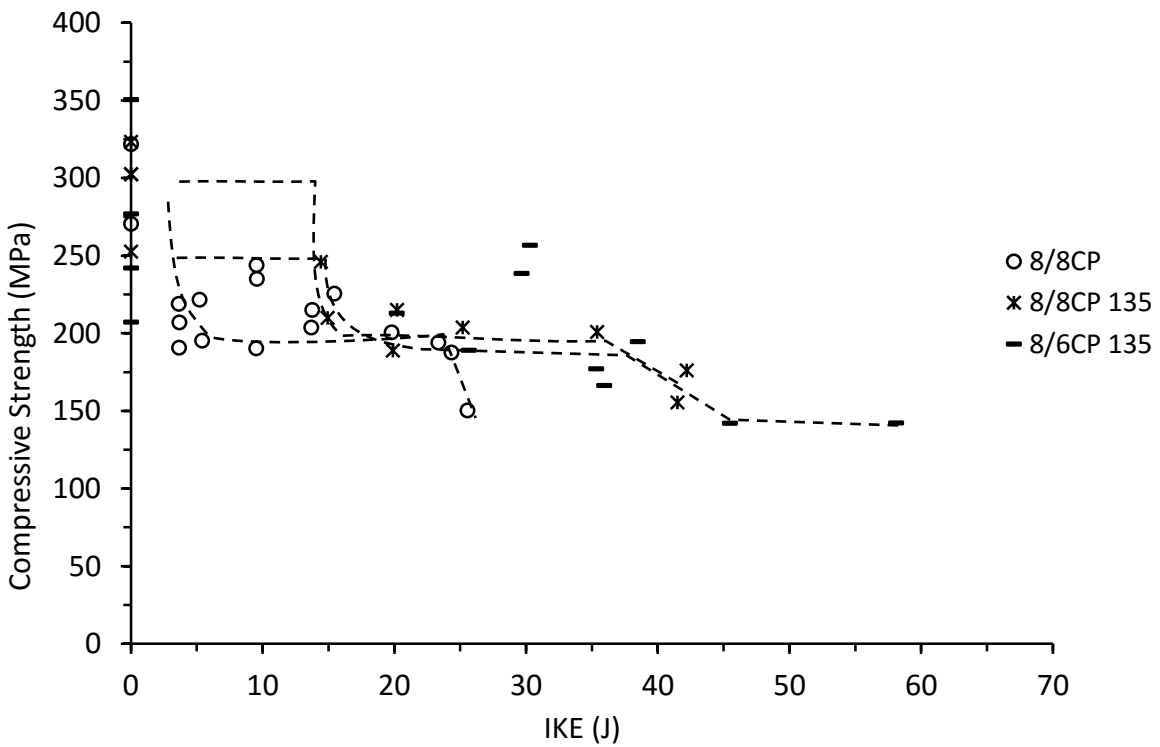


Figure 7.6.2. Compressive strength vs incident kinetic energy for thin symmetrical and unsymmetrical CP carbon/epoxy panels with 70 and 135kg/m³ core density

The effect of further increasing the core density up to 135kg/m^3 is also shown in Figure 7.6.1 and Figure 7.6.2. The decaying trend of their CAI strength values can be seen to be very similar to that of the sandwich panels with 110kg/m^3 core. That is, at the lower end (about 15J) of IKEs, the denser panels with the greater rigidities have shown much greater CAI strength values. After that, their CAI strengths values at the same IKE are the same when their CAI behaviour was dominated by delamination in the impacted skin. Yet again, the denser panels have demonstrated the greater damage tolerance with the same CAI strength for a much greater level of IKE. Increasing the core density as a means to increase the effective range of the damage tolerance of a panel over increasing the thickness of the skin offers a more weight effective design solution.

7.7. Effects of different skin material on CAI strengths

The CAI strength data of thin and thick symmetrical CP E-glass/epoxy panels with 70kg/m^3 core are shown in Figure 7.7.1-Figure 7.7.4. The overall CAI performance of the thin panels in terms of trend for the given IKE was very similar to that of the carbon/epoxy, which was slightly surprising. Further examining the CAI strength data in terms of the delamination extent in the impacted skin is seen in Figure 7.7.2. The E-glass/epoxy panels clearly suffered much less delamination than the carbon/epoxy panels, explaining why two of the five panels did not fail in the mid-section region, though their CAI strength values fortuitously fall on the trend. The overall CAI performance of the thick E-glass/epoxy panels was again similar to their carbon/epoxy counterparts, even though three out of the five panels did not fail in the mid-section region. Interestingly, those two panels that failed in the mid-section region have produced slightly greater CAI strength values (at 18J and 40J). Since the panel that was impacted at 18J failed in the mid-section, technically, those two impacted at 25J and 35J should also have failed in the mid-section region and hence their lower CAI stress values do not affect the trend. Moreover, the E-glass/epoxy panels are heavier and suffered less damage at the same given IKE but have not offered a greater damage tolerance performance.

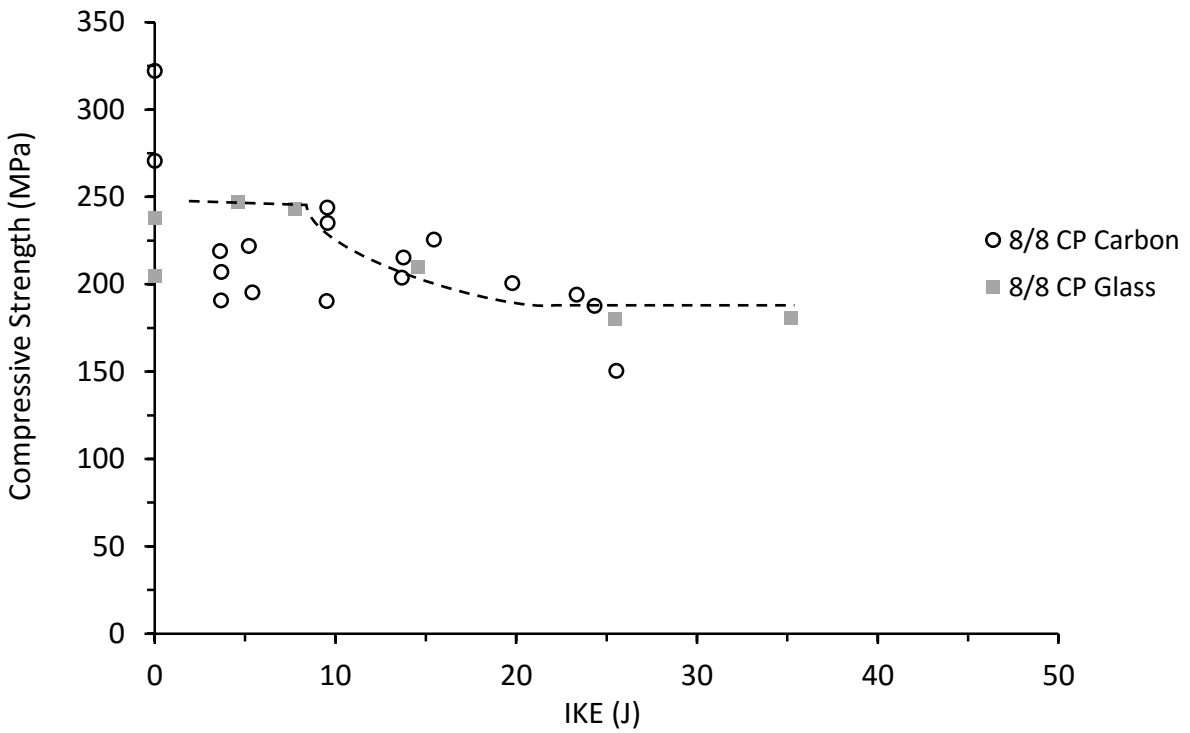


Figure 7.7.1. Compressive strength vs incident kinetic energy for thin symmetrical CP carbon and E-glass/epoxy panels with 70kg/m³ core density

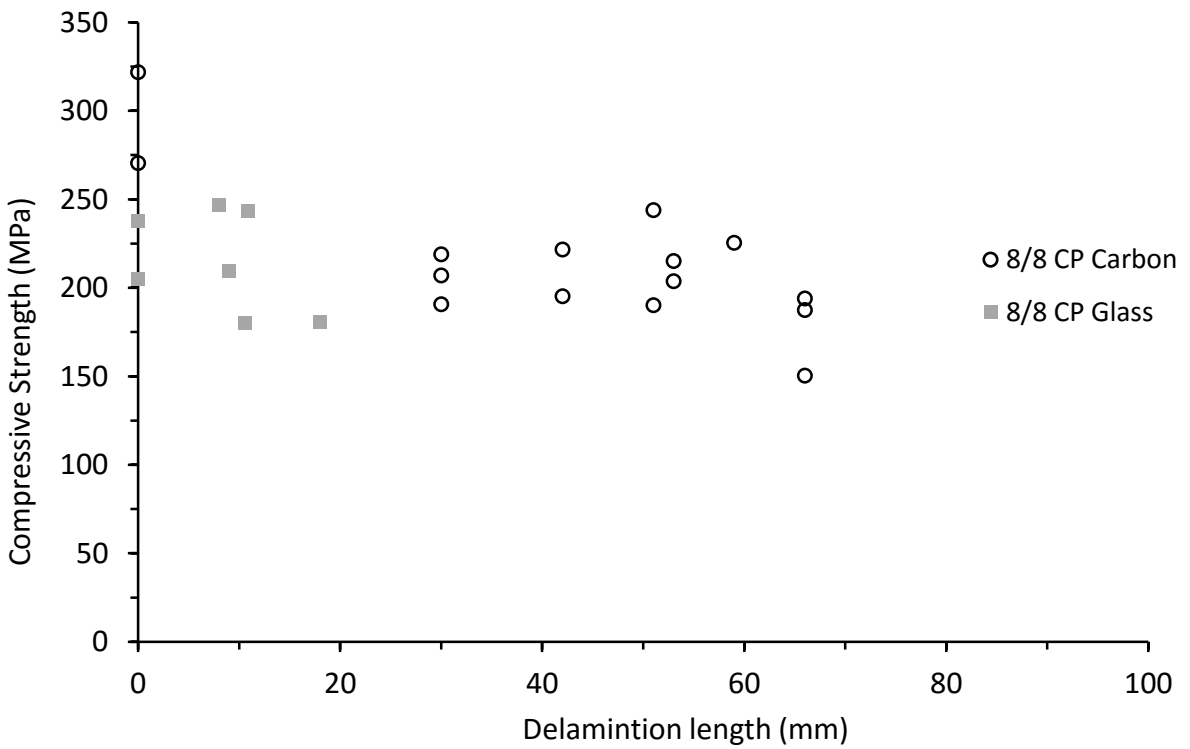


Figure 7.7.2. Compressive strength vs delamination length for thin symmetrical CP carbon and E-glass/epoxy panels with 70kg/m³ core density

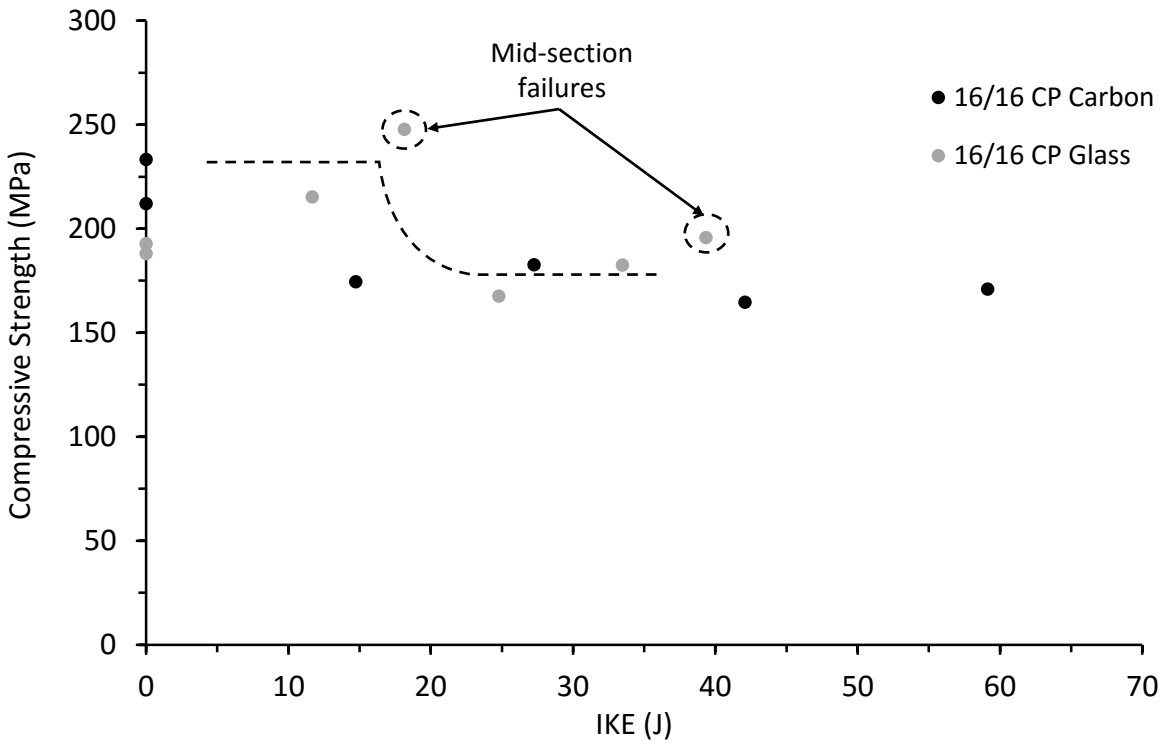


Figure 7.7.3. Compressive strength vs incident kinetic energy for thick symmetrical CP carbon and E-glass/epoxy panels with 70kg/m³ core density

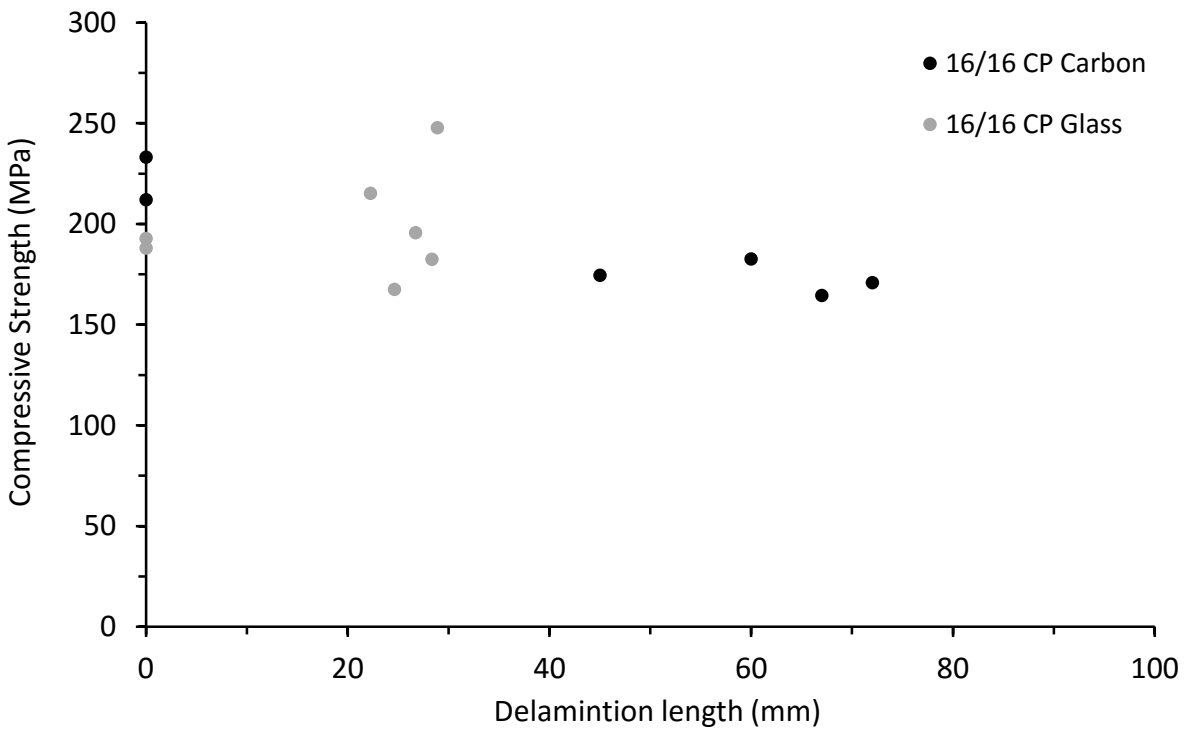


Figure 7.7.4. Compressive strength vs delamination length for thick symmetrical CP carbon and E-glass/epoxy panels with 70kg/m³ core density

7.8. Effects of removed core on CAI strengths of carbon/epoxy skinned sandwich panels

Core removed panels

The effect of removing portions of the core on the compressive strengths of thin and thick symmetrical and unsymmetrical CP and QI panels is shown below in Figure 7.8.1 and Figure 7.8.2. In the thin panels, a clear correlation exists between the reduction in compressive strength and the length of core removed from the panels. As shown from the strain responses in Section 7.2.2, the removal of plies from one skin created an uneven compressive resistance between the skins in the mid-section inducing a local bending moment, and without the cores stabilising presence, the mid-section became very susceptible to the in-plane compressive load, and led to a large reduction in compressive strength. For the panels with the larger section of core removed (40mm), this condition itself made the overwhelming contribution to their in-plane compressive behaviour, much greater than the effects of symmetry and skin lay-up. Therefore, their respective in-plane compressive strengths were much closer together. What is clear is that without the core support, the in-plane compressive strengths of the sandwich panels suffered very significantly.

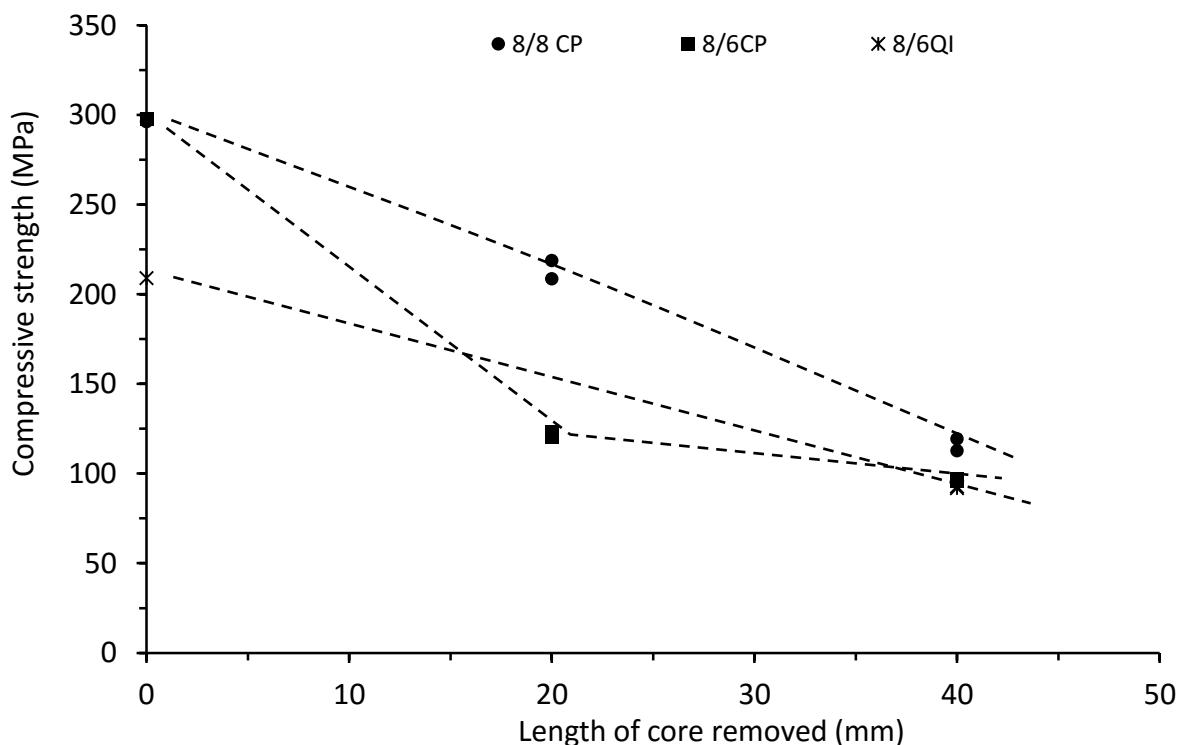


Figure 7.8.1. Compressive strengths of core removed thin symmetrical and unsymmetrical CP and QI carbon/epoxy panels with 70kg/m³ core density

For the thick symmetrical and unsymmetrical CP panels, the removal of 40mm length of core still dominated their in-plane compressive behaviour with more or less linear responses up to failure. The doubling of the skin thickness increased the local buckling resistance in the mid-section region,

resulting in a significantly higher compressive strength compared to the thin panels with the core removed.

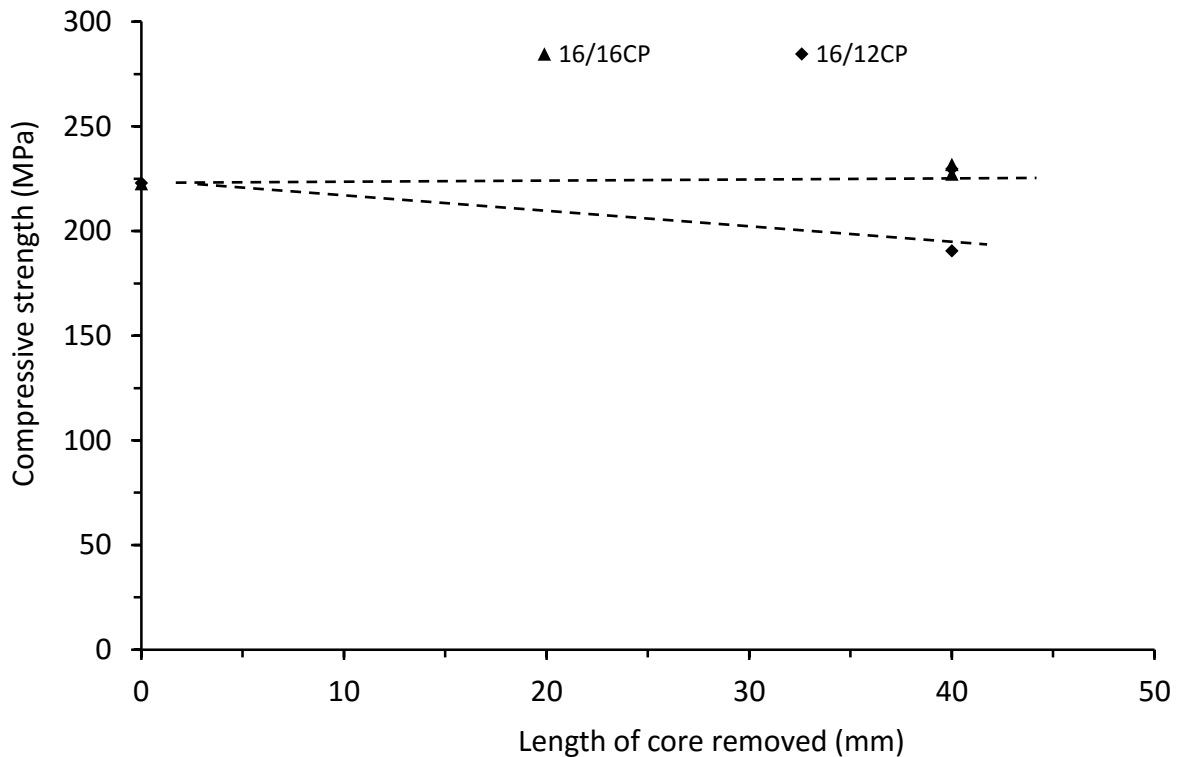


Figure 7.8.2. Compressive strengths of core removed of thick symmetrical and unsymmetrical CP carbon/epoxy panels with 70kg/m³ core density

Impacted core removed panels

In order to further examine the effects of core support on the in-plane compressive behaviour, four selected panels were impacted before the core was removed from them so that the skin conditions were identical to the impact damaged panels. The CAI strengths of thin symmetrical and unsymmetrical CP panels are shown below in Figure 7.8.3 and Figure 7.8.4 along with the CAI strength data from sandwich panels of the same skin configurations. It is conclusive from these figures that without the support of the core, the CAI strengths of the sandwich panels suffer significantly as the IKE is increased.

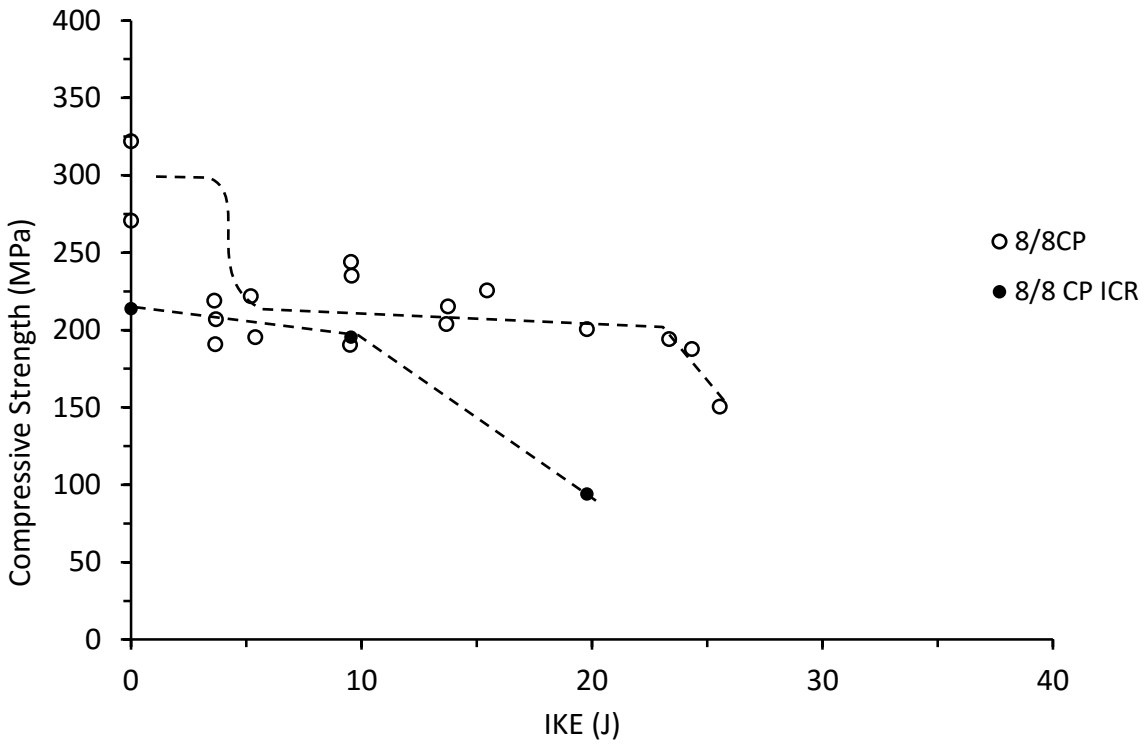


Figure 7.8.3. Compressive strength against IKE for thin symmetrical CP carbon/epoxy panels with and without 20mm of core removed

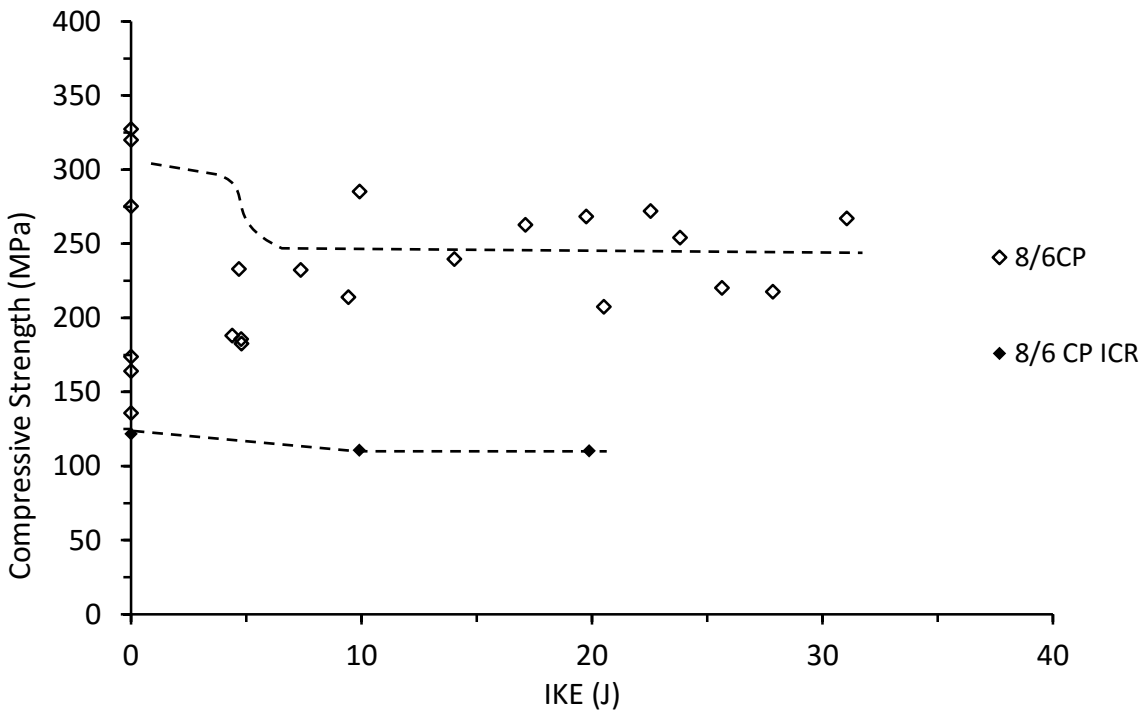


Figure 7.8.4. Compressive strength against IKE for thin unsymmetrical CP carbon/epoxy panels with and without 20mm of core removed

7.9. Effects of holes on CAI strengths of thin carbon/epoxy skinned sandwich panels

As an extreme condition opposite to the removal of the core, drilling a sufficiently large hole in the skin(s) could have a similar overwhelming effect on their in-plane compressive strengths, even though the hole diameter of 40mm is only 29% of the panel width. It can be seen in Figure 7.9.1 that the in-plane compressive strengths were reduced by the presence of hole(s). For panels with one hole in one skin, the unsymmetrical panel offered a much greater compressive strength than the symmetrical one. This suggests that the presence of the hole in the symmetrical panel introduced a significant shift of the local mid-plane and thus inducing a local bending moment, so that the panel failed earlier in compression. On the contrary, as mentioned in earlier sections, drilling a hole in the 8 ply skin of the unsymmetrical panel somewhat re-balanced the local in-plane compressive resistance, thereby not suffering a significant loss in compressive strength. For the two hole precondition, the difference between the compressive strengths was no longer there. This suggests that the overall effect of holes on the in-plane compressive strengths was much greater than the local imbalance induced due to the two ply difference in the two skins.

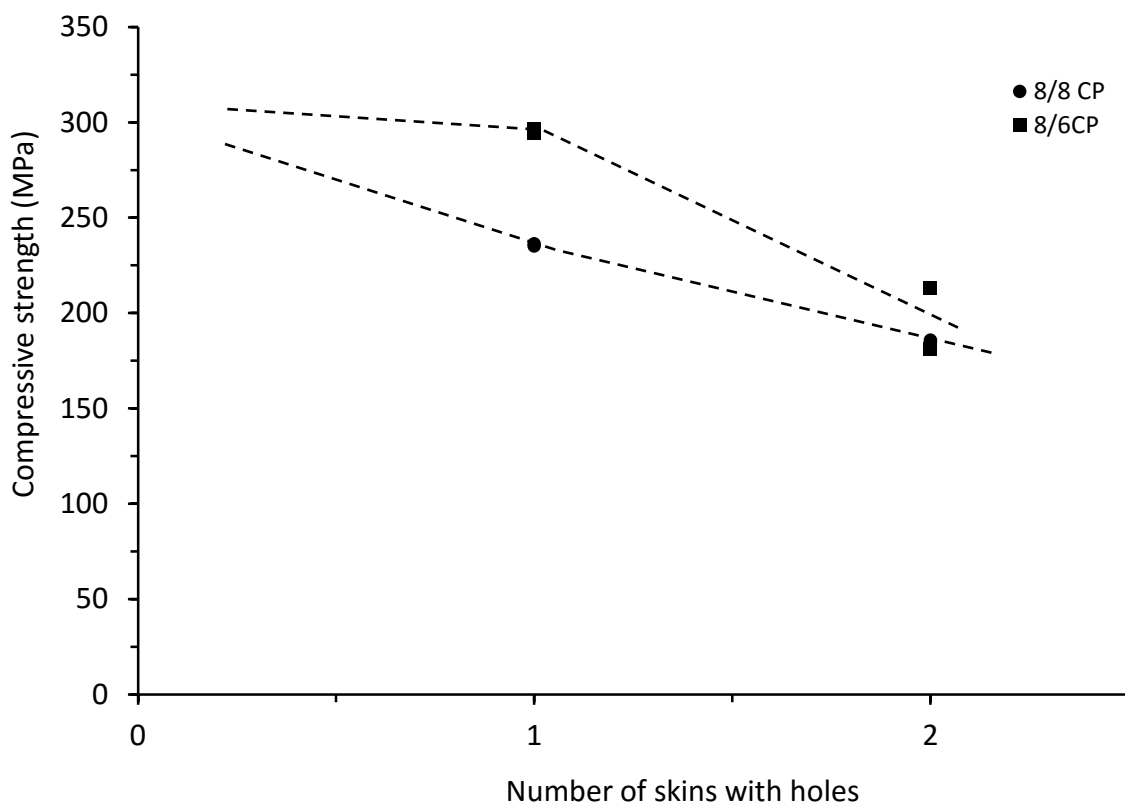


Figure 7.9.1. Compressive strengths of thin symmetrical and unsymmetrical CP carbon/epoxy panels with 40mm hole drilled in skins

7.10. Deformation interactions between skins and core under in-plane compression

To ultimately understand how the dominant characteristics of impact damage degrade the in-plane compressive strengths of the impact damaged sandwich panels, various extreme preconditions were introduced into the sandwich panels and their in-plane compressive behaviour have been examined along with the baseline and impact damaged panels. Although the definition of the in-plane compressive strength of sandwich panels takes into account only the cross-sectional area of two skins, it is never in doubt, as confirmed experimentally in the early sections, that the core of the sandwich contributes significantly to their in-plane compressive strengths, but it is completely unknown how this actually takes place. To this end, at one extreme, the core around the mid-section was removed simply to see how the two skins without the support of the core react to the in-plane compressive load. Moreover, one skin of some sandwich panels was impacted before the core was removed so that the skin conditions would be identical to those impacted panels compression tested with the core in place. At the other extreme, a sufficiently large hole(s) of 40mm diameter was/were drilled in the skin(s) to see how a significant reduction of the skin properties alone would affect their in-plane compressive strengths with the full support of the core.

The usual impact damage characteristics include material damage such as delamination and fibre fracture in addition to local curvature changes in the impacted area. The effects of these elements of the impact damage on the in-plane compressive strengths are generally coupled. They affect the in-plane shear, flexural and TTT resistances of the sandwich panels. Moreover, during in-plane compression, the lack of symmetry associated with the local curvature changes could induce further local bending moments. Whilst the in-plane shear resistance of the whole panel is critical to the transmission of the in-plane compressive load, the flexural and TTT resistance are critical to the in-plane compressive behaviour only around the mid-section region, especially the edge regions (or effective width). The introductions of the aforementioned preconditions in thin and thick as well as symmetrical and unsymmetrical sandwich panels were some preliminary efforts in an attempt to separate the effects of the two elements of the impact damage. With the central section of core being removed, the flexural and TTT resistance should be reduced significantly, whereas the in-plane shear resistance should not be affected. For panels with hole(s), the in-plane shear and flexural resistance should be reduced significantly, whereas the TTT resistance should be affected only marginally.

To facilitate the thorough understanding of the in-plane compressive behaviour of sandwich panels, aided with various preconditions, it is essential to establish the deformation sequence in terms of strain responses as shown in Figure 7.10.1(a)-(c), similar to that for monolithic laminate panels [87]. In this way, the interaction between skins and core during in-plane compression could be examined

before an analytical framework for predicting the in-plane compressive strength of sandwich panels could ultimately be developed. It is well known that a clamped sandwich panel with unloaded edges simply supported in Figure 7.10.1(a) and Figure 7.10.2(a) undergoes local buckling if its width-to-thickness ratio is sufficiently large, even though it was not the case in the present investigation due to the aforementioned reasons. For this local buckling to occur, the compressive load must be transmitted to the mid-section region by overcoming the in-plane shear rigidity and the transmitted load in turn overcomes the local flexural and TTT rigidities, as depicted in Figure 7.10.1(b) and Figure 7.10.2(b). Moreover, for this local buckling to induce instability, it must grow in the transverse direction into the edge regions or effective width, as illustrated in Figure 7.10.3. This crucial aspect is clearly demonstrated by the in-plane compressive behaviour of the core removed panels, in which the inward local buckling at the edge regions dictated the behaviour. Thus, the in-plane compressive load must be continued until the local buckling in a single half wave propagates and develops to two smaller half waves as illustrated in Figure 7.10.1(c) in the mid-section region. At this stage, the panel should fail across the width along the nodal line, which is where the two half waves meet in the mid-section. That is because the mode transition in the transverse direction should reach the edge regions.

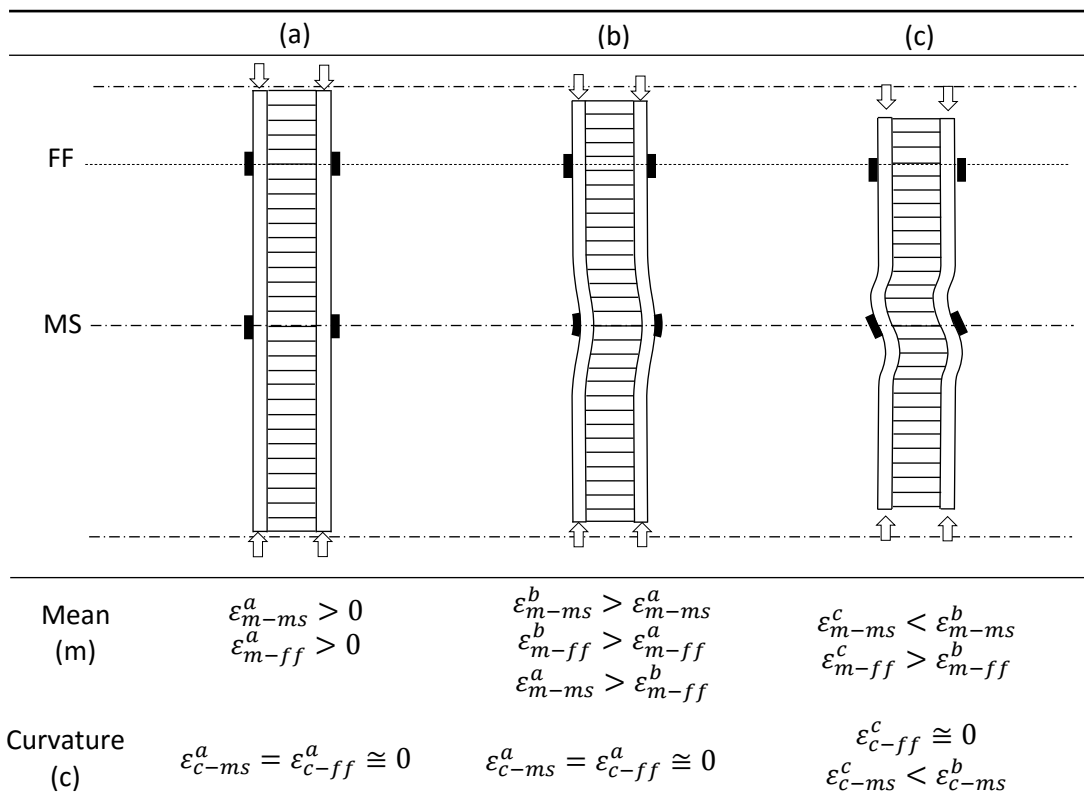


Figure 7.10.1. Illustration of the expected buckling deformation process of undamaged control panels under in-plane compression in the longitudinal loading direction

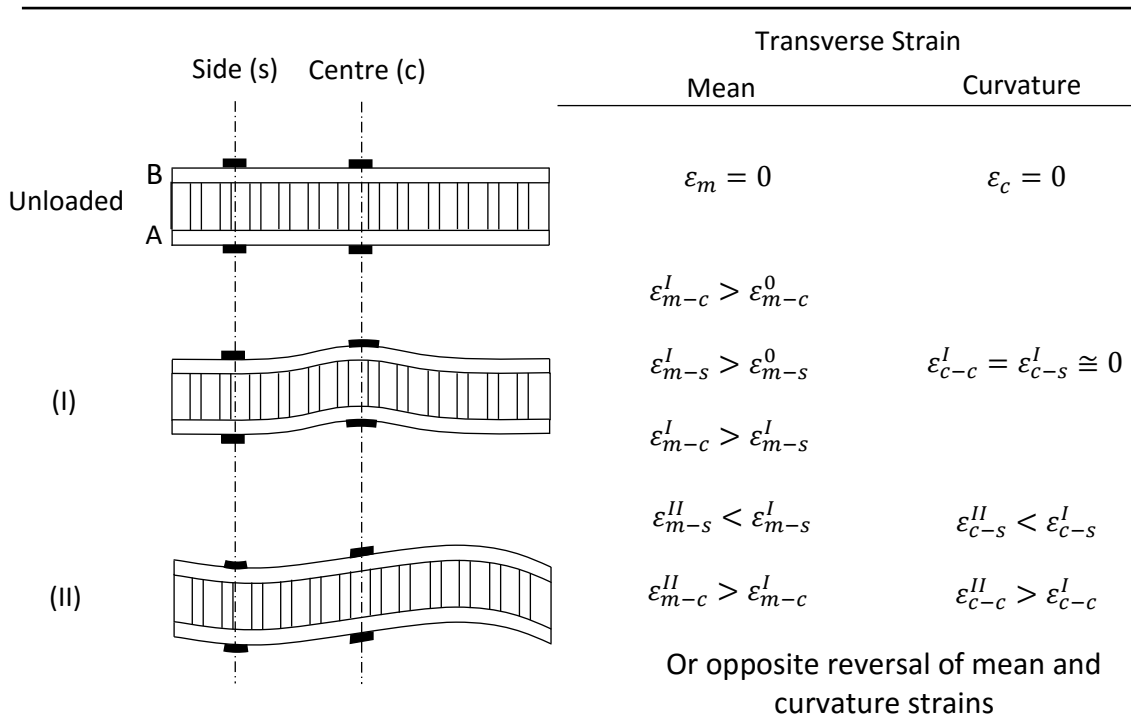


Figure 7.10.2. Illustration of the expected buckling deformation process of undamaged control panels under in-plane compression in the transverse direction

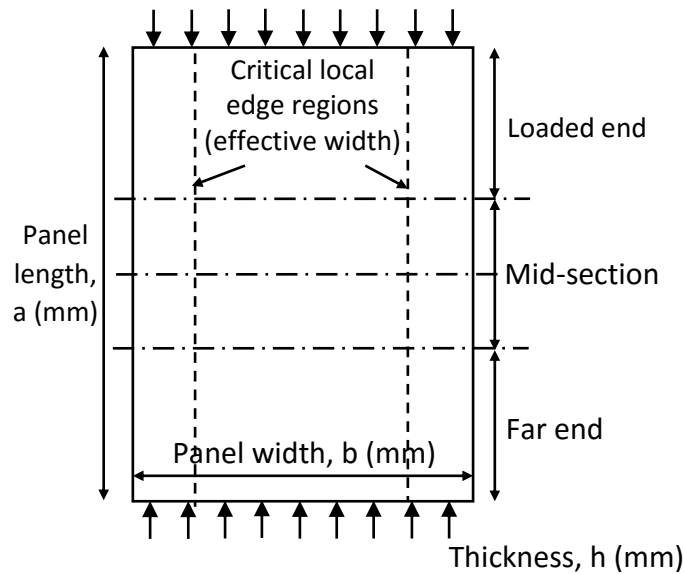


Figure 7.10.3. Illustration identifying panel regions, geometries, and critical regions

However, the present width-to-thickness ratio of the panel of between 8 and 10 was not large enough to allow the baseline panels and panels impacted at the very low IKEs to fail in the sequence as described above. In those cases, the compressive load transmitted to the mid-section was insufficient to overcome the local flexural rigidity and/or local TTT rigidity so that the panels became susceptible to stress concentrations at the loaded ends, leading to end crushing.

Clearly for the moderate and high IKEs, the localised impact damage in the mid-section region not only degraded the in-plane shear, local flexural and TTT shear rigidities, but also induced local curvature and un-even skin resistances which induced a local bending moment in the mid-section, further increasing the susceptibility to develop further local buckling in the mid-section. Hence, these impact damaged panels could follow the similar deformation sequence, as illustrated by Figure 7.10.4 (a) – (b) and Figure 7.10.5 (I) – (II). In particular, under the continued compressive load, the delaminated areas with the relatively large sizes could either continue to delaminate transversely or simply buckle outwards, whichever offers the least resistance. An additional perspective for the fact that the moderate and severer impact damage or a hole of 40mm diameter could induce the in-plane compressive failure is that the transverse size of the condition could be large enough to reach the critical edge regions of the mid-section region.

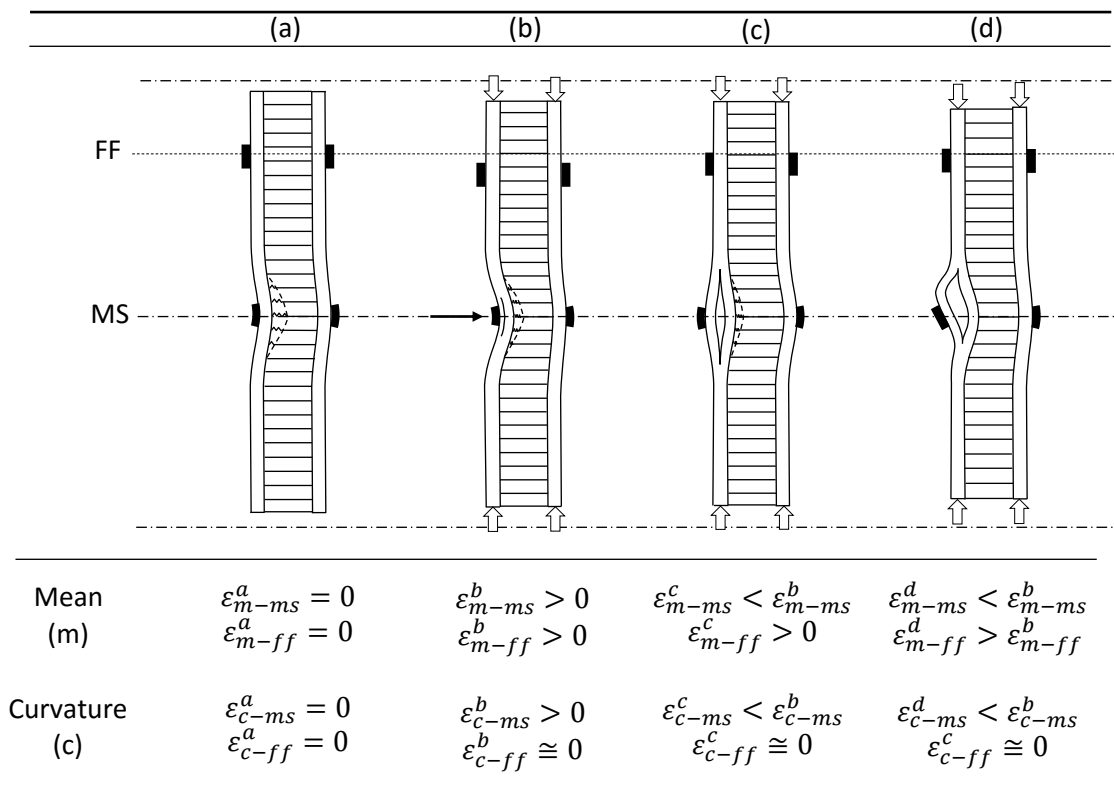


Figure 7.10.4. Illustration of the probable buckling deformation process of impact damaged panels under in-plane compression in the longitudinal loading direction.

Interestingly, the thin unsymmetrical panels have a pre-existing imbalance in in-plane shear rigidity and hence have an inherent bending moment. The preconditions such as impact damage and hole in the unsymmetrical panels could 'restore' the balance of weakened in-plane shear resistance. Consequently, their in-plane compressive strengths at the same IKEs could actually be greater than the thin symmetrical panels. For thick unsymmetrical panels, the effect of four ply difference on the

in-plane shear rigidity is much smaller so that thick unsymmetrical panels under in-plane compression behaved pretty much like the thick symmetrical panels.

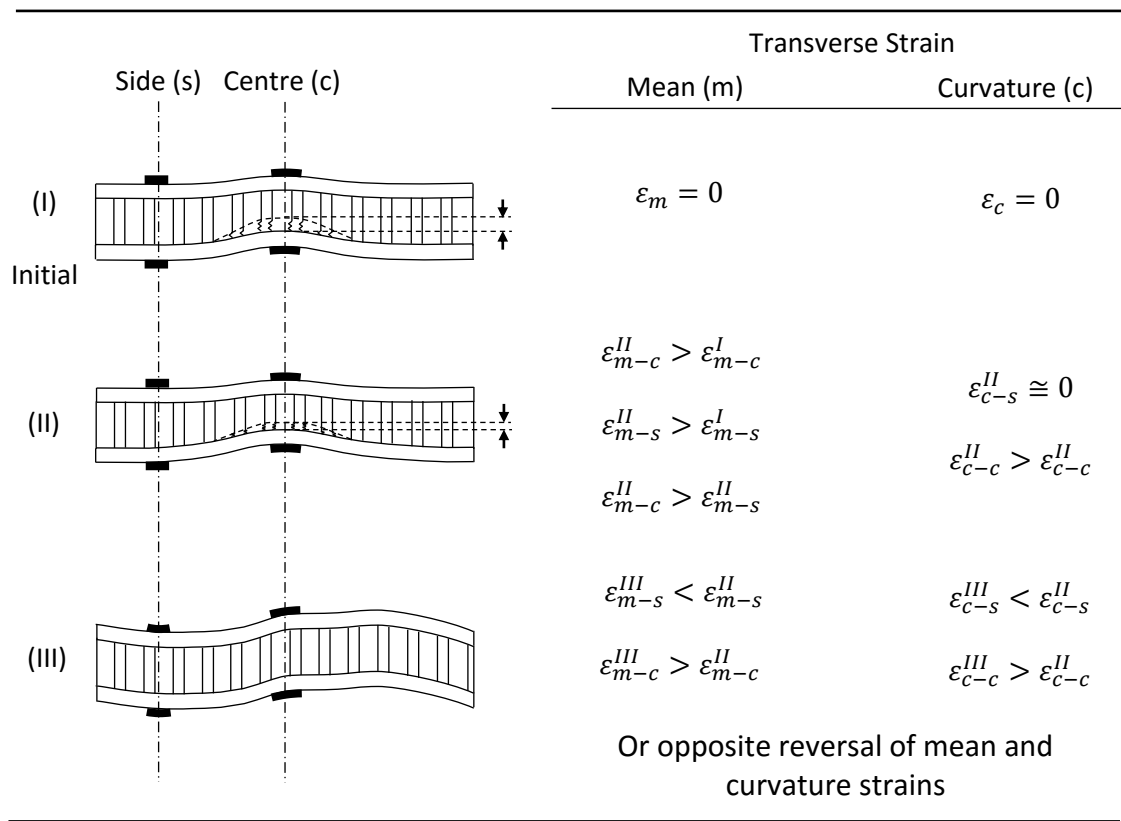


Figure 7.10.5. Illustration of the probable buckling deformation process of impact damaged panels under in-plane compression in the transverse loading direction.

The exclusive contribution of two skins to the in-plane compressive behaviour of the sandwich panels could be estimated further by comparing the average in-plane compressive strength of 216MPa from the thin symmetrical CP panels with 20mm core removed to the average in-plane compressive strength of 257MPa from 2mm thick monolithic QI laminates in [120]. The in-plane shear resistance of the sandwich panels should not be reduced a great deal by the removal of core of a short length, as the skins remained intact. However, the fact that the baseline panels could not fail in the mid-section region suggests that the in-plane shear resistance of the sandwich panels is much greater than its local buckling resistance so that the panels with the laterally unsupported skin portions of 20 mm length buckle and fail in in-plane compression eventually, therefore, imagining that to split the single 2mm thick laminate into two identical 1mm thick laminates spaced by the thickness of a core could increase the upper limit of the in-plane compressive strength.

This indicated that there were two significant contributions of the core. Firstly, the edge regions with intact core across the panel which contributed a significant amount to the compressive resistance under in-plane loading, as demonstrated by the core removal specimens. Yet, this could materialise

only if the in-plane shear resistance of the panels (including unsymmetrical ones) has already been weakened substantially by the presence of either substantial impact damage or hole(s) around the central part of the region so that the compressive load is able to be transmitted effectively to the mid-section region. An unsymmetrical weakening in the mid-section region also induces a local bending moment around the central part of the region, which reduces the local residual flexural rigidity further. Secondly, the influence of the core is apparent in the reduction of the effects of impact damage in the central mid-section of the panel, significantly reducing the levels of propagation of the impact damaged regions, opposing the de-stabilising effect of the damage mechanisms, which was clearly observed in the impacted panels with core removed before compression testing with delamination failure mechanisms being observed in the edge regions.

8. CONCLUSIONS AND RECOMMENDATIONS

8.1. Conclusions

The impact damage resistance and damage tolerance of composite sandwich panels with aluminium honeycomb core have been studied experimentally in addition to the in-plane compression of various preconditioned panels. These sandwich panels consist of carbon/epoxy skins of two different thicknesses, two different lay-ups and sandwich asymmetry, along with three different core densities; sandwich panels with translucent E-glass/epoxy skins were used purely for tracking the damage development generated at the two different phases (damage resistance and CAI testing).

All sandwich panels were manufactured using a two-step approach. That is, two skins in each panels were individually cured in an autoclave (first step), following manufacturer's instructions. Each skin-core bonding with a meshed adhesive was cured separately (second step) with the bonding line at the bottom of the curing set-up in an oven to ensure that the 'telegraphic effect' and resin dripping did not occur. Impact damage resistance testing was carried out using a bespoke instrumented drop-weight impact rig at low impact velocity over a range of IKEs for each sandwich configuration (group). The upper end IKE was decided for each sandwich configuration, when the occurrence of fibre fracture in the impacted skin was observed. In each test, impact force response history, impact and rebound velocities were measured, aided with the results of post-mortem measurements and diagnostic cross-sectioning of selected specimens, to develop an in-depth understanding of the onset and propagation of dominant damage mechanisms. The effects of skin thickness, material, asymmetry and lay-up and core density on their damage development were thus consistently evaluated quantitatively through an extensive set of 'damage maps'. All impact damaged and preconditioned panels were strain-gauged back-to-back at several strategically selected pivotal locations. After in-plane compression testing, their compressive responses in conjunction with in-situ photographic evidence and post-mortem observations were thoroughly interrogated to ascertain the occurrence of local buckling in a single half wave, its transition to two half waves and ultimate catastrophic failure. Their CAI and in-plane compressive strengths were used to establish several sets of 'damage tolerance maps', through which the reduction trends of the CAI strengths of all the panels were evaluated using IKE, delamination and crushed core extents and dent depth to ascertain how the presence of core affected the in-plane compressive resistance. Under these conditions, the following conclusions are reached:

(i) Two dominant damage mechanisms were a combination of delamination in the impacted skin and core crushing underneath and fibre fracture in the impacted skin plus more core crushing. In each panel group, the former occurred at all IKEs, whereas the latter occurred at the upper end of the IKE

range. While core crushing occurred in both in-plane and TTT directions, after the occurrence of fibre fracture, the crushing in the TTT direction became dominant. In thin panels with the denser cores (especially 135kg/m^3), some limited debonding occurred at the relatively high IKEs.

(ii) The increase in skin thickness did not alter the damage mechanisms in the sandwich panels but extended the capacity of the thick panels in dealing with IKE, as expected. Similarly, the change in skin lay-up did not alter the damage mechanisms. However, the delamination extent in thin panels with quasi-isotropic lay-up was 50% smaller than that of panels with cross-ply skins at the same IKEs in the mid to upper range of impact energies. The energy absorption by all panels was observed to be around 70% before the occurrence of fibre fracture and about 95% after, regardless of skin thickness, lay-up or material. The lack of symmetry in similar panels had the negligible effect on the nature of the damage mechanisms. Increasing the core density moderately (to 110 kg/m^3) yet again had little effect, similar to the lack of symmetry, and however, further increasing the density (to 135 kg/m^3), some limited debonding occurred at the relatively high IKEs. The effect of changing the skin material was substantial. Although not altering the damage mechanisms, the panels with E-glass/epoxy skins had delamination extent six times smaller at 15J and 25J impact energies than that of panels in carbon/epoxy skins.

(iii) All baseline panels with the width-to-thickness ratio of about 10 failed prematurely either near one of the loaded ends or through the end crushing. A few impact-damaged thick panels also failed in this way, unfortunately. While some (panels with thick skins) were due to limited degradation induced at the low IKEs, the remaining were associated with the panels with denser core. The remaining and overwhelming majority of the CAI panels plus all preconditioned panels failed in the mid-section.

(iv) Thin symmetrical panels of both lay-ups had the moderately greater CAI strengths than the thick symmetrical panels of the same configuration, using any damage tolerance measure. The respective effects of skin lay-up on the CAI strengths in both thin and thick symmetrical panels became marginal. I, it was found that when the narrow section of core was removed of the panels with still intact skins that their in-plane compressive strengths could be as low as those of the impact-damaged panels, if not lower. The fact that both thickness and lay-up effects were no more than being very moderate reflects that the influence of the skins in the mid-section region over the in-plane compressive resistance was substantially absorbed through their interaction with the same core.

(v) The unique contribution of the skin-core interaction to the in-plane compressive strengths was confirmed through the fact that the thin CP panels with denser cores (110kg/m^3 and 135kg/m^3)

showed the moderately greater CAI strengths than those with 70kg/m^3 core, as their TTT normal and shear resistances were greater, even though this indication faded when IKE levels went up.

(vi) The most significant unusual finding of the unsymmetrical panels was that rather than the well-established nonlinearly decaying trends for the CAI strengths the thin unsymmetrical panels showed the steady rising trend for their CAI strengths due possibly to the fact that the deleterious effects of the impact damage were evened out as the IKEs increased until fibre fracture occurred. The rest of the findings from the unsymmetrical panels were similar to those symmetrical panels, especially thick ones.

(vii) The in-plane compressive strengths of the core removed and impacted core removed thin panels were significantly smaller than those with holes in the skins. This finding shows that the core support at the compression resistance-critical areas (i.e. the edge regions in the mid-section region) is very significant to the in-plane compressive strength of any sandwich panel. In particular, without the core support at the resistance-critical areas, these in-plane compressive strengths of all the core removed panels with the intact skins were even slightly lower than the CAI strengths of the impact damaged panels, whose impacted skins were severely damaged.

8.2. Recommendations of further work

As a result of this research, a number of recommendations can be made for future work. In terms of impact damage resistance, one aspect that could be worthy pursuing is that different combinations of thicker (thus stiffer) skins with the denser cores such that 16 ply skin be used with a core density of 110kg/m^3 or in particular 135kg/m^3 to improve the sandwich performance to minimise the compatibility issue such as skin-core debonding.

In terms of CAI strength or impact damage tolerance, one key issue is for a baseline sandwich panel to have such width-to-thickness and AR ratios that it could fail in in-plane compression in the mid-section region. In this way, the valid baseline in-plane compressive strength could be obtained to make the impact damage tolerance assessment more complete and accurate. Nevertheless, pursuing this could mean to require increasing the width-to-thickness and AR ratios of each sandwich panel by 3.5 times. With the in-plane dimensions of around 675mm by 450mm, an overall cost of research investigation for the similar depth and scope could be too prohibitive to be practically realistic. The ultimate issue that should have been attempted in the present investigation is to establish an analytical model to predict the CAI strength for a given condition, which will be immensely valuable to a design stress analysis of sandwich structures.

9. REFERENCES

- [1]. Hill, M.D. 2007, "Damage resistance and tolerance of carbon/epoxy skinned honeycomb sandwich panels", PhD Thesis, Loughborough University.
- [2]. Bull, P.H. & Hallstrom, S. 2004, "High-Velocity and quasi-static impact of large sandwich panels", *Journal of Sandwich Structures and Materials*, vol. 6, no. 2, pp. 97-113.
- [3]. Vadakke, V. & Carlsson, L.A. 2004, "Experimental investigation of compression failure mechanisms of composite faced foam core sandwich specimens", *Journal of Sandwich Structures and Materials*, vol. 6, no. 4, pp. 327-342.
- [4]. Kepler, J. 2004, "Impact penetration of sandwich panels at different velocities - An experimental parameter study: Part II - Parameters and results", *Journal of Sandwich Structures and Materials*, vol. 6, no. 4, pp. 357-374.
- [5]. Kepler, J. 2004, "Impact penetration of sandwich panels at different velocities – An experimental parameter study: Part II – Interpretation of results and modelling", *Journal of Sandwich Structures and Materials*, vol. 6, no. 5, pp. 379-397.
- [6]. Erickson, M.D., Kallmeyer, A.R. & Kellogg, K.G. 2005, "Effect of temperature on the low-velocity impact behaviour of composite sandwich panels", *Journal of Sandwich Structures and Materials*, vol. 7, no. 3, pp. 245-264.
- [7]. Lee, J.Y. Shin, K.B. & Jeong, J.C. 2009, "Experimental and numerical simulation studies of low-velocity impact responses on sandwich panels for a BIMODAL tram", *Advanced Composite Materials*, vol. 18, no. 1, pp. 1-20.
- [8]. Shipsha, A. & Zenkert, D. 2005, "Compression-after-impact strength of sandwich panels with core crushing damage", *Applied Composite Materials*, vol. 12, no. 3-4, pp. 149-164.
- [9]. Tsotsis, T. & Lee, S. 1996, "Characterisation of localised failure modes in honeycomb sandwich panels using indentation", *Composite Materials: Testing and Design (Twelfth Volume)*, ASTM STP 1274, vol. 12, pp. 139-165.
- [10]. Koissin, V., Shipsha, A. & Skvortsov, V. 2009, "Compression strength of sandwich panels with sub-interface damage in the foam core", *Composites Science and Technology*, vol. 69, no. 13, pp. 2231-2240.
- [11]. Zenkert, D., Shipsha, A., Bull, P. & Hayman, B. 2005, "Damage tolerance assessment of composite sandwich panels with localised damage", *Composites Science and Technology*, vol. 65, no. 15–16, pp. 2597-2611.
- [12]. Williams, H.R., Trask, R.S. & Bond, I.P. 2008, "Self-healing sandwich panels: Restoration of compressive strength after impact", *Composites Science and Technology*, vol. 68, no. 15–16, pp. 3171-3177.
- [13]. Herup, E.J. & Palazotto, A.N. 1998, "Low-velocity impact damage initiation in graphite/epoxy/Nomex honeycomb-sandwich plates", *Composites Science and Technology*, vol. 57, no. 12, pp. 1581-1598.
- [14]. Anderson, T. & Madenci, E. 2000, "Experimental investigation of low-velocity impact characteristics of sandwich composites", *Composite Structures*, vol. 50, no. 3, pp. 239-247.
- [15]. Shin, K.B., Lee, J.Y. & Cho, S.H. 2008, "An experimental study of low-velocity impact responses of sandwich panels for Korean low floor bus", *Composite Structures*, vol. 84, no. 3, pp. 228-240.
- [16]. Davies, G.A.O., Hitchings, D., Besant, T., Clarke, A. & Morgan, C. 2004, "Compression after impact strength of composite sandwich panels", *Composite Structures*, vol. 63, no. 1, pp. 1-9.
- [17]. Akay, M. & Hanna, R. 1990, "A comparison of honeycomb-core and foam-core carbon-fibre/epoxy sandwich panels", *Composites*, vol. 21, no. 4, pp. 325-331.
- [18]. Besant, T., Davies, G.A.O. & Hitchings, D. 2001, "Finite element modelling of low velocity impact of composite sandwich panels", *Composites Part A: Applied Science and Manufacturing*, vol. 32, no. 9, pp. 1189-1196.
- [19]. Schubel, P.M., Luo, J. & Daniel, I.M. 2005, "Low velocity impact behaviour of composite sandwich panels", *Composites Part A: Applied Science and Manufacturing*, vol. 36, no. 10, pp. 1389-1396.

- [20]. Schubel, P.M., Luo, J. & Daniel, I.M. 2007, "Impact and post impact behaviour of composite sandwich panels", *Composites Part A: Applied Science and Manufacturing*, vol. 38, no. 3, pp. 1051-1057.
- [21]. Leijten, J., Bersee, H.E.N., Bergsma, O.K. & Beukers, A. 2009, "Experimental study of the low-velocity impact behaviour of primary sandwich structures in aircraft", *Composites Part A: Applied Science and Manufacturing*, vol. 40, no. 2, pp. 164-175.
- [22]. Baral, N., Cartié, D.D.R., Partridge, I.K., Baley, C. & Davies, P. 2010, "Improved impact performance of marine sandwich panels using through-thickness reinforcement: Experimental results", *Composites Part B: Engineering*, vol. 41, no. 2, pp. 117-123.
- [23]. Tomblin, J.S. 2004, "Damage resistance and tolerance of composite sandwich panels – Scaling effects", Report DOT/FAA/AR-03/75, USA.
- [24]. Nettles, A. & Jackson, J. 2010, "Compression after impact testing of sandwich composites for usage on expendable launch vehicles", *Journal of Composite Materials*, vol. 44, no. 6, pp. 707-738.
- [25]. Bhuiyan, M.A., Hosur, M.V. & Jeelani, S. 2009, "Low-velocity impact response of sandwich composites with nanophased foam core and biaxial braided face sheets", *Composites Part B: Engineering*, vol. 40, no. 6, pp. 561-571.
- [26]. Bull, P.H. & Edgren, F. 2004, "Compressive strength after impact of CFRP-foam core sandwich panels in marine applications", *Composites Part B: Engineering*, vol. 35, no. 6–8, pp. 535-541.
- [27]. Gustin, J., Joneson, A., Mahinfalah, M. & Stone, J. 2005, "Low velocity impact of combination Kevlar/carbon fibre sandwich composites", *Composite Structures*, vol. 69, no. 4, pp. 396-406.
- [28]. Ishai, O. & Hiel, C. 1992, "Damage tolerance of a composite sandwich with interleaved foam core", *Journal of Composites Technology and Research*, vol. 14, no. 3, pp. 155-168.
- [29]. Kassapoglou, C., Jonas, P.J. & Abbott, R. 1988, "Compressive strength of composite sandwich panels after impact damage: An Experimental and analytical study", *Journal of Composites Technology and Research*, vol. 10, no. 1, pp. 65-73.
- [30]. Kassapoglou, C. 1996, "Compression strength of composite sandwich structures after barely visible impact damage", *Journal of Composites Technology and Research*, vol. 18, no. 4, pp. 274-284.
- [31]. Lee, J.H., Cheong, S.K. & Shin, K.H. 2006, "Impact characteristics of a honeycomb sandwich panel", *Key Engineering Materials*, vol. 326-328, pp. 1761-1764.
- [32]. Meo, M., Vignjevic, R. & Marengo, G. 2005, "The response of honeycomb sandwich panels under low-velocity impact loading", *International Journal of Mechanical Sciences*, vol. 47, no. 9, pp. 1301-1325.
- [33]. Raju, K.S., Smith, B.L., Tomblin, J.S., Liew, K.H. & Guarddon, J.C. 2008, "Impact damage resistance and tolerance of honeycomb core sandwich panels", *Journal of Composite Materials*, vol. 42, no. 4, pp. 385-412.
- [34]. Raju, M., Reddy, C.R., Swamy, M.R.N., Giridhar, G., Srikanth, L., Prakash, M.R. & Rao, R. 2006, "Repair effectiveness studies on impact damaged sandwich composite constructions", *Journal of Reinforced Plastics and Composites*, vol. 25, no. 1, pp. 5-16.
- [35]. Vaidya, U.K., Ulven, C., Pillay, S. & Ricks, H. 2003, "Impact damage of partially foam-filled co-injected honeycomb core sandwich composites", *Journal of Composite Materials*, vol. 37, no. 7, pp. 611-626.
- [36]. Wen, H., Reddy, T., Reid, S. & Soden, P. 1998, "Indentation, penetration and perforation of composite laminates and sandwich panels under quasi-static and projectile loading", *Key Engineering Materials*, vol. 141-143, pp. 501-552.
- [37]. Xia, F. & Wu, X. 2010, "Study on impact properties of through-thickness stitched foam sandwich composites", *Composite Structures*, vol. 92, no. 2, pp. 412-421.
- [38]. Koissin, V., Shipsha, A. & Skvortsov, V. 2009, "Compression strength of sandwich panels with sub-interface damage in the foam core", *Composites Science and Technology*, vol. 69, no. 13, pp. 2231-2240.

- [39]. Edgren, F., Soutis, C. & Asp, L.E. 2008, "Damage tolerance analysis of NCF composite sandwich panels", *Composites Science and Technology*, vol. 68, no. 13, pp. 2635-2645.
- [40]. Williams, H.R., Trask, R.S. & Bond, I.P. 2008, "Self-healing sandwich panels: Restoration of compressive strength after impact", *Composites Science and Technology*, vol. 68, no. 15–16, pp. 3171-3177.
- [41]. Stapleton, S.E. & Adams, D.O. 2011, "Structural enhancements for increased energy absorption in composite sandwich structures", *Journal of Sandwich Structures and Materials*, vol. 13, no. 2, pp. 137-158.
- [42]. Moslemian, R., Quispitupa, A., Berggreen, C. & Hayman, B. 2012, "Failure of uniformly compression loaded debond damaged sandwich panels — an experimental and numerical study", *Journal of Sandwich Structures and Materials*, vol. 14, no. 3, pp. 297-324.
- [43]. Staal, R.A., Mallinson, G.D., Jayaraman, K. & Horrigan, D.P.W. 2009, "Predicting Failure Loads of Impact Damaged Honeycomb Sandwich Panels", *Journal of Sandwich Structures and Materials*, vol. 11, no. 2-3, pp. 213-244.
- [44]. Nanayakkara, A., Feih, S. & Mouritz, A.P. 2012, "Experimental impact damage study of a z-pinned foam core sandwich composite", *Journal of Sandwich Structures and Materials*, vol. 14, no. 4, pp. 469-486.
- [45]. Zheng, Q., Li, Z. & Wu, D. 2000, "Damage analysis of honeycomb core composite sandwich plate subjected low velocity impact", *Journal of Reinforced Plastics and Composites*, vol. 19, no. 1, pp. 58-68.
- [46]. Edgren, F., Asp, L.E. & Bull, P.H. 2004, "Compressive failure of impacted NCF composite sandwich panels - Characterisation of the failure process", *Journal of Composite Materials*, vol. 38, no. 6, pp. 495-514.
- [47]. Aminanda, Y., Castanié, B., Barrau, J. & Thevenet, P. 2009, "Experimental and numerical study of compression after impact of sandwich structures with metallic skins", *Composites Science and Technology*, vol. 69, no. 1, pp. 50-59.
- [48]. Henao, A., Carrera, M., Miravete, A. & Castejón, L. 2010, "Mechanical performance of through-thickness tufted sandwich structures", *Composite Structures*, vol. 92, no. 9, pp. 2052-2059.
- [49]. Nettles, A.T., Jackson, J.R. & Hodge, A.J. 2012, "Change in damage tolerance characteristics of sandwich structure with a Thermal Protection System (TPS)", *Journal of Composite Materials*, vol. 46, no. 2, pp. 211-226.
- [50]. Nettles, A., Hodge, A. & Jackson, J. 2011, "An Examination of the Compressive Cyclic Loading Aspects of Damage Tolerance for Polymer Matrix Launch Vehicle Hardware", *Journal of Composite Materials*, vol. 45, no. 4, pp. 437-458.
- [51]. Aviles, F. & Carlsson, L.A. 2006, "Experimental study of debonded sandwich panels under compressive loading", *Journal of Sandwich Structures and Materials*, vol. 8, no. 1, pp. 7-31.
- [52]. Zhang, G., Wang, B., Ma, L., Xiong, J., Yang, J. & Wu, L. 2013, "The residual compressive strength of impact-damaged sandwich structures with pyramidal truss cores", *Composite Structures*, vol. 105, no. 0, pp. 188-198.
- [53]. Park, H. & Kong, C. 2011, "A study on low velocity impact damage evaluation and repair technique of small aircraft composite structure", *Composites Part A: Applied Science and Manufacturing*, vol. 42, no. 9, pp. 1179-1188.
- [54]. Salehi-Khojin, A., Mahinfalah, M., Bashirzadeh, R. & Freeman, B. 2007, "Temperature effects on Kevlar/hybrid and carbon fibre composite sandwiches under impact loading", *Composite Structures*, vol. 78, no. 2, pp. 197-206
- [55]. Zhou, J., Hassan, M.Z., Guan, Z. & Cantwell, W.J. 2012, "The low velocity impact response of foam-based sandwich panels", *Composites Science and Technology*, vol. 72, no. 14, pp. 1781-1790.
- [56]. Crupi, V., Epasto, G. & Guglielmino, E. 2011, "Low-velocity impact strength of sandwich materials", *Journal of Sandwich Structures and Materials*, vol. 13, no. 4, pp. 409-426.
- [57]. Baba, B.O. 2013, "Impact response of sandwich beams with various curvatures and debonds", *Journal of Sandwich Structures and Materials*, vol. 15, no. 2, pp. 137-155.

- [58]. Li, Z., Zheng, Z. & Yu, J. 2013, "Low-velocity perforation behaviour of composite sandwich panels with aluminium foam core", *Journal of Sandwich Structures and Materials*, vol. 15, no. 1, pp. 92-109.
- [59]. Butukuri, R., Bheemreddy, V., Chandrashekhara, K. & Samaranayake, V. 2012, "Evaluation of low-velocity impact response of honeycomb sandwich structures using factorial-based design of experiments", *Journal of Sandwich Structures and Materials*, vol. 14, no. 3, pp. 339-361.
- [60]. Xia, F. & Wu, X. 2010, "Work on impact properties of foam sandwich composites with different structure", *Journal of Sandwich Structures and Materials*, vol. 12, no. 1, pp. 47-62.
- [61]. Du, L. & Jiao, G. 2009, "Indentation study of Z-pin reinforced polymer foam core sandwich structures", *Composites Part A: Applied Science and Manufacturing*, vol. 40, no. 6–7, pp. 822-829.
- [62]. Ávila, A.F., Carvalho, M.G.R., Dias, E.C. & da Cruz, D.T.L. 2010, "Nano-structured sandwich composites response to low-velocity impact", *Composite Structures*, vol. 92, no. 3, pp. 745-751.
- [63]. Hosur, M.V., Mohammed, A.A., Zainuddin, S. & Jeelani, S. 2008, "Processing of nanoclay filled sandwich composites and their response to low-velocity impact loading", *Composite Structures*, vol. 82, no. 1, pp. 101-116.
- [64]. Heimbs, S., Cichosz, J., Klaus, M., Kilchert, S. & Johnson, A.F. 2010, "Sandwich structures with textile-reinforced composite foldcores under impact loads", *Composite Structures*, vol. 92, no. 6, pp. 1485-1497.
- [65]. Xia, F. & Wu, X. 2010, "Study on impact properties of through-thickness stitched foam sandwich composites", *Composite Structures*, vol. 92, no. 2, pp. 412-421.
- [66]. Yang, F.J., Hassan, M.Z., Cantwell, W.J. & Jones, N. 2013, "Scaling effects in the low velocity impact response of sandwich structures", *Composite Structures*, vol. 99, no. 0, pp. 97-104.
- [67]. Zhou, J., Guan, Z.W. & Cantwell, W.J. 2013, "The impact response of graded foam sandwich structures", *Composite Structures*, vol. 97, no. 0, pp. 370-377.
- [68]. Wang, Z., Jing, L., Ning, J. & Zhao, L. 2011, "The structural response of clamped sandwich beams subjected to impact loading", *Composite Structures*, vol. 93, no. 4, pp. 1300-1308.
- [69]. Manes, A., Gilioli, A., Sbarufatti, C. & Giglio, M. 2013, "Experimental and numerical investigations of low velocity impact on sandwich panels", *Composite Structures*, vol. 99, pp. 8-18.
- [70]. Navarro, P., Aubry, J., Marguet, S., Ferrero, J.F., Lemaire, S. & Rauch, P. 2012, "Experimental and numerical study of oblique impact on woven composite sandwich structure: Influence of the firing axis orientation", *Composite Structures*, vol. 94, no. 6, pp. 1967-1972.
- [71]. Wang, J., Waas, A.M. & Wang, H. 2013, "Experimental and numerical study on the low-velocity impact behaviour of foam-core sandwich panels", *Composite Structures*, vol. 96, no. 0, pp. 298-311.
- [72]. Othman, A.R. & Barton, D.C. 2008, "Failure initiation and propagation characteristics of honeycomb sandwich composites", *Composite Structures*, vol. 85, no. 2, pp. 126-138.
- [73]. Serrano-Perez, J.C., Vaidya, U.K. & Uddin, N. 2007, "Low velocity impact response of autoclaved aerated concrete/CFRP sandwich plates", *Composite Structures*, vol. 80, no. 4, pp. 621-630.
- [74]. Lascoup, B., Aboura, Z., Khellil, K. & Benzeggagh, M. 2010, "Impact response of three-dimensional stitched sandwich composite", *Composite Structures*, vol. 92, no. 2, pp. 347-353.
- [75]. Boyle, M.P., Roberts, J.C., Wienhold, P.D., Bao, G. & White, G.J. 2001, "Experimental, numerical, and analytical results for buckling and post-buckling of orthotropic rectangular sandwich panels", *Composite Structures*, vol. 52, no. 3–4, pp. 375-380.
- [76]. Christopherson, J., Mahinfalah, M., Jazar, G.N. & Aagaah, M.R. 2005, "An investigation on the effect of a small mass impact on sandwich composite plates", *Composite Structures*, vol. 67, no. 3, pp. 299-306.
- [77]. Fagerberg, L. 2004, "Wrinkling and compression failure transition in sandwich panels", *Journal of Sandwich Structures and Materials*, vol. 6, no. 2, pp. 129-144.
- [78]. Gustin, J., Joneson, A., Mahinfalah, M. & Stone, J. 2005, "Low velocity impact of combination Kevlar/carbon fibre sandwich composites", *Composite Structures*, vol. 69, no. 4, pp. 396-406.

- [79]. Lagace, P.A. & Mamorini, L. 2000, "Factors in the compressive strength of composite sandwich panels with thin face sheets", *Journal of Sandwich Structures and Materials*, vol. 2, no. 4, pp. 315-330.
- [80]. Mahfuz, H., Islam, S., Saha, M., Carlsson, L. & Jeelani, S. 2005, "Buckling of sandwich composites; effects of core/skin debonding and core density", *Applied Composite Materials*, vol. 12, no. 2, pp. 73-91.
- [81]. Soutis, C. & Spearing, S.M. 2002, "Compressive response of notched, woven fabric, face sheet honeycomb sandwich panels", *Plastics, Rubber and Composites*, vol. 31, no. 9, pp. 392-397.
- [82]. Thomsen, O.T. & Banks, W.M. 2004, "An improved model for the prediction of intra-cell buckling in CFRP sandwich panels under in-plane compressive loading", *Composite Structures*, vol. 65, no. 3-4, pp. 259-268.
- [83]. Thomson, R.S. & Mouritz, A.P. 1999, "Skin wrinkling of impact damaged sandwich composite", *Journal of Sandwich Structures and Materials*, vol. 1, no. 4, pp. 299-322.
- [84]. Turner, K.M. & Vizzini, A.J. 2004, "Response of impacted sandwich panels with integral stiffeners", *Journal of Sandwich Structures and Materials*, vol. 6, no. 4, pp. 313-326.
- [85]. Wadee, M.A. 1999, "Experimental evaluation of interactive buckle localization in compression sandwich panels", *Journal of Sandwich Structures and Materials*, vol. 1, no. 3, pp. 230-254.
- [86]. Abrate, S. 1997, "Localized impact on sandwich structures with laminated facings", *Applied Mechanics Reviews*, vol. 50, no. 2, pp. 69-82.
- [87]. Zhou, G. & Rivera, L.A. 2005, "Investigation for the reduction of in-plane compressive strength in preconditioned thin composite panels", *Journal of Composite Materials*, vol. 39, no. 5, pp. 391-422.
- [88]. Zhou, G. & Rivera, L.A. 2007, "Investigation on the reduction of in-plane compressive strength in thick preconditioned composite panels", *Journal of Composite Materials*, vol. 41, no. 16, pp. 1961-1994.
- [89]. Zhou, G. & Hill, M.D. 2009, "Impact damage and energy-absorbing characteristics and residual in-plane compressive strength of honeycomb sandwich panels", *Journal of Sandwich Structures and Materials*, vol. 11, no. 4, pp. 329-356.
- [90]. Zhou, G., Hill, M. & Hookham, N. 2007, "Investigation of parameters governing the damage and energy absorption characteristics of honeycomb sandwich panels", *Journal of Sandwich Structures and Materials*, vol. 9, no. 4, pp. 309-342.
- [91]. Tomblin, J.S. 1999, "Review of damage tolerance for composite sandwich airframe structures", Report DOT/FAA/AR-99/49, USA.
- [92]. Czabaj, M., Zehnder, A., Eisenberg, D., Singh, A. & Davidson, B. 2010, "Compression after impact of sandwich composite structures: experiments and modelling", American Institute of Aeronautics and Astronautics.
- [93]. McQuigg T.D., Kapania R.K., Scotti S.J., and Walker S.P. 2012, "Compression after impact on honeycomb core sandwich panels with thin face sheets, Part 1: Experiments" Fifty third AIAA/ASME/ASCE/AHS/ASC Structures, Structural Dynamics and Materials Conference.
- [94]. Tomblin, J.S., Raju, K.S., Liew, J. and Smith, B.L. 2001, "Impact damage characterisation and damage tolerance of composite sandwich airframe structures", Report DOT/FAA/AR-00/44, USA.
- [95]. Tomblin, J.S., Raju, K.S., Liew, J. and Smith, B.L. 2002, "Impact damage characterization and damage tolerance of composite sandwich airframe structures – Phase II", Report DOT/FAA/AR-02/80, USA.
- [96]. Zhou, G., Hill, M., Loughlan, J. & Hookham, N. 2006, "Damage Characteristics of Composite Honeycomb Sandwich Panels in Bending under Quasi-static Loading", *Journal of Sandwich Structures and Materials*, vol. 8, no. 1, pp. 55-90.
- [97]. Sharma, S.C., Narasimha Murthy, H.N. & Krishna, M. 2004, "Low-velocity impact response of polyurethane foam composite sandwich structures", *Journal of Reinforced Plastics and Composites*, vol. 23, no. 17, pp. 1869-1882.

- [98]. Hoo Fatt, M.S. & Park, K.S. 2001, "Dynamic models for low-velocity impact damage of composite sandwich panels – Part A: Deformation", *Composite Structures*, vol. 52, no. 3–4, pp. 335-351.
- [99]. Dost, E.F., Ilcewicz, L.B., and Avery, W.B. 1991, "The effects of stacking sequence on impact damage resistance and residual strength for quasi-isotropic laminates", *Composite Materials: Fatigue and Fracture*, ASTM STP 1110.
- [100]. Liu, D. 1988, "Impact-induced delamination—A view of bending stiffness mismatching", *Journal of Composite Materials*, vol. 22, no. 7, pp. 674-692.
- [101]. McGowan, D.M. & Ambur, D.R. 1998, "Damage characteristics and residual strength of composite sandwich panels impacted with and without compression loading", 39th AIAA/ASME /ASCE/AHS/ASC Structures, Structural Dynamics and Materials Conference, Paper No. 98-1783.
- [102]. McGowan, D.M., Ambur, D.R. 1997, "Damage-tolerance characteristics of composite fuselage sandwich structures with thick face sheets", NASA Technical Memorandum 110303.
- [103]. Anon. 2007, "Standard test method for edgewise compressive strength of sandwich constructions", ASTM C364/C364M – 07.
- [104]. Anon. 2011, "Standard test method for flatwise compressive properties of sandwich cores", C365/C365M - 11a.
- [105]. Anon. 2012, "Standard test method for measuring the damage resistance of a fibre-reinforced polymer-matrix composite to a concentrated quasi-static indentation force", D6264/D6264M – 12.
- [106]. Anon. 2005, "Standard test method for measuring the damage resistance of a fibre-reinforced polymer matrix composite to a drop-weight impact event", ASTM D7136/D7136M - 15.
- [107]. Anon. 2005, "Standard test method for compressive residual strength properties of damaged polymer matrix composite plates", ASTM D7137/D7137M – 12.
- [108]. Anon. 1983, "Standard tests for toughened resin composites", NASA reference publication 1092.
- [109]. Anon. 2009, "Carbon-fibre-reinforced plastics – Determination of compression-after-impact-properties at a specific impact-energy levels", BS ISO 18352:2009.
- [110]. Anon. 2011, "Standard Test method for core shear properties of sandwich constructions by beam flexure", ASTM C393/C393M – 11.
- [111]. Anon. 2011, "Standard practice for damage resistance testing of sandwich constructions", ASTM D7766/D7766M-11
- [112]. Anon. 2013, "Standard test method for short-beam strength of polymer matrix composite materials and their laminates", ASTM D2344/D2344M – 13.
- [113]. Anon. 2014, "Standard test method for tensile properties of polymer matrix composite materials", ASTM D3039/D3039M – 14.
- [114]. Anon. 2008, "Standard test method for compressive properties of polymer matrix composite materials with unsupported gage section by shear loading", ASTM D3410/D3410M – 03(2008)
- [115]. Anon. 2013, "Standard test method for in-plane shear response of polymer matrix composite materials by tensile test of a $\pm 45^\circ$ laminate", ASTM D3518/D3518M – 13.
- [116]. Anon. 2015, "Standard test method for in-plane shear response of polymer matrix composite materials by tensile test of a $\pm 45^\circ$ laminate", ASTM D790 – 15.
- [117]. Anon. 2002, *Military Handbook - MIL-HDBK-17-3F: Composite Materials Handbook, Volume 3 - Polymer Matrix Composites Materials Usage, Design, and Analysis*.
- [118]. Anon. "Recommended test method for compression after impact properties of oriented fibre-resin composites", SACMA, SRM 2-88.
- [119]. Airbus Industries Test Method 1-0010. "Fibre reinforced plastics - Determination of compression strength after impact", ISO 179 / EN 6038.
- [120]. Lloyd, J.C., 2002, "Impact damage and damage tolerance of fibre reinforced advanced composite laminate structures", PhD thesis, Loughborough University.
- [121]. Ratcliffe, J., Jackson, W., Schaff J., 2004, "Predicting the compression strength of impact-damaged sandwich panels", *Proceedings of the American Helicopter Society 60th Annual Forum*, Baltimore, MD.

- [122]. Cytec Industrial Materials, "<https://www.cytec.com/sites/default/files/datasheets/VTA260.pdf>", VTA-260 adhesive properties.
- [123]. Hexcel, "<http://www.hexcel.com/resources/honeycomb-data-sheets>", Hexweb™ 5052 Alloy Hexagonal Aluminium Honeycomb data sheets.
- [124]. Zhou, G., 2008 "Principles of composite materials & structures", Loughborough University, Departmental Publication.

APPENDIX A

Laminate skin manufacture

Skin lay-up procedure

1. Gloves were to be worn at all times when handling the prepreg material to avoid contamination from grease from fingers, allows for easier handling and protects the skin from the resin when at room temperature. All surfaces used must be cleaned using Propanol to remove dust and grease.
2. Remove the carbon or glass fibre prepregs roll from the freezer immediately prior to cutting.
3. Using the guillotine for 0° and 90° plies mark and cut a length of 300mm in the fibre direction, ensuring that the manufactured edge of the prepregs material is aligned parallel to the fibre direction using the guides on the guillotine. For glass/epoxy UD prepregs (430mm wide), rotate the ply 90° and cut the width down to 300mm. Cut the required number of plies for the intended lay-up, mark the 0° direction for easy reference and return each ply to the freezer prior to laying up.
4. For ±45° carbon/epoxy plies, using a pen, set-square and a ruler, accurately mark out the semi-diamond shape across the 300mm width prepregs roll. Cut the shape using a sharp Stanley knife blade, ensuring to keep the blade at an acute angle to the material to ensure the fibres are cut cleanly, and do not drag across with the blade. Using tape, attach an additional triangle material to complete the diamond, ensuring that the fibre orientations match and there is no gap between the two pieces.
5. Return the roll to the freezer, creating as air tight a seal on the bag to keep the moisture out of the prepregs roll.
6. To keep accurate track of the number and orientation of plies whilst laying up, prepare a simple tick sheet before the laminate is laid up (example shown in Table 2.2.1). To avoid compounding errors in laying up or wasting significant amounts of material, the laminates are to be laid up in smaller sub-laminates of 4 plies (8 and 16 ply laminates) or 3 plies (6 or 12 ply laminates) at a time.
7. Remove one ply from the freezer, and remove the white paper backing sheet, and place the ply down on the table with the other backing sheet facing down and orientate it in the required direction. Tick this off on the sheet.
8. Remove the next ply from the freezer ensuring the fibre direction is as required from the tick sheet, and once again remove the white paper backing sheet.
9. Using the perpendicular aluminium guides on the lay-up table, carefully place the 2nd ply on top of the 1st ply, ensuring all edges are in line. Smooth out any air bubbles that get trapped between the plies.
10. Repeat until the sub-laminate is complete, mark the bottom left corner to maintain orientation in the aluminium guides, the laminate 0° direction, and the fibre direction of the top ply, and return to the freezer.
11. Repeat steps 7-10 for each sub-laminate.
12. For thin laminates (6 or 8 ply), remove both sub-laminates from the freezer, remove the top brown wax paper backing sheet from the bottom sub-laminate and place between the guides on the lay-up table. Remove the bottom brown wax paper backing sheet from the top sub-laminate, and place on top of the other making sure the central ply orientations match at the mid-plane, ensuring the edges are in line in both the 0° and 90° directions.
13. For thick laminates (12 or 16 ply), remove 2 sub-laminates from the freezer, and remove the top brown wax paper backing sheet from the bottom sub-laminate and place between the guides on the lay-up table. Remove the bottom brown wax paper backing sheet from the top

sub-laminate and place on top of the other making sure the fibre orientations of the plies at the interface match the tick sheet, creating one half of the laminate.

14. Repeat step 13 to create the second half of the laminate.
15. To complete the thick laminate, repeat step 12 for the two thicker half sub-laminates.
16. Mark on the backing sheet of the top ply the laminate thickness, the lay-up configuration and the 0° fibre direction.
17. Return the completed laminate to the freezer prior to curing.

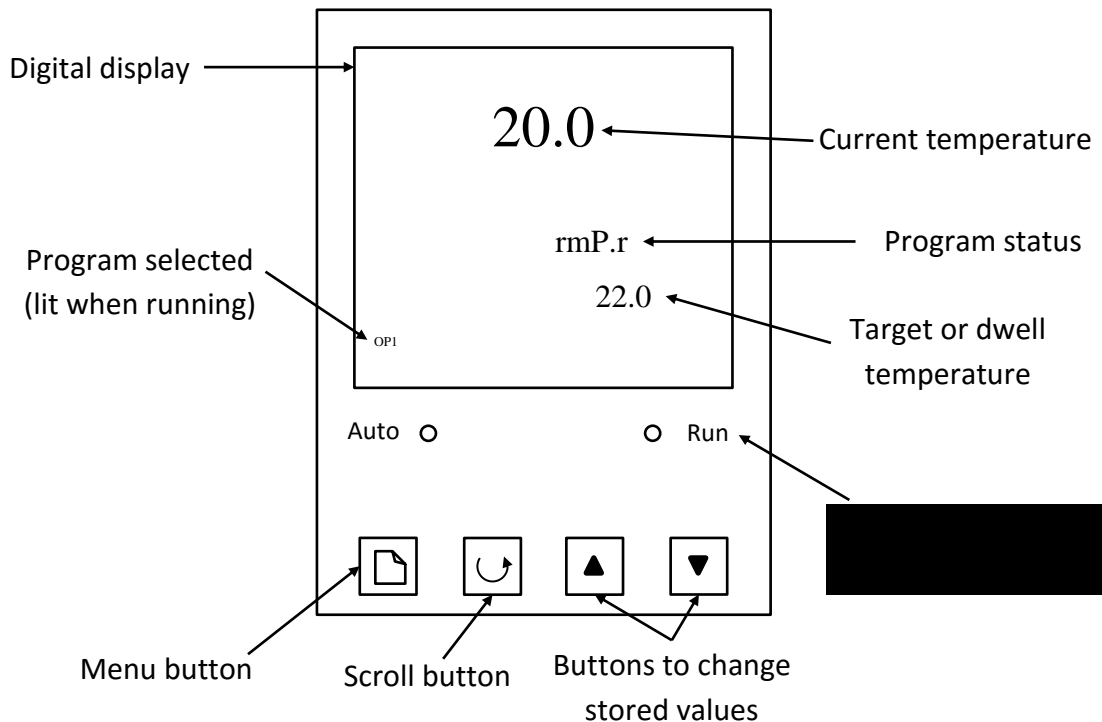
Curing procedure

1. Before removing the laminate from the freezer, a number of consumable and non-consumable materials need to be prepared. A diagram of the autoclave chamber containing the consumables is shown in Figure 2.2.7
2. Cut the following materials:
 - 2 x porous PTFE 340mm x 340mm (Consumable)
 - 2/4 x Bleeder Fabric 340mm x 340mm (Consumable)
 - 1 x Bagging Film 330mm x 330mm (Consumable)
 - 1 x Bagging Film 650mm x 650mm (Non-Consumable)
 - 1 x Breather Fabric 350mm x 350mm (Non-Consumable)
 - 1 x non-porous brown PTFE 450mm x 450mm (Non-Consumable)
3. Remove the laminate from the freezer, place on a cleaned surface, and remove the bottom backing sheet.
4. Place one sheet of the porous PTFE on the exposed surface of the laminate. Starting from the centre of the laminate, working outwards to the edges gently smooth out any significant wrinkles or air bubbles such the porous PTFE is in contact with the whole laminate surface. Any wrinkles or folds in the porous PTFE will be permanently imprinted on the laminate surface under the pressure of the autoclave during curing, and may impair the performance of the laminate or affect the bonding surface.
5. Repeat the process on the other side of the laminate, and transfer the information recorded in the bottom corner to the inside of the bottom piece of porous PTFE material.
6. Place the non-porous brown PTFE material on the base of the autoclave, ensuring that it is significantly larger than the laminate and bleeder fabric to ensure any excess resin does not come in contact with the autoclave base.
7. Place either one or two pieces of bleeder fabric, for thin and thick laminates respectively, in the centre of the non-porous PTFE fabric.
8. Place the porous PTFE covered laminate centrally on top of the bleeder fabric, ensuring that there are no significant wrinkles in the bleeder fabric.
9. Place the other piece or pieces of bleeder fabric on top of the porous PTFE on the laminate.
10. Place the 330mm x 330mm piece of bagging material on top of the bleeder fabric. This piece needs to be smaller than the bleeder material to allow for an air path for the vacuum.
11. On top of the bagging material place the 300mm x 300mm steel caul plate, ensuring no folds of material get caught between the laminate and the caul plate. Position the caul plate such that the edges of the uncured laminate are directly in-line with the caul plate.
12. Place the breather fabric on top of the caul plate so that all the corners and edges of the caul plate are covered, allowing for better circulation of air from the vacuum, as well as providing protection to the vacuum bag from piercing or splitting on the caul plate.
13. Cover the vacuum holes at the rear of the autoclave base with a spare strip of breather fabric, ensuring that none of the curing materials overlap these holes. The breather material prevents any excess resin from being sucked into the vacuum pump should excess resin bleeding occur. This also ensures that no holes will be blocked up allowing the air path to maintain the vacuum environment in the chamber.

14. Place the 650mm x 650mm bagging film over the autoclave, materials and laminate. Ensure that there is enough slack in the bagging material to contour to around the materials, laminate and caul plate without risking splitting or excess stretching of the bagging material when the vacuum is applied. Also ensure that the bagging material extends past the rubber seals at the edge of the chamber to allow for a seal to be formed when the lid of the chamber is put on top.
15. Use a sharp implement to create two holes in the corner of the bagging material over the 2 locator pin holes in the autoclave base corners.
16. Check all rubber seals are intact around the base of the autoclave and on the spacer plate, then place the spacer on top of the vacuum bag and autoclave base plate, ensuring that no wrinkles in the vacuum bag are trapped between the rubber seals. This can be checked by looking between the spacer and the autoclave base, and applying pressure to the top of the spacer, if all the light holes disappear, there is likely a good seal not interrupted by wrinkles in the bagging material.
17. Place the autoclave lid on top of the spacer, ensuring not misalign or jolt the lower plates and materials, aligning the holes in the corner with the spacer plate and the autoclave base. Insert the locator pins to hold the plates in place.
18. Place the three steel transverse members on top of the plate, and feed through the 6 high tensile bolts, ensuring they are vertically aligned. Initially finger tighten the nuts on to the bolts. Use a torque wrench set to 25Nm to tighten the bolts without damaging the seals or threads on the bolts. Tighten the bolts sequentially alternating between the 6 bolts, not tightening them to the required torque immediately allowing for compression of the seals evenly around the autoclave perimeter.
19. Connect the air hose at the rear of the autoclave to allow pressure to be fed into the autoclave.
20. Slowly increase the air pressure in the chamber. When 90psi is reached on the gauge, allow for the air pressure to equalise in the chamber, and make adjustments if the pressure is over or under shot. Listen around the perimeter of the autoclave for hissing sounds, indicating that there is an incomplete seal. If a leak is found, release the pressure from the chamber and remove the bolts and lid and repeat steps 14-19.
21. Switch on the autoclave and the vacuum pump. The required vacuum is 25mmHg. If this level is not reached, there may be a hole in the vacuum bag, and it will need to be replaced.
22. Set the autoclave to run a store program that adheres to the required cure cycle for the laminate material. Check that the correct dwell temperature is achieved. (See below for full autoclave programming details).
23. Once the curing cycle is complete, allow the temperature to reside naturally until it is back to room temperature, release the pressure from chamber and turn off the vacuum, undo the bolts and remove the lid and plate separator.
24. Take the laminate out of the autoclave, and mark the fibre direction, thickness and other laminate information on the top right corner of the laminate. Throw away the consumable materials, and retain the non-consumables for the next laminate cure cycle.
25. For pre-conditioned panels with a hole in the skin, after curing they should be marked, as in Figure 2.4.2, and sent to the workshop to be drilled. Care should be taken in the drilling process not to cause damage to the fibres in the region adjacent to the hole.

Autoclave operation and programming instructions

Autoclave display and significant buttons



To check or change a stored program

1. Press the menu button three times to display: Prog → List
2. Press the scroll button to scroll through the program options. The components of the cure cycle will be as followed:
 - w Hb → OFF
 - Hb u → 0.0
 - rmP.U → min
 - dwL.U → Hour
 - CYC.n → 1
 - SEG.n → 1
 - tYPE → rmP.r
 - tGt → 60.0
 - rATE → 2.0
 - SEG.n → 2
 - tYPE → dwEll
 - dur → (hour) 18.0
 - SEG.n → 3
 - tYPE → End
 - End.t → rSEt
3. Pressing the scroll button at the end will return the display to: : Prog → List
4. For different dwell times for the glass/epoxy and carbon/epoxy laminates, the dwell time must be correct depending on which material is being cured. (16 hours for carbon/epoxy and 6 hours for glass/epoxy).

5. Ramp rate and target temperature must be ensured to be the correct values before accepting the program.
6. The program must end with End.t → rSEt otherwise the cure cycle will not finish, and the laminate may be compromised.

To run a stored program

1. Press the menu button twice to display: Run → List
2. Press the scroll button twice to display: Stat → OFF
3. Press the down arrow button once to display: Stat → Run
4. This starts the cure program, and is indicated by the lighting up of OP1 on the autoclave digital display and the run light on the right hand side underneath the display will also light up. The program status will indicate the first portion of the cure cycle is running, indicating rmP.r for the ramp cycle, and the target temperature will be displayed, intermittently flashing 1LSP and 2HSP.

Skin/core bonding and oven procedure

1. To prepare the cured laminate to be bonded to the core, first the edges must be trimmed using the diamond coated water cooled saw. First, fill the saw with water up to the indicated line, mark cutting lines on the panel edges using a metallic marker, ensuring the proposed cuts will not reduce the dimensions of panel below 300mm x 300mm.
2. Position the laminate on the tile saw, lowering the grinding disk to ensure correct alignment with the cutting line. Start the saw and allow the cooling water to circulate. In a single, slow and smooth motion cut along the marked line while holding the panel in position. Repeat 3-4 for all four edges. After cutting has been completed drain and dispose of the water in the saw.
3. Clean all work surfaces, and both the top and bottom of the trimmed laminate, with propanol to remove all dirt and grease.
4. The honeycomb core material is supplied in large sheets, and hence must be cut down to the required size. To ensure a good bond between the laminate and the core at the edges, and to remove any possibility of any cells damaged during the cutting of the honeycomb being included in the panel, the core is to be cut to 40-50mm larger than the laminate size.
5. The honeycomb core should be inspected for damage incurred from storage or handling, or manufacturing defects. The core should be cut to 340mm x 340mm using a sharp Stanley knife. Care must be taken to avoid leaning on the core when making the cut. Store the core safely between layers of bubble wrap until ready to be bonded.
6. Remove the adhesive roll from the freezer and allow to thoroughly defrost prior to un-bagging and unrolling, so as not to damage the bonds and mesh material within the adhesive which are brittle when frozen.
7. Cut a sheet of adhesive measuring 340mm x 340mm using a sharp Stanley knife. Place the adhesive on the lay-up table ensuring that it is flat and wrinkle free. Remove one of the backing sheets and place the laminate skin, bonding surface down, centrally on the adhesive. Smooth over the laminate to release any trapped air bubbles. For core removal panels, a gap should be left in the adhesive, as shown in Figure 2.4.1.
8. Turn the laminate over and remove the other backing sheet from the adhesive. Hold the honeycomb above the laminate and position so that the nodal direction of the honeycomb is

precisely aligned with the 0° fibre direction of the laminate. When happy with the alignment lower the honeycomb and press down gently to fix its position.

9. Prepare the oven table by cleaning it with propanol and ensure there is no excess dried adhesive or resin on the surface from previous cures and line it with a piece of bagging film to prevent the adhesive sticking to the surface.
10. Place the laminate and core assembly on to the table, with the laminate underneath the core, to avoid the adhesive running under gravity when heated.
11. To protect the core from the caul plate, place a single layer of bagging material on top of the core, then place a single sheet of breather material on to the bagging film. Both of these materials should be larger than the laminate, but smaller than the core.
12. To help provide and distribute the required pressure during the cure, a steel caul plate is put on top of the bagging and breather material, ensuring not to damage to the core when placing it on top. The caul plate should be positioned to be in-line with the edges of the laminate underneath.
13. Slide the oven table into the oven, making sure not to misalign the caul plate. Once in the oven, place additional weights on to the caul plate to achieve the required pressure for the cure, making sure to spread them evenly over the plate.
14. Close the oven door and initiate the oven cure procedure using a digital display similar to the autoclaves above. Ensure the correct program is selected, to provide a ramp rate of 2°C/min to the dwell temperature of 60°C to dwell for 16 hours. After the cure cycle is finished, open the oven doors, and allow the heat to dissipate naturally to prevent any damage in the adhesive from rapid cooling.
15. Once cooled remove from the oven and trim off the excess honeycomb with a Stanley knife taking care not to damage the cell walls. This makes it easier to align the second skin directly above the first.
16. To bond the second skin to the core, the same steps should be undertaken as for the first, however there will be no overhanging core material, making alignment easier.
17. Once bonded the sandwich panel edge can be trimmed and individual specimens cut using the diamond edged water cooled saw. Using a metallic silver pen, mark the transverse and longitudinal central lines on both the front and back of the specimen, and for specimens to be impacted, draw a circle of radius 100mm on the top skin to allow for easy placement in the impact test rig.

End potting procedure

1. To allow for easy separation after end potting, smear silicon grease on to the mating surfaces of the two base sections of the mould whilst wearing a Latex glove. Attach the base sections together using the bolts provided, and tighten significantly so that resin does not leak through the bottom of the mould.
2. Smear additional silicon grease on the base cavity to prevent the epoxy resin from sticking the moulds, keep the thickness of the grease uniform, and ensure that the corners are sufficiently coated.
3. Mix the required amount epoxy resin in a mixing cup using the 1:1 mixing ratio of resin to hardener defined by the manufacturer's recommendations. For one end pot, 30-32g of total weight of the constituent parts must be mixed up. Mixing time should be at least 5 minutes

in order to ensure thorough amalgamation of the constituent parts. Allow time after mixing for the epoxy resin to settle, allowing for large trapped air pockets to escape.

4. Pour the resin into the mould to a depth of approximately 10mm; this will rise to approximately 15mm once the panel is inserted.
5. Using a Stanley knife, carefully score 3-4mm into the centre of the honeycomb at the end of the panel being end potted. This allows the mid-section of the core to be depressed without causing the core to detach from the skin.
6. Using a 10mm square section piece of aluminium, carefully depress the honeycomb in o a 'V' shape across the whole width of the panel evenly. This allows a larger bonding area for the resin, resulting in a stronger bond.
7. Slowly place the panel in the mould, one corner first, to allow the resin to fill the void in the end of the panel and allowing air bubbles to escape.
8. Once the panel is fully in position the two top sections of the mould can be screwed into position to ensure that panel remains immobile and vertical during the curing process. Use a set square to ensure the panel is sitting vertically in the mould. Prior to fitting the top section ensure the mating surfaces are smeared with silicon grease to ensure no sticking occurs.
9. Allow the epoxy resin to cure for 24hrs at room temperature.
10. Once cured, remove the top sections of the moulds and remove the bolts that fix the base sections together.
11. Using a thin wooden strip, tap it into the chamfers at either of the base section, the split the two base parts very easily and will release the panel.
12. Repeat steps 1-11 for the other end of the panel.
13. Once both ends have been potted the panel the end pots are then machined to give a perfectly flat surface ready for compressive loading, ensuring that both ends are parallel with each other.

Strain gauge placement

1. Mark out the position of the strain gauges, which are detailed in Figure 2.5.2, with a silver metallic pen with a cross to allow for the strain gauge to be aligned in the x and y axis.
2. To prepare the surface to allow a good adhesion, lightly sand the regions with wet and dry sandpaper where the strain gauges are to be positioned and clean with acetone.
3. Remove the strain gauge from its' protective plastic sheath with use of tweezers and place on a piece of tape with the bonding surface of the strain gauge facing outwards.

NOTE: Do not handle the strain gauge directly as the bonding surface is pre-cleaned and will easily pick up dirt or grease. Also, due to the fragile nature of the strain gauge foil and legs, excessive handling could cause damage to the gauge.

4. Position the strain gauge using the tape directly on the cross marked on the panel, such that the arrows on the gauge are aligned with the markings.
5. Once positioned correctly, peel back the tape enough to expose the bottom bonding surface of the strain gauge.
6. Add a drop of quick drying adhesive to the bonding surface and return the tape back to its position on the panel surface. Apply a very light pressure to the gauge to prevent inducing pre-strain on the gauge to ensure it is fully adhered to the panel. Use a piece of non-stick

paper supplied with the gauge to absorb any excess glue escaping from around underneath the strain gauge.

7. Allow to dry for 5 minutes before removing the tape, taking care not to pull off the strain gauge wires. The strain gauge should be dark red in colour if bonded correctly. If any light red patches are present air is trapped underneath.
8. Carefully bend the gauge wires back over the strain gauge using a pair of tweezers.
9. Cut out one terminal from the sheet of terminals, and place a piece of tape over the terminal, such that the metal contacts are directly under the tape, and position the terminal so that it is just touching the strain gauge underneath the legs.
10. Once correctly placed, peel back the tape and place one drop of glue on dull bottom surface of the terminal. Re-position the terminal. Apply a small amount of pressure to the terminal and leave to dry. Remove the tape.
11. Bend the terminal wires back down and position above the gold terminal contacts. Stick the wires down to the panel with masking tape to keep the wires in contact with the terminals.
12. Using a soldering iron, solder the left terminal wire to the left contact and the right wire to the right contact. Do not touch the soldering iron directly to the strain gauge wires as this can cause the small solder dot to detach, also keep the time the soldering iron is in contact with the terminal to a minimum to further ensure the wires from the strain gauge do not heat up excessively. The solder on each contact must not touch the other contact otherwise the terminals will be bridged and the strain gauge will give incorrect readings.

NOTE: When soldering, ensure that the soldering iron does not touch the panel surface as this can damage the surface.

13. When soldered, cut the excess off the strain gauge wires that extend past the terminal contacts. Strip and pre-coat an electrical wire to allow for it to be applied easily to the terminal. Solder an electrical wire to each terminal to allow connection with the computer.
14. Check the resistance across the strain gauge to ensure it has been bonded correctly and no bridges exist. The resistance should be $120\Omega \pm 1.0\Omega$ if correct. If this resistance is not within this range, check to see if the circuit is bridged and the all electrical wires are firmly in place.
15. Stick the electrical wires to the panel using a large piece of tape to prevent damage to the wires or connection during storage. Mark each wire with a number using masking tape to identify quickly which gauge the wires belong to, this will help easily identify which strain gauge the wires belong to when in-situ during testing.
16. Record the strain gauge factor written on the packet, as it is needed for programming of the Data-logger.
17. Repeat steps 2-16 for remaining strain gauges.

Impact testing procedure and data logger set-up

Impactor and Panel Set up

1. Raise the impactor away from the impact rig base using the pulley lever and position specimen in impact rig over the 100mm circular cut-out.
2. Lower the impactor down to the panel surface carefully to ensure the photodiodes are in correct position giving consideration to different panel thickness.

3. Centralise the panel using the impactor as a guide. Do not strike honeycomb core from the side whilst centralising the panel.
4. Clamp panel in place using 4 Nm of torque on each of the 4 bolts.
5. Position impactor back into cradle, ensuring it is straight and level.
6. Raise Impactor up to required position, using a tape measure to finalise the height needed for testing. Either insert the safety bar or a thick piece of wood over the specimen to prevent damage in case the impactor is accidentally released.
7. Ensure the wiring for the impactor load cell is free from the release string and clear of the impactor as it drops.

Data Acquisition Set Up

1. Power up the Computer, the Microlink 4000 data acquisition unit, strain gauge amplifier, time counters, and power supply units. If the computer does not boot correctly see below steps:
 - a. Hit Ctrl-Alt-Delete to restart
 - b. F1 to access menu
 - c. Advanced – System Boot Up Sequence – Enter – Select C;A – Enter
 - d. Esc back to Advanced
 - e. Tab to Select IDE Set Up – Yes to settings – Esc
 - f. Save Changes and Exit
2. On Desktop Access Directory to Wavecap – Open Wavecap.exe
3. File- Load Setup – Impact.wcs – OK. Ensure window is now titled Impact
4. Click Run
5. Click Arm
6. Reset both timers for the Photodiodes just before testing

Testing Procedure

1. Ensure both testers are ready to test, two testers are required since both the data acquisition software and the impactor release need to be triggered manually
2. Countdown to release of impactor
3. Trigger data acquisition program to coincide with impact event (2 second window). Trigger will need to be altered depending on height of impact. Click TRIGGER on computer when tester releases impactor.
4. Immediately after the impactor has hit the specimen, slide the wooden impact stopper between the specimen and the impactor to ensure no secondary impacts.
5. Record immediately both timer displays for incident and rebound times recorded. Do not move impactor whilst this is being done.
6. Save Data on Wavecap, only the file “AD703.asc” is required. Import this file into Excel and manipulate as required and save under a file name that identifies the test and specimen carried out.
7. Undo the four bolts holding the clamping plate, return the impactor to the carriage and remove the specimen.

Denison test procedure and data logger set-up

Denison machine set up and operating procedures

The Denison machine applies load using hydraulic pressure, which is controlled by 3 valves connected to the oil reservoir. The main valve is used for large movements of the loading head whilst the fine control valve is used for adjustment of the loading head position at higher loads. Both these valves must be turned clockwise to increase the rate of oil delivery. The third valve is a release valve and is used to rapidly return the loading head to its upper most location by moving the lever upwards.

1. Turn on the main power supply.
2. Turn on the power switch lever located at the right hand side of the machine.
3. Turn on the motor by pressing the button located on the front panel.
4. As the machine is hydraulically controlled allow it to warm up for 30 minutes before using.
5. Remove the cover cage from the machine.
6. Place the loading table in the machine, ensure the bed is level by using a spirit level and adjusting the 4 screws at the base of the bed as required.
7. Place the jig on the loading bed such that the front face of the panel will face the front of the machine. Use shims where necessary to get the jig level.
8. Brush the testing area to clear it from debris from any previous test. Place the specimen into the compression jig taking care not to trap the strain gauge wires and ensure the specimen is level and centred in the jig by using a spirit level. When level, systematically finger tighten the six bolts to hold the specimen in place. Start with the central bolts, and tighten from both sides at the same time.
9. Press the reset button on the control panel.
10. Turn the fine control valve anti-clockwise until it is fully closed.
11. Turn the main valve clockwise to lower the loading head to approximately 1mm above the specimen. The oil flow rate is displayed on the oil delivery indicator and the main valve should be opened enough to let the oil delivery indicator read between 4 and 5.
12. Place the LVDT on the loading bed such that it is only very slightly compressed. This will allow a maximum amount of travel and therefore displacement measurement to be recorded during the test. Note the LVDT must be removed during the test prior to it being compressed to its limit to prevent it being damaged.
13. Turn on the Orion data logger and computer.
14. Connect the LVDT to the strain gauge amplifier connected to the data logger.
15. Connect the Load output from the Denison to the data logger using the grey wire labelled 'Load Channel 18'. Connect the strain gauges to the data logger using the 16 point connection blocks and check the resistance across the strain gauge wires is 120.1 ± 1.0 .
16. Program the data logger as per the below instructions noting the strain gauge factor is generally 2.13 for single FLA-5-11 strain gauges and 2.12 for double FCA-3-11 rosette strain gauges.
17. Open the DATALOGGER 2000.HT program on the computer.
18. From the main menu select TRANSER and CAPTURE TEXT.
19. Enter the file name and path for the test data to be stored; currently default setting of 'hope.txt' must be used.
20. Start the data logger after channels have been initialised (See Step 4 below) by pressing RUN.

21. Begin loading the specimen using first the main valve then the control valve when the main valve reaches its limit (at around 50kN). The loading rate should be kept steady throughout loading at a rate around 0.1kN/s.
22. Remove the LVDT just prior to it reaching its compressive limit and before specimen failure. As loading must be controlled manually throughout the test an assistant will be needed to remove the LVDT.
23. After failure move the release lever upwards to return the loading head to its top most position, and turn both the main and fine control valves anti-clockwise until fully closed.
24. Press RUN on the data logger to stop capturing the data.
25. To process the data open DATASORT.EXE program and type 'reformat' to reformat the data collected into a text file which can be opened in Excel, split the data columns using "Text to columns" command using a delimitation with a space. Save the data file in personalised folder.
26. Remove the specimen from the Denison machine.
27. Repeat steps 8-26 for additional tests.

Data Acquisition Machine Set-Up

1. Programming of Strain Gauges

This sequence is to be carried out for each strain gauge, where each gauge uses two channels, and are typically placed in channels 1-16 and 21-24.

Display with Multifunction button options	Operation
Set up channels	<Channel>
Enter channel numbers	Type <1-16,21-24>
	<Enter>
Select items to be defined [Analogue In]	
Sensor Conv Alarm Output Text	[Sensor]
Select measurement type	
Volts Amp Ohms Thcpl Prt Strain	[Strain]
Select bridge configuration	
FullBr 1/2Br 1/4Br	[1/4Br]
Select thermal drift compensation	
On Off	[On]
Select dummy	
Rem120 UserX UserY UserZ	[Rem120]
Select energisation current	
8mA 1mA User	[1mA]
Enter gauge factor	2.11 (get from SG packet)
	<Enter>

Note the strain gauge factor is generally 2.12 for single FLA-5-11 strain gauges and 2.11 for double FCA-3-11 rosette strain gauges.

2. Programming in Position and Load Outputs from Denison and LVDT

Note: channel for Denison load = 18; channel for LVDT = 38

Display with Multifunction button options	Operation
Set up channels	<Channel>
Enter channel numbers	Type <18,38>
	<Enter>
Select items to be defined [Analogue In]	
Sensor Conv Alarm Output Text	[Sensor]
Select measurement type	
Volts Amp Ohms Thcpl Prt Strain	[Volts]
Select DC or AC measurement	
DC AC	[DC]

3: Programming in the task of the Data Logger

Display with Multifunction button options	Operation
Set up Task	<Task>
Enter task number [1-8]	Type <1>
	<Enter>
Enter task title [18 characters max]	Type <A>
Select task function	
Scan Event Off	[Scan]
Select task trigger source	
Timer Clock Task	[Timer]
Enter delay to start [dd-hh:mm:ss.t]	
00-00:00:00.0	Type <0>
0	<Enter>
Enter number of scans	
*	[*]
Select of fixed interval scan	
Cont Inter	[Inter]
Enter delay to start [dd-hh:mm:ss.t]	
00-00:00:00.0	
Enter scan interval	Type <1>
	<Enter>
Enter channels to be scanned	Type <1-16, 21-23, 18, 38>
Select measurement rate	
500/s 100/s 40/s 10/s	[40/s]
Select end-of-scan	
Off On	[Off]
Select data to be logged	
All Alarm Proc Al+Pr None	[All]
Select when the output task header	
Always Log Data	[Always]
Select output device	
Tape Print RS232 422/a Dsply GPIB	[RS232]
Select format required	
Coded Full Compact	[Full]
Enter task triggered in alarm [x,y,z]	
0	[0]
Enter task aborted in alarm [x,y,z]	
0	[0]
Ready for command	

4: Initialising the Data logger to prepare it to carry out the task

Display with Multifunction button options	Operation
Select facility required	<Init>
Chans Refs Clock Print Edit Exit	[Chans]
Enter Channels to be initialised	Type <1-16, 21-24, 18, 38>
	<Enter>
Ready for command	

To carry out repeat tests with the same set up, repeat only step 4 for the data logger set-up.

APPENDIX B

Load displacement responses from all impacted tested panels

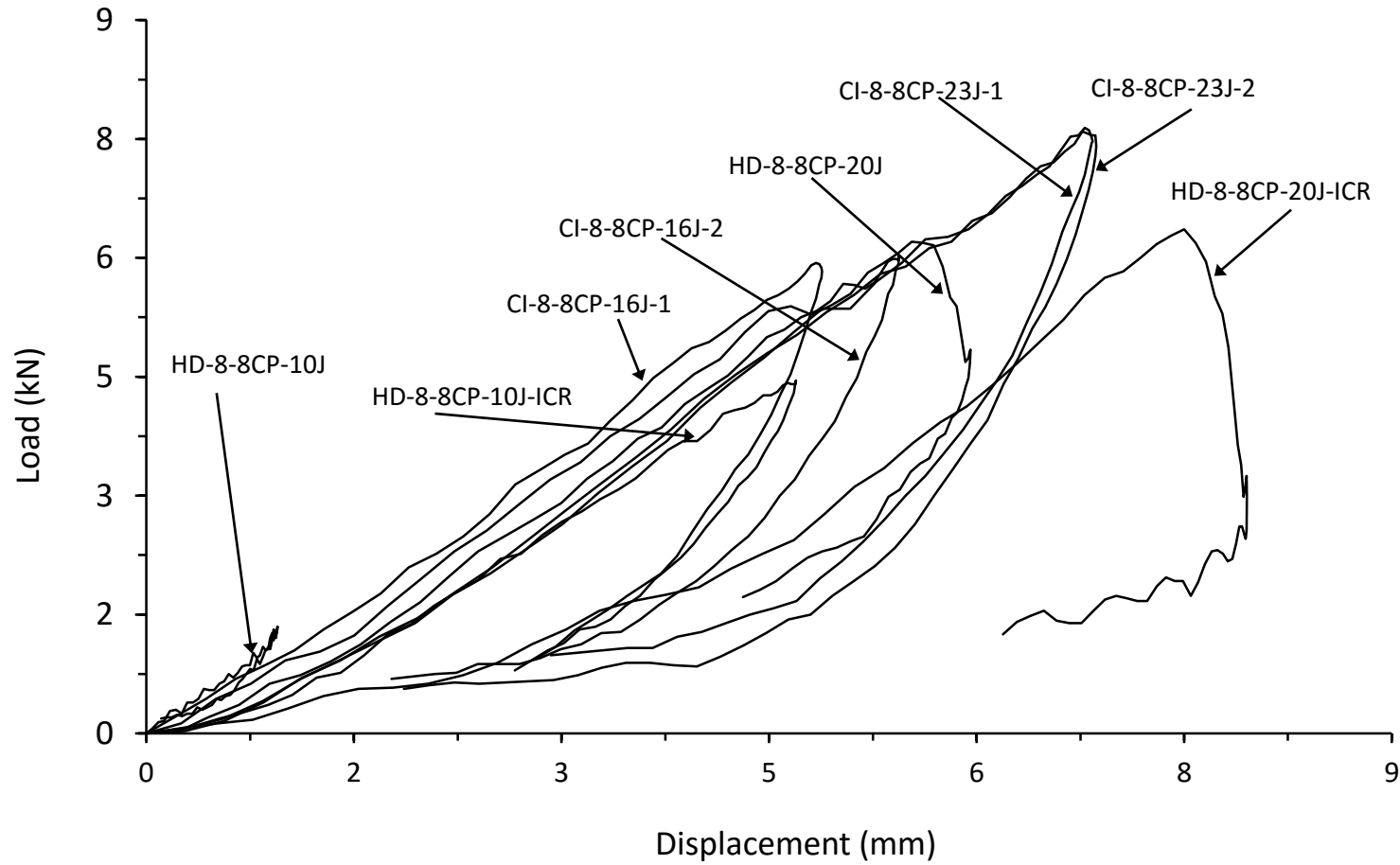


Figure B1. All impact testing load displacement responses from thin symmetrical CP carbon/epoxy panels with 70kg/m³ core density

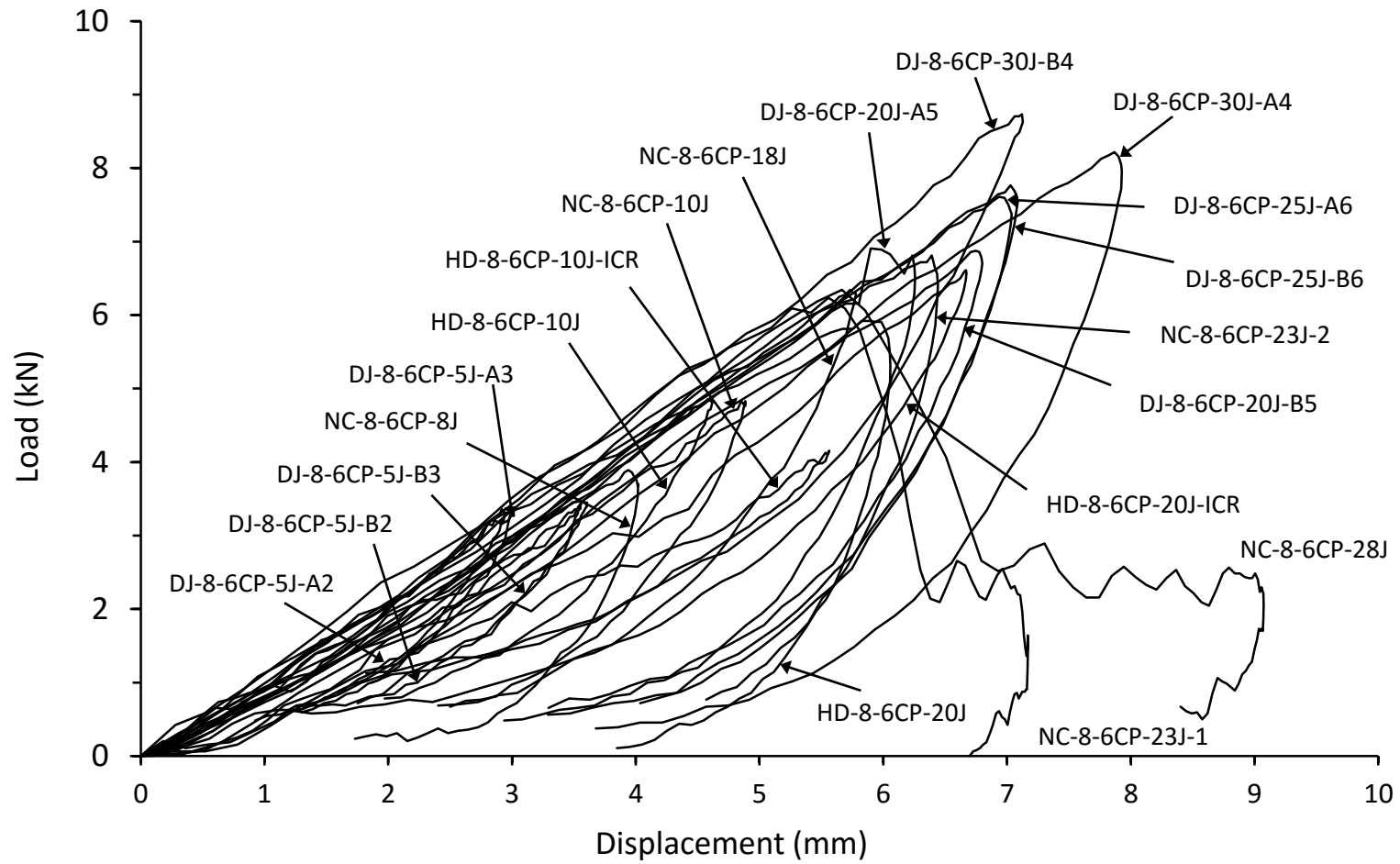


Figure B2. All impact testing load displacement responses from thin unsymmetrical CP carbon/epoxy panels with 70kg/m³ core density

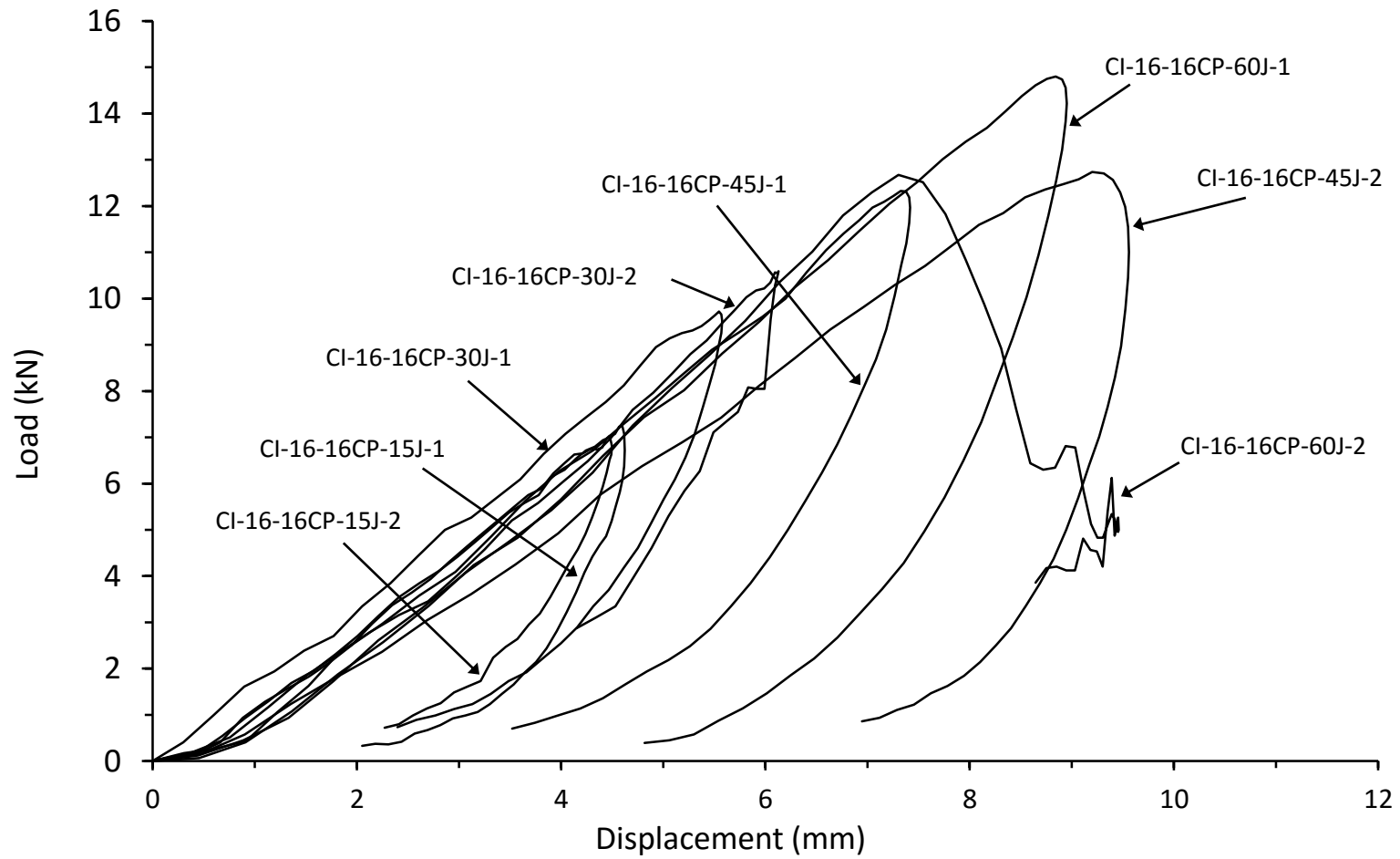


Figure B3. All impact testing load displacement responses from thick symmetrical CP carbon/epoxy panels with 70kg/m³ core density

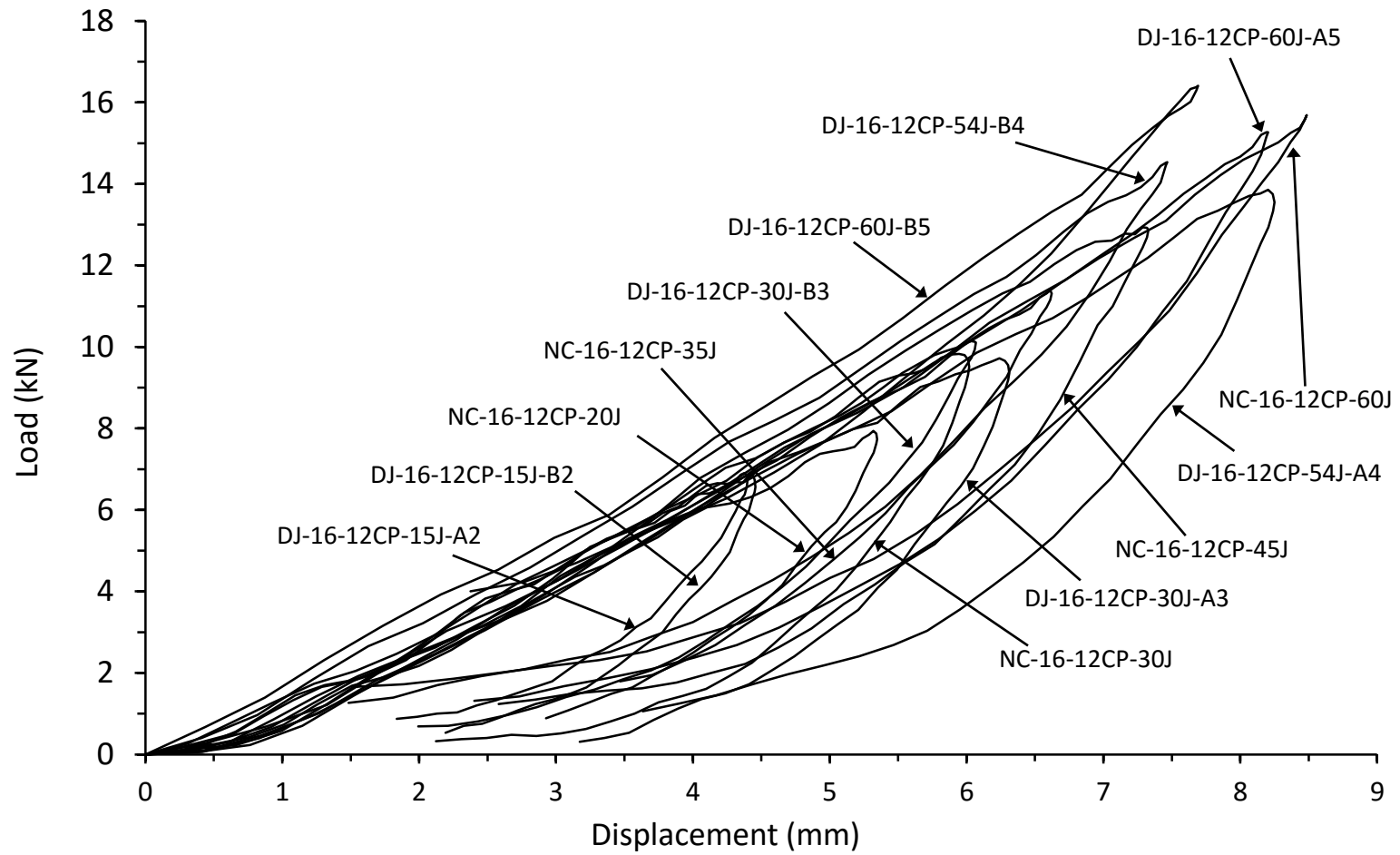


Figure B4. All impact testing load displacement responses from thick unsymmetrical CP carbon/epoxy panels with 70kg/m³ core density

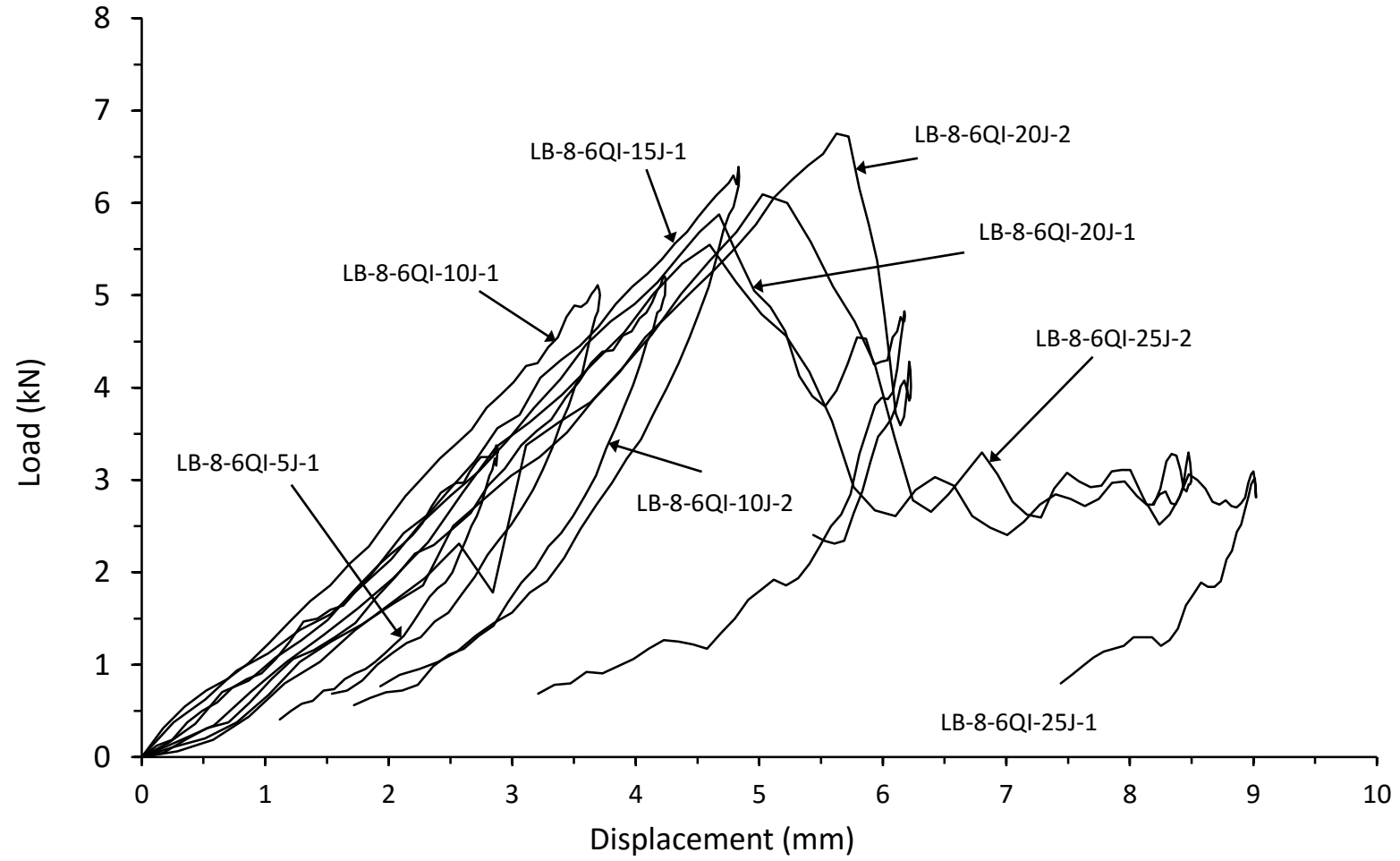


Figure B5. All impact testing load displacement responses from thin symmetrical QI carbon/epoxy panels with 70kg/m^3 core density

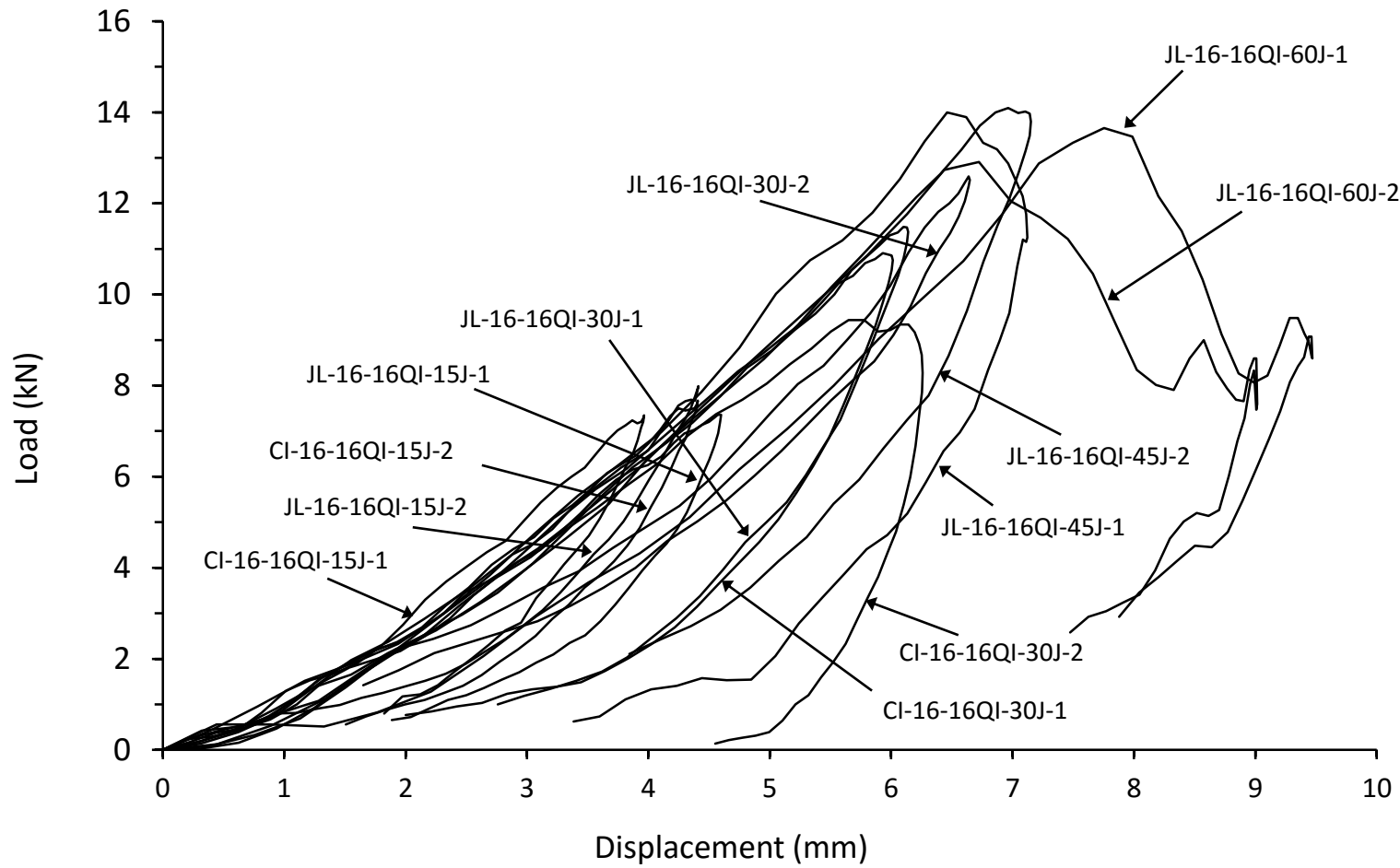


Figure B6. All impact testing load displacement responses from thick symmetrical QI carbon/epoxy panels with 70kg/m³ core density

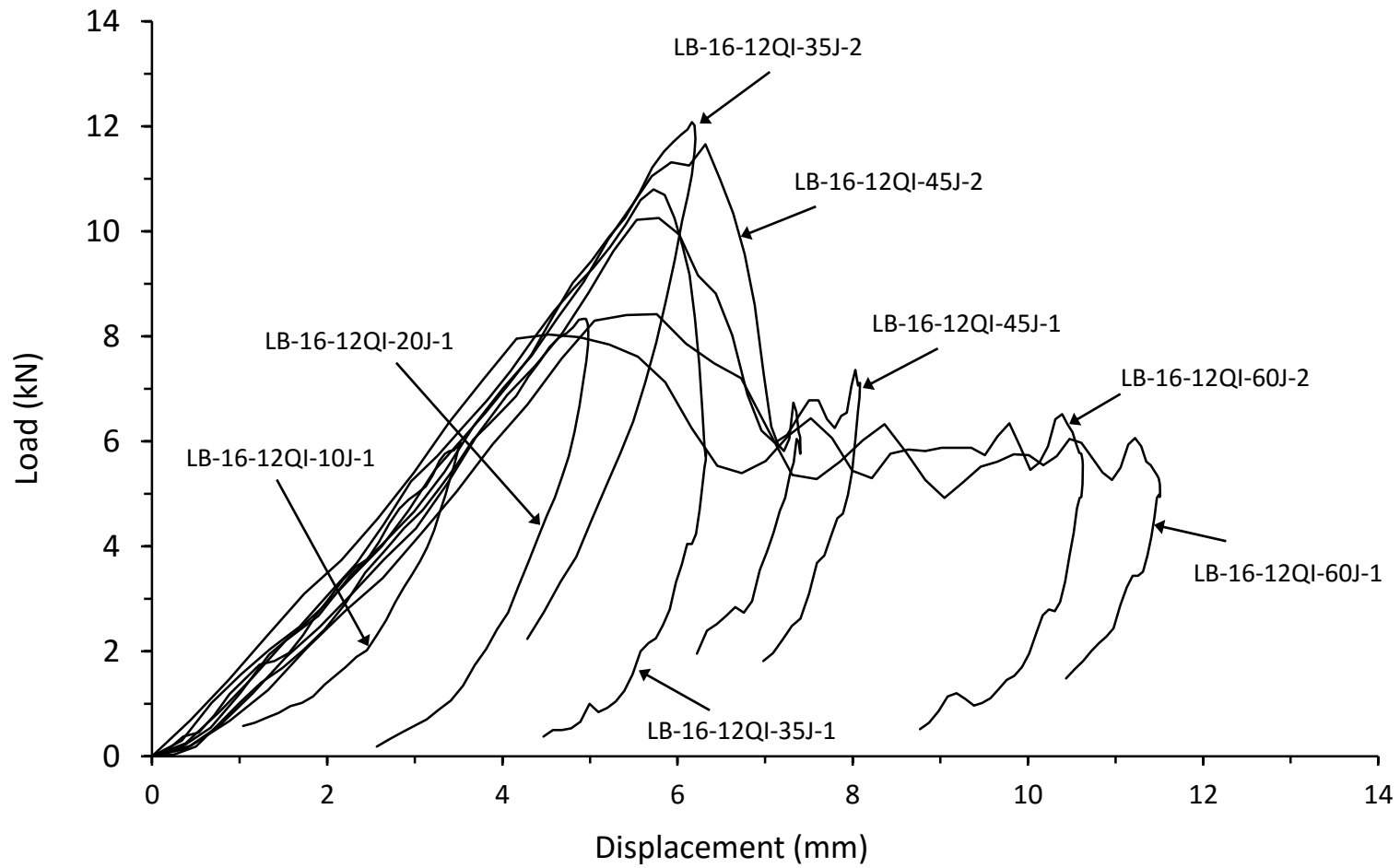


Figure B7. All impact testing load displacement responses from thick unsymmetrical QI carbon/epoxy panels with 70kg/m³ core density

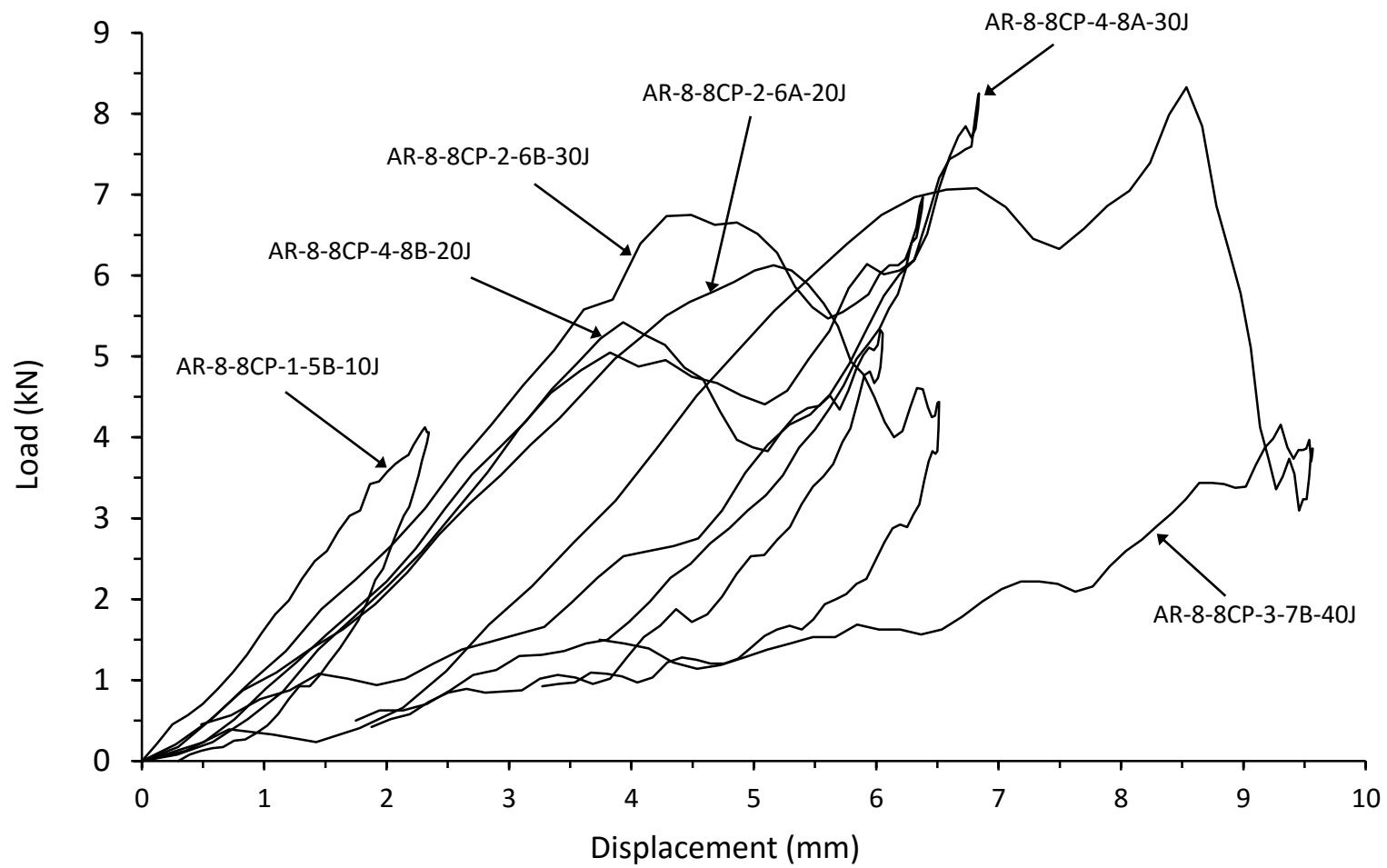


Figure B8. All impact testing load displacement responses from thin symmetrical CP carbon/epoxy panels with 110kg/m³ core density

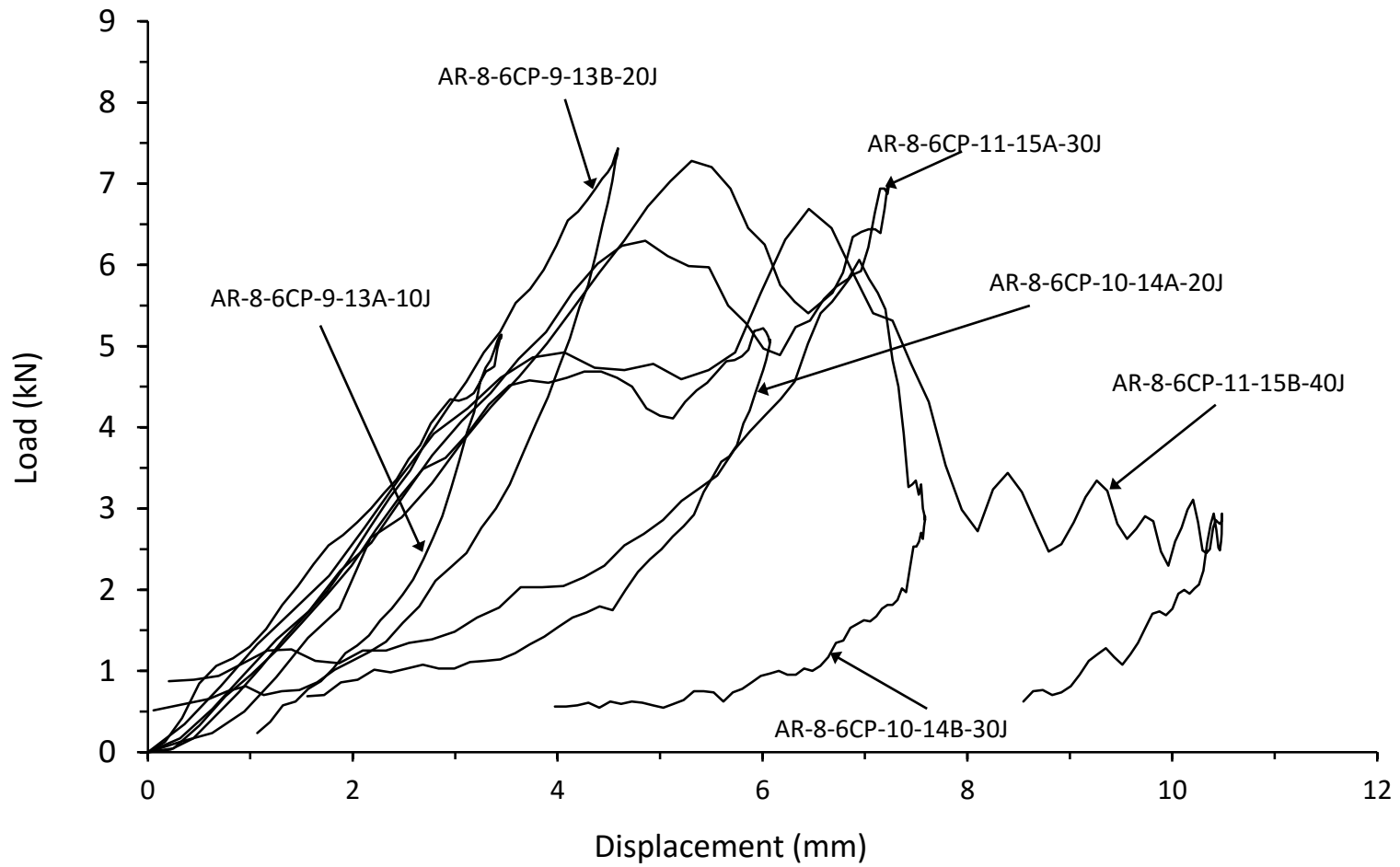


Figure B9. All impact testing load displacement responses from thin unsymmetrical CP carbon/epoxy panels with 110kg/m³ core density

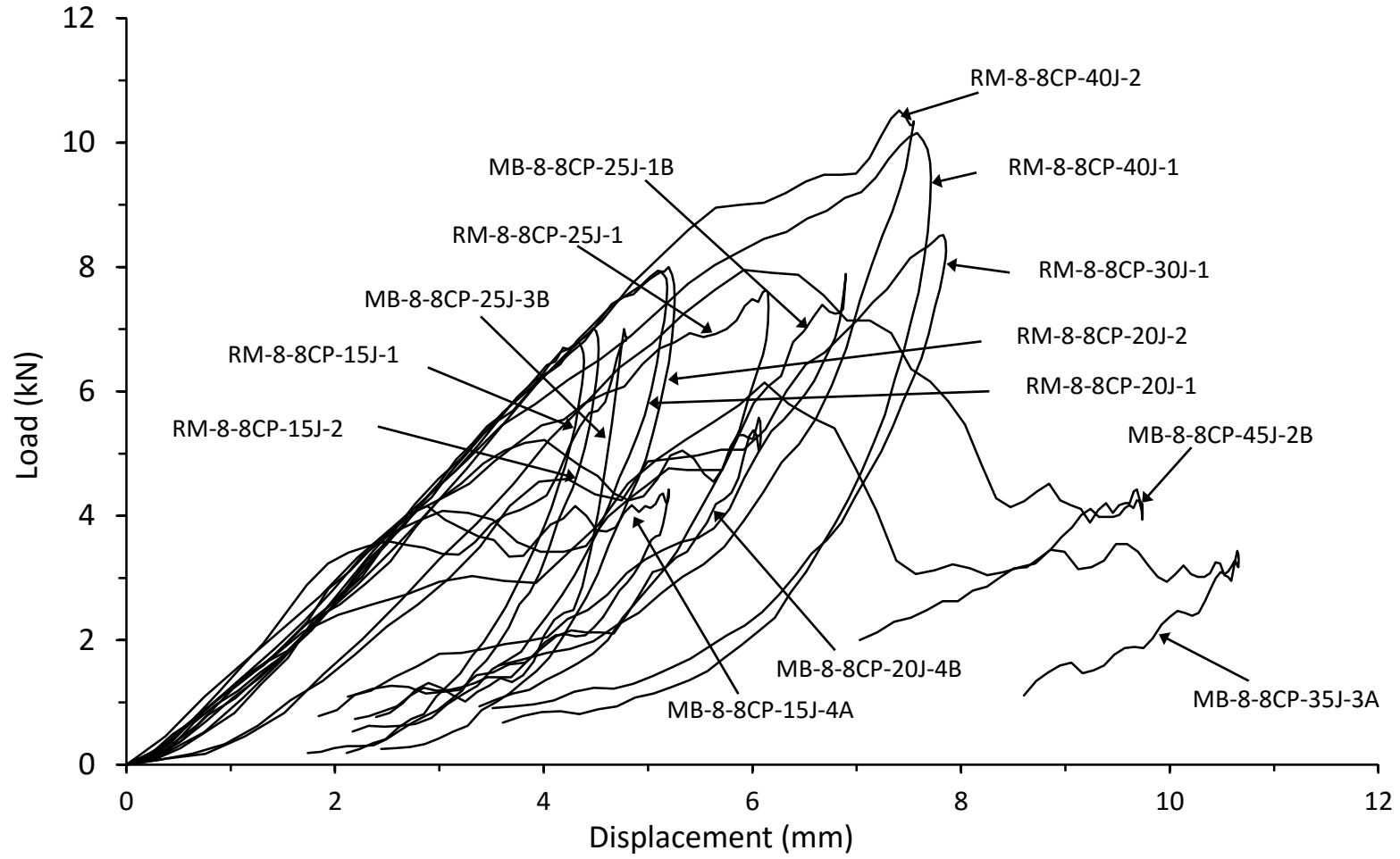


Figure B10. All impact testing load displacement responses from thin symmetrical CP carbon/epoxy panels with 135kg/m³ core density

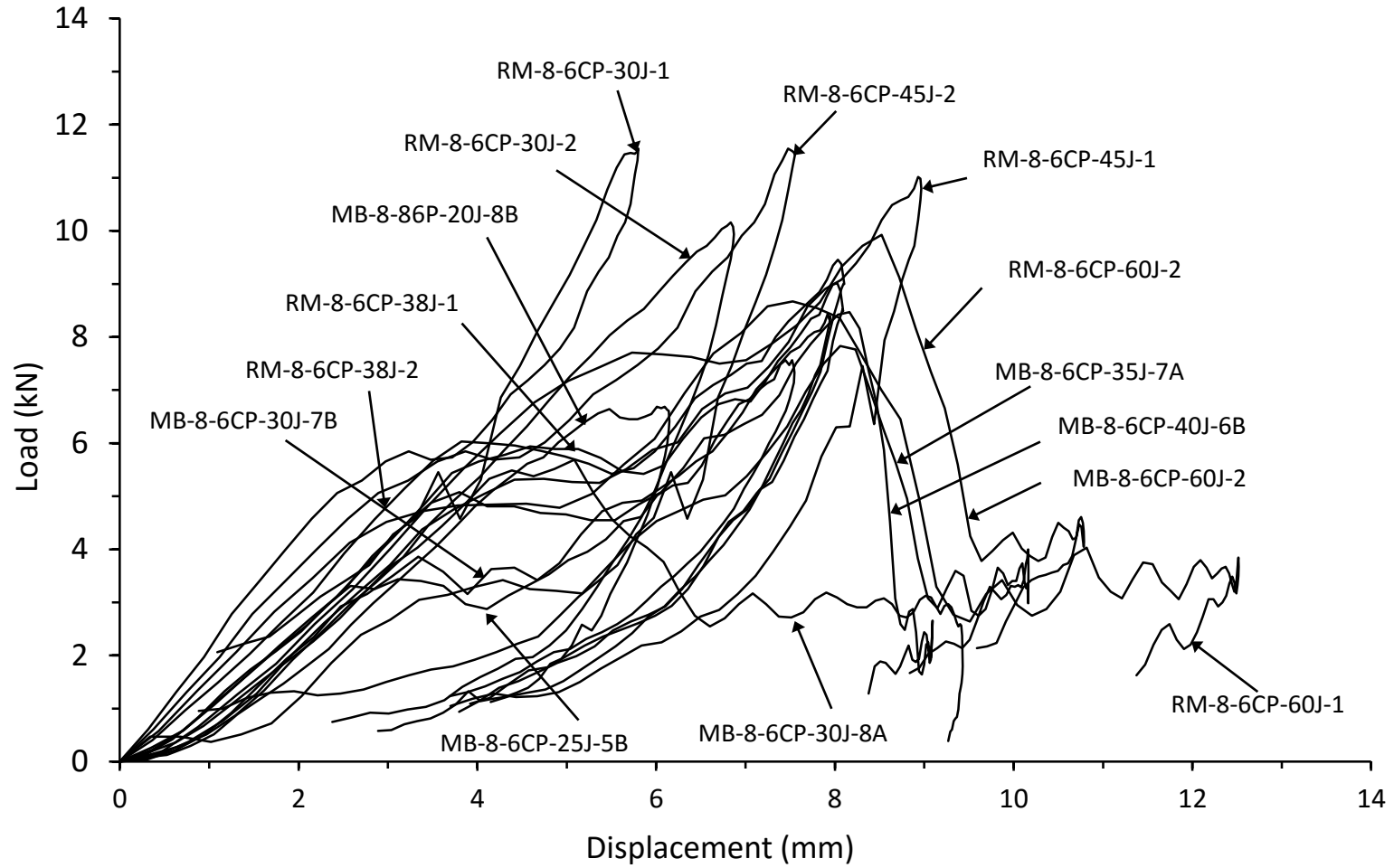


Figure B11. All impact testing load displacement responses from thin unsymmetrical CP carbon/epoxy panels with 135kg/m³ core density

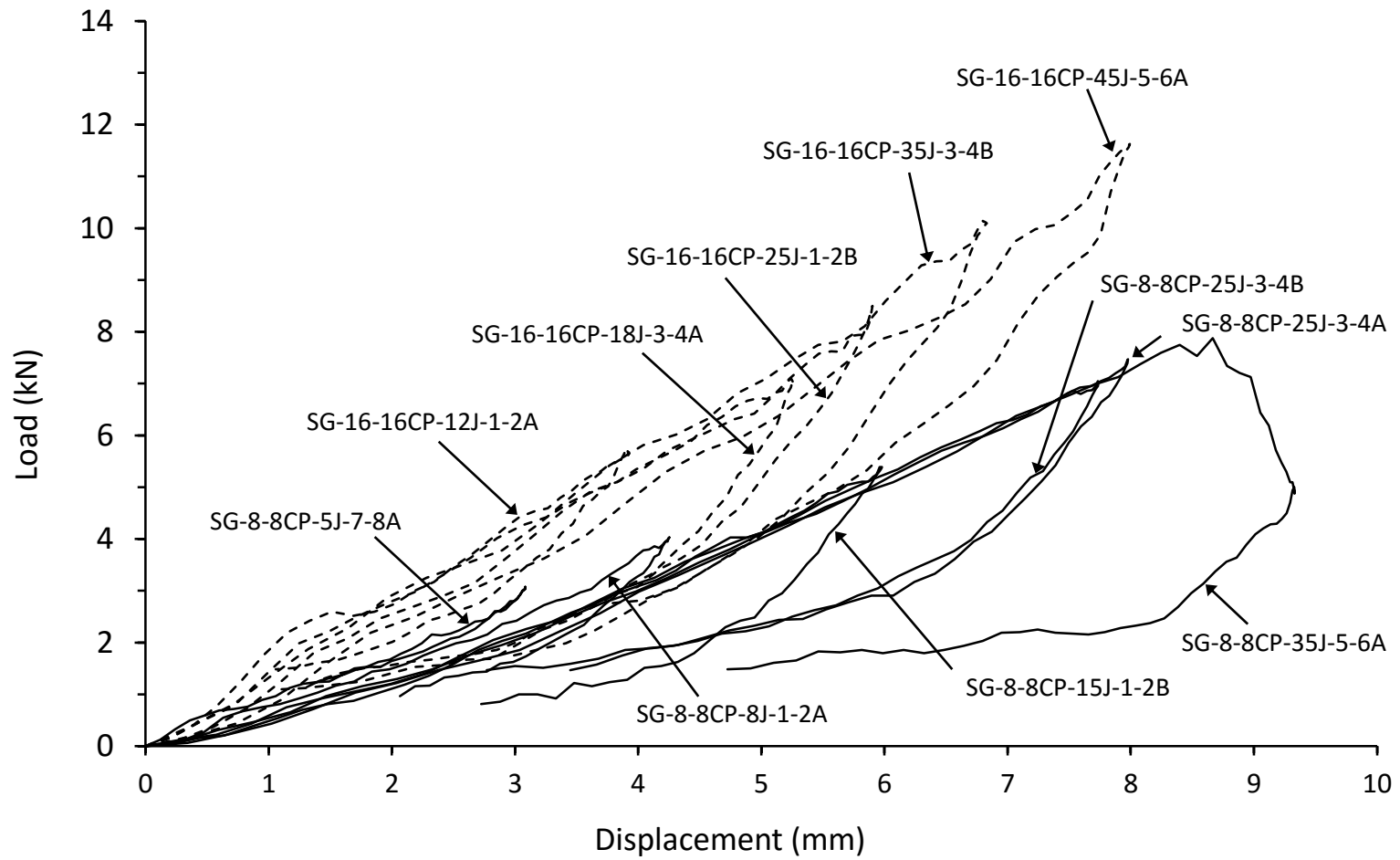


Figure B12. All impact testing load displacement responses from thin and thick symmetrical CP E-glass/epoxy panels with 70kg/m³ core density

APPENDIX C

Mean and curvature strain responses from all tested CAI panels

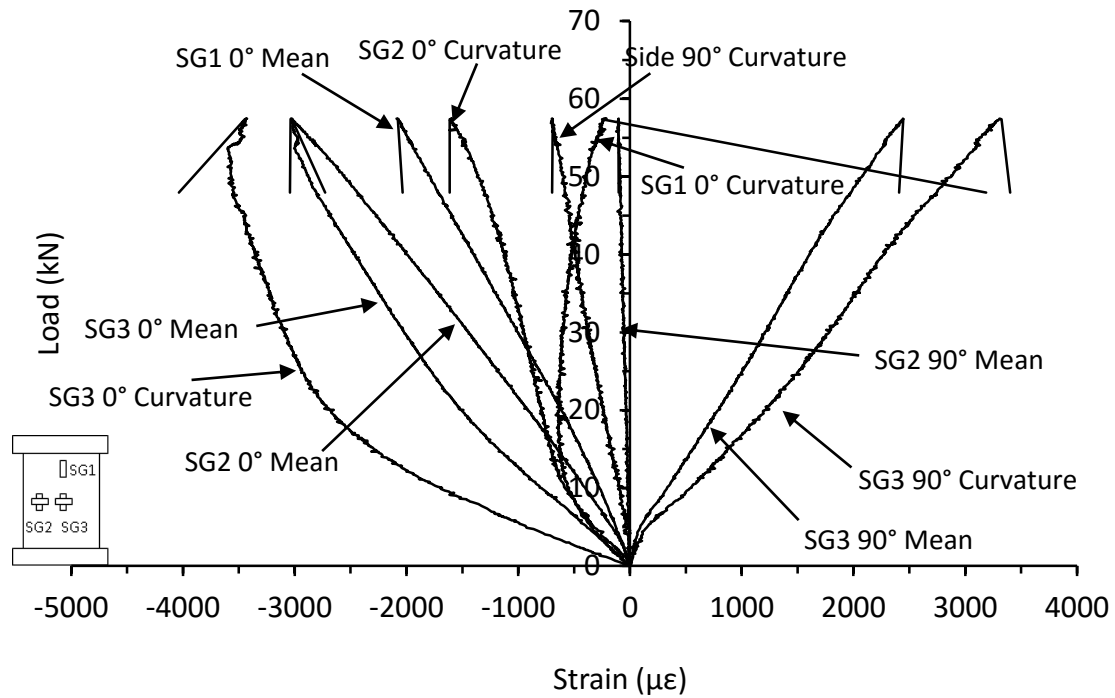


Figure C.1. Mean and curvature strain responses from thin symmetrical CP carbon/epoxy panel with 70kg/m^3 core density impacted at 23J (CI-8-8-CP-23J)

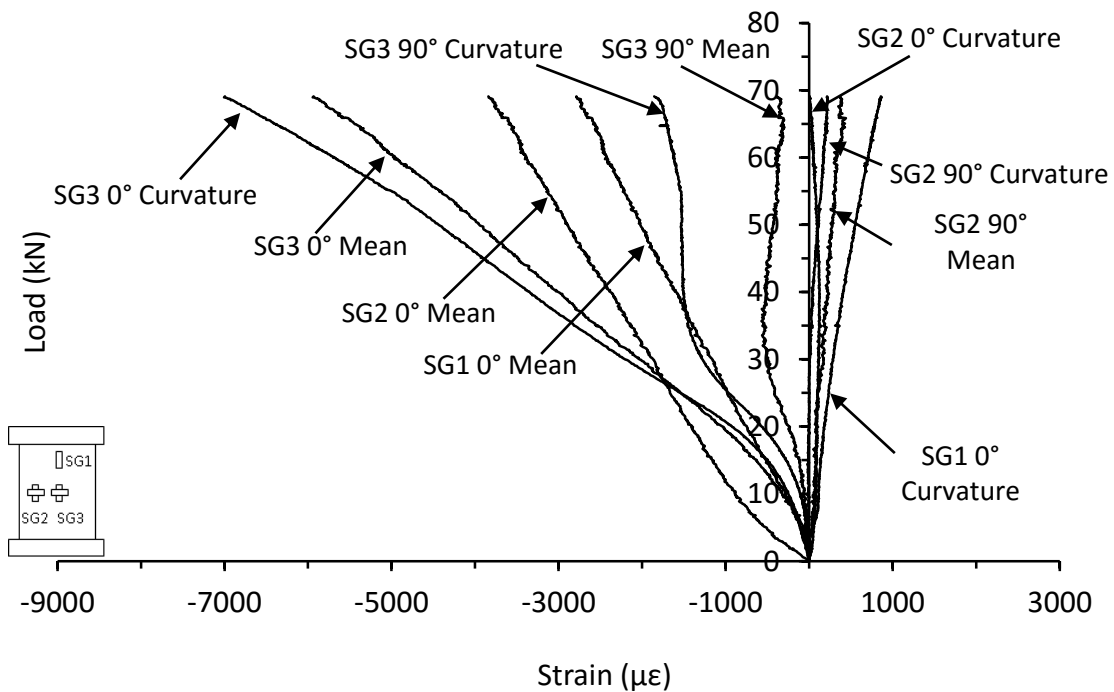


Figure C.2. Mean and curvature strain responses from thin symmetrical CP carbon/epoxy panel with 70kg/m^3 core density impacted at 10J (HD-8-8-CP-10J)

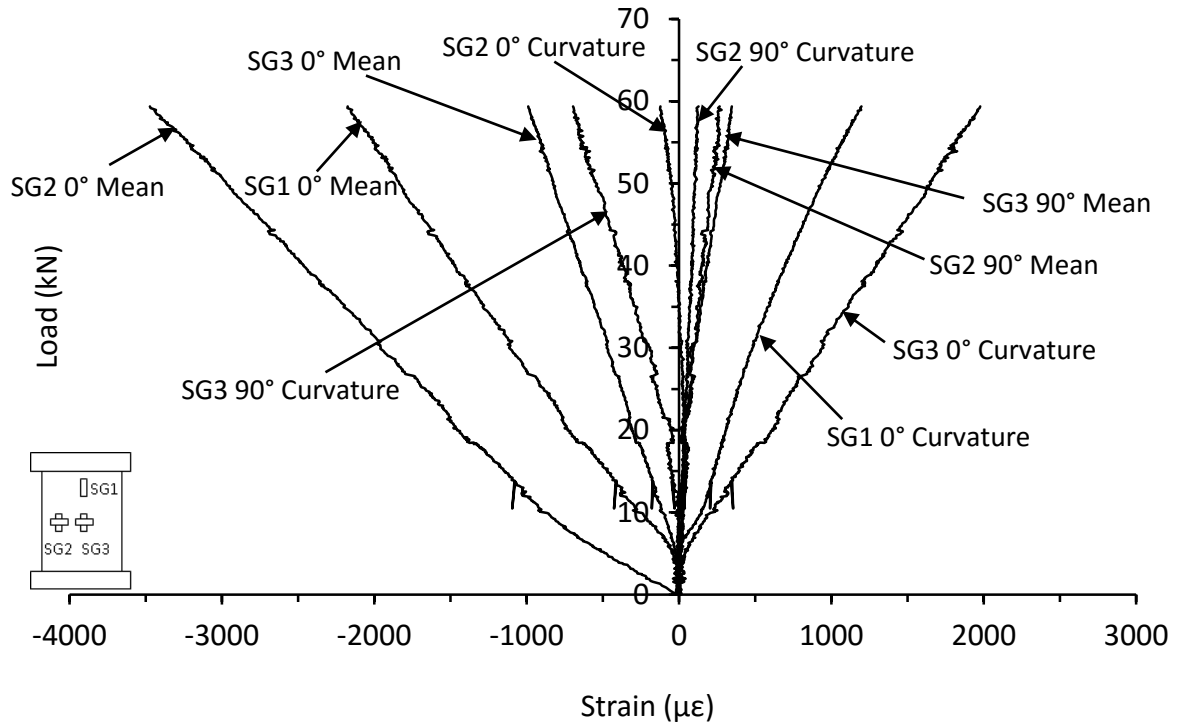


Figure C.3. Mean and curvature strain responses from thin symmetrical CP carbon/epoxy panel with 70kg/m^3 core density impacted at 20J (HD-8-8-CP-20J)

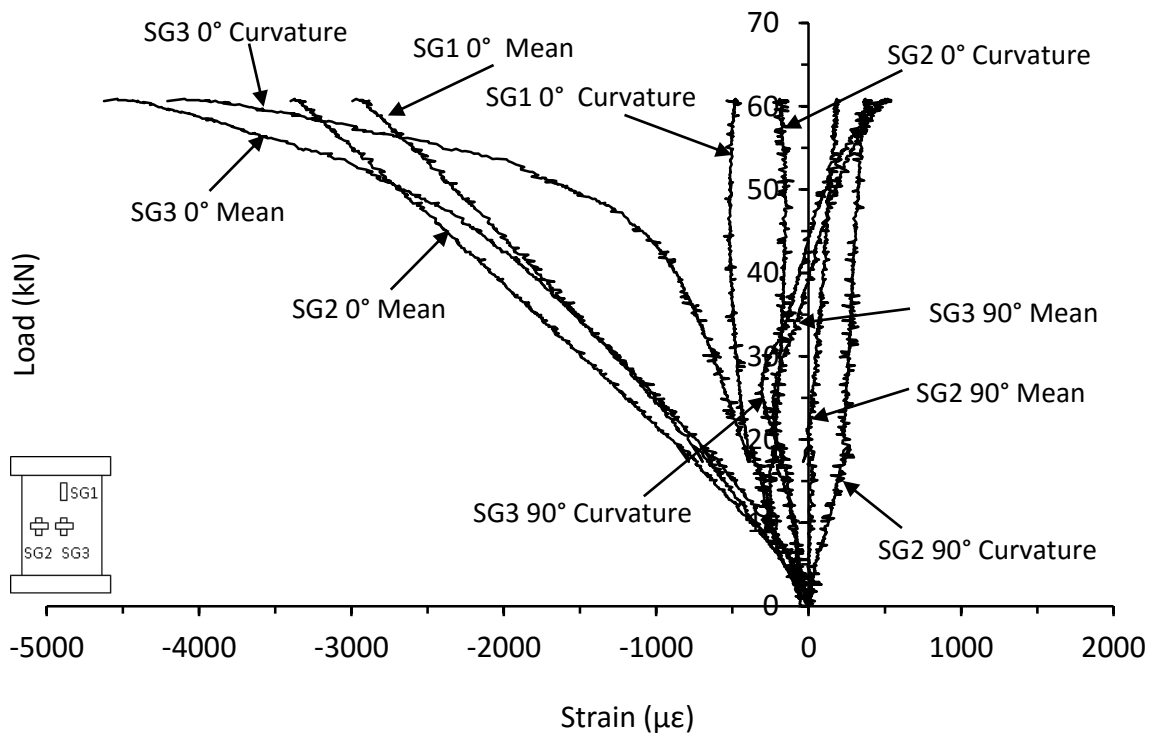


Figure C.4. Mean and curvature strain responses from thin unsymmetrical CP carbon/epoxy panel with 70kg/m^3 core density impacted at 5J (DJ-8-6-CP-5J-A2)

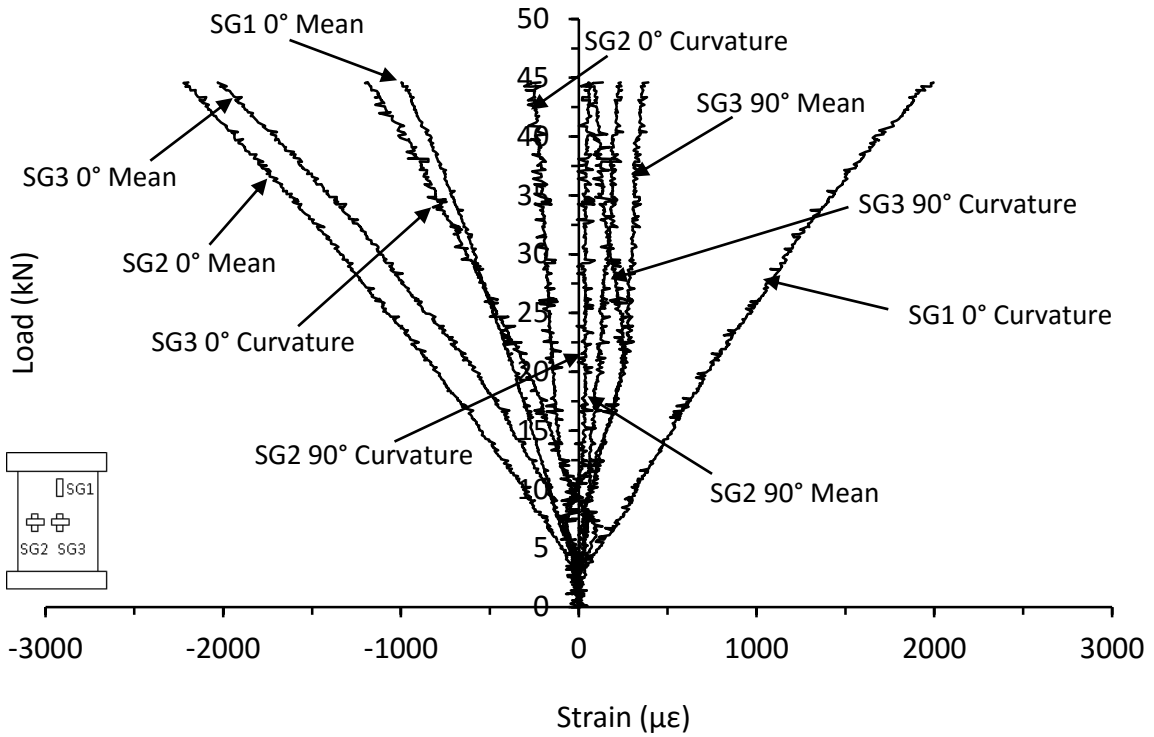


Figure C.5. Mean and curvature strain responses from thin unsymmetrical CP carbon/epoxy panel with 70kg/m³ core density impacted at 5J (DJ-8-6-CP-5J-A3)

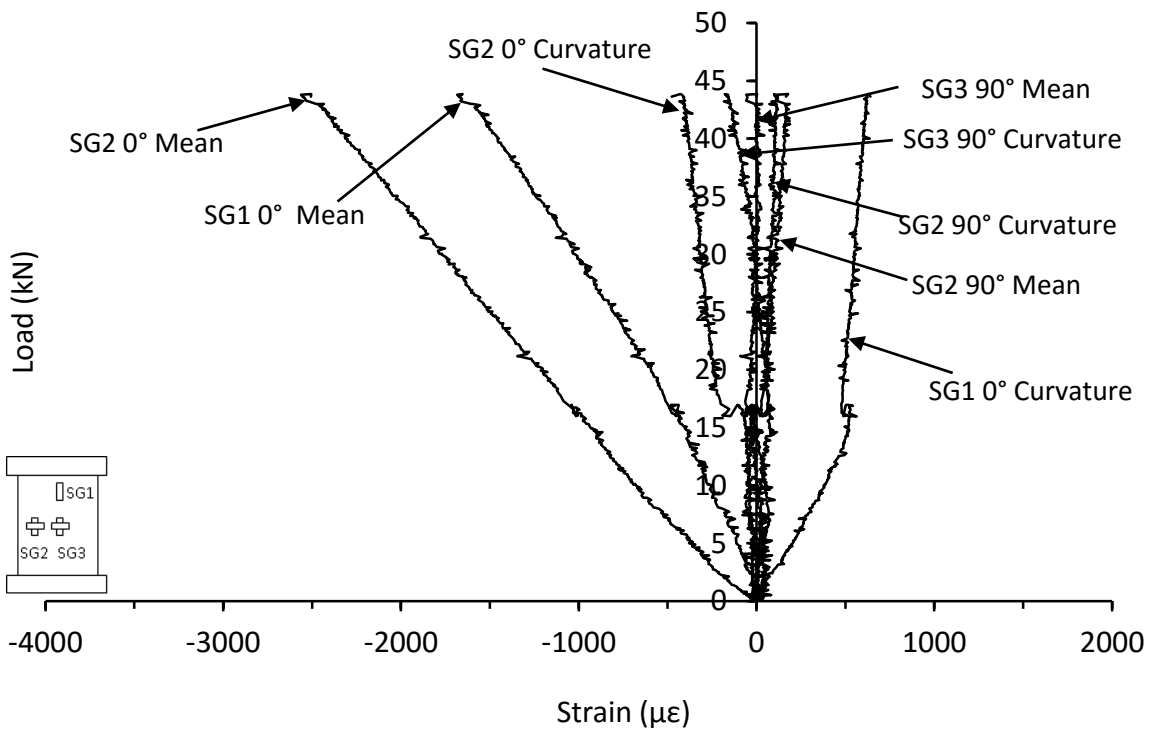


Figure C.6. Mean and curvature strain responses from thin unsymmetrical CP carbon/epoxy panel with 70kg/m³ core density impacted at 5J (DJ-8-6-CP-5J-B3)

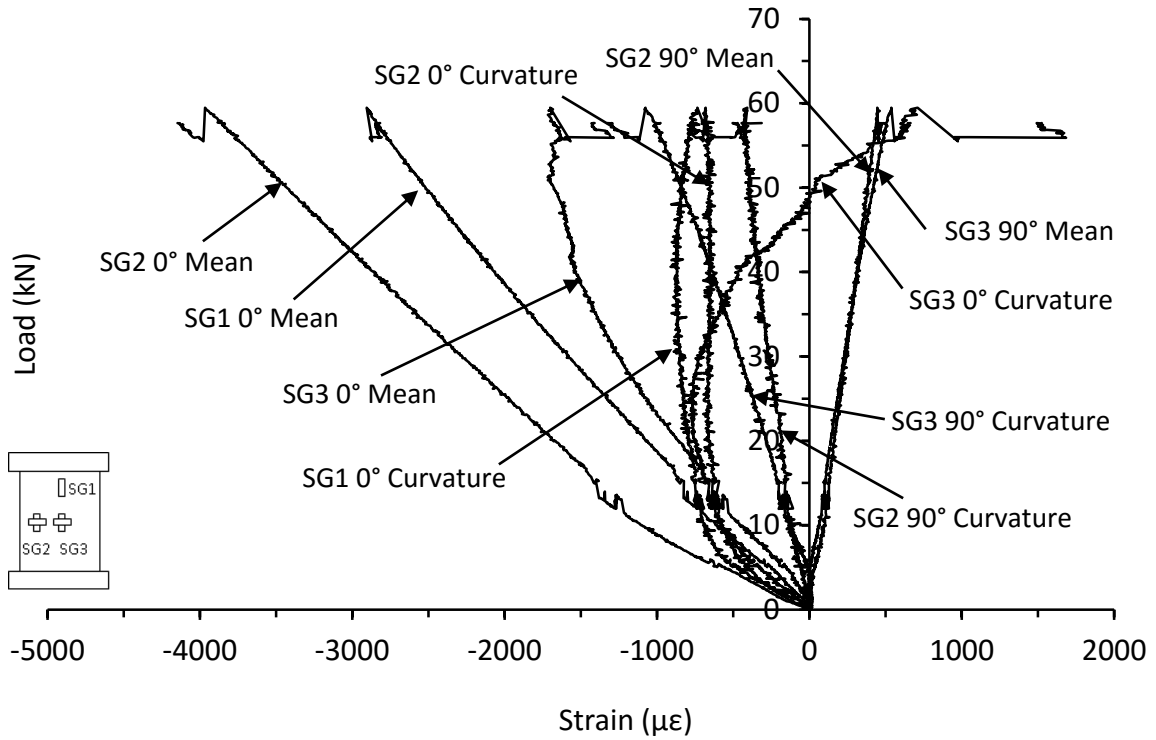


Figure C.7. Mean and curvature strain responses from thin unsymmetrical CP carbon/epoxy panel with 70kg/m³ core density impacted at 8J (NC-8-6-CP-8J)

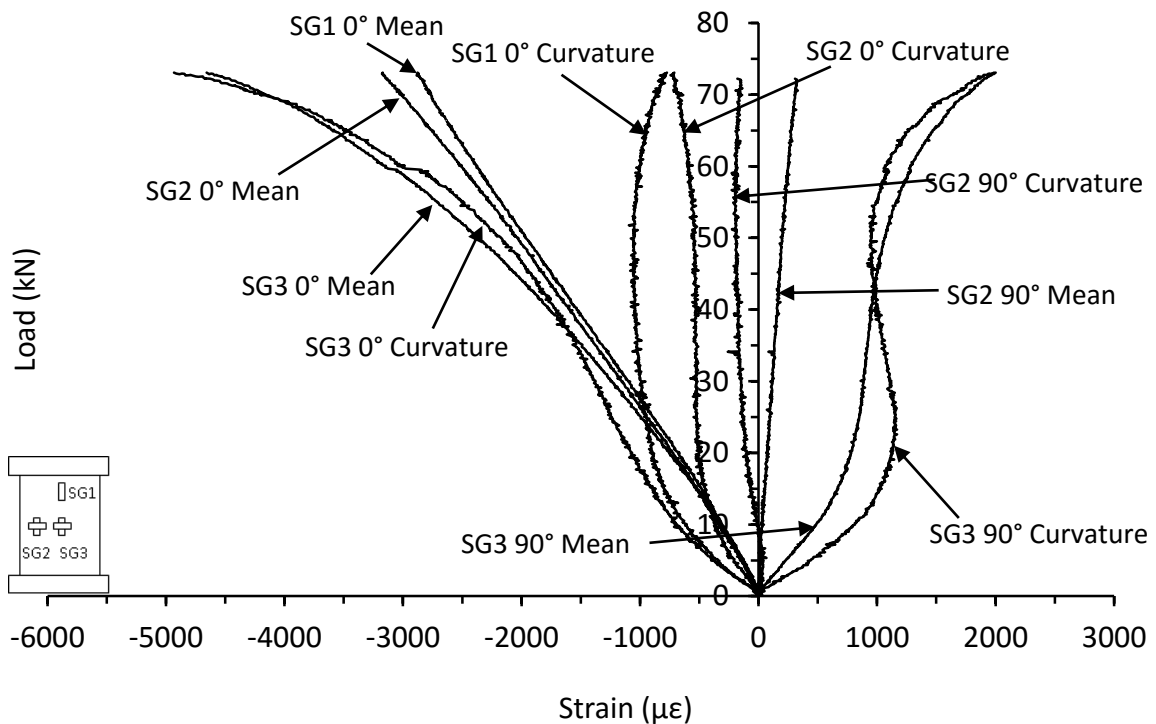


Figure C.8. Mean and curvature strain responses from thin unsymmetrical CP carbon/epoxy panel with 70kg/m³ core density impacted at 10J (NC-8-6-CP-10J)

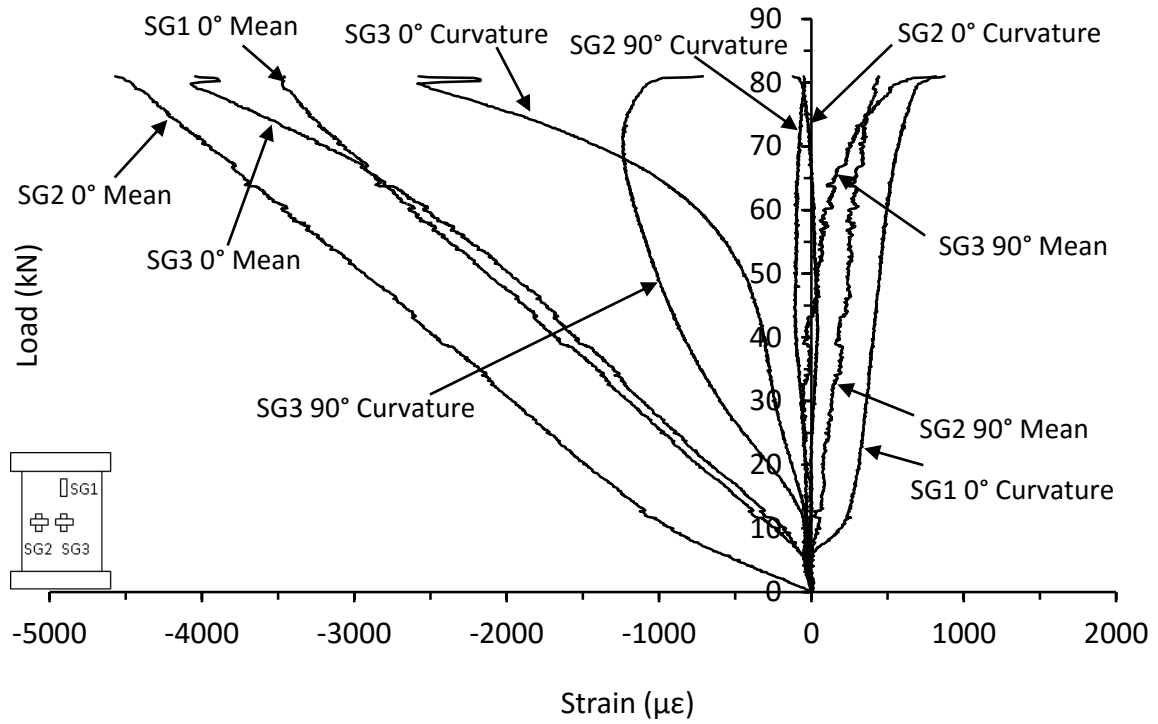


Figure C.9. Mean and curvature strain responses from thin unsymmetrical CP carbon/epoxy panel with 70kg/m³ core density impacted at 10J (HD-8-6-CP-10J)

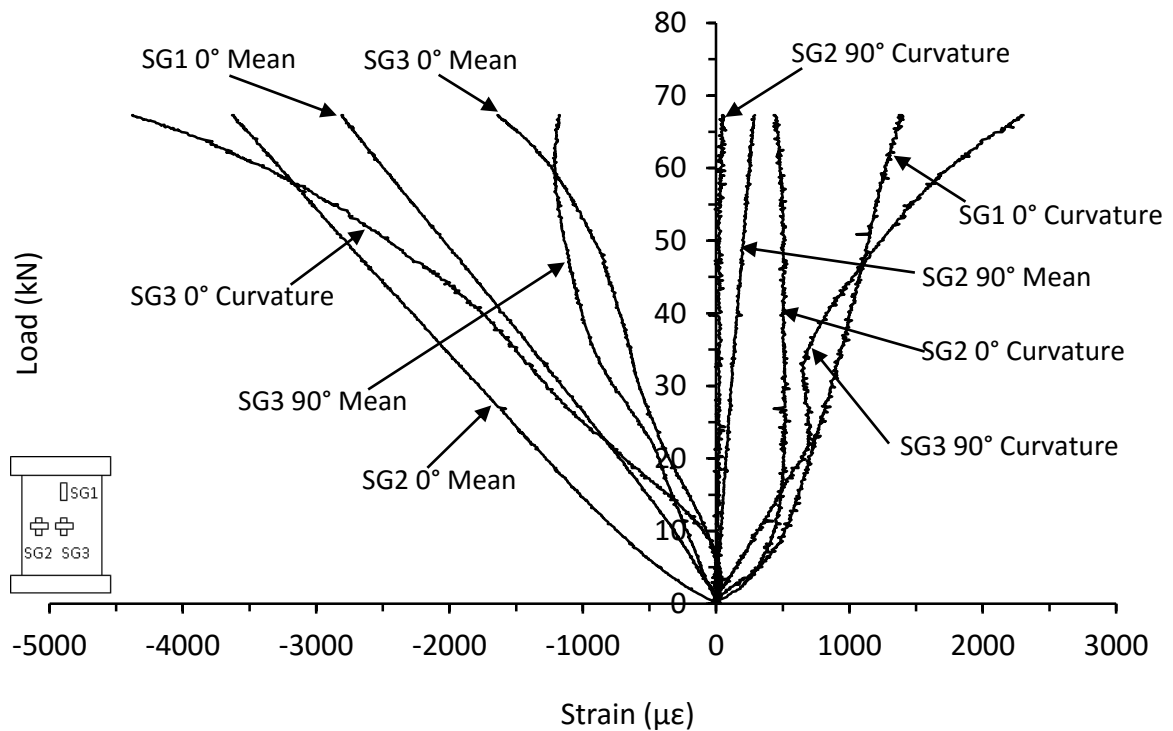


Figure C.10. Mean and curvature strain responses from thin unsymmetrical CP carbon/epoxy panel with 70kg/m³ core density impacted at 18J (NC-8-6-CP-18J)

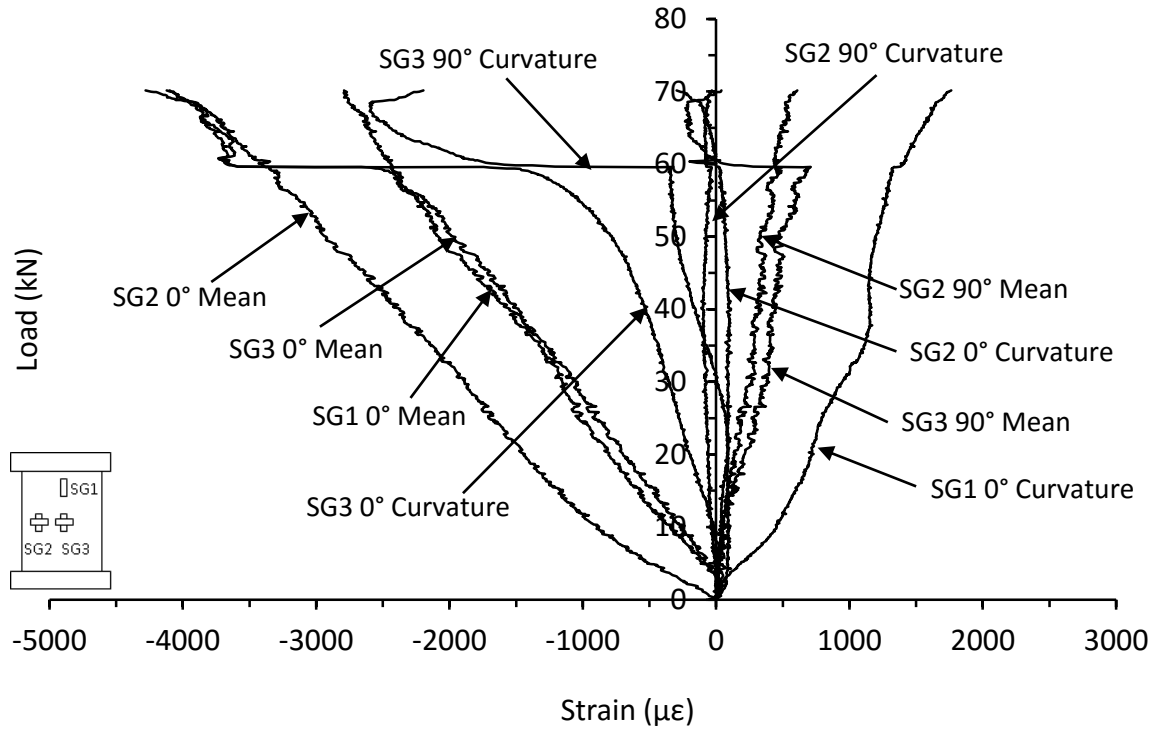


Figure C.11. Mean and curvature strain responses from thin unsymmetrical CP carbon/epoxy panel with 70kg/m³ core density impacted at 20J (HD-8-6-CP-20J)

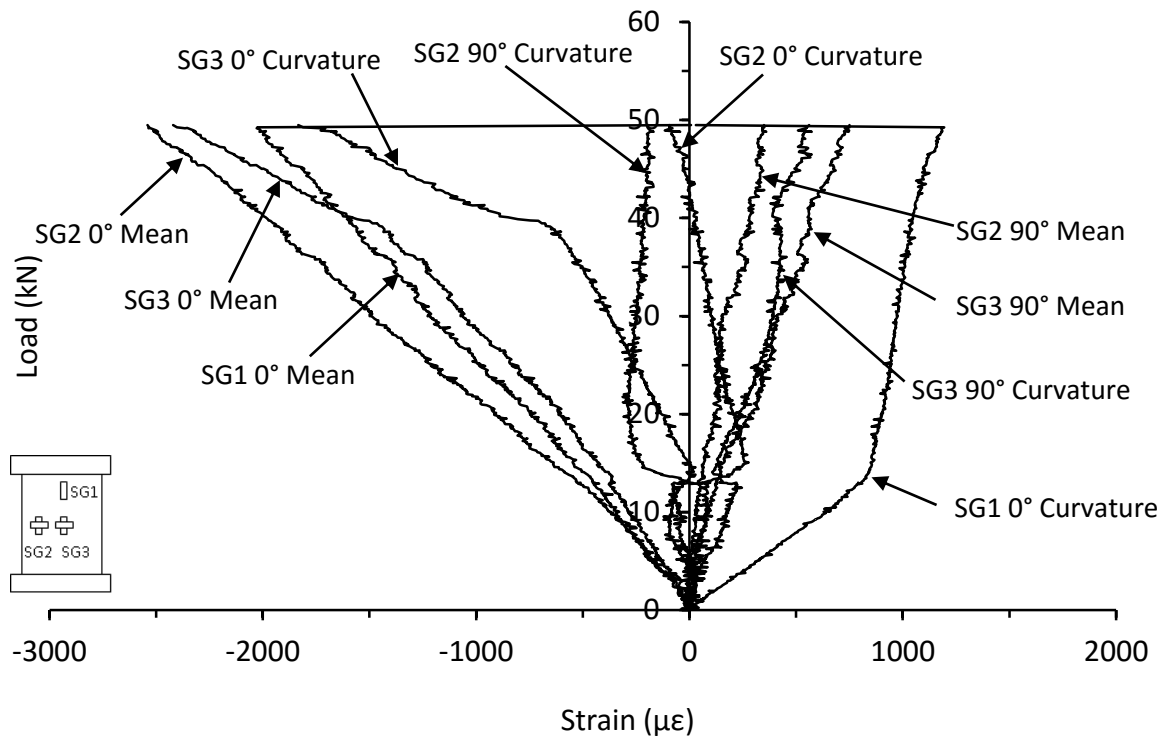


Figure C.12. Mean and curvature strain responses from thin unsymmetrical CP carbon/epoxy panel with 70kg/m³ core density impacted at 20J (DJ-8-6-CP-20-A)

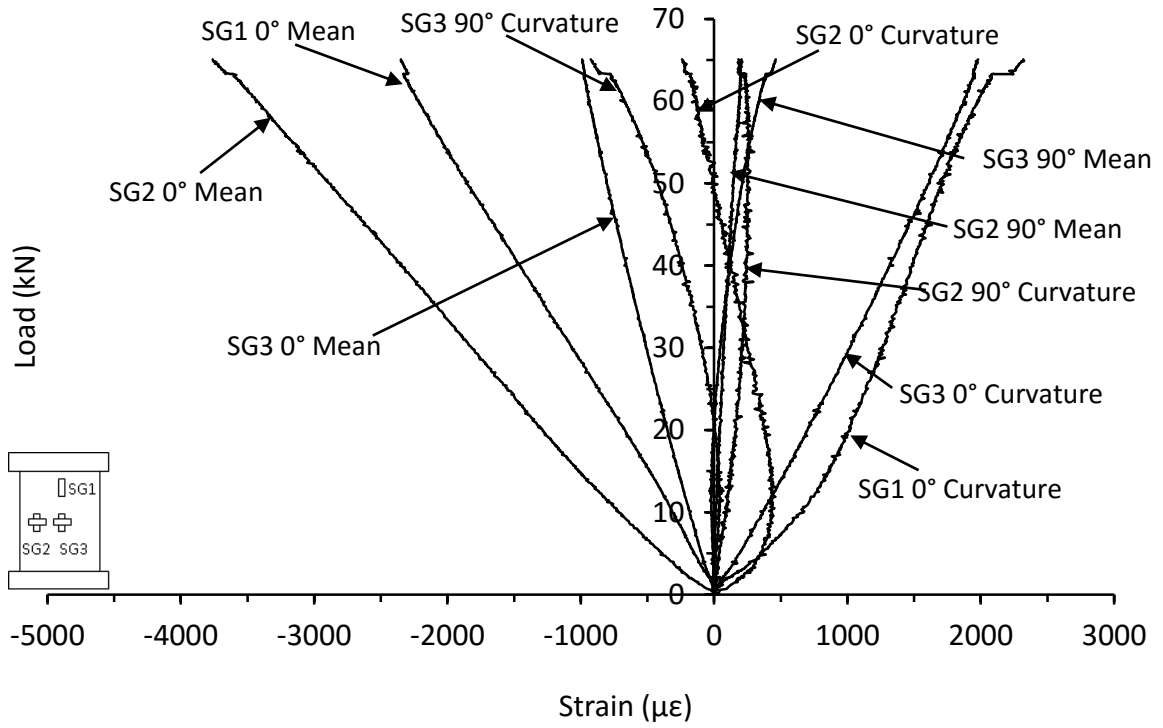


Figure C.13. Mean and curvature strain responses from thin unsymmetrical CP carbon/epoxy panel with 70kg/m^3 core density impacted at 23J (NC-8-6-CP-23J-1)

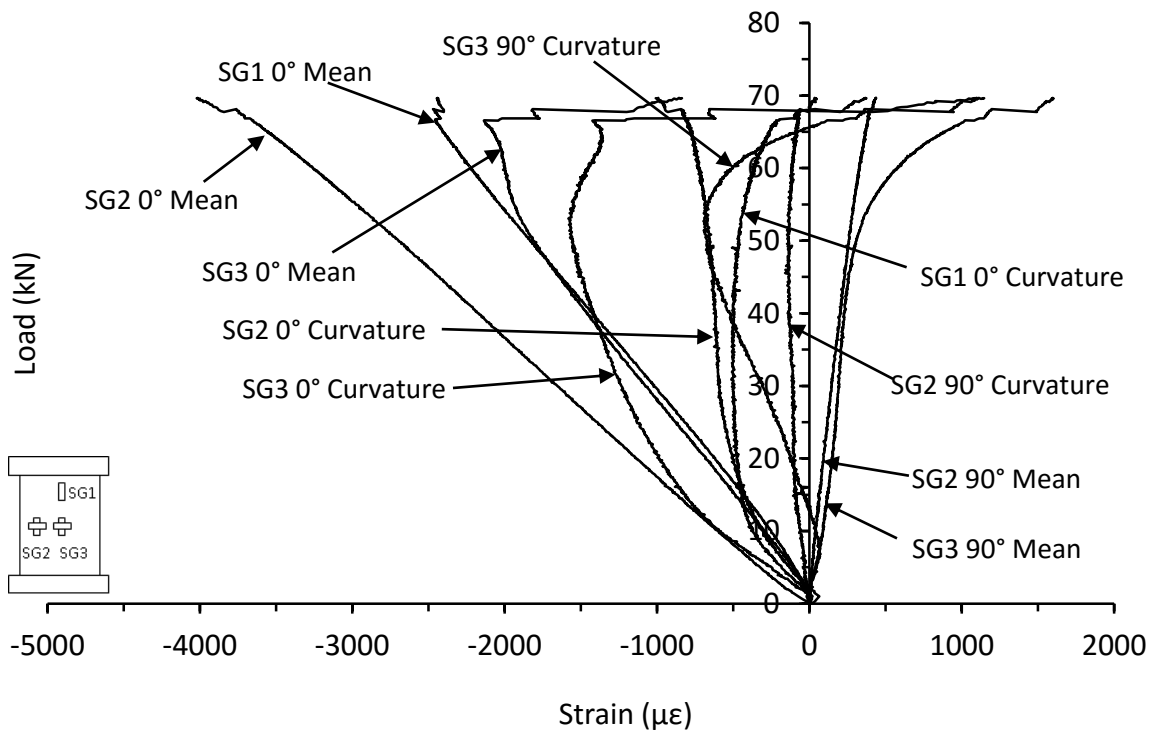


Figure C.14. Mean and curvature strain responses from thin unsymmetrical CP carbon/epoxy panel with 70kg/m^3 core density impacted at 23J (NC-8-6-CP-23J-2)

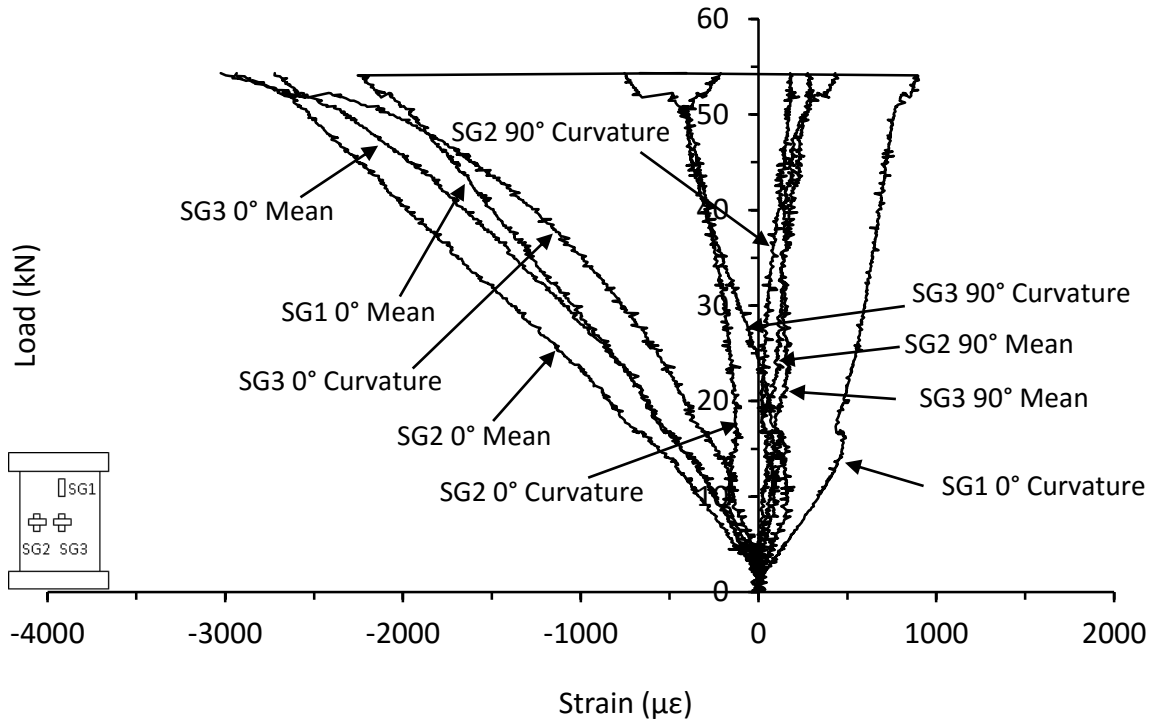


Figure C.15. Mean and curvature strain responses from thin unsymmetrical CP carbon/epoxy panel with 70kg/m³ core density impacted at 25J (DJ-8-6-CP-25J-A)

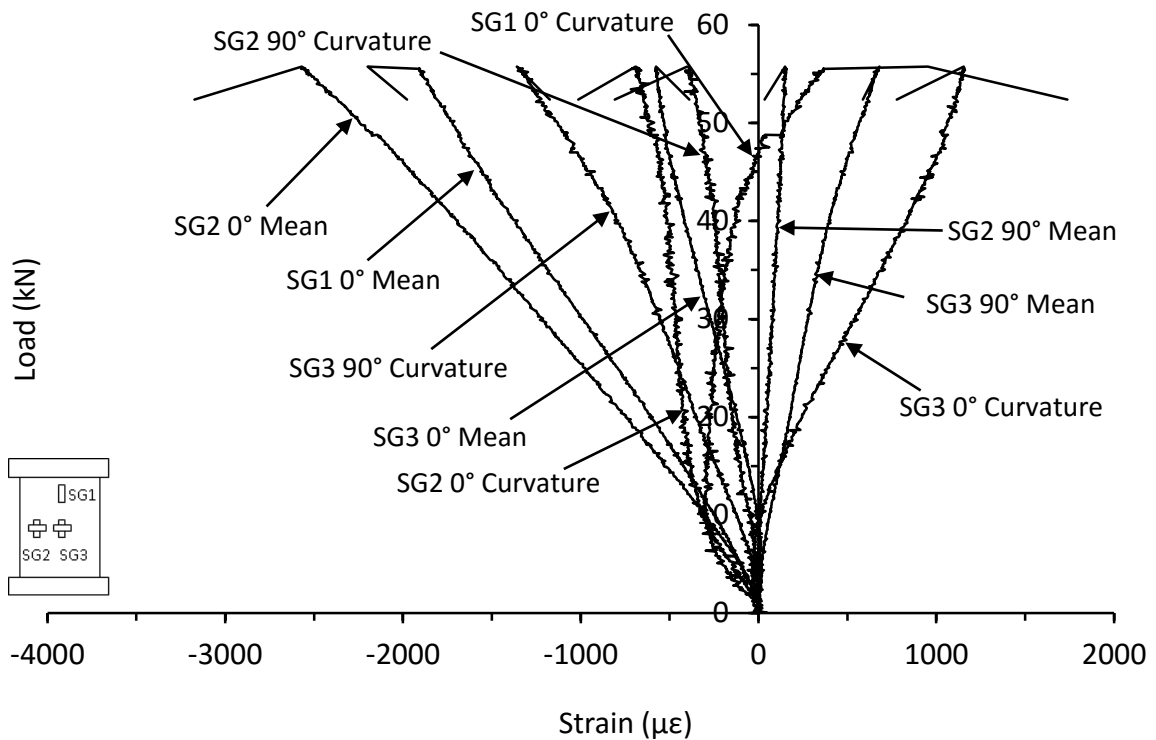


Figure C.16. Mean and curvature strain responses from thin unsymmetrical CP carbon/epoxy panel with 70kg/m³ core density impacted at 28J (NC-8-6-CP-28J)

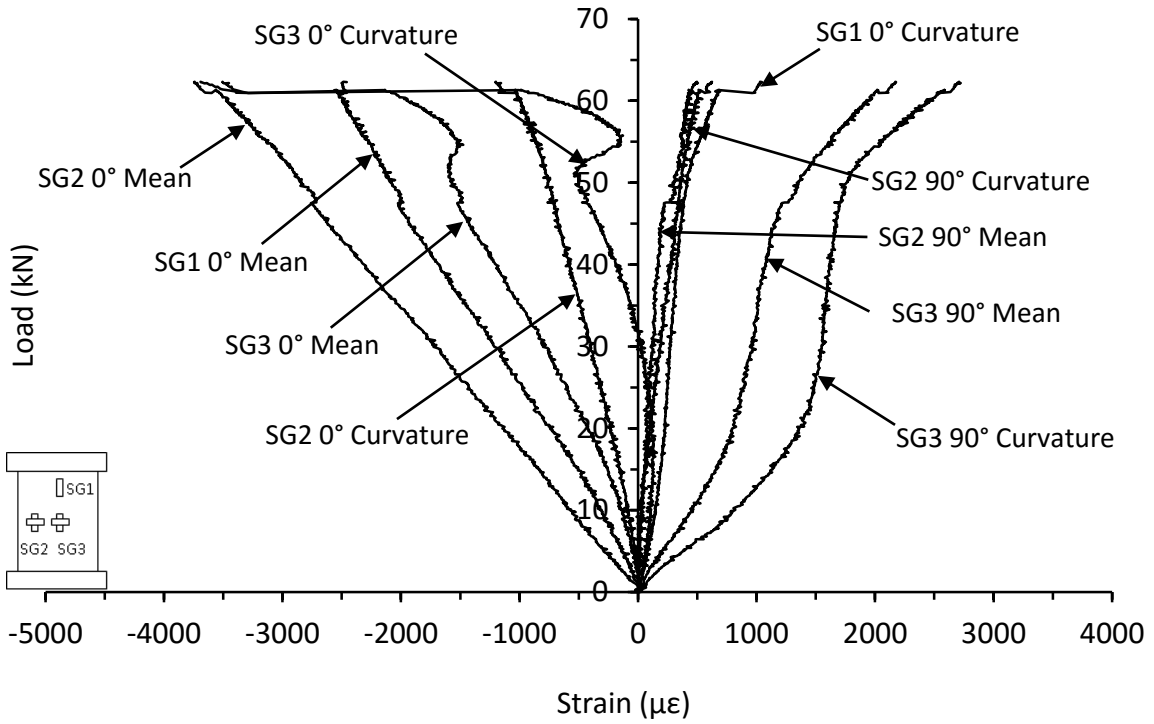


Figure C.17. Mean and curvature strain responses from thin unsymmetrical CP carbon/epoxy panel with 70kg/m³ core density impacted at 30J (DJ-8-6-CP-30J-A)

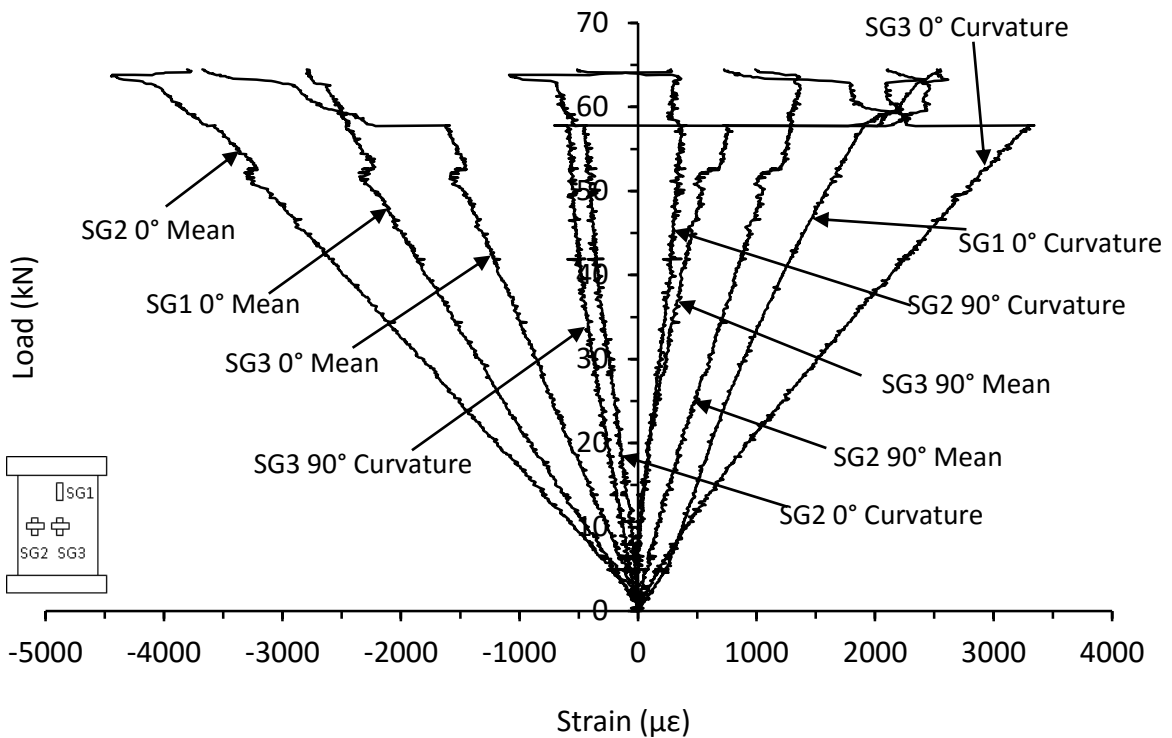


Figure C.18. Mean and curvature strain responses from thin symmetrical QI carbon/epoxy panel with 70kg/m³ core density impacted at 5J (JL-8-8-QI-5J-B)

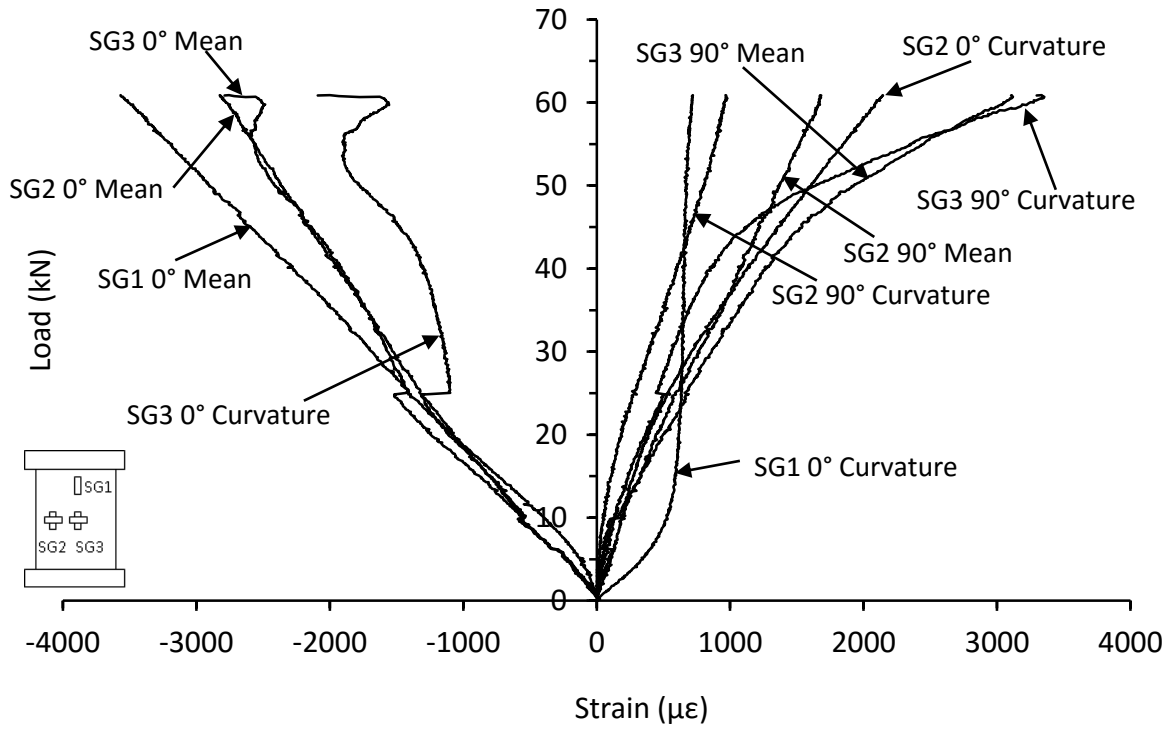


Figure C.19. Mean and curvature strain responses from thin symmetrical QI carbon/epoxy panel with 70kg/m³ core density impacted at 10J (JL-8-8-QI-10J-B)

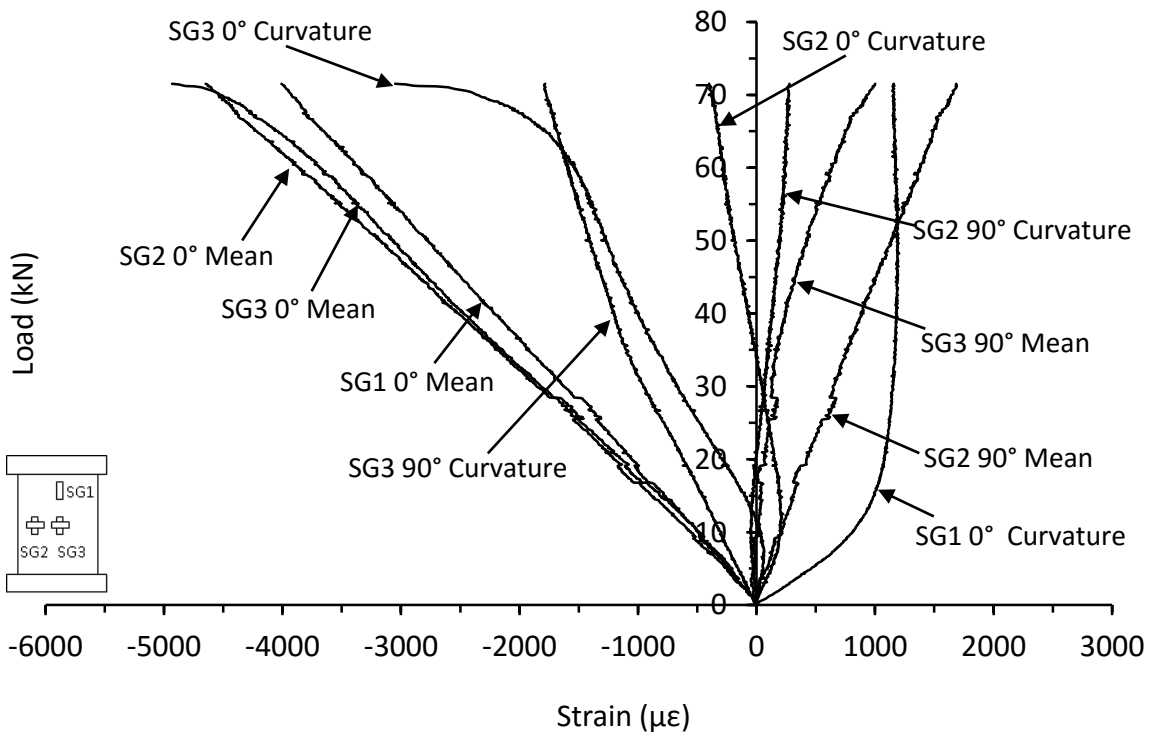


Figure C.20. Mean and curvature strain responses from thin symmetrical QI carbon/epoxy panel with 70kg/m³ core density impacted at 15J (JL-8-8-QI-15J-B)

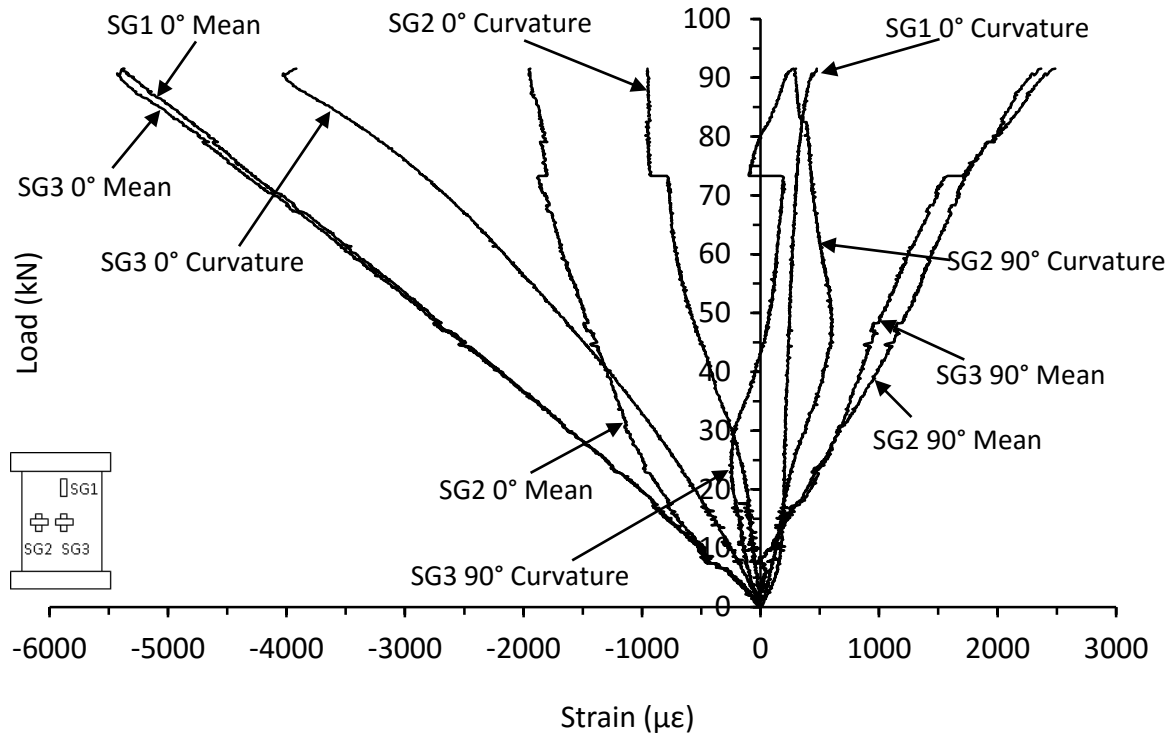


Figure C.21. Mean and curvature strain responses from thin symmetrical QI carbon/epoxy panel with 70kg/m³ core density impacted at 20J (JL-8-8-QI-20J-B)

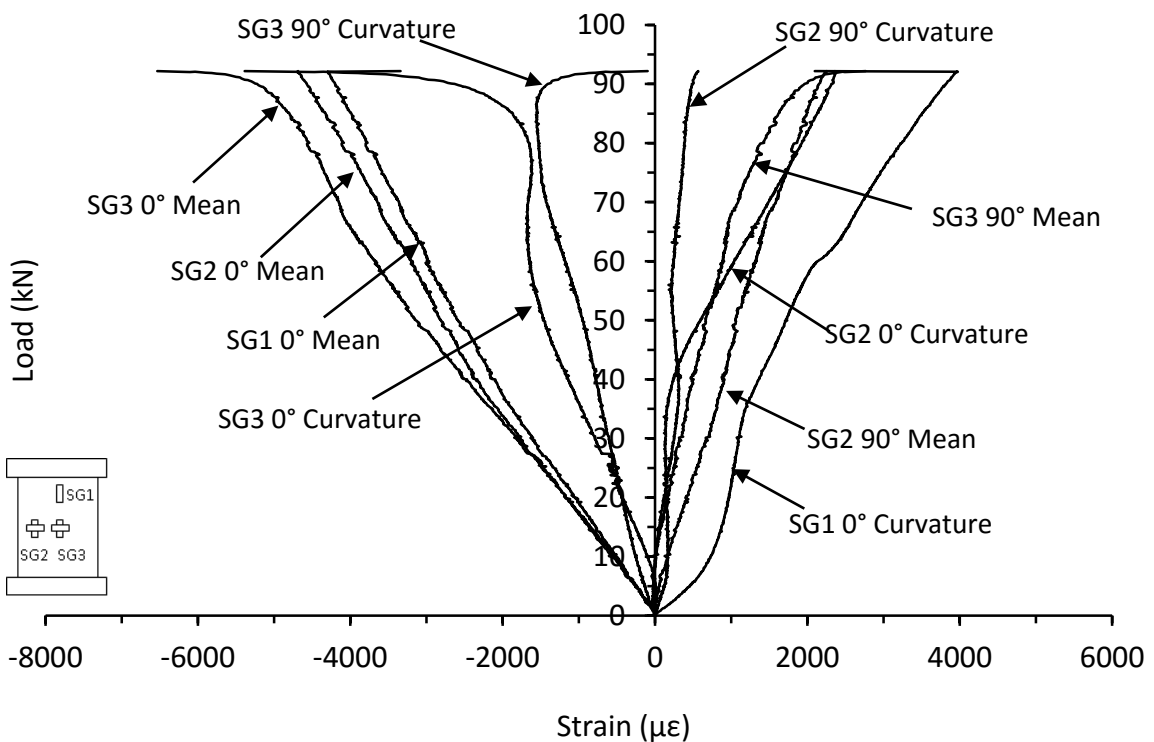


Figure C.22. Mean and curvature strain responses from thin symmetrical QI carbon/epoxy panel with 70kg/m³ core density impacted at 25J (JL-8-8-QI-25J-B)

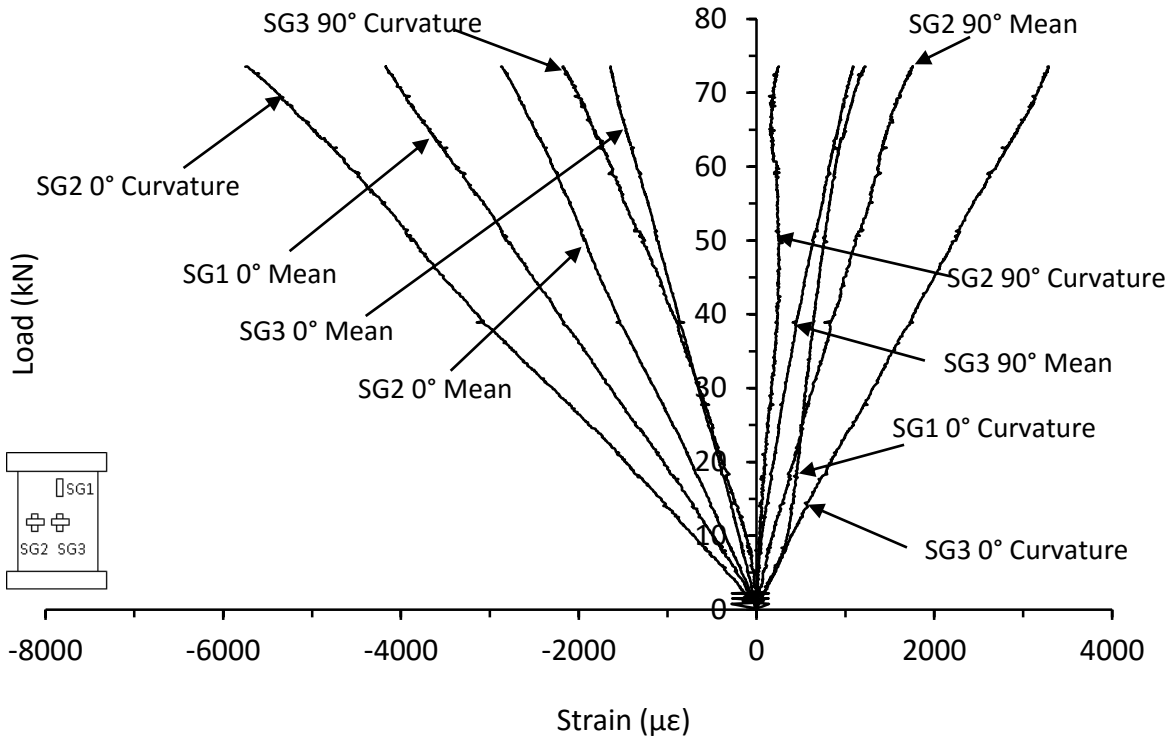


Figure C.23. Mean and curvature strain responses from thin symmetrical QI carbon/epoxy panel with 70kg/m^3 core density impacted at 30J (JL-8-8-QI-30J-B)

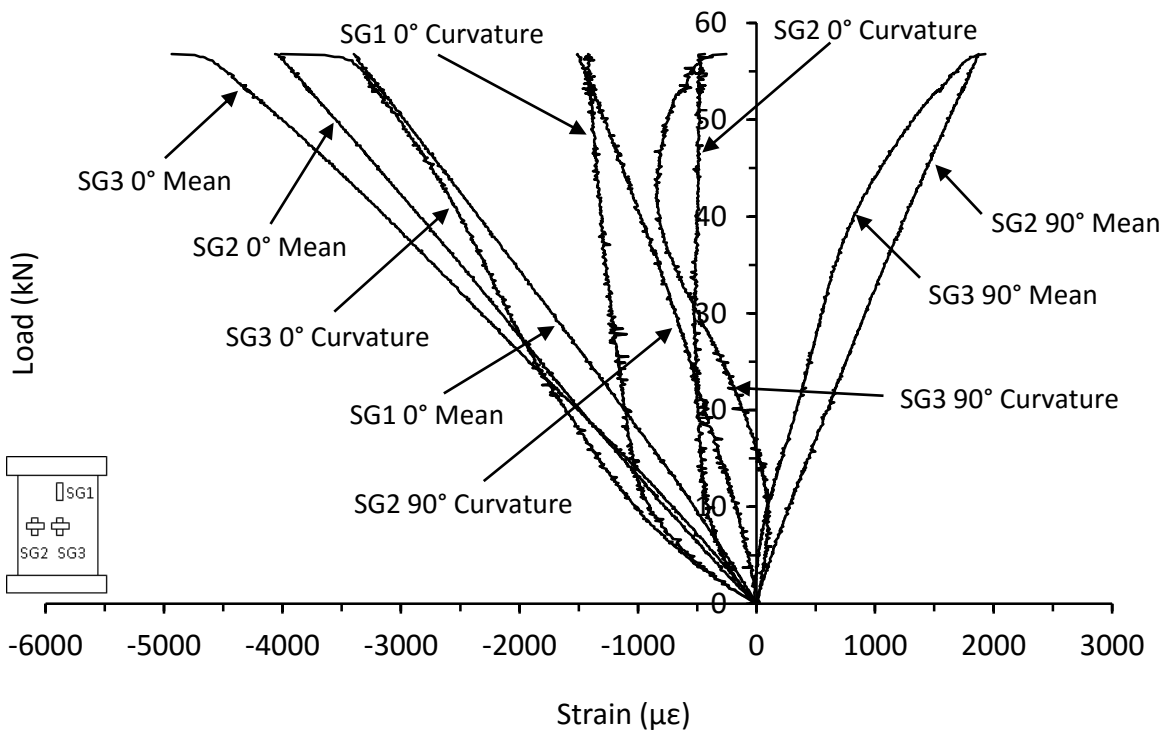


Figure C.24. Mean and curvature strain responses from thin unsymmetrical QI carbon/epoxy panel with 70kg/m^3 core density impacted at 5J (LB-8-6-QI-5J-A)

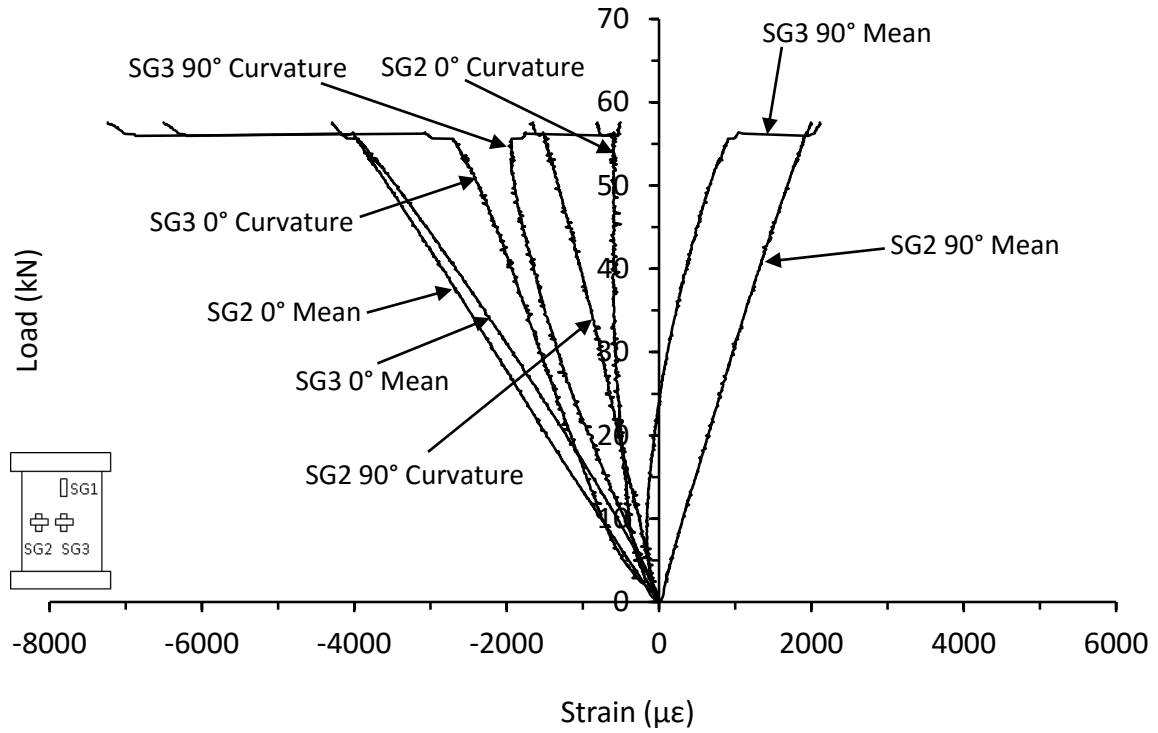


Figure C.25. Mean and curvature strain responses from thin unsymmetrical QI carbon/epoxy panel with 70kg/m³ core density impacted at 10J (LB-8-6-QI-10J-B)

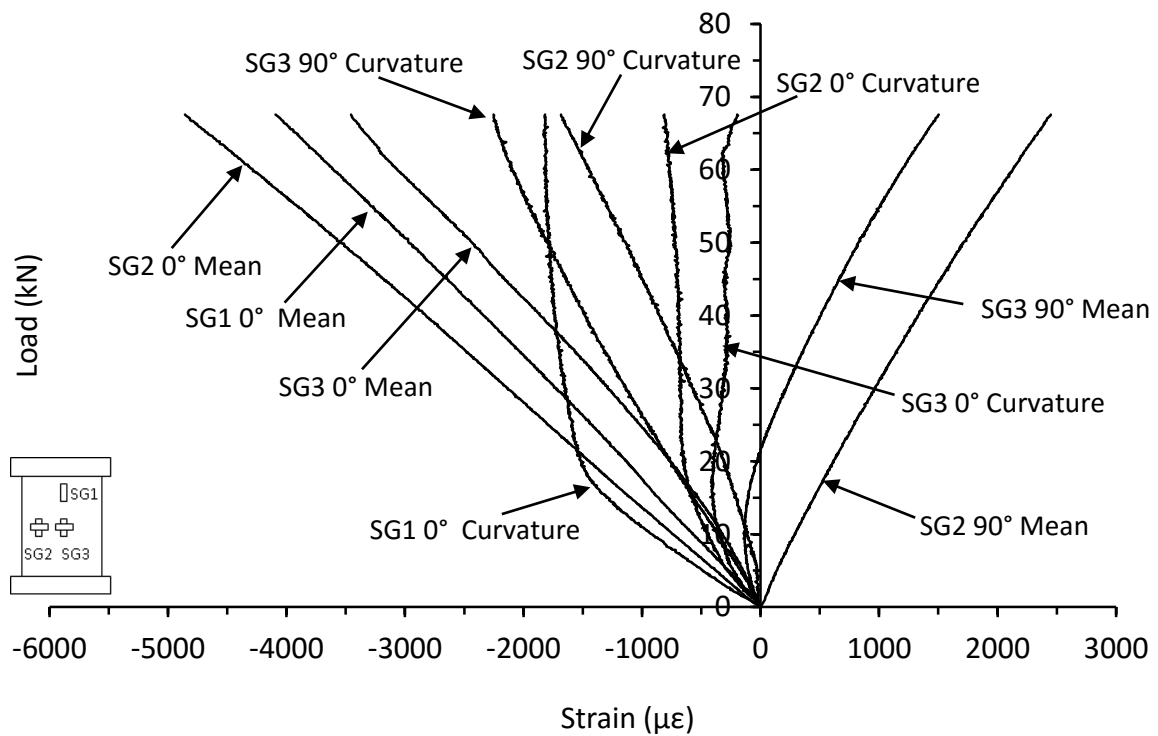


Figure C.26. Mean and curvature strain responses from thin unsymmetrical QI carbon/epoxy panel with 70kg/m³ core density impacted at 15J (LB-8-6-QI-15J-B)

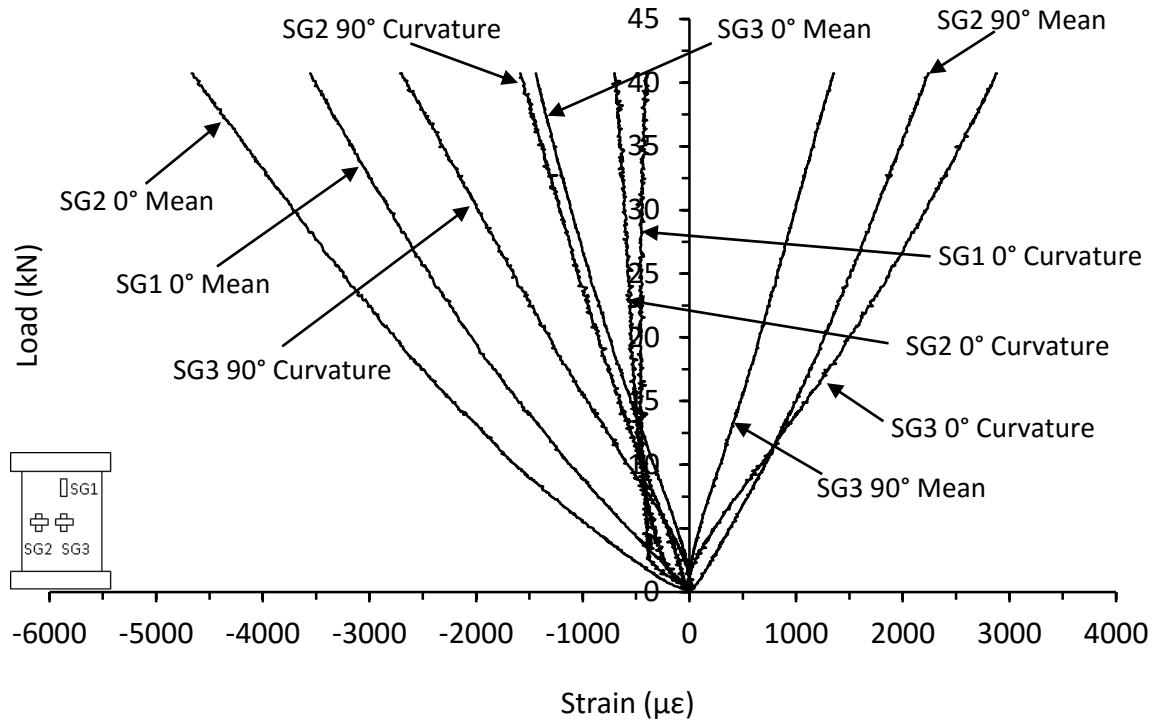


Figure C.27. Mean and curvature strain responses from thin unsymmetrical QI carbon/epoxy panel with 70kg/m³ core density impacted at 20J (LB-8-6-QI-20J-B)

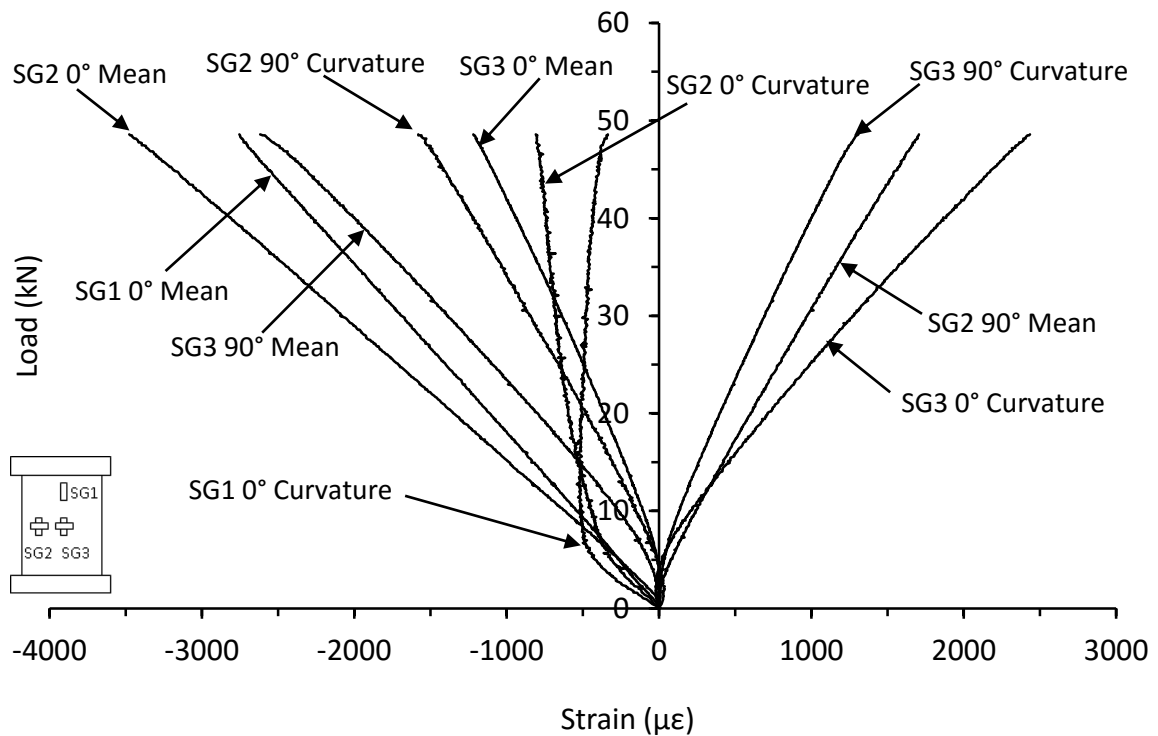


Figure C.28. Mean and curvature strain responses from thin unsymmetrical QI carbon/epoxy panel with 70kg/m³ core density impacted at 25J (LB-8-6-QI-25J-A)

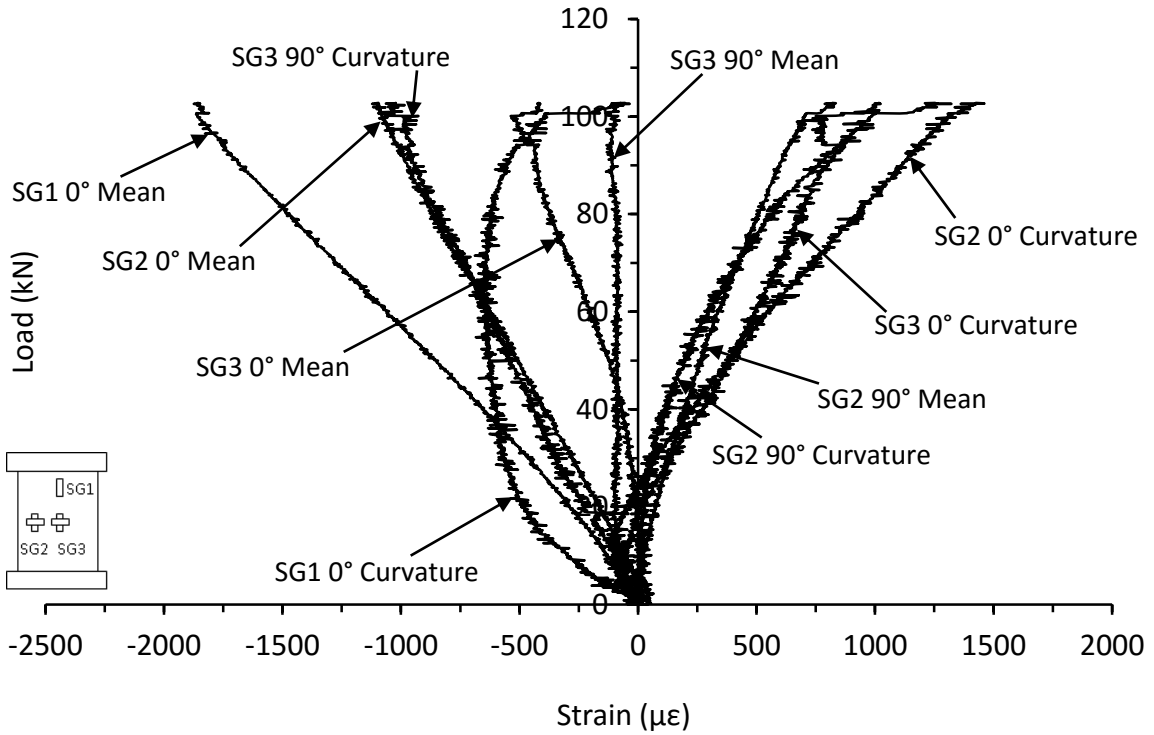


Figure C.29. Mean and curvature strain responses from thick symmetrical CP carbon/epoxy panel with 70kg/m³ core density impacted at 15J (CI-16-16-CP-15J)

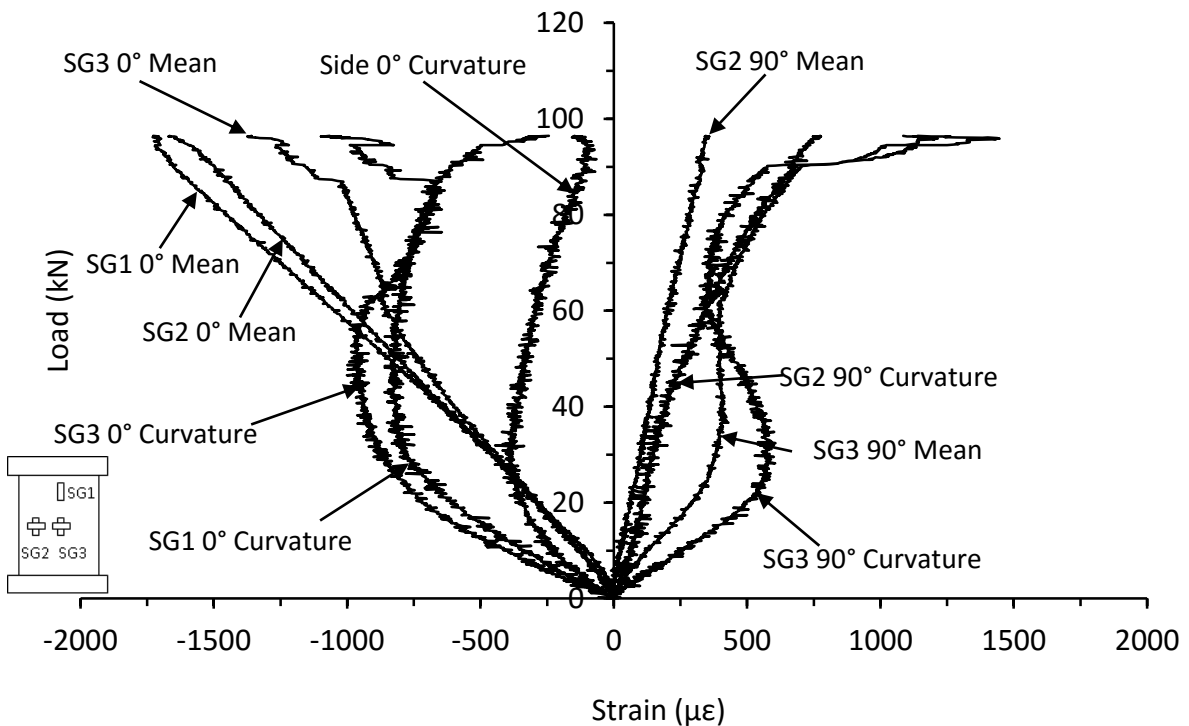


Figure C.30. Mean and curvature strain responses from thick symmetrical CP carbon/epoxy panel with 70kg/m³ core density impacted at 45J (CI-16-16-CP-45J)

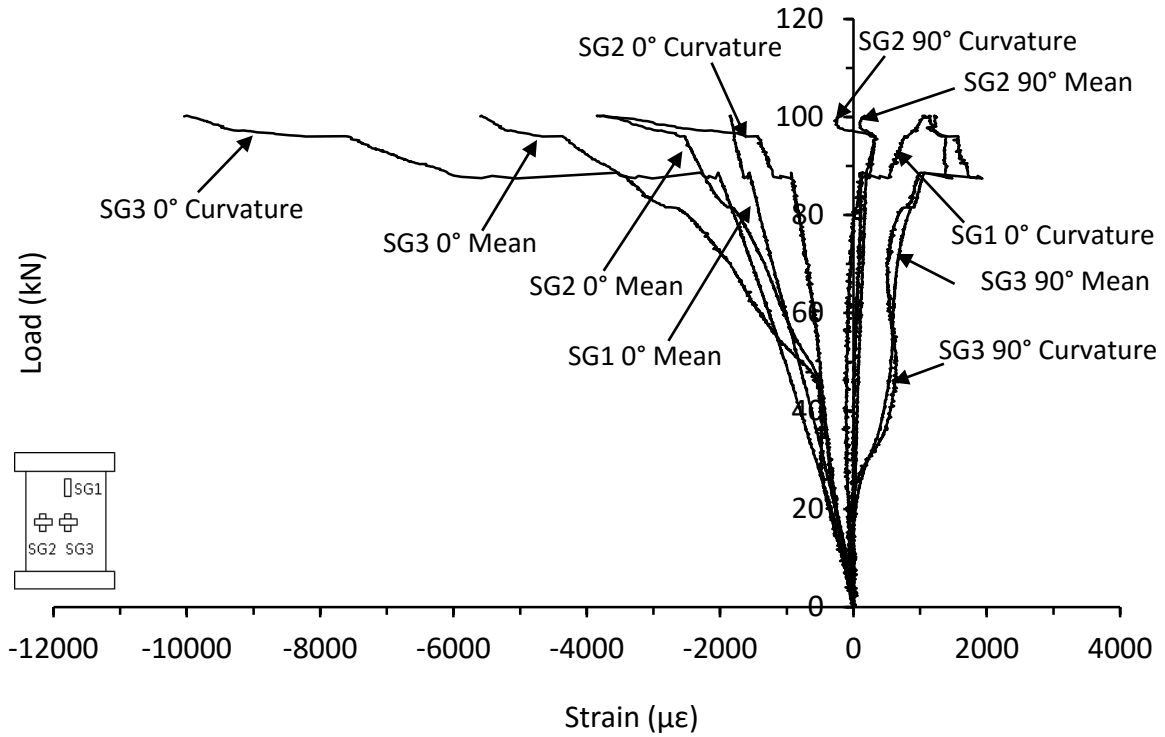


Figure C.31. Mean and curvature strain responses from thick symmetrical CP carbon/epoxy panel with 70kg/m³ core density impacted at 60J (CI-16-16-CP-60J)

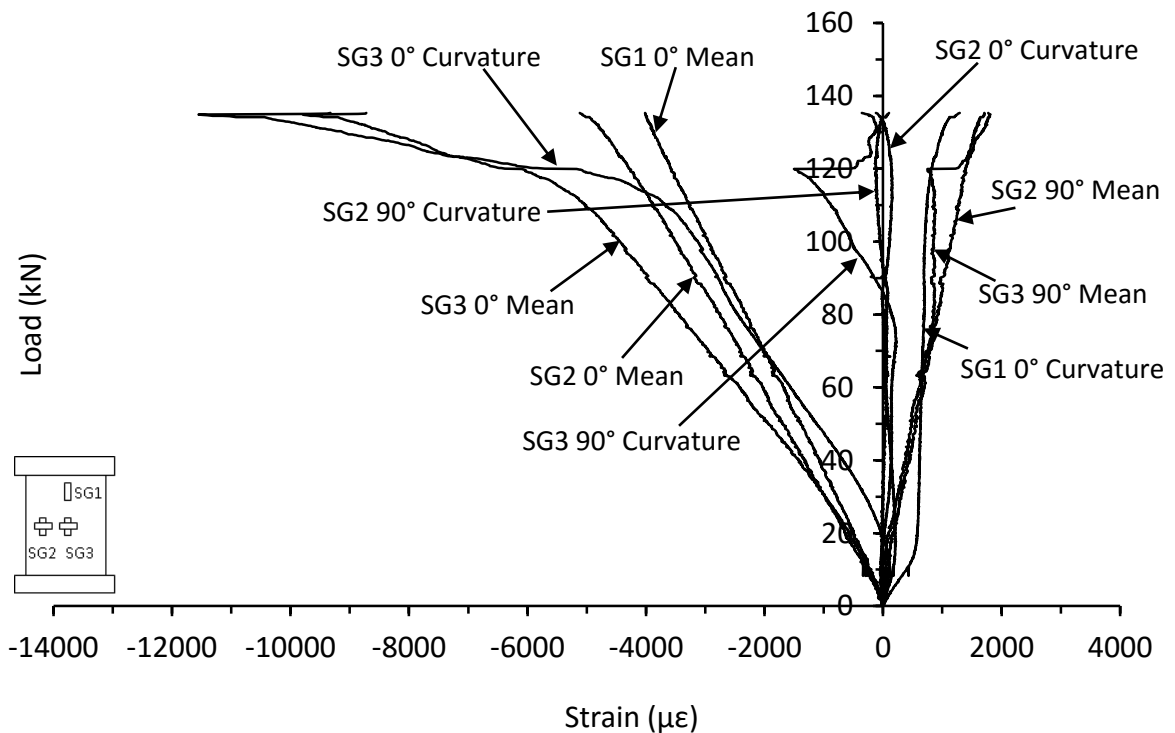


Figure C.32. Mean and curvature strain responses from thick symmetrical QI carbon/epoxy panel with 70kg/m³ core density impacted at 15J (JL-16-16-QI-15J-B)

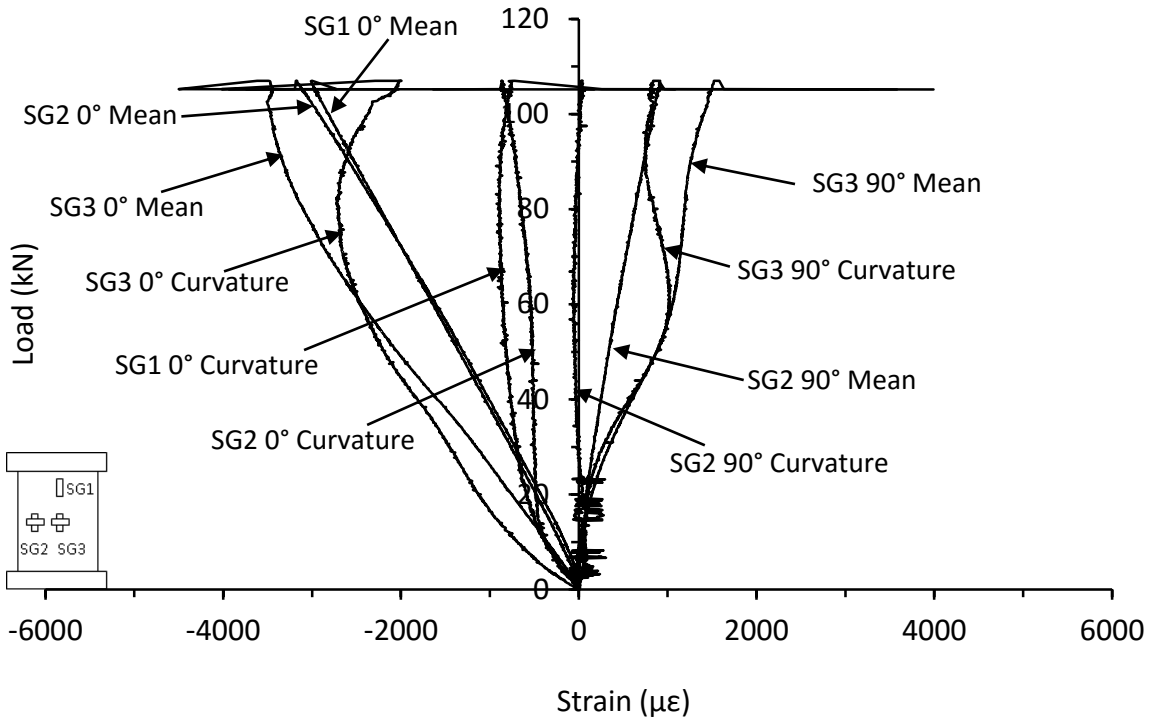


Figure C.33. Mean and curvature strain responses from thick symmetrical QI carbon/epoxy panel with 70kg/m³ core density impacted at 15J (CI-16-16-QI-15J)

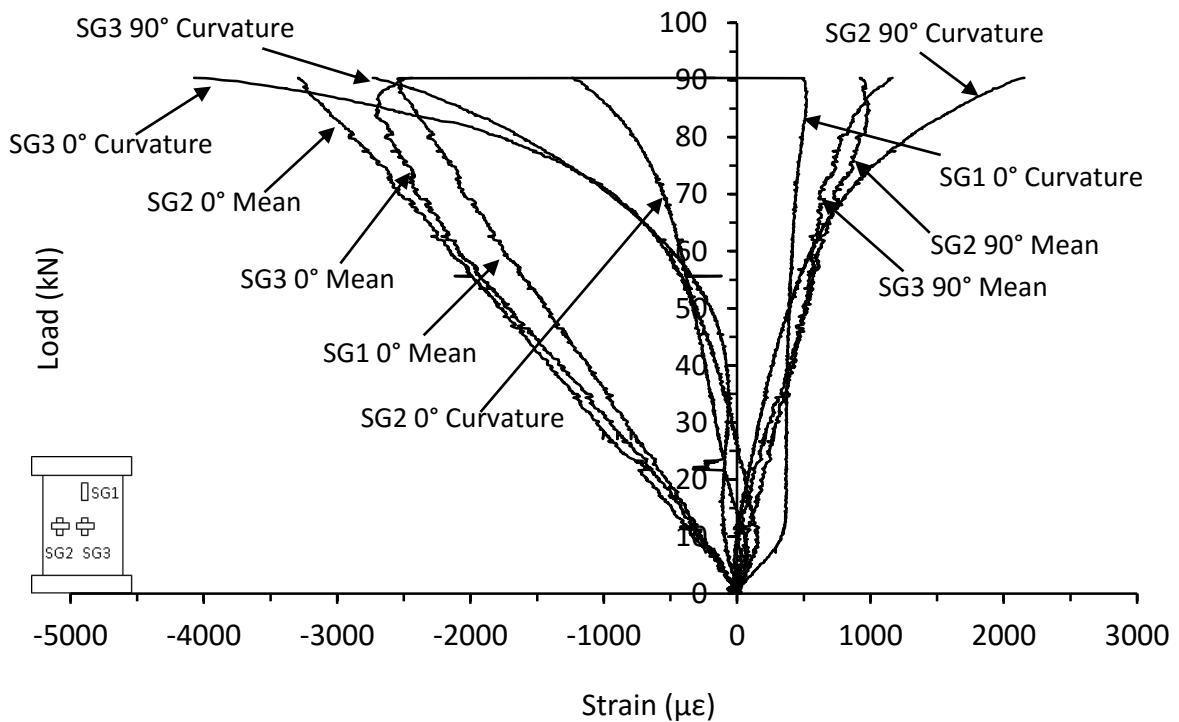


Figure C.34. Mean and curvature strain responses from thick symmetrical QI carbon/epoxy panel with 70kg/m³ core density impacted at 30J (JL-16-16-QI-30J-B)

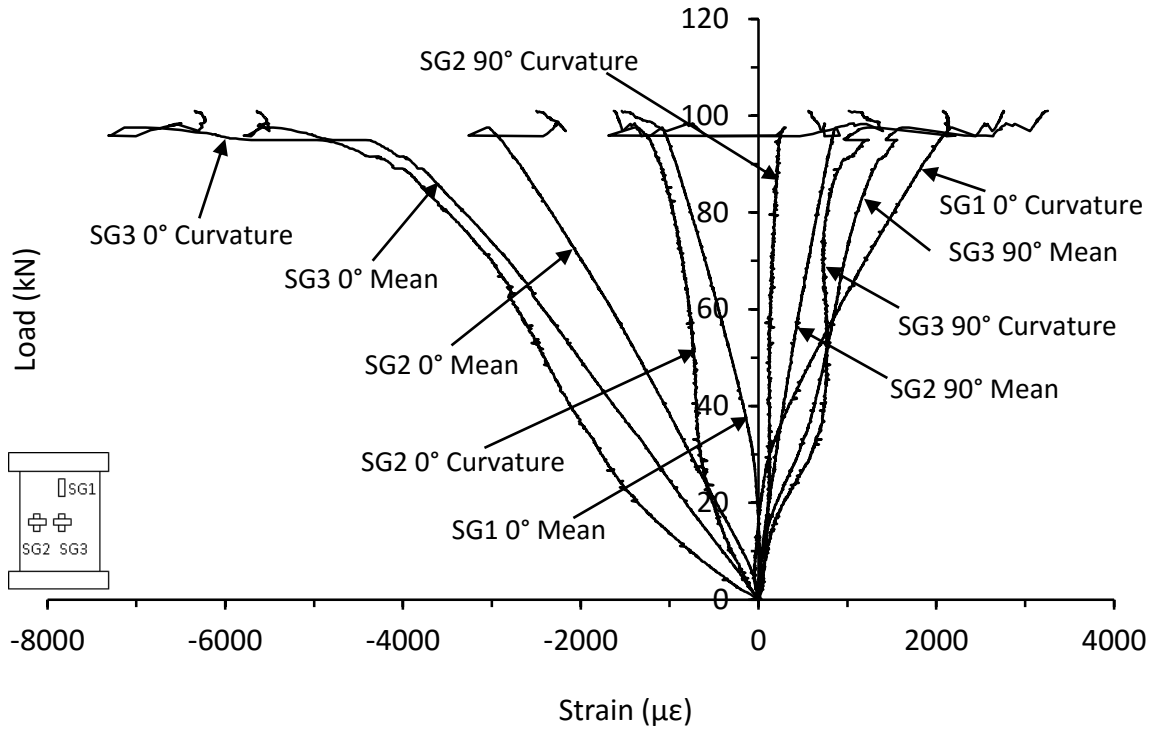


Figure C.35. Mean and curvature strain responses from thick symmetrical QI carbon/epoxy panel with 70kg/m³ core density impacted at 30J (CI-16-16-QI-30J)

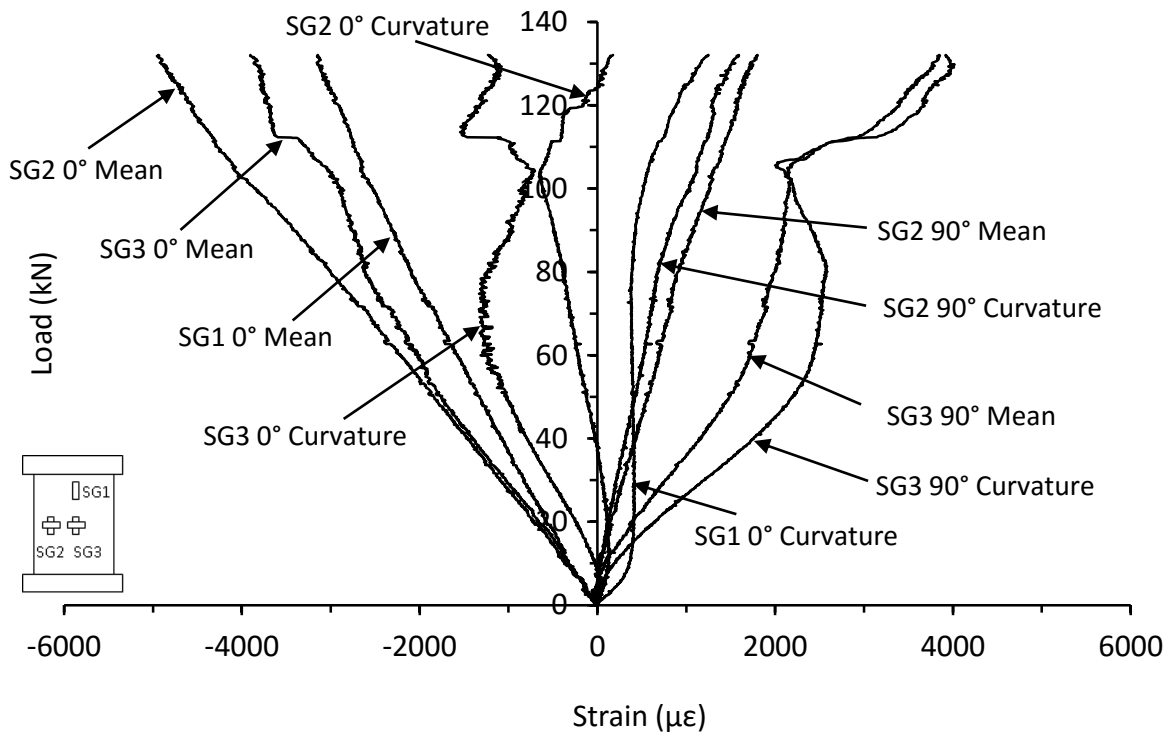


Figure C.36. Mean and curvature strain responses from thick symmetrical QI carbon/epoxy panel with 70kg/m³ core density impacted at 45J (JL-16-16-QI-45J-B)

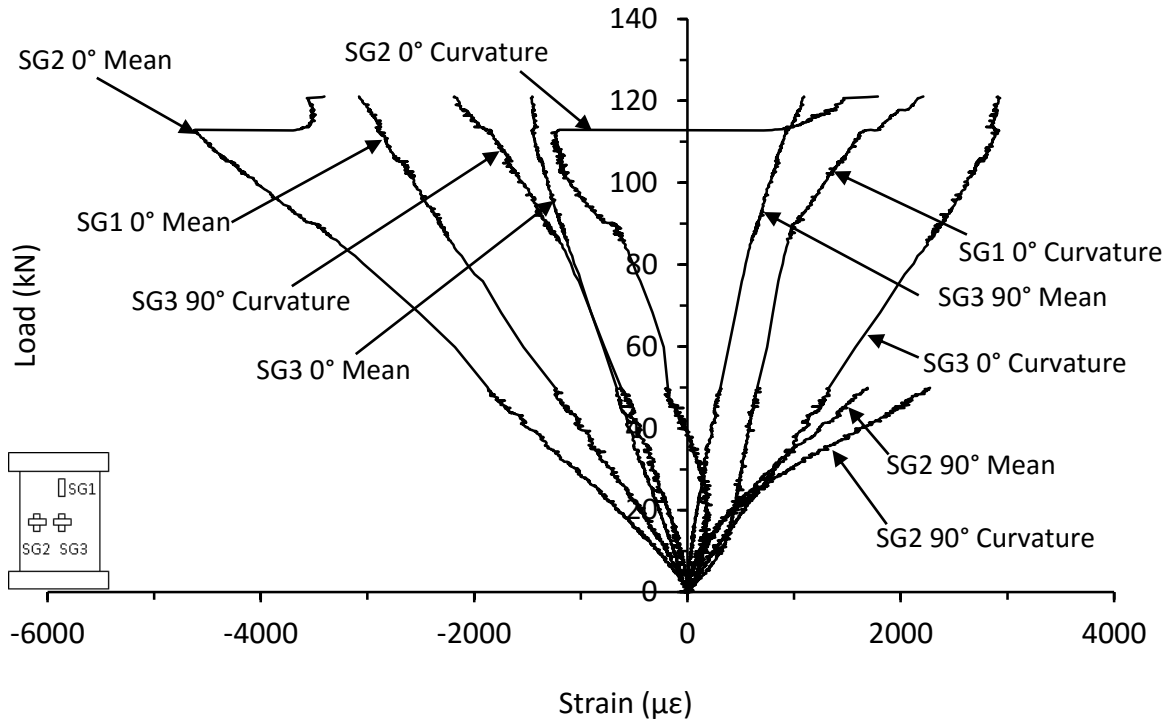


Figure C.37. Mean and curvature strain responses from thick symmetrical QI carbon/epoxy panel with 70kg/m³ core density impacted at 60J (JL-16-16-QI-60J-B)

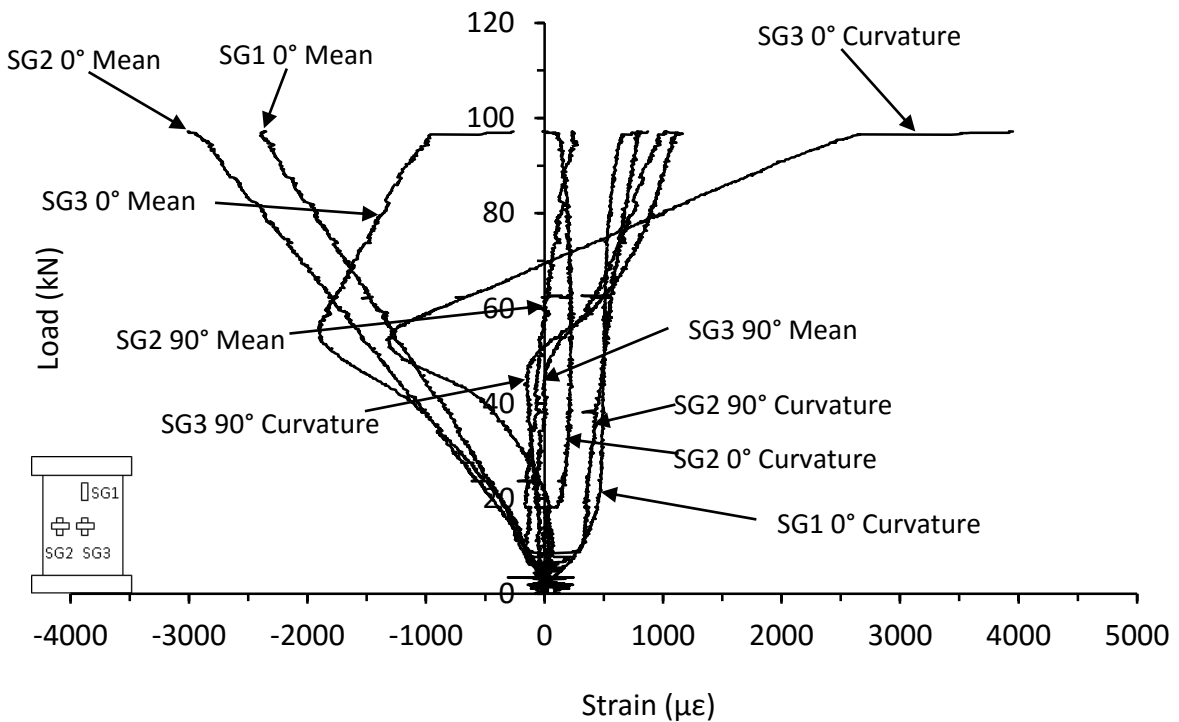


Figure C.38. Mean and curvature strain responses from thick unsymmetrical CP carbon/epoxy panel with 70kg/m³ core density impacted at 15J (DJ-16-12-CP-15J-A)

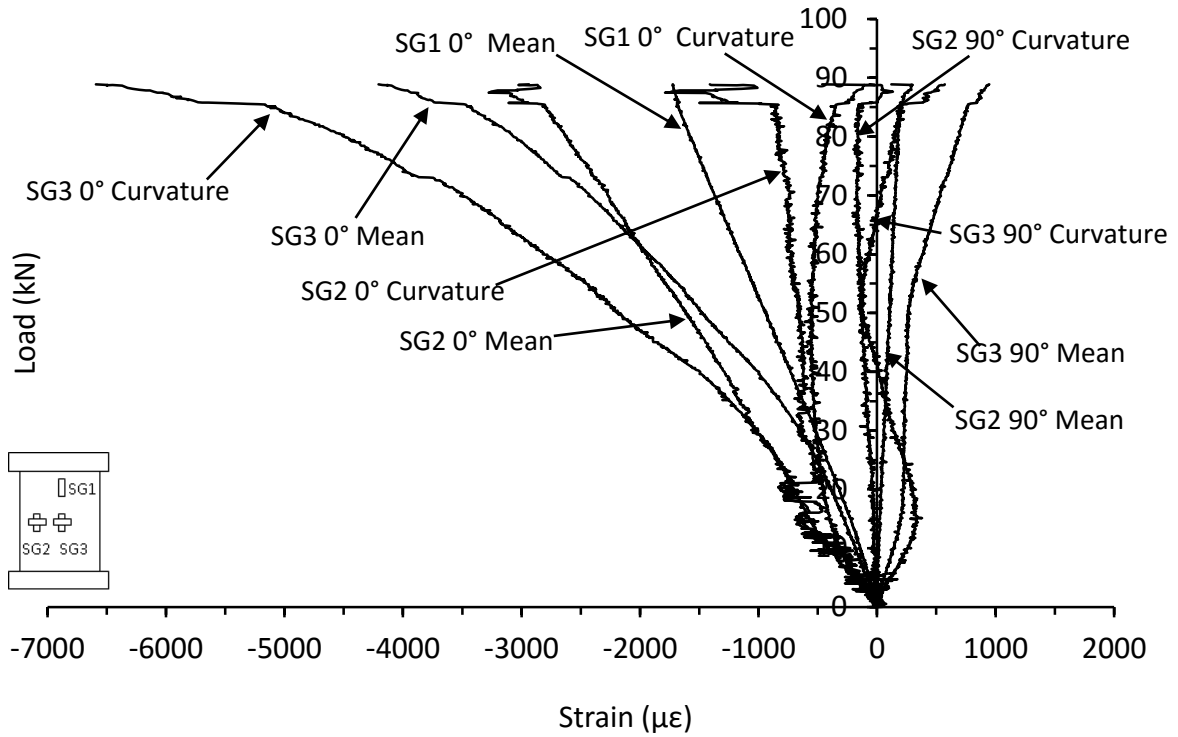


Figure C.39. Mean and curvature strain responses from thick unsymmetrical CP carbon/epoxy panel with 70kg/m³ core density impacted at 20J (NC-16-12-CP-20J)

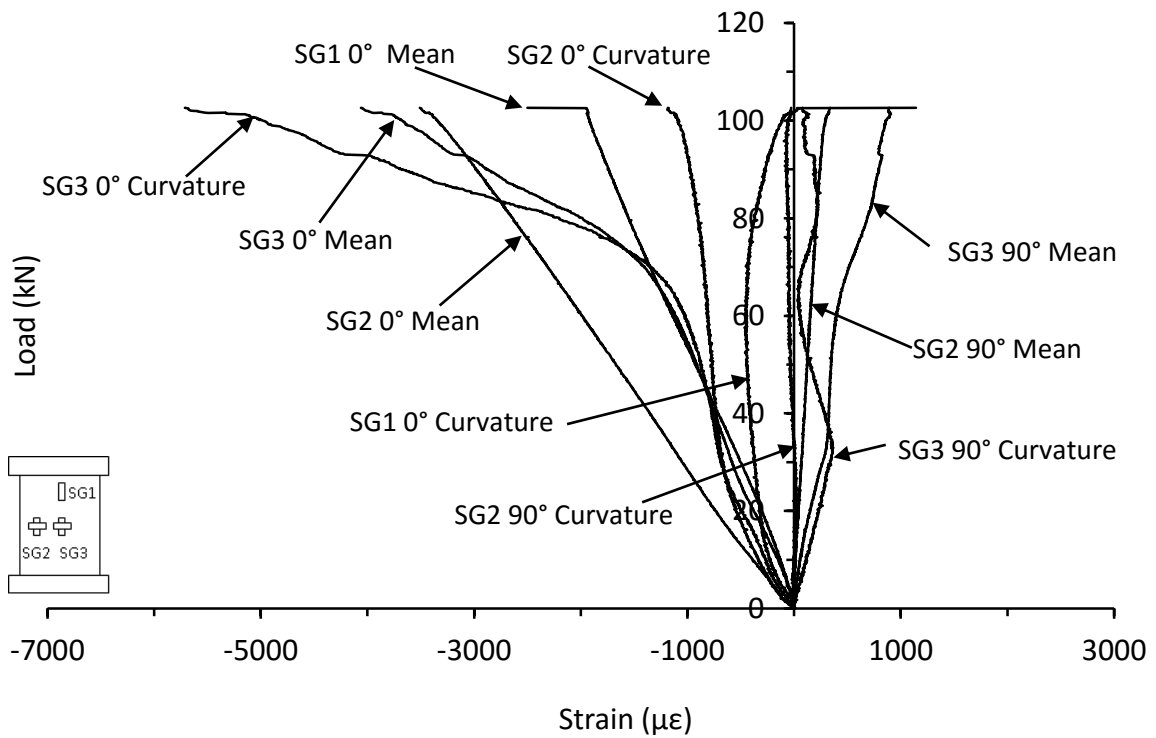


Figure C.40. Mean and curvature strain responses from thick unsymmetrical CP carbon/epoxy panel with 70kg/m³ core density impacted at 30J (NC-16-12-CP-30J)

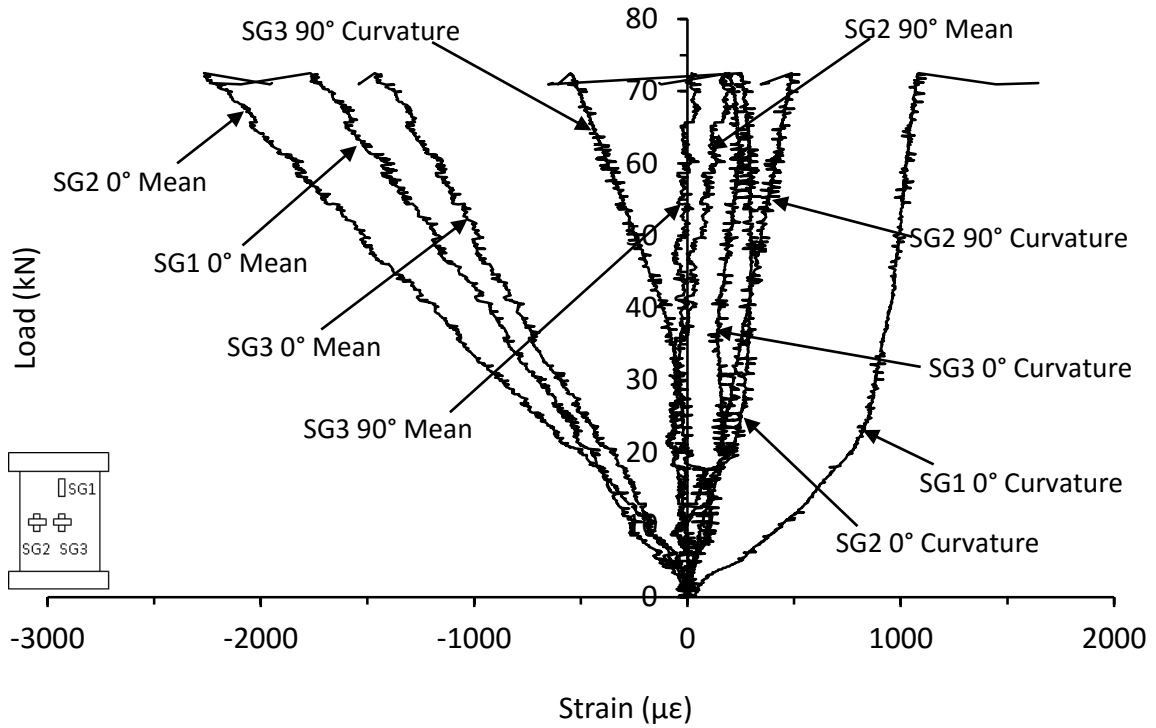


Figure C.41. Mean and curvature strain responses from thick unsymmetrical CP carbon/epoxy panel with 70kg/m³ core density impacted at 30J (DJ-16-12-CP-30J-A)

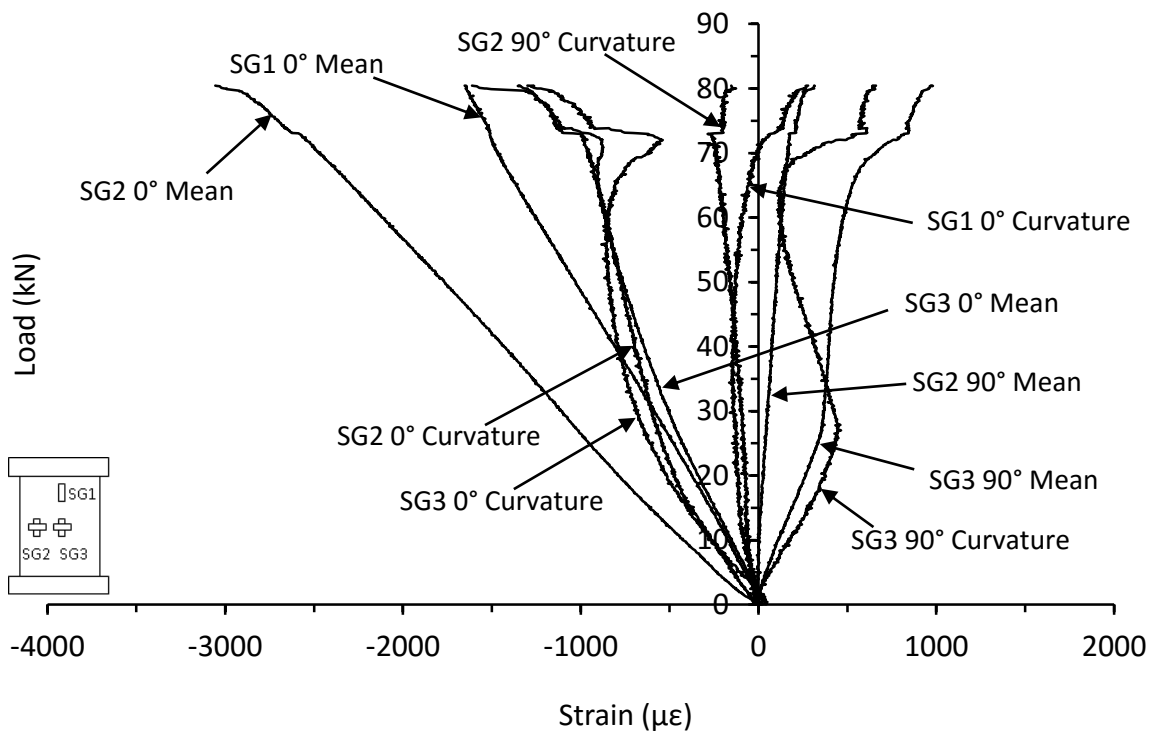


Figure C.42. Mean and curvature strain responses from thick unsymmetrical CP carbon/epoxy panel with 70kg/m³ core density impacted at 35J (NC-16-12-CP-35J)

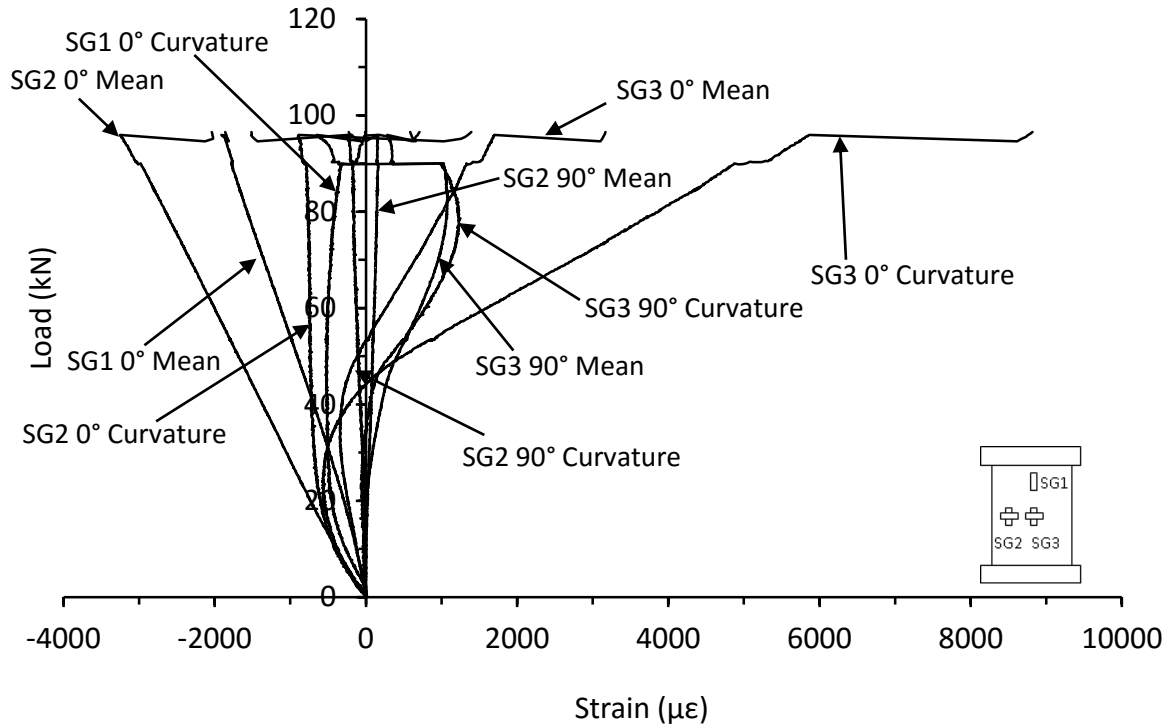


Figure C.43. Mean and curvature strain responses from thick unsymmetrical CP carbon/epoxy panel with 70kg/m^3 core density impacted at 45J (NC-16-12-CP-45J)

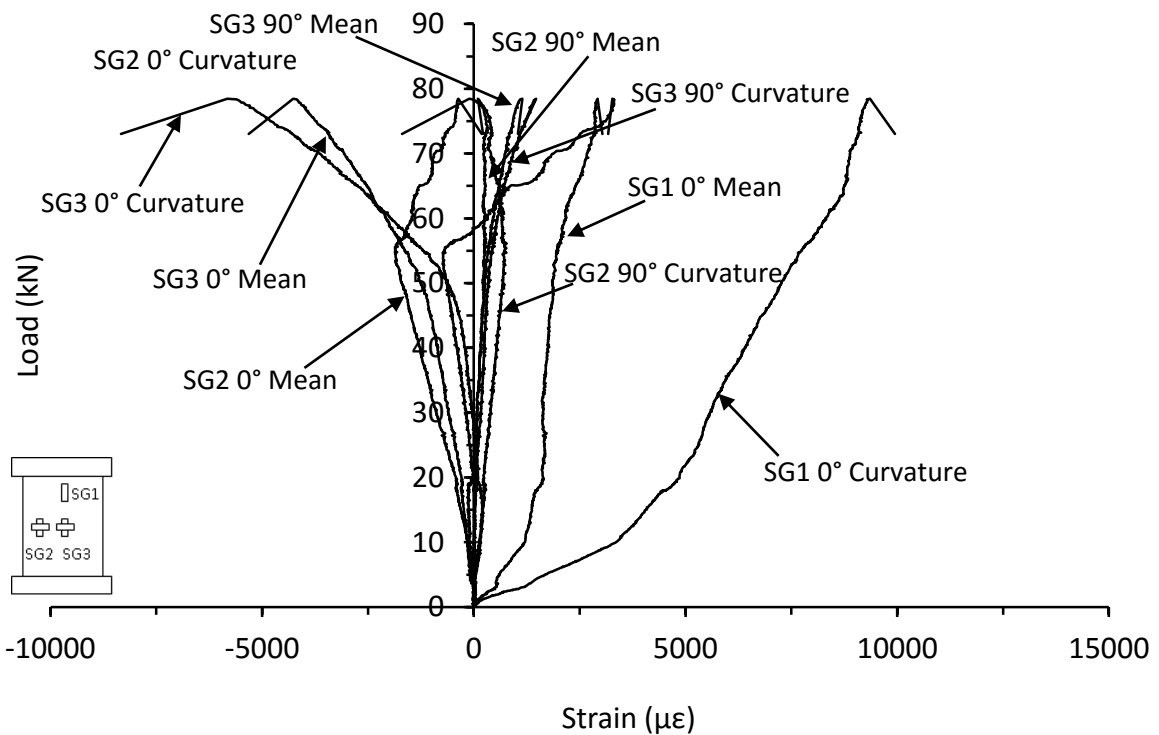


Figure C.44. Mean and curvature strain responses from thick unsymmetrical CP carbon/epoxy panel with 70kg/m^3 core density impacted at 54J (DJ-16-12-CP-54J-A)

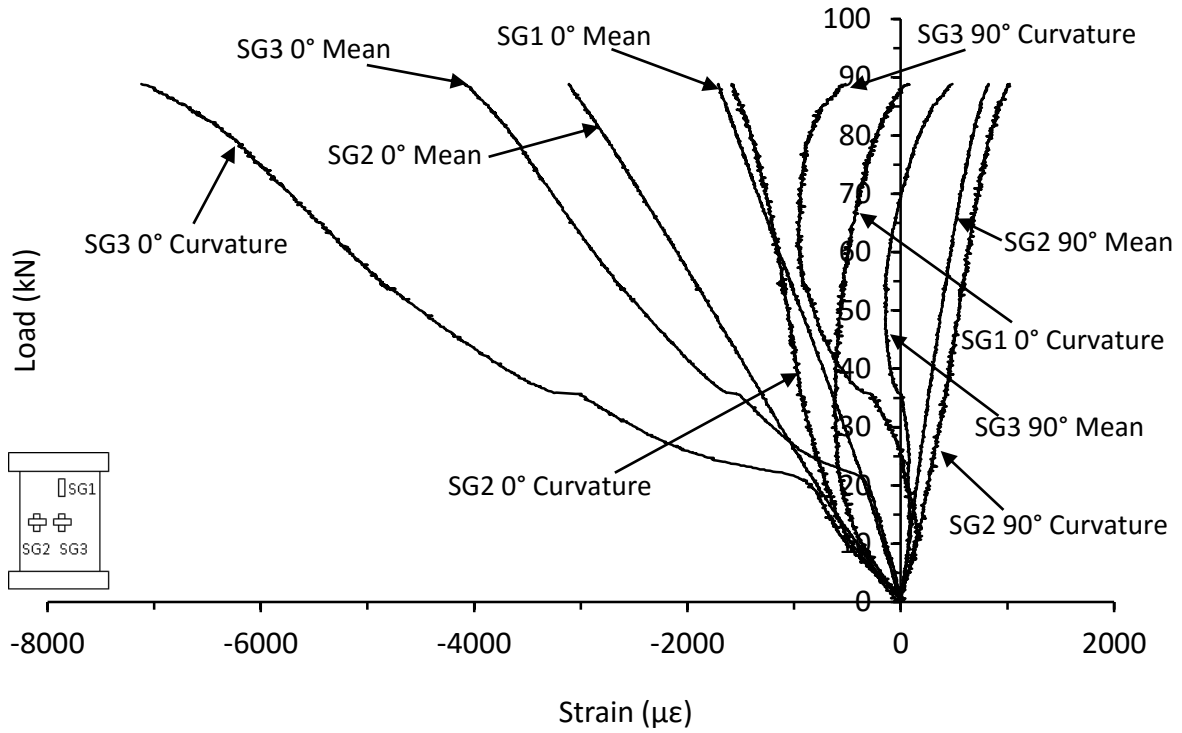


Figure C.45. Mean and curvature strain responses from thick unsymmetrical CP carbon/epoxy panel with 70kg/m³ core density impacted at 60J (NC-16-12-CP-60J)

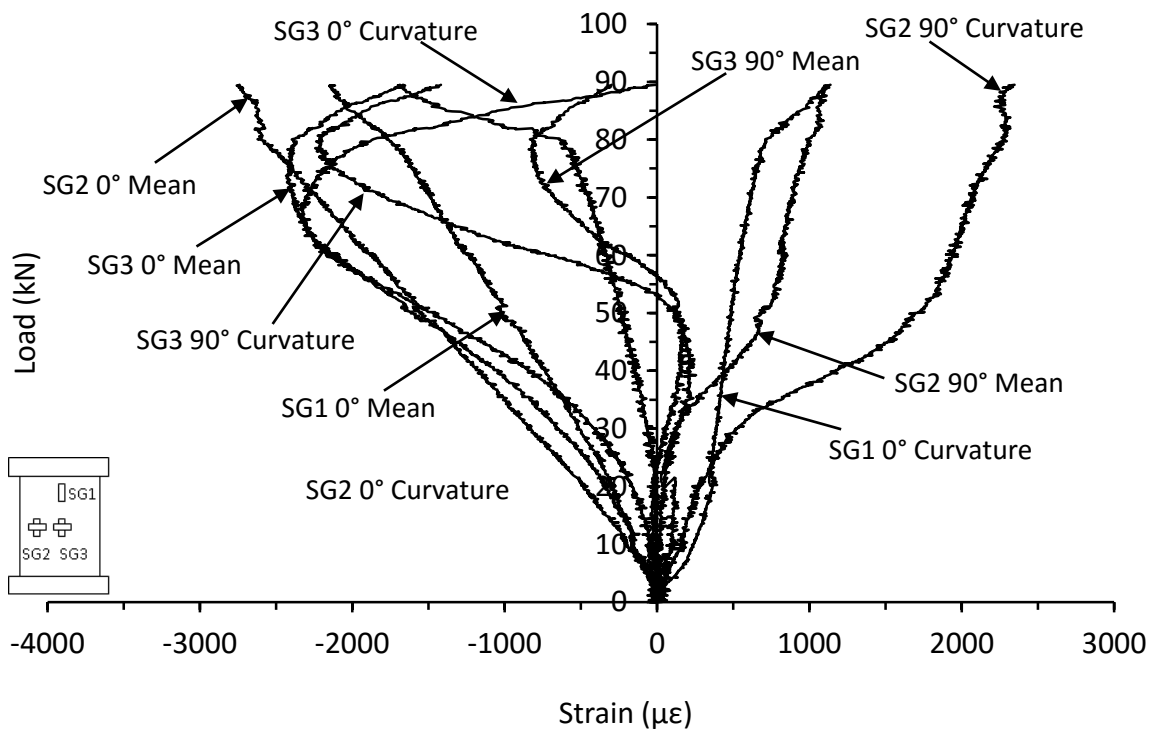


Figure C.46. Mean and curvature strain responses from thick unsymmetrical CP carbon/epoxy panel with 70kg/m³ core density impacted at 60J (DJ-16-12-CP-60J-A)

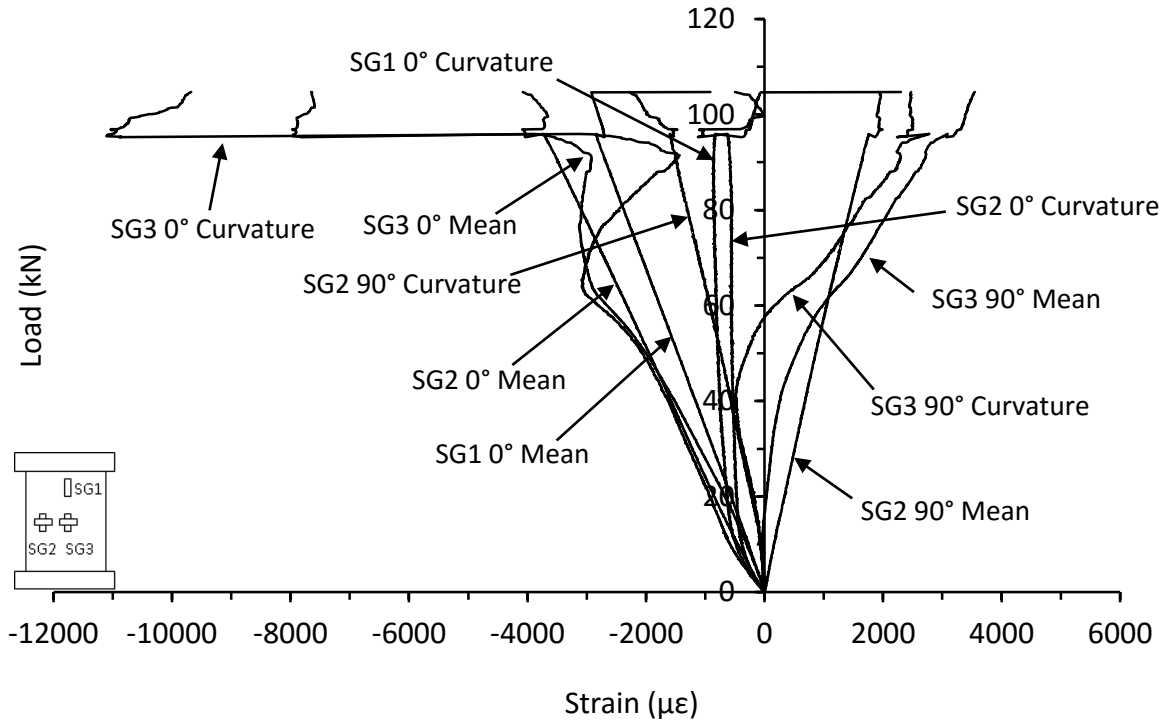


Figure C.47. Mean and curvature strain responses from thick unsymmetrical QI carbon/epoxy panel with 70kg/m³ core density impacted at 10J (LB-16-12-QI-10J-A)

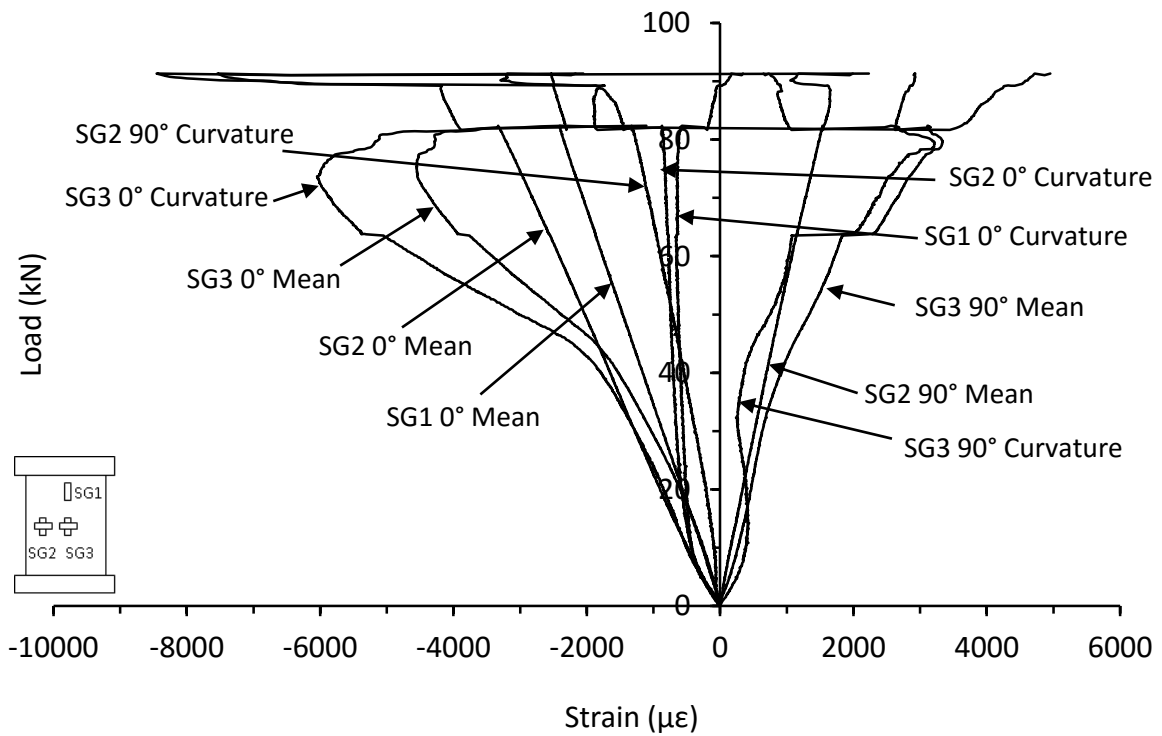


Figure C.48. Mean and curvature strain responses from thick unsymmetrical QI carbon/epoxy panel with 70kg/m³ core density impacted at 20J (LB-16-12-QI-20J-B)

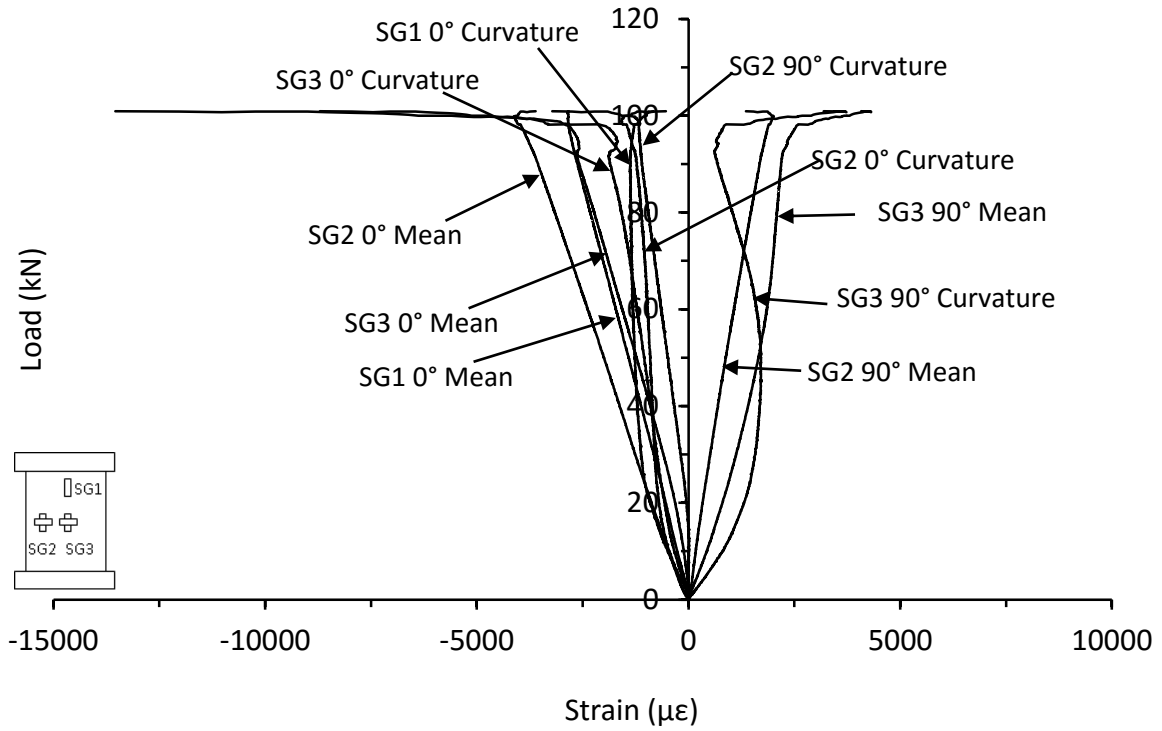


Figure C.49. Mean and curvature strain responses from thick unsymmetrical QI carbon/epoxy panel with 70kg/m³ core density impacted at 35J (LB-16-12-QI-35J-B)

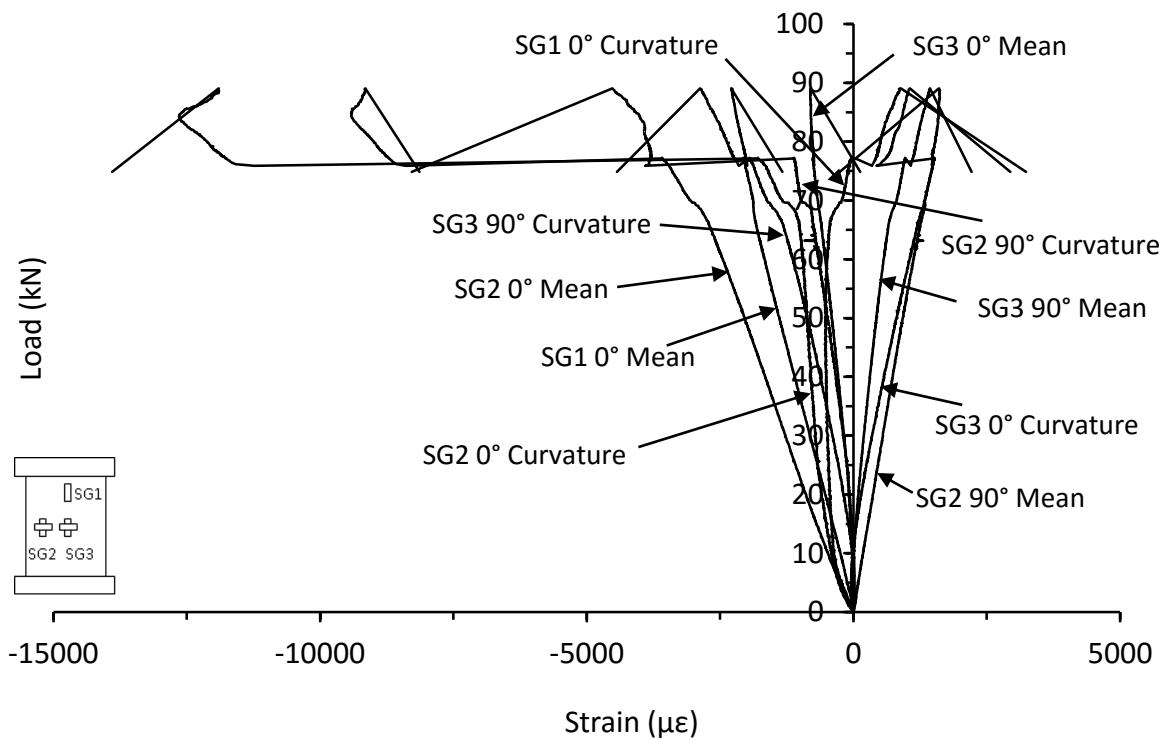


Figure C.50. Mean and curvature strain responses from thick unsymmetrical QI carbon/epoxy panel with 70kg/m³ core density impacted at 45J (LB-16-12-QI-45J-A)

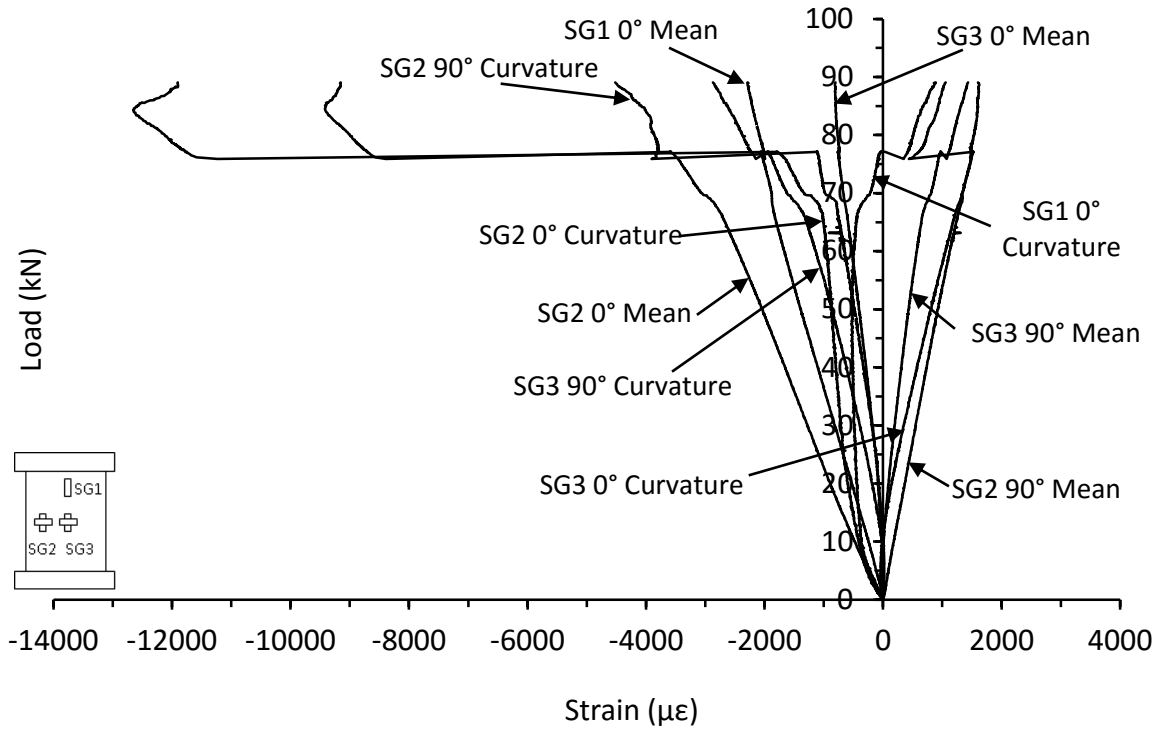


Figure C.51. Mean and curvature strain responses from thick unsymmetrical QI carbon/epoxy panel with 70kg/m³ core density impacted at 45J (LB-16-12-QI-45J-B)

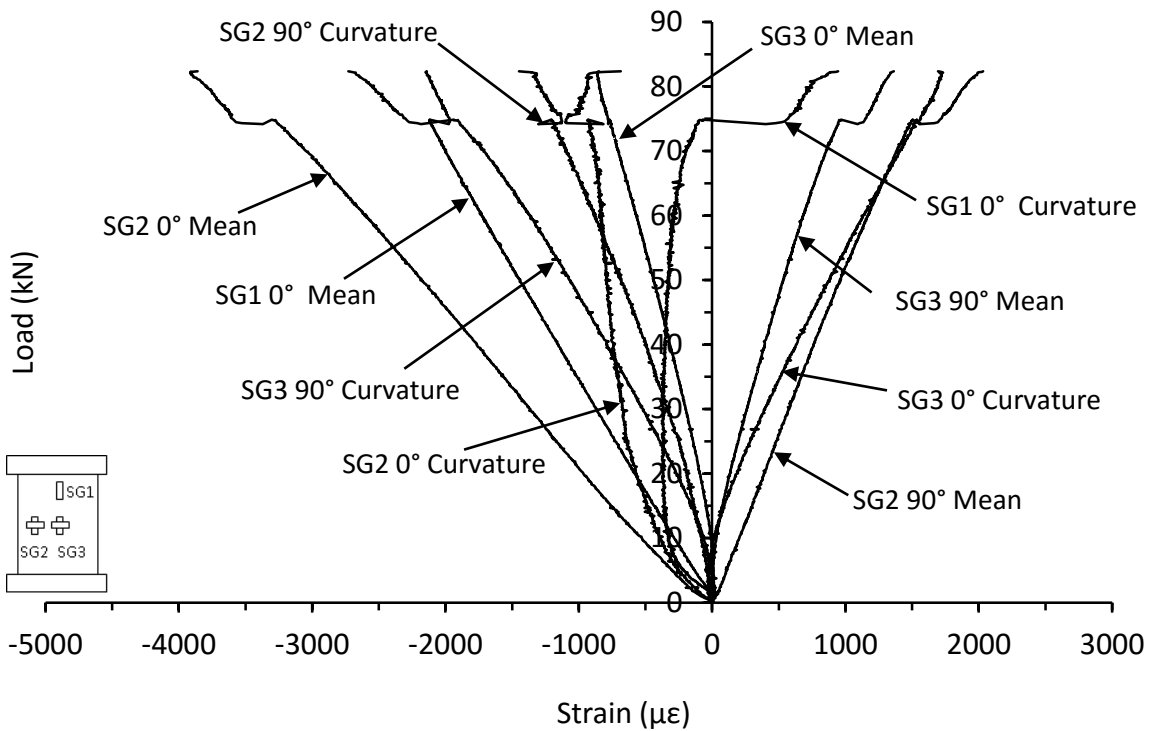


Figure C.52. Mean and curvature strain responses from thick unsymmetrical QI carbon/epoxy panel with 70kg/m³ core density impacted at 60J (LB-16-12-QI-60J-A)

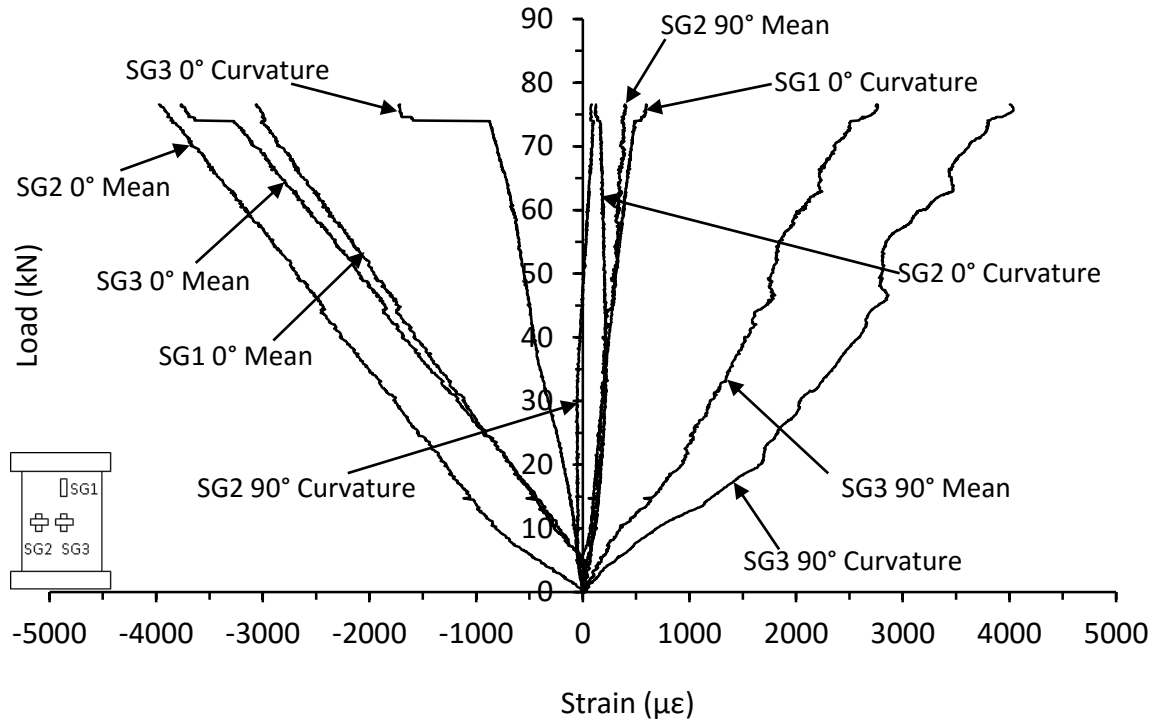


Figure C.53. Mean and curvature strain responses from thin symmetrical CP carbon/epoxy panel with 110kg/m³ core density impacted at 10J (AR-8-8-CP-10J)

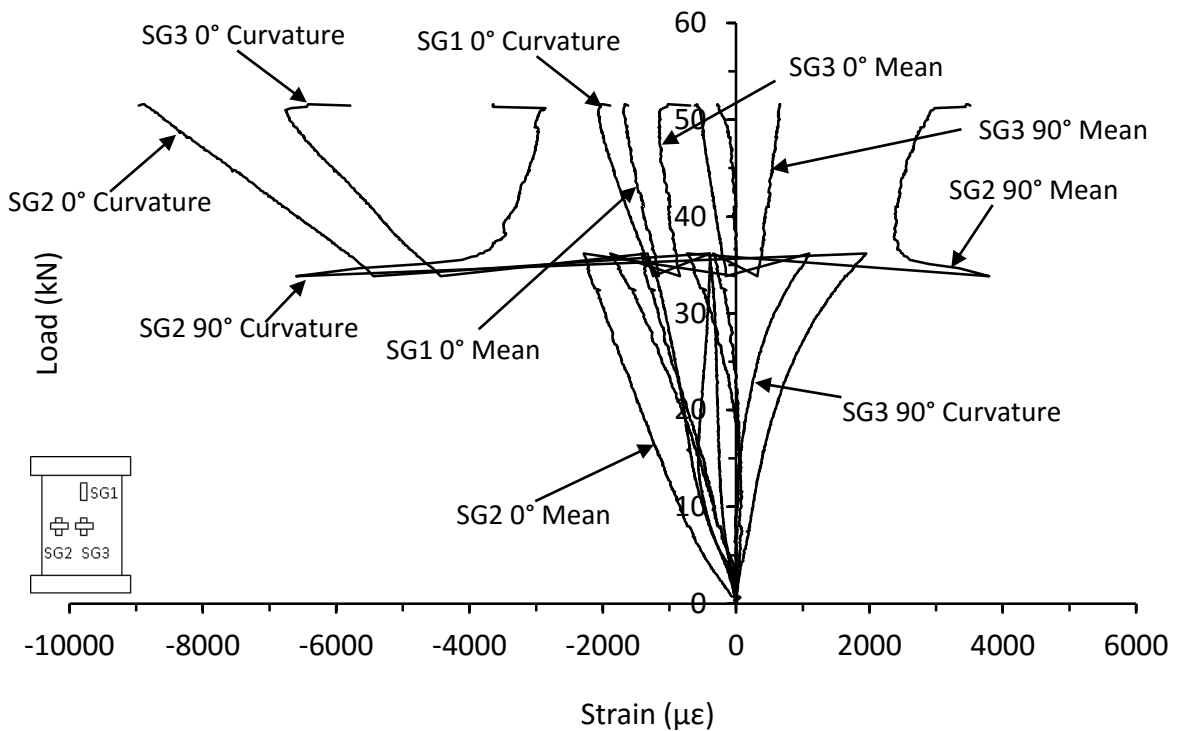


Figure C.54. Mean and curvature strain responses from thin symmetrical CP carbon/epoxy panel with 110kg/m³ core density impacted at 20J (AR-8-8-CP-20J-A)

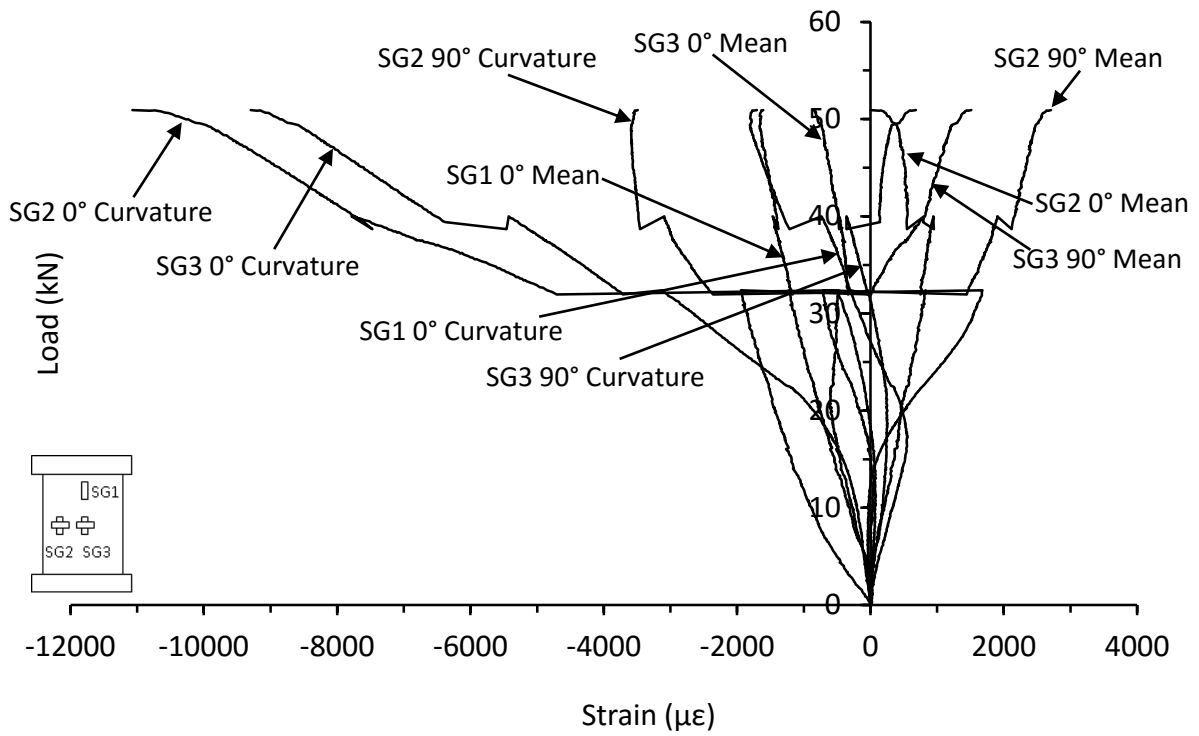


Figure C.55. Mean and curvature strain responses from thin symmetrical CP carbon/epoxy panel with 110kg/m³ core density impacted at 20J (AR-8-8-CP-20J-B)

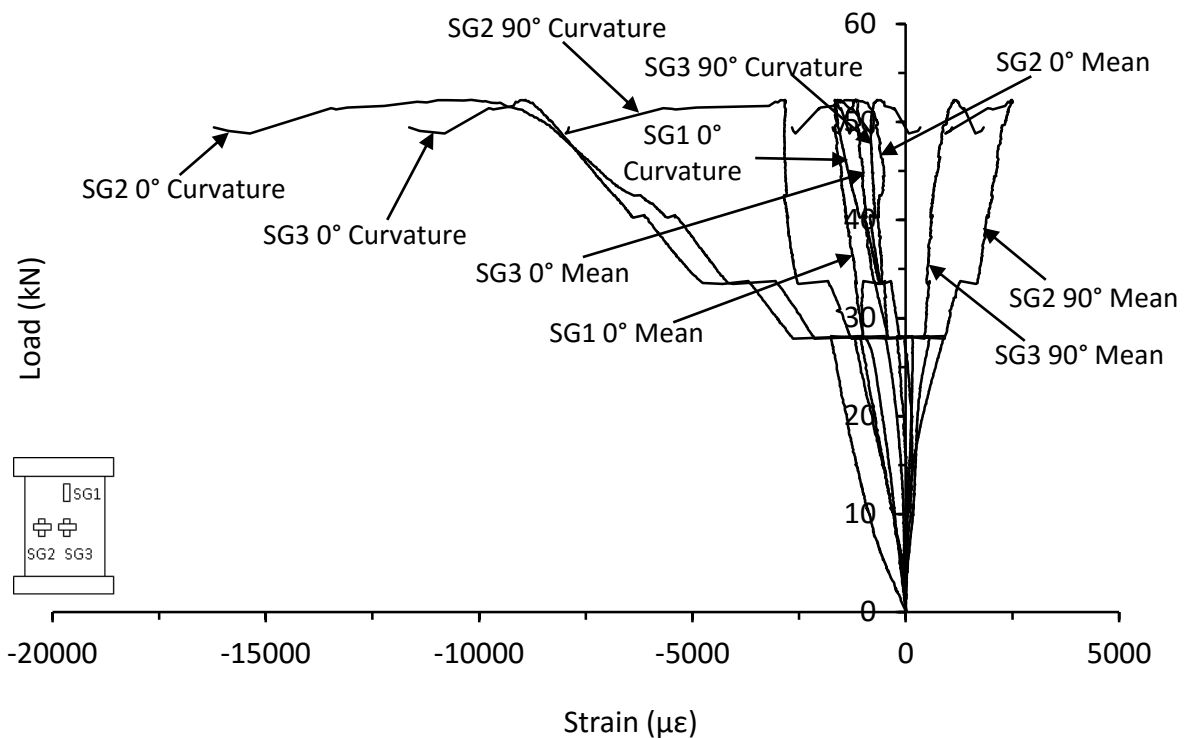


Figure C.56. Mean and curvature strain responses from thin symmetrical CP carbon/epoxy panel with 110kg/m³ core density impacted at 30J (AR-8-8-CP-30J)

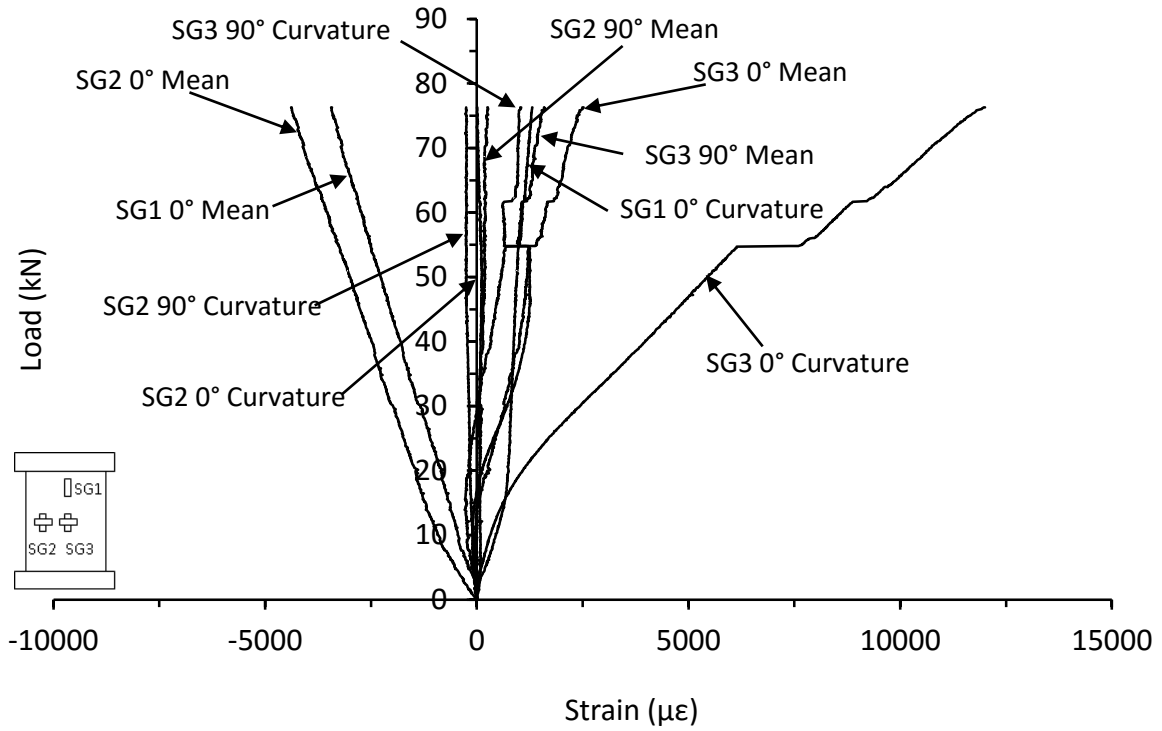


Figure C.57. Mean and curvature strain responses from thin unsymmetrical CP carbon/epoxy panel with 110kg/m³ core density impacted at 10J (AR-8-6-CP-10J)

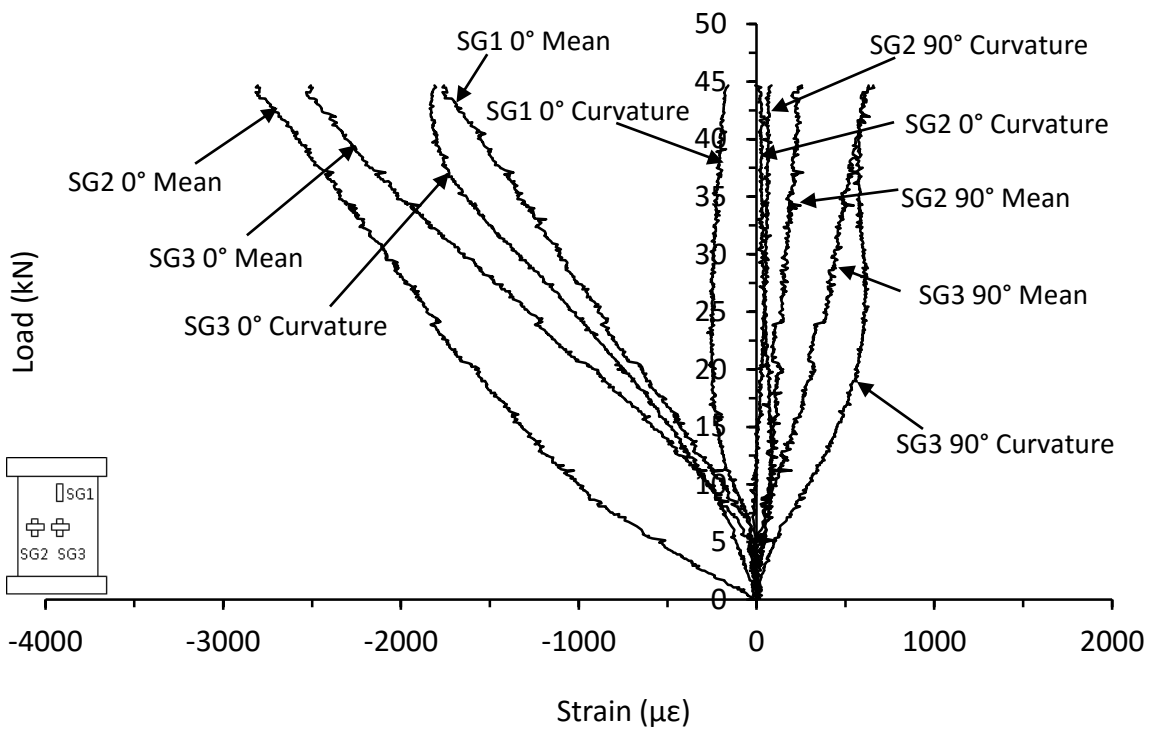


Figure C.58. Mean and curvature strain responses from thin unsymmetrical carbon/epoxy CP panel with 110kg/m³ core density impacted at 20J (AR-8-6-CP-20J-B)

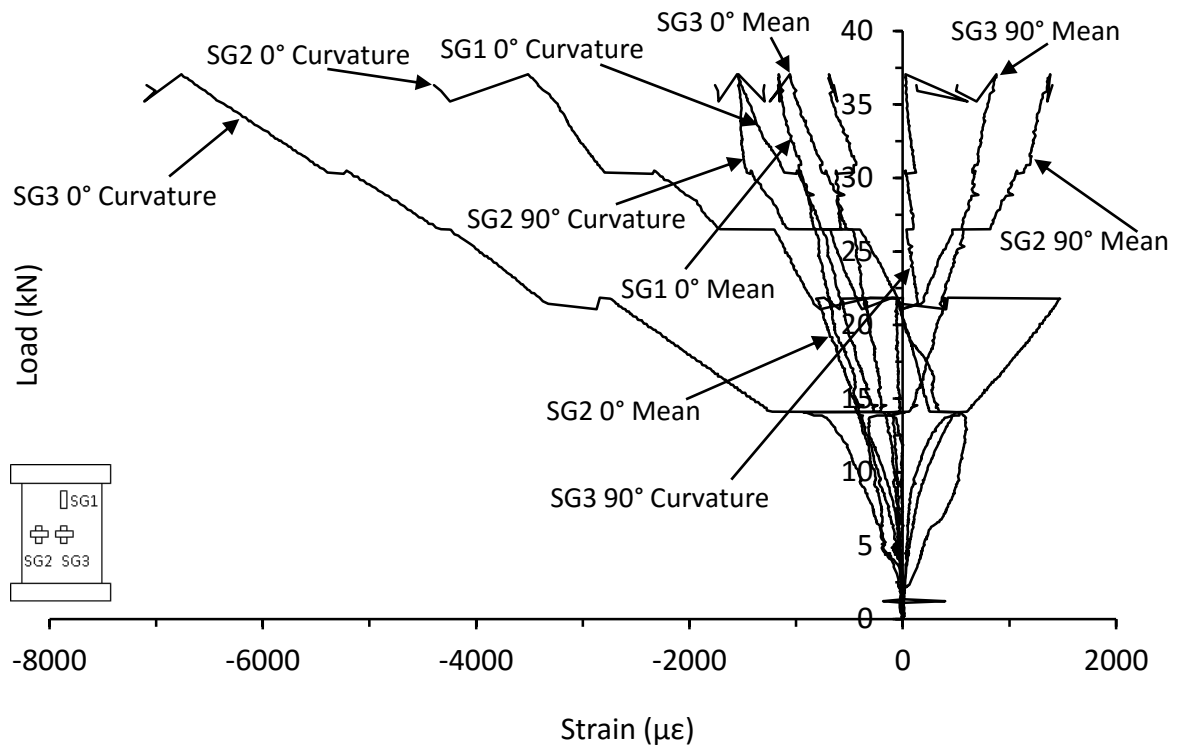


Figure C.59. Mean and curvature strain responses from thin unsymmetrical CP carbon/epoxy panel with 110kg/m³ core density impacted at 20J (AR-8-6-CP-20J-A)

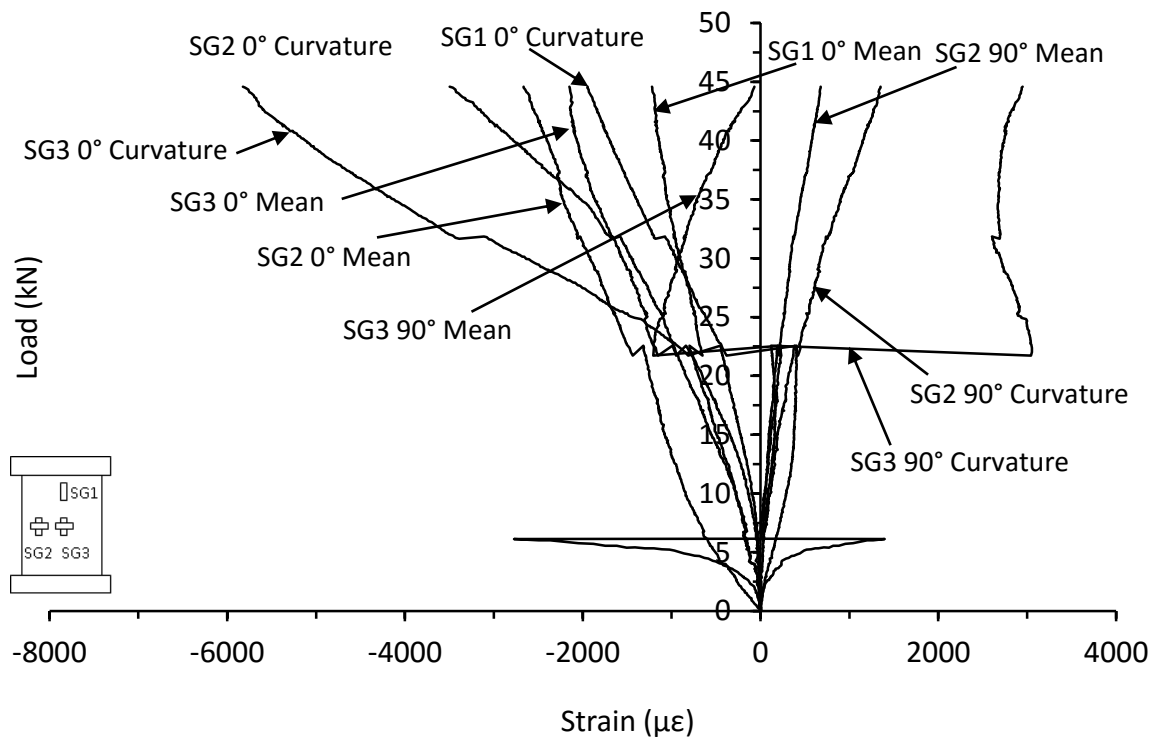


Figure C.60. Mean and curvature strain responses from thin unsymmetrical CP carbon/epoxy panel with 110kg/m³ core density impacted at 30J (AR-8-6-CP-30J)

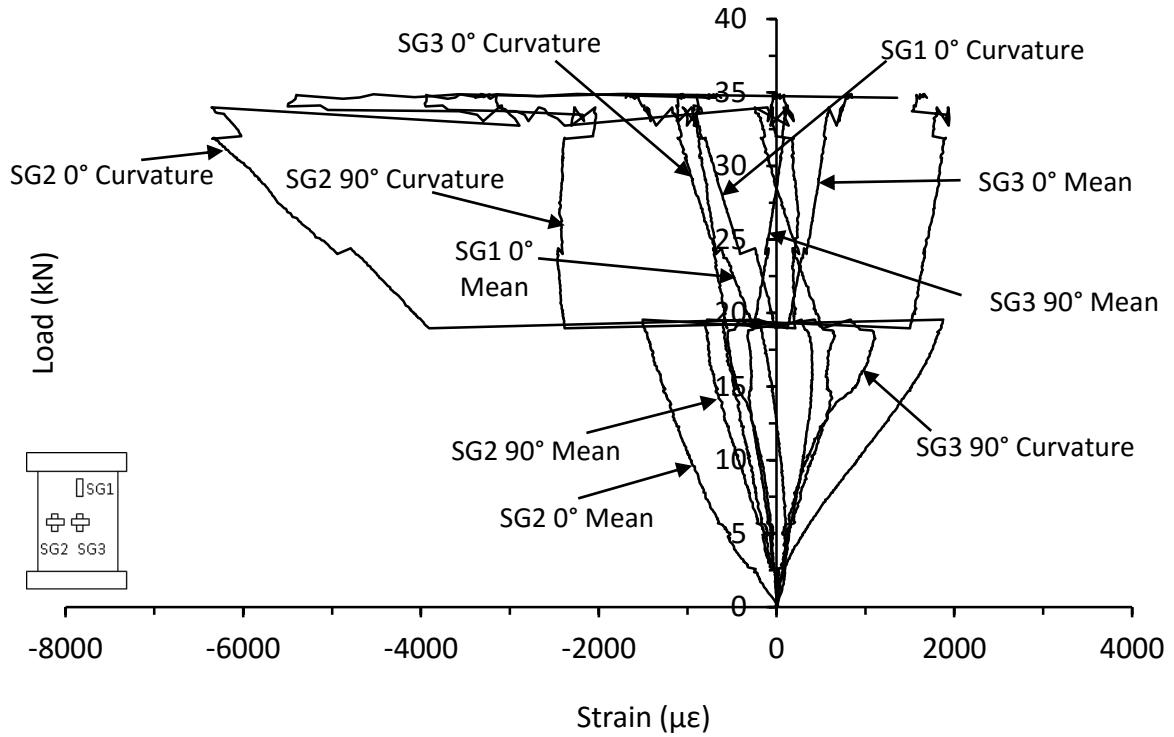


Figure C.61. Mean and curvature strain responses from thin unsymmetrical CP carbon/epoxy panel with 110kg/m³ core density impacted at 40J (AR-8-6-CP-40J)

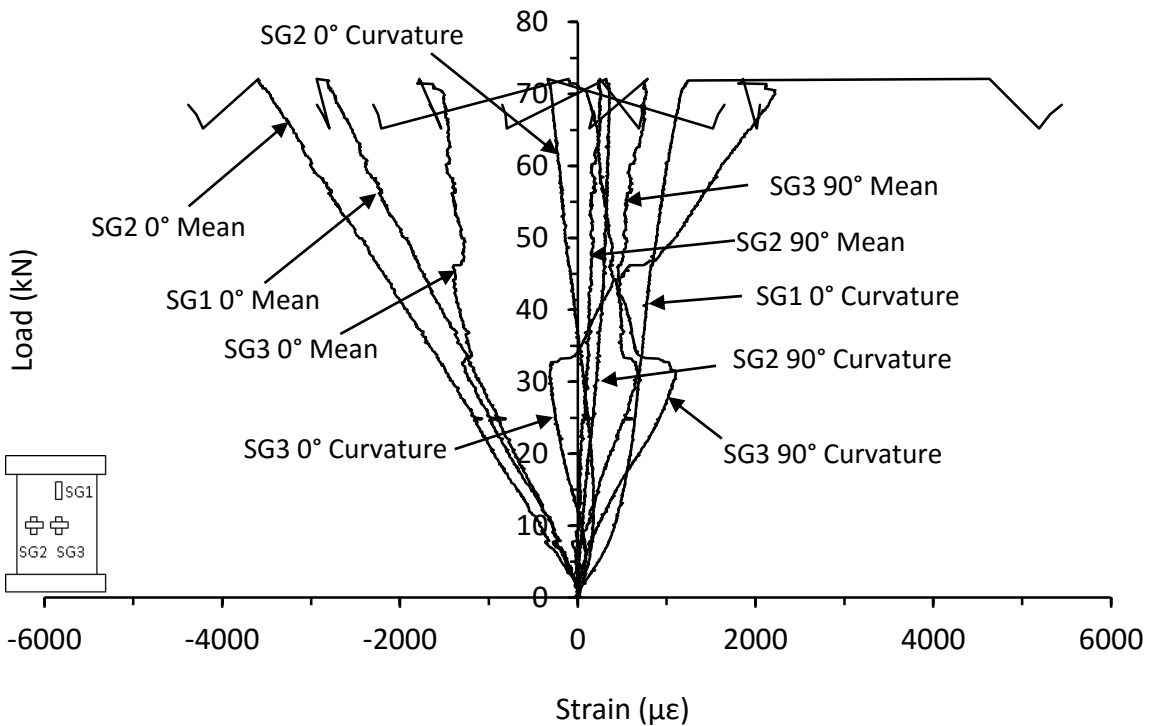


Figure C.62. Mean and curvature strain responses from thin symmetrical CP carbon/epoxy panel with 135kg/m³ core density impacted at 15J (RM-8-8-CP-15J-A)

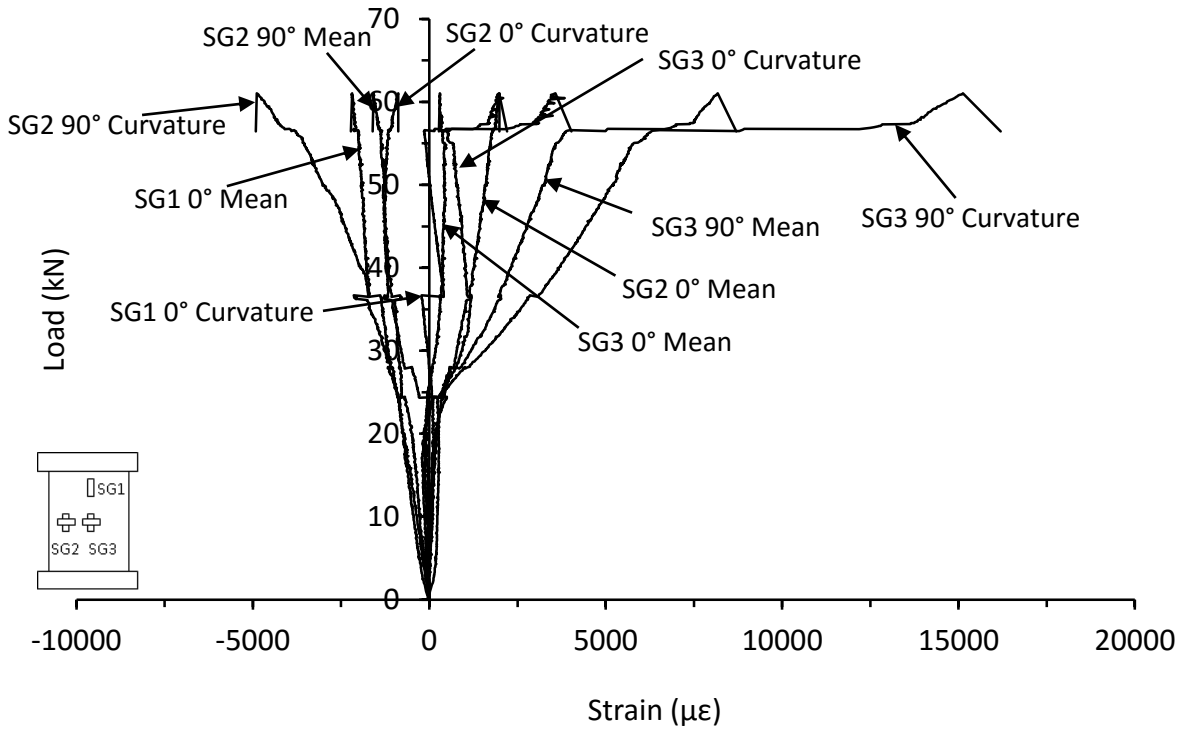


Figure C.63. Mean and curvature strain responses from thin symmetrical CP carbon/epoxy panel with 135kg/m³ core density impacted at 15J (MB-8-8-CP-15J)

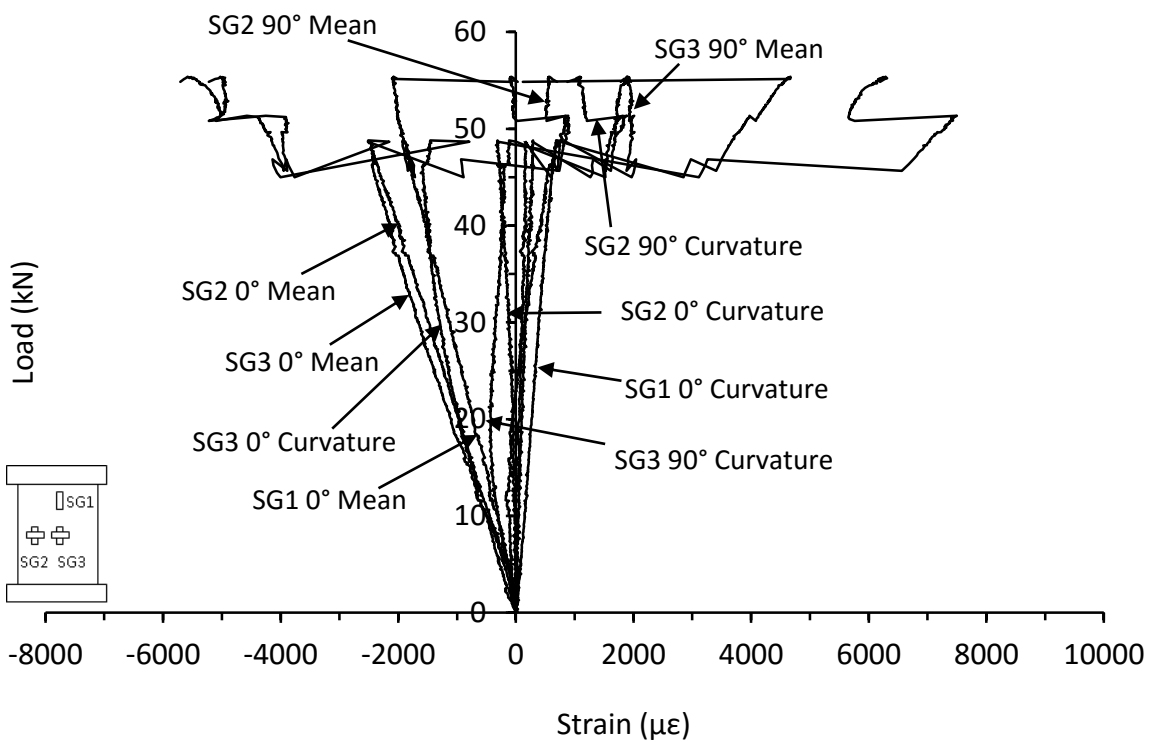


Figure C.64. Mean and curvature strain responses from thin symmetrical CP carbon/epoxy panel with 135kg/m³ core density impacted at 20J (RM-8-8-CP-20J-A)

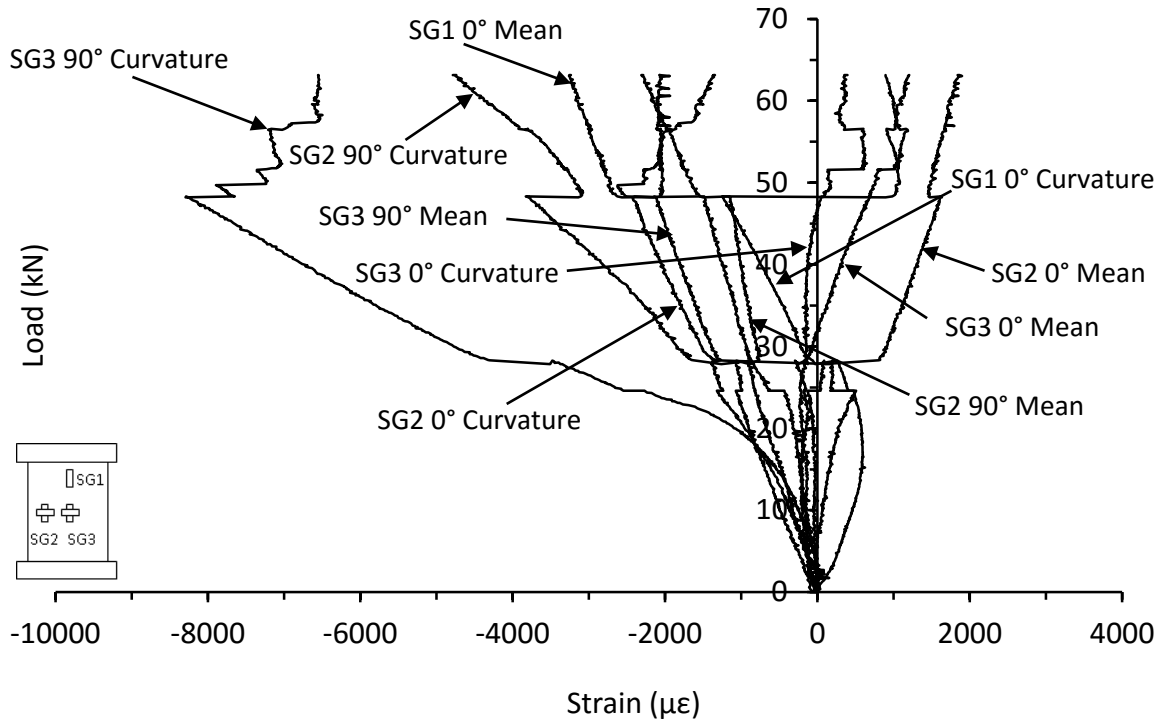


Figure C.65. Mean and curvature strain responses from thin symmetrical CP carbon/epoxy panel with 135kg/m³ core density impacted at 20J (MB-8-8-CP-20J)

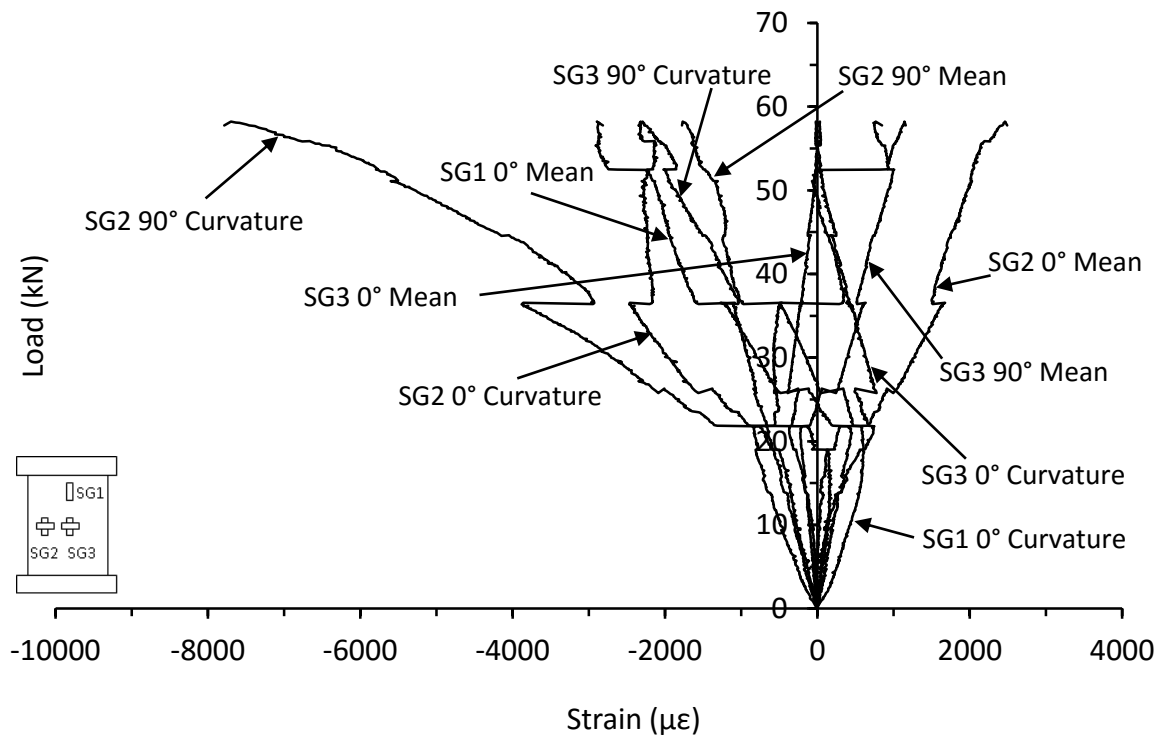


Figure C.66. Mean and curvature strain responses from thin symmetrical CP carbon/epoxy panel with 135kg/m³ core density impacted at 25J (MB-8-8-CP-25J)

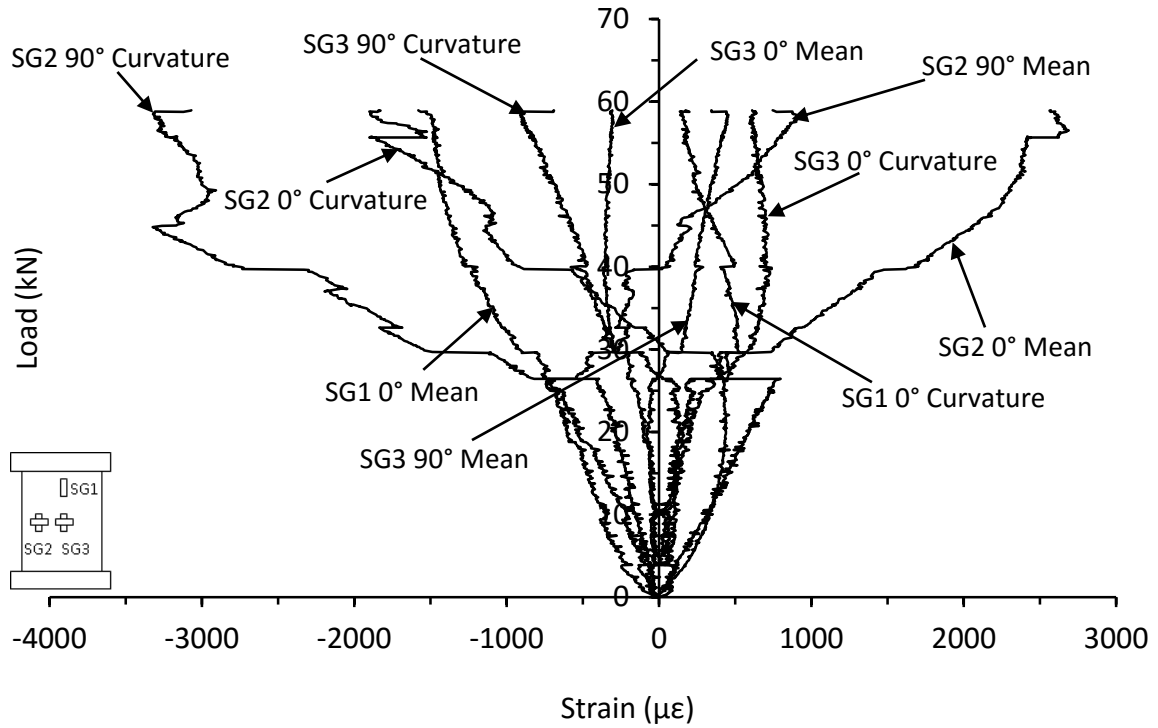


Figure C.67. Mean and curvature strain responses from thin symmetrical CP carbon/epoxy panel with 135kg/m³ core density impacted at 35J (MB-8-8-CP-35J)

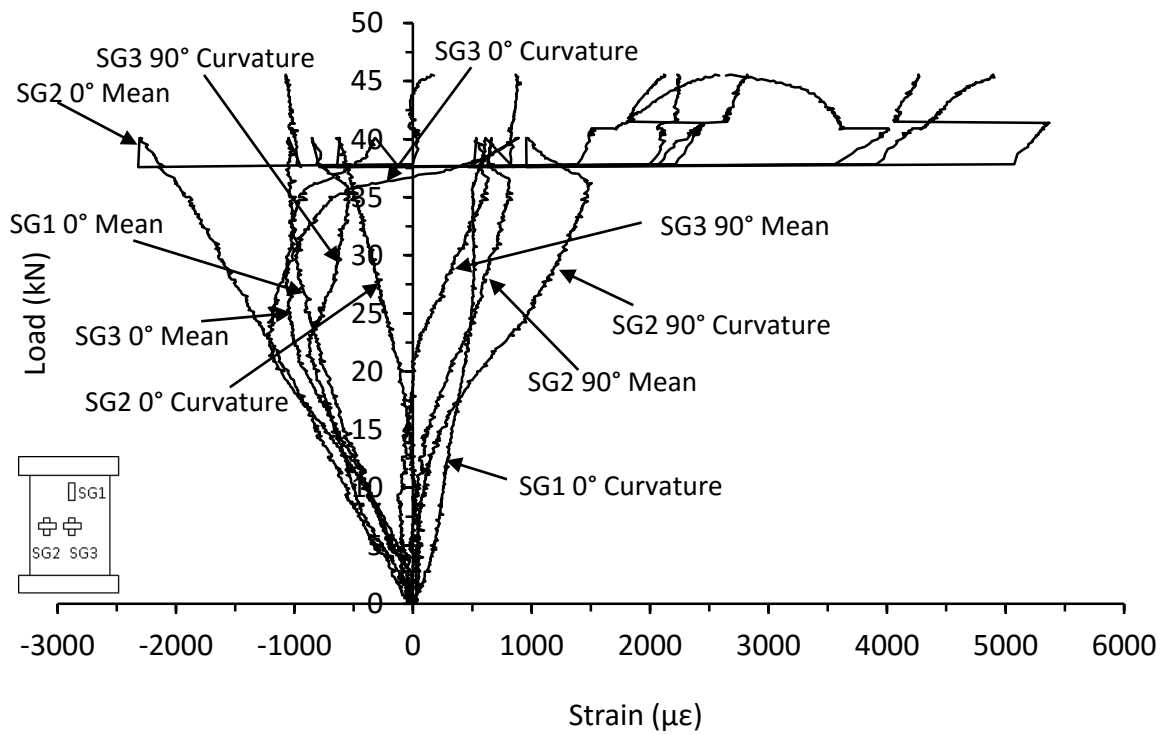


Figure C.68. Mean and curvature strain responses from thin symmetrical CP carbon/epoxy panel with 135kg/m³ core density impacted at 40J (RM-8-8-CP-40J-A)

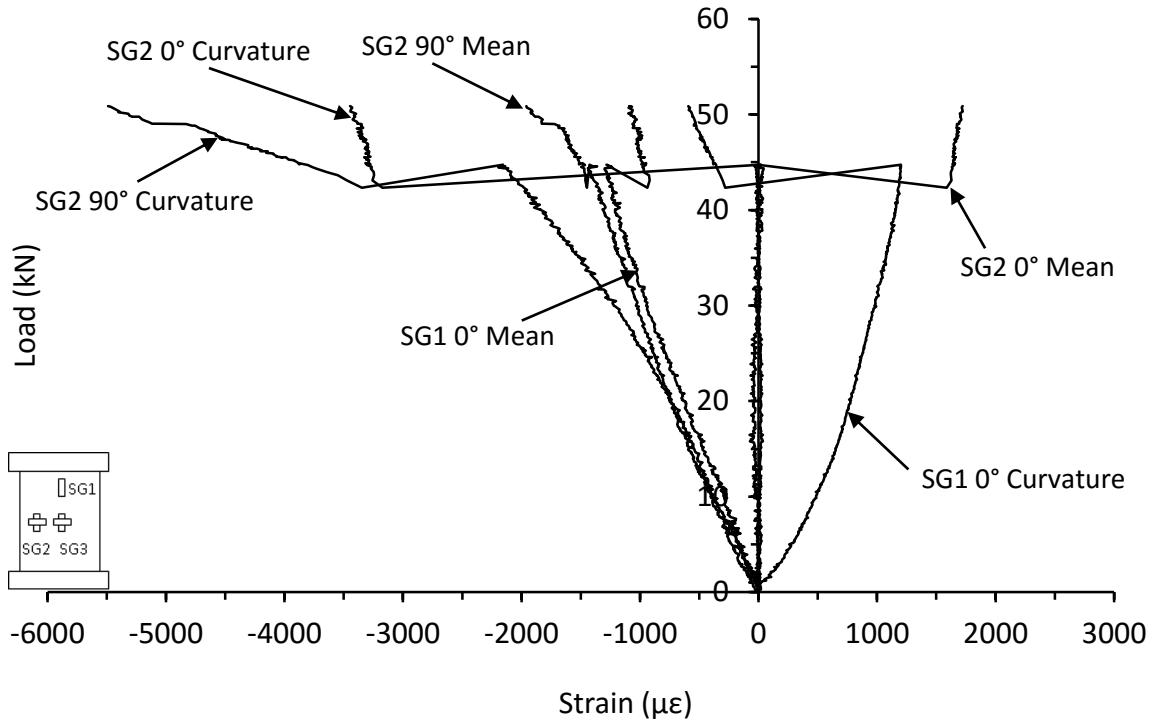


Figure C.69. Mean and curvature strain responses from thin symmetrical CP carbon/epoxy panel with 135kg/m³ core density impacted at 45J (MB-8-8-CP-45J)

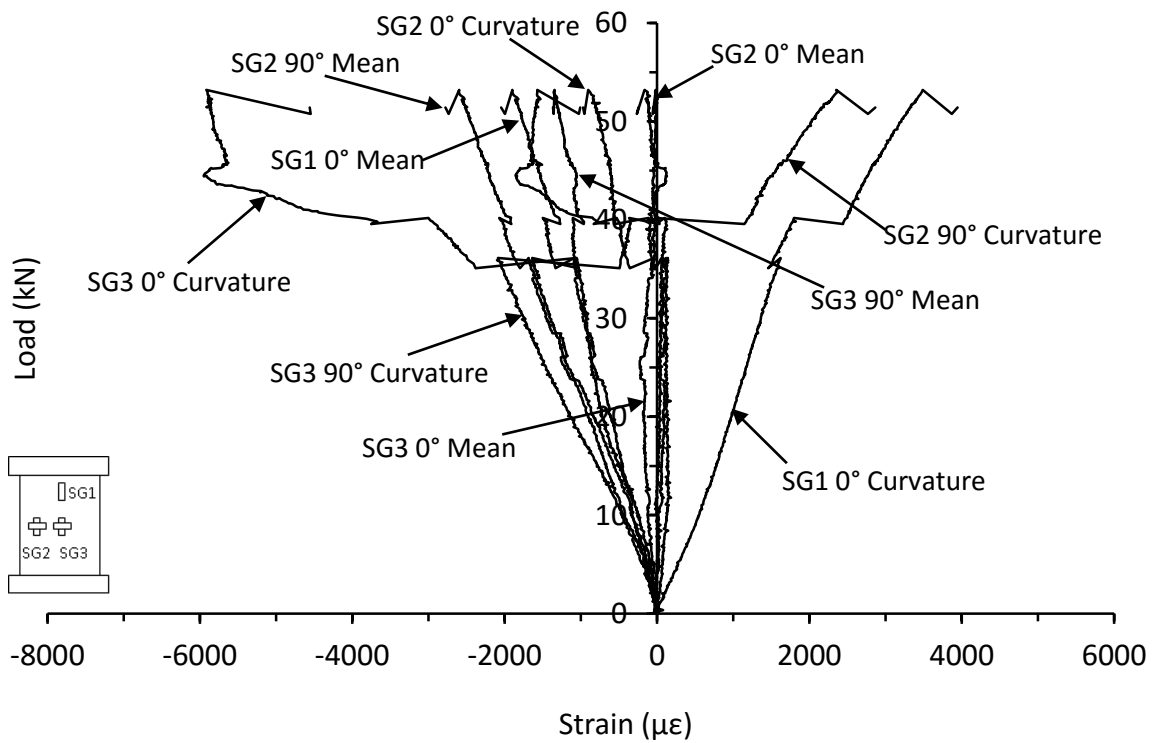


Figure C.70. Mean and curvature strain responses from thin unsymmetrical CP carbon/epoxy panel with 135kg/m³ core density impacted at 20J (MB-8-6-CP-20J)

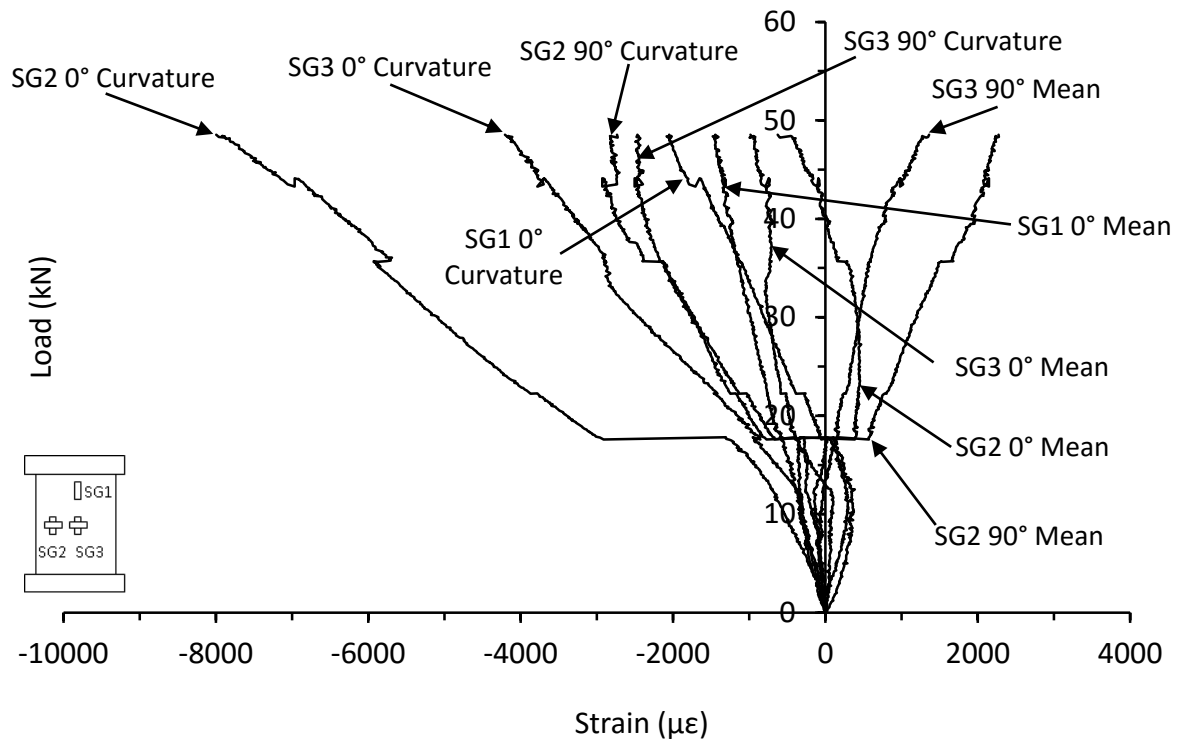


Figure C.71. Mean and curvature strain responses from thin unsymmetrical CP carbon/epoxy panel with 135kg/m³ core density impacted at 25J (MB-8-6-CP-25J)

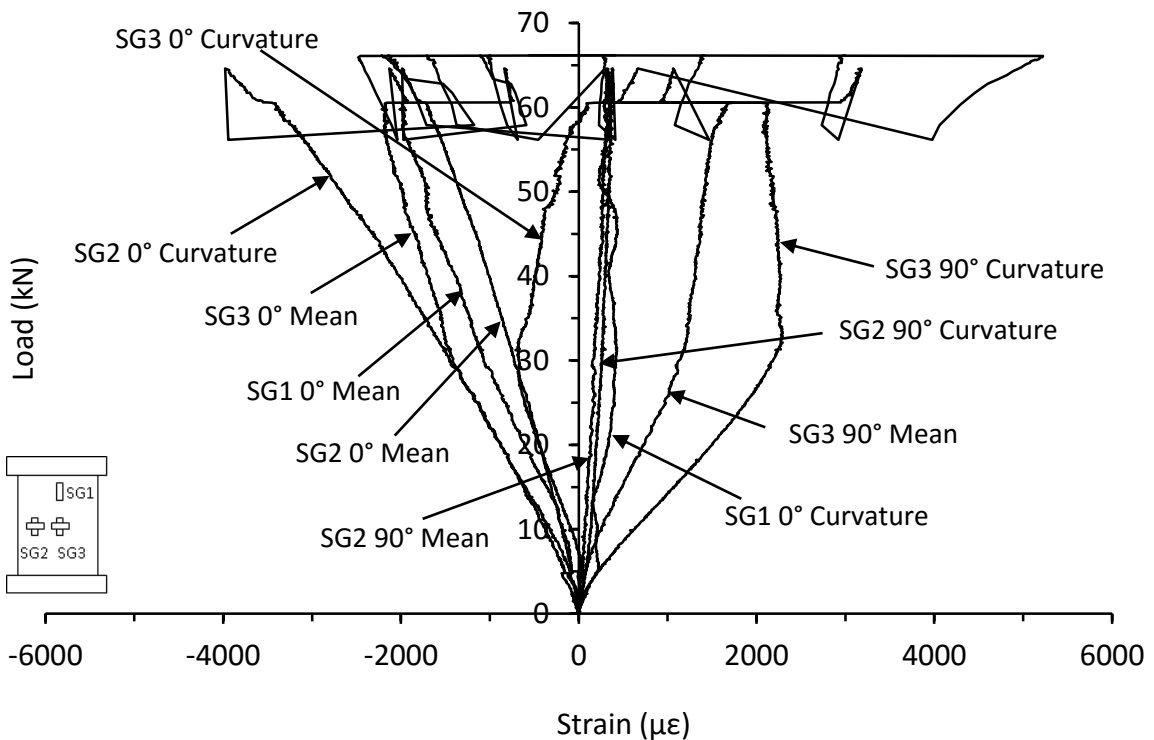


Figure C.72. Mean and curvature strain responses from thin unsymmetrical CP carbon/epoxy panel with 135kg/m³ core density impacted at 30J (RM-8-6-CP-30J-A)

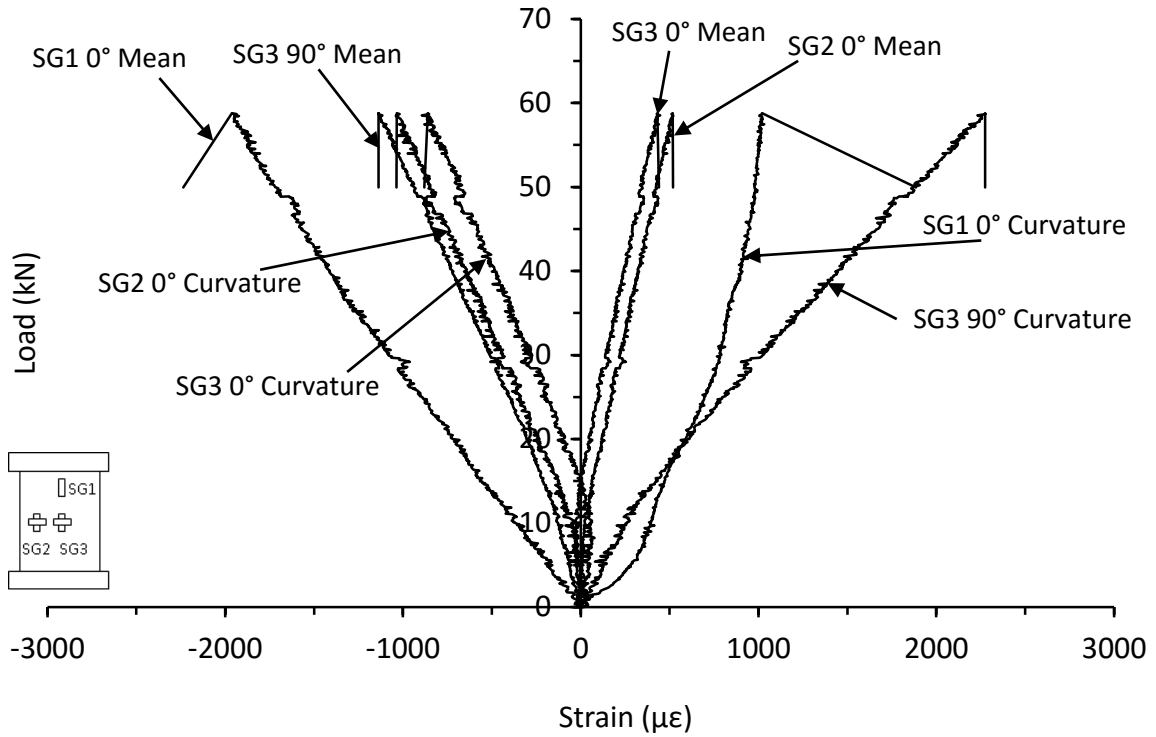


Figure C.73. Mean and curvature strain responses from thin unsymmetrical CP carbon/epoxy panel with 135kg/m³ core density impacted at 30J (MB-8-6-CP-30J)

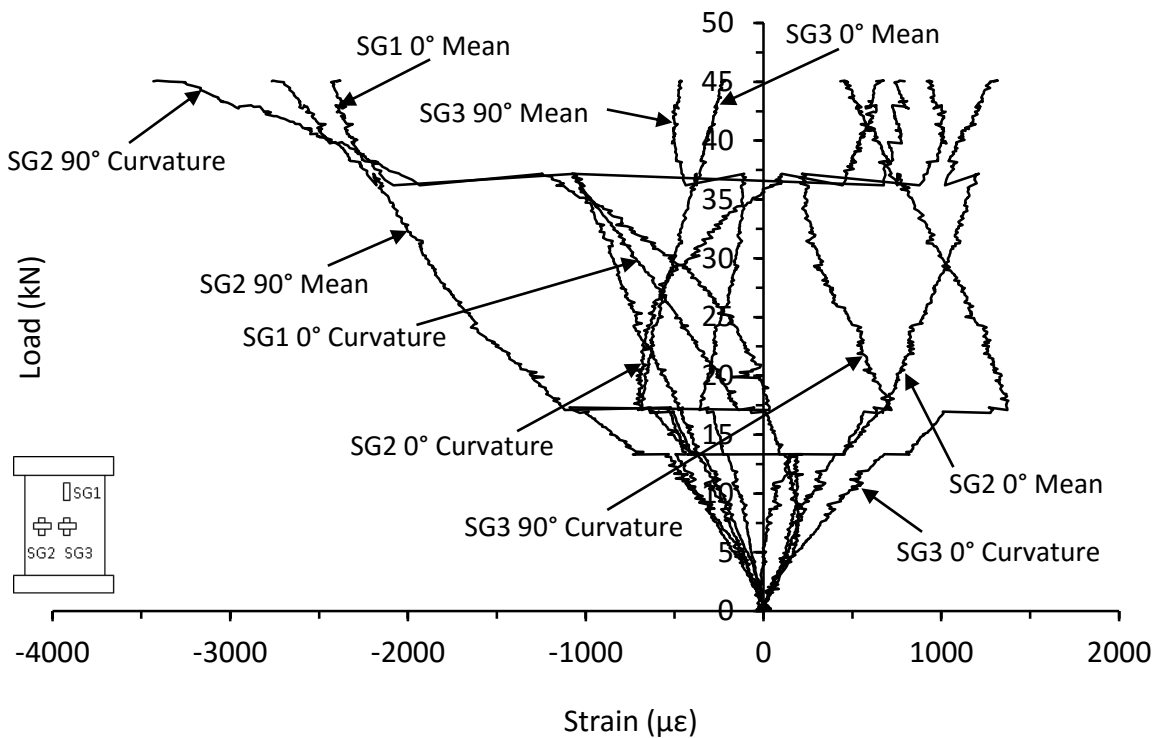


Figure C.74. Mean and curvature strain responses from thin unsymmetrical CP carbon/epoxy panel with 135kg/m³ core density impacted at 35J (MB-8-6-CP-35J)

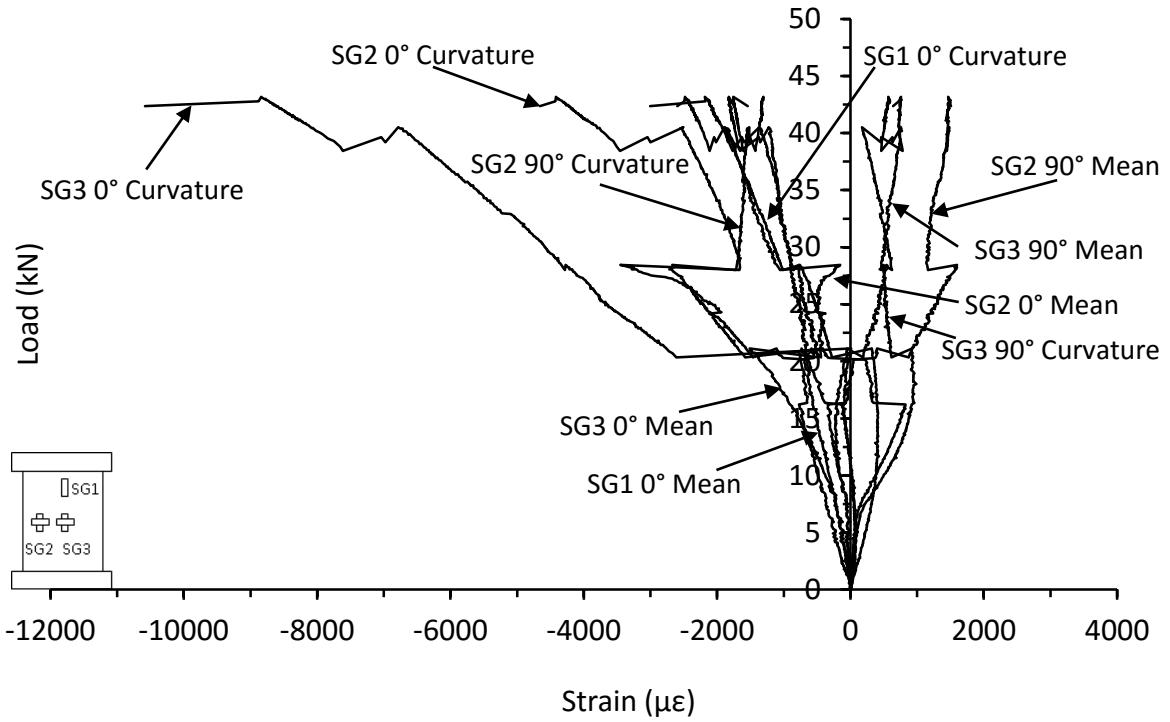


Figure C.75. Mean and curvature strain responses from thin unsymmetrical CP carbon/epoxy panel with 135kg/m³ core density impacted at 38J (RM-8-6-CP-38J-A)

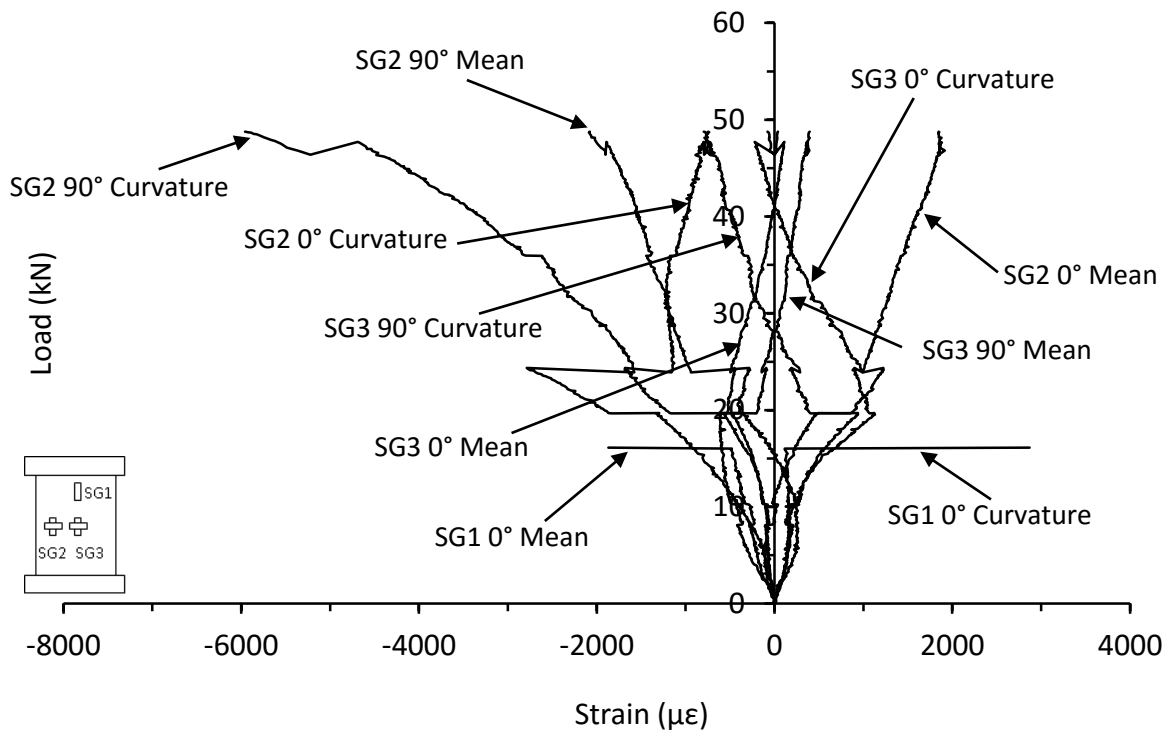


Figure C.76. Mean and curvature strain responses from thin unsymmetrical CP carbon/epoxy panel with 135kg/m³ core density impacted at 40J (MB-8-6-CP-40J)

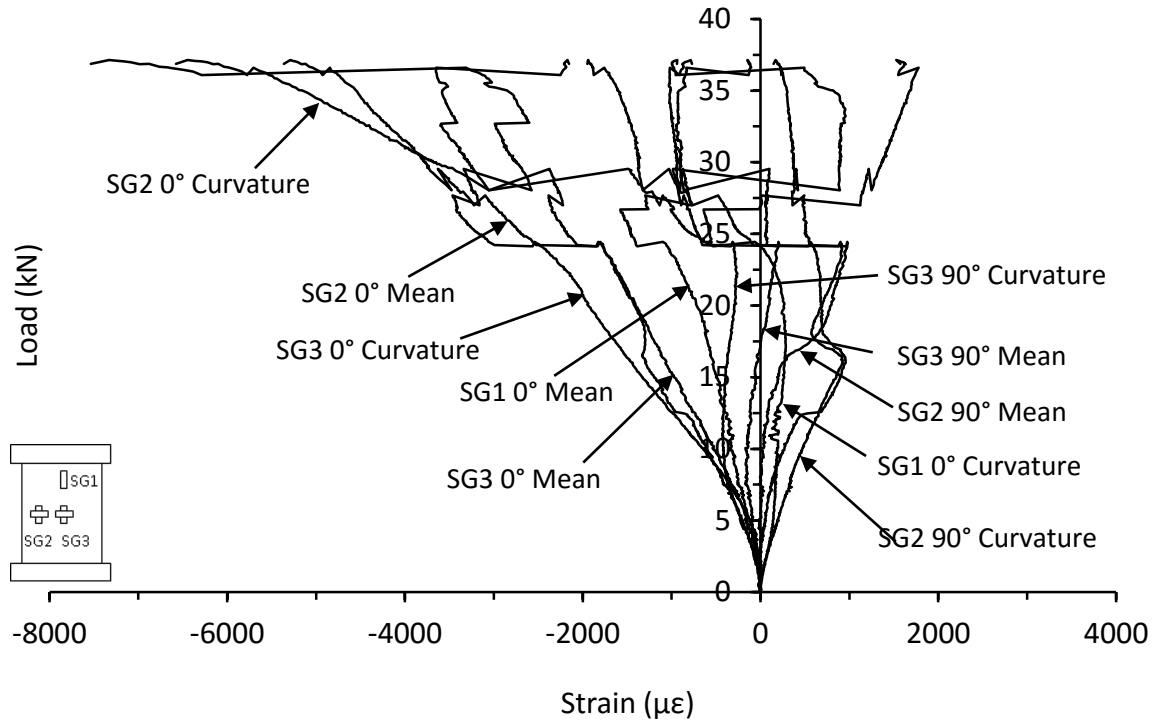


Figure C.77. Mean and curvature strain responses from thin unsymmetrical CP carbon/epoxy panel with 135kg/m^3 core density impacted at 45J (RM-8-6-CP-45J-A)

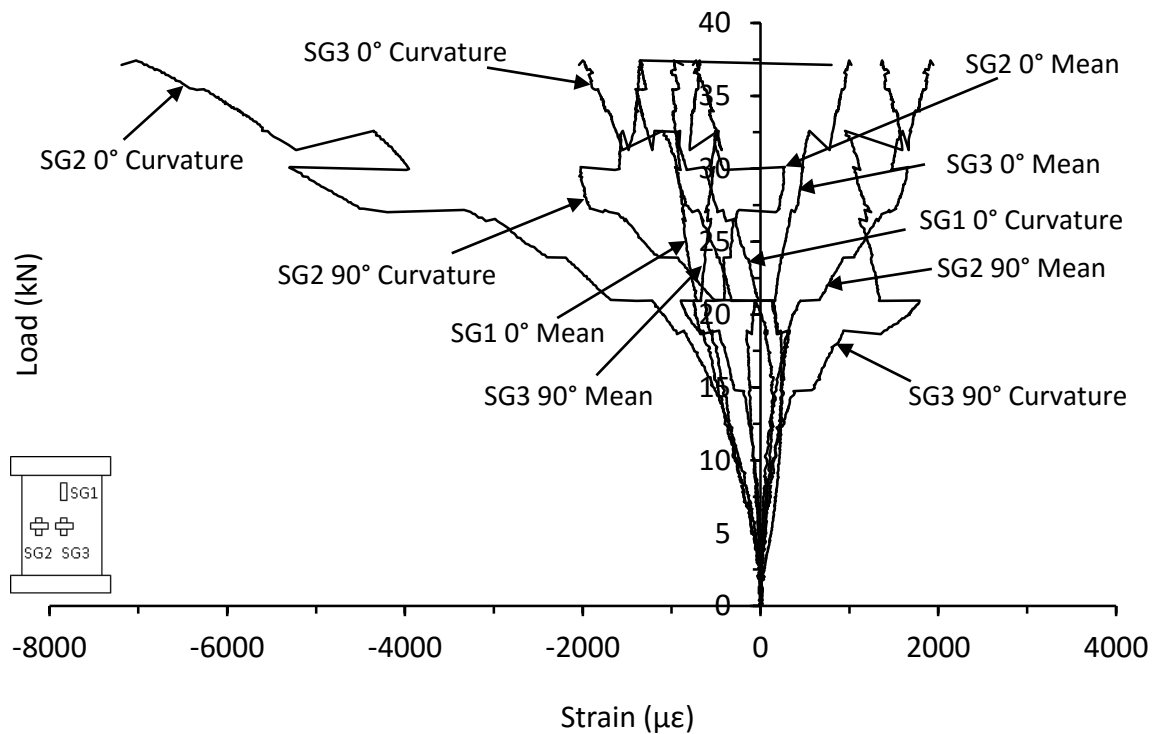


Figure C.78. Mean and curvature strain responses from thin unsymmetrical CP carbon/epoxy panel with 135kg/m^3 core density impacted at 60J (RM-8-6-CP-60J-A)

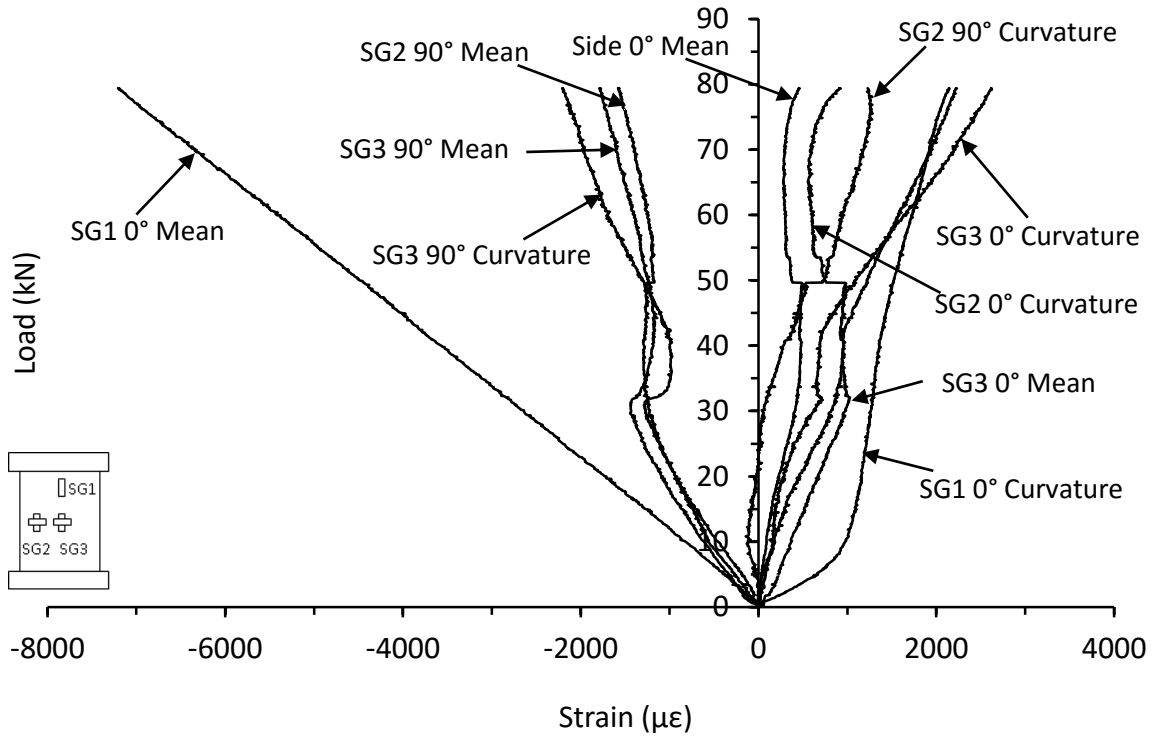


Figure C.79. Mean and curvature strain responses from thin symmetrical CP E-glass/epoxy panel with 70kg/m^3 core density impacted at 8J (SG-8-8-CP-8J)

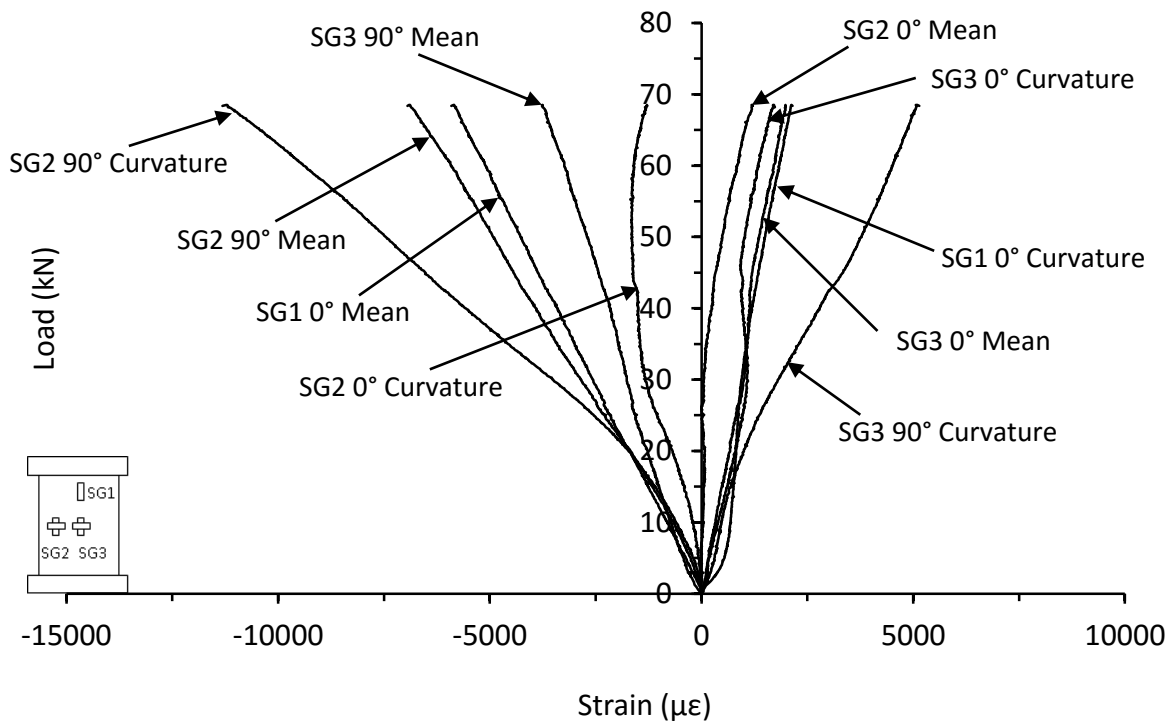


Figure C.80. Mean and curvature strain responses from thin symmetrical CP E-glass/epoxy panel with 70kg/m^3 core density impacted at 15J (SG-8-8-CP-15J)

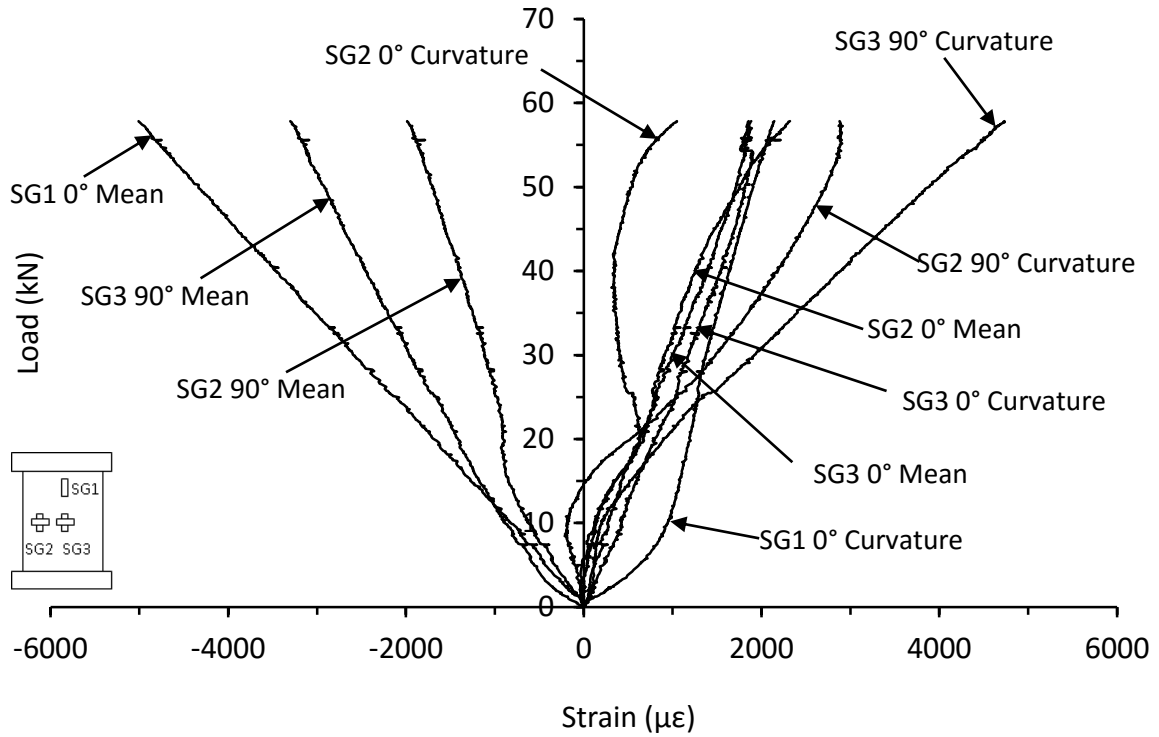


Figure C.81. Mean and curvature strain responses from thin symmetrical CP E-glass/epoxy panel with 70kg/m³ core density impacted at 25J (SG-8-8-CP-25J)

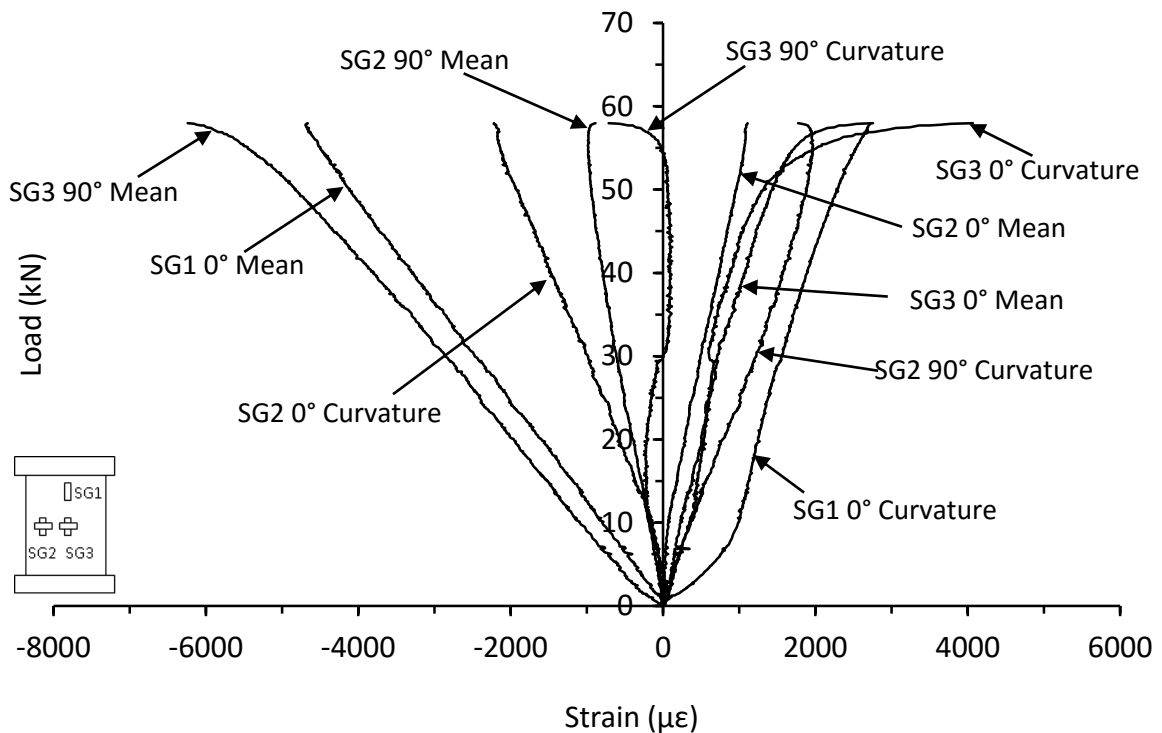


Figure C.82. Mean and curvature strain responses from thin symmetrical CP E-glass/epoxy panel with 70kg/m³ core density impacted at 35J (SG-8-8-CP-35J)

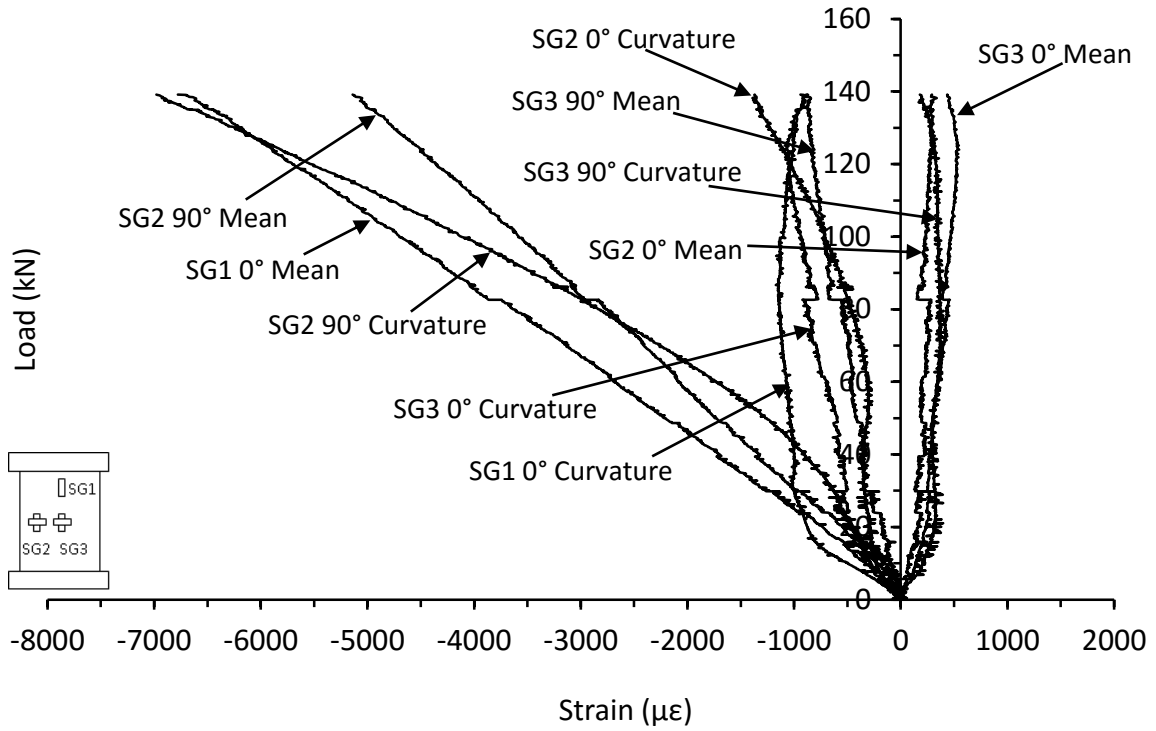


Figure C.83. Mean and curvature strain responses from thick symmetrical CP E-glass/epoxy panel with 70kg/m³ core density impacted at 12J (SG-16-16-CP-12J)

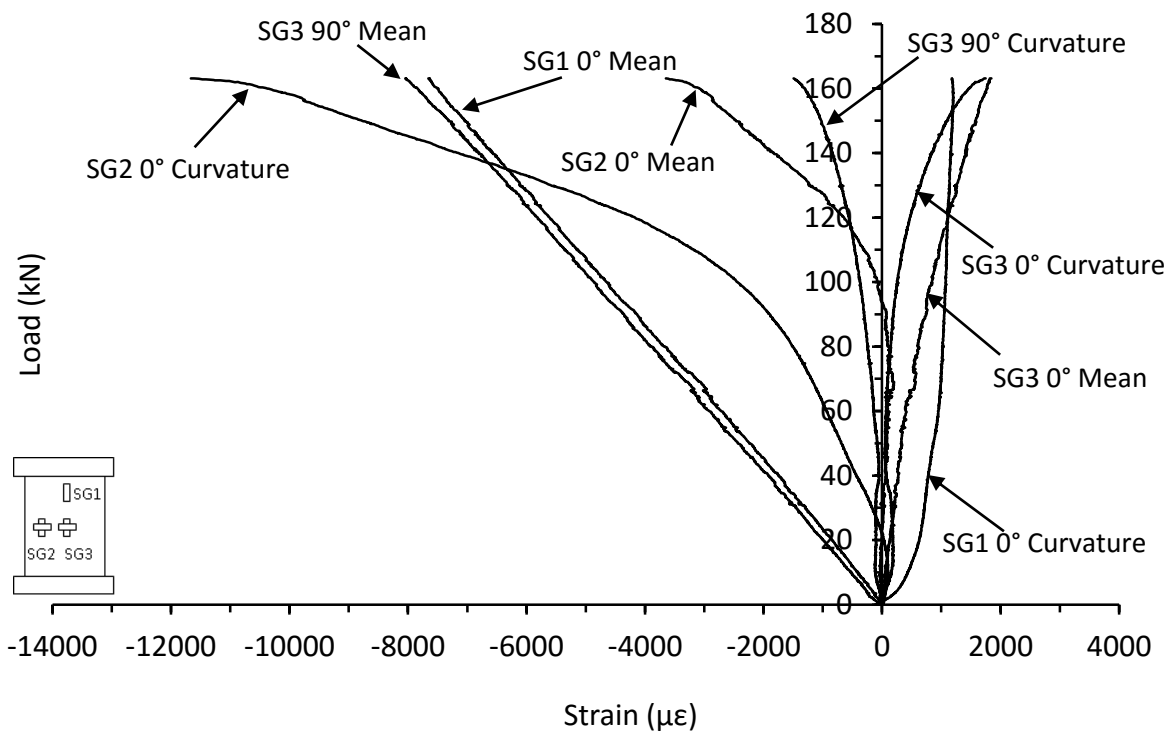


Figure C.84. Mean and curvature strain responses from thick symmetrical CP E-glass/epoxy panel with 70kg/m³ core density impacted at 18J (SG-16-16-CP-18J)

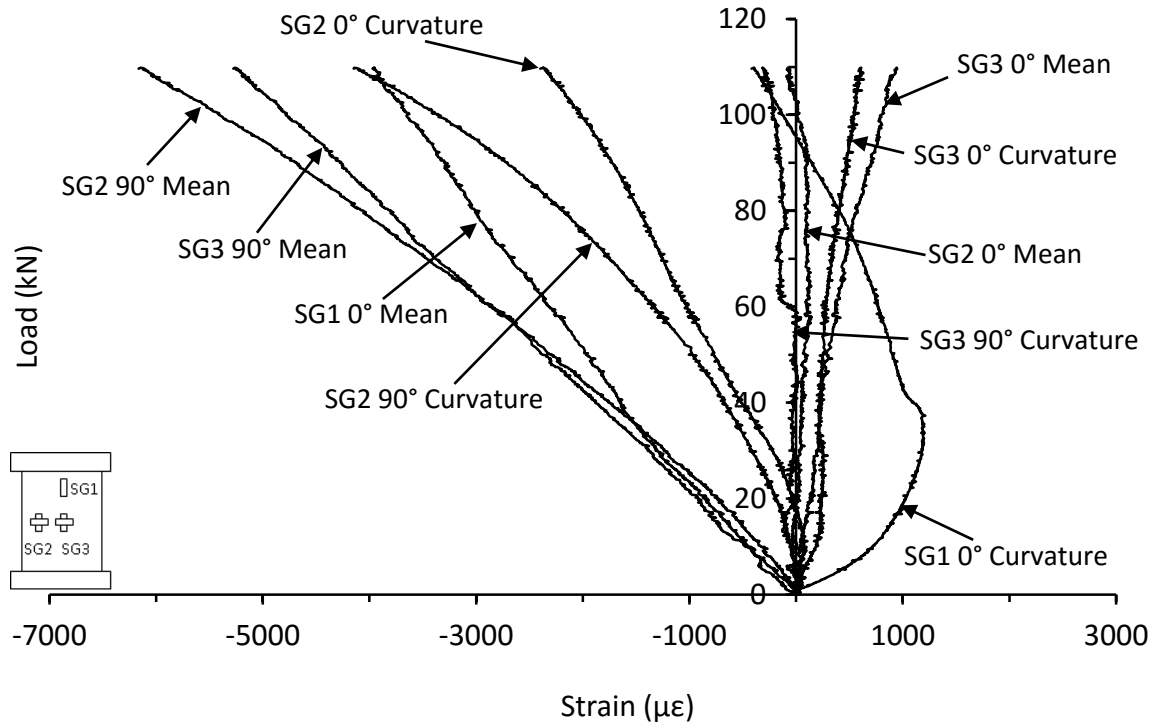


Figure C.85. Mean and curvature strain responses from thick symmetrical CP E-glass/epoxy panel with 70kg/m³ core density impacted at 25J (SG-16-16-CP-25J)

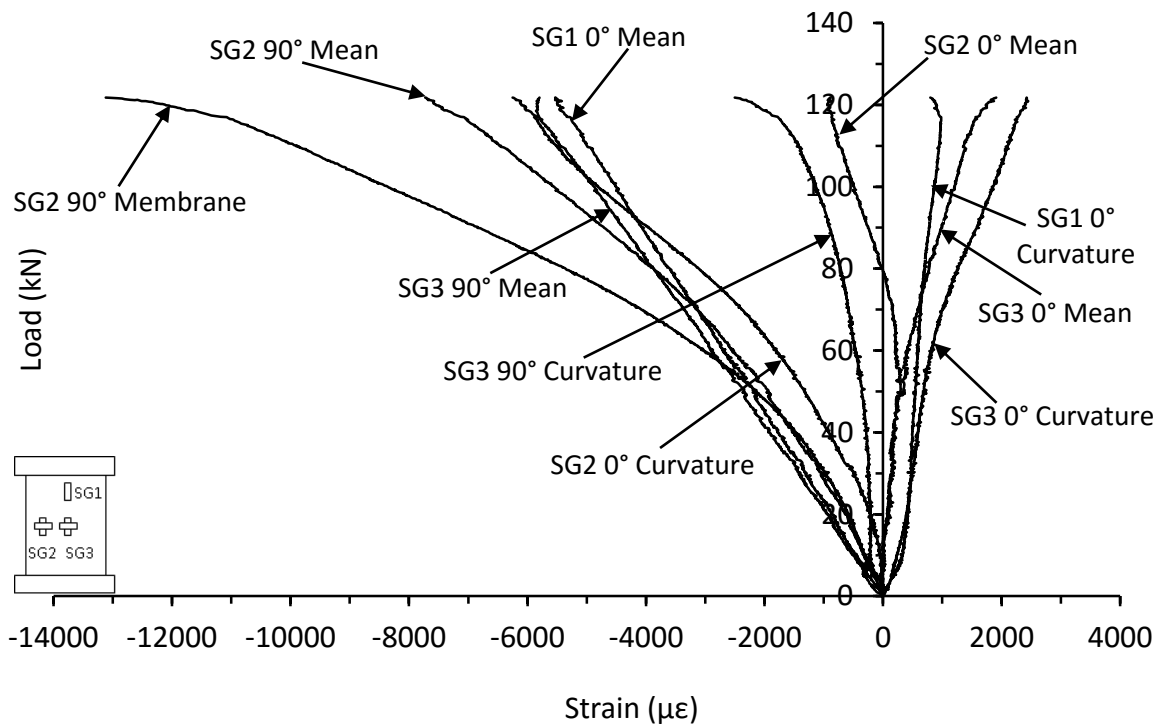


Figure C.86. Mean and curvature strain responses from thick symmetrical CP E-glass/epoxy panel with 70kg/m³ core density impacted at 35J (SG-16-16-CP-35J)

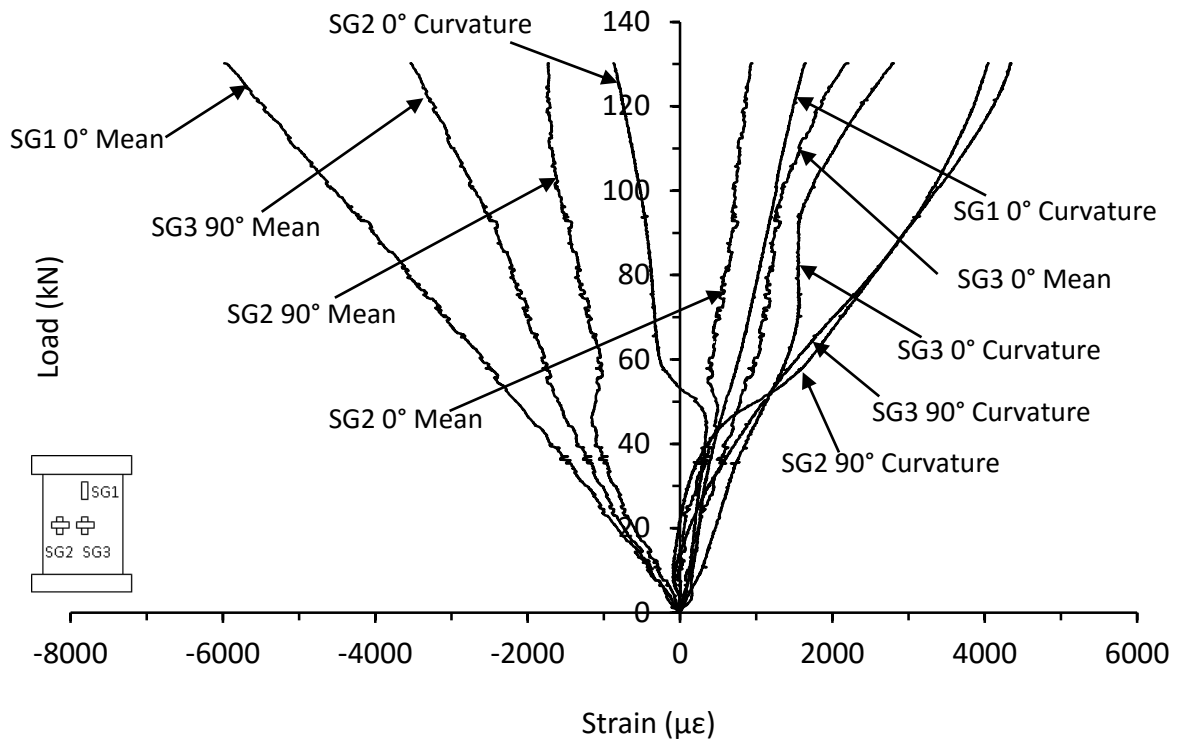


Figure C.87. Mean and curvature strain responses from thick symmetrical CP E-glass/epoxy panel with 70kg/m^3 core density impacted at 45J (SG-16-16-CP-45J)

APPENDIX D

Mean and curvature strain responses from all tested pre-conditioned panels

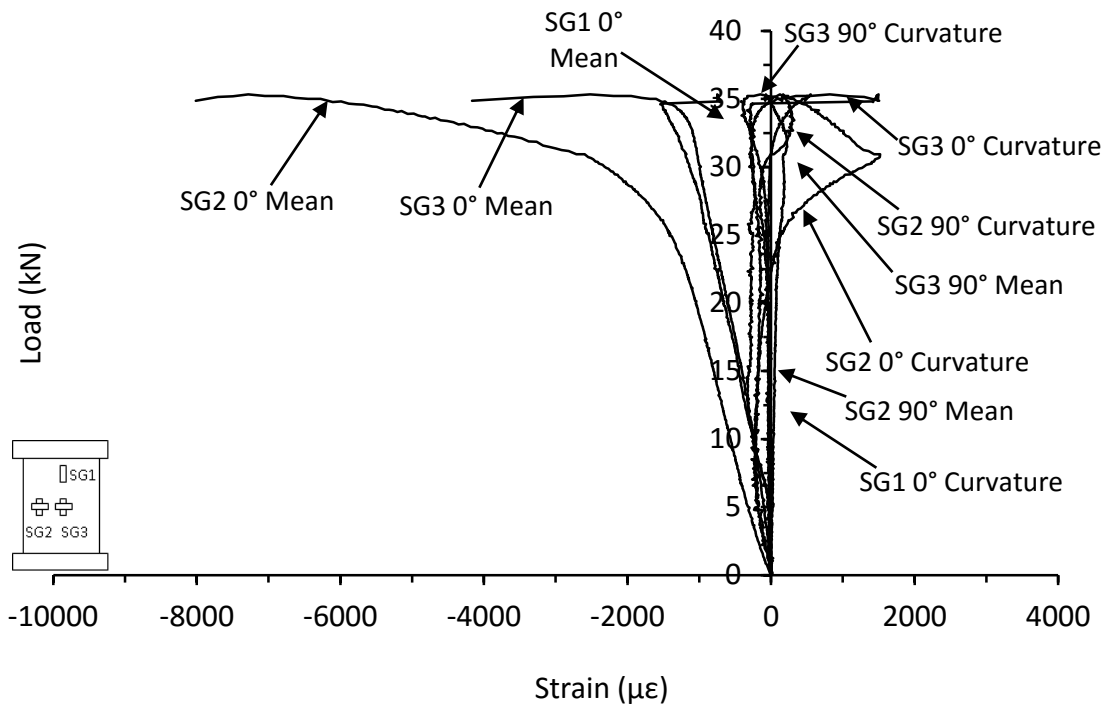


Figure D.1. Mean and curvature strain responses from thin symmetrical CP carbon/epoxy panel with 70kg/m³ core density with 40mm of core removed (CI-8-8-CP-CR-1)

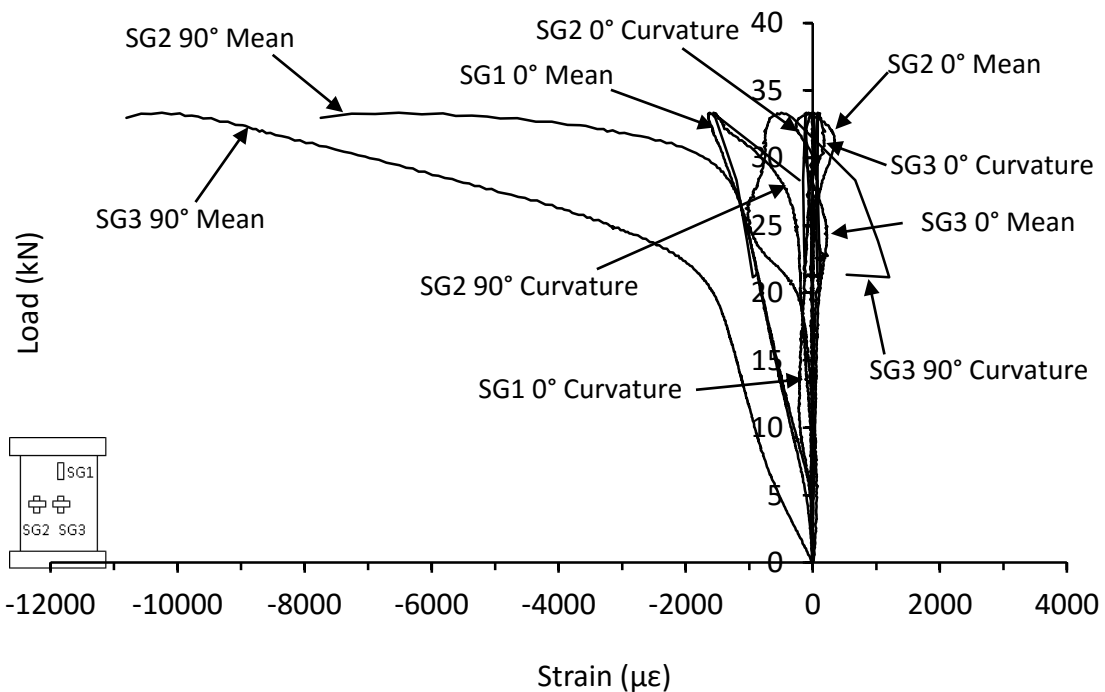


Figure D.2. Mean and curvature strain responses from thin symmetrical CP carbon/epoxy panel with 70kg/m³ core density with 40mm of core removed (CI-8-8-CP-CR-2)

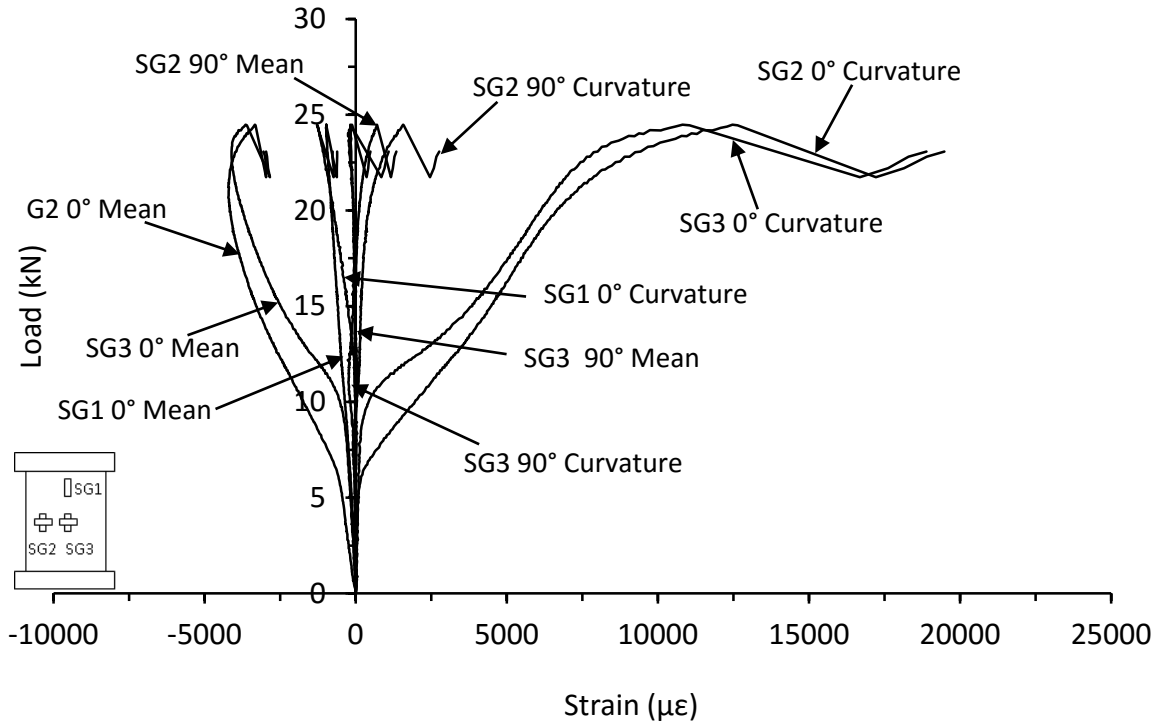


Figure D.3. Mean and curvature strain responses from thin unsymmetrical CP carbon/epoxy panel with 70kg/m^3 core density with 40mm of core removed (NC-8-6-CP-CR-A)

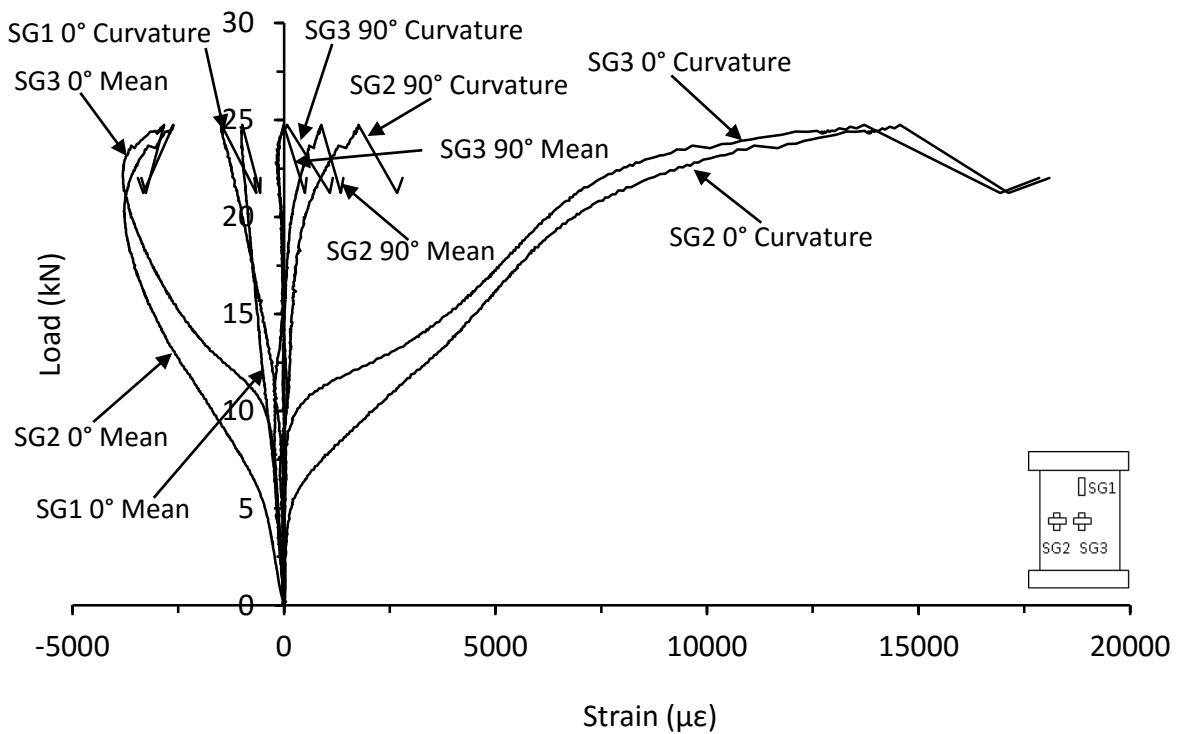


Figure D.4. Mean and curvature strain responses from thin unsymmetrical CP carbon/epoxy panel with 70kg/m^3 core density with 40mm of core removed (NC-8-6-CP-CR-B)

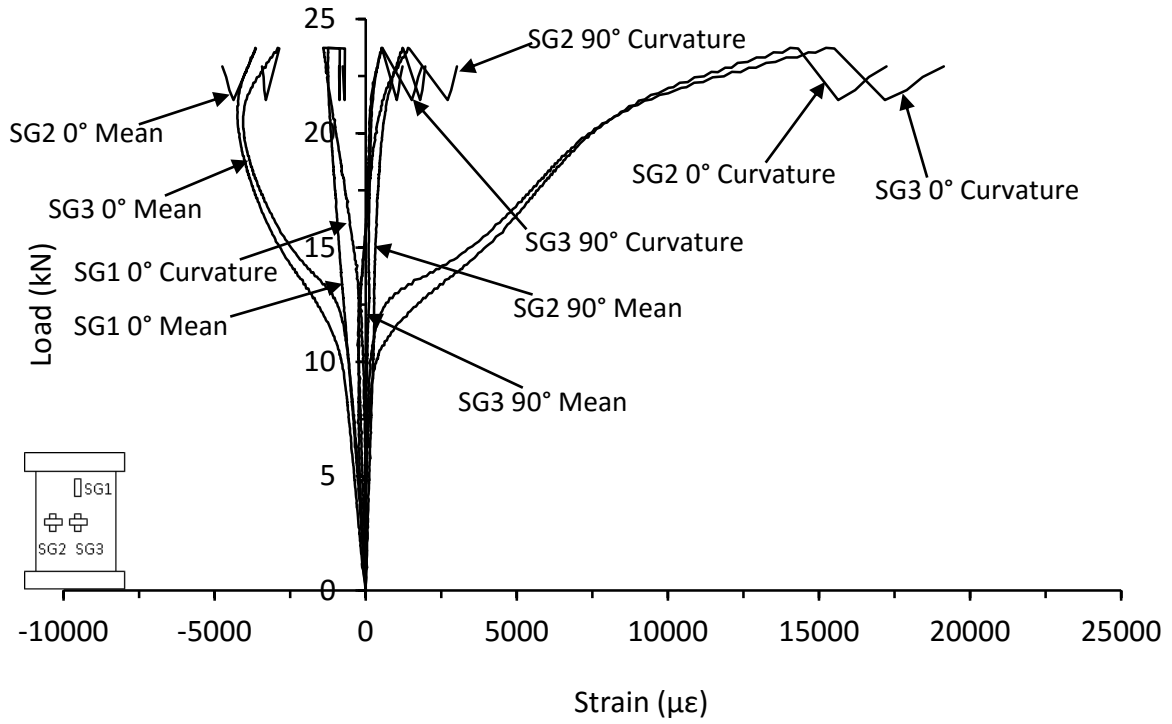


Figure D.5. Mean and curvature strain responses from thin unsymmetrical QI carbon/epoxy panel with 70kg/m^3 core density with 40mm of core removed (LB-8-6-QI-CR-A)

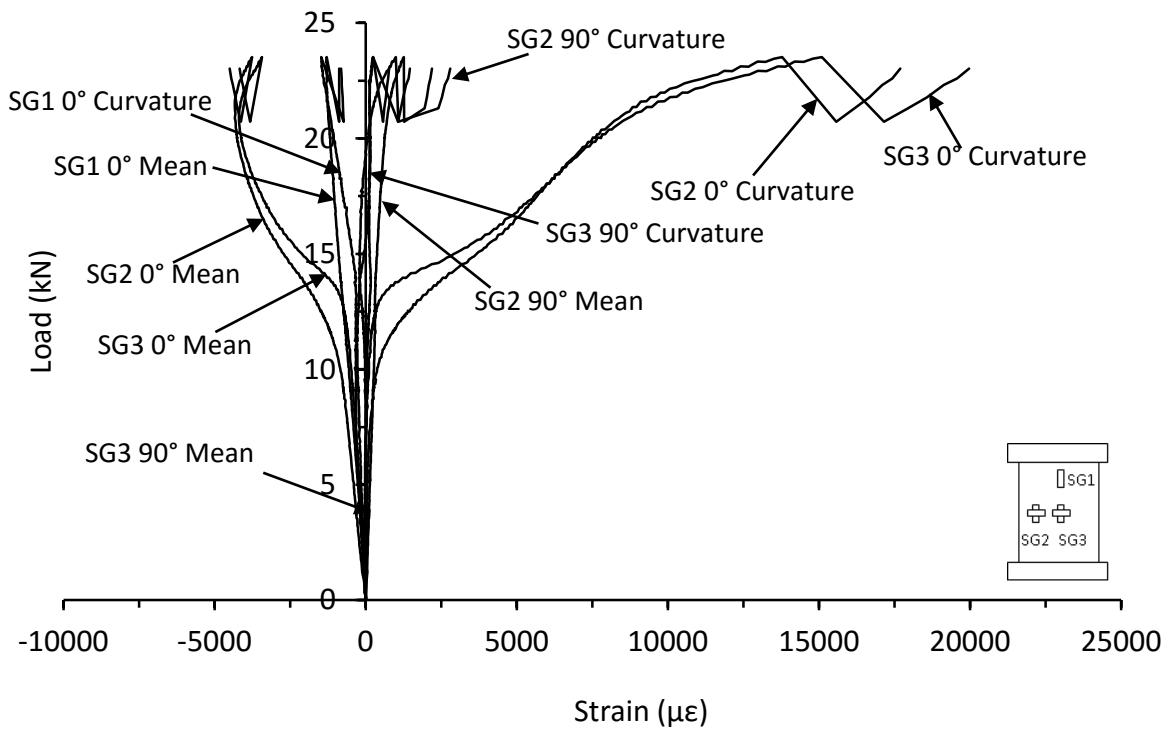


Figure D.6. Mean and curvature strain responses from thin unsymmetrical QI carbon/epoxy panel with 70kg/m^3 core density with 40mm of core removed (LB-8-6-QI-CR-B)

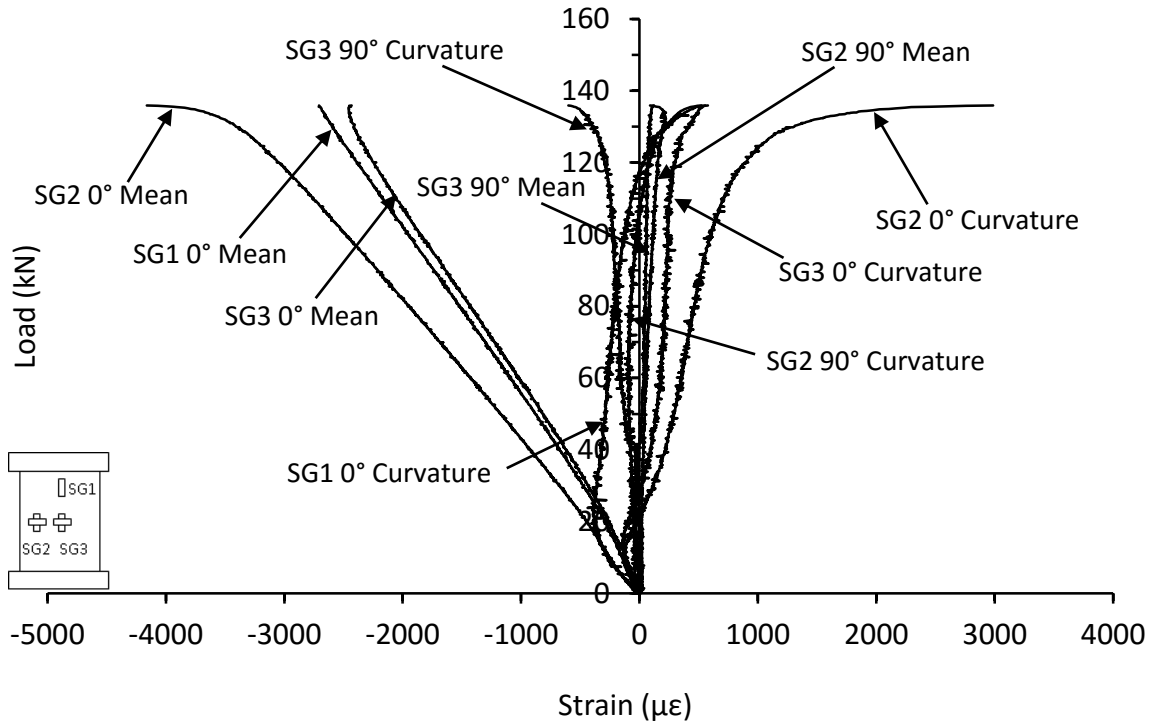


Figure D.7. Mean and curvature strain responses from thick symmetrical CP carbon/epoxy panel with 70kg/m³ core density with 40mm of core removed (CI-16-16-CP-CR-1)

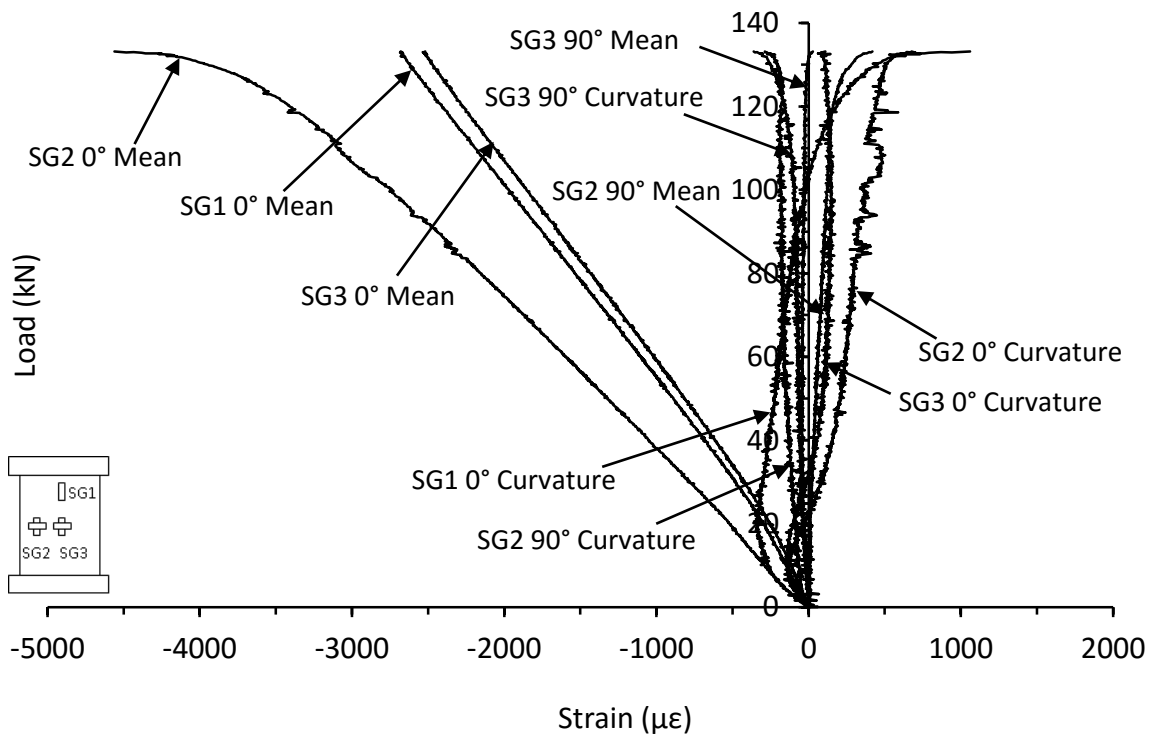


Figure D.8. Mean and curvature strain responses from thick symmetrical CP carbon/epoxy panel with 70kg/m³ core density with 40mm of core removed (CI-16-16-CP-CR-2)

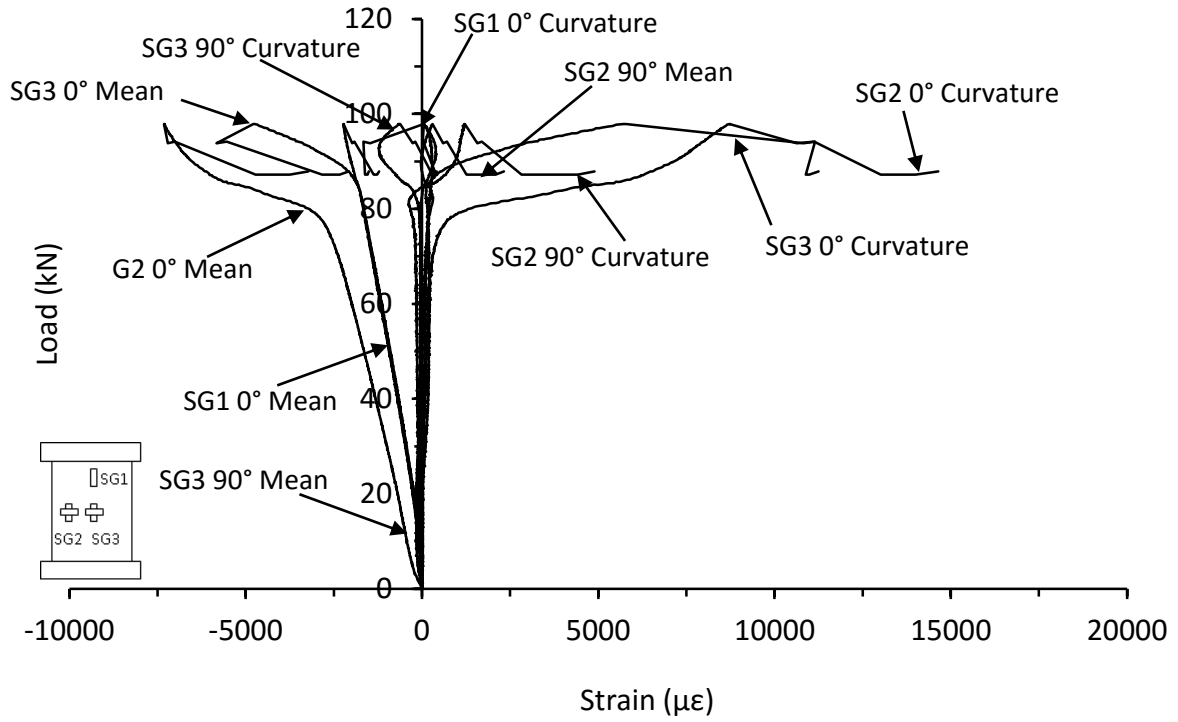


Figure D.9. Mean and curvature strain responses from thick unsymmetrical CP carbon/epoxy panel with 70kg/m³ core density with 40mm of core removed (NC-16-12-CP-CR-A)

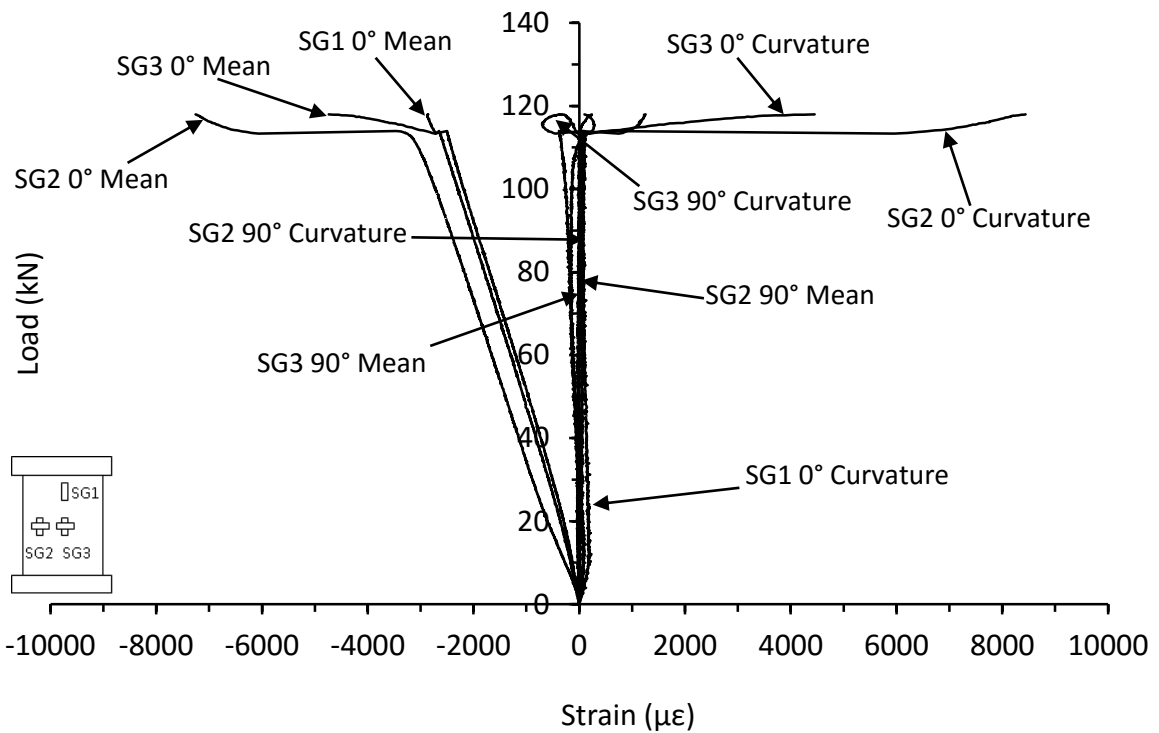


Figure D.10. Mean and curvature strain responses from thick unsymmetrical CP carbon/epoxy panel with 70kg/m³ core density with 40mm of core removed (NC-16-12-CP-CR-B)

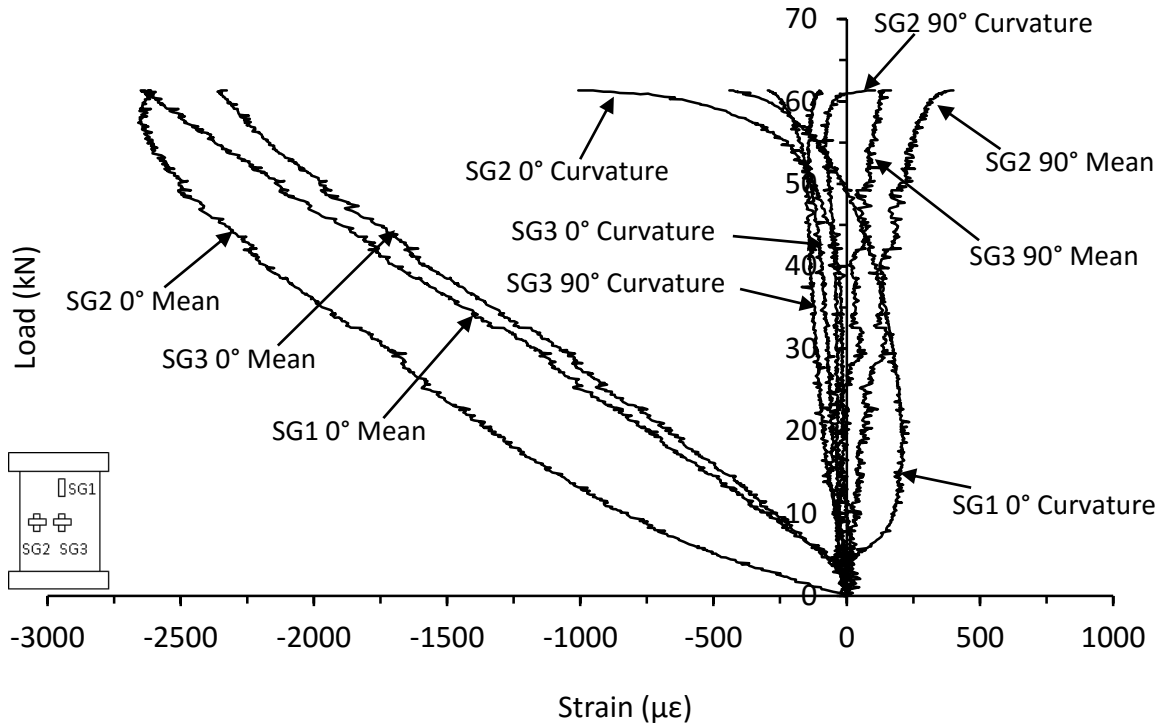


Figure D.11. Mean and curvature strain responses from thin symmetrical CP carbon/epoxy panel with 70kg/m^3 core density with 20mm of core removed (HD-8-8-CP-CR-A)

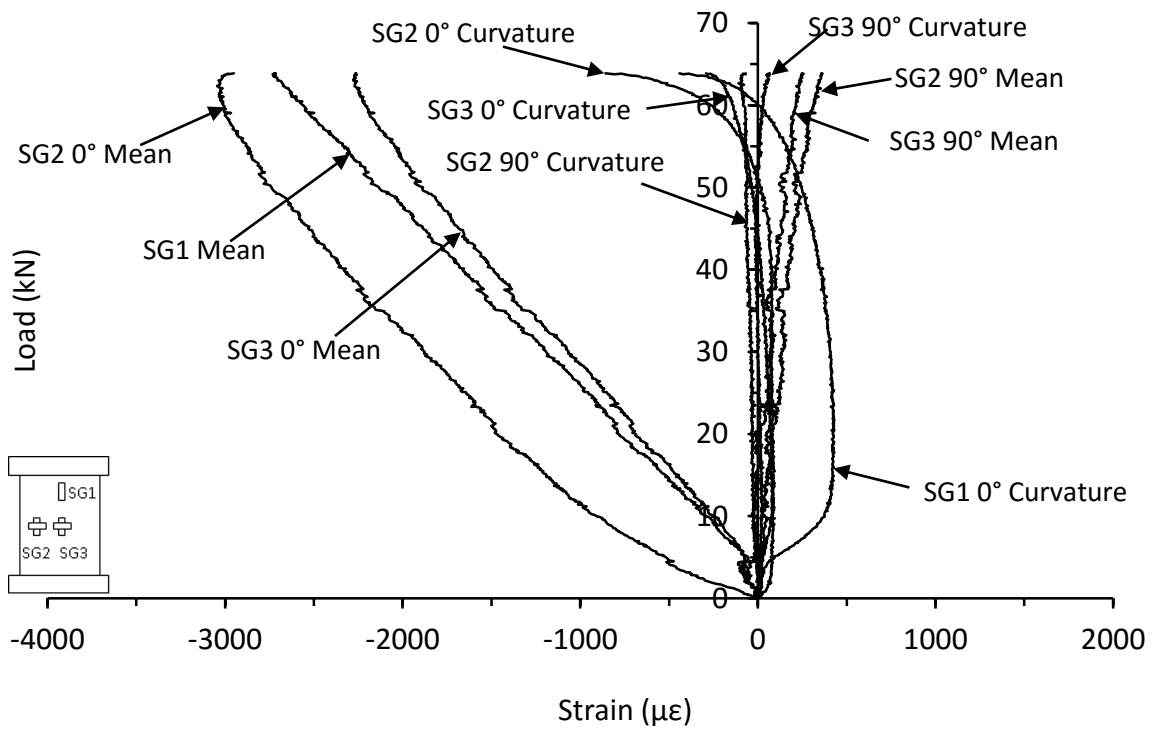


Figure D.12. Mean and curvature strain responses from thin symmetrical CP carbon/epoxy panel with 70kg/m^3 core density with 20mm of core removed (HD-8-8-CP-CR-B)

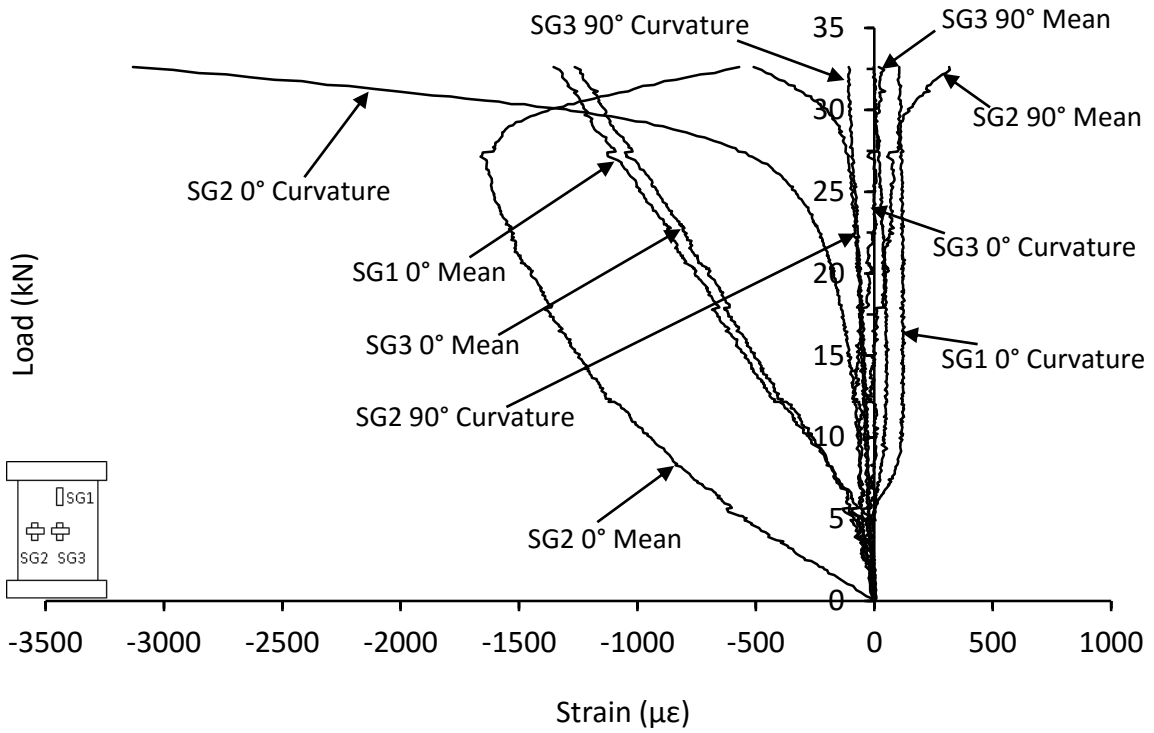


Figure D.13. Mean and curvature strain responses from thin unsymmetrical CP carbon/epoxy panel with 70kg/m^3 core density with 20mm of core removed (HD-8-6-CP-CR-A)

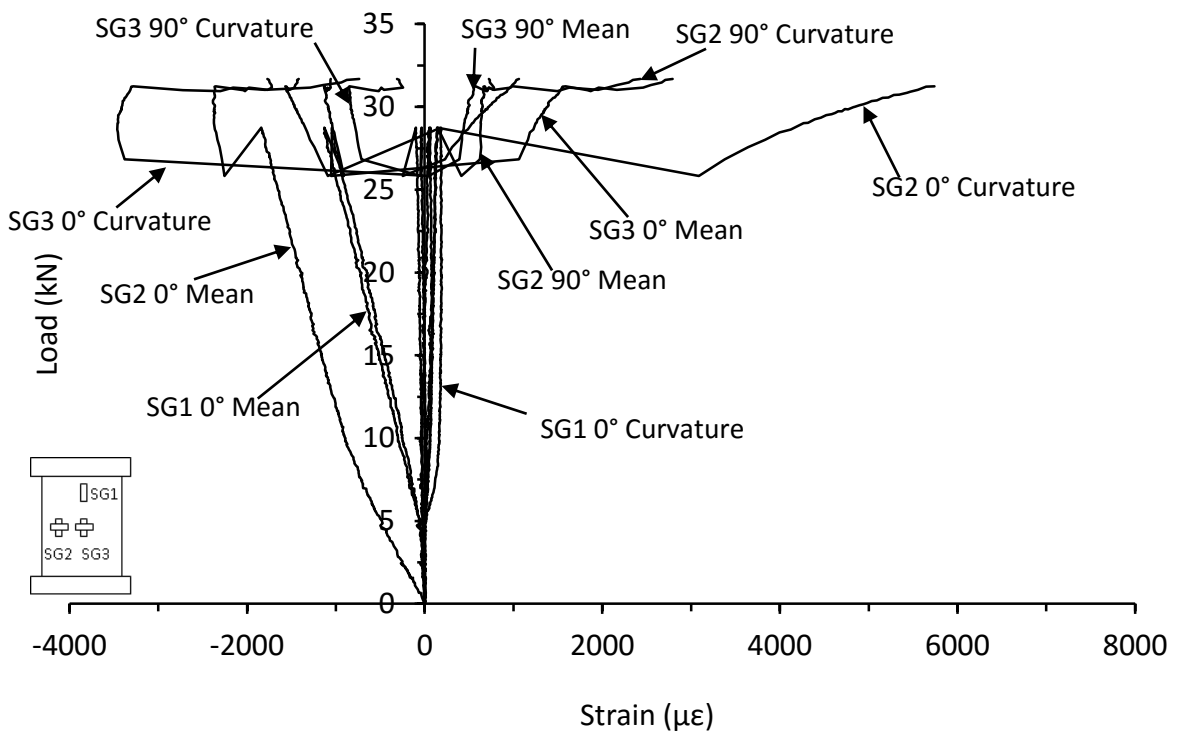


Figure D.14. Mean and curvature strain responses from thin unsymmetrical CP carbon/epoxy panel with 70kg/m^3 core density with 20mm of core removed (HD-8-6-CP-CR-B)

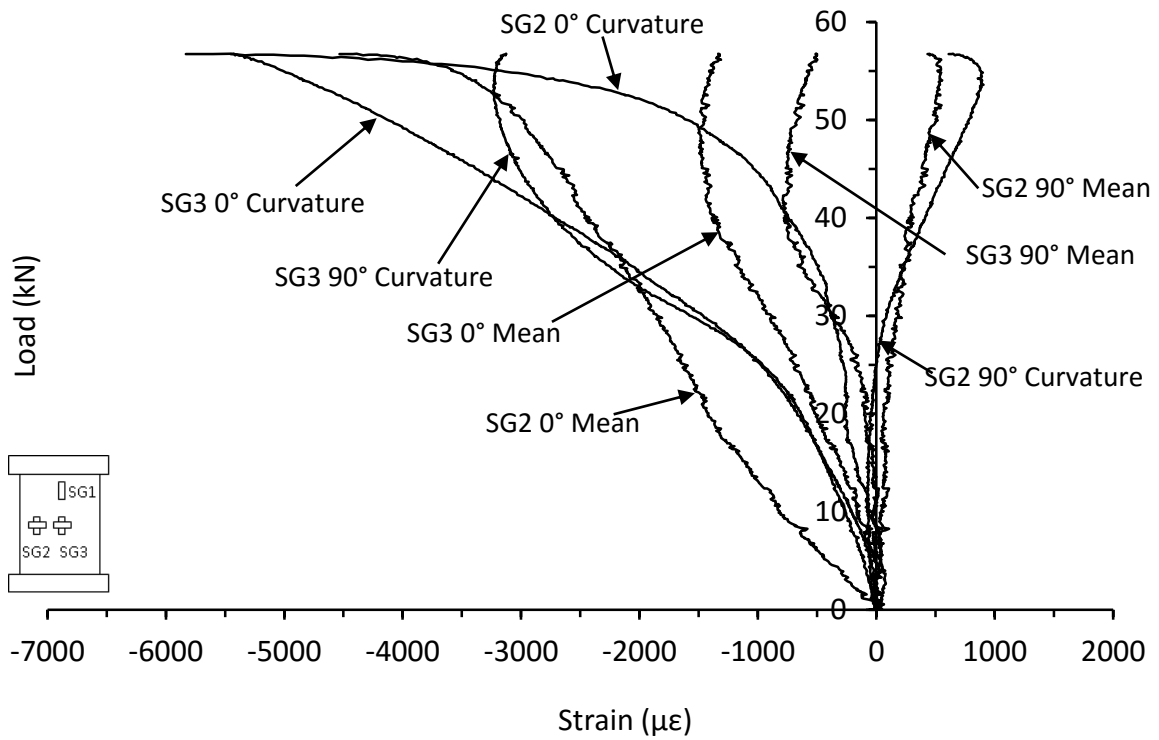


Figure D.15. Mean and curvature strain responses from thin symmetrical CP carbon/epoxy panel with 70kg/m^3 core density with 20mm of core removed impacted at 10J (HD-8-8-CP-ICR-10J)

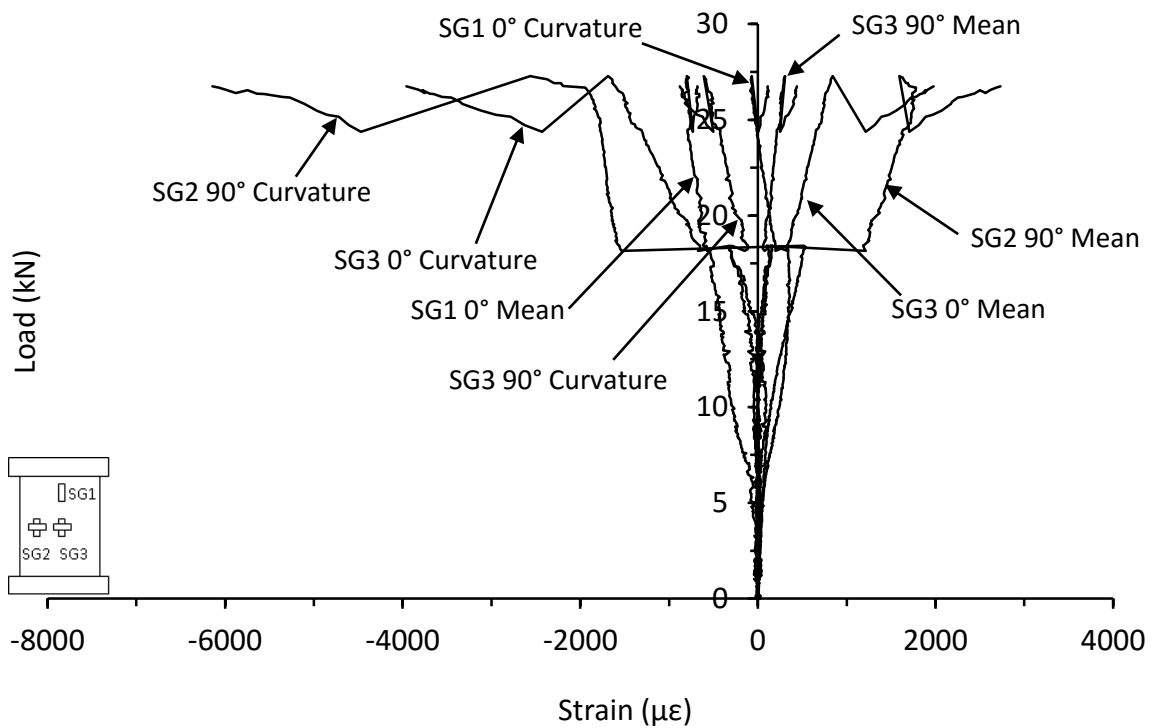


Figure D.16. Mean and curvature strain responses from thin symmetrical CP carbon/epoxy panel with 70kg/m^3 core density with 20mm of core removed impacted at 20J (HD-8-8-CP-ICR-20J)

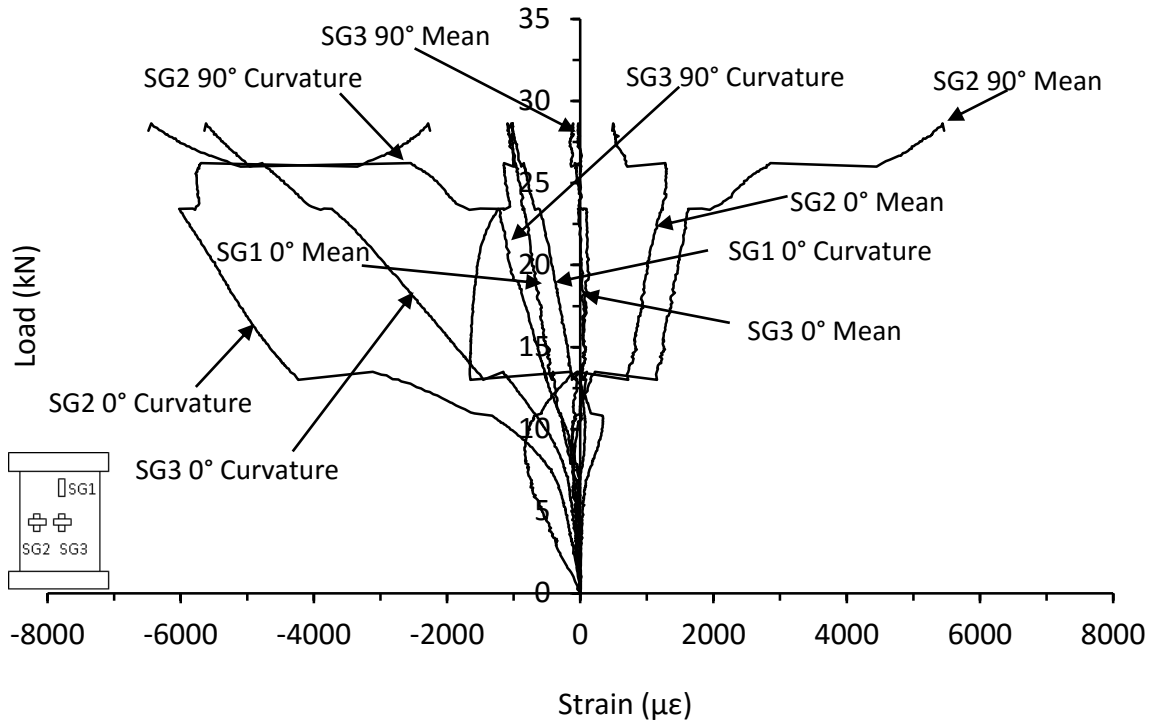


Figure D.17. Mean and curvature strain responses from thin unsymmetrical CP carbon/epoxy panel with 70kg/m^3 core density with 20mm of core removed impacted at 10J (HD-8-6-CP-ICR-10J)

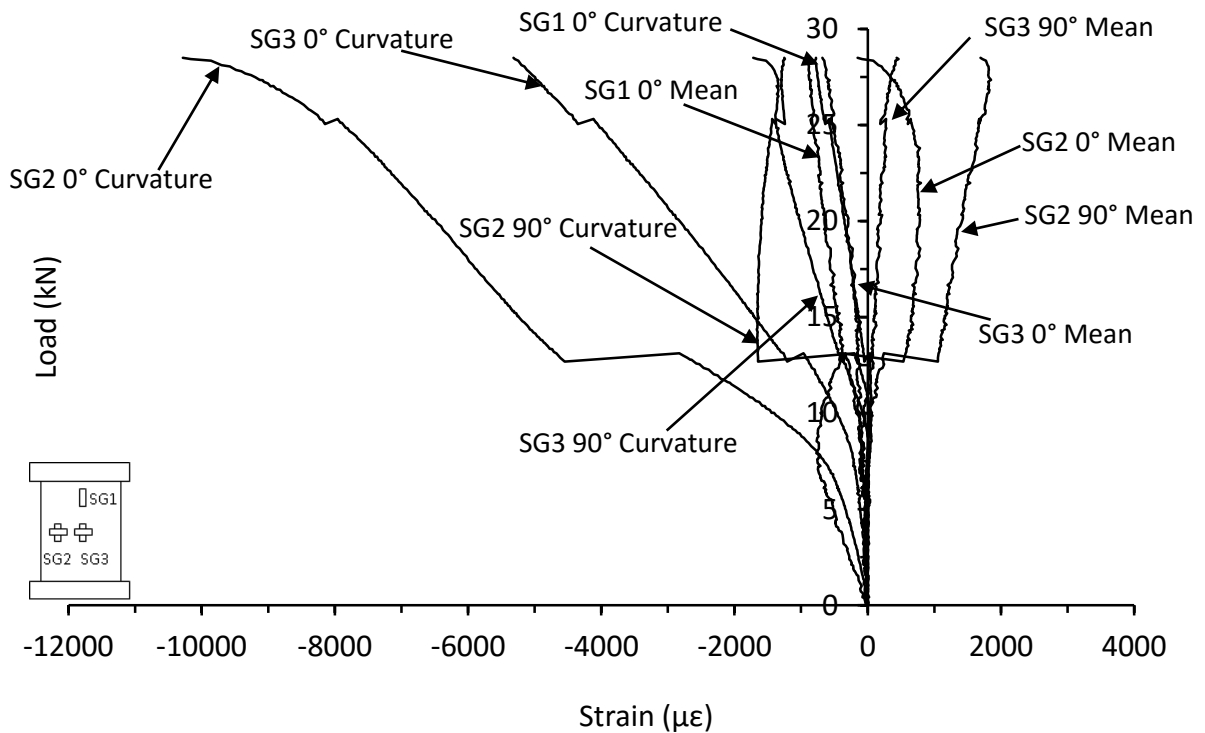


Figure D.18. Mean and curvature strain responses from thin unsymmetrical CP carbon/epoxy panel with 70kg/m^3 core density with 20mm of core removed impacted at 20J (HD-8-6-CP-ICR-20J)

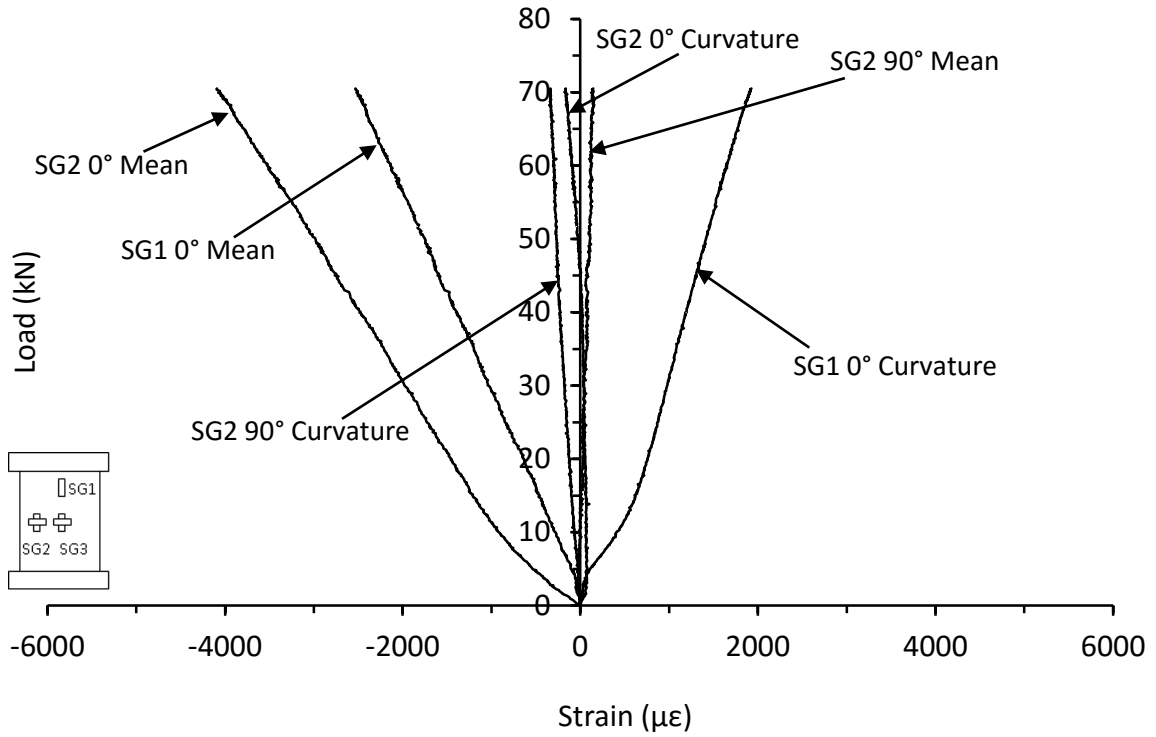


Figure D.19. Mean and curvature strain responses from thin symmetrical CP carbon/epoxy panel with 70kg/m^3 core density with 40mm hole drilled in the top skin (HD-8-8-CP-1H-A)

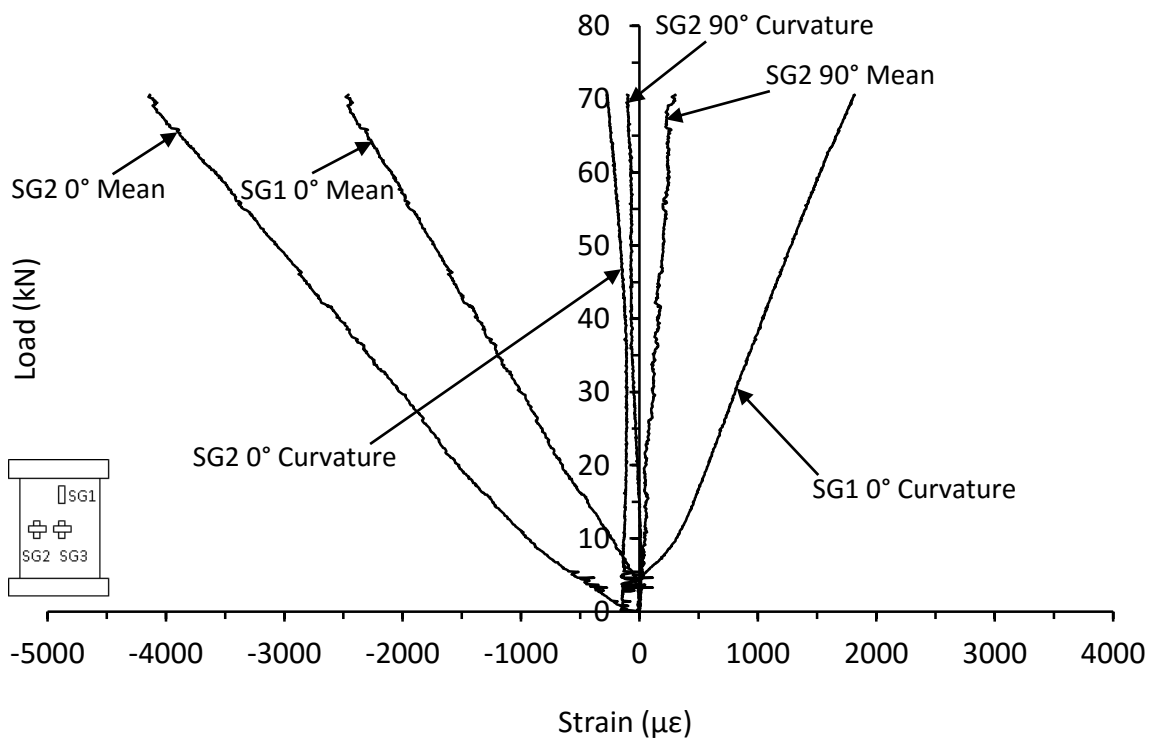


Figure D.20. Mean and curvature strain responses from thin symmetrical CP carbon/epoxy panel with 70kg/m^3 core density with 40mm hole drilled in the top skin (HD-8-8-CP-1H-B)

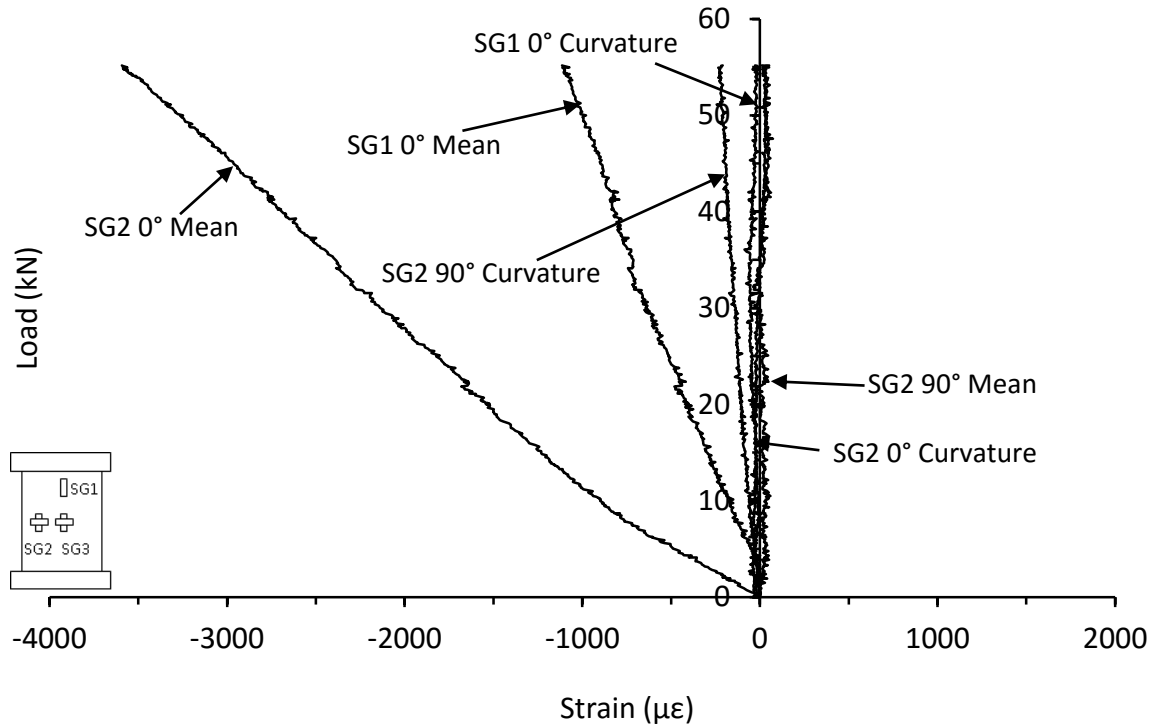


Figure D.21. Mean and curvature strain responses from thin symmetrical CP carbon/epoxy panel with 70kg/m³ core density with 40mm hole drilled in both skins (HD-8-8-CP-2H-A)

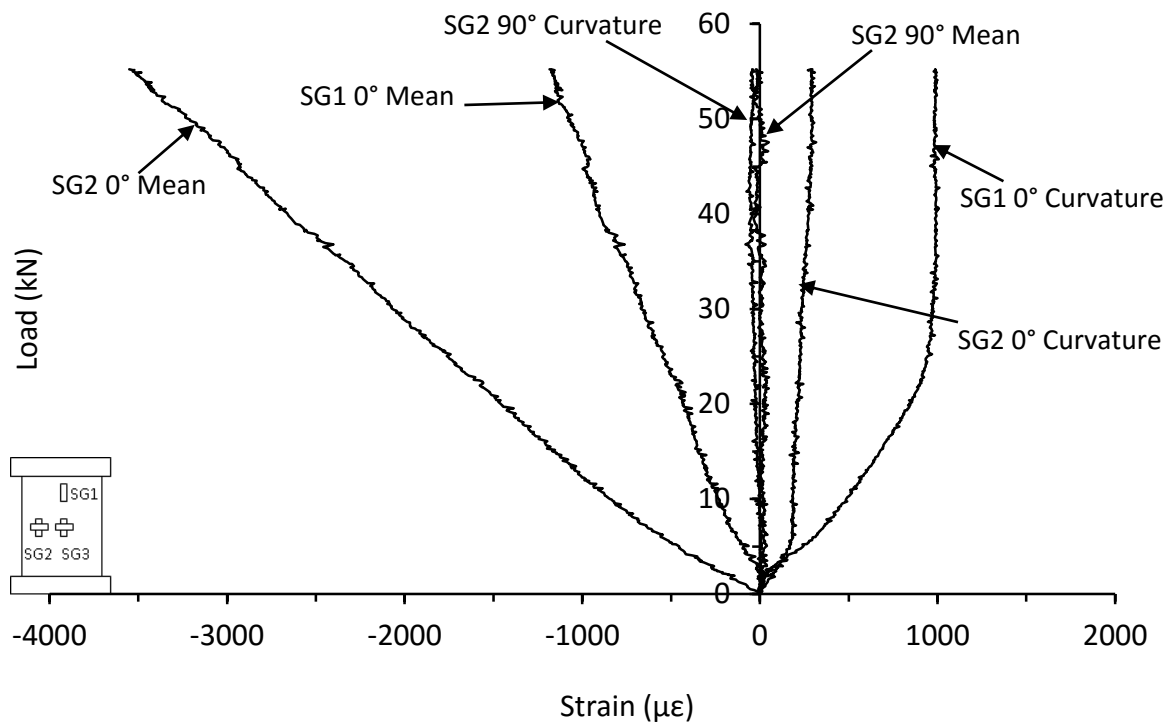


Figure D.22. Mean and curvature strain responses from thin symmetrical CP carbon/epoxy panel with 70kg/m³ core density with 40mm hole drilled in both skins (HD-8-8-CP-2H-B)

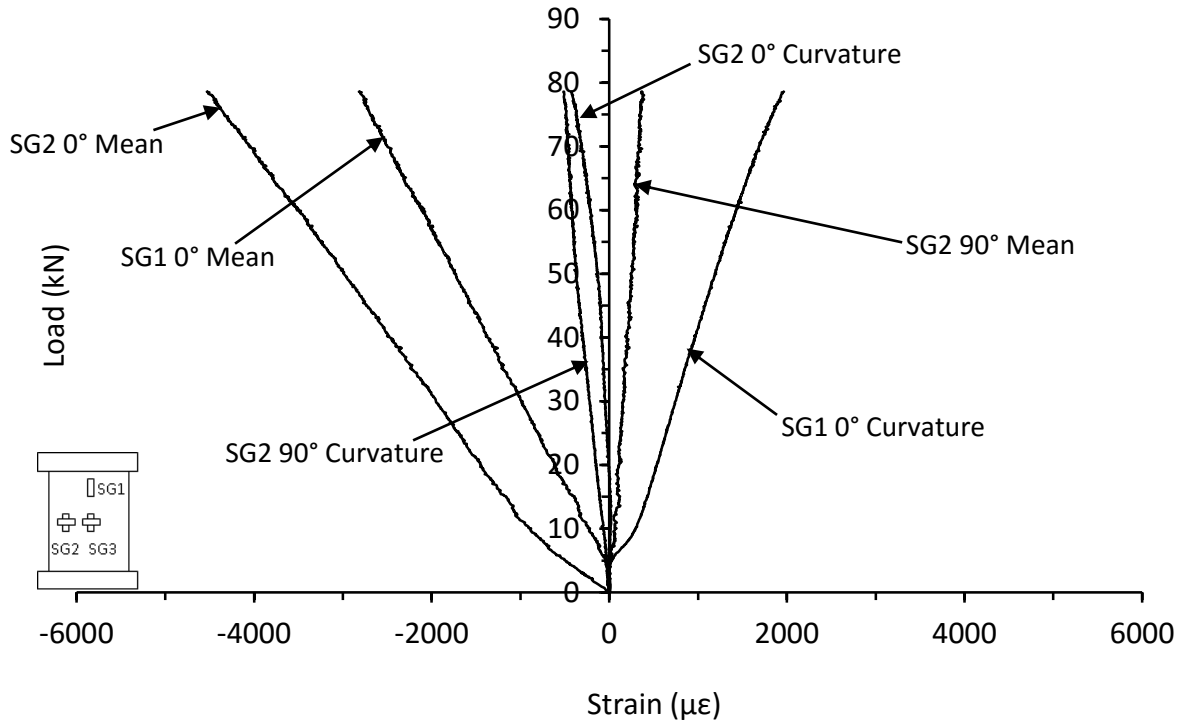


Figure D.23. Mean and curvature strain responses from thin unsymmetrical CP carbon/epoxy panel with 70kg/m³ core density with 40mm hole drilled in the top skin (HD-8-6-CP-1H-A)

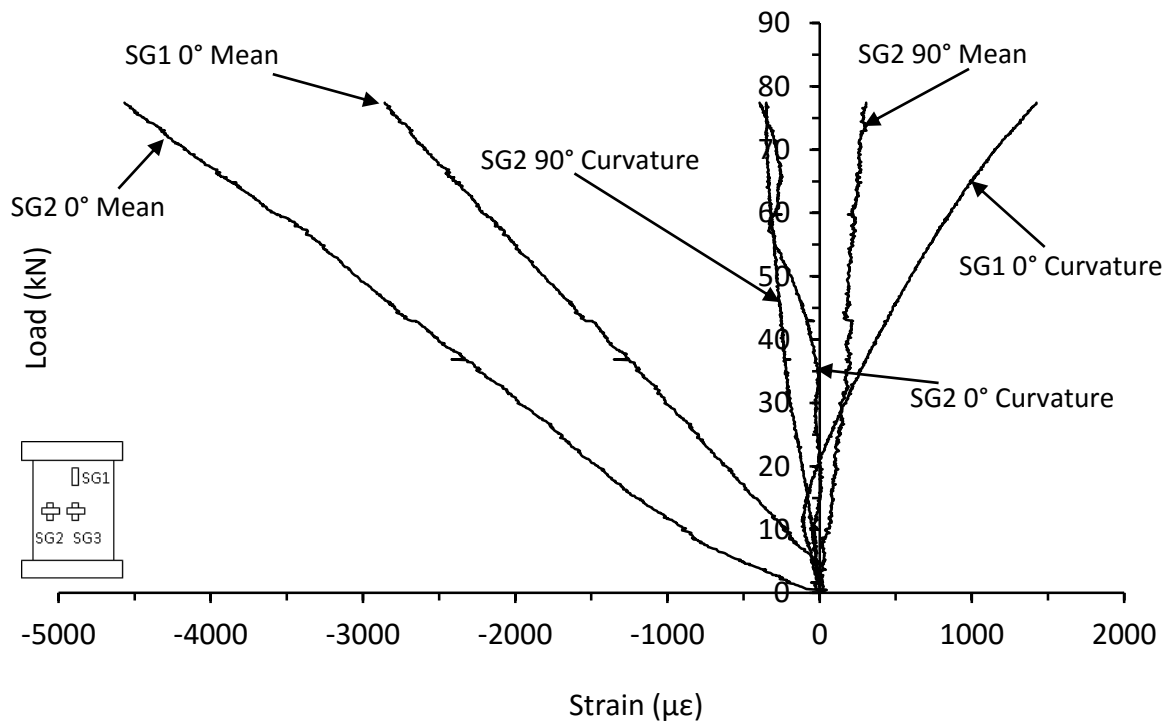


Figure D.24. Mean and curvature strain responses from thin unsymmetrical CP carbon/epoxy panel with 70kg/m³ core density with 40mm hole drilled in the top skin (HD-8-6-CP-1H-B)

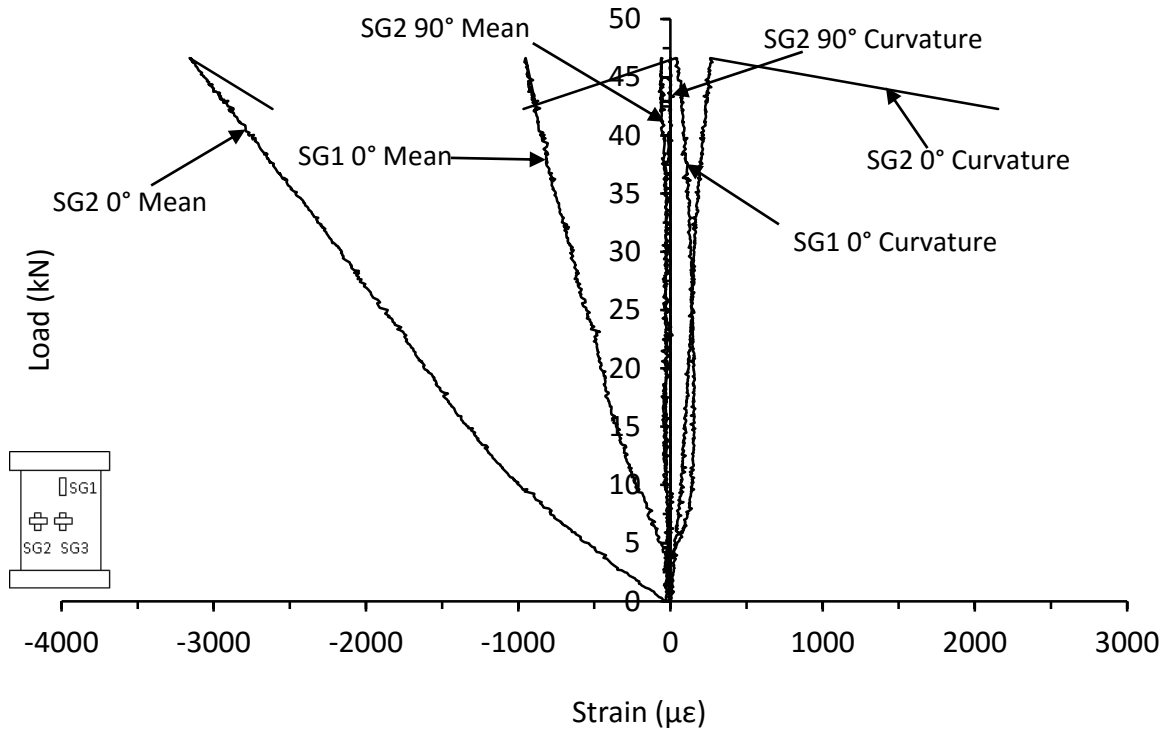


Figure D.25. Mean and curvature strain responses from thin unsymmetrical CP carbon/epoxy panel with 70kg/m³ core density with 40mm hole drilled in both skins (HD-8-6-CP-2H-A)

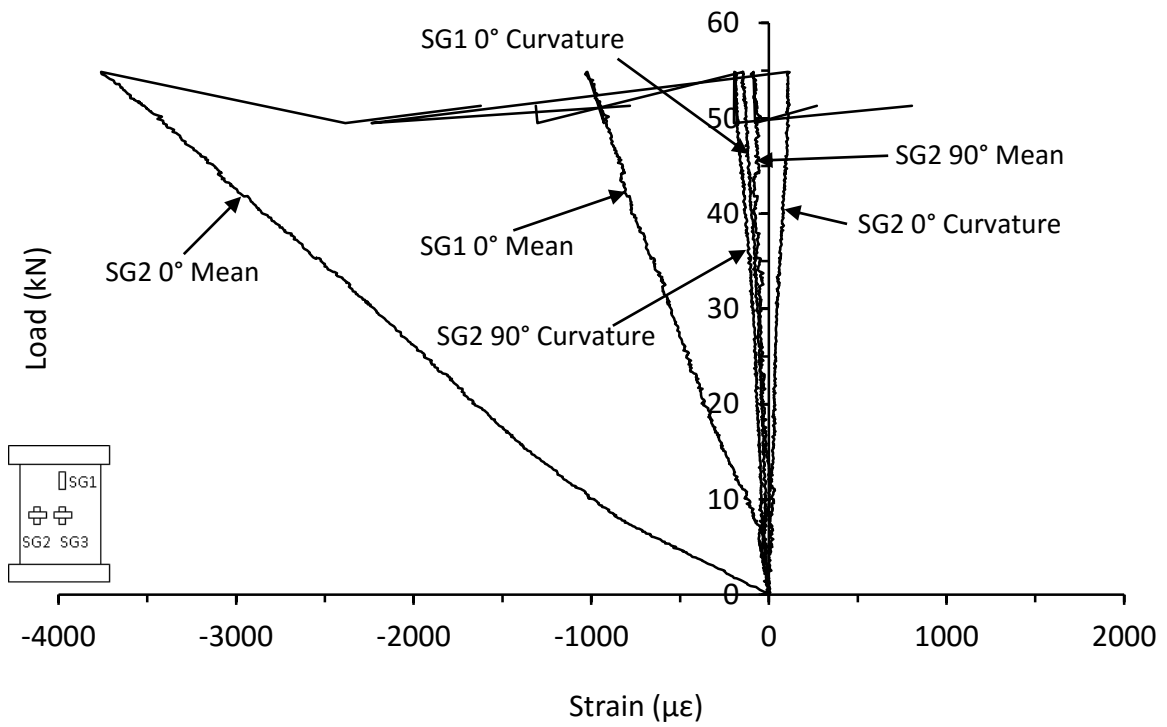


Figure D.26. Mean and curvature strain responses from thin unsymmetrical CP carbon/epoxy panel with 70kg/m³ core density with 40mm hole drilled in both skins (HD-8-6-CP-2H-B)P